

---

# Proceedings of the High Energy Density Matter (HEDM) Contractors' Conference held 5-7 June 1994 in Crystal Bay NV

T.L. Thompson, editor  
S.L. Rodgers, editor

December 1994

Special Report

---

APPROVED FOR PUBLIC RELEASE; DISTRIBUTION UNLIMITED.

---

19950223 127



**PHILLIPS LABORATORY**  
**Propulsion Directorate**  
**AIR FORCE MATERIEL COMMAND**  
**EDWARDS AIR FORCE BASE CA 93524-7048**

---

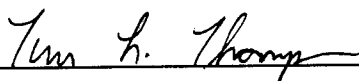
## NOTICE

When U.S. Government drawings, specifications, or other data are used for any purpose other than a definitely related Government procurement operation, the fact that the Government may have formulated, furnished, or in any way supplied the said drawings, specifications, or other data, is not to be regarded by implication or otherwise, or in any way licensing the holder or any other person or corporation, or conveying any rights or permission to manufacture, use or sell any patented invention that may be related thereto.

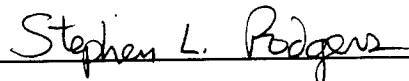
## FOREWORD

This Conference Proceedings was compiled and edited by Capt Tim Thompson and Dr. Stephen L. Rodgers, OLAC Phillips Laboratory, Edwards AFB CA.

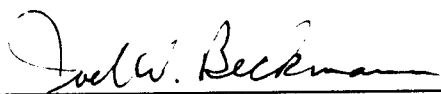
This report has been reviewed and is approved for release and distribution in accordance with the distribution statement on the cover and on the SF Form 298.



TIM L. THOMPSON, Capt, USAF  
Editor



STEPHEN L. RODGERS  
Editor



JOEL W. BECKMANN  
Acting Director  
Fundamental Technologies Division



ROBERT C. CORLEY  
Chief Scientist (Propulsion)

Accession For	
NTIS GRA&I	<input checked="" type="checkbox"/>
DTIC TAB	<input type="checkbox"/>
Unannounced	<input type="checkbox"/>
Justification	
By _____	
Distribution/Availability Codes	
Dist	Avail and/or Special
A-1	

REPORT DOCUMENTATION PAGE			Form Approved OMB No 0704-0188	
Public reporting burden for this collection of information is estimated to average 1 hour per response, including the time for reviewing instructions searching existing data sources gathering and maintaining the data needed, and completing and reviewing the collection of information. Send comments regarding this burden estimate or any other aspect of this collection of information, including suggestions for reducing this burden to Washington Headquarters Services, Directorate for Information Operations and Reports, 1215 Jefferson Davis Highway, Suite 1204, Arlington, VA 22202-4302, and to the Office of Management and Budget, Paperwork Reduction Project (0740-0188), Washington DC 20503.				
1. AGENCY USE ONLY (LEAVE BLANK)		2. REPORT DATE December 1994	3. REPORT TYPE AND DATES COVERED Special Report 9 Jun 93 - 7 Jun 94	
4. TITLE AND SUBTITLE Proceedings of the High Energy Density Matter (HEDM) Contractor's Conference held 5-7 June 1994 in Crystal Bay NV			5. FUNDING NUMBERS C: PE: 62302F PR: 3058 TA: 00N2	
6. AUTHOR(S) Tim L. Thompson and Stephen L. Rodgers, editors				
7. PERFORMING ORGANIZATION NAME(S) AND ADDRESS(ES) Phillips Laboratory OLAC PL/RKFE 10 East Saturn Blvd. Edwards AFB CA 93524-7680			8. PERFORMING ORGANIZATION REPORT NUMBER	
9. SPONSORING/MONITORING AGENCY NAME(S) AND ADDRESS(ES)			10. SPONSORING/MONITORING AGENCY REPORT NUMBER  PL-TR-94-3036	
11. SUPPLEMENTARY NOTES Extended abstracts from the Eighth High Energy Density Matter Contractor's Conference  COSATI CODE(S): 2005; 2109				
12a. DISTRIBUTION/AVAILABILITY STATEMENT  APPROVED FOR PUBLIC RELEASE DISTRIBUTION IS UNLIMITED			12b. DISTRIBUTION CODE  A	
13. ABSTRACT (MAXIMUM 200 WORDS)  This report documents the information presented at the eighth annual High Energy Density Matter (HEDM) Contractors' Conference held 5-7 June 1994 in Crystal Bay NV. This report contains the extended abstracts of the oral, workshop, and poster presentations given by the Air Force funded contractors and by the in-house researchers from the Phillips Laboratory.  <b>DTIC QUALITY INSPECTED 4</b>				
14. SUBJECT TERMS HEDM, High Energy Density Matter, propellant, solid hydrogen, cryogenic materials, potential energy surfaces.			15. NUMBER OF PAGES	
			16. PRICE CODE	
17. SECURITY CLASSIFICATION OF REPORT Unclassified	18. SECURITY CLASSIFICATION OF THIS PAGE Unclassified	19. SECURITY CLASSIFICATION OF ABSTRACT Unclassified	20. LIMITATION OF ABSTRACT SAR	

## Table of Contents

<b>Introduction</b> .....	1
<b>Conference Agenda</b> .....	2
<b>List of Poster Presentations</b> .....	7
<b>List of Attendees</b> .....	9
 <b><u>Extended Abstracts from Technical Sessions</u></b>	
“New Developments in Theory and their Role in Studying High Energy Density Matter;” R. Bartlett, University of Florida .....	20
“Potential Energy Surfaces for High Energy Species;” M. Gordon, K. Nguyen, N. Matsunaga, G. Chaban; Iowa State University and J. Boatz; Phillips Laboratory .....	31
“Theoretical Studies of Nonadiabatic Processes Relevant to the Stability and Detection of Energetic Species;” D. Yarkony; John Hopkins University .....	39
“Laser and Fourier Transform Spectroscopy of Novel Propellant Molecules;” P. Bernath; University of Waterloo .....	46
“Cubane and Derivatives as Combustion Modifiers. Synthetic Results;” R. Moriarty and M. Rao; University of Illinois .....	53
“Novel High Energy Compounds;” K. Christe, W. Wilson; Rocketdyne.....	54
“Progress Towards the Synthesis of Polymeric Nitrogen;” H. Lorenzana, A. McMahan, C. Yoo, and T. Barbee; Lawrence Livermore National Laboratory .....	59
“Progress on Atom Doped Cryogenic Solid Propellants;” M. Fajardo, S. Tam, J. Boatz, M. Cordonnier, and T. Thompson; Phillips Laboratory .....	64
“Quantum Computer Simulations of the Structure and Dynamics of Impurities in Solid Hydrogen;” G. Voth; University of Pennsylvania .....	66

“Mobilities and Reaction Dynamics of Atoms in Cryogenic Solids;” .....	71
E. Ryan, D. LaBrake and E. Weitz; Northwestern University	
“Ultrahigh Resolution Spectroscopy of the $Q_1(0)$ Transitions Induced .....	77
by Laser Radiation Field, External Electric Field, Impurity Quadrupole Field, and $\gamma$ -Ray Radiolysis;” T. Oka; University of Chicago	
“Diffusion in Crystalline and Amorphous Solid Hydrogen;” J. Gaines, .....	91
University of Hawaii; G. Collins, P. Souers, and J. Sater, Lawrence Livermore National Laboratory; and P. Fedders, Washington University	
“Solid Hydrogen Structure;” G. Collins, E. Mapoles, F. Magnotta and .....	99
T. Bernat; Lawrence Livermore National Lab	
“Triple Point of the BSP-DA-HCP Insulating Phase in Megabar Pressure .....	100
Deuterium;” I. Silvera; Harvard University	
“Spectroscopy of Alkali Atoms and Molecules Attached to Highly .....	102
Quantum Clusters;” F. Stienkemeier, W. Ernst, J. Higgins and G. Scoles; Princeton University	
“Novel Phenomena Involving Contact Between Alkali Atoms and Helium .....	109
or Hydrogen;” M. Cole and W. Ernst; Pennsylvania State University	
“Characterization of van der Waals Complexes Involving B and Al Atoms.....	112
Through Laser Fluorescence Excitation Spectroscopy;” P. Dagdigian and E. Hwang; John Hopkins University	
“Weakly Bound Complexes Involving Atomic Boron;” M. Alexander, .....	117
University of Maryland	
“Time Resolved Dynamics in Molecular Cluster Ions;” C. Lineberger, .....	121
S. Leone, R. Parson and S. Oneil; University of Colorado	
“The Newly Synthesized Tetranitrogen Monoxide Molecule: Why is the .....	122
Observed Form Higher in Energy than the Unobserved Cyclic Structure?” J. Galbraith and F. Schaefer; University of Georgia	
“Magnetic Circular Dichroism Spectroscopy of Metal/Rare Gas and .....	123
Metal/Hydrogen Systems;” J. Kenney; Eastern New Mexico University	
“Demonstration of a High Gain Visible Wavelength Chemical Laser .....	135
Based on Energy Transfer from Metastable $NF(a^1\Delta)$ to Boron Hydride;” D. Bernard and E. Boehmer; Rockwell International Science Center	

“Irvine University Research Initiative on Advanced Cryogenic Propellants;” V. Apkarian, R. Gerber, K. Janda, J. Rutledge, and P. Taborek; University of California at Irvine	138
“Current Experiments on the Combustion of Cryogenic Solid Propellants;” P. Carrick, Phillips Laboratory	150
“Structure, Thermochemistry and Performance of Advanced Propellants;” H. Michels, J. Montgomery, D. Tzeng and E. Lee; United Technologies	154
“A Survey of Rocket Propulsion Systems;” E.J. Wucherer, Hughes STX	172

### **Extended Abstracts from Poster Session**

“Production and Decay of Diazidoborane (DAB) and Tetra-azidodiborane (TADB);” E. Boehmer, Rockwell Science Center	176
“Characterization of Quadricyclane;” E.J. Wucherer, Hughes STX	179
“Thermoluminescence Studies of Atomic Species in Cryogenic Solid Matrices;” T.L. Thompson, M.E. Cordonnier, M.E. Fajardo, Phillips Laboratory	183
“Collision Dynamics of Small Molecular Hydrogen and Deuterium Clusters with Light Atoms;” Zhiming Li, R. Benny Gerber; University of California, Irvine	185
“Molecular Impurities in Quantum Clusters;” Michele McMahon, K. Birgitta Whaley; University of California, Berkeley	193
“Dynamics of Processes in Doped Hydrogen Clusters;” R.B. Gerber, Z. Li, S. Broude, A.B. McCoy; University of California, Irvine	201
“Fourier Transform Vibrational Spectroscopy of Novel $\text{Li}_x\text{B}_y$ Propellant Additive Clusters in Solid Argon;” J.D. Presilla-Marquez, P.G. Carrick; Phillips Laboratory	216
“Theoretical Studies of the Molecular and Electronic Structure of $\text{Li}_2\text{B}_2$ ;” Jerry Boatz, Phillips Laboratory	217
“Prediction of Triplet Absorption Lineshape for NA Atoms in Liquid Ar;” Mario Fajardo, Jerry Boatz, Phillips Laboratory	228

“Theoretical Methods for Cryogenically Trapped Metal Radical Spectra;” .....	229
J. Boatz, M.E. Fajardo, Phillips Laboratory and P.W. Langhoff, Indiana University	
“Optical Spectroscopy and Photochemistry of Atoms in Solid Molecular .....	237
Hydrogen;” William Stwalley, John Bahns, University of Connecticut	
“Optical Absorption, Emission and Radiation Transfer in High- .....	238
Temperature Metal Vapors;” J.D. Mills, C.W. Larson, Phillips Laboratory, P.S. Erdman, W.S. Stwalley, University of Connecticut, and P.W. Langhoff, Indiana University	
“Emission Spectroscopy of B <sub>2</sub> and BH;” C.R. Brazier and P.G. Carrick, .....	245
Phillips Laboratory	
“Emission Spectra of the (1) <sup>1</sup> Σ <sub>u</sub> <sup>+</sup> - (1) <sup>1</sup> Σ <sub>g</sub> <sup>+</sup> Transition of B <sub>2</sub> ;” .....	252
Michelle Cordonnier, Patrick Carrick and Christopher Brazier, Phillips Laboratory	
“A Theoretical Study of B-N Analog of Prismane;” Nikita Matsunaga .....	259
and Mark Gordon, Iowa State University	
“Potential Energy Surfaces for High Energy Compounds Containing .....	268
Nitrogen;” Galina Chaban, Kiet Nguyen, and Mark Gordon, Iowa State University	
“Metal Clusters and Metal Complexes: Models for Metal-Seeded .....	275
Energetic Materials;” Michael Duncan, University of Georgia	
“Velocity Selected Laser Ablation Metal Atom Source;” Michel Macler .....	279
and Mario E. Fajardo, Phillips Laboratory	
“Laser Pyrolysis of Explosives;” Charles Wight, University Of Utah .....	286
“Strained Ring Hydrocarbon Pyrolysis;” Angelo Alfano, Phillips Laboratory .....	290
“Spectroscopy of Atom-Dihydrogen ver der Waals Complexes;” .....	295
J. Spotts, M. Johnson, G. Olsen, M. Okumura; California Institute of Technology	

## INTRODUCTION

The main purpose of the High Energy Density Matter (HEDM) program is to research and develop advanced high energy compounds containing increased energy densities (energy to mass ratios) to produce greater specific impulses (thrust per weight flow rate of propellant) which will enable spacecraft to carry larger payloads. With these advanced propellants, future space-bound payloads could be possibly four times greater than they are today. Theoretical and experimental research is carried out by in-house researchers at the Phillips Laboratory at Edwards Air Force Base and through Air Force funded contracts with numerous researchers in academic and industrial communities.

The HEDM program is administered by a steering group made up of representatives from the Propulsion Directorate of the Phillips Laboratory and the Air Force Office of Scientific Research (AFOSR). A technical panel administered by the National Research Council (NRC) assists the steering group in ensuring the high technical content of the program.

Annual conferences, alternatively hosted by the AFOSR and the Phillips Laboratory are arranged in order to allow in-house and contract researchers to report on their progress and new developments. The Eighth High Energy Density Matter Contractors' Conference was held 5-7 June 1994 in Crystal Bay, Nevada. This year's conference was held in conjunction with the AFOSR's Contractor's Conference in Propulsion and consisted of sessions on New HEDM Molecules, HEDM Synthesis, Cryogenic Solids, Metal Atoms and Clusters, Advanced Cryogenic Propellants, Solid Propellant Rocket Dynamics, Advanced Propellants and Propulsion Systems, and HEDM Program Overview. There was also a workshop session on Synthesis.

This report documents the information presented at this conference and contains extended abstracts of the poster and oral presentations given at the conference.

The next HEDM Contractors' Conference is scheduled for 4 - 6 June 95 at Woods Hole, MA.



# HIGH ENERGY DENSITY MATTER CONTRACTORS CONFERENCE

Cal-Neva Lodge

Crystal Bay, NV

## AGENDA

Sunday, 5 June 1994

11:00 AM - 1:00 PM **Registration and Lunch**

1:00 PM **Introductory Remarks**

Michael R. Berman, AFOSR, and Stephen L. Rodgers, Phillips Laboratory

### New HEDM Molecules

1:30 "New Developments In Theory And Their Role In

Studying High Energy And Density Matter"

Rod Bartlett, University of Florida

2:00 "Potential Energy Surfaces For High Energy Species"

Mark Gordon, Iowa State University

2:30 "Nonadiabatic Processes Revelant To The Stability

And Detection Of Energetic Materials"

David Yarkony, Johns Hopkins University

3:00 "Fourier Transform Emission Spectroscopy Of

Novel Propellant Molecules"

Peter Bernath, University of Waterloo and University of Arizona

3:30 - 4:00 **Break**

### HEDM Synthesis

4:00 "Cubane and Derivatives as Combustion Modifiers: Synthetic Results"

Robert Moriarty, University of Illinois at Chicago

4:30 "Novel High Energy Compounds"

Karl Christie, Rocketdyne Division of Rockwell International Corporation

5:00 "Progress Towards The Synthesis Of Polymeric Nitrogen"

Hector Lorenzana, Lawrence Livermore National Laboratory

5:30 **Adjourn**

7:30-9:30 **Synthesis Workshop**

Monday, 6 June 1994

7:30 - 8:30 AM      **Breakfast**

**Cryogenic Solids**

8:30 AM      "Progress On Atom Doped Cryogenic Solid Propellants"  
Mario Fajardo, Phillips Laboratory, Edwards AFB CA

9:00            "Quantum Computer Simulations Of The Structure And  
Dynamics Of Impurities In Solid Hydrogen"  
Gregory Voth, University of Pennsylvania

9:30            "Mobilities And Reaction Dynamics Of  
Atoms In Cryogenic Solids"  
Eric Weitz, Northwestern University

10:00          **Break**

10:30          "Ultra-High Resolution Spectroscopy Of The  $Q_{\nu}(0)$   
Transitions Induced By Impurity Quadrupole Field,  
Laser Radiation Field, External Electric Field And  
 $\gamma$ -Ray Radiolysis"  
Takeshi Oka, University of Chicago

11:00          "Diffusion In Crystalline And Amorphous Solid Hydrogen"  
James Gaines, University of Hawaii

11:30          "Solid Hydrogen Structure"  
Gilbert Collins, Lawrence Livermore National Laboratory

12:00          "Triple-Point Of The BSP-DA-HCP Insulating  
Phase In Megabar Pressure Deuterium"  
Isaac Silvera, Harvard University

12:30-1:45    **Lunch**

Monday, 6 June 1994  
(Continued)

**Metal Atoms and Clusters**

- 1:45 PM "Spectroscopy Of Alkali Atoms And Molecules Attached To Highly Quantum Clusters (H<sub>2</sub>, He)"  
Frank Stienkemeier and Giacinto Scoles, Princeton University
- 2:15 "Novel Phenomena Involving Contact Between Alkali Atoms And Helium Or Hydrogen"  
Milton Cole, Pennsylvania State University
- 2:30 "Characterization Of Van Der Waals Complexes Involving B And Al Atoms Through Laser Fluorescence Excitation Spectroscopy"  
Paul Dagdigian, Johns Hopkins University
- 3:00 "Investigation Of Weakly Bound Complexes Involving Boron Atoms"  
Millard Alexander, University of Maryland
- 3:30 **Break**
- 4:00 "Time Resolved Dynamics In Molecular Clusters"  
Carl Lineberger, University of Colorado
- 4:30 "The Newly Synthesized Tetranitrogen Monoxide Molecule: Why is the Observed Form Higher in Energy than the Unobserved Cyclic Structure?"  
H. Fritz Schaefer, III, University of Georgia
- 5:00 "Magnetic Circular Dichroism Spectroscopy Of Metal/Rare Gas And Metal/Hydrogen Systems"  
John Kenney, III, Eastern New Mexico University
- 5:30 "Demonstration Of A High Gain Visible Wavelength Chemical Laser Based On Energy Transfer From Metastable NF (a<sup>1</sup>Δ) To Boron Hydride"  
David Benard, Rockwell International Science Center
- 5:45 **Adjourn**
- 7:30-10:00 **Poster Session and Reception**

Tuesday, 7 June 1994

7:30 - 8:30 AM      **Breakfast**

**Advanced Cryogenic Propellants**

8:30 AM      **"University Research Initiative: Advanced Cryogenic Propellants"**  
V. A. Apkarian, R. B. Gerber, K. Janda, L. Nosanow, J. Rutledge,  
P. Taborek, University of California, Irvine

10:00          **Break**

**Solid Propellant Rocket Dynamics (joint with AFOSR/NA)**

10:30          **"Nonsteady Combustion Mechanisms Of Advanced  
Solid Propellants (URI)"**  
M Branch, University of Colorado; M Beckstead, Brigham Young University,  
M Smooke, Yale University; V Yang, Pennsylvania State University

11:30          **"Thermal Decomposition Mechanisms Of New Polycyclic Nitramines"**  
T B Brill, University of Delaware

12:00          **"Combustion Kinetics Of HEDMs And Metallic Fuels"**  
A Fontijn, RPI

12:30-1:45      **Lunch**

Tuesday, 7 June 1994  
(Continued)

**Advanced Propellants and Propulsion Systems**

- 1:45 PM "Current Experiments On The Combustion Of Cryogenic Solid Propellants"  
Patrick Carrick, Phillips Laboratory, Edwards AFB CA
- 2:15 "Structure, Thermochemistry And Performance Of Advanced Propellants"  
Harvey Michels, United Technologies Research Center
- 2:45 "A Survey Of Rocket Propulsion Systems"  
E. J. Wucherer, Hughes STX, Edwards AFB CA
- 3:15-4:15 Open Discussion of HEDM Propulsion Concepts
- 4:15-4:30 Break

**HEDM Program Overview and Directions**

- 4:30 "Future Directions of Air Force Spacelift"  
Lt Col Dave Lewis
- 5:00 Concluding Remarks  
Michael R. Berman, AFOSR, and Stephen L. Rodgers, Phillips Laboratory

## POSTER PRESENTATIONS

Production and Decay of Diazaborane (DAB) and Tetra-azidodiborane (TADB)  
E. Boehmer, Rockwell Science Center

Non-Toxic Replacements for Aerozine-50  
E.J. Wucherer, Hughes STX

Thermoluminescence Studies of Atomic Species in Cryogenic Solid Matrices  
T.L. Thompson, M.E. Cordonnier, M.E. Fajardo, Phillips Laboratory

Collision Dynamics of Small Molecular Hydrogen and Deuterium Clusters with  
Light Atoms  
Zhiming Li, R. Benny Gerber; University of California, Irvine

Molecular Impurities in Quantum Clusters  
Michele McMahon, K. Birgitta Whaley; University of California, Berkeley

Dynamics of Processes in Doped Hydrogen Clusters  
R.B. Gerber, Z. Li, S. Broude, A.B. McCoy; University of California, Irvine

Fourier Transform Vibrational Spectroscopy of Novel  $\text{Li}_x\text{B}_y$  Propellant Additive  
Clusters in Solid Argon  
J.D. Presilla-Marquez, P.G. Carrick; Phillips Laboratory

Theoretical Studies of the Molecular and Electronic Structure of  $\text{Li}_2\text{B}_2$   
Jerry Boatz, Phillips Laboratory

Prediction of Triplet Absorption Lineshape for Na Atoms in Liquid Ar  
Mario Fajardo, Jerry Boatz, Phillips Laboratory

Optical Potential Methods for the Spectra of Metal Radicals Trapped in Low-  
Temperature Rare Gas Matrices  
J. Boatz, M.E. Fajardo, Phillips Laboratory and P.W. Langhoff; Indiana University

Optical Spectroscopy and Photochemistry of Atoms in Solid Molecular Hydrogen  
William Stwalley, John Bahns, University of Connecticut

Optical Absorption, Emission and Radiation Transfer in High-Temperature Metal  
Vapors  
J.D. Mills, C.W. Larson, Phillips Laboratory, P.S. Erdman, W.S. Stwalley, University of  
Connecticut, and P.W. Langhoff, Indiana University

Emission Spectroscopy of  $\text{B}_2$  and BH  
Christopher Brazier and Patrick Carrick, Phillips Laboratory

Emission Spectra of the  $(1)^1\Sigma_u^+ - (1)^1\Sigma_g^+$  Transition of  $B_2$   
Michelle Cordonnier, Patrick Carrick and Christopher Brazier, Phillips Laboratory

A Theoretical Study of B-N Analog of Prismane  
Nikita Matsunaga and Mark Gordon, Iowa State University

Potential Energy Surfaces for High Energy Compounds Containing Nitrogen  
Galina Chaban, Kiet Nguyen, and Mark Gordon, Iowa State University

Metal Clusters and Metal Complexes: Models for Metal-Seeded Energetic Materials  
Michael Duncan, University of Georgia

Velocity Selected Laser Ablation Metal Atom Source  
Michel Macler and Mario E. Fajardo, Phillips Laboratory

Laser Pyrolysis of Explosives  
Charles Wight, University Of Utah

**AIR FORCE  
HIGH ENERGY DENSITY MATERIALS  
CONTRACTORS' CONFERENCE**

CAL-NEVA Lodge

Crystal Bay, NV

June 5-7, 1994

Participants List

Millard H. Alexander  
Department of Chemistry  
University of Maryland  
College Park, MD 20742  
Tel: (301) 405-1823  
Fax: (301) 314-9121  
mha@hibridon.Umd.Edu

Angelo J. Alfano  
Phillips Laboratory  
OLAC PL/RKFA Bldg. 8451  
10 E. Saturn Boulevard  
Edwards AFB, CA 93524-7660  
Tel: (805) 275-6176  
Fax: (805) 275-6233

V. Ara Apkarian  
Department of Chemistry  
University of California at Irvine  
Irvine, CA 92717  
Tel: (714) 856-6851  
Fax: (714) 725-3168  
aapkaria@uci.edu

Young K. Bae  
Phillips Laboratory  
Hughes STX  
10 E. Saturn Boulevard  
Edwards AFB, CA 93526-7680  
Tel: (805) 275-5761  
Fax: (805) 275-5886

Rodney J. Bartlett  
Department of Chemistry  
University of Florida  
P. O. Box 118435  
Gainesville, FL 32611-8435  
Tel: (904) 392-1597  
Fax: (904) 392-8722  
bartlett@qtp.Ufl.Edu

Charles Bauschlicher  
NASA Ames Research Center  
RTC 230-3  
Moffett Field, CA 94035  
Tel: (415) 604-6231  
Fax: (415) 604-0350  
bauschli@pegasus.Arc.Nasa.Gov

Robert Behdadnia  
Phillips Laboratory  
10 E. Saturn Boulevard  
Edwards AFB, CA 93524-7680  
Tel: (805) 275-5799 or 5410  
Fax: (805) 275-5471  
behdadnia@lablink.ple.af.mil

David J. Benard  
Rockwell International Science Center  
1049 Camino Dos Rios  
Thousand Oaks, CA 91360  
Tel: (805) 373-4278  
Fax: (805) 373-4775



Michael Berman  
Air Force Office of Scientific Research  
110 Duncan Avenue, Suite B115  
Bolling AFB, DC 20332-0001  
Tel: (202) 767-4963  
Fax: (202) 767-4961  
berman@afosr.mil

Peter F. Bernath  
Department of Chemistry  
University of Waterloo  
Waterloo, Ontario CANADA N2L 3G1  
Tel: (519) 888-4814  
Fax: (519) 746-0435  
bernath@watsci.uwaterloo.ca

Jerry A. Boatz  
Phillips Laboratory  
OLAC PL/RKFE  
10 E. Saturn Boulevard  
Edwards AFB, CA 93524-7680  
Tel: (805) 275-5364  
Fax: (805) 275-5471  
boatzj@scivx2.ple.af.mil

Ellen Boehmer  
Rockwell International Science Center  
1049 Camino Dos Rios  
Thousand Oaks, CA 91360  
Tel: (805) 373-4139  
Fax: (805) 373-4775  
eboehme@scimail.ormnet.cb.com

Melvin Branch  
Department of Mechanical Engineering  
University of Colorado  
Boulder, CO 80309-0427  
Tel: (303) 492-6318  
Fax: (303) 492-2863

Chris Brazier  
Hughes STX/Phillips Laboratory  
10 E. Saturn Boulevard  
Edwards AFB, CA 93524-7680  
Tel: (805) 275-5951  
Fax: (805) 275-5886  
brazier@lablink.ple.af.mil

H. F. Calcote  
Aerochem Research Labs, Inc.  
P. O. Box 12  
Princeton, NJ 08542  
Tel: (609) 921-7070  
Fax: (908) 329-8292

Louis F. Cannizzo  
Thiokol Corporation  
P. O. Box 707, M/S 244  
Brigham City, UT 84302  
Tel: (801) 863-3782  
Fax: (801) 863-2271

Patrick G. Carrick  
Phillips Laboratory  
10 E. Saturn Boulevard  
Edwards AFB, CA 93524-7680  
Tel: (805) 275-5883  
Fax: (805) 275-5471  
carrickp@lablink.ple.af.mil

Galina Chaban  
Iowa State University  
316 Wilhelm  
Ames, IA 50011  
Tel: (515) 294-2582  
Fax: (515) 294-5204  
galina@si.fi.amelab.gov

Karl O. Christe  
Rocketdyne BA 26  
6633 Canoga Avenue  
Canoga Park, CA 91309  
Tel: (818) 586-6736  
Fax: (818) 586-8605

Robert Cohn  
Phillips Laboratory  
OL-AC PL/CA-R  
5 Pollux Drive  
Edwards Air Force Base, CA 93524-7048  
Tel: (805) 275-6112  
Fax: (805) 275-5086  
cohn@lablink.Ple.Af.Mil

Milton W. Cole  
Pennsylvania State University  
104 Davey Laboratory  
University Park, PA 16802  
Tel: (814) 863-0165  
Fax: (814) 865-3604  
mwc@psuvm.psu.edu

Gilbert W. Collins  
Lawrence Livermore National Laboratory  
7000 East Avenue, L-482  
Livermore, CA 94550  
Tel: (510) 423-2204  
Fax: (510) 422-4982  
collins7@llnl.gov

Michelle E. Cordonnier  
Phillips Laboratory  
OLAC PL/RKFE  
10 E. Saturn Boulevard  
Edwards AFB, CA 93524-7680  
Tel: (805) 275-5798  
cordonnr@lablink.ple.af.mil

Paul J. Dagdigian  
Remsen Hall  
Johns Hopkins University  
Baltimore, MD 21209  
Tel: (410) 516-7438  
Fax: (410) 516-8420  
p13z2681@jhuvvm.hcf.jhu.edu

William Dailey  
Department of Chemistry  
University of Pennsylvania  
231 South 34th Street  
Philadelphia, PA 19104  
Tel: (215) 898-2704  
Fax: (215) 573-2112  
dailey@a.chem.upenn.edu

Ed Delaney  
SPARTA, Inc.  
244 E. Avenue, K-4  
Lancaster, CA 93536  
Tel: (805) 723-3148  
Fax: (805) 723-1379

Michael A. Duncan  
Department of Chemistry  
University of Georgia  
Athens, GA 30602  
Tel: (706) 542-1998  
Fax: (706) 542-9454  
maduncan@uga.cc.uga.edu

Mario Fajardo  
Phillips Laboratory  
OLAC PL/RKFE  
10 E. Saturn Boulevard  
Edwards AFB, CA 93524-7680  
Tel: (805) 275-5946  
Fax: (805) 275-5471

Ponzi Ferraraccio  
Phillips Laboratory  
3550 Aberdeen Avenue  
Kirtland AFB, NM  
Tel: (505) 846-6936  
Fax: (505) 846-5034

Arthur Fontijn  
Department of Chemistry  
Rensselaer Polytechnic Institute  
Troy, NY 12180-3590  
Tel: (518) 276-6508  
Fax: (518) 276-4030  
fontijn@rpi.tsmts

Robert L. Forward  
Forward Unlimited  
P. O. Box 2783  
Malibu, CA 90265-7783  
Tel: (805) 983-7652  
Fax: (206) 579-1363

Patrick E. Frye  
Rockwell International Corporation  
Rocketdyne Division  
P. O. Box 7922 - Mailstop IB59  
6633 Canoga Avenue  
Canoga Park, CA 91309-7922  
Tel: (818) 586-0363  
Fax: (818) 586-0579  
frye@mrbig.rdyne.rockwell.com

James R. Gaines  
Department of Physics  
University of Hawaii  
2505 Correa Road  
Honolulu, HI 96822  
Tel: (808) 956-2922  
Fax: (808) 956-9496

Alon Gany  
Department of Mechanical  
and Aerospace Engineering  
Princeton University  
Princeton, NJ 08544  
Tel: (609) 258-5041  
Fax: (609) 258-5963

Bruce C. Garrett  
Battelle Northwest  
PSL Building  
908 Battelle Boulevard  
Richland, WA 99352  
Tel: (509) 375-2587  
Fax: (509) 375-6916  
d3e057@pnl.gov

Robert B. Gerber  
Department of Chemistry  
University of California at Irvine  
Irvine, CA 92717  
Tel: (714) 856-6758  
Fax: (714) 856-8571  
benny@batata.fh.huji.ac.il

Irvin Glassman  
Department of Engineering  
Princeton University  
Princeton, NJ 08544  
Tel: (609) 258-5199  
Fax: (609) 258-5967

Mark S. Gordon  
Department of Chemistry  
Iowa State University  
Ames, IA 50011  
Tel: (515) 294-0452  
Fax: (515) 294-5204  
mark@si.fi.ameslab.gov

V. E. Haloulakos  
McDonnell Douglas Aerospace  
5301 Bolsa Avenue, M/S 13-3  
Huntington Beach, CA 92647  
Tel: (714) 896-3456  
Fax: (714) 896-3171

Mohammed Hariballah  
ONERA  
B.P. 72  
92323 Chatillon, Cedex  
FRANCE  
Tel: 33-1-46734337  
Fax: 33-1-46734147

Kenneth C. Janda  
Department of Chemistry  
University of California at Irvine  
44 Ulrey Court  
Irvine, CA 92717  
Tel: (714) 856-5266  
Fax: (714) 856-8571  
kcjanda@uci.edu

Paul Jones  
Phillips Laboratory  
OLAC PL/RKFE  
10 East Saturn Bldg  
Edwards AFB, CA 93524-7680  
Tel: (805) 275-5410  
Fax: (805) 275-5471

Daniel H. Katayama  
Phillips Laboratory (GPID)  
29 Randolph Road  
Hanscom AFB, MA 01731-3010  
Tel: (617) 377-5088  
Fax: (617) 377-7091  
dh.kata@al.plh.af.mil

John W. Kenney, III  
Eastern New Mexico University  
Dept of Physical Sciences Station 33  
Portales, NM 88130  
Tel: (505) 562-2152  
Fax: (505) 562-2578

Michael Klein  
University of Pennsylvania  
3231 Walnut St.  
Philadelphia, PA 19104-6202  
Tel: (215) 898-8571  
Fax: (215) 898-8296  
klein@sol.drsm.upenn.edu

Dan Konowalow  
Phillips Laboratory  
OLAC PL/RKFE  
25 Franklyn Dr.  
Lansing, NY 14882  
Tel: (607) 533-4295  
dank@tc.Cornell.Edu

Takako Kudo  
Department of Chemistry  
Iowa State University  
Ames, IA 50011  
Tel: (515) 292-9925  
Fax: (515) 294-5204

Peter W. Langhoff  
Department of Chemistry  
Indiana University  
Bloomington, IN 47405  
Tel: (812) 855-8621  
Fax: (812) 855-8310  
langhoff@ucs.indiana.edu

Stephen R. Langhoff  
NASA Ames Research Center  
RTC 230-3  
Moffett Field, CA 94035  
Tel: (415) 604-6213  
Fax: (415) 604-6213  
langhoff@pegasus.arc.nasa.gov

William C. Larson  
Phillips Laboratory  
OLAC PL/RKFE  
10 E. Saturn Boulevard  
Edwards AFB, CA 93524-7680  
Tel: (805) 275-6104  
Fax: (805) 275-5471

Chung K. Law  
Princeton University  
P. O. Box CN5263  
Princeton, NJ 08544-5263  
Tel: (609) 258-3900  
Fax: (609) 258-6746

Stephen Leone  
University of Colorado  
JILA, Campus Box 440  
Boulder, CO 80309  
Tel: (303) 492-5128  
srl@jila.colorado.edu

David W. Lewis  
Phillips Laboratory  
8 Draeo Drive  
Edwards AFB, CA 93524-7230  
Tel: (805) 275-5230  
Fax: (805) 275-5034

Zhiming Li  
Department of Chemistry  
University of California at Irvine  
Irvine, CA 92717  
Tel: (714) 725-2789  
Fax: (714) 856-8571  
zhiming@prince.ps.uci.edu

W. Carl Lineberger  
JILA/University of Colorado  
C.B. 440  
Boulder, CO 80309-0440  
Tel: (303) 492-7834  
Fax: (303) 492-8994  
wcl@jila.colorado.edu

Hector E. Lorenzana  
Lawrence Livermore National Laboratory  
L-299 H-Division  
Livermore, CA 94550  
Tel: (510) 422-8982  
Fax: (510) 422-2851  
hlorenzana@llnl.gov

Michel Macler  
Phillips Laboratory  
OLAC PL/RKFE  
10 East Saturn Blvd  
Edwards AFB, CA 93524-7680  
Tel: (805) 275-5931  
Fax: (805) 275-5471

Frank Magnotta  
Lawrence Livermore National Laboratory  
PO Box 808; L278  
Livermore, CA 94549  
Tel: (510) 422-7285  
Fax: (510) 423-9178  
magnotta1@llnl.gov

John Margrave  
Department of Chemistry  
Rice University  
P. O. Box 1892  
Houston, TX 77251  
Tel: (713) 527-4813  
Fax: (713) 285-5155  
chem@ricevml.rice.edu

Nikita Matsunaga  
Department of Chemistry  
Iowa State University  
Wilhelm Hall #402  
Ames, IA 50011  
Tel: (515) 294-9925  
Fax: (515) 294-5204  
mik.4a@si.fi.ameslab.gov

Donald S. McClure  
Department of Chemistry  
Princeton University  
Washington Road  
Princeton, NJ 08544  
Tel: (609) 258-4980  
Fax: (609) 258-6746  
dmclure@chemvax.princeton.edu

Tim McKelvey  
Phillips Laboratory  
OLAC PL/RKFE  
Edwards AFB, CA 93523  
Tel: (805) 275-5955  
Fax: (805) 275-5471  
mckelveyt@lab.Link.Ple.Af.Mil

Michele A. McMahon  
University of California, Berkeley  
Berkeley, CA 94720  
Tel: (510) 643-7885  
Fax: (510) 642-8369  
michele@holmium.cchem.berkeley.edu

Harvey H. Michels  
United Technologies Research Center  
411 Silver Lane  
East Hartford, CT 06108  
Tel: (203) 727-7489  
hhm@utrc.utc.com

Jeffrey D. Mills  
Indiana University and Phillips Laboratory  
3615 South Leonard Springs Road  
Bloomington, IN 47403  
Tel: (812) 855-8621  
Fax: (812) 855-8310  
jdmills@ucs.indiana.edu

Robert M. Moriarty  
University of Illinois at Chicago  
5417 SES Bldg  
Chicago, IL 60680  
Tel: (312) 996-2364  
Fax: (312) 966-0431

Robert A. Nichols  
Phillips Laboratory  
4 Draco Drive  
Edwards AFB, CA 93523-5000  
Tel: (805) 275-6074  
Fax: (805) 275-5049

Lewis H. Nosanow  
Department of Physics  
University of California at Irvine  
P-2, Room 4129  
Irvine, CA 92717-4575  
Tel: (714) 856-5034  
Fax: (714) 725-2174

Takeshi Oka  
Department of Chemistry  
University of Chicago  
5785 S. Ellis Avenue  
Chicago, IL 60637  
Tel: (312) 702-7070  
Fax: (312) 702-0805  
oka@biovax.uchicago.edu

Mitchio Okumura  
California Institute of Technology  
Chemistry 127-72  
1201 East California Boulevard  
Pasadena, CA  
Tel: (818) 395-6557  
Fax: (818) 568-8824  
mo@celia.clatech.edu

Stephen O'Neil  
JILA, CB 440  
University of Colorado  
Boulder, CO 80309-0440  
Tel: (303) 492-7817  
Fax: (303) 492-5235

Robert Parson  
JILA, Campus Box 440  
University of Colorado  
Boulder, CO 80309-0440  
Tel: (303) 492-7751  
Fax: (303) 492-5235  
rparson@jila.colorado.edu

J.D. Presilla-Marquez  
Phillips Laboratory  
OLAC PL/RKFE  
10 East Saturn Blvd.  
Edwards AFB, CA 93524-7680  
Tel: (805) 275-5412

Douglas J. Raber  
National Research Council  
2101 Constitution Avenue, N. W.  
Washington, D. C. 20418  
Tel: (202) 334-2156  
Fax: (202) 334-2154  
draber@nas.Edu

Michael J. Redmon  
Hughes STX Corp.  
10 Saturn Blvd, MS 8451/44  
Edwards AFB, CA 93524-7680  
Tel: (805) 275-5796  
Fax: (805) 275-5882

Eric Rice  
ORBITEC  
402 Gammon Place  
Madison, WI 53719  
Tel: (608) 833-1992  
Fax: (608) 833-5050

Steven M. Robbins  
Thiokol Corporation  
43770 15th Street West #135  
Lancaster, CA 93536  
Tel: (805) 942-8423  
Fax: (805) 942-5910

Wayne E. Roe  
Phillips Laboratory  
5 Pollux Drive  
Edwards AFB, CA 93524-7680  
Tel: (805) 275-5206  
Fax: (805) 275-8352

James E. Rutledge  
Department of Physics  
University of California at Irvine  
Irvine, CA 92717  
Tel: (714) 856-5141  
Fax: (714) 725-2174

Robert J. Santoro  
Department of Chemistry  
Pennsylvania State University  
University Park, PA 16802  
Tel: (814) 863-1285  
Fax: (814) 865-3389

Roberta P. Saxon  
SRI International  
333 Ravenswood Avenue  
Menlo Park, CA 94025  
Tel: (415) 859-3465  
Fax: (415) 859-4321  
roberta\_saxon@qm.sri.com

Richard J. Saykally  
Department of Chemistry  
University of California at Berkeley  
Berkeley, CA 94720-1460  
Tel: (510) 642-8269  
Fax: (510) 642-8369  
rjs@hydrogen.cchem.berkeley.edu

Henry F. Schaefer, III  
Center for Computational  
Quantum Chemistry  
University of Georgia  
Athens, GA 30602-2556  
Tel: (706) 542-2067  
Fax: (706) 542-0406  
hfsiii@uga

Giacinto Scoles  
Department of Chemistry  
Princeton University  
Princeton, NJ 08544  
Tel: (609) 258-5570  
Fax: (609) 258-6746  
gscoles@pucc.princeton.edu

George M. Seidel  
Department of Physics  
Brown University  
Providence, RI 02912  
Tel: (401) 863-2584  
Fax: (401) 863-2024

Jeffrey A. Sheehy  
Eloret Corporation  
NASA Ames Research Center  
Mail Stop 230-3  
Moffett Field, CA 94035  
Tel: (415) 604-3471  
Fax: (415)-604-0350

Isaac F. Silvera  
Department of Physics  
Harvard University  
Cambridge, MA 02138  
Tel: (617) 495-9075  
Fax: (617) 496-5144  
silvera@huhepl

Alan Smooke  
Yale University  
15 Prospect Street  
New Haven, CT 06511  
Tel: (203) 432-4344  
Fax: (203) 432-6775

Alan Snelson  
IIT Research Institute  
10 West 35th Street  
Chicago, IL 60616  
Tel: (312) 567-4260  
Fax: (312) 567-4286

Paul Sokol  
Department of Physics  
Pennsylvania State University  
University Park, PA 16802  
Tel: (814) 863-0528  
Fax: (814) 865-3604  
sokol@phys.psu.edu

James M. Spotts  
California Institute of Technology  
127-72 Division of Chemistry  
Pasadena, CA 91125  
Tel: (818) 395-6014  
Fax: (818) 568-8824

William C. Stwalley  
Department of Physics, U-46  
University of Connecticut  
2152 Hillside Road  
Storrs, CT 06269-3046  
Tel: (203) 486-4924  
Fax: (203) 486-3346  
stwalley@uconnvm.uconn.edu

Heidi Terrill-Stolper  
Department of Physical Sciences  
Eastern New Mexico University  
Station 33  
Portales, NM 88130  
Tel: (505) 562-2152  
Fax: (505) 562-2578

Peter Taborek  
Department of Chemistry  
University of California at Irvine  
Irvine, CA 92717  
Tel: (714) 725-2254  
Fax: (714) 725-8571

Donald L. Thompson  
Department of Chemistry  
Oklahoma State University  
Stillwater, OK 74078  
Tel: (405) 744-5174  
Fax: (405) 744-6007  
chemdlt@osucc.bitnet

Capt Tim Thompson  
Phillips Laboratory  
OL-AC PL/RK  
5 Pollux Dr  
Edwards AFB, CA 93524-7048  
Tel: (805) 275-6115  
Fax: (805) 275-5086  
thompsot@lablink.ple.af.mil

Donald D. Tzeng  
United Technologies / CSD  
600 Metcalf Road  
San Jose, CA  
Tel: (408) 776-4423  
Fax: (408) 776-5995

James J. Valentini  
Department of Chemistry  
Columbia University  
Box 766 Havemeyer Hall  
New York, NY 10027  
Tel: (212) 854-7590  
Fax: (212) 932-1289  
valvalentini@cuchem

Greg Voth  
Department of Chemistry  
University of Pennsylvania  
Philadelphia, PA 19104-6323  
Tel: (215) 898-3048  
Fax: (215) 573-2112  
voth@a.chem.upenn.edu

Albert F. Wagner  
Argonne National Laboratory  
Bldg. 200, R108  
9700 S. Cass Avenue  
Argonne, IL 60439  
Tel: (708) 252-3597  
Fax: (708) 252-4470

David P. Weaver  
Phillips Laboratory  
10 East Saturn Boulevard  
Edwards AFB, CA 93524-7660  
Tel: (805) 275-6177  
Fax: (805) 275-5471

Scott T. Weidman  
National Research Council  
2101 Constitution Avenue, N. W.  
Washington, D. C. 20418  
Tel: (202) 334-2156  
Fax: (202) 334-2154  
sweidman@nas.Edu

Eric Weitz  
Department of Chemistry  
Northwestern University  
2145 Sheridan Road  
Evanston, IL 60208-8113  
Tel: (708) 491-5583  
weitz@casbah.Edu



Stewart Wesson  
Eastern New Mexico University  
Dept of Physical Sciences  
Station 33  
Portales, NM 88130  
Tel: (505) 562-2152  
Fax: (505) 562-2578

K. Birgitta Whaley  
Department of Chemistry  
University of California at Berkeley  
Berkeley, CA 94720-1460  
Tel: (510) 643-6820  
Fax: (510) 642-8369  
whaley@holmium.cchem.berkeley.edu

Carl E. Wieman  
JILA/University of Colorado  
Box 390  
Boulder, CO 80309-0440  
Tel: (303) 492-6963  
Fax: (303) 492-8994  
cwieman@jila.colorado.edu

Charles A. Wight  
Department of Chemistry  
University of Utah  
Henry Eyring Building  
Salt Lake City, UT 84112  
Tel: (801) 581-8796  
Fax: (801) 585-3207  
wight@chemistry.utah.edu

Jack K. Willis  
Eastern New Mexico University  
Station 33  
Portales, NM 88130  
Tel: (505) 562-2152  
Fax: (505) 562-2578

Angelica C. Wilson  
Hughes STX / Phillips Laboratory  
OLAC PL/RKFE  
10 E. Saturn Boulevard  
Edwards AFB, CA 93524  
Tel: (805) 275-5317  
Fax: (805) 275-5471

E. J. Wucherer  
Hughes STX / Phillips Laboratory  
OLAC PL/RKFE  
10 E. Saturn Boulevard  
Edwards AFB, CA 93524  
Tel: (805) 275-2759  
Fax: (805) 275-5471  
wucherere@lablink.ple.af.mil

Edward J. Yadlowsky  
HY-Tech Research Corp  
104 Centre Court  
Radford, VA 24141  
Tel: (703) 639-4019  
Fax: (703) 639-4027

David R. Yarkony  
Department of Chemistry  
Johns Hopkins University  
3400 N. Charles Street  
Baltimore, MD 21218  
Tel: (410) 516-4663  
Fax: (410) 516-8410  
yarkony@jhuvms.hcf.jhu.edu

# *Oral Presentations*

# **EXTENDED ABSTRACT**

## **1994 AIR FORCE HIGH ENERGY DENSITY MATERIALS (HEDM) CONTRACTORS CONFERENCE**

**Cal-Neva Lodge  
Crystal Bay, Nevada  
June 5-7, 1994**

**Rodney J. Bartlett**  
*Quantum Theory Project*  
*University of Florida*  
*Gainesville, Florida 32611-8435*

## Summary of Principal Recent Results

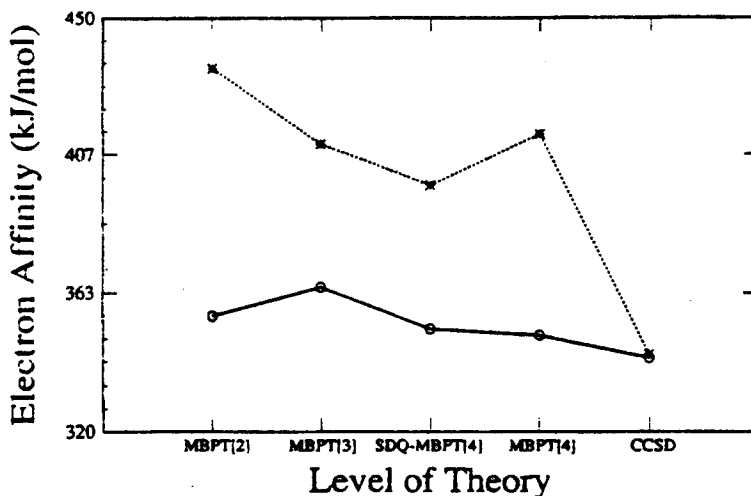
To date, the successes of our effort for the HEDM program, both methodological and in terms of metastable molecule chemistry, have been many. Considering the latter first, recognizing the prospects for highly energetic metastable species based upon nitrogen, we initiated our study of a variety of such potential molecules. These included  $N_3H_3$  [18], which is isoelectronic with the well-known species ozone, cyclopropane and propene; tetrahedral  $N_4$  [11] which is isovalent with  $P_4$  or  $As_4$ , and is forbidden by symmetry from decaying to ground state  $N_2$  molecules; octahedral  $N_8$  [11], isoelectronic with cubane and similarly forbidden from direct decomposition to  $N_2$  in its ground state; and pentazole,  $HN_5$  [10]. Each of these was found to contribute a metastable minimum on the global potential energy surface. The minima were fully characterized by calculation of the Hessian (second derivative matrix) frequently using our recently developed analytical MBPT(2) methods [14,17], which also provided the IR spectra of these unknown molecules. At this level of approximation the vibrational frequencies are normally within 5% of experiment and the relative intensities typically to within about 20% [1]. I might add, the character of a critical point on an energy surface can change depending upon whether electron correlation is included, so this is a critical test for every potential metastable molecule. Furthermore, some regard must be paid to low-lying excited states that might offer a decomposition path to ensure that the molecule is stable to unimolecular decomposition. In the absence of matrix isolation, bimolecular mechanisms can also offer ways for the target molecule to disappear.

Although sometimes postulated, there is no experimental evidence for the existence of any of these molecules. This tends to be a recurring theme in the investigation of metastable molecules. Yet, the accuracy of modern *ab initio* correlated predictions is sufficiently reliable that barring rapid bimolecular kinetics and certain possible excited state decomposition paths, the proposed metastable molecule should be capable of synthesis at least in matrix isolation and can be identified from our predicted frequencies.

## Methodological Advances

The ability to provide accurate energetic and spectroscopic results for candidate HEDM molecules rests upon new developments in *ab initio*, electronic structure theory. Several such advances have been accomplished in the last period of this grant. All are incorporated into the ACES II program system which is now widely used throughout the world, including industry (Lubrizol, Dupont, Ford, etc.) and other government agencies (NASA Ames, DOE's Battelle, Pacific Northwest Laboratory, etc.).

1. Open shell molecules are frequently more difficult to describe accurately than those where all electrons are paired. The most widely used procedure for open shells is to start with an unrestricted Hartree Fock (UHF) reference and add electron correlation via MBPT (also known as MP) theory. However, for many problems, UHF solutions suffer from spin-contamination as the UHF function is not an eigenfunction of spin. For some problems, a restricted open shell Hartree Fock (ROHF) reference, which is a spin eigenfunction, is a better choice. However, because the ROHF method uses different Fock operators in its determination, one for doubly orbital orbitals, and one for singly occupied orbitals, it was not clear how to use an ROHF reference in MBPT calculations. We solved this problem to provide a non-iterative ROHF-MBPT method for second, third and fourth order [17], that is no more expensive than the usual UHF-MBPT calculations, but one that offers vastly better convergence to the exact result for spin contaminated cases. This is illustrated in Fig. 1 for the CN radical.



Electron affinity of CN radical. (O) ROHF; (\*) UHF.

Note that at the ROHF-MBPT(2) level, there is good agreement with infinite order CCSD results, while UHF-MBPT(2) is far from the converged answer. Furthermore, finite order MBPT failed to rectify this failing of the UHF, spin contaminated reference.

2. To locate critical points on an energy surface,  $E(R)$ , as minima or transition states, requires the facile evaluation of the forces on the atoms in a molecule,  $\nabla E(R)$ . Since molecules have  $3N-6$  degrees of freedom where  $N$  is the number of atoms, repeated calculation of  $E(R)$  in

all degrees of freedom is a hopeless procedure for most polyatomic molecules. However, by also evaluating  $\nabla E(\mathbf{R})$  *analytically*, in about the same time as  $E(\mathbf{R})$  itself, it is comparatively easy to locate the minimum energy geometry where the atomic forces vanish. We provided the initial ROHF-MBPT(2) analytical gradients under this grant [14], and used it in several applications to transient molecules like FCS.

3. The other primary methodological advance achieved last year is the general formulation and implementation of the equation-of-motion (EOM-CCSD) method for excited states, UV-visible spectra, and associated properties. This is a very general method that shows promise of being the method of choice for excited states. The theory [1,5,6] and several applications [4-6,8] have been recently reported.

The basic idea of EOM-CC is that most of the dynamical correlation in a ground (or reference) state is quite similar to that in an excited, ionized, or electron attached state; but the non-dynamical correlation is quite different, and any suitable method must account for this difference.

Consider the Schrödinger equation for the general single state and  $k$ th excited state:

$$H\psi_o = E_o\psi_o$$

$$H\psi_k = E_k\psi_k$$

where  $\psi_k = R_k\psi_o$ , we have

$$HR_k\psi_o = E_k R_k\psi_o$$

$$R_k H\psi_o = E_o R_k\psi_o$$

$$\text{or, } [H, R_k]\psi_o = (E_k - E_o)R_k\psi_o = \omega_{ko}R_k\psi_o$$

By choosing  $\psi_o = \exp(T)\Phi_o$ , the CC choice, we obtain

$$[e^{-T}He^T, R_k]\Phi_o = \omega_{ko}R_k\Phi_o$$

$$[\bar{H}, R_k]\Phi_o = \omega_{ko}R_k\Phi_o$$

$$(\bar{H}R_k)_c\Phi_o = \omega_{ko}R_k\Phi_o$$

In matrix form, we have

$$\bar{H}R_k = R_k\omega_{ko}$$

One appropriate application of EOM will be to study the spectroscopic signatures of atoms and molecules embedded in cryogenic matrices. A few examples are attached.

## Papers Developed Under AFOSR-HEDM Support

1. R.J. Bartlett and J.F. Stanton, "Application of Post Hartree-Fock Methods: A Tutorial," in *Revs. Comp. Chem.* **5**, pp. 65-169, 1994, VCH Publishers, Eds. K.B. Lipkowitz and D.B. Boyd.
2. W.J. Lauderdale, J.F. Stanton and R.J. Bartlett, "The Novel Anion  $\text{Be}(\text{BH}_4)_3^-$ ," to be published.
3. I. Cernusak, P. Ertl, M. Urban and R.J. Bartlett, " $\text{C}_2\text{H}_4\text{B}_2\text{N}_2$ : New Compound. Prediction of Structure and Stability," *J. Phys. Chem.*, in press.
4. N. Oliphant and R.J. Bartlett, "The Theoretical Determination of Charge Transfer and Ligand Field Transition Energies for  $\text{FeCl}_4^-$  Using the EOM-CC Method," *J. Am. Chem. Soc.* **116**, 4091 (1994).
5. J.F. Stanton and R.J. Bartlett, "The Equation of Motion Coupled-Cluster method. A Systematic Biorthogonal Approach to Molecular Excitation Energies, Transition Probabilities and Excited State Properties," *J. Chem. Phys.* **98**, 7029 (1993).
6. D.C. Comeau and R.J. Bartlett, "The Equation-of-Motion Coupled-Cluster Method: Applications of Open- and Closed-Shell Reference States," *Chem. Phys. Lett.* **207**, 414 (1993).
7. T.R. Burkholder, L. Andrews and R.J. Bartlett, "Reaction of Boron Atoms With Carbon Dioxide. Matrix and *Ab Initio* Calculated Infrared Spectra of OBCO," *J. Phys. Chem.* **97**, 3500 (1993).
8. J.F. Stanton and R.J. Bartlett, "Does Chlorine Peroxide Exhibit a Strong Ultraviolet Absorption near 250nm?" *J. Chem. Phys.* **98**, 3022 (1993).
9. D. Cremer, J. Gauss, E. Kraka, J.F. Stanton and R.J. Bartlett, "A CCSD(T) Investigation of Carbonyl Oxide and Dioxirane. Equilibrium Geometries, Dipole Moments, Infrared Spectra, Heats of Formation and Isomerization Energies," *Chem. Phys. Lett.* **209**, 547 (1993).
10. K. Ferris and R.J. Bartlett, "Hydrogen Pentazole: Does It Exist?" *J. Am. Chem. Soc.* **114**, 8302 (1992).
11. W.J. Lauderdale, J.F. Stanton and R.J. Bartlett, "Stability and Energetics of Metastable Molecules: Tetraazatetrahedrane ( $\text{N}_4$ ), Hexaazabenzene ( $\text{N}_6$ ) and Octaazacubane ( $\text{N}_8$ ), *J. Phys. Chem.* **96**, 1173 (1992).
12. I. Cernusak, S. Beck and R.J. Bartlett, "Potential Energy Surface of Borazirene ( $\text{HCNBH}$ )," *J. Phys. Chem.* **96**, 10284 (1992)
13. J.F. Stanton, J. Gauss, R.J. Bartlett, T. Helgaker, P. Jørgensen and H.J. Aa. Jensen, "Interconversion of Diborane(4) Isomers," *J. Chem. Phys.* **97**, 1211 (1992).

14. W.J. Lauderdale, J.F. Stanton, J. Gauss, J.D. Watts and R.J. Bartlett, "Restricted Open-Shell Hartree-Fock Based Many-Body Perturbation Theory: Theory and Initial Application of Energy and Gradient Calculations," *J. Chem. Phys.* **97**, 6606 (1992).
15. I. Cernusak, M. Urban, P. Ertl and R.J. Bartlett, " $C_2H_4B_2N_2$ : A Prediction of Ring and Chain Compounds," *J. Am. Chem. Soc.* **114**, 10955 (1992).
16. J.F. Stanton, J. Gauss, J.D. Watts, W.J. Lauderdale and R.J. Bartlett, "The Aces II Program System," *Int. J. Quantum Chem.* **S26**, 879 (1992).
17. W.J. Lauderdale, J.F. Stanton, J. Gauss, J.D. Watts and R.J. Bartlett, "Many-Body Perturbation Theory with a Restricted Open-Shell Hartree-Fock Reference," *Chem. Phys. Lett.* **187**, 21 (1991).
18. D.H. Magers, E.A. Salter, R.J. Bartlett, C. Salter, B.A. Hess, Jr., and L.J. Schaad, "Do Stable Isomers of  $N_3H_3$  Exist?" *J. Am. Chem. Soc.* **110**, 3435 (1988).



<i>State</i>	<i>Main Excitation</i>	<i>EE-EOMCC (Li)</i>	<i>Exp.</i>
$2p^0$	$2s \rightarrow 2p$	1.85	1.85
$2S$	$2s \rightarrow 3s$	3.37	3.37
$2p^0$	$2s \rightarrow 3p$	3.83	3.83
$2D$	$2s \rightarrow 3d$	3.96	3.88
	$\Delta$ CCSD	IP-EOMCC	Exp.
First IP	5.38	5.38	5.39

**Li Atom Excitation Energies.**

<i>State</i>	<i>Main Excitation</i>	<i>EE-EOMCC (B*)</i>	<i>Exp.</i>	<i>FSCC(1,2)</i>
$4P$	$2s \rightarrow 2p$	—	3.57	3.70
$2S$	$2p \rightarrow 3s$	4.96	4.96	—
$2D$	$2s \rightarrow 2p$	—	5.93	6.10
$2p^0$	$2p \rightarrow 3p$	5.99	—	—
$2D$	$2p \rightarrow 3d$	6.65	6.79	—
		$\Delta$ CCSD	Exp.	
First IP		8.20	8.30	

**B Atom Excitation Energies.**

<i>State</i>	<i>EE-EOMCC</i>	<i>Exp.</i>
2s2p <sup>1</sup> P <sup>0</sup>	5.282	5.277
2s3s <sup>1</sup> S	6.812	6.779
2p <sup>2</sup> <sup>1</sup> D	7.225	7.050
2s3p <sup>1</sup> P <sup>0</sup>	7.484	7.462
2s3d/2p <sup>2</sup> <sup>1</sup> D	9.778	7.988

**Be excitation spectrum: Singlet states**

<i>State</i>	<i>EE-EOMCC</i>	<i>Exp.</i>
2s2p <sup>3</sup> P <sup>0</sup>	2.706	2.725
2s3s <sup>3</sup> S	6.460	6.457
2s3p <sup>3</sup> P <sup>0</sup>	7.316	7.303
2p <sup>2</sup> <sup>3</sup> D	—	7.401
2s3d <sup>3</sup> D	8.810	7.694

**Be excitation spectrum: Triplet states**

<i>State</i>	<i>EE-EOMCC</i>	<i>Exp.</i>
3s3p <sup>1</sup> P <sup>0</sup>	4.354	4.346
3s4s <sup>1</sup> S	5.444	5.394
3s3d/3p <sup>2</sup> <sup>1</sup> D	5.973	5.753
3s4p <sup>1</sup> P <sup>0</sup>	7.179	6.118
3p <sup>2</sup> /3s3d <sup>1</sup> D	8.138	6.588

**Mg excitation spectrum: Singlet states**

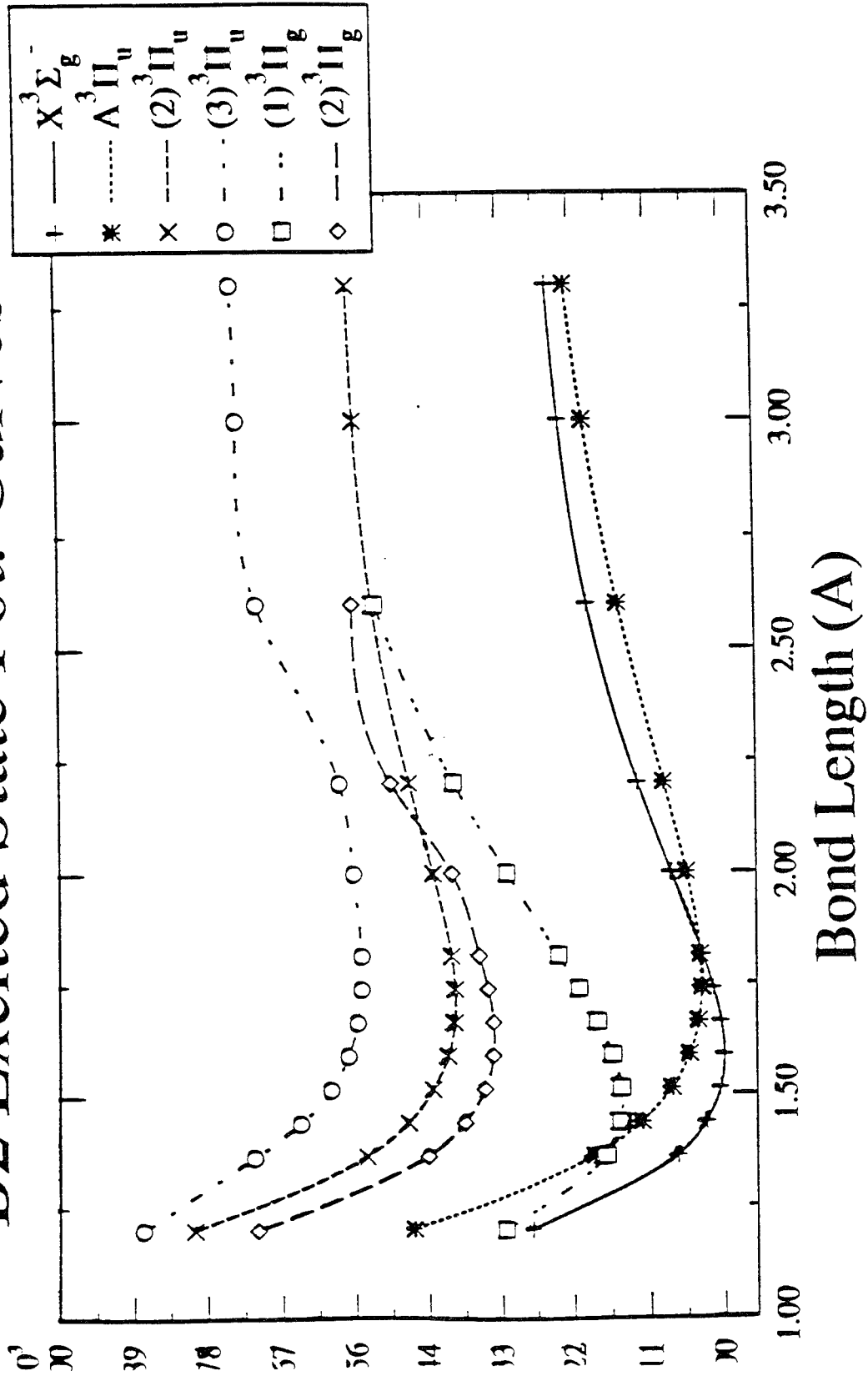
<i>State</i>	<i>EE-EOMCC</i>	<i>Exp.</i>
3s3p <sup>3</sup> P <sup>0</sup>	2.672	2.712
3s4s <sup>3</sup> S	5.104	5.108
3s3d <sup>3</sup> D	6.342	5.946
3s4p <sup>3</sup> P <sup>0</sup>	6.742	5.932

**Mg excitation spectrum: Triplet states**

<i>State</i>	<i>Main Excitation</i>	<i>EE-EOMCC (AI*)</i>	<i>Exp.</i>	<i>FSCC (1,2)</i>
$^2S$	$3p \rightarrow 4s$	3.17	3.14	—
$^4P$	$3s \rightarrow 3p$	—	3.60	3.66
$^2D$	$3p \rightarrow 3d$ $3s \rightarrow 3p$	4.18	4.02	4.46
$^2P^0$	$3p \rightarrow 4p$	4.09	4.09	—
		$\Delta\text{CCSD}$	<i>Exp.</i>	
First IP		5.91	5.98	

Al Atom Excitation Energies.

# B2 Excited State Pot. Curves



# Acetaldehyde

state	EOM-CC	expt	osc. str.	AEL
1 <sup>1</sup> A'' (valence)	4.32	4.28	6x10 <sup>-5</sup>	1.08
2 <sup>1</sup> A' (3s)	6.79	6.82	0.015	1.08
3 <sup>1</sup> A' (3p)	7.47	7.46	0.075	1.08
2 <sup>1</sup> A'' (3p)	7.75		0.011	1.08
4 <sup>1</sup> A' (3p)	7.80	7.75	0.020	1.08
5 <sup>1</sup> A' (3d)	8.54	8.43	0.014	1.08
6 <sup>1</sup> A' (3d)	8.75	8.69	0.055	1.08
3 <sup>1</sup> A'' (3d)	8.90		8x10 <sup>-5</sup>	1.08
4 <sup>1</sup> A'' (3d)	9.07		0.024	1.08
7 <sup>1</sup> A' (3d)	9.11		0.005	1.08
5 <sup>1</sup> A'' (valence)	9.28		5x10 <sup>-5</sup>	1.08
8 <sup>1</sup> A' (valence)	9.43		0.210	1.08

# POTENTIAL ENERGY SURFACES FOR HIGH ENERGY SPECIES

AFOSR HEDM MEETING  
JUNE 5-7, 1994

MARK S. GORDON, KIET A. NGUYEN, NIKITA MATSUNAGA, AND GALINA CHABAN  
DEPARTMENT OF CHEMISTRY  
IOWA STATE UNIVERSITY  
AMES, IOWA 50011

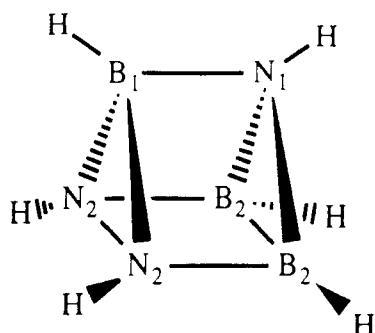
JERRY A. BOATZ  
PHILLIPS LABORATORY  
EDWARDS AFB, CA

## EXTENDED ABSTRACT

The potential energy surfaces for several types of high energy species have been investigated using *ab initio* electronic structure theory. Discussed in turn below are the BN analog of prismane, the tetrasilaaanalog of bicyclobutane, high energy structures of  $N_2O_2$  and some preliminary probes of metal- $H_2$  Van der Waals complexes. Many of these calculations have benefitted greatly from the use of parallel computers, and this aspect of the calculations will be discussed first.

*Parallel Computing.* Most of the calculations described here have been performed with the electronic structure program GAMESS<sup>1</sup>. Most of the essential functionalities of this code have been implemented in parallel mode. This includes restricted closed (RHF) and open (ROHF) shell and unrestricted open shell (UHF) Hartree Fock wave functions, generalized valence bond (GVB), multi-configurational self consistent field (MCSCF)<sup>2</sup> and configuration interaction (CI) wave functions. The analytic gradients are available for all but the CI wave functions, and these may be computed in parallel as well. Analytic Hessians are available for the RHF, ROHF and GVB wave functions, and a parallel code has been developed for calculating the Hessians in parallel using a small number of nodes. Finally, MP2 energies for RHF, ROHF, and UHF wave functions may be determined with the aid of parallel algorithms, and the MP2 gradient codes are under development. All of the parallel algorithms have been written in a manner that takes advantage of distributed memory computers, so they may be used on networks of (either identical or different) workstations or on massively parallel computers. Locally, at Iowa State University, these codes are currently run on networks of IBM RS6000 computers connected by Ethernet, and an IBM SP2 with a high speed switch is expected by the end of August. Use is also made of the Intel Delta at Caltech (under the auspices of ARPA), the Connection CM5 at the Army High Performance Computing Center at the University of Minnesota, the Intel Paragon at the San Diego Supercomputer Center, and the SP2 at Maui.

An example of the performance (and the difficulties) of parallel SCF calculations is provided by the BN analog of prismane,



a high energy isomer of the benzene analog borazene. The results are summarized in Table 1, where the speedups for an energy plus gradient run are presented as a function of the number of processors. The overall speedup (last column) is essentially perfect (100%) through 8 processors 92% through 16 processors, and slowly tails off as the number of processors increases to 256. Even at 256 processors there is a better than 25% speedup. The source of the loss in efficiency as the number of processors increases may be determined by analyzing the middle three columns of the table. While the two-electron gradients are essentially perfectly parallel, the efficiency of the Hartree-Fock part of the calculation parallels that of the overall job. Further analysis reveals that, while the calculation is dominated by the (almost perfectly parallel) integrals plus gradients for small numbers of processors, the sequential Fock matrix diagonalization becomes a larger percentage of the calculation as the number of processors is increased. Since matrix diagonalizations are such an important part of electronic structure calculations, an effective treatment of this part of the calculation in parallel computations must be addressed.

**High Energy Species.** The known potential energy surface for *BN prismane* is shown in Figure 1. At the MP2/SBK(d)//RHF/SBK(d) level of theory, BN prismane is 161 kcal/mol higher in energy than the borazene global minimum. Several other minima have been found on this surface, including a planar isomer of borazene that is itself 100 kcal/mol higher in energy than borazene. To date, no direct route from BN prismane to borazene has been found, and all routes leading from BN prismane appear to involve energy barriers in the range of 30-40 kcal/mol. Of particular interest is the pair of three-membered rings shown at the right in the figure. Since these rings lie 40 kcal/mol *above* BN prismane, they may provide a synthetic route to this high energy species. Potential syntheses are being explored at Rockwell Science.

The *tetrasilane-analog of bicyclobutane* has been of interest for several years, since it is predicted by electronic structure theory to exist as two isomers that differ primarily in the length of the bridgehead Si-Si distance, a normal 2.35Å in the short bond (SB) isomer and a much longer 2.9Å in the long bond (LB) isomer. In the unsubstituted compound, the LB isomer is predicted to lower in energy. The only analog that has been synthesized is highly substituted, with *t*-butyl groups replacing the hydrogens at both bridgehead positions. In contrast to the theoretical predictions, only the SB isomer is found for this substituted compound. This difference between theory and experiment is important to understand, since the unsubstituted compound (which has not yet been synthesized), when used as an additive to LOX/LH2 in 2.5 mole % is found to increase the specific impulse by 11 seconds. Therefore, GVB/6-31G(d) calculations were performed on the SB->LB isomerization as a function of the group R in the bridgehead positions. As shown in Figure 2, increasing the size of the bridgehead substituents, destabilizes the LB isomer, relative to the LB isomer. This explains why only the SB isomer is found experimentally. Of particular interest is our prediction that the two isomers of the dimethyl analog are nearly isoenergetic, separated by about a 6 kcal/mol barrier. This suggests that both isomers of the dimethyl compound may be synthesized.

Several high energy isomers of  $N_2O_2$  have been identified on the MCSCF(10,10)/6-31G(d) potential energy surface. Four of these are shown in Figure 3. The most reliable energies are those calculated with multi-reference second order perturbation theory (CASPT2) and the 6-311+G(2d) basis set. At this level of theory, all four isomers are predicted to be about 50-80 kcal/mol higher in energy than 2 NO. It is important to recognize, however, that unusual metastable species frequently have low-lying excited states, and these excited states may well be repulsive. If this is the case, an apparently stable species may be non-adiabatically unstable. Indeed, it has been shown that isomer 4 is non-adiabatically unstable to dissociation to O +  $N_2O^3$ . The non-adiabatic stability of other  $N_2O_2$  isomers is currently under investigation by Yarkony and co-workers and is discussed in a separate abstract. Our most recent calculations have focused on that part of the potential energy surface corresponding to decomposition of isomer 1 to 2 NO. The transition state for this decomposition has been identified, and the minimum energy path determined at both the MCSCF and CASPT2 levels of theory. At the highest level of theory, CASPT2(10,10)/6-311+G(2d)//MCSCF(10,10)/6-31G(d), the barrier to the decomposition is predicted to be 52 kcal/mol with an exothermicity of 49 kcal/mol. The potential energy surfaces for dissociations of the other high energy isomers are currently being explored.

Preliminary calculations have been performed on Van der Waals complexes between main group *metal atoms and clusters of  $H_2$* . Our initial concern is with the ground state potential energy surface, so it is of interest to determine the reliability of single-configuration-based methods for this purpose. Therefore, the first series of calculations were performed on B-- $H_2$  and Li-- $H_2$  with QCISD(T) and the Dunning augmented correlation consistent polarized triple zeta basis set (aug-cc-pVTZ), since both of these species have been investigated by others using multi-reference CI methods. For B-- $H_2$  QCISD(T) predicts a well of 128  $cm^{-1}$ , in comparison with the well of 121  $cm^{-1}$  predicted by MRCI calculations<sup>4</sup>. For Li-- $H_2$  the QCISD(T) well of 9  $cm^{-1}$  compares favorably with the 11  $cm^{-1}$  found by MRCI<sup>5</sup>. These results give us confidence in the accuracy of the predictions for other metals. A potential energy well of 33  $cm^{-1}$  is found for linear Be-- $H_2$ , while the  $C_{2v}$  perpendicular structure is found to be a transition state. Successive additions of  $H_2$  to Be up to four hydrogen molecules is predicted to be additive, with the binding of Be( $H_2$ )<sub>4</sub> predicted to be 132  $cm^{-1}$ . Similar results are found for Al, where the Al-- $H_2$  and Al--( $H_2$ )<sub>4</sub> binding energies are predicted to be 184 and 747  $cm^{-1}$ , respectively. So, Al is a particularly promising metal dopant in solid hydrogen. Other elements appear to be less appealing. Although C has a 324  $cm^{-1}$  well relative to separated C and  $H_2$  on the  $^3A_2$  surface, a barrier of only 10  $cm^{-1}$  separates this well from covalent  $CH_2$  in  $C_{2v}$  symmetry. Distortion of the symmetry is likely to lower this barrier. The analogous well for Si is 720  $cm^{-1}$ . This appears to be quite promising, but the  $^3A_2$  state crosses the  $^1A_1$  state. The latter leads to the ground state of  $SiH_2$ , and it is likely that non-adiabatic interactions between these two states will diminish or remove the stability of the Si-- $H_2$  Van der Waals complex.

## References

1. M.W. Schmidt, K.K. Baldridge, J.A. Boatz, S.T. Elbert, M.S. Gordon, J.H. Jensen, S. Koseki, N. Matsunaga, K.A. Nguyen, S. Su, T.L. Windus, M. Dupuis, and J.A. Montgomery, Jr., *J. Comp. Chem.*, **14**, 1347 (1993).
2. T.L. Windus, M.W. Schmidt, and M.S. Gordon, *Theor. Chim. Acta*, in press.
3. K.A. Nguyen, M.S. Gordon, J.A. Montgomery, Jr., H.H. Michels, and D.R. Yarkony, *J. Chem. Phys.*, **98**, 3845 (1993).



4. M.H. Alexander, J. Chem. Phys., 99, 6014 (1993)

5. D. Konowalow, private communication.

Speed-up (efficiency)

**Proc.**

	int + RHF	1e- grad	2e- grad	total
8	1.0	1.0	1.0	1.0
16	1.87(93.5)	1.89(94.5)	1.98(99.0)	1.84(92.0)
32	3.26(81.5)	1.56(39.0)	3.91(97.8)	3.09(77.2)
64	5.22(65.2)	1.59(19.9)	7.64(95.5)	4.74(59.2)
128	7.77(48.6)	3.19(19.9)	14.74(92.1)	6.74(42.1)
256	10.02(31.3)	3.36(10.5)	27.32(85.4)	8.35(26.1)

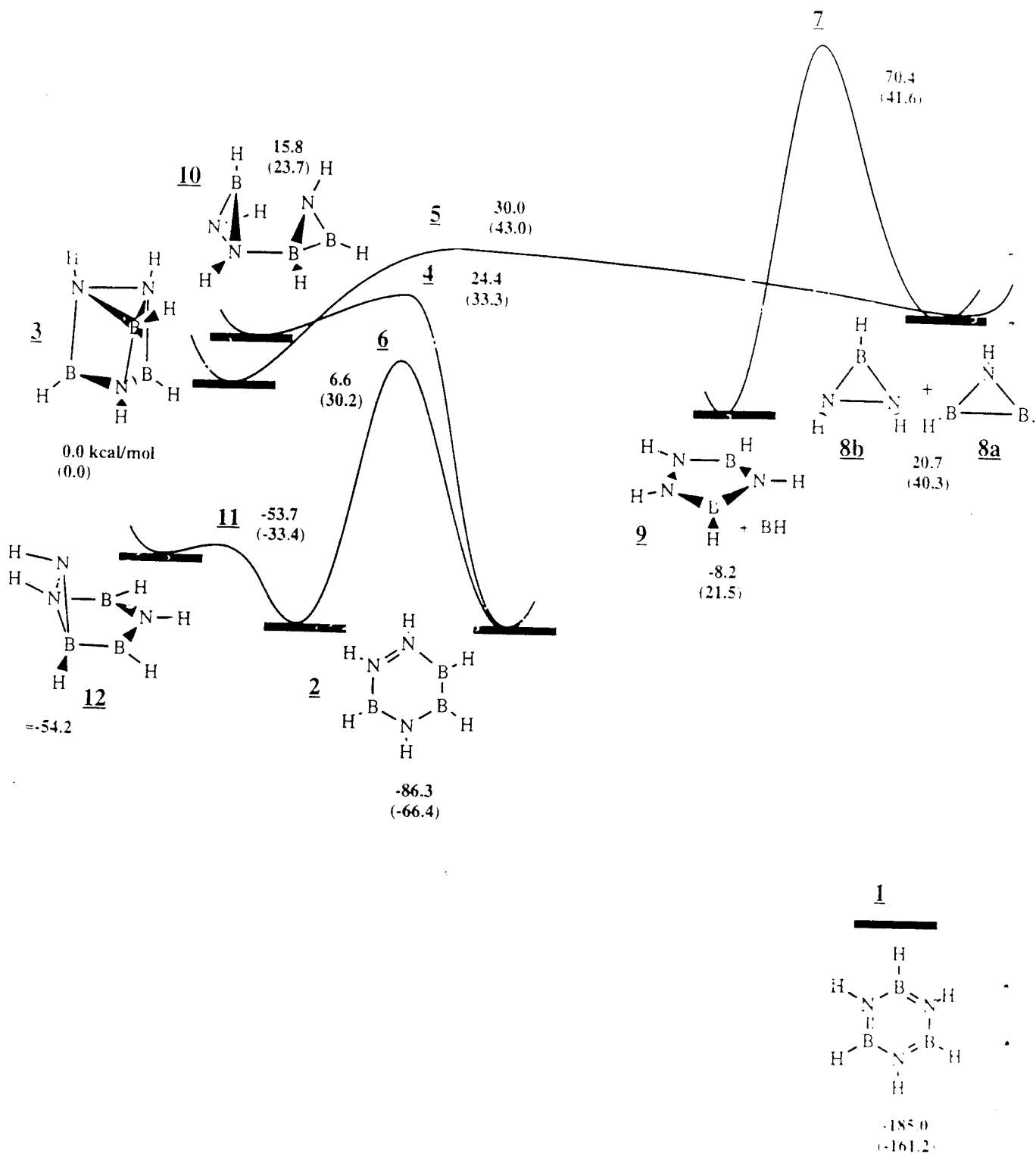
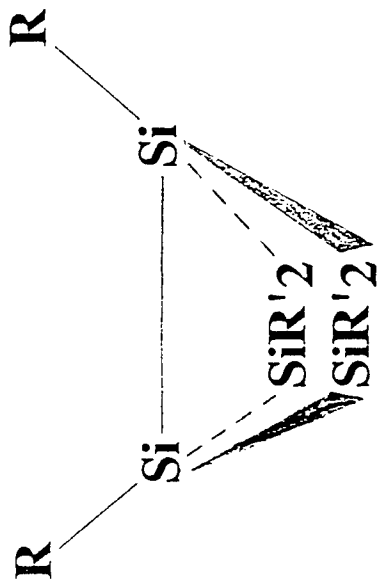


Figure 1. RHF/SBK(d) Potential Energy Surface of B-N Prismane  
 The values are in kcal/mol. The values in parentheses are of MP2  
 relative energies.



R	R'	$E(LB) - E(SB)$ (kcal/mol)	# basis fns
H	H	-9.6	88
CH <sub>3</sub>	H	-1.9	114
$\begin{array}{c} \text{CH}_3 \\   \\ \text{CH}_3\text{-C} \\   \\ \text{CH}_3 \end{array}$	H	$\geq 3.2$	192

Figure 2.  
37.

## N<sub>2</sub>O<sub>2</sub> HIGH ENERGY ISOMERS

MCSCF(10,10)/6-31G(d) geometries (A,deg.) and relative energies (kcal/mol) with reference to 2 NO

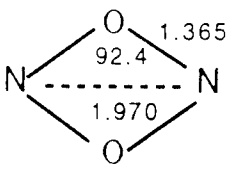
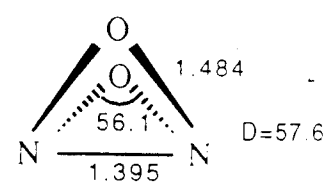
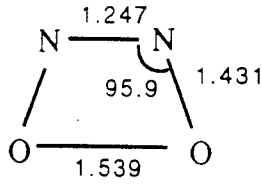
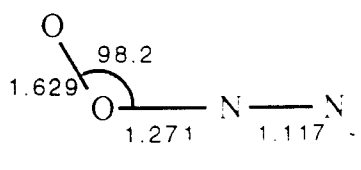
	1. D <sub>2h</sub>	2. C <sub>2v</sub>
		
<b>E rel.</b>		
MCSCF/6-31G(d)	<b>71.0</b>	<b>71.2</b>
CASPT2/6-31G(d)	<b>49.0</b>	<b>77.3</b>
MCSCF/6-311+G(2d)	<b>71.7</b>	<b>73.2</b>
CASPT2/6-311+G(2d)	<b>48.7</b>	<b>81.9</b>
	3. C <sub>2v</sub>	4. C <sub>s</sub>
		
MCSCF/6-31G(d)	<b>43.4</b>	<b>60.3</b>
CASPT2/6-31G(d)	<b>49.4</b>	<b>79.3</b>
MCSCF/6-311+G(2d)	<b>44.4</b>	<b>57.1</b>
CASPT2/6-311+G(2d)	<b>52.9</b>	<b>75.5</b>

Figure 3.

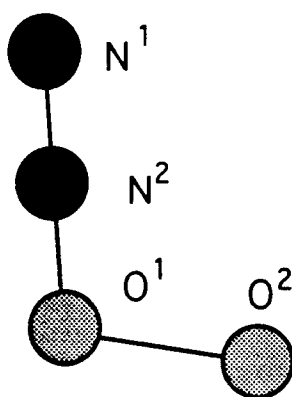
# Theoretical Studies of Nonadiabatic Processes Relevant to the Stability and Detection of Energetic Species

David R. Yarkony  
Department of Chemistry  
Johns Hopkins University  
Baltimore, MD 21218

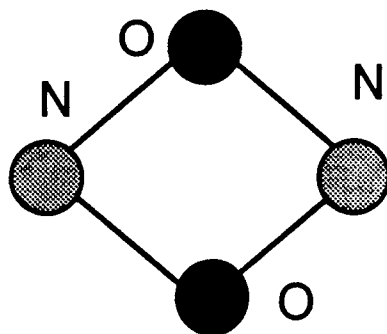
## I. Radiationless decay of geometrical isomers of $N_2O_2$

### Motivation

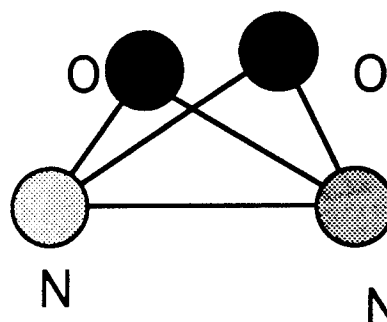
In 1988 Michels and Montgomery<sup>1</sup> characterized the geometric isomer of  $N_2O_2$ ,  $a-N_2O_2$ , pictured below



as potential high energy density material (HEDM). However we subsequently showed<sup>2</sup> that this potential HEDM is in fact rapidly predissociated to  $N_2O + O(^3P)$  through an intersystem crossing with the  $^3A''$  state. Recently Gordon and coworkers<sup>3</sup> identified two additional isomers of  $N_2O_2$  the rhomboidal ( $D_{2h}$ ) and bicyclo ( $C_{2v}$ ) isomers pictured below:



$D_{2h}$  Isomer



Bicyclo  $C_{2v}$  Isomer

as potential HEDMs.

### Computational Studies

Motivated by our previous study of  $\alpha$ -N<sub>2</sub>O<sub>2</sub> we are in the process of studying the stability of these proposed HEDMs with respect to spin-forbidden radiationless decay. The potential decay pathways for these two isomers are interrelated since, as shown by Gordon and coworkers<sup>4</sup> they can interconvert along an approximately C<sub>2v</sub> preserving pathway with a barrier less than 40 kcal/mol. Thus we are considering two modes of spin-forbidden radiationless decay (i) C<sub>s</sub> symmetry decay in which the molecular plane of the D<sub>2h</sub> structure is preserved and (ii) C<sub>s</sub> symmetry decay in which the equivalence of the two oxygens in the bicyclo isomer is preserved. This latter pathway can be interpreted as spin-forbidden predissociation 'along' the bicyclo $\leftrightarrow$ rhomboidal interconversion pathway. The current state of our calculations is summarized below.

For pathway (i) multireference CI calculations using DZP basis sets (4s2p1d) and TZP (6s4p1d) basis sets were used to characterize the ground <sup>1</sup>A' state at the rhomboidal structure and its minimum energy crossing(MEX) with the <sup>3</sup>A'' state in the vicinity of this structure. These calculations were performed at the MRCI level, with only the N and O 1s orbitals kept doubly occupied, in spaces comprised of 357389[1063685]-<sup>1</sup>A' and 794449[2406753]-<sup>3</sup>A'' configuration state functions using the DZP [TZP] bases. A distorted rhombus was identified as the MEX structure. The geometrical parameters and energetics are summarized below:

	Rhomboidal Minimum	MEX( <sup>1</sup> A'- <sup>3</sup> A'') <sup>a</sup>			
R(NN)	3.665[3.664](3.72) <sub>a0</sub>	3.840			
R(NO)	2.543[2.548] (2.580)	2.318	2.447	2.655	3.30
$\angle$ ONO	87.8 [87.6] (87.6)	76.1	102.1		
$\Delta E$	147Kcal/mol	61[~47]			

<sup>a</sup>MEX denotes minimum energy crossing point.  $\Delta E \equiv E(^3A'') - E(^1A')(eq)$ . (eq) denotes the equilibrium geometry of the rhomboidal structure. Energies at crossing structure are degenerate to  $< 1\text{cm}^{-1}$ . Results obtained with TZP basis in []. Geometries from Ref. <sup>4</sup> in ().

For the TZP calculations  $\Delta E$  is reduced by  $\sim 14$  kcal/mol but remains appreciable  $\sim 47$  kcal/mol.

These results show that the  $^1A' \sim ^3A''$  intersystem crossing on pathway (i) will not limit the lifetime of the rhomboidal structure.  $^1A' \sim ^3A'$  intersystem crossing will be considered shortly.

For pathway (ii) the following results have been obtained to date using the DZP basis and FOCI wavefunctions again with only the nitrogen and oxygen 1s orbitals frozen.

	Bicyclo Minimum	MEX( $^1A' - ^3A''$ )		MEX( $^1A' - ^3A'$ ) <sup>a</sup>
R(NN)	3.665(2.636)	3.280		in progress
R(NO)	2.747 (2.804)	4.409	2.497	
R(OO)	3.919	3.477		
$\Delta E$	196 Kcal/mol	184		

<sup>a</sup>MEX denotes minimum energy crossing point.  $\Delta E \equiv E(^3A'') - E(^1A')(eq)$ . (eq) denotes the equilibrium geometry of the bicyclo structure. Energies at crossing structure are degenerate to  $< 1$  cm<sup>-1</sup>. Geometries from Ref. <sup>4</sup> in ().

Clearly a  $^1A' - ^3A''$  intersystem crossing will not limit the lifetime of these species. An assessment of the importance of the ( $^1A' - ^3A'$ ) intersystem crossing for pathway (ii) awaits the results of calculations in progress.

## II. Radiative Decay $BH(a^3\Pi) \rightarrow BH(X^1\Sigma^+)$

$BH(a^3\Pi)$  has been suggested as a possible energy source in an energy transfer chemical laser.<sup>5</sup> The metastable  $a^3\Pi$  state stores approximately 1.3 eV of energy for use in a collisional energy transfer chemical laser system analogous to the oxygen-iodine laser system. In this regard it is desirable to know the fluorescence lifetime of the  $a^3\Pi$  state corresponding to the spin-forbidden dipole-allowed transition,  $a^3\Pi \rightarrow X^1\Sigma^+$ .

The  $a^3\Pi \rightarrow X^1\Sigma^+$  radiative transition is attributable to the spin-forbidden dipole-allowed transition moments connecting the  $a^3\Pi_{\Omega} \Omega = 1, 0^+$  and  $X^1\Sigma_0^+ \Omega = 0^+$  electronic states of the nonrotating molecule, given by

$$\mu_{\perp} \equiv \langle \Psi(a^3\Pi_1) | \mu_{\perp}^e | \Psi(X^1\Sigma_0^+) \rangle \quad 1a$$



$$\mu_{\parallel} \equiv \langle \Psi(a^3\Pi_{0^+}) | \mu_0^e | \Psi(X^1\Sigma_0^+) \rangle \quad . \quad 1b$$

In order to determine the transition moments the wavefunctions,  $\Psi(a^3\Pi_{\Omega})$  and  $\Psi(X^1\Sigma_0^+)$  must be evaluated to first order in perturbation theory as:

$$\Psi(a^3\Pi_1) = \Psi^0(a^3\Pi_1) + \Psi^1(^1\Pi_1, a^3\Pi_1) \quad 2a$$

$$\Psi(a^3\Pi_{0^+}) = \Psi^0(a^3\Pi_{0^+}) + \Psi^1(^1\Sigma_0^+, a^3\Pi_{0^+}) \quad 2b$$

$$\Psi(X^1\Sigma_0^+) = \Psi^0(X^1\Sigma_0^+) + \Psi^1(^3\Pi_{0^+}, X^1\Sigma_0^+) + \Psi^1(^3\Sigma_0^+, X^1\Sigma_0^+) \quad 2c$$

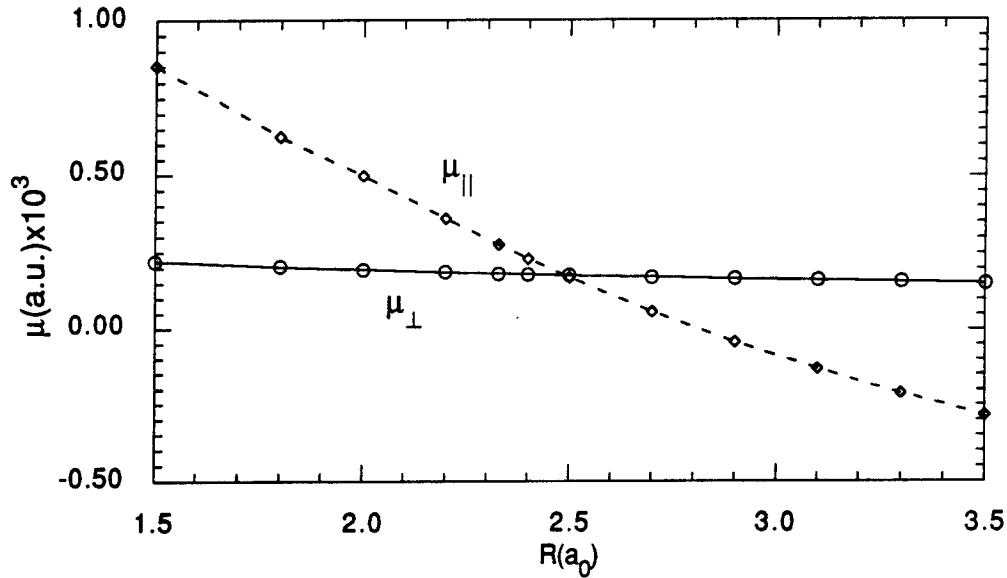
The  $\Psi^1(K,I)$  are determined from :

$$[H^0 - E^0(I)]\Psi^1(K,I) = -H^{so}\Psi^0(I) \quad . \quad 3b$$

rather than the equivalent but computationally intractable eigenstate representation<sup>6</sup>

$$\Psi^1(K,I) = \sum_{J \in K} \frac{H_{IJ}^{so}\Psi^0(J)}{E^0(I) - E^0(J)} \quad . \quad 4$$

The computed  $\mu_i$ <sup>7</sup> are pictured below:



Using this data the radiative lifetime of the the individual fine structure transitions ( $a^3\Pi, v, N, F_i, e/f \rightarrow X^1\Sigma^+$  transitions were determined. The average radiative lifetime was found to be approximately 16 s for  $v = 0 - 3$  with the shortest lifetime being longer than 8 s.

### III. Nonadiabatic Effects in the Electronic Spectra of B<sub>2</sub>

The spectrum of B<sub>2</sub> is relevant to the study of boron containing HEDMs. Brazier and Carrick<sup>8</sup> observed significant deviations from the expected isotopomer relations in the (2<sup>3</sup>Π<sub>g</sub>,v=0) – (A<sup>3</sup>Π<sub>u</sub>,v=0) band, deviations they attributed to perturbations in the 2<sup>3</sup>Π<sub>g</sub> state. The fine structure splitting constant of the 1<sup>3</sup>Π<sub>g</sub> state is of practical importance as its inference was key to a recent assignment<sup>8</sup> of the (2<sup>3</sup>Π<sub>u</sub>,v=0) – (1<sup>3</sup>Π<sub>g</sub>,v=0) band. An avoided crossing of the 1,2<sup>3</sup>Π<sub>g</sub> states is expected to significantly effect the vibrational level dependence of the fine structure splitting constant in both these states.

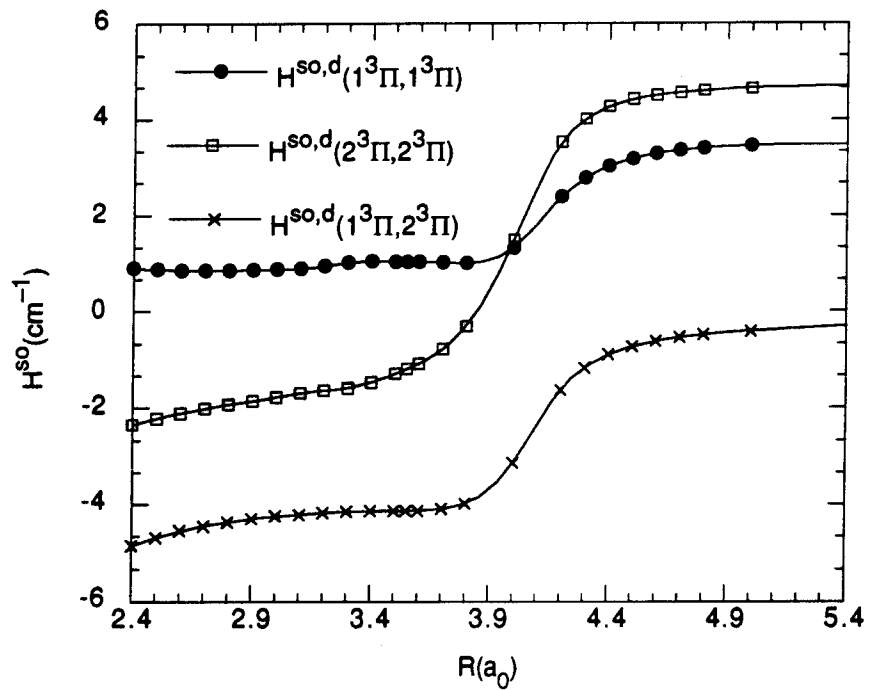
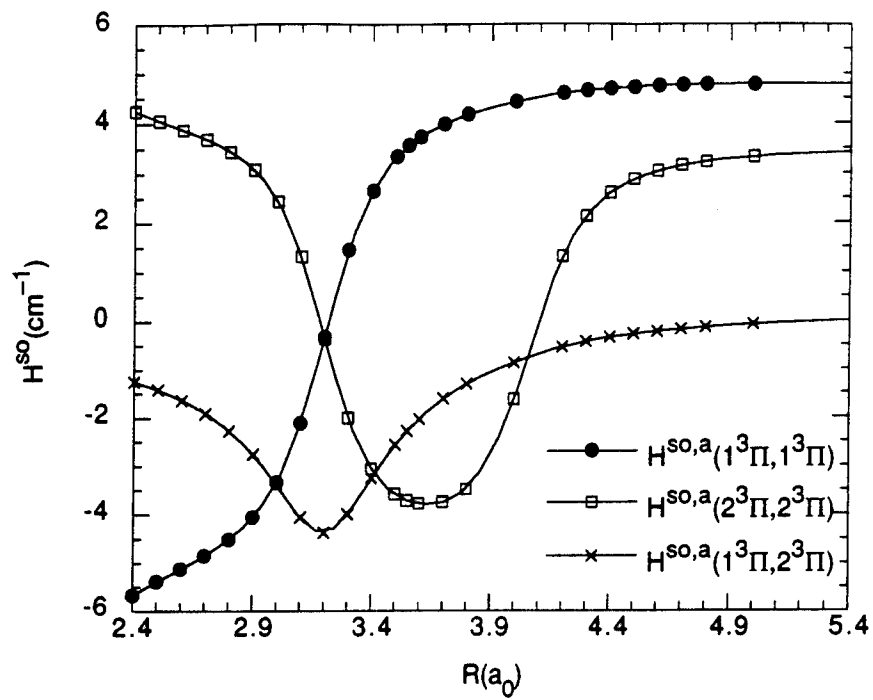
A computational study was undertaken to quantify the nonadiabatic interactions in the 1,2<sup>3</sup>Π<sub>g</sub> states of B<sub>2</sub>.<sup>9</sup> The following calculations were performed. The adiabatic electronic states Ψ<sup>a</sup>(1<sup>3</sup>Π<sub>g</sub>) and Ψ<sup>a</sup>(2<sup>3</sup>Π<sub>g</sub>) and derivative couplings  $f_R^{IJ}(R) \equiv \left\langle \Psi_j^a(\mathbf{r}; R) \left| \frac{d}{dR} \Psi_i^a(\mathbf{r}; R) \right\rangle_r$  were determined using MCSCF/CI wavefunctions. The corresponding diabatic states, defined by

$$\left\langle \Psi_j^d(\mathbf{r}; R) \left| \frac{d}{dR} \Psi_i^d(\mathbf{r}; R) \right\rangle_r = 0, \text{ were determined from}$$

$$\begin{pmatrix} \Psi_i^d(\mathbf{r}; R) \\ \Psi_j^d(\mathbf{r}; R) \end{pmatrix} = \begin{pmatrix} \cos \theta(R) & \sin \theta(R) \\ -\sin \theta(R) & \cos \theta(R) \end{pmatrix} \begin{pmatrix} \Psi_i^a(\mathbf{r}; R) \\ \Psi_j^a(\mathbf{r}; R) \end{pmatrix}$$

with  $\theta(R) - \theta(R_0) = -\int_{R_0}^R f_R^{II}(R) dR$ . Spin-orbit interactions  $H^{\text{so},e}(I,J) =$

$\left\langle \Psi^e(J^3\Pi_g) \left| H^{\text{so}} \right| \Psi^e(I^3\Pi_g) \right\rangle$  were determined in the adiabatic (a=e) basis and transformed to the diabatic basis (e=d). It is interesting to compare  $H^{\text{so},e}(I,J)$  for e = a and e = d. Such a comparison is provided in the figures below. Note that as expected  $H^{\text{so},d}(I,J)$  exhibits a much more limited geometry dependence than does  $H^{\text{so},a}(I,J)$ .



The nuclear motion problem was then solved in the coupled adiabatic and coupled diabatic state bases that is

$$\Psi_{L,J,\Omega,p}(\mathbf{r}, \mathbf{R}) = \sum_{l,v} a_{lv}^{LJ\Omega p} \chi_v^{lJ\Omega}(\mathbf{R}) \Psi_{lJ\Omega p}^{er}(\mathbf{r}; \mathbf{R}) / R \quad , \quad 5$$

was determined where  $\Psi_{lJ\Omega p}^{er}(\mathbf{r}; \mathbf{R})$  is a rotational–electronic function specifying the electronic state  $I_{\Omega} \equiv 2S+1\Lambda_{\Omega}$ , the total angular momentum  $J$ , its body fixed projection  $\Omega$  and the overall parity  $p$ , and  $\chi_v^{lJ\Omega}(\mathbf{R})$  is a single potential energy curve (adiabatic or diabatic) vibrational eigenstate .

The results of the coupled state treatment provide the following values for the fine structure splittings ( $1^3\Pi_g, v=0 - 4$ ):  $-4.2(-4.4), -3.7, -2.8, -1.8, -0.83 \text{ cm}^{-1}$  and ( $2^3\Pi_g, v=0 - 2$ ):  $1.224, 0.767, 0.425 \text{ cm}^{-1}$ . Good agreement with the only available experimental result<sup>8</sup> ( $1^3\Pi_g, v=0$ ) given parenthetically is evident. By comparing the results of the adiabatic and diabatic state treatments it was concluded that while the diabatic basis provides illuminating qualitative insights into the electronic structure of the states in question -as illustrated in the figuresn above, the adiabatic basis is preferred computationally.

## REFERENCES

1. H. H. Michels and J. J. A. Montgomery, *J. Chem. Phys.* **88**, 7248 (1988).
2. K. A. Nguyen, M. S. Gordon, J. A. Montgomery, H. H. Michels, and D. R. Yarkony, *J. Chem. Phys.* **98**, 3845 (1993).
3. K. A. Nguyen, N. Matsunaga, M. S. Gordon, J. A. Montgomery, and H. H. Michels, in preparation.
4. K. A. Nguyen, M. S. Gordon, and J. A. Boatz(1994).
5. D. J. Benard *Abstracts of the High Energy Density Materials Contractors Meeting*, 1993, 200.
6. D. R. Yarkony, *Int. Reviews of Phys. Chem.* **11**, 195 (1992).
7. L. A. Pederson, H. Hettema, and D. R. Yarkony, *J. Phys. Chem* (1994).
8. C. R. Brazier and P. G. Carrick, *J. Chem. Phys.* **96**, 8683 (1992).
9. M. R. Manaa and D. R. Yarkony, *J. Chem. Phys.* (1994).

## Laser and Fourier Transform Spectroscopy of Novel Propellant Molecules

Peter Bernath  
Department of Chemistry  
University of Waterloo  
Waterloo, Ontario, Canada N2L 3G1

and

Department of Chemistry  
University of Arizona  
Tucson, Arizona 85721 USA

A variety of molecules important as potential advanced propellants were studied by high resolution Fourier transform emission spectroscopy. It is proposed to make high energy density materials (HEDM) in a high temperature carbon furnace.

### A. Vibration-Rotation Emission Spectroscopy: AlCl, HCl, AlH, AlD, BF, AlF

One promising scheme for boosting the performance of the hydrogen/oxygen propellant system is to trap light metal atoms or metal hydrides in solid hydrogen. We are exploring the chemical interaction of light metals such as aluminum with hydrogen at high temperatures by Fourier transform emission spectroscopy. We find high resolution emission spectroscopy to be a very sensitive diagnostic tool for high temperature chemistry.

In order to trap a metal atom in solid hydrogen, it first must be vaporized probably in the presence of hydrogen gas. Our gas phase studies are, therefore, the first steps in any practical trapping scheme.

Aluminum powder is currently used in conventional solid propellants and Al atoms are a very favorable additive to solid hydrogen. Aluminum liquid and aluminum vapors are very corrosive, but we have found that a carbon liner protects the alumina furnace tube at high temperatures. At 1550°C aluminum and hydrogen react to give AlH in the gas phase<sup>1</sup> with no

LiH & LiD

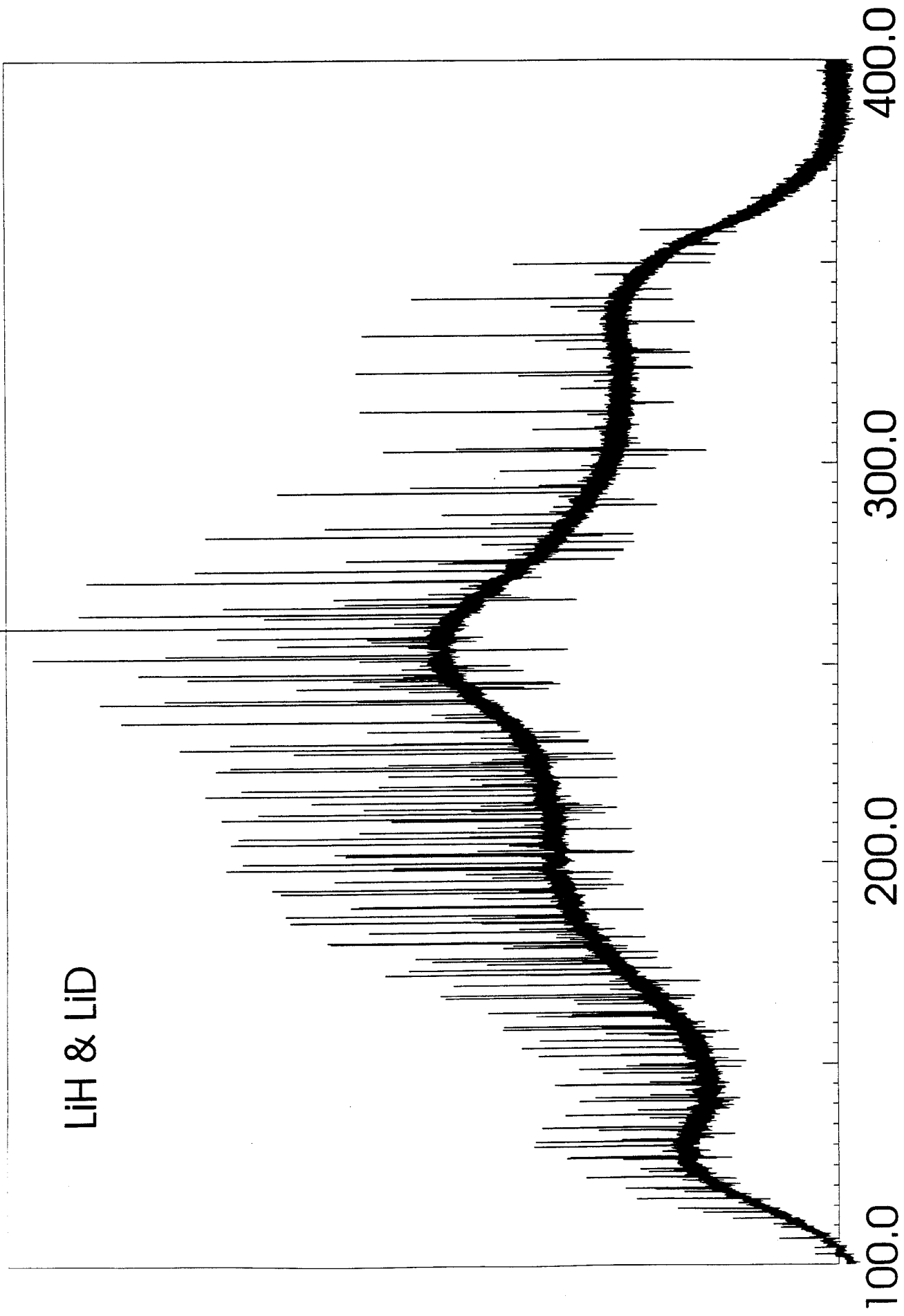


FIGURE 1

evidence for the formation of  $\text{AlH}_2$  or  $\text{AlH}_3$ . The remarkably strong  $\text{AlH}$  emission allowed the line positions to be measured with a precision of  $\pm 0.0001 \text{ cm}^{-1}$  (in the most favorable cases) with our Bruker IFS 120 spectrometer at Waterloo. This precision is unprecedented for an unstable molecule such as  $\text{AlH}$ . Similar experiments were carried out on  $\text{AlD}^1$  as well as  $\text{BF}$  and  $\text{AlF}$ . These molecules were measured to test our new data reduction methods (see below).

The long wavelength limits of our emission technique were explored by recording the vibration-rotation spectrum of  $\text{AlCl}^2$  and the pure rotational spectrum of hot  $\text{HCl}^3$  at 20 microns. Both  $\text{HCl}$  and  $\text{AlCl}$  are observed in the plumes of rockets burning aluminized solid propellants with an ammonium perchlorate oxidizer.

#### B. Pure Rotational Emission Spectroscopy: $\text{LiH}$

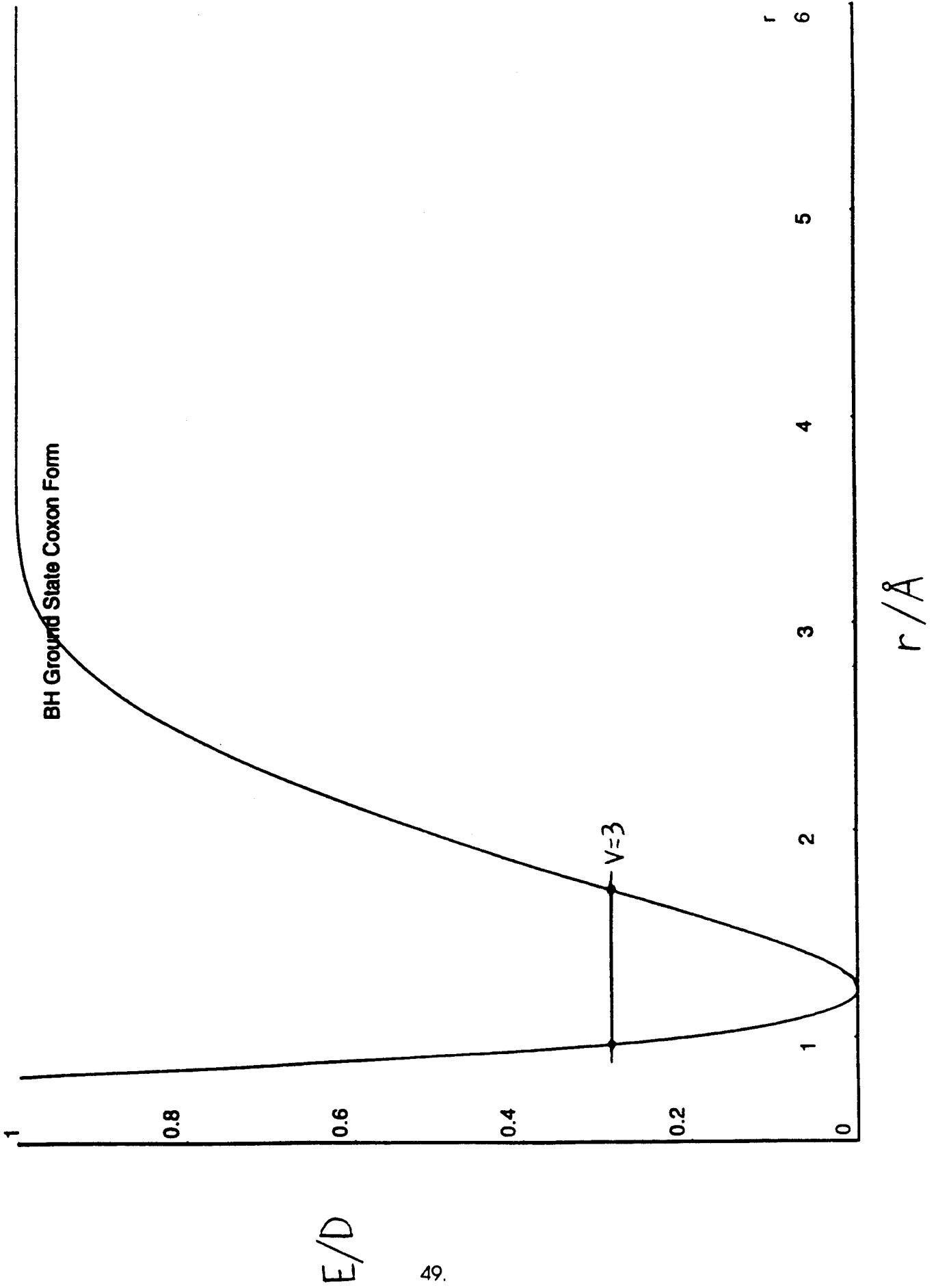
Following our detection of the pure rotational emission spectra of the stable molecules  $\text{HCl}$  and  $\text{HF}^3$ , we tried this technique on the transient molecule  $\text{LiH}$ . We recorded improved  $\text{LiH}$  spectra in the  $100\text{-}400 \text{ cm}^{-1}$  range after we inadvertently recorded some  $\text{LiH}$  impurity spectra during a failed attempt to find  $\text{LiAl}$ . The far infrared spectra of  $\text{LiH}$  are very extensive (Figure 1) and have an excellent signal-to-noise ratio.

#### C. "New" Data Reduction Techniques

We typically measure thousands of line positions for a molecule, but we would like to represent these data in a more compact form. Spectroscopists traditionally fit their data to polynomials to extract spectroscopic constants. However, the most physically meaningful quantity is the potential energy curve. With accurate potential energy curves (and dipole moment functions) all spectra could be calculated. Moreover the potential energy curves are the key ingredients for any simulation of the physical properties in a condensed state.

We are directly fitting the experimental data to the eigenvalues of the Schrödinger

FIGURE 2





equation ("inverse perturbation approach"). The Schrödinger equation is solved numerically using a parameterized modified-Morse potential energy function of the form<sup>2</sup>

$$V(r) = D_e (1 - e^{-\beta(r)})^2 / (1 - e^{-\beta(r_\infty)})^2$$

with

$$\beta(r) = z(\beta_0 + \beta_1 z + \beta_2 z^2 + \dots) \text{ and } z = (r - r_e)/(r + r_e).$$

Corrections for Born-Oppenheimer breakdown are made by adding mass-dependent terms to  $V(r)$ . This approach is a modification of one proposed by Coxon. The potential energy function obtained for BH is drawn in Figure 2. The last vibrational level for which there is data is  $v=3$  so that it is proposed to extend the data set by working at very high temperatures.

The advantage of our approach is that the potential energy function,  $V(r)$ , is quantitatively correct for the lower part of the curve (Figure 2) where we have spectroscopic data and is qualitatively correct for the upper part of the curve. Our approach is also capable of incorporating all the available information and represents the "best" potential curve.

#### D. Large Scale Production of HEDM

One advantage of the production of a high energy density material in a furnace is that technology can be applied on both a laboratory or an industrial scale. One possible HEDM production scheme is illustrated in Figure 3. The starting material such as boron or carbon could be introduced into the furnace as powder mixed with hydrogen. After the desired species form in the furnace they are diluted rapidly with cold He and deposited on a cold surface. The HEDM/solid hydrogen mixture is mechanically removed and stored. The problem with such a scheme is the enormous thermal load placed on the cryogenic part of the apparatus by the use of an oven. Our work is aimed at testing the feasibility of using high temperature furnaces to

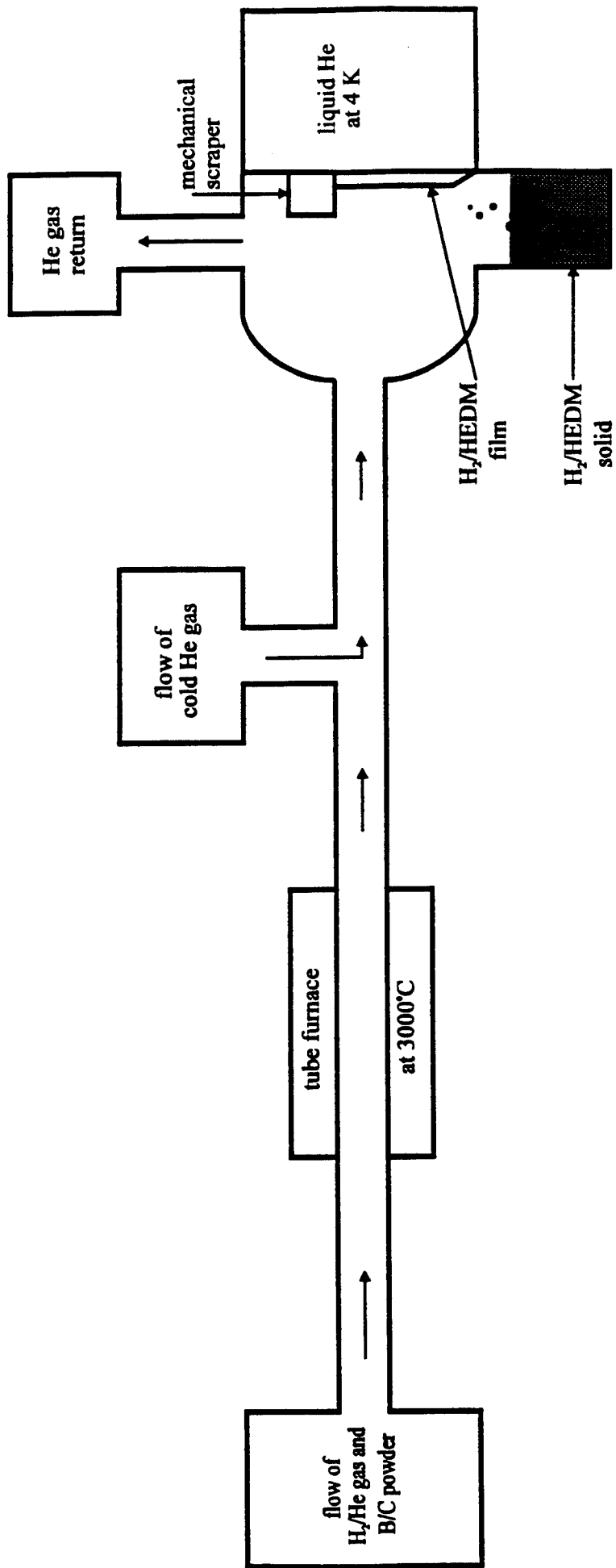


FIGURE 3: Proposed scheme for the large scale production of HEDM.

create new high energy density materials.

#### References

1. J.B. White, M. Dulick and P.F. Bernath, *J. Chem. Phys.* **99**, 8371 (1993).
2. H.G. Hedderich, M. Dulick and P.F. Bernath, *J. Chem. Phys.* **99**, 8363 (1993).
3. R.B. LeBlanc, J.B. White and P.F. Bernath, *J. Mol. Spectrosc.* **164**, 574 (1994).

# Cubane and Derivatives as Combustion Modifiers. Synthetic Results

*Robert M. Moriarty and M. Rao*

Cubane,  $C_8H_8$ , is a high density, high energy substance of considerable interest as a fuel or fuel additive. Application studies of this material have been hampered by the unavailability via synthesis of multi kilogram quantities. We have recently modified the Eaton synthesis using visible light and pyrex reactors in the place of ultraviolet irradiation using quartz components. This modification potentially allows for the production of sufficient cubane for broad scale evaluation. In collaboration with C.K. Law at Princeton the occurrence of microexplosions in fuels using added 1,4 - dicarboxycubane monoethyl ester has been observed. This result opens up the possibility of designing a superior additive either in the form of an alkylcubane or an alkylazidocubane. The synthesis and properties of these type compounds will be presented.

# NOVEL HIGH ENERGY COMPOUNDS

*Karl O. Christe and W.W. Wilson*

*Rocketdyne Division of Rockwell International Corporation, Canoga Park, CA 91309*

This paper describes our effort from June 1993 through August 1993, when this contract ended. The main objective of the study was to explore the synthesis of novel high energy compounds for HEDM applications.

Salts containing the  $F_3^-$  anion would be of significant interest for storing elemental fluorine in a safe manner, for solid propellant  $F_2$  gas generators, and for use as a fluorinating agent. Therefore, efforts were made to explore the possibility of preparing  $F_3^-$  salts.

The trifluoride anion,  $F_3^-$ , has been the subject of numerous theoretical calculations [1-4] ranging from SCF (Self Consistent Field) to CCSDT (Coupled Cluster Single Double Triple). The most sophisticated methods [3] duplicated well the vibrational frequencies which were observed [5] by Ault and Andrews for the  $Cs^+F_3^-$  and  $Rb^+F_3^-$  ion pairs in argon matrices at 15K. The best estimates for the stability of  $F_3^-$  indicate that  $F_3^-$  is thermodynamically more stable than  $(F_2 + F^-)$  by about  $110\text{kJ mol}^{-1}$  [3]. This value is comparable to those found for  $Br_3^-$  ( $D_0 = 105\text{kJ mol}^{-1}$ ) and  $I_3^-$  ( $D_0 = 109\text{kJ mol}^{-1}$ ) and larger than that of  $Cl_3^-$  ( $D_0 = 75\text{kJ mol}^{-1}$ ). Since the  $Cl_3^-$ ,  $Br_3^-$  and  $I_3^-$  anions are all well known, both in solution and in the solid state, and anhydrous  $N(CH_3)_4F$  provides a source of soluble fluoride anions in the presence of a large and oxidizer resistant cation [6], it was interesting to examine whether  $N(CH_3)_4^+F_3^-$  can be prepared on a macroscopic scale using experimental techniques which recently provided novel anions such as  $XeF_5^-$  [7],  $IOF_6^{2-}$  [8],  $TeOF_6^{2-}$  [9],  $PF_4^-$  [10] or  $ClF_6^-$  [11].

The possibility of preparing  $\text{N}(\text{CH}_3)_4^+\text{F}_3^-$  was examined by pressurizing solutions of  $\text{N}(\text{CH}_3)_4^+\text{F}^-$  with up to five hundred torr of  $\text{F}_2$  in either  $\text{CH}_3\text{CN}$  at  $-31^\circ\text{C}$  or  $\text{CHF}_3$  at  $-142^\circ\text{C}$  (Caution! These experiments are potentially hazardous and appropriate safety precautions must be used at all times). The resulting mixtures were gently agitated for about two hours, followed by removal of all material, volatile at these low temperatures, in a dynamic vacuum. The solid residues were then allowed to warm in the closed Teflon-FEP reaction vessels to room temperature. No fluorine evolution was observed during these warm-up steps. The nonvolatile residues were characterized by the observed material balances and vibrational spectra. In the case of the  $\text{CHF}_3$  solution, the low-temperature product was the known [6]  $\text{N}(\text{CH}_3)_4^+\text{F}^- \cdot n\text{CHF}_3$  adduct which decomposed at higher temperature to  $\text{N}(\text{CH}_3)_4\text{F}$  and  $\text{CHF}_3$ . In the case of the  $\text{CH}_3\text{CN}$  solution, the solid product was  $\text{N}(\text{CH}_3)_4^+\text{HF}_2^-$  formed by slow attack of the solvent by both  $\text{F}_2$  and  $\text{F}^-$  [12]. The absence of an oxidizing species in the solid products was also demonstrated by their inability to liberate iodine from aqueous KI solutions.

These results demonstrate that, in spite of the large and strongly stabilizing  $\text{N}(\text{CH}_3)_4^+$  counter ion,  $\text{N}(\text{CH}_3)_4^+\text{F}_3^-$  is not stable at temperatures as low as  $-142^\circ\text{C}$ . The failure of  $\text{F}_3^-$  formation under the above conditions, in spite of the bond energy of  $\text{F}_2$  and the dissociation energy of  $\text{F}_3^-$  being comparable to those of  $\text{I}_2$  and  $\text{I}_3^-$ , respectively, is surprising and might be attributed to the high solvation energies of  $\text{F}^-$  in highly polar solvents, such as  $\text{CHF}_3$  or  $\text{CH}_3\text{CN}$ . Reactions between  $\text{N}(\text{CH}_3)_4\text{F}$  and  $\text{F}_2$  in the absence of a solvent were not studied due to experimental difficulties encountered with controlling the reaction.

The second area of interest were tetravalent mercury compounds. Recent ab initio calculations [13] predicted that  $\text{HgF}_4$  might be stable and preparable from  $\text{HgF}_2$  and  $\text{KrF}_2$ .  $\text{HgF}_4$  would be the first group IIb compound with an oxidation state higher than +II and would be of interest as either a fluorinating agent or an ingredient for high energy density batteries. The  $\text{HgF}_2$ - $\text{KrF}_2$  system in HF solution was studied but did not yield any

evidence for the formation of  $\text{HgF}_4$ . Similarly, efforts to stabilize the +IV oxidation state by formation of the  $\text{HgF}_6^{2-}$  anion were unsuccessful. When an intimate mixture of  $2\text{CsCl}$  and  $\text{HgCl}_2$  was fluorinated at  $160^\circ\text{C}$  with 1200 psi of  $\text{F}_2$ , the only reaction products were  $\text{ClF}_5$  and  $\text{Cs}_2\text{HgF}_4$ .

The synthesis of  $\text{ClF}_5\text{O}$  was further pursued.  $\text{ClF}_5\text{O}$  is expected to be stable and would be the highest performing earth-storable liquid rocket oxidizer with an  $I_{sp}$  improvement of about 10 seconds over that of  $\text{ClF}_5$ , the highest performing presently known liquid oxidizer. The synthesis of  $\text{ClF}_5\text{O}$  has been attempted by us and others for more than 25 years.

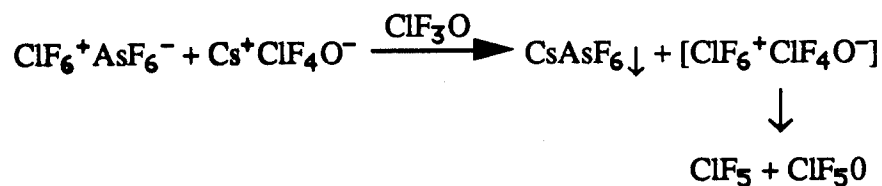
A hot wire reactor which was originally developed in Russia [14], was built and checked out for the production of  $\text{KrF}_2$ . Production rates of about 500mg  $\text{KrF}_2$  per hour were achieved. Attempts to oxidatively fluorinate either  $\text{FClO}_2$  or  $\text{ClF}_3\text{O}$  to  $\text{ClF}_5\text{O}$ , however, have been unsuccessful so far. Higher reaction temperatures might be required and attempts will be made to modify the reactor accordingly.

Other attempts at the synthesis of  $\text{ClF}_5\text{O}$  involved the fluorination reaction of  $\text{ClF}_3\text{O}$  with  $\text{KrF}_2$  in HF solution. However, instead of oxidative fluorination of the chlorine central atom, the following oxygen-fluorine exchange reaction was observed.



This result suggests that fluorination of  $\text{ClF}_3\text{O}_2$  with  $\text{KrF}_2$  might offer a potential route to  $\text{ClF}_5\text{O}$ . Although  $\text{ClF}_3\text{O}_2$  is known [15], its reported synthesis is extremely difficult and an improved synthesis will be required for studying its reaction chemistry. An attempt was made to improve on the reported synthesis from  $\text{FClO}_2$  and  $\text{PtF}_6$  by using HF as a solvent and  $\text{KrF}_2$  as an additional fluorinating agent. However, the only observed product was  $\text{ClO}_2^+\text{PtF}_6^-$  and none of the desired  $\text{ClO}_2\text{F}_2^+\text{PtF}_6^-$ .

Another approach toward ClF<sub>5</sub>O, which we investigated, involved a metathetical reaction between ClF<sub>6</sub><sup>+</sup>AsF<sub>6</sub><sup>-</sup> and Cs<sup>+</sup>ClF<sub>4</sub>O<sup>-</sup> in ClF<sub>3</sub>O solution. Instead of the desired reaction,



the following displacement reaction occurred.

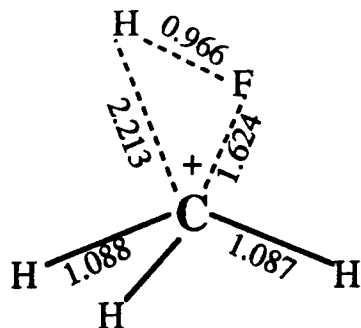


The reaction will be repeated in ClF<sub>5</sub> solution which does not displace ClF<sub>6</sub><sup>+</sup> from its salts.

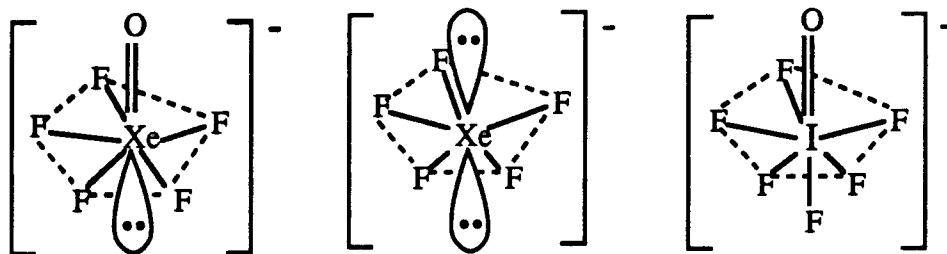
Our computations on azidamines, a new class of highly energetic polynitrogen compounds, were completed in collaboration with Drs. H. Michels, J. Montgomery, and D. Dixon. It is predicted that N(N<sub>3</sub>)<sub>2</sub><sup>-</sup>, HN(N<sub>3</sub>)<sub>2</sub>, N(N<sub>3</sub>)<sub>3</sub>, and N(N<sub>3</sub>)<sub>4</sub><sup>+</sup> are all vibrationally stable and that their energy barriers toward N<sub>2</sub> elimination are comparable to that of FN<sub>3</sub>, i.e., ~45 to 60 kJ/mol.

In collaboration with Prof. Olah's group from USC, the electrophilic fluorination of CH<sub>4</sub> was studied, both experimentally and by ab initio calculations. Since a naked "F<sup>+</sup>" is not available on a macroscopic scale, N<sub>2</sub>F<sup>+</sup> and NF<sub>4</sub><sup>+</sup> salts which were developed under this program were used as "F<sup>+</sup>" substitutes. The experimental data agree with our expectations for an electrophilic reaction and the theoretical calculations support a mechanism involving a direct "F<sup>+</sup>" insertion into a C-H bond resulting in a 2e-3c bonded pentacoordinate carbonium ion intermediate.





The  $\text{XeOF}_5^-$  anion was successfully combined with the  $\text{N}(\text{CH}_3)_4^+$  cation to form a salt which is thermally stable up to  $\sim 145^\circ\text{C}$  but which is highly friction and shock sensitive. In collaboration with Prof. Schrobilgen's group, the salt was characterized. Theoretical calculations, carried out by Dr. Dixon, and the experimentally observed vibrational spectra show that  $\text{XeOF}_5^-$  has a pseudo-pentagonal bipyramidal structure of symmetry  $\text{C}_{5v}$  which is analogous to those previously found for  $\text{XeF}_5^-$  [7] and  $\text{IOF}_6^-$  [8].



## REFERENCES

1. P.A. Cahill, C.E. Dykstra, and J.C. Martin, *J. Am. Chem. Soc.*, **107** (1985) 6359.
2. J.J. Novoa, F. Mota, and S. Alvarez, *J. Phys. Chem.*, **92** (1988) 6561.
3. G.L. Heard, C.J. Marsden, and G.E. Scuseria, *J. Phys. Chem.*, **96** (1992) 4359.
4. C. Sosa, C. Lee, G. Fitzgerald, and R.A. Eades, *Chem. Phys. Letters*, **211** (1993) 265.
5. B.S. Ault and L. Andrews, *Inorg. Chem.*, **16** (1977) 2024, and *J. Am. Chem. Soc.*, **98** (1976) 1591.

6. K.O. Christe, W.W. Wilson, R.D. Wilson, R. Bau, and J. Feng, *J. Am. Chem. Soc.*, **112** (1990) 7619.
7. K.O. Christe, E.C. Curtis, D.A. Dixon, H.P. Mercier, J.C.P. Sanders, G.J. Schrobilgen, and W.W. Wilson, *J. Am. Chem. Soc.*, **113** (1991) 3351.
8. K.O. Christe, D.A. Dixon, A.R. Mahjoub, H.P.A. Mercier, J.C.P. Sanders, K. Seppelt, G.J. Schrobilgen, and W.W. Wilson, *J. Am. Chem. Soc.*, **115** (1993) 2696.
9. K.O. Christe, D.A. Dixon, J.C.P. Sanders, G.J. Schrobilgen, and W.W. Wilson, *Inorg. Chem.*, **32** (1993) 4089.
10. K.O. Christe, W.W. Wilson, H.P.A. Mercier, J.C.P. Sanders, G.J. Schrobilgen, and W.W. Wilson, *J. Am. Chem. Soc.*, in press.
11. K.O. Christe, W.W. Wilson, R.V. Chirakal, J.C.P. Sanders, and G.J. Schrobilgen, *Inorg. Chem.* **29** (1990) 3506.
12. W.W. Wilson, K.O. Christe, J. Feng, and R. Bau, *Can. J. Chem.*, **67** (1989) 1898.
13. M. Kaupp and H.G. von Schnering, *Angew. Chem. Int. Ed. Engl.*, **32** (1993) 861.
14. V.N. Bezmel'nitsyn, V.A. Legasov, and B.B. Chaivonov, *Dok. Akad. Nauk. SSSR*, **235** (1977) 96.
15. K.O. Christe, *Inorg. Nucl. Chem. Lett.*, **8** (1972) 457; K.O. Christe and R.D. Wilson, *Inorg. Chem.*, **12** (1973) 1356; K.O. Christe and E.C. Curtis, *Inorg. Chem.*, **12** (1973) 2245.

# Progress Towards the Synthesis of Polymeric Nitrogen

Hector E. Lorenzana, A. K. McMahan, C. S. Yoo, and T. W. Barbee, III  
Lawrence Livermore National Laboratory  
Livermore, CA 94551

## Introduction

Current conventional energetic compounds rely on strong covalent bonds within individual molecules for energy storage. A new class of energetic compounds has been recently proposed that entirely replaces weak van der Waals interactions with strong covalent bonds arranged in a continuous, uniform network, thus tremendously enhancing the energy per volume. In particular, recent theoretical calculations have suggested that a phosphorus-like or polymeric form of nitrogen may exist metastably at atmospheric pressure as a hard, insulating solid with an enhanced energy per unit volume.<sup>1-3</sup> It is predicted that the polymeric phase of nitrogen should be stable at high pressure, and therefore the megabar diamond anvil cell might provide the ideal vehicle for carrying out proof-of-existence experiments. Currently, we are bringing to bear technologies for achieving multimegabar pressures and temperatures of several thousand K.<sup>4</sup> These conditions are necessary to rearrange the bonds of strongly covalent systems into highly energetic configurations. There is no doubt that the transformations will show strong hysteresis making the initial synthesis difficult, but for these very same reasons, these new compounds potentially will be metastable at ambient conditions in their energetic state. We discuss our results and progress to date, indicating that we are well on our way to understanding the high pressure equation-of-state of solid N<sub>2</sub>.

## Background

The low pressure phases of N<sub>2</sub> have been characterized amply and are believed to be well-understood from theoretical considerations.<sup>3, 5-12</sup> At pressures greater than a few 10's of GPa, knowledge of the structures of N<sub>2</sub> becomes much more sketchy. Tentative structural identifications have been proposed based on low temperature Raman data to 52 GPa (Fig. 1).<sup>10</sup> Since many N<sub>2</sub> phases are stable only at low temperature, the phase diagram at room temperature is markedly different.<sup>9</sup> A transition from a cubic disordered ( $\delta$ ) to a rhombohedral ordered ( $\epsilon$ ) phase occurs at 18 GPa. Identification is based on Raman as well as X-ray diffraction data. At the slightly higher pressure of 22 GPa, a new phase ( $\eta$ ) has been reported based on Raman vibrational (vibron) modes.<sup>10</sup> X-ray diffraction patterns do not demonstrate a transition at this pressure.<sup>12</sup> X-ray and Raman vibron and lattice (phonon) measurements suggest no transitions up to 44 and 54 GPa respectively.<sup>9, 12</sup> Based only on Raman vibron determinations extending to 110 GPa, transitions at 66 GPa ( $\eta \rightarrow \theta$ ) and at 100 GPa ( $\theta \rightarrow \iota$ ) have been reported.<sup>7</sup> These high pressure crystalline structures have not been established experimentally. Theoretically, various high-pressure molecular phases have

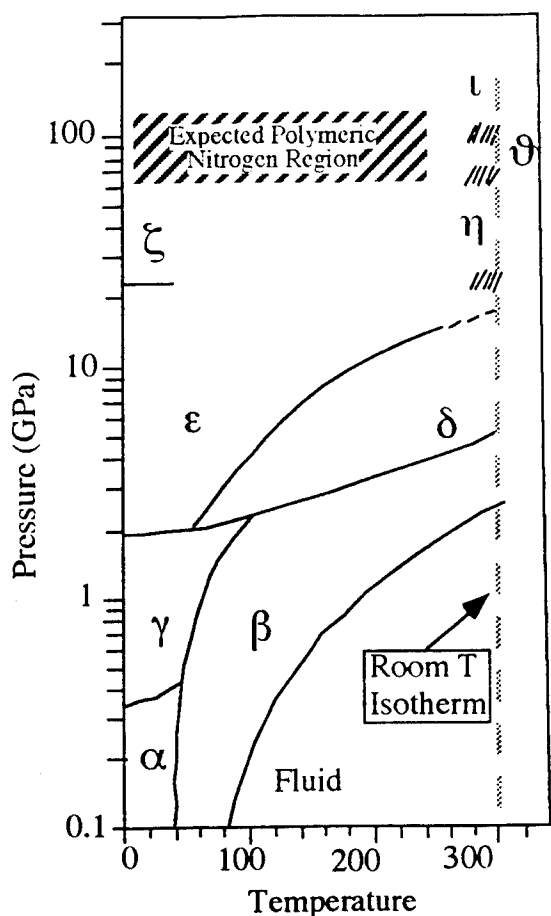


Fig. 1 Phase diagram of nitrogen. (Adapted from Ref. 9)

been studied with the  $\epsilon$  phase found to be the preferred form above 2 GPa at low temperature in agreement with experiment.<sup>13</sup> Recently calculations suggest that at about 65 GPa, nitrogen will undergo a molecular to polymeric transition. This phase is predicted to be insulating.<sup>1-3</sup>

## Results

We report new Raman vibron and phonon results that, while consistent with previously published data, demonstrate new phenomena and subtleties in the high-pressure behavior of  $N_2$ . Specifically, our Raman data do not support the previously identified transitions at 66 GPa and 100 GPa.<sup>7</sup> On the other hand, extremely low-intensity vibron peaks about two orders of magnitude less than the fundamental demonstrate that a completely new and unexpected transition occurs in  $N_2$  at about 70 GPa. This newly measured phase probably involves a minor crystallographic rearrangement of the molecules.

Raman scattering has proven to be an indispensable probe for high-pressure research.  $N_2$  exhibits two manifolds of Raman active modes, internal (vibrons at  $\sim 2400$   $cm^{-1}$ ) and lattice (phonons at  $\sim 100$   $cm^{-1}$ ) vibrational modes. Both sets of modes have

been used to identify phase transitions in molecular solids including  $N_2$ . The power of characterizing both the phonons and vibrons can be exemplified by the  $\delta \rightarrow \epsilon$  and the  $\epsilon \rightarrow \eta$  transitions in  $N_2$  where *one* of the sets of modes exhibit changes but *not* the other. First-principles theoretical calculation of both sets of modes can also provide additional insight constraining structural identification.<sup>14</sup>

Our primary goal for these experiments was to characterize the nature of the high-pressure phase transitions in  $N_2$ . Consequently, we have reproduced previous measurements, and though we obtain very similar data, there are enough differences that we arrive at very different conclusions. According to X-ray diffraction measurements, an  $R\bar{3}c$ -like structure is stable with increasing pressure up to 44 GPa.<sup>12</sup> The  $R\bar{3}c$  structure allows three distinct Raman-active vibron modes, although it is usually assumed that the two modes arising from counterparts of the  $\delta$ -phase disk sites are essentially degenerate, an assumption which is not borne out in recent theoretical calculations.<sup>14</sup> Nevertheless, a third vibron peak (a shoulder on the low frequency vibron peak) at 22 GPa has been interpreted as indicating the onset of the  $\epsilon \rightarrow \eta$  phase transition.<sup>10</sup> The crystalline structure of the  $\eta$  phase is unknown but clearly is a close relative of the  $R\bar{3}c$  structure. The phonons show no measurable change across this pressure range implying no major symmetry change, consistent with x-ray measurements.

With increasing pressure, we find that vibron peaks split in a continuous fashion possibly starting as low as  $\sim 25$  GPa.<sup>9</sup> Since the X-ray data show no phase transformation in this pressure range and since the splitting appears continuous rather than abrupt, we interpret this splitting as resulting from growing crystal field interactions and implying no sudden symmetry change. In fact, we infer *no phase transitions* until  $\sim 70$  GPa, since there are no discontinuous splittings or intensity changes in the vibrational modes, in contrast to previous reports (Fig. 2).<sup>7</sup> Our phonon measurements support our conclusions, as the modes show no obvious discontinuity in intensity or frequency.

At about 70 GPa, we observe very low intensity structure in the vibrational spectrum that appear discontinuously. These new peaks are emphasized in Fig. 3. The peak marked by an asterisk is the  $N_{14}$ - $N_{15}$  vibrational mode, the  $N_{15}$  atom occurring at a 0.37% abundance. This structure is being interpreted as evidence for a new phase transition, though because the major vibron and phonon branches do not show obvious changes, we interpret the transition as involving a minor crystallographic rearrangement. One possibility is the doubling of the previous unit cell, which would permit previously forbidden modes to become Raman active. X-ray scattering results support our conclusion that a phase transition occurs in this pressure range.<sup>11</sup> We measure no changes in the phonon spectra across this pressure range.

Lastly, we observe no discontinuous changes in intensity or frequency in both the vibron and phonon modes up to 130 GPa. Previous identifications of a transition occurring at 100 GPa reported discontinuous behavior in intensities (the disappearance of a peak) in the vibron spectra. We observe no evidence for a phase transition occurring at 100 GPa.

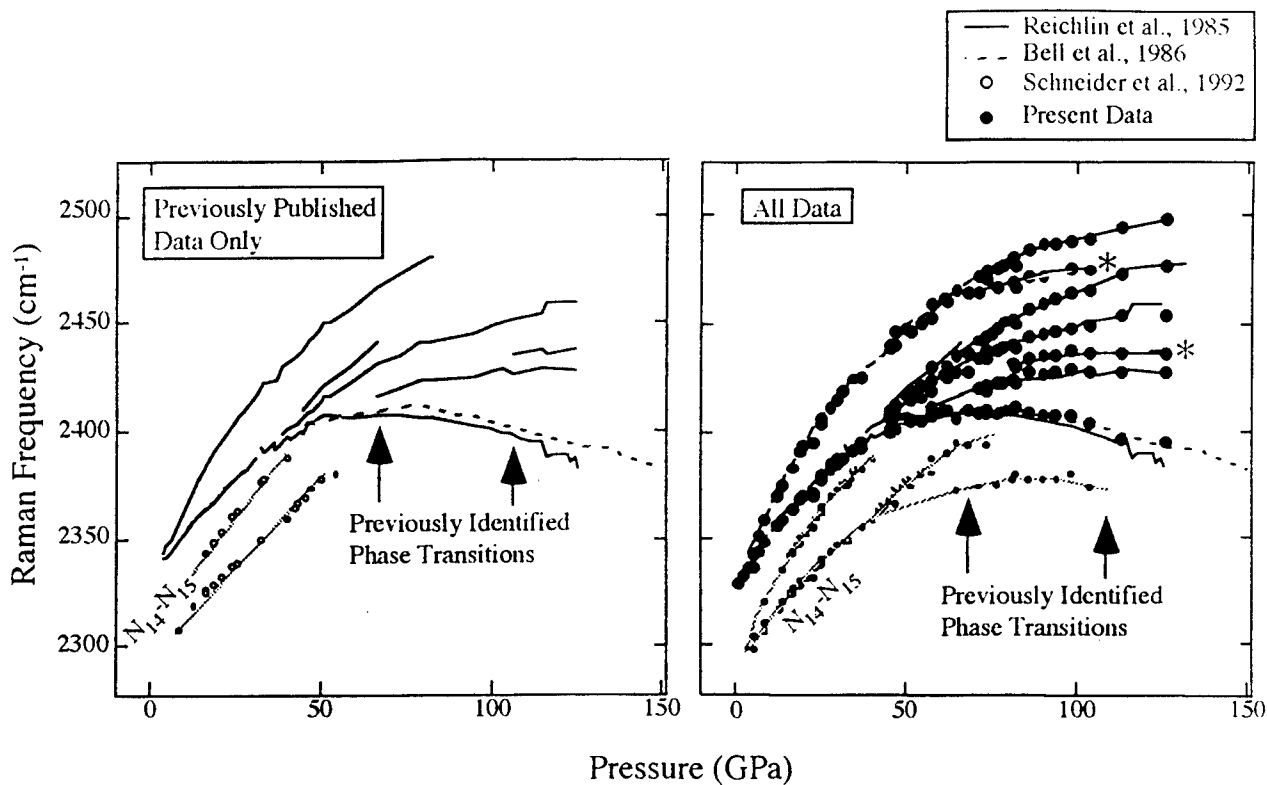


Fig. 2 Vibron mode frequencies versus pressure. We observe continuity in intensity and frequency of major peaks across 66 GPa and 100 GPa implying no major phase transition occurs. We see new peaks (branches noted by asterisks) appearing at about 70 GPa suggesting a minor phase transition occurs.

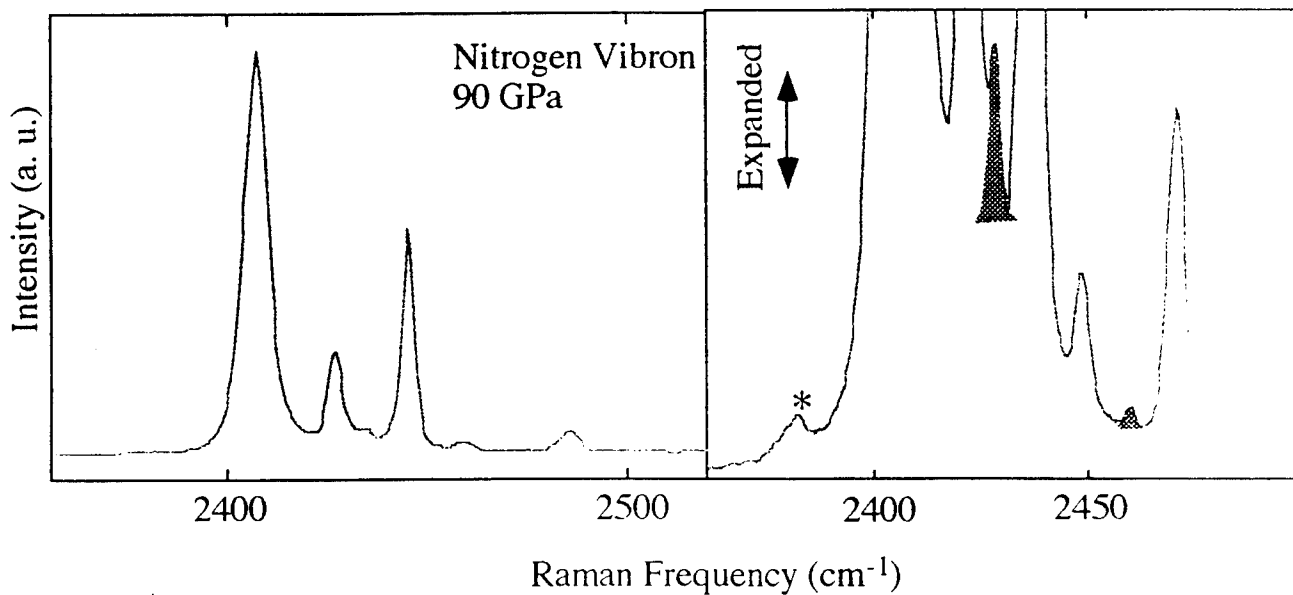


Fig. 3 Vibron spectra. The new peaks are shaded in as a guide to the eye. The peak marked by the asterisk is the signal from the  $N_{15}$ - $N_{14}$  isotopic impurities.

## Summary

We have significantly revised the phase diagram of N<sub>2</sub> at high pressures and identified a new phase transition. The one transition at ~70 GPa would appear to involve a minor crystallographic distortion. Starting at about 120 GPa, N<sub>2</sub> gradually transforms with increasing pressure to a coffee-brown color, though we point out the system remains molecular. This observation is interesting for two reasons: (1) because the bandgap in N<sub>2</sub> is showing indications that it is closing and possibly *en route* to becoming metallic and (2) because metallic behavior is expected on general grounds to weaken the molecular bond. We are now in the regime where the molecular character is measurably weakening, perhaps presaging a dissociation transition to the polymeric phase.

## References

1. C. Mailhot, L. H. Yang, A. K. McMahan, *Phys. Rev. B*, **46**, 14419 (1992).
2. R. M. Martin, R. J. Needs, *Phys. Rev. B*, **34**, 5082 (1986).
3. A. K. McMahan, R. LeSar, *Phys. Rev. Lett.*, **54**, 1929 (1985).
4. D. L. Heinz, R. Jeanloz, in *High Pressure Research in Mineral Physics* M. H. Manghnani, Y. Syono, Eds. (American Geophysical Union, Washington DC, 1987) pp. 113.
5. R. D. Ethers, V. Chandrasekharan, E. Uzan, K. Kobashi, *Phys. Rev. B*, **33**, 8615 (1986).
6. P. M. Bell, H. K. Mao, R. J. Hemley, *Physica*, **139 & 140B**, 16 (1986).
7. R. Reichlin, D. Schiferl, S. Martin, C. Vanderborgh, R. L. Mills, *Phys. Rev. Lett.*, **55**, 1464 (1985).
8. J. Belak, R. LeSar, R. D. Ethers, *J. Chem. Phys.*, **92**, 5430 (1990).
9. H. Schneider, W. Häfner, A. Wokaun, H. Olijnyk, *J. Chem. Phys.*, **96**, 8046 (1992).
10. S. Buchsbaum, R. L. Mills, D. Schiferl, *J. Phys. Chem.*, **88**, 2522 (1984).
11. A. P. Jephcoat, R. J. Hemley, H. K. Mao, D. E. Cox, *Bulletin of the American Physical Society*, **33**, 522 (1988).
12. H. Olijnyk, *J. Chem. Phys.*, **93**, 8968 (1990).
13. D. Schiferl, R. LeSar, D. S. Moore, *Simple Molecular Systems at Very High Density*. P. L. A. Polian and N. Boccara, Eds., (Plenum, N.Y., 1989).
14. T. W. Barbee III, *Proceedings of the 14th AIRAPT Int. High Pressure Conference*, 1993).

Work performed under the auspices of the U.S. Department of Energy by the Lawrence Livermore National Laboratory under contract number W-7405-ENG-48.

HIGH ENERGY DENSITY MATTER CONTRACTORS CONFERENCE  
North Lake Tahoe, NV 5 to 7 June, 1994

**Progress on Atom Doped Cryogenic Solid Propellants**

Mario E. Fajardo, Simon Tam, Jerry Boatz, Michelle Cordonnier, Tim Thompson, and  
Michel Macler (NRC Research Associate)

Emerging Technologies Branch, Propulsion Directorate, Phillips Laboratory  
(OLAC PL/RKFE Bldg. 8451, Edwards AFB, CA 93524-7680)

**ABSTRACT**

I will take the time during this talk to show highlights of our recent efforts towards trapping light atoms in cryogenic solids; detailed presentations of this work will be made during tonight's poster session. These presentations will include: the ongoing saga of the quest for B atoms in solid hydrogen, the observation of thermoluminescence due to atomic recombination in N/D<sub>2</sub> and O/D<sub>2</sub> matrices, the prediction of "triplet like" (i.e. three peaks) absorption spectra from Monte Carlo simulations of Na atoms in disordered rare gas systems, and the successful demonstration of a novel, tunable, velocity selected metal atom source based on modifications to the laser ablation method.

**Al, B, N, and O Atoms in Solid Molecular Hydrogen Matrices**

Our experimental data demonstrating the trapping of Al, B, N, and O atoms in cryogenic solid molecular hydrogen matrices have been summarized in ref. [1]. Detailed presentations and analyses of our results are currently in preparation as manuscripts on the optical absorptions of matrix isolated Al atoms [2] and B atoms [3], and on the thermoluminescence spectra of N and O atoms recombining in solid deuterium matrices [4].

**Na Atoms in Disordered Ar Systems**

Our recent experiments on Li atoms trapped in mixed Ar/Xe host matrices demonstrated that "triplet-like" (i.e. three peaks) optical absorption features can be observed even in highly disordered systems [5]. This result encouraged us to apply our theoretical scheme for simulating



the structures [6] and optical absorption spectra [7] of matrix isolated metal atoms to higher temperature, disordered Na/Ar systems. The simulated optical absorption spectrum for a Na atom in "liquid" Ar showed three broad, but resolved, peaks at 17160, 17840, and 18320  $\text{cm}^{-1}$  (the free Na atom transition is a narrowly spin-orbit split doublet centered at 16968  $\text{cm}^{-1}$ ). The liquid Ar conditions were approximated by constraining the ensemble of one Na atom and 107 Ar atoms to have a bulk density of 1.42  $\text{g}/\text{cm}^3$  and a temperature of 84 K, corresponding to the conditions for liquid Ar at its triple-point. Simulations of solid Ar at its triple point density and temperature (1.62  $\text{g}/\text{cm}^3$ , 84K) also yielded a well defined triplet absorption feature, but with a slightly larger gas-to-matrix centroid blue shift and somewhat smaller peak splittings (e.g.: peaks at 17450, 17870, and 18370  $\text{cm}^{-1}$ ). Simulations at the Ar critical point (0.53  $\text{g}/\text{cm}^3$ , 151 K) yielded a peak centered at 16870  $\text{cm}^{-1}$ , with both blue- and red-degraded wings, in qualitative agreement with previous simulations performed at a lower Ar density and higher temperature (0.13  $\text{g}/\text{cm}^3$ , 450 K) [8]. Further details and discussions of our simulations will be reported in an upcoming publication [9].

### Velocity Selected Metal Atom Source

The results of our efforts to produce a compact, intense source of velocity selected metal atoms with kinetic energies tunable throughout the 1 to 20 eV range are reported in detail in another manuscript in these proceedings [10] and elsewhere [11,12]. Briefly: pulses of atoms with broad velocity distributions are produced by laser ablation of aluminum metal. A second pulsed laser, delayed by  $\sim 1 \mu\text{s}$  and crossed at a right angle to the atomic beam, is used to photoionize only those atoms with unwanted velocities, i.e.: atoms moving too fast or too slow to be hidden behind an opaque mask placed  $\sim 1 \text{ cm}$  from the ablated surface. The photoions are subsequently deflected from the beam by a static magnetic field. We have demonstrated velocity selected Al atom fluxes equivalent to  $\Phi \sim 10^{11} \text{ atoms}/(\text{cm}^2\text{-eV-pulse})$  at a working distance of 10 cm. We hope to use this new source to elucidate the mechanisms of non-reactive (e.g.: trapping site formation) and reactive processes occurring during matrix deposition.

## REFERENCES

1. M.E. Fajardo, S. Tam, T.L. Thompson, and M.E. Cordonnier, "Spectroscopy and reactive dynamics of atoms trapped in molecular hydrogen matrices," Chem. Phys. accepted (1994).
2. S. Tam and M.E. Fajardo, manuscript in preparation. "Matrix Isolation Spectroscopy of Aluminum Atoms."
3. S. Tam and M.E. Fajardo, manuscript in preparation. "Matrix Isolation Spectroscopy of Boron Atoms and Molecules."
4. J. Petroski, M.E. DeRose, T.L. Thompson, and M.E. Fajardo, manuscript in prep. "Thermoluminescence of Atomic Species in Solid Deuterium Matrices."
5. R.A. Corbin and M.E. Fajardo, J. Chem. Phys. **101**, 2678 (1994). "Optical Absorptions of Li Atoms in Mixed Ar/Xe Matrices."
6. M.E. Fajardo, J. Chem. Phys. **98**, 119 (1993). "Classical Monte Carlo Simulations of Relaxed Trapping Site Structures in Li Atom Doped Solid Ne."
7. J.A. Boatz and M.E. Fajardo, J. Chem. Phys. **101**, 3472 (1994). "Monte Carlo Simulations of the Structures and Optical Absorption Spectra of Na Atoms in Ar Clusters, Surfaces, and Solids."
8. G.J. Erickson and K.M. Sando, "Molecular-dynamics simulation of pressure broadening of sodium resonance line by argon," Phys. Rev. A **22**, 1500 (1980).
9. M.E. Fajardo and J.A. Boatz, manuscript in preparation. "Monte Carlo Simulations of Na Atoms in Disordered Ar Systems."
10. M. Macler and M.E. Fajardo, "Velocity Selected Laser Ablation Metal Atom Source," these proceedings.
11. M. Macler and M.E. Fajardo, Appl. Phys. Lett., accepted (1994). "Velocity Selection of Fast Laser Ablated Aluminum Atoms by Temporally and Spatially Specific Photoionization."
12. M. Macler and M.E. Fajardo, Appl. Phys. Lett. **65**, 159 (1994). "Comparison of Short Range and Asymptotic Measurements of the Kinetic Energy Distributions of Laser Ablated Aluminum Atoms."

# Quantum Computer Simulations of the Structure and Dynamics of Impurities in Solid Hydrogen

Gregory A. Voth

*Department of Chemistry, University of Pennsylvania, Philadelphia, Pennsylvania  
19104-6323*

## Introduction

Solid hydrogen doped with atomic impurities<sup>1</sup> (e.g., Li, B) is a potential high energy density material (HEDM) for use in rocket propulsion. One critical issue in these materials is the metastable structure of the impurity trapping sites. A second and at least equally important issue is the diffusion and recombination rates of the impurities in the solid hydrogen host. Indeed, the rates of the latter processes determine the overall stability, or useful lifetime, of low temperature HEDMs.

Quantum computer simulation techniques have been shown to yield important information on the structure of impurity trapping sites in high energy density matter.<sup>2-6</sup> However, an even more challenging problem is the simulation of dynamical diffusion and recombination. Such simulations of impurity mobility in solid hydrogen are particularly difficult because the solid is so strongly influenced by quantum effects, thereby requiring a *quantum dynamical* method. Such a method has recently been developed<sup>7</sup> and will be described in the following section. This research is complementary to our research on the structure of impurities in solid hydrogen which includes the following accomplishments:

- A determination<sup>2</sup> of the nature of the impurity site for a lithium atom in solid *para*-H<sub>2</sub> and *ortho*-D<sub>2</sub>. The electronic excitation spectrum was also calculated and found to agree quite well with the experimental spectrum of Fajardo and co-workers<sup>1</sup> obtained at Edwards for this potential HEDM.
- The electron spin resonance (ESR) linewidth for a hydrogen atom impurity in solid *p*-H<sub>2</sub> was calculated from first principles<sup>3</sup> and found to be in essentially exact agreement with experiment. The linewidth was predicted to be the same for substitutional and interstitial impurity sites in the lattice.
- Two analytical models for atomic impurities in solid hydrogen were developed which can be used to predict the equilibrium structure and thermodynamic properties of such HEDMs.<sup>4</sup>
- The behavior liquid and cluster *p*-H<sub>2</sub> with and without a Li impurity was studied with quantum computer simulation methods.<sup>5</sup> The electronic excitation spectrum was also predicted for these systems.

- A boron atom impurity in solid  $p$ -H<sub>2</sub> is being studied using a combination of path integral and electronic density functional techniques.<sup>6</sup>

### Quantum Dynamical Simulations

The rate constant  $k_r$  for recombination of two impurities in a low temperature solid can be approximately described by the equation

$$\frac{1}{k_r} \approx \frac{1}{k_{in}} + \frac{1}{k_D} \quad , \quad (1)$$

where  $k_{in}$  is the intrinsic recombination rate for the two impurities (i.e., when at the contact distance  $r_c$ ) and  $k_D$  is the rate at which the two impurities diffuse into proximity with one another. The latter rate is related to the diffusion constant  $D$  such that  $k_D \approx 4\pi r_c D$ . If the intrinsic rate of recombination is very fast and/or the diffusion rate is slow, it is clear from Eq. (1) that the overall rate of recombination will be limited by the impurity diffusion. In an ideal cryogenic HEDM, one would obviously like the diffusion constant of the impurities to be small in order to obtain a stable material.

Computer simulation will be invaluable in determining the factors which influence impurity diffusion in HEDMs. The diffusion constant can be obtain from one of two formulas:

$$D = \frac{1}{6} \lim_{t \rightarrow \infty} \frac{d}{dt} \langle |\mathbf{q}(t) - \mathbf{q}(0)|^2 \rangle \quad (2)$$

or

$$D = \frac{1}{3} \int_0^\infty dt \langle \dot{\mathbf{q}}(t) \cdot \dot{\mathbf{q}}(0) \rangle \quad , \quad (3)$$

where the notation  $A(t) \equiv e^{iHt/\hbar} A e^{-iHt/\hbar}$  denotes a quantum Heisenberg operator for any operator "A". Both of the above functions are quantum dynamical correlation functions (or, in the case of Eq. (2), can be related to one). Therefore, the simulation of impurity diffusion in low temperature HEDMs requires a quantum dynamical simulation method which will now be described.

Our method revolves around the intriguing properties of the path centroid variable in the Feynman path integral formulation of quantum statistical mechanics.<sup>7,8</sup> The path centroid is defined by<sup>8</sup>

$$q_0 = \frac{1}{\hbar\beta} \int_0^{\hbar\beta} d\tau q(\tau) \quad , \quad (4)$$

which can be used to define a classical-like equilibrium "centroid density"  $\rho_c(q_c)$  at the point in space  $q_c$ . The latter quantity is given by the "imaginary time" (i.e., equilibrium) Feynman path integral expression<sup>7,8</sup>

$$\rho_c(q_c) = \int \cdots \int Dq(\tau) \delta(q_c - q_0) \exp\{-S[q(\tau)]/\hbar\} \quad , \quad (5)$$

where the preceding expressions have been written for a single degree-of-freedom. Extension to many degrees-of-freedom is straightforward. Note that the path centroid is defined and seemingly has meaning only within the context of equilibrium statistical mechanics. However, insight into the *dynamical* role of the centroid variable in the computation of quantum time correlation functions has been uncovered, resulting in a method called "Centroid Molecular Dynamics".<sup>7</sup>

The basic result of Centroid MD is that the position or velocity correlation function for quantum particles in many-body systems is related to a centroid correlation function obtained by running *classical-like trajectories* on an effective quantum potential.<sup>7</sup> In Centroid MD, the centroid trajectories  $q_c(t)$  are generated by the classical-like equation

$$m\ddot{q}_c(t) = - \frac{dV_c(q_c)}{dq_c} \quad , \quad (6)$$

where the effective potential, which is the quantum *centroid potential*, is defined as

$$V_c(q_c) = - k_B T \ln \left[ \rho_c(q_c) / (m / 2\pi\hbar^2\beta)^{1/2} \right] \quad . \quad (7)$$

The classical-like centroid time correlation function  $C^*(t)$  is then computed via the formula

$$C^*(t) = \langle q_c(t)q_c(0) \rangle_{\rho_c} \quad , \quad (8)$$

where the initial conditions have been weighted by the phase space version of the centroid density in Eq. (5).<sup>7</sup> From Eq. (8), the quantum position correlation function  $C(t)$  can be determined from the Fourier relation<sup>7</sup>

$$\tilde{C}(\omega) = (\hbar\beta\omega/2) [\coth(\hbar\beta\omega/2) + 1] \tilde{C}^*(\omega) \quad , \quad (9)$$

where  $\tilde{C}(\omega)$  and  $\tilde{C}^*(\omega)$  denote Fourier transforms of the two correlation functions. The quantum velocity correlation function can be determined in the same manner by computing the centroid velocity correlation function  $\langle v_c(t)v_c(0) \rangle$ . Moreover, the method has been extended to treat general quantum time correlation functions.<sup>7</sup>

The Centroid MD method provides a way to include quantum delocalization, zero point energy, and tunneling directly and efficiently in molecular dynamics simulations. The method is certainly approximate, but the supporting analysis and numerical data seems quite compelling at this point in time. For example, Centroid MD has proven to be very accurate in several test cases,<sup>7</sup> and it has been justified through a mathematical analysis,<sup>7</sup> as well as from a variational perspective.<sup>7</sup> Furthermore, when barriers are encountered by the centroid trajectories, the insights from path integral quantum transition state theory<sup>9</sup> confirm that those trajectories will surmount (i.e., tunnel through) such barriers with the correct probability. Most importantly, Centroid MD allows one to compute an accurate approximation to the quantum position correlation function for general systems, and the numerical effort in such a calculation, although greater than for a classical MD calculation, scales in the same way with number of particles  $N$  as does the classical calculation. This scaling is proportional to  $N$  or  $N^2$ , depending on the range of the classical force.

rather than scaling exponentially in  $N$  as does a direct numerical solution of the Schrödinger equation.

Several powerful algorithms have been devised to perform the quantum averaging implicit in the Centroid MD equations for many-body quantum systems [cf. Eq. (7)] "on the fly" while integrating those equations in time.<sup>7</sup> Figure 1 depicts the quantum dynamical diffusion of a light quantum particle having 100 times the electron mass in a classical Lennard-Jones fluid. Shown also is the classical limit of the diffusion which is seen to be substantially faster than the quantum case.

### Displacement of a Solvated Quantum Particle

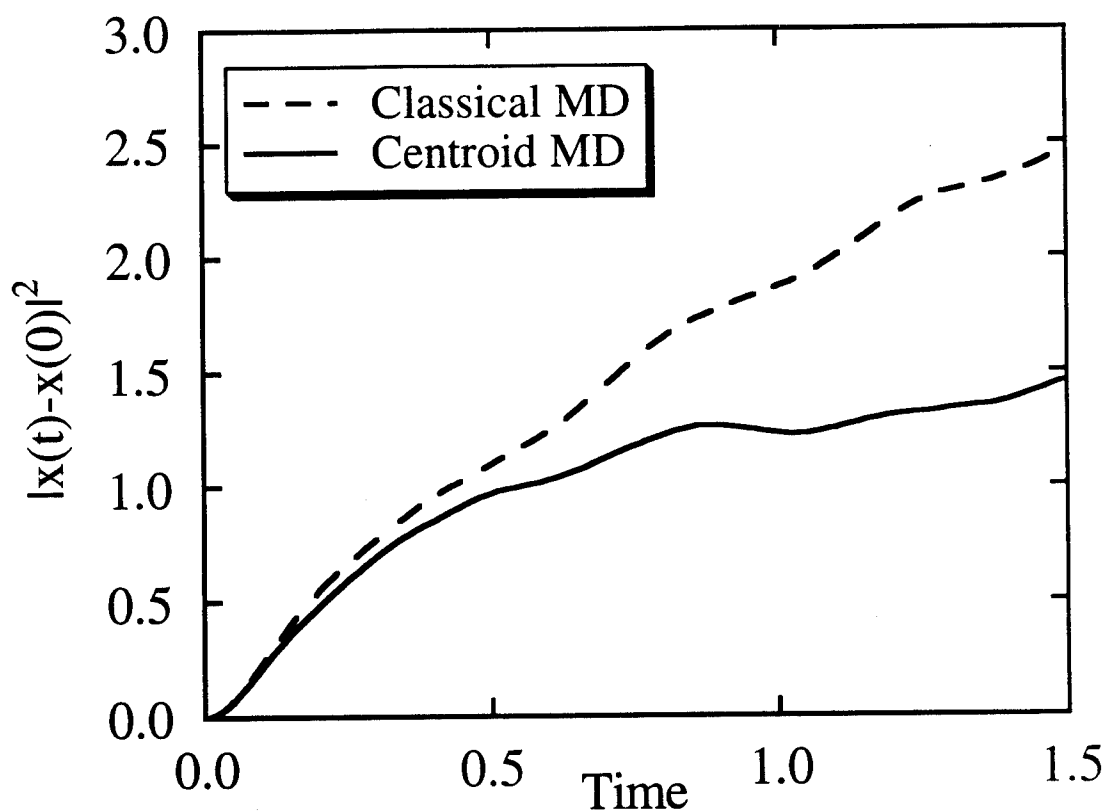


**Figure 1:** A plot of the mean square displacement for a quantum particle of 100 times the electron mass solvated in a classical neon fluid. The solid line is the Centroid MD result, while the dashed line is for the classical limit.

## Conclusions

With the Centroid MD method, one can directly and efficiently calculate the quantum dynamical properties of condensed matter systems as they are described by time correlation functions. This breakthrough will allow us to simulate impurity diffusion in low temperature HEDM systems and to learn about the factors which influence the stability of potential HEDMs. Such calculations will be the target of future research in the HEDM Program.

## References

- (1) M. E. Fajardo, in *Proceedings of the High Energy Density Matter Conference*, edited by M. E. Cordonnier (USAF Phillips Laboratory, Edwards AFB, CA, 1991); *J. Chem. Phys.* **98**, 110 (1993).
- (2) D. Scharf, G. J. Martyna, D. H. Li, G. A. Voth, and M. L. Klein, *J. Chem. Phys.* **99**, 9013 (1993).
- (3) D. H. Li and G. A. Voth, *J. Chem. Phys.* **100**, 1785 (1994).
- (4) D. H. Li and G. A. Voth, *J. Chem. Phys.* **96**, 5340(1992); *J. Chem. Phys.* **98**, 5734 (1993).
- (5) D. Scharf, G. J. Martyna, and M. L. Klein, *J. Chem. Phys.* **99**, 8997 (1993); D. Scharf, M. L. Klein, and G. J. Martyna, *J. Chem. Phys.* **97**, 3590 (1992); D. Scharf, G. J. Martyna, and M. L. Klein, *Chem. Phys. Lett.* **197**, 231 (1992); *Low Temp. Phys.* **19**, 364 (1993).
- (6) D. H. Li, I. Bhattacharya-Kodali, and G. A. Voth (to be submitted).
- (7) J. Cao and G. A. Voth, *J. Chem. Phys.* **99**, 10070 (1993); *J. Chem. Phys.* **100**, 5093 (1994); *J. Chem. Phys.* **100**, 5106 (1994); *J. Chem. Phys.* (submitted, 1994); *J. Chem. Phys.* (submitted, 1994); *J. Chem. Phys.* (submitted, 1994).
- (8) R. P. Feynman, *Statistical Mechanics*, (Addison-Wesley, Reading, MA, 1972).
- (9) G. A. Voth, D. Chandler, and W. H. Miller, *J. Chem. Phys.* **91**, 7749 (1989); G. A. Voth, *Chem. Phys. Lett.* **170**, 289 (1990); For a review, see G. A. Voth, *J. Phys. Chem.* **97**, 8365 (1993).

# Mobilities and Reaction Dynamics of Atoms in Cryogenic Solids

E. Todd Ryan, Dwayne LaBrake and Eric Weitz

Department of Chemistry  
Northwestern University  
Evanston, IL 60208-3113

## Introduction

The technique of matrix isolation spectroscopy<sup>1</sup> has served as a powerful tool for the study of reactive chemical species. The species of interest can be prepared in various ways. One common technique involves the photolysis of a precursor molecule in the matrix to produce a reactive species directly as a photoproduct. Another technique involves the production of an atom or radical by photolysis which subsequently reacts with some other radical or molecule in the matrix to produce the species of interest.<sup>1,2</sup>

In both of the above techniques, the rates for atomic and molecular mobility in the matrix are of prime importance. If the radical is produced by reaction of two species in the matrix, the timescale for its production will be effected by the diffusion time of the reactant in the matrix. Once a radical is produced, its lifetime will be determined in part by the time that it takes for the radical to diffuse to some other reactant in the matrix.

It is also possible that the reactive species can absorb electromagnetic radiation. This radiation can then be degraded into energy in translational and/or internal degrees of freedom. If a significant amount of the initially absorbed energy eventually resides in translational degrees of freedom of the reactive species, the mobility of this species can be enhanced. This processes has been termed "photoinduced mobility"<sup>3-5</sup> and will occur any time the absorption of a photon results in the complex residing on the repulsive portion of a barrierless potential energy surface. Such a process may occur as a result of direct photodissociation or when the excited state of the reactive species can form a complex with the host material. Under the later circumstances relaxation of the complex will typically lead to a transition where the constituents of the complex are placed on the repulsive wall of the ground state potential energy surface leading to translational excitation of the species. Such behavior has been reported for F atoms in rare gas solids<sup>5</sup> and we have observed such behavior for XeO complexes and have published results in this area<sup>3</sup>. We have also observed this behavior for H atoms and discuss initial results in this area in this report.

We also report on some recent results regarding the reactions of O atoms in cryogenic solids. We demonstrate that the maximum O atom concentration attainable by photodissociation of N<sub>2</sub>O in a concentrated N<sub>2</sub>O:Xe matrix is limited by reactions of O atoms with N<sub>2</sub>O which occur in N<sub>2</sub>O clusters. We also show that O atoms generated by photolysis of N<sub>2</sub>O can react with N<sub>2</sub>. Using an isotopically labeled starting material we can distinguish the N<sub>2</sub>O that is formed as a result of reaction from the N<sub>2</sub>O that serves as an O atom source. This photolysis process and the resulting reactions have been studied as a function of temperature and matrix deposition conditions.<sup>6</sup>

## Experimental

The experimental apparatus used in these studies has been reported on in detail previously<sup>3,6,7</sup>. For H atom studies, the output of an ArF or KrF excimer laser is used to photolyze HBr. The 193 nm output of this laser is also used to excite H atom - xenon exciplexes. These



exciplexes have been reported to have an  $\text{Xe}_2\text{H}$  structure, analogous to the  $\text{Rg}_2\text{X}$  structure of rare gas - halogen exciplexes<sup>6</sup>. Pulses of approximately  $10 \text{ mJ/cm}^2$  are used to photolyze the samples while significantly reduced energy pulses are used to probe the H atom concentration via  $\text{Xe}_2\text{H}$  emission. The output of a XeF excimer laser is used to probe Br atom concentrations by exciting  $\text{Xe}_2\text{Br}$  emission. For O atom experiments, the output of an excimer laser operating on either ArF (193 nm) or KrF (248 nm) with fluences typically in the range of  $10.0 \text{ mJ/cm}^2$  is used to irradiate an  $\text{N}_2\text{O}:\text{Xe}$  or an  $\text{N}_2\text{O}:\text{N}_2$  matrix. For both systems exciplex emission produced upon matrix irradiation, is viewed by a gated optical multichannel analyzer (OMA) (Princeton Instruments model IRY700) attached to an ISA HR-320 monochromator equipped with a 300 grooves/mm grating blazed at 600 nm. The gate width of the OMA is set to be significantly longer than the fluorescence decay time. The output from the OMA is thus the integrated fluorescence signal over the entire duration of fluorescence which is normalized by the excimer laser energy. In some experiments a phototube is used in place of the OMA. IR spectroscopy is also used to monitor these systems.

## Results

Figure 1 and 2 are of  $\text{Xe}_2\text{Br}$  emission produced by probing matrices irradiated with  $7.0 \text{ mJ/cm}^2$  ArF laser pulses with approximately  $1.0 \text{ mJ/cm}^2$  XeF laser pulses. The first figure is for a 1:800 HBr:Xe matrix while the second figure is for a very dilute matrix with an approximate composition of 1:100,000. Since HBr is a very "sticky" gas it is very difficult to make up reproducible mixtures at high dilution. Thus the concentration of a highly dilute mixture was judged by the relative intensity of the Br atom exciplex emission at a point corresponding to complete photolysis. This emission has been shown to be linear in Br atom concentration. The insets to the Figures are plots of  $1/(I_{\text{MAX}} - I)$  and  $\log(I_{\text{MAX}} - I)$  respectively. The linearity of these plots implies that the data in Figure 1 follows kinetics that are second order in HBr concentration and the data in Figure 2 follows kinetics that are first order in HBr concentration. Similar behavior is observed for 248 nm photolysis of HBr.<sup>7</sup>

Figure 3 shows "photoproduction curves" for O atoms probed by 193 nm irradiation of various  $\text{N}_2\text{O}:\text{Xe}$  matrices using  $7.1 \text{ mJ/cm}^2$  pulses. Figure 4 shows infrared spectra for a  $\text{N}_2\text{O}(546):\text{Xe}$  matrix (1:354) deposited at 36 K. Panel A is for the matrix prior to photolysis while panel B is for the matrix subsequent to photolysis with 1800 ArF laser pulses. The absorptions that grow in are at  $2169$  and  $2135 \text{ cm}^{-1}$  and are identified as due to the  $\nu_3$  mode of  $\text{N}_2\text{O}$  (456) and the  $\nu_1 + \nu_3$  and possibly the  $\nu_3$  modes of  $\text{O}_3$ .

## Discussion

### A. Br Atom Production

The second order production of Br atoms is accompanied by second order loss of HBr as probed by infrared spectroscopy. This second order behavior implies that a mobile species that is produced on photolysis of HBr reacts with another HBr molecule leading to its reactive loss. It has been demonstrated that Br atoms and HBr are thermally stable and that Br atoms are not significantly photomobilized.<sup>7</sup> Thus the mobile species must be H atoms. The transition from second order production of Br atoms to first order production is then a reflection of the finite range of H atom motion in a rare gas matrix. The fact that the same qualitative behavior is observed subsequent to 248 or 193 nm dissociation of HBr is an indication that photoinduced mobility of H

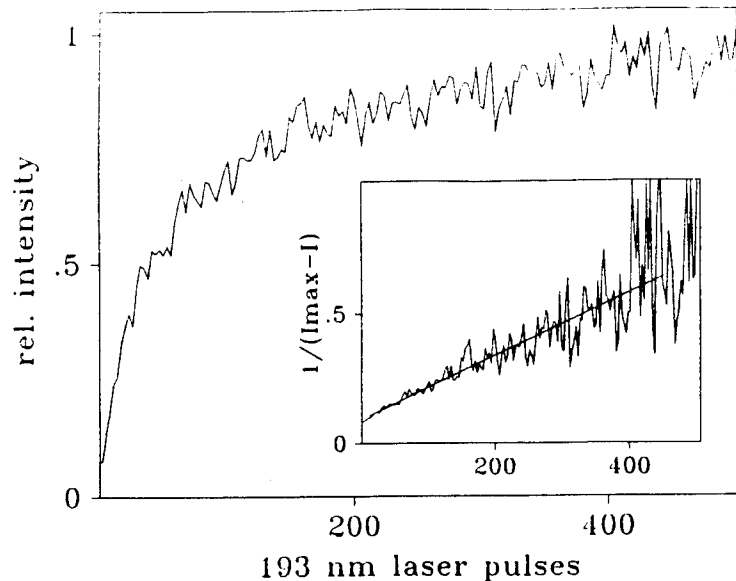


Figure 1. The intensity of  $\text{Xe}_2\text{Br}$  fluorescence versus number of 193 nm laser pulses. The 1:800 HBr:Xe sample was photolyzed at 10 K using a 193 nm laser fluence of  $7.0 \text{ mJ/cm}^2$ . A plot of  $1/(I_{\text{MAX}}-I)$  versus laser pulses is shown as an inset.

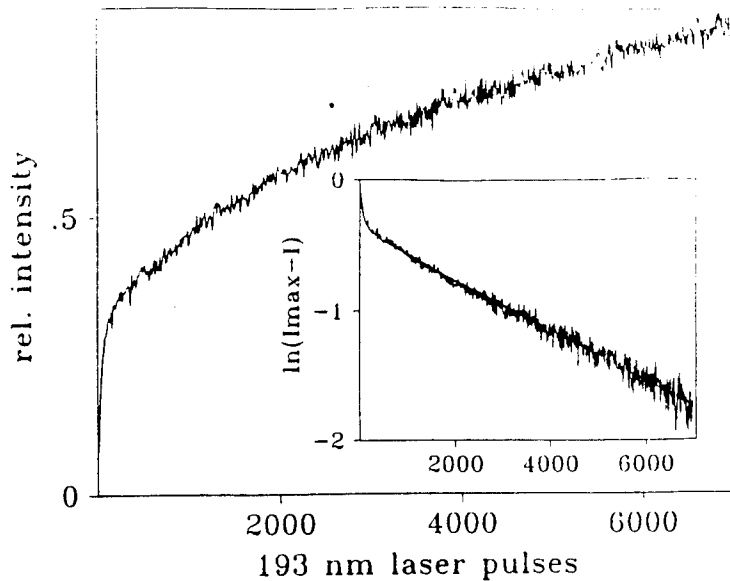


Figure 2. A plot of the intensity of fluorescence from  $\text{Xe}_2\text{Br}$  exciplexes versus 193 nm laser pulses at 10 K. The HBr:Xe mole ratio was approximately 1:100,000. The sample was photolyzed using a 193 nm laser fluence of  $7.0 \text{ mJ/cm}^2$ . A plot of  $\ln(I_{\text{MAX}}-I)$  versus laser pulses is shown as an inset.

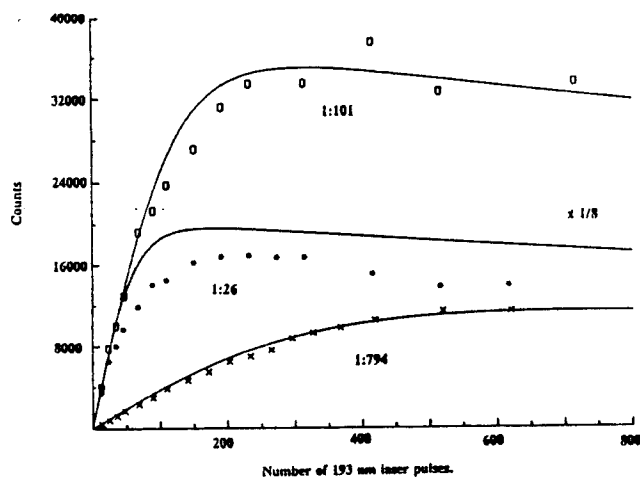


Figure 3. O atom photoproduction curves obtained at 10 K by 193 nm photolysis of  $\text{N}_2\text{O}/\text{Xe}$  matrices with doping ratios: (1:794) (\*), (1:101) (x), and (1:26) (o). The solid lines were generated by numerically integrating the equations in reference 3. The predicted fit to the (1:26) data was scaled by a factor of 8 so it would not be off the scale of the plot.

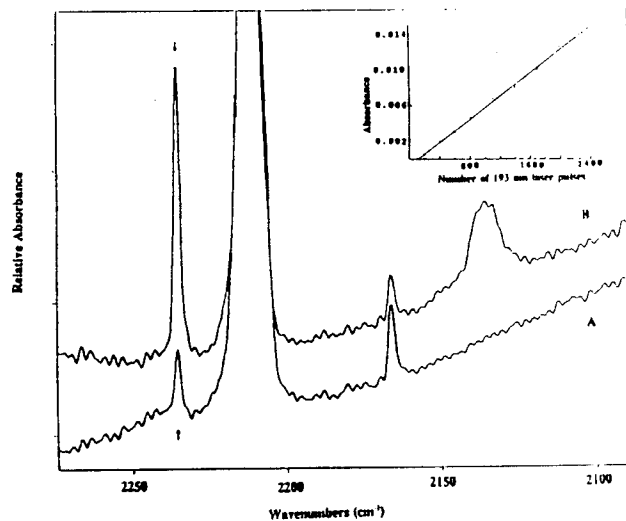
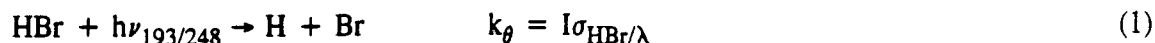


Figure 4. 4A displays an infrared spectrum of an unphotolyzed  $\text{N}_2\text{O}$  (546)/ $\text{N}_2$ (1:354) matrix deposited at 15 K. The (546)  $\nu_3$  monomer absorption is at  $2213 \text{ cm}^{-1}$ . The absorptions at  $2166$  and  $2235 \text{ cm}^{-1}$  are due to (556) and (446) impurities, respectively. 4B displays the same matrix after irradiation with 1800 193 nm laser pulses. The (546) and (556) absorptions decrease upon photolysis while the (446) absorption (marked by the arrows) grows. An ozone absorption ( $\nu_1 + \nu_3$  and possibly  $2\nu_3$ ) also grows in at  $2135 \text{ cm}^{-1}$ . The insert displays a plot of ozone absorption intensity versus the number of 193 nm laser pulses.

atoms as a result of dissociative relaxation of  $\text{Xe}_2\text{H}$  exciplexes is not a dominant source of the atom mobility that leads to HBr loss since these exciplexes are not excited by 248 nm radiation.<sup>8</sup> Thus the source of mobility must be translational energy release on direct photodissociation of HBr. This energy is preferentially disposed in the translational degrees of freedom of the H atom. Given this picture the following minimal set of kinetic equations describes the processes taking place in the system.



In this formulation  $I$  is the laser pulse intensity in photons/cm<sup>2</sup>/sec and  $\sigma$  is the effective absorption cross-section in cm<sup>2</sup>. As discussed previously in detail,  $\sigma$  can be written as  $\sigma_1\phi_1$  where  $\sigma_1$  is the intrinsic absorption cross-section and  $\phi_1$  is the cage exit probability.<sup>12</sup> As a first approximation, the rate constants,  $k$  for equations 2-4, are assumed to be the same since each reaction is expected to be limited by the mobility of the H atom reactant.

In the regime where second order kinetics are applicable, H atoms can be considered to be a transient species whose overall concentration does not vary significantly in time once an initial growth period has occurred. This issue will be explored in more detail in a subsequent publication dealing with the details of H atom production and loss.<sup>8</sup> As such, equation 4, which involves the square of a small concentration, can be neglected. Given these assumptions, the following differential rate expression can be written

$$\frac{d[\text{H}]}{dt} = k_\theta[\text{HBr}] - k[\text{H}][\text{HBr}] - k[\text{H}][\text{Br}] \quad (5)$$

Under these conditions the application of the steady state approximation to the transient H atom species gives

$$[\text{H}]_{ss} = \frac{k_\theta[\text{HBr}]}{k([\text{HBr}] + [\text{Br}])} \quad (6)$$

using the Br atom mass balance

$$[\text{Br}] = [\text{HBr}]_0 - [\text{HBr}] \quad (7)$$

This can be rewritten as

$$[\text{H}]_{ss} = \frac{k_\theta[\text{HBr}]}{k[\text{HBr}]_0} \quad (8)$$

Using

$$\frac{d[\text{HBr}]}{dn} = -k_{\theta}[\text{HBr}] - k[\text{H}][\text{HBr}] + k[\text{H}][\text{Br}] \quad (9)$$

and the expression for  $[\text{H}]_{ss}$  in eqn. 8 and  $[\text{Br}]$  in eqn. 7 gives:

$$\frac{d[\text{HBr}]}{dn} = \frac{-d[\text{Br}]}{dn} = \frac{-2k_{\theta}}{[\text{HBr}]_0} [\text{HBr}]^2 \quad (10)$$

After integrating equation 10 over the number of laser pulses, the following expressions for the laser pulse dependence of the HBr and Br atom concentrations are obtained.

$$[\text{HBr}] = \frac{[\text{HBr}]_0}{1 + 2k_{\theta}n} \quad (11)$$

and

$$[\text{Br}] = [\text{HBr}]_0 - \frac{[\text{HBr}]_0}{1 + 2k_{\theta}n} \quad (12)$$

Equation 10 relates the phenomenological rate constant for the photolytic loss of HBr and the production of Br atoms to microscopic rate constants. It is essentially the effective photodissociation cross section for HBr weighted by the initial concentration of HBr, i.e.,

$$k = \frac{2I\sigma_{\text{HBr}/\lambda}}{[\text{HBr}]_0} \quad (13)$$

Therefore,

$$\sigma_{\text{HBr}/\lambda} = \frac{k[\text{HBr}]_0}{2I} \quad (14)$$

These equations immediately provide a method for computing the effective photodissociation cross-section for HBr in the matrix and demonstrates why the phenomenological rate constant for HBr loss and Br production should be equal, as they are observed to be, at a given wavelength for a constant fluence photolysis pulse.

In the first order regime the predicted form of the Br atom growth curve is simple exponential. This prediction is realized by the data in Figure 2.

H atom growth curves have a more complex form due to the reactions that produce and consume these species. This exact behavior of this species will be dealt with in detail in a future publication.<sup>8</sup>

### B. $N_2O$ Photolysis

Attempts to fit the O atom photoproduction curves shown in Figure 3 to the mathematical model of reference 3 were successful for the two sets of data taken at higher concentrations. The model predicts a much higher steady state concentration for O atoms in the highest concentration matrix than is realized by the data. This difference is explainable by chemistry that occurs between O atoms and  $N_2O$  molecules in clusters that are present in higher concentration matrices. Consistent with this explanation much higher concentrations of dimers and higher order multimers are seen in the 1:32 matrix than are observed in the IR spectra of the more dilute matrices. Formation of NO and  $NO_2$  are observed on prolonged photolysis of  $N_2O$  containing Xe matrices. These products are compatible with  $O(^1D)$  chemistry. To provide more verification that this type of chemistry can occur in a matrix environment we photolyzed isotopically labeled  $N_2O$  (546) in a normal  $N_2$  matrix. Photolysis led to the formation of  $N_2O$  (446) as a result of reaction of O atoms with the  $^{14}N_2$  in a normal nitrogen matrix. This chemistry has not been observed for  $O(^3P)$  atoms but is consistent with the formation and reaction of  $O(^1D)$  atoms in a matrix environment. Though  $O(^1D)$  atoms are formed there is evidence that they are rapidly quenched before they can travel long distance through the matrix. This evidence comes from a prior study on the reaction of O atoms with  $N_2$  in  $N_2$  doped Xe matrices<sup>3</sup> and from a recent study of the reaction of O atoms generated by photolysis of  $O_3$  with  $N_2$ .<sup>9</sup> In that latter study evidence is presented that relaxation of O atoms from  $O(^1D)$  to  $O(^3P)$  occurs in approximately 10 collisions with the  $N_2$  host material. These data indicate that loss of O atoms due to reactions in clusters may be a limiting factor in the ability to produce higher O atom concentrations by photolysis of dopants in cryogenic solids. Nevertheless the maximum concentration of O atoms that has been generated already exceeds 32 mmolar.

### Acknowledgments

We acknowledge support of this work by Phillips Laboratory at Edwards Air Force Base under contract #F29601-91-C-0016.

### References

1. M. E. Jacox in Chemistry and Physics of Matrix-Isolated Species, L. E. Andrews and M. Moskovits eds., (Elsevier, Amsterdam, 1989).
2. For example, B. Brocklehurst and G. C. Pimentel, *J. Chem. Phys.* **36**, 2040 (1962); J. Fournier, C. Lalo, J. Deson and C. Vermiel, *J. Chem. Phys.* **66**, 2656 (1977); R. N. Perutz, *Chem. Rev.* **85**, 77 (1985).
3. E. T. Ryan and Eric Weitz, *J. Chem. Phys.* **99**, 8628 (1993).
4. A. I. Katz and V. A. Apkarian, *J. Phys. Chem.* **94**, 6671 (1990).
5. H. Kunttu, J. Feld, R. Alimi, A. Becker and V. A. Apkarian, *J. Chem. Phys.* **92**, 4856 (1990) and R. Alimi, R. B. Gerber and V. A. Apkarian, *ibid.* **92**, 3551 (1990).
6. E. T. Ryan and E. Weitz - *Chemical Physics*, in press.
7. D. LaBrake, E. T. Ryan and E. Weitz - manuscript in preparation.
8. D. LaBrake, E. T. Ryan and E. Weitz - manuscript in preparation.
9. A. V. Benderskii and C. A. Wight, *Chem. Phys.*, in press.

Ultrahigh Resolution Spectroscopy of the  $Q_1(0)$  Transitions Induced by  
Laser Radiation Field, External Electric Field, Impurity Quadrupole Field,  
and  $\gamma$ -Ray Radiolysis

Takeshi Oka

Department of Chemistry and  
Department of Astronomy and Astrophysics,  
The Enrico Fermi Institute  
The University of Chicago  
Chicago, IL 60637

## 1. Introduction

Let me start by reminding you of the two beautiful characteristics of the para-  $H_2$  crystal.

### A. *Quantum Crystal.*

Solid hydrogen is a weakly bound system. The  $H_2$ - $H_2$  dispersion interaction has the equilibrium binding energy of  $D_e \sim 25 \text{ cm}^{-1}$ ,<sup>1</sup> but after subtracting the zeropoint energy, the energy of stabilization is only  $D_0 \sim 2.9 \text{ cm}^{-1}$ .<sup>2</sup> This weakness of binding together with the small mass of  $H_2$  makes solid hydrogen (together with solid He) a special category of crystals which Lou Nosanow christened with the name of "Quantum Crystal".<sup>3</sup> For such crystals "the root-mean-square deviation of a particle from its lattice site is not small compared to the nearest-neighbor distance. The problem is not simply that the anharmonic terms are large; it is that the harmonic approximation itself breaks down."<sup>3</sup> Moreover the constituents of a quantum crystal may exchange their positions due to quantum mechanical tunneling effect. This is well established for solid  $^3\text{He}$  from spin resonance experiments and observation of phase transitions in the mK region, in which the exchange was shown to occur with the time scale of microseconds.<sup>4, 5</sup> This type of exchange is expected also in solid hydrogen<sup>6</sup> although its

frequency is likely to be lower than that of He because of higher binding energy ( $D_e \sim 25 \text{ cm}^{-1}$  versus  $7.1 \text{ cm}^{-1}$  for He). Theoretical estimates of the exchange time of  $10^4 \sim 10 \text{ sec}^7$  and  $10^{-4} \text{ sec}^8$  have been given. It will be awfully nice if this effect is observed experimentally. In any case this tunneling, even after the formation of crystals, makes solid hydrogen *self repairing*. This agrees with our experience; nature helps us making nice crystals in spite of our clumsiness and the crystal keeps its order after harsh  $\gamma$ -ray irradiation.

### *B. Singly Occupied Quantum State.*

Because of the weak intermolecular interaction which keep the molecules at the intermolecular distance of  $3.793 \text{ \AA}$  and because of the high symmetry of the crystal, the motion of constituent molecules are well quantized. Unlike in other molecular crystals, the rotational quantum number  $J$  may be regarded as a good quantum number. The unique aspect of the para- $\text{H}_2$  crystal as a spectroscopic specimen is that all molecules in the crystal occupy the single lowest state. This is the state in which all quantum numbers are zero; not only the quantum numbers associated with motion such as the electronic orbital angular momentum  $L$ , the vibrational quantum number  $v$ , and the rotational quantum number  $J$ , but also the total electron and nuclear spin numbers  $S$  and  $I$  are zero due to the principle of superposition. All molecules with the number density of  $2.61 \times 10^{22} \text{ cm}^{-3}$ , except for the  $J = 1$  ortho- $\text{H}_2$  impurity ( $\geq 0.06\%$ ) and HD ( $\sim 0.03\%$ ) in natural abundance, are in the identical quantum state ready to interact with radiation. Such uniform crystal state has quantum mechanical translational symmetry in addition to the point group symmetry of  $D_{3h}$ . This symmetry leads to the momentum quantum number  $\mathbf{k}$  which is also zero in the ground state but may take any of the  $N$  values in the first Brillouin zone if a molecular quantum state is excited.<sup>9</sup> It is its selection rule  $\Delta \mathbf{k} = 0$  which plays a major role in the discussion of this talk.

## **2. Pure Vibrational $Q_1(0)$ Transitions<sup>10, 11</sup>**

The pure vibrational transition  $Q_1(0)$ , in which the vibrational state of  $\text{H}_2$  is excited  $v = 1 \leftarrow 0$ , but the rotational state remains in the lowest state  $J = 0 \leftarrow 0$ , is dipole forbidden

since  $\langle J=0 | \mu \cdot \mathbf{E} | J=0 \rangle = 0$ , where  $\mu$  is the dipole moment operator and  $\mathbf{E}$  is the radiation electric field. It is doubly forbidden for an electric dipole moment through the parity rule and the angular momentum triangle relation. It becomes allowed if there exists an additional field which mixes a small fraction of electronic excited state with opposite parity and  $J=1$  with the ground state. The transition moment then is given by the well known Kramers Heisenberg formula,

$$\sum_n \frac{\langle 0 | \mu \cdot \mathbf{E} | n \rangle \langle n | \mu \cdot \mathbf{E}' | 0 \rangle}{W_0 - W_n + \hbar\omega}$$

where  $\mathbf{E}'$  is the additional field and  $\omega$  is its frequency and  $W_0$  and  $W_n$  are energies of the ground state and the  $n$ -th electronic state, respectively.

In this talk I give four examples of this type of transitions induced in para- $\text{H}_2$  crystals through different electronic fields. The effects, the electric fields, and their orders of magnitude are summarized below.

	Effects	Electric Fields	Orders of Magnitude
a	Stimulated Raman	Laser radiation field	1 kV/cm
b	Condon	External D.C. field	10 kV/cm
c	Impurity	Quadrupolar field of $J=1 \text{ H}_2$	1 MV/cm
d	Ionization	Coulomb field of charges	100 MV/cm

While all these four are electric field induced effects, there are qualitative differences in the observed spectrum and its analysis. In the former two effects a and b, all molecules more or less experience the same field; the translational symmetry is maintained and the resulting  $\Delta\mathbf{k} = 0$  rule is well obeyed. In the latter two effects c and d, the source of the field is localized on impurity or charge and varies drastically depending on the relative positions of molecules. The given orders



of magnitude of the electric field are those for the nearest neighbor. For the impurity induced spectrum, the short range  $1/R^4$  quadrupolar field destroys the translational symmetry and the  $\Delta\mathbf{k} = 0$  rule is not followed. On the other hand, for the charge induced spectrum we found, to our surprise, that the  $\Delta\mathbf{k} = 0$  rule is observed due to the long ranged nature of the Coulomb field. The orders of magnitude of the electric field given above for a and b are those applicable at this stage of development but by no means limited to those values. In particular, for the Condon effect, we should be able to increase the field by an order of magnitude. Since the transition intensity is proportional to the square of the field this should greatly increase the signal. In the following I give the results of our experiment briefly.

### 3. Stimulated Raman Spectrum<sup>12, 13</sup>

We used an  $\text{Ar}^+$  ion laser at 476.6 nm for pump and a dye laser at 594.1 nm for tunable probe radiation. A block diagram of the apparatus is given in Fig. 1 (next page). The Ar laser radiation is either amplitude or tone burst modulated and the gain of the probe radiation at resonance is detected. Two examples of observed spectrum are given in Fig. 2. When the impurity concentrations are low, the signal is very sharp indicating the remarkable purity of the vibron Bloch state and the  $\Delta\mathbf{k} = 0$  selection rule. When the impurity concentration is increased, the spectrum starts to show structure which is yet to be interpreted.

### 4. Condon Spectrum<sup>14</sup>

After observing the beautiful  $\Delta\mathbf{k} = 0$  Raman signal, we attempted to observe the variation of its frequency and lineshape depending on temperature. This turned out to be not easy; since the accuracy of locating the center of the peak is  $\sim 1$  MHz, we have to stabilize frequencies of both the Ar laser and the dyes laser to a fraction of MHz and measure their frequency individually to the same accuracy. This looked a little beyond our expertise and so my students and I drove to Colorado to work with John Hall, to attempt this; this was unsuccessful. Then it occurred to us that, for this purpose, it is much easier to use an external electric field to

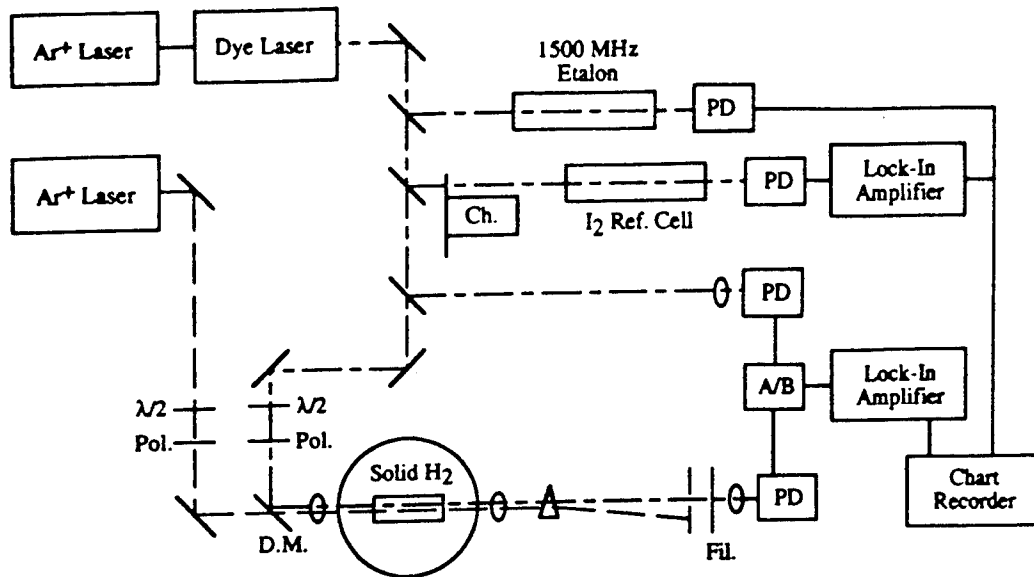


Fig. 1 Block diagram of the experiment for simulated Raman Spectroscopy.

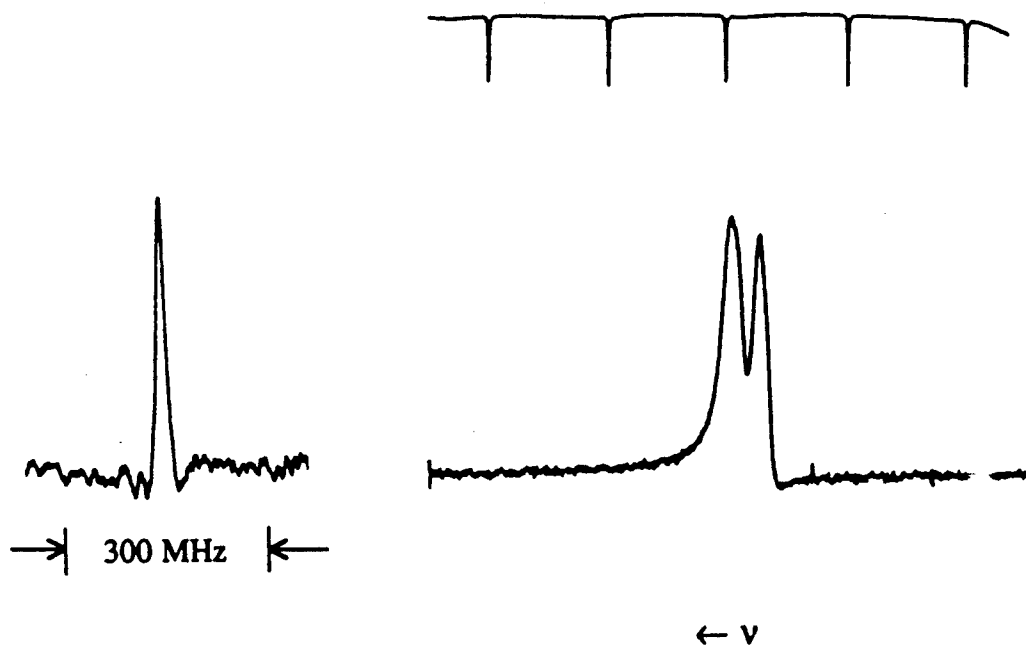


Fig. 2 Stimulated Raman gain spectrum of para- $H_2$  crystal. On the left is a sharp spectral line ( $\Delta\nu \sim 7$  MHz *hwhm*) for low ortho- $H_2$  concentration (0.06%) indicating the purity of the vibron Bloch state and the  $\Delta k = 0$  rule. On the right is broader lines for higher ortho- $H_2$  concentration (2%). The cause of the structure is yet to be understood. The interference markers are separated by  $0.05$   $cm^{-1}$ .

cause the  $Q_1(0)$  transition. Since it is trivial to switch the field on and off we should be able to use the effect as molecular modulation. Such effect has been predicted by Condon<sup>15</sup> in the early years of spectroscopy; we call this effect the Condon effect and the modulation Condon modulation. More background of this effect and the detail of the experiment is given in Ref. 14.

A few technical difficulties related to inserting the high voltage electrode in the cell and growing a good transparent crystal between the electrode and the wall of the sample cell, and applying high electric field without breakdown, have been overcome by the graduate student Karen Kerr. An example of the observed signal is shown in Fig. 3. The use of Condon modulation has improved the sensitivity of our spectroscopy by two orders of magnitude ( $\Delta I/I \sim 5 \times 10^{-6}$ ). Now the experiment is much simpler. We use a color center laser as the tunable infrared source which can be stabilized to  $\lesssim 0.5$  MHz if necessary. This technique has been used to observe the variation of the  $Q_1(0)$  spectral line depending on temperature. An example is shown in Fig. 4. Details of the observation and its interpretation are in Ref. 14. This technique is very versatile and has already been applied to many cases.<sup>11</sup>

## 5. Impurity Induced Spectrum

The  $J = 1$  ortho- $H_2$  molecules, which exist in para- $H_2$  crystals as impurities (typically 0.2 %) as a result of imperfect para conversion, have average quadrupole moment and thus exert  $1/R^4$  electric quadrupolar field to surrounding para- $H_2$  molecules. This field at the position of the  $i$ -th molecule,

$$E(\mathbf{R}_i) = Q \nabla \sum_m C_{2m}(\Omega) C_{2m}^*(\mathbf{R}_i) / R_i^3$$

is on the order of  $E \sim \sqrt{3}Q/R^4 \sim 1$  MV/cm at the position of nearest neighbors and induces the  $Q_1(0)$  transition. Because of the strong field, the induced spectrum has higher integrated intensity than the previous two cases. However, the short ranged, randomly localized field destroys the translational symmetry of the crystal and the  $\Delta \mathbf{k} = 0$  rule is not followed leading to a broad spectral line. An example is shown in Fig. 5. Included in the figure is theoretical vibron

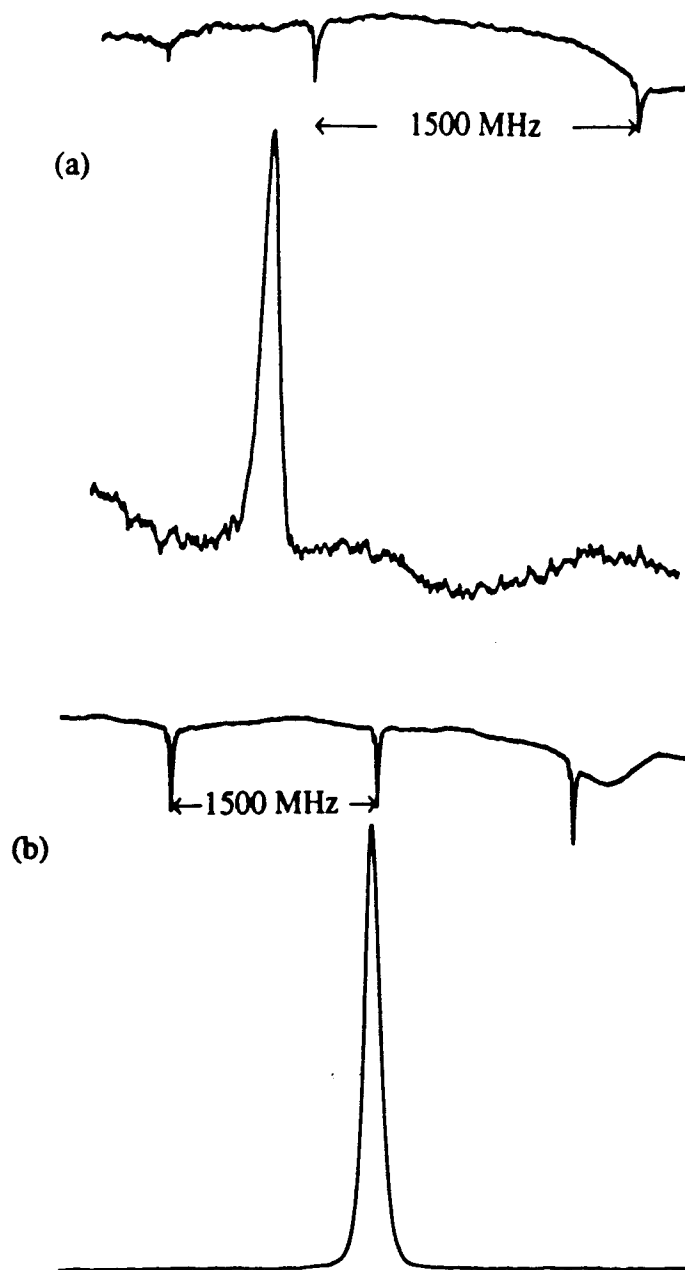


Fig. 3 Observed electric field induced  $Q_1(0)$  transition in 99.8% pure para- $H_2$  crystal. A difference frequency system was used as the radiation source. The wavenumber of the spectral line was measured to be  $4149.6918 \text{ cm}^{-1}$ . In the upper figure, a D.C. electric field of 8 kV/cm was applied and videodetection using a chopper was employed. In the lower figure Condon modulation with a 10 kHz sine wave A.C. field of 6 kV/cm peak to peak was used followed by  $2f$  detection. The laser polarizer is parallel to the applied field. The signal disappears when they are perpendicular. A sensitivity of  $\Delta I/I \sim 5 \times 10^{-6}$  was obtained for a time constant of 3 sec.

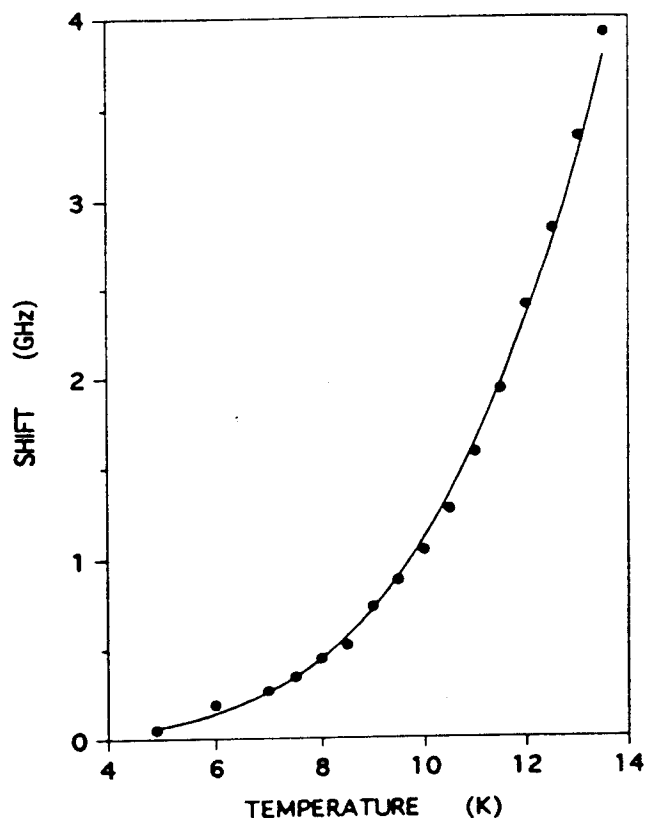
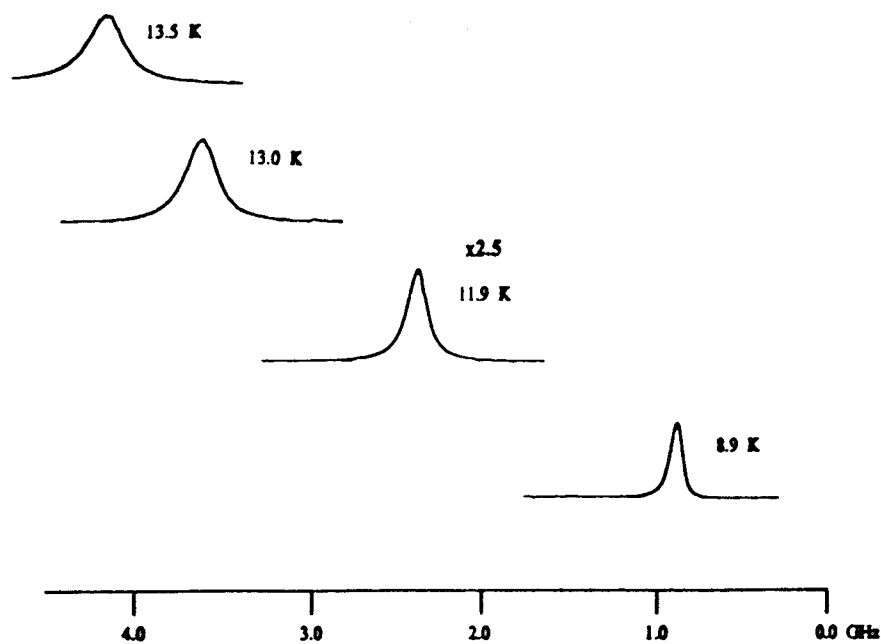


Fig. 4 Temperature variation of the  $Q_1(0)$  transition. The spectral frequency varies  $\sim 4$  GHz as the temperature is varied from 4.2 K to 13.5 K. The linewidth increases by a factor of  $\sim 4$ . Note that the lineshape changes from near Gaussian shape to almost perfect Lorentzian. For the discussion see Ref. 14.

energy spectrum calculated by Bose and Poll,<sup>16</sup> which agrees with the observation semiquantitatively.

While the quadrupolar field of  $J = 1$   $H_2$  acting on the host  $J = 0$   $H_2$  induces broad spectrum, it induces sharp spectrum on impurities such as  $J = 0$   $D_2$  or HD which are embedded randomly in the crystal in small concentration. In this case the vibron is well localized because of the large energy mismatch between the impurity  $D_2$  or HD and surrounding para- $H_2$ . The resulting  $Q_1(0)$  transition of  $D_2$  or HD, however, are accompanied by simultaneous transitions of the  $J = 1$   $H_2$  and show intricate structure which has been a puzzle for us for the last few years.<sup>17</sup> We have now completely understood this structure thanks to a very thorough and persistent effort by graduate student David Weliky and theoretical calculations by Teri Byers.<sup>11</sup> I regard this to be a major progress. When the concentration of impurity  $D_2$  or HD is small, vibrons are well localized on impurity sites and the spectral lines are observed to be extremely sharp ( $\Delta\nu \sim 2$  MHz *hwhm*). When the concentration of the impurity is increased, however, each spectral line starts to show structure which somewhat resembles that of vibron bands as shown in Fig. 6. It is likely that this structure is caused by vibron hopping among randomly distributed impurities which produce some Bloch-type state. I believe this phenomenon poses a well defined interesting theoretical problem.

## 6. Charge Induced Spectrum<sup>18</sup>

In our attempt to possibly obtain high energy density matter, we energized solid hydrogen by ionization using accelerated electrons (3 MeV) and  $\gamma$ -ray radiation. After a few years of trial and error we found that the latter method is superior because of its efficiency, its ability to produce uniform ionization, and its ease of operation. High energy  $\gamma$ -ray (1.17 MeV and 1.33 MeV) ionize  $H_2$  to form  $H_2^+$  initially by Compton scattering. The scattered electrons have energies of a fraction of MeV and they initiate cascades of ionizations. Altogether approximately  $1.5 \times 10^{17}$  cm<sup>-3</sup> of ionizations occur in the crystal after one hour of  $\gamma$ -ray irradiation. Such intense ionization would leave the ordinary dielectric materials as rubble of

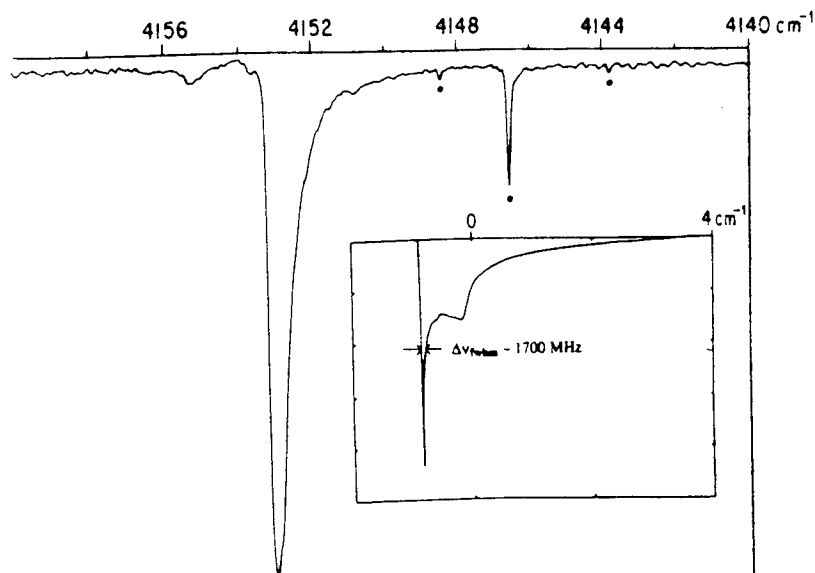


Fig. 5 Broad spectral feature corresponding to the  $Q_1(0)$  transition of  $H_2$  induced by the quadrupolar electric field of  $J=1$   $H_2$ . Breakdown of translational symmetry violates the  $\Delta k = 0$  rule. Inset shows the vibron energy spectra calculated by Bose and Poll.<sup>16</sup>

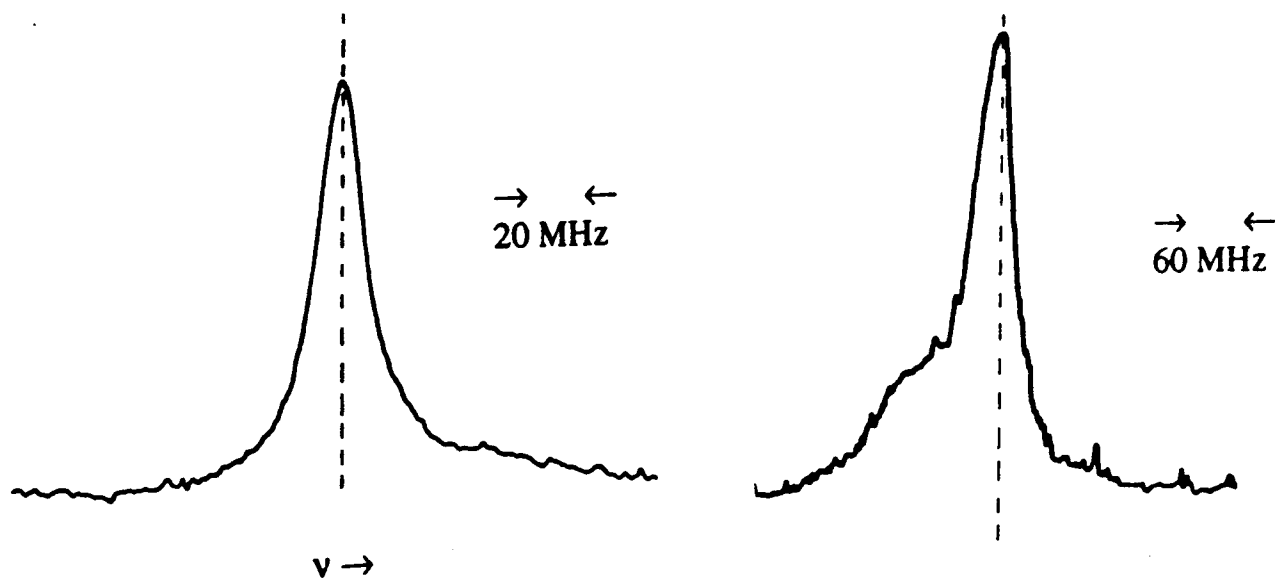
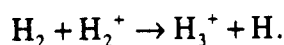


Fig. 6 Sharp spectral line of  $D_2$  induced by the electric field of  $J=1$   $H_2$ . On the left is a spectrum of a sample containing 0.1%  $J=0$   $D_2$ . On the right is a spectrum of a sample containing 0.4%  $J=0$   $D_2$ . The latter shows asymmetric vibron-like lineshape due to vibron hopping among randomly localized  $D_2$ . Both samples contain 0.2% ortho- $H_2$  impurity.

radiation damage, but the extraordinary self-repairing nature of solid hydrogen keeps the crystal still ordered and transparent to radiation.

An example of the charge induced spectrum is shown in Fig. 7. To our surprise, the spectrum is very sharp and intense, and appears very close in frequency to the position of the Raman (or Condon) spectrum. This clearly shows that the spectrum is induced by the electric field of charges introduced in the crystal by  $\gamma$ -ray radiolysis and that there exist well defined vibron Bloch state and the  $\Delta k = 0$  selection rule. The structure of the line seen in Fig. 7 depends on individual crystals and resembles that of Raman spectrum with high ortho concentration (Fig. 5); we have not understood it yet. Based on Condon's theory, the intensity of the signal gives estimates of average charge induced electric field to be 4 ~ 12 kV/cm. One surprising aspect of the charge induces signal is its stability. When the crystal temperature was varied from 4.2 K to 13.5 K near the triple point, the frequency of the spectrum was blue shifted by ~ 4 GHz similar to the Condon spectrum discussed earlier. When the temperature was brought back to 4.2 K, the signal came back to the original position with the original intensity. The reproduction of the signal after temperature cycles demonstrates the amazing stability of the charges distributed in the crystal.

We speculate that positive charges are stabilized and localized by the following processes. The  $H_2^+$  ions produced by  $\gamma$ -ray radiolysis immediately react with surrounding  $H_2$  to form  $H_3^+$  through the well known efficient reaction,<sup>19</sup>



The  $H_3^+$  thus produced attracts neighboring  $H_2$  and stabilizes in the form of cluster ions  $H_3^+(H_2)_n$ . An estimate of the number density of the positive charge thus stabilized depends a lot on the fate of negative charges. The electrons ejected by  $\gamma$ -ray radiolysis cannot stabilize on  $H_2$  and migrate around in the crystal. Most of them recombine with the positive charges and are neutralized. Some of them may reach the wall of the container and fall into it (the work function



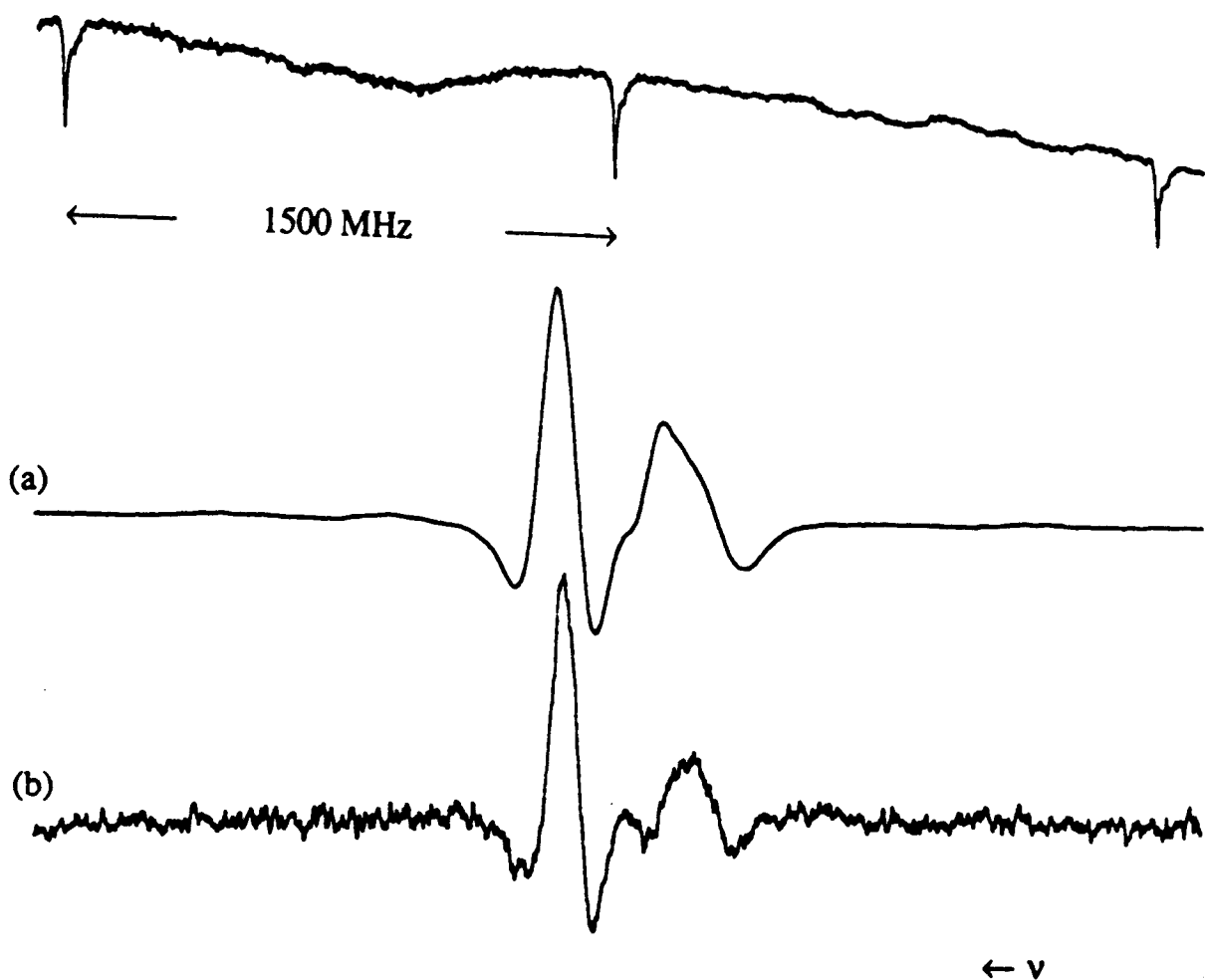


Fig. 7 Simultaneously recorded signal of the  $\gamma$ -ray induced  $Q_1(0)$  transition using infrared spectroscopy (middle trace) and stimulated Raman spectroscopy (lower trace). The upper trace gives interference fringe of a spectrum analyzed separated by 1500 MHz

of Cu is 4.56 eV). However some of them may combine with hydrogen atoms that are copiously produced by the  $\gamma$ -ray radiolysis,<sup>20</sup> and get stabilized in the form of  $H^-(H_2)_n$ . If we assume the extreme case in which no negative charge is stabilized in the crystal, the observed electric field of  $\sim 10$  kV/cm gives the positive charge density estimate of  $\sim 10^{10}$  cm<sup>-3</sup> from Gauss' theorem. On the other hand, if we assume the opposite extreme in which the number densities of the positive and negative charges are equal and the crystal is overall neutral, then we obtain an estimate of  $\sim 10^{15}$  cm<sup>-3</sup>. We shall attempt to determine the charge density by directly observing spectrum of  $H_3^+(H_2)_n$  cations. For both extreme cases, the long range Coulomb field covers sufficient domain of crystal that vibron Bloch states exist and give  $\Delta k = 0$  rules. More detail of this argument is given in Ref. 18.

## References

1. I.F. Silvera, *Rev. Mod. Phys.* **52**, 393 (1980).
2. A.R.W. McKellar, *J. Chem. Phys.* **92**, 3261 (1990).
3. L.H. Nosanow, *Phys. Rev.* **146**, 120 (1966).
4. M.C. Cross and D.S. Fisher, *Rev. Mod. Phys.* **57**, 881 (1985).
5. M.J. Roger, J.H. Hetherington, and J.M. Debrieu, *Rev. Mod. Phys.* **55**, 1 (1983).
6. M. Meyer, *Can. J. Phys.* **65**, 1453 (1987).
7. R. Oyarzun and J. Van Kranendouk, *Can. J. Phys.* **50**, 1494 (1972).
8. J.M. Delrieu and N.S. Sullivan, *Phys. Rev.* **B23**, 3197 (1981).
9. J. Van Kranendouk, **Solid Hydrogen**, Plenum Press, New York (1983).
10. T. Oka, *Annu. Rev. Phys. Chem.* **44**, 299 (1993).
11. D.P. Weliky, T.J. Byers, K.E. Kerr, T. Momose, R.M. Dixon and T. Oka, *Appl. Phys.* **B59**, (1994) in press.
12. T. Momose, D.P. Weliky, and T. Oka, *J. Mol. Spectrosc.* **153**, 760 (1992).
13. T. Momose, K.E. Kerr, R.M. Dixon, Y. Zhan and T. Oka, manuscript in preparation.
14. K.E. Kerr, T. Momose, D.P. Weliky, C.M. Gabrys and T. Oka, *Phys. Rev. Lett.*, **72**, 3957 (1994).
15. E.U. Condon, *Phys. Rev.* **41**, 759 (1932).
16. S.K. Bose and J.D. Poll, *Can. J. Phys.* **68**, 159 (1990).
17. M.-C. Chan, L.-W. Xu, C.M. Gabrys, and T. Oka, *J. Chem. Phys.* **95**, 9404 (1991).
18. T. Momose, K.E. Kerr, D.P. Weliky, C.M. Gabrys, D.M. Dickson and T. Oka, *J. Chem. Phys.*, **100**, 7840 (1994).
19. T. Oka, *Rev. Mod. Phys.* **64**, 1141 (1992).
20. T. Miyazaki, S. Kitamura, H. Morikita, and K. Fueki, *J. Phys. Chem.* **96**, 10331 (1992).

## Diffusion in Crystalline and Amorphous Solid Hydrogen

James R. Gaines<sup>(1)</sup>, Gilbert W. Collins<sup>(2)</sup>, P. Clark Souers<sup>(2)</sup>, James D. Sater<sup>(2)</sup>,  
and Peter A. Fedders<sup>(3)</sup>

### I. INTRODUCTION

Nuclear magnetic resonance (NMR) is one of the few experimental methods that can study diffusion directly as the hopping motion of particles with nuclear spin causes a predictable dephasing of the NMR signal so that the diffusion coefficient can be measured in situ negating the need for a radioactive tracer element. The solid molecular hydrogens represent an especially interesting class of solids in which to study diffusion since there are three isotopes (H, D, and T) from which molecules with masses of 2, 3, 4, 5, and 6 can be formed. We will present new data on molecular diffusion and some different theoretical models to extract the atom diffusion coefficient for comparison with the molecular diffusion coefficient.

### II. Theoretical Background

Consider only the so called "monovacancy limit" where the concentration of vacancies,  $c_v$ , is very small. We define  $\Gamma_0$  as our basic rate. It is the probability per unit time that a host molecule (eg  $H_2$ ) will hop to a vacant neighboring site. Then the vacancy diffusion coefficient  $D_v$ , the diffusion constant associated with vacancy motion, is:

$$D_v = \frac{1}{6} Z a^2 \Gamma_0 \quad (1)$$

where  $Z$  is the number of neighbors (12 for hcp), and  $a$  is the distance of one hop. The probability per unit time that a vacancy will hop is  $Z\Gamma_0$  because a vacancy has  $Z$  sites to jump to. On average 1/6 of the jumps take the vacancy in a given direction.

**A. The diffusion of molecules.** The probability that any site neighboring a given molecule is vacant (and thus a molecule can hop to it) is  $c_v$ . Thus, roughly, the diffusion coefficient for a molecule is  $c_v D_v$ . In fact this is not quite correct since the molecule under consideration and the vacancy can undergo multiple scattering. Thus the diffusion coefficient for a molecule is written as

$$D_m = f_m c_v D_v \quad (2)$$

where  $f_m$  is the (tracer) correlation factor,  $f_m = 0.781$  for an fcc lattice and certain motions on an hcp lattice.

We define the "molecular hopping rate",  $\Gamma_m$ , the rate calculated by Ebner and Sung [1] as  $\Gamma_m = c_v Z f_m \Gamma_0 = 1/\tau_c$ , where  $\tau_c$ , used below, is the correlation time. Except for details like  $f_m$ , one can think of  $\Gamma_m$  as the "effective hopping rate" of a host molecule to any site and

$$D_m = \left(\frac{Z}{6}\right) f_m c_v \Gamma_0 a^2 = \Gamma_m \left(\frac{a^2}{6}\right) \quad (3)$$

---

(1) Dept. of Physics  
2505 Correa Road  
Honolulu, HI 96822

(2) Lawrence Livermore National Laboratory  
ICF Program  
Livermore, CA 94550

(3) Dept. of Physics  
Washington University  
St. Louis, Missouri 63130.

*Expressions used to obtain D from the data.* Our NMR data consists of a measurement of the temperature dependence of the NMR time constant denoted  $T_{ss}$  (usually denoted  $T_2$  but we will use  $T_{ss}$  to avoid confusion with molecular tritium in this section), roughly the inverse linewidth, from spin-echo experiments. We will relate the measured quantity  $T_{ss}$  to the correlation time  $\tau_c$  by the expression:

$$\frac{1}{T_{ss}} = 1.338 M_2 \tau_c \quad (4)$$

where  $\tau_c$  is the correlation time and  $M_2$ , is the rigid lattice second moment. Including the factor  $f_m$ , the diffusion coefficient for molecules,  $D_m$ , will be calculated from the expression:

$$D_m = [1.338 M_2 T_{ss}] \left( \frac{a^2}{6} \right) \quad (5)$$

*The Theory of Ebner and Sung.* The single theoretical study was performed by Ebner and Sung [1]. The Ebner and Sung paper was reviewed and augmented in the paper by Zhou et al [2]. Ebner and Sung considered two possible mechanisms: (i) thermally activated diffusion over a barrier into a vacancy and (2) tunneling through the barrier into a vacancy. The former process would dominate at high temperatures with the latter process dominating the low temperature behavior. A diffusion coefficient of the form

$$D = D_0 \exp\left(-\frac{E_a}{kT}\right) \quad (6)$$

was predicted in both temperature regimes, with the values of both  $D_0$  and  $E_a$  depending on the specific limit with  $E_a = E_v + E_b - E_t$  for high temperature and  $E_a = E_v$  for low temperatures where  $E_v$  is the energy to create a vacancy,  $E_b$  is the barrier height,  $E_t$  is the energy of the first tunneling level.

**B. The diffusion of atoms.** There have been no direct measurements of  $D$  for atoms. However measurements of the recombination coefficient can be analyzed to yield the atom hopping rate and hence the diffusion coefficient. Defining  $2\alpha$  as the atom recombination coefficient,  $v_0$ , the volume per molecule ( $a^3/\sqrt{2}$ ),  $Z$  the number of nearest neighbors,  $\tau_{hs}$ , the time to hop to a specific site,  $\tau_r$ , the recombination time, and  $\xi_1$  a constant of order unity, the recombination coefficient can be shown to be equal to:

$$2\alpha = \frac{2Z^2 v_0}{\xi_1 \tau_{hs} + Z\tau_r} \quad (7)$$

If we assume that  $\xi_1 \tau_{hs} \gg Z\tau_r$ , then  $2\alpha = 2v_0 Z \Gamma_{any}$ , where  $\Gamma_{any}$  is the rate for an atom to hop to any site and thus  $Z$  times larger than the rate to hop to a specific site. Thus from the recombination coefficient, we obtain the atom hopping rate which can then be compared to the molecular hopping rate.

### III. EXPERIMENTAL DATA

We have made new measurements of the molecular self diffusion coefficient in the solid hydrogens by conventional pulsed NMR techniques in  $T_2$ , DT, and HD and have verified the original measurements in  $H_2$  [3-5]. Our new measurements, at 30 MHz, when combined with earlier ones provide a more complete picture of molecular diffusion in these quantum solids and can be interpreted to give some additional insight into the relationship between atomic diffusion and molecular diffusion.

**A. The new NMR data.** Experimentally, we measure the temperature dependence of the transverse relaxation time (spin-spin),  $T_{SS}$ , in the region where motional effects dominate the observed linewidth. The samples are loaded into the cell as liquids. The temperature is then reduced in increments of about 0.5 K. A Carr-Purcell-Meiboom-Gill pulse sequence was used to measure  $T_{SS}$  at the higher temperatures but a single  $90^\circ$  pulse was used when  $T_{SS}$  became too short for the longer sequence to be practical. Quadrature detection was used so that the signals had to be phase corrected and then extrapolated to  $t = 0$ . All other work on the diffusion coefficient in molecular hydrogen has used this approach with the exception of the work on  $D_2$  by Meyer and co-workers [6,7]. They used a more sophisticated approach involving rotating frame measurements, a technique that is well grounded theoretically.

Our new NMR measurements of  $T_{SS}$  in HD, D-T and  $T_2$ , expressed as diffusion coefficients,  $D(T)$ , are given in Figure 1. Points taken in the liquid phase are included in this figure but are not included in the analysis of the solid data. Data taken on the isotopes  $H_2$  and  $D_2$  by H. Meyer and co-workers are included for comparison and completeness. Since the parameters that characterize the 6-12 potential in all the isotopes are the same, the diffusion coefficients should have universal behavior but don't. The behavior, while not universal, is smooth, showing only simple thermal activation. Accordingly, we used Eqn. 6 to fit the data and extracted  $E_a$  and  $D_0$ . The activation energies for all the isotopes are given in Table 1.

TABLE 1. The activation energies and diffusion coefficient prefactors used in our analysis, for molecules, are summarized in the table below.

Isotope	$E_a$ (K)	Heat Sub. (K)	$D_0$ (cm <sup>2</sup> /s)
$H_2$	197	92.6	$3.64 \times 10^{-3}$
HD in $H_2$	197		$5.7 \times 10^{-3}$
HD	250	116.7	$6.84 \times 10^{-3}$
$D_2$	300	138.3	$1.30 \times 10^{-2}$
D-T	372	150.3	0.443
$T_2$	432	164.8	2.62

#### IV. ANALYSIS AND INTERPRETATION

In this section we will analyze and interpret data taken on molecules and atoms in the solid hydrogens. Some of the samples will have been made by slow crystallization from the liquid phase while others will have been formed by deposition of vapor on a cold substrate.

**A. Molecules.** In attempting to compare data on different quantum solids, it is customary to use reduced variables, an approach similar to that used in applying the "law of corresponding states" to the behavior of different gases in an attempt to see the universal features of all gases. The reduced variables in this case are formed from dimensionless combinations obtained from the two Lennard-Jones parameters,  $\epsilon$  and  $\sigma$ . Unfortunately, these parameters are approximately the same for all the hydrogen isotopes so that one prediction of this approach would be that the product of the diffusion coefficient ( $D$ )

and the square root of the mass ( $\sqrt{M}$ ) would be the same for all the hydrogen isotopes. This is clearly incorrect for the data in Figure 1. For instance, by drawing a horizontal line, it is seen that the same values of  $D$  occur for widely different values of  $1/T$  or, for a given value of  $T$ , the diffusion coefficient of the lightest isotope,  $H_2$ , is far larger than that of the heaviest isotope,  $T_2$ . This is a clear quantum effect. A different method of comparing the isotope data is required.

**1. Temperature scaling.** What we seek is a non-trivial scaling so that we can find how the parameters  $D_0$  and  $E_a$  vary from isotope to isotope--even though the potentials are essentially the same--except for the equilibrium spacings of the molecules. We have found one method that works, namely "temperature scaling" based on the quantum parameter [8]. The basic idea can be illustrated by plotting the triple point temperature of each isotope ( $T_{tp}$ ), multiplied by the quantum parameter for that isotope as a function of the quantum parameter,  $\Lambda$ . The product  $\Lambda T_{tp}$  is roughly constant with a mean value of 22.8 and an rms deviation of 6% even though the triple point temperatures range from 13.8 for  $H_2$  to 20.6 for  $T_2$ .

This approach to scaling is tested in Figure 2, where the diffusion coefficients for all the isotopes are plotted as a function of  $[\Lambda T]^{-1} = 1/T_s$ , where  $T_s$  is the "scaled temperature". The "parallel lines" formed by the data points indicate that the activation energy scales with the quantum parameter. A plot of the product of  $D(T)\Lambda^4$  vrs the  $E_a/T$ , groups the data points into two series; one for the non-radioactive isotopes and one for the radioactive ones.

**3. The vacancy hop frequency.** From our determination of the hopping frequencies for the isotopes, we can calculate the hop frequency of a vacancy at the triple point for comparison. If we try to isolate the hop frequency of vacancies, at the triple point, for comparison, we write:

$$(\Gamma_{any})_{H_2} = 12 c_v f_m \Gamma_0 = 12(\Gamma_0) f_m \exp(-E_v/T) \quad (8)$$

Thus, to within a factor of four, the vacancy hop rate, at the triple point temperature, is the same for all the hydrogen isotopes.

**B. Atoms.** The hopping of atoms controls the steady-state population of atoms trapped in solid hydrogen. This has never been studied directly through a measurement of the atom diffusion coefficient but there are two other approaches that have probed the steady-state atom population and the atom dynamics. These are EPR (electron paramagnetic resonance) studies and measurements (and modeling) of the ortho to para conversion of molecules of  $T_2$  in solid  $T_2$ . In this case, there have been measurements on crystalline solids and also measurements on amorphous solids.

**1. Crystalline Solids.** Leach and Fitzsimmons [9] produced H atoms in crystalline  $H_2$  by electron bombardment and studied atom recombination after the electron beam was turned off. Defining  $n$  to be the atom density, after the beam is off,

$$\frac{dn}{dt} = - (2\alpha) n^2 \quad (9)$$

where  $\alpha$  is the atom recombination coefficient. They could measure it directly from the time decay of the EPR signal which was proportional to the density of atoms,  $n$ . They found that

$$\alpha = \alpha_0 \exp(- E_\alpha/T)$$

where the activation energy  $E_\alpha = 195 \pm 10$  K, remarkably like that found for  $H_2$  molecules in solid  $H_2$ . Our

relationship between the recombination coefficient and the atom hopping rate ( $\Gamma$ ), Eqn. 7, can be used to extract  $\Gamma$  from the measured values of  $\alpha$ . We find that (after setting the activation energies to a common value)

$$(\Gamma)^H = (5.9 \times 10^{13} \text{ sec}^{-1})\exp(-197/T)$$

This can be compared with the molecular hopping rate obtained from the NMR data

$$(\Gamma)^{H_2} = (1.56 \times 10^{13} \text{ sec}^{-1})\exp(-197 \text{ K}/T)$$

showing that the atom and molecule hopping rates are almost identical in  $H_2$ , differing only by a factor of four.

Other important information about crystalline solids is provided by our data taken using NMR techniques on the ortho to para conversion in solid  $T_2$  [9]. There have been no direct measurements of the atom recombination coefficient in solid tritium. Because the ortho-para conversion process is catalyzed by the presence of atoms [ref.], the rate is a sensitive function of the steady-state atom population. Using this fact, we were able to extract the atom recombination coefficient from that data and calculate the atom hopping rate as well. The details have been given in Ref. 9.

In Figure 3, we show the recombination coefficient obtained by EPR techniques for H atoms in crystalline  $H_2$  plotted for comparison with the T atom recombination coefficient obtained by modeling the NMR data on solid  $T_2$ . The temperature is scaled by the quantum parameter for  $H_2$ , namely  $\Lambda = 1.731$  since the quantum parameter for  $T_2$  is unity. The agreement is outstanding even though the recombination coefficients are no longer following a simple thermally activated form.

**2. Amorphous Solids.** The data taken in Russia on atoms in  $H_2$  and  $D_2$  [11,12] represent data on amorphous, not crystalline solids. Up to now there has been the attempt to understand the two sets of data in terms of the extensive data base that we have on the crystalline hydrogens. We will depart from that approach. Their samples were prepared by depositing streams of  $H_2$  or  $D_2$  gas, containing atoms produced by microwave discharge, onto cold substrates, held at 2 K or below. The recombination coefficients for the amorphous samples are compared in Figure 4 with those from crystalline samples. Note that there is not good agreement even between the amorphous  $H_2$  and  $D_2$  experiments nor is there agreement between the amorphous and crystalline samples.

## V. CONCLUSIONS

Based on this data and our analysis, we can draw the following conclusions:

(1) the diffusion of these crystalline solids c- $H_2$  etc. is controlled by the number of vacancies in the lattice. This is in agreement with the theory of diffusion in hydrogen by Ebner and Sung.

(2) the non-radioactive isotopes,  $H_2$ , HD, and  $D_2$  have values of  $D_0$  that are very regular and predictable from the relationship  $D_0 = (0.0241)\Lambda^{-3.6}$ . The radioactive isotopes have much larger values of  $D_0$ , that compensate, in part, for their much larger activation energies. The "apparent activation energies" arise from lattice damage due to the radioactivity that acts to suppress hopping and diffusion.

(3) we have determined values of the vacancy formation energy,  $E_v$ , the barrier height energy,  $E_b$ , and the energy of the first tunneling level in the hydrogen potential,  $E_t$ , defined by Ebner and Sung.



(4) values for the microscopic hopping rates of the molecules can be obtained from the data. We obtain essentially the same vacancy hopping rate, at the triple point, for all the isotopes.

(5) the microscopic atom hopping rates for crystalline samples are slightly larger, but nearly identical, to the corresponding hopping rates for molecules. Thus by studying the molecule hopping rates (say via NMR measurements) one can infer the atom hopping rates.

(6) the recombination coefficients (and hence hopping rates) for crystalline solids differ from those of amorphous solids. Possibly the recombination coefficients for the amorphous solids, at low temperatures, depend on the atom recombination time rather than the vacancy hopping rate.

(7) extrapolation of the data on crystalline-solids to higher temperatures shows that atom diffusion is also dominated by vacancies and that at the triple point the atom hop frequency is somewhat larger than the molecule hop frequency.

## REFERENCES

1. C. Ebner and C.C. Sung, Phys. Rev. A5, 2625 (1972).
2. D. Zhou, M. Rall, E.G. Kisvarsanyi, and N.S. Sullivan, Phys. Rev. B45, 2800 (1992).
3. M. Bloom, Physica 23, 767 (1957). This paper contains both H<sub>2</sub> and HD data.
4. W.P. Haas, N.J. Poulis, and J.J.W. Bonleffs, Physica 27, 1037 (1961).
5. F. Weinhaus and H. Meyer, Phys. Rev. B7, 2974 (1973).
6. F. Weinhaus, S.M. Myers, B. Maraviglia, and H. Meyer, Phys. Rev. B3, 626 (1971).
7. F. Weinhaus, H. Meyer, S.M. Myers, and A.B. Harris, Phys. Rev. B7, 2960 (1973).
8. P. Clark Souers, "Hydrogen Properties for Fusion Energy", University of California Press 1986, 10 ff.
9. R.K. Leach, "A Paramagnetic Resonance Study of Hydrogen Atom Production and Recombination in Solid H<sub>2</sub> from 1.4 to 8 K", Ph. D. thesis, University of Wisconsin, Madison, Wis. (1972). University Microfilms, Ann Arbor, Mich. 48106, 1972, No. 72-23060.
10. J.R. Gaines, J.D. Sater, E.M. Fearon, P.C. Souers, F.E. McMurphy, and E.R. Mapoles, Phys. Rev. B37, 1482 (1988).
11. A.Y. Katunin et al, Soviet Phys. J.E.T.P. Lett. 34, 357 (1981).
12. A.V. Ivliev et al, Soviet Phys. J.E.T.P. Lett. 36, 472 (1982).

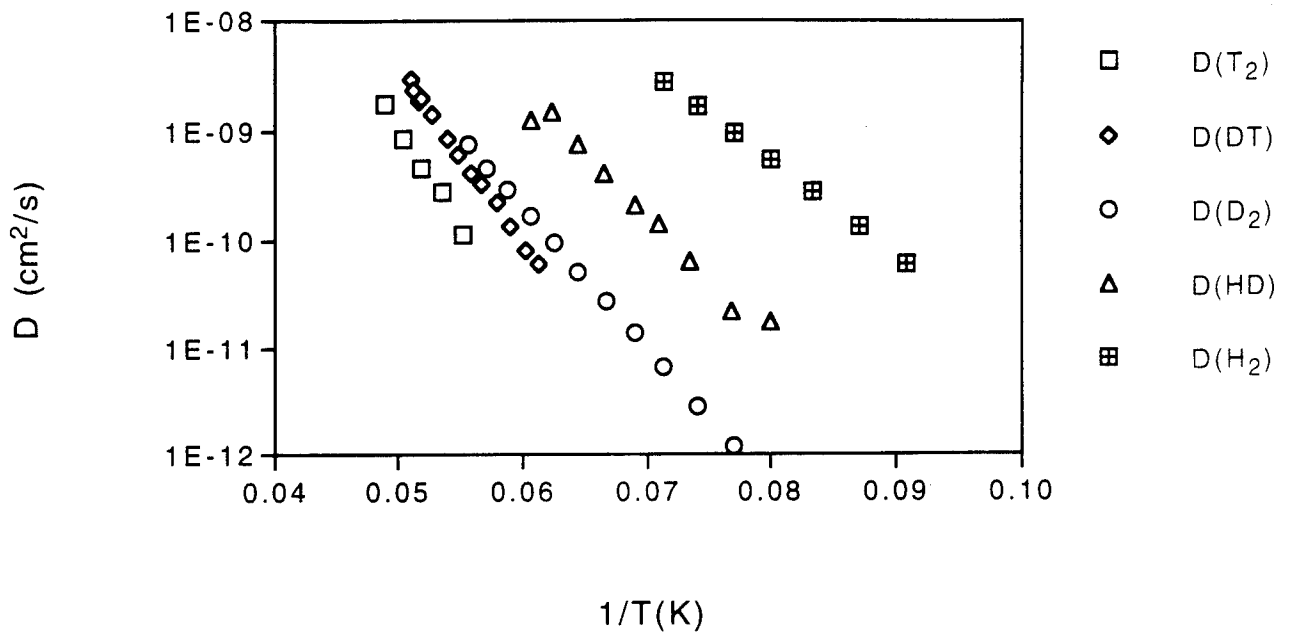


Fig. 1. Diffusion coefficient versus temperature for all isotopes.

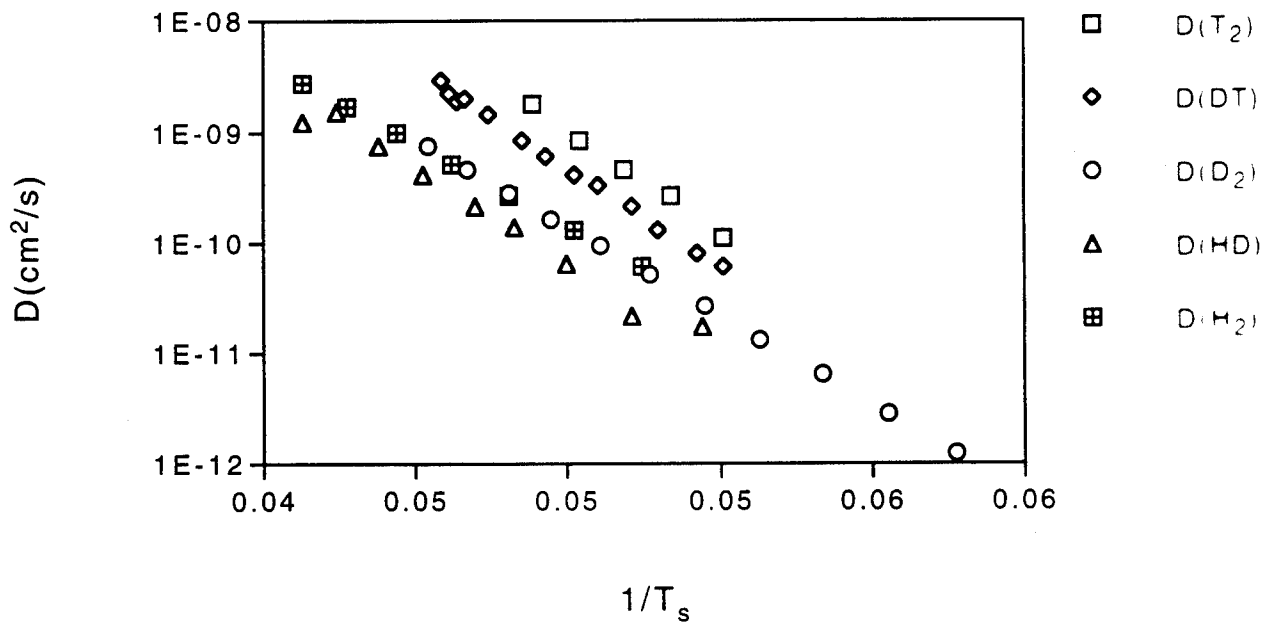


Fig. 2. Diffusion coefficient versus scaled temperature for all isotopes.

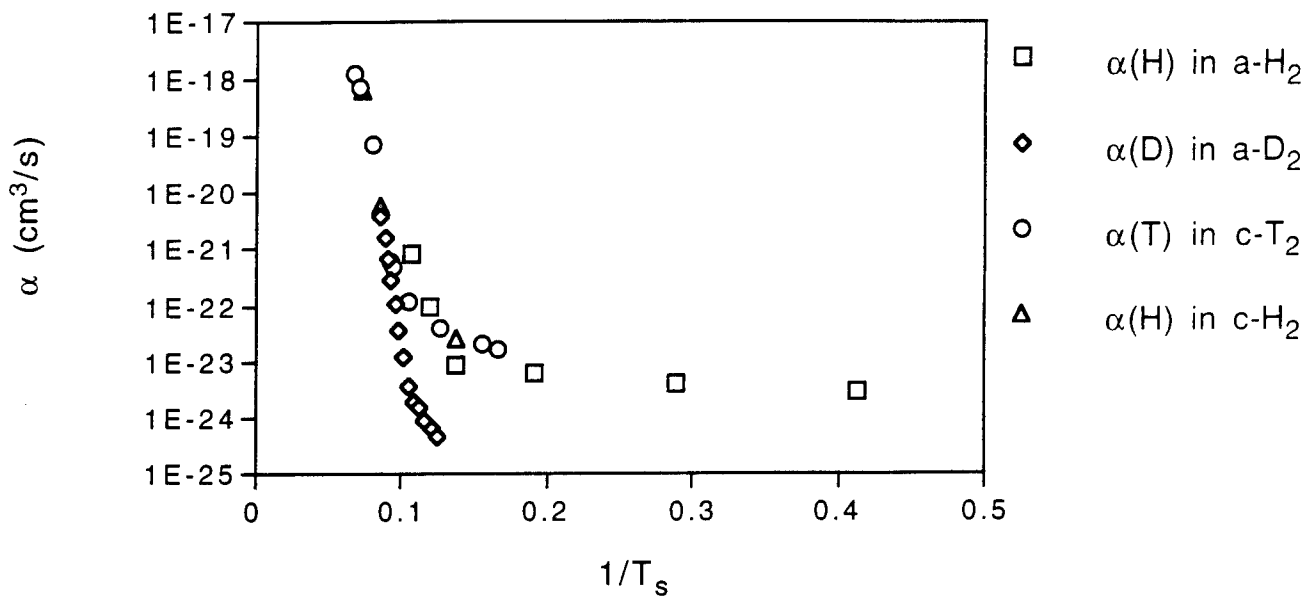


Fig. 3. Coefficient  $\alpha$  versus scaled temperature for all isotopes.

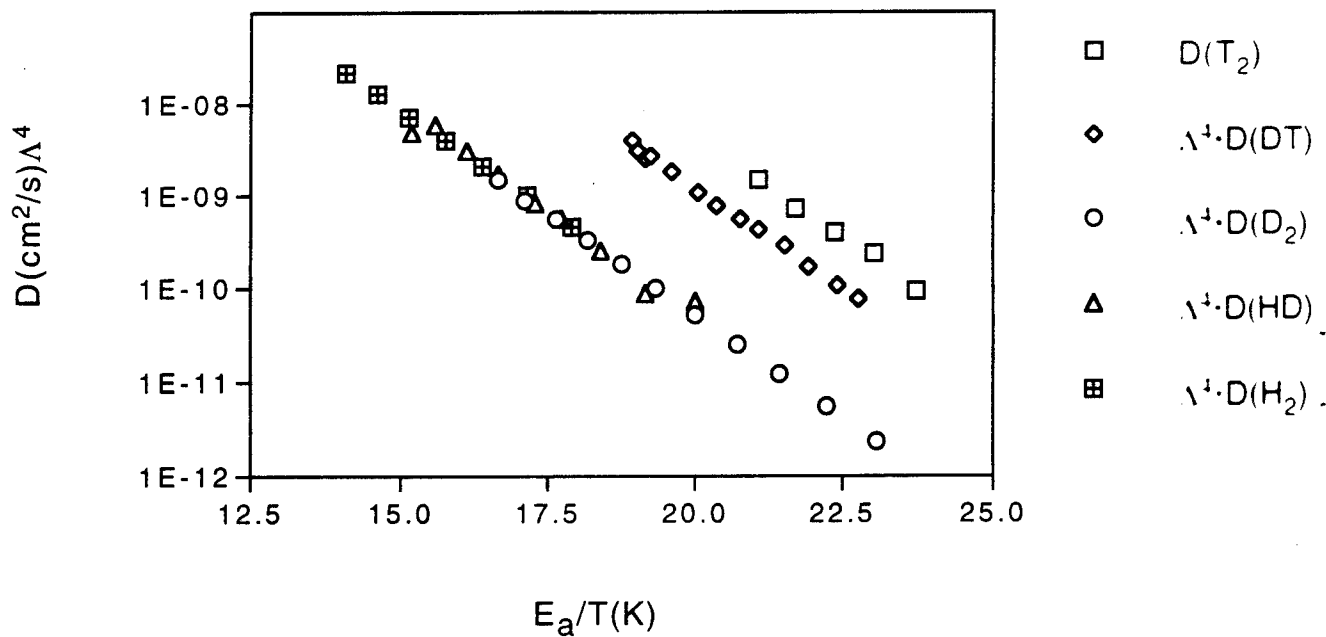


Fig. 4. Diffusion coefficient times  $\Lambda^4$  versus energy/temperature.

## Solid Hydrogen Structure \*

Gilbert Collins, Evan Mapoles, Frank Magnotta, and Tom Bernat

We report on the structure of solid hydrogen films deposited from the gas phase from the triple point temperature down to 3 K. From the rotational Raman spectrum of  $J=0$  hydrogen and deuterium deposited below half their respective triple point temperature, we find four peaks instead of the three crystal field split peaks expected from the HCP phase. This is similar to the rotational Raman signal observed in rapidly pressurized solid hydrogen from Professor Silvera's lab. We find that the sample transforms into an HCP phase continuously and irreversibly as the temperature increases through about half the triple point temperature. We also find that impurities can inhibit this transformation to an HCP phase. At low temperature the deposited crystals are microcrystalline. As the deposition temperature approaches the triple point, single crystals of millimeter extent are easily formed. We report the roughening transition temperature from these crystals.

\* Work performed under the auspices of the U.S. Department of Energy by Lawrence Livermore National Laboratory under Contract W-7405-ENG-48.

## Triple Point of the BSP-DA-HCP Insulating Phase in Megabar Pressure Deuterium

Isaac F. Silvera  
Lyman Laboratory of Physics  
Harvard University, Cambridge, MA 02138

A sample of solid deuterium has been studied in a diamond anvil cell to pressures over 2 megabar using both IR and Raman spectroscopy. Using IR spectroscopy the phase lines of the D-A and BSP phases were determined as well as a triple point where these phases meet the hcp phase. From the observations of both Raman and IR modes possible crystal structures for the various phases are proposed.

Although it is believed that the isotopes H<sub>2</sub> and D<sub>2</sub> should behave similarly at high pressure because they are isoelectronic, most high pressure research has been carried out on H<sub>2</sub> and very little on D<sub>2</sub>. At very high pressure in hydrogen, the phase known as the H-A phase has been studied extensively. The onset at low temperature is at 149 GPa and with increasing pressure the phase line rises sharply in the T-P phase diagram. It has been reported that this line terminates in a critical point [1, 2]. However, other than this, the phase has not been characterized, although it has been proposed that this may be the molecular metallic phase of hydrogen. For deuterium, only one point has been observed for a high pressure phase transition at 77K and 165 GPa [3]; this has been assigned to the D-A phase, but for a rigorous identification the phase line should be determined. Both hydrogen and deuterium have a broken-symmetry transition, the transition to orientational order of para-hydrogen or ortho-deuterium; however, the T-P phase line has not been well investigated. Deuterium has been studied from the low pressure onset at 28 GPa to 40 GPa and only a single point in hydrogen has been determined at the onset, 113 GPa. It is not known how the BSP and the H-A (D-A) phases merge. In the work reviewed here [4], we study deuterium to a pressure of 210 GPa, determining the BSP and D-A phase lines and find a triple point where the BSP, H-A, and low pressure hcp phases merge. Our results imply that the critical point in hydrogen was erroneously identified.

We have loaded normal deuterium into a diamond anvil cell (DAC) in a cryostat with the capability of varying the temperature from 4.2 K to room temperature. The sample could be held at low temperature for extended periods of time so that it converts to pure ortho-D<sub>2</sub>. It is important to have a pure crystal, for then the selection rules which find their origin in the translational symmetry for perfect crystals applies, whereas a mixed ortho-para crystal does not have translational symmetry. We studied the sample by both Raman and IR spectroscopy. For the latter we used a tunable Burleigh color-center laser. Our objective was to determine the phase lines by observing changes in the spectra as the lines were crossed. Pressures as high as 210 GPa were achieved.

It turns out that the IR spectrum of the vibrons is a very sensitive probe and the phase lines determined by this technique are shown in fig. 1. In the discussion it is more convenient to first call the three phases I, II, and III. In the low pressure phase no IR absorption was observed. This is consistent with phase I having hcp symmetry in agreement with the known crystal structure for this phase. In phase two, three distinct IR vibron modes have been detected; in phase III, just one vibron is observed. The crystal structure of both of these phases is unknown. We see that we have been able to identify the D-A phase line, the phase corresponding to the H-A phase line. In addition we have determined the BSP phase line up to the point where it meets the D-A, to determine the triple point of the hcp, BSP, and the D-A phases. From IR spectroscopy above the

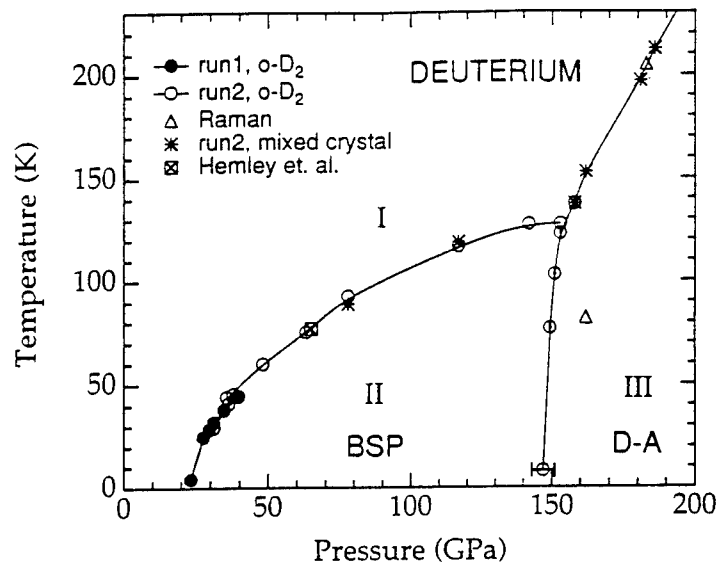


Fig. 1. The phase lines of deuterium as determined by infrared spectroscopy showing the triple point.

triple point we find that a phase line still exists, separating the hcp and D-A phases.

The H-A phase was earlier determined by a discontinuity in the Raman active vibron frequency in crossing from the low pressure phase to the H-A phase. Above a certain pressure and density, this continuity went to zero and this was the basis for the identification of the "critical point". In our deuterium work, we have evidence that the Raman vibron discontinuity goes to zero above the triple point. Thus, we are led to propose that the "critical point" in hydrogen was probably misidentified and it is probably a triple point, as in deuterium. This can be verified by a spectroscopic study in hydrogen similar to the one we have carried out in deuterium.

Finally, from our spectroscopic data, along with a group theoretical analysis which we have carried out, we can comment on the possible structures of the high pressure phases of deuterium; the comments are probably applicable to hydrogen, but this awaits a detailed spectroscopic study. The single IR vibron of the D-A phase means that it cannot have the hcp structure. A possible structure which is compatible with the single IR, and single Raman vibron is P2/m. A possible structure for the BSP phase is Pca2<sub>1</sub>. This phase should have 3 IR vibrons, but 4 Raman vibrons are expected, where only one is observed. It is possible that some of these Raman modes are degenerate or very weak, so that only one distinct mode is observed. Such a determination will require further detailed study.

This research has been supported by U.S. Air Force contract No. F29601-92-C-0019 from the Phillips Laboratories.

#### References

1. R.J. Hemley and H.K. Mao, *Science* **249**, 391 (1990).
2. H.E. Lorenzana, I.F. Silvera, and K.A. Goettel, *Phys. Rev. Lett.* **65**, 1901 (1990).
3. R.J. Hemley and H.K. Mao, *Phys. Rev. Lett.* **63**, 1393 (1989).
4. L. Cui, N.H. Chen, S.J. Jeon, and I.F. Silvera, *Phys. Rev. Lett.* **72**, 3048 (1994).

## SPECTROSCOPY OF ALKALI ATOMS AND MOLECULES ATTACHED TO HIGHLY QUANTUM CLUSTERS

F. Stienkemeier, W. Ernst\*, J. Higgins and G. Scoles  
Chemistry Department, Princeton University, Princeton, N.J. 08544

We have assembled a molecular beam laser spectrometer for the study of chromophore-doped clusters. The clusters are prepared by expansion of a gas through a small nozzle at temperatures variable from 12K to room temperature and at pressures up to 100 atm. Because of the very high pumping speed available in the expansion chamber ( $32,000 \text{ l s}^{-1}$ ) the nozzle can discharge a relatively large quantity of gas (in excess of  $10 \text{ cm}^3 \text{ STP}$ ) producing, therefore, a large flux of clusters. Approximately 1% of the condensed gas flux is collimated by a conical skimmer and is admitted to a second vacuum chamber pumped by a  $5,000 \text{ l s}^{-1}$  diffusion pump. Assuming that 10% of the gas admitted to the second chamber is in the form of large clusters, with an average cluster size of  $10^3$  atoms, the cluster beam flux results to be of the order of  $10^{14}$  clusters per second. The temperature of these clusters is estimated to be 0.4K. A few centimeters after the skimmer the clusters cross a scattering (pick-up) box which is connected to an alkali atom reservoir located outside the apparatus. Both scattering box and reservoir can be heated up to 1000K. The scattering box is kept normally at a temperature 100K higher than the reservoir to avoid alkali atom distillation and to keep the alkali vapor contained in the box (typically at a partial pressure between  $10^{-4}$  and  $10^{-3}$  torr) free of dimers. According to the value of the alkali pressure in the box, the clusters pick-up one or more alkali atoms without being appreciably deflected from their (straight) path. A few centimeters downstream of the pick-up cell the clusters are crossed with the well baffled output beam of a tunable dye laser (Spectra Physics 380) at the center of a two-mirror laser induced fluorescence (LIF) detector of standard design.<sup>(1)</sup> A Langmuir-Taylor surface ionization detector, located beyond the LIF detector, monitors the presence of alkali atoms in the beam and helps in establishing the optimum cluster source and pick-up cell conditions for maximum cluster flux conditions and desired alkali dopant concentration in the clusters. A schematic of the set-up is shown in fig. 1.

With this apparatus we have, during the last two months, measured four spectra of different alkali species. Three of the spectra have been assigned while the fourth, which is, by far, the most intense feature, has so far escaped assignment. These four spectra will be presented in succession hereafter. Their discussion will help to illustrate the capability of the present set up. A brief discussion about possible future developments will conclude this abstract.

---

\*Permanent address: Physics Department, Penn State University, University Park, PA. 16802

a) Monomer spectrum

The spectrum of the Na monomer attached to the He clusters, measured by chopping the doped-cluster beam and detecting the phase-related LIF signal with a lock-in amplifier, is shown in fig. 2. The two arrows on the wavelength scale indicate the position of the free Na ( $3^2S_{1/2} \rightarrow 3^2P_{1/2}$ ,  $3^2P_{3/2}$ ) doublet. Notable are the very small shift of the absorptions and their long blue tails. Since the Na atoms are believed to reside on the cluster surface <sup>(2)</sup> a relatively small "bubble" blue shift <sup>(3)</sup> is expected. Adding a polarizability-induced red shift would help to reduce the shift further. The blue tails seem to increase in importance with increasing cluster size.

b) Dimer spectrum: the ( $A^1\Sigma_u^+ \leftarrow X^1\Sigma_g^+$ ) transition

The left hand side of fig. 3 shows the LIF spectrum of a Na<sub>2</sub> molecule also believed to reside on the cluster's surface. The frequency of these transitions is very close to the gas phase values of the  $A \leftarrow X$  vibronic progression of the Na<sub>2</sub> molecule. The vibrational spacings, which vary according to the anharmonicity of the excited state potential, help to establish that the shift is no more than 10 cm<sup>-1</sup> which is at least two order of magnitude smaller than the shift measured for the corresponding spectrum of the Na<sub>2</sub> molecule imbedded in liquid He. <sup>(3)</sup> In the course of these measurements we made the important observation that some of the oscillations detected in the bands were reproducibly resolvable into a well defined structure. (see fig.4). This structure is likely related to the rotational motion of the Na<sub>2</sub> molecule and may contain also satellite lines produced by the combined excitation of the Na<sub>2</sub> and the (superfluid) helium cluster. We are presently installing a Coherent 699 dye laser in order to use its MHz wide output to resolve the structure of this spectrum further. The presence of the narrow features in this spectrum, and the information which they carry about the structure of the chromophore, combined with the small size of the spectral shifts, illustrate the potential use of He clusters as an almost ideal matrix for matrix isolation spectroscopy.

c) Dimer spectrum: the ( $1^3\Sigma_g^+ \leftarrow 1^3\Sigma_u^+$ ) transition

Since in the He clusters there is no mechanism to induce spin-changing transitions in the atoms that stick to its surface, the formation of high spin alkali aggregates becomes possible or, actually, probable. To be precise a van der Waals bound Na<sub>2</sub> (triplet) dimer should form with 3 to 1 higher probability than a Na<sub>2</sub> singlet molecule. The LIF detected excitation spectrum of the Na<sub>2</sub> lowest triplet state is shown in the right hand side of fig. 3. The assignment is based on the energy of the photons which generate the transition, on the position of the first excited  $\Sigma$  triplet (the  $1^3\Sigma_g^+$  state) potential energy curve (as reported by Magnier et al. <sup>(4)</sup>) and, most importantly, by the calculated vibrational spacings of this potential in the region located vertically above the potential minimum of the lowest triplet ( $1^3\Sigma_u^+$ ) state. The calculated spacings are, within a few percent, in



agreement with the separation of the vibronic progression located between 670 and 690 nm. (see fig.3). As far as we know this is only the second vibrationally resolved spectrum obtained exciting a van der Waals bound alkali triplet (see ref.5 for the spectrum of the  $\text{Cs}_2\ ^3\Sigma_u$  dimer formed in a free jet expansion) and the only one in which the lowest triplet is excited in a matrix-like environment. These observations illustrate the potential for optical pumping experiments and for the spectroscopy of other exotic high spin states in the He cluster environment.

#### d. The mystery spectrum

At the beginning of these measurements we detected, in the region between 610 and 633 nm, a very strong spectrum which, so far, has resisted assignment. As it can be seen in fig. 5, this feature dwarfs the two dimer spectra discussed above, which are barely visible in the figure as small wiggles on the baseline between 633 and 690 nm. As the intensity of the feature appears to be proportional to the third power of the Na atom concentration in the pick-up cell, the spectrum may be due to a species containing 3 Na atoms. We stop short of attributing the spectrum to the  $\text{Na}_3$  bound trimer since, at the contrary of what happened for  $\text{Na}_2$ , the measured feature carries little resemblance with the gas phase  $\text{Na}_3$  spectrum other than being more or less in the right frequency region. Various different options for the interpretation of this spectrum are presently being evaluated. Fig. 6 shows the potential energy curves for a few significant states of  $\text{Na}_2$ . The arrows mark the assigned transitions.

The above results clearly show the feasibility of analogous measurements using Li doped  $\text{H}_2$  clusters, which we intend to start soon, but also open the door onto several new research avenues which we would like to briefly mention here.

- a) Starting with a He cluster-alkali atom complex it should be possible, using two lasers, and/or external fields to access the Rydberg states of the exotic atom formed by an alkali ion located at the core of a He cluster coupled with an electron orbiting around the cluster.
- b) Loading the clusters with a stable molecule and subsequently picking up (in a low pressure discharge) an atomic or molecular free radical one could form, and characterize spectroscopically, free radicals and other transient species which could not be produced by more standard methods.
- c) Loading the clusters with one or more transition metal atoms and molecular ligands, such as  $\text{CO}$ ,  $\text{NH}_3$  and  $\text{C}_2\text{H}_2$ , it should be possible to obtain precise spectroscopic and structural information which could shed light on several important issues related to transition metal-transition metal bonding and ligand field theory.

In summary, it appears that highly quantum clusters can be used as low perturbation, low temperature matrices for high resolution spectroscopy. Since they allow for the relatively easy formation of uncommon and unstable species their applicability to interesting chemical and physical problems seems to be assured.

### Acknowledgements

This work was carried out under contract number F04611-91-K-001 from the AF-HEDM program. It is our pleasure to acknowledge very useful discussions with K.K. Lehmann, R.W. Field, M.D. Morse, W.C. Cole and W.C. Stwalley. W.C. Stwalley and C.C.Tsai are also thanked for sending us an extremely useful high quality plot of the electronic states of Na<sub>2</sub>.

### References

- 1\_ See Hefter and Bergmann's chapter on optical detection methods in "Atomic and Molecular Beam Methods", G. Scoles, Ed., Oxford U.P., N.Y. 1988.
- 2\_ F. Dalfovo, Z. Physik D29 (1994) 61; F. Ancilotto, E. Cheng, M.W. Cole and F. Toigo, Z. Physik D (to be published).
- 3\_ Y. Takahashi, K. Sano, T. Kinoshita and T. Yabuzaki. Phys.Rev. Lett. 71 (1993) 1035.
- 4\_ S. Magnier, Ph. Millié, O. Dulieu and F. Masnou-Seeuws. J. Chem.Phys. 99 (1993) 7113.
- 5\_ U. Dimer, J. Gress and W. Demtröder. Chem. Phys. Lett. 178 (1991) 330.

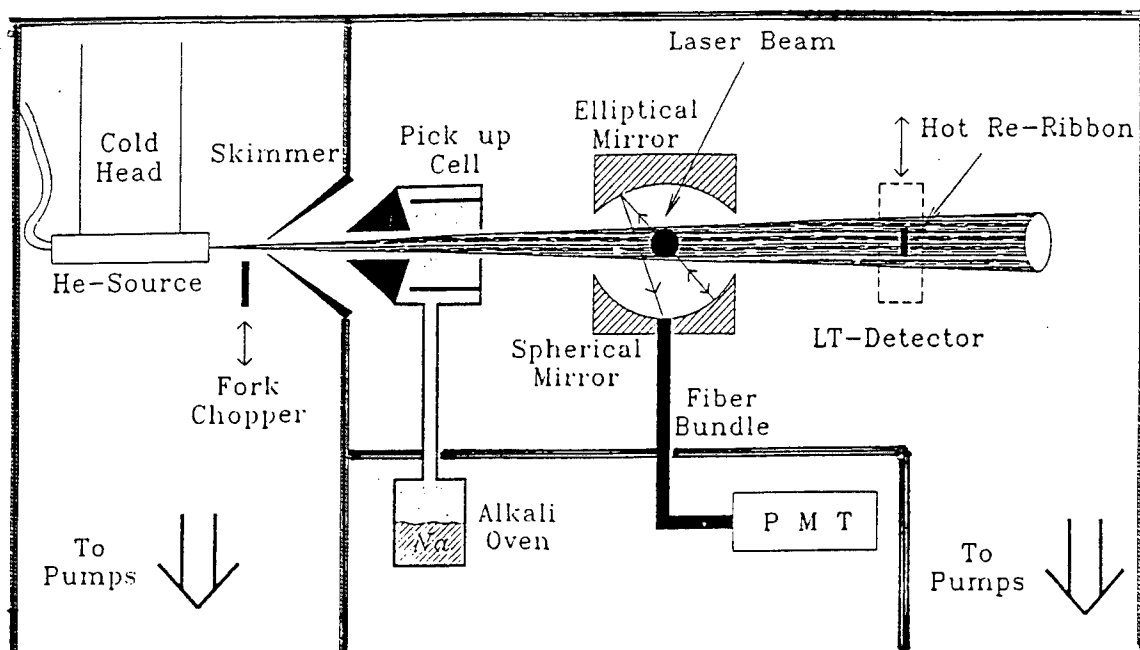


Fig.1 Schematic drawing of the apparatus.

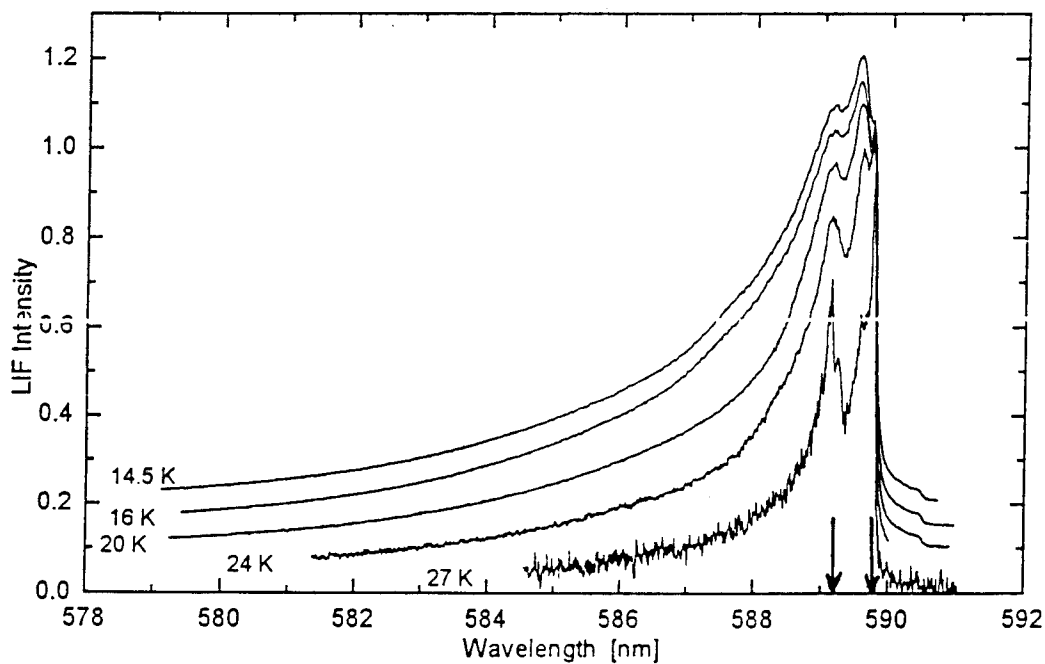


Fig.2 Spectrum of the Na monomer attached to He clusters as a function of the temperature of the cluster source nozzle (i.e. of the cluster size).  $P_0 = 70$  atm. For clarity the spectra have been shifted vertically by .05 each.

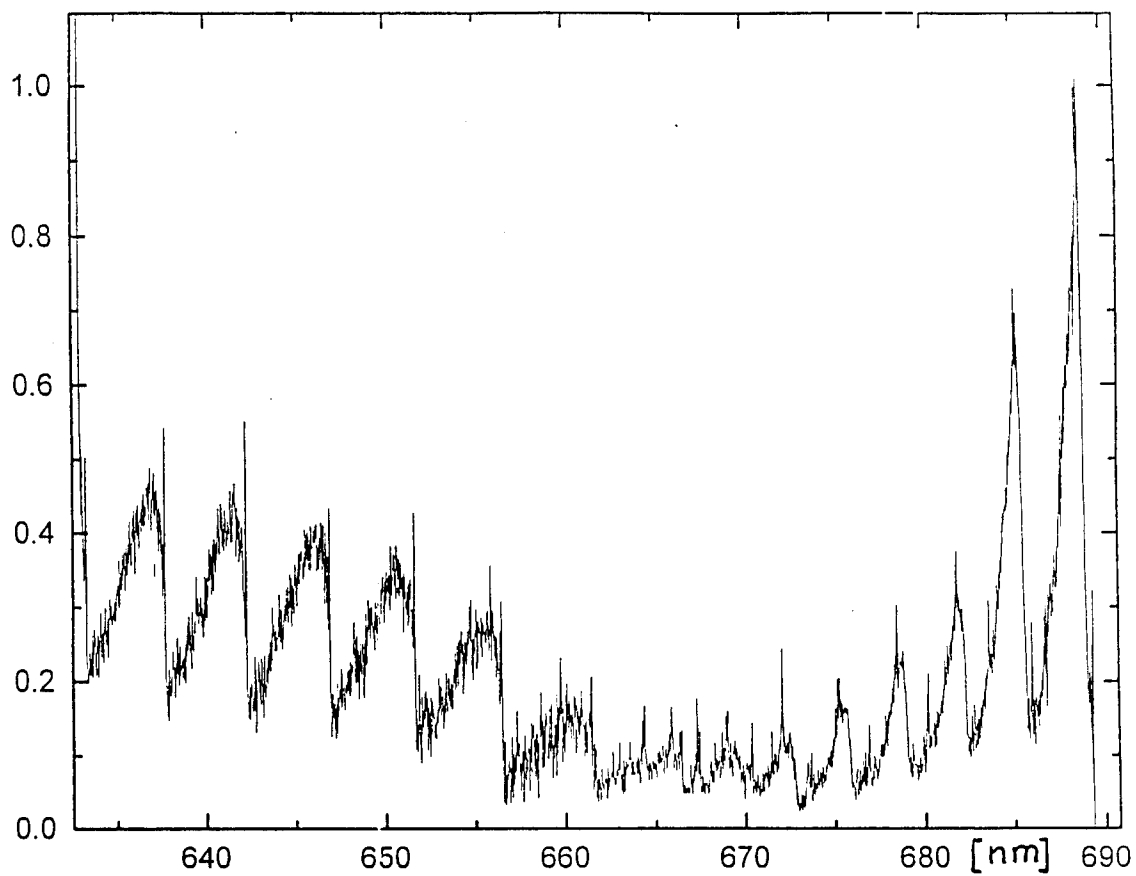


Fig.3 Spectrum of the  $A \leftarrow X$  band and the  $1^3\Sigma_g^+ \leftarrow 1^3\Sigma_u^+$  band of  $\text{Na}_2$  attached to liquid He clusters.  $T_{\text{nozzle}} = 21.5\text{K}$ ,  $P_0 = 80 \text{ atm}$

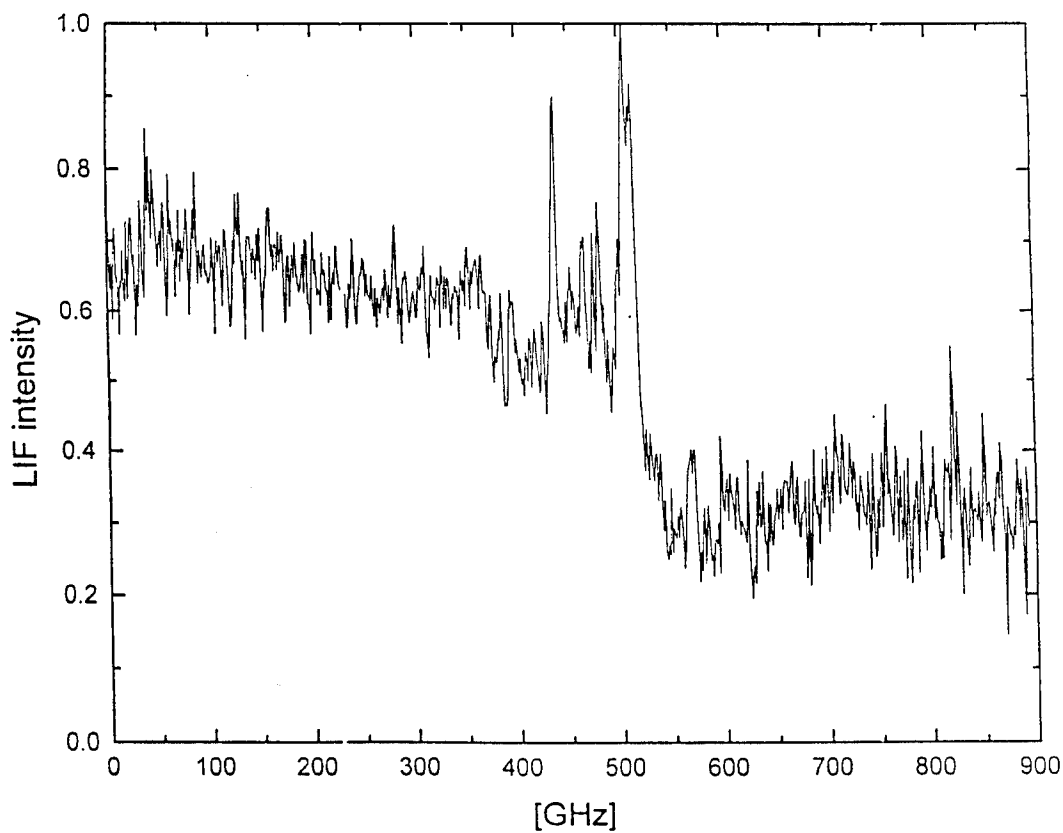


Fig.4 The portion from 636 to 638 nm of the spectrum of fig.3 expanded to show the narrow features around 637 nm

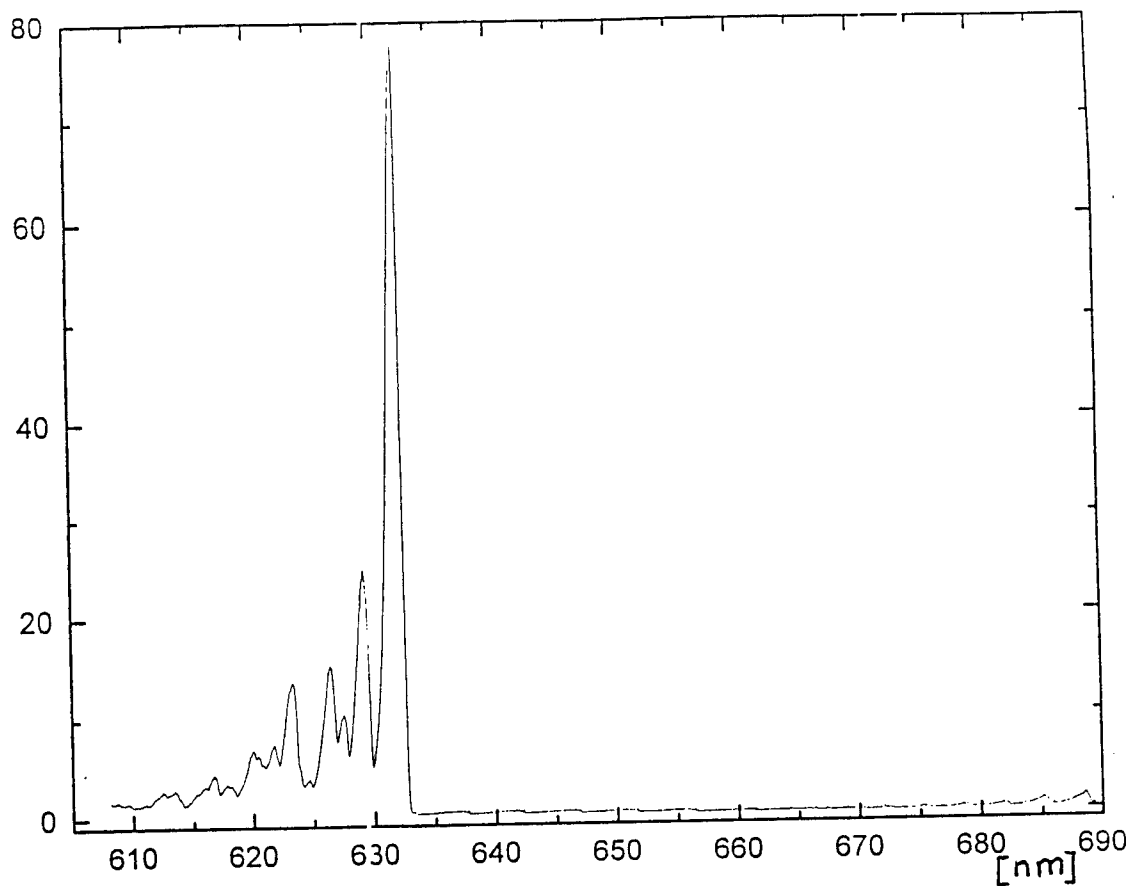


Fig.5 Spectrum due to  $\text{Na}_n$  moieties attached to He cluster in the spectral region from 610 and 690 nm.  $T_{\text{nozzle}} = 21.5\text{K}$ ,  $P_0 = 80 \text{ atm}$

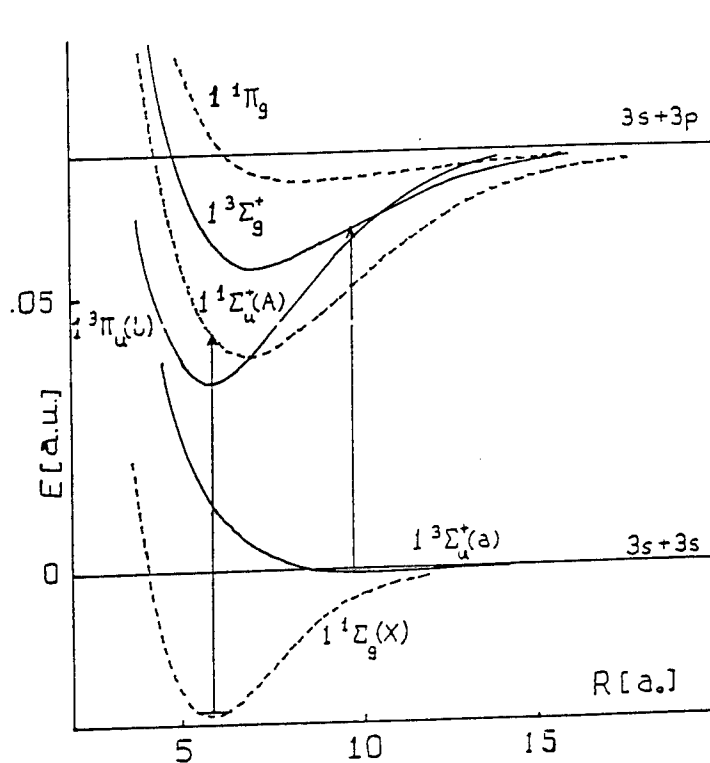


Fig.6 Potential energy curves for a few significant electronic states of  $\text{Na}_2$ . Dashed lines: singlet states. Continuous lines: triplet states. The assigned transitions are indicated by arrows.

NOVEL PHENOMENA INVOLVING CONTACT BETWEEN ALKALI ATOMS AND  
HELIUM OR HYDROGEN

Milton W. Cole and Wolfgang E. Ernst  
Department of Physics, 104 Davey Laboratory  
Pennsylvania State University  
University Park, PA 16802

1. Introduction

Recent years have seen an explosion of activity in the field of alkali atoms, clusters, and bulk metals interacting with helium and/or hydrogen gases, liquids, and clusters. This diverse research has had impact and repercussions for both fundamental science and a wide range of applications. In this talk, a discussion will be provided of some of the more remarkable results and considerations. The project in which we are involved is a collaboration with Professor Giacinto Scoles, of Princeton. Our talk focuses on the theoretical background, as well as some recently explored phenomena involving *qualitatively* new science at the interface of chemistry and physics. There will be seen an obvious connection to the experiments being carried out at Princeton, some results of which are mentioned below.

One striking, and possibly surprising, fact has led to the very unusual kinds of behavior exhibited by the systems of interest here: alkali atoms and metals have *incredibly weak interactions* with helium, hydrogen molecules, and other closed-shell species [1,2]. A simple comparison is indicative: the well depth of the He-Cs interatomic interaction is about one-tenth that of the He-He interaction! This fact arises from (a) the huge size of the Cs atom, and (b) the Pauli principle, which assures that an external electron's wave function must be orthogonal to the He core electronic wave functions. This implies that the former must oscillate rapidly in the core region, corresponding to a high kinetic energy and a repulsive interaction. In the case of Cs, this keeps that atom far from the He nucleus; the equilibrium distance is of order 8 Å for this dimer. Since the attractive van der Waals potential varies as the inverse sixth power of the separation, this yields a very small well depth ( $\sim 10^{-4}$  eV), the *smallest* in nature.

The consequences of this weakness are numerous, of which we cite a few:

1. Of all surfaces in nature that one might consider for adsorption of helium, only Cs is believed to be *not* wet by He [2,3].
2. Most alkali metal surfaces are expected to exhibit "prewetting" transitions for He, H<sub>2</sub>, Ne,.... [4,5]. This means that the film thickness undergoes an abrupt jump in thickness

This transition has been seen in *no* other adsorption system [6].

3. Helium liquid and large clusters are both believed to expel alkali atoms [7]. There is, we believe, a stable surface bound state, involving a microscopic dimple induced by the atom [8]. Our group's preliminary data with Na are consistent with this.

4. Liquid hydrogen is believed to expel Li atoms, which then reside (in equilibrium) on the surface [8]. The other alkalis are believed to prefer energetically to go inside the fluid.

This paper will provide a brief introduction to these phenomena. We hope to make clear why the study of alkali atoms and small clusters near and inside of helium and hydrogen clusters is particularly interesting scientifically. We will then describe briefly the relation to the current and future experimental and theoretical program involving cluster spectroscopy.

## 2. Background

The terms "wetting" and "prewetting" may require brief definitions. They refer to how a film grows in equilibrium with its own vapor on a foreign surface. A wetting system is one for which the film thickness diverges as the vapor pressure approaches saturation; any other behavior is called "nonwetting" or "incomplete wetting". Let us now consider the case of H<sub>2</sub> on Rb [9,10]. Because the attractive force responsible for the film's presence is very weak, virtually no film adsorbs at low temperature  $T$ . As one approaches  $T=19$  K, however, a very thick film suddenly appears at saturated pressure; this is the wetting transition. For temperatures lying between 19 and 22.7 K a related phenomenon occurs: prewetting. This means that a film thickness jump occurs at a pressure somewhat below saturation. Finally, for  $T>22.7$  K, no transition at all occurs. This set of phenomena had not been seen prior to 1992. It has been predicted by our group for many closed shell adsorbates on the alkalis and has been seen subsequently in almost all of these cases which have been studied; see Refs 2 and 11 for a review of both experiment and theory, and Ref.9 for the most recent and comprehensive set of predictions [12].

The preceding paragraph describes consequences for inert gas adsorption on alkalis. What about the *reverse phenomenon*? This turns out to be equally intriguing! There are experimental indications that alkali atoms in liquid helium reside in "bubbles" created by the desire to keep the alkalis apart from their environment [13,14]. These are calculated to be very energetic structures [7]. This has led us to predict the existence of alkali *surface* states [8]. Our calculations for the planar interface have yielded the existence of stable states with typical binding energy  $\sim 10$  meV. The alkali atom creates a little dimple (about 3 Å deep) immediately below it. The distance of closest approach is about 90 % of the equilibrium distance for the He-alkali interatomic potential. In marked contrast with this situation is the case of alkalis interacting with liquid H<sub>2</sub>. We find that Li alone among the alkalis forms a stable surface state (bound by about 10 meV) on H<sub>2</sub>; the others form instead stable bulk states of the completely submerged atom.

These interesting predictions are based on models of varying simplicity and accuracy. Evidently, comparison with existing and future experiments requires a refinement of our methodology, which is feasible, and a careful look at the relation between the configuration of the alkali complex (including variable numbers of alkali atoms) and the resulting spectral features.

The first results of a spectroscopic investigation of sodium atoms and molecules attached to large helium clusters is being presented in a different talk. So far, the measured spectra of Na and Na<sub>2</sub> exhibit transitions characteristic of the free species, with a broadening which may be attributed to the coupling to the host cluster. Since the vibrational frequencies of the dimer appear unaltered, and even rotational structure is resolved, we conclude that the chromophore resides at the surface instead of diffusing inside. A detailed analysis and comparison with predictions derived from the theoretical configuration remain to be done.

#### References

1. G. Scoles, *Ann.Rev.Phys.Chem.* 31,81 (1980)
2. M.W.Cole, E.Cheng, C.Carraro, W.F.Saam, M.R.Swift, and J.Treiner, *Physica B*197, 254 (1994)
3. P.J.Nacher, and J.Dupont-Roc, *Phys.Rev.Lett.* 67, 2966 (1991); B.Demolder, N.Bigelow, P.J.Nacher, and J.Dupont-Roc, *J.Low Temp.Phys.*, in press
4. K.S.Ketola, S.Wang, and R.B.Hallock, *Phys.Rev. Lett.* 68,201 (1992);  
P.Taborek and J.E.Rutledge, *ibid* 68,2184 (1992)
5. E.Cheng, G.Mistura, H.C.Lee, M.H.W.Chan, M.W. Cole, C.Carraro, W.F.Saam, and F.Toigo, *Phys. Rev. Lett.* 70,1854 (1993)
6. Prewetting has been seen more recently in surface melting [S.Chandavarkar, R.M.Geertman, and W.H.de Jeu, *Phys. Rev.Lett.*69,2384 (1992)] and in surface segregation near the binary mixture consolute point [H.Kellay, D.Bonn, and J.Meunier, *ibid* 71, 2607 (1993)]
7. K.E.Kürten and M.L.Ristig, *Phys.Rev.B* 27,5479 (1983); F.Dalfovo, *Z.Phys. D* 29,61 (1994)
8. F.Ancilotto, E.Cheng, M.W.Cole, and F.Toigo, *Z.Phys.B*, to be published
9. E.Cheng, M.W.Cole, W.F.Saam, and J.Treiner, *Phys.Rev.B*48, 18214 (1993)
10. G.Mistura, H.C.Lee and M.H.W.Chan, *Physica B*194, 661 (1994) and *J.Low Temp. Phys.*, in press
11. P.Taborek and J.E.Rutledge, *Physica B*197, 283 (1994)
12. The existing discrepancies may be attributable to either an inadequate potential or perhaps a more exotic mechanism, the role of zero-point surface phonons. See. M.W. Cole, M.R.Swift, and F.Toigo, *Phys.Rev.Lett.*69,2682(1992)
13. Proceedings of the Symposium on Atoms and Ions in Superfluid Helium, Heidelberg, 1994, to be published in *Z.Phys.B*
14. Y.Takahashi, K.Sano, T.Kinoshita, and T.Yabuzaki, *Phys. Rev.Lett.*71,1039 (1993)



# Characterization of van der Waals complexes involving B and Al atoms through laser fluorescence excitation spectroscopy

Paul J. Dagdigian and Eunsook Hwang

*Department of Chemistry, The Johns Hopkins University,  
Baltimore MD 21218*

## *Introduction*

Laser fluorescence excitation spectra of van der Waals complexes involving B and Al atoms, formed in a free-jet expansion, have been recorded and analyzed in order to derive information about the structure and weak binding in these species. Our interpretation of the spectra has been carried out in close collaboration with Millard Alexander's group, who have calculated *ab initio* potential energy surfaces for these systems and, subsequently, vibrational energies of the complexes.

## *Complexes Involving Boron Atoms*

At the 1993 HEDM meeting, we presented a detailed collaborative experimental and theoretical study of the BAr electronic states [ $X^2\Pi$ ,  $A^2\Sigma^+$ ,  $B^2\Sigma^+$ ] which correlate with the ground and resonance excited atomic asymptotes [B( $2p^2P$ ,  $3s^2S$ ) + Ar].<sup>1-3</sup> We have more recently sought to observe the laser fluorescence excitation spectra of several other boron – rare gas van der Waals complexes. We have attempted, thus far unsuccessfully, to detect BNe complexes in supersonic beams seeded in He/Ne mixtures with atomic B( $2p^2P$ ] spin-orbit temperatures as low as 3 K. The BNe ground state binding energy  $D_0$  is estimated by exploratory *ab initio* calculations<sup>4</sup> to be quite small ( $\approx 18 \text{ cm}^{-1}$ ).

We have also observed several complicated features which we believe correspond to fluorescence excitation of  $BKr_n$  complexes. Since the BKr binding energy is expected to be less than that for  $Kr_2$ , we have carried out these experiments by first setting up the apparatus to generate BAr complexes in a He/Ar flow. Then a small flow of Kr is added to the gas flow through a flowmeter. We have observed the loss of the BAr signal as the Kr is added, and the concomitant growth of small signals which correlate with 2 separate molecular carriers. The complexity of the observed bands precludes either of these as the diatomic BKr complex. We suspect that the BKr complex is not kinetically stable in the supersonic flow and readily is converted into higher clusters, presumably  $BKr_n$ .

### The BH-Ar Complex

Our source of boron atoms in the above beam experiments is the 193 nm photolysis of diborane. We have been exploring another important fragment from this photolysis process, namely the BH diatomic molecule, which is conveniently detected by laser fluorescence excitation in its  $A^1\Pi - X^1\Sigma^+$  band system near 433 nm. We have observed BH molecules in our supersonic beam and, in addition, have detected for the first time the ArBH van der Waals complex and recorded its electronic spectrum, which occurs in the region of the BH  $A - X$  (0,0) band.<sup>5</sup>

A survey spectrum of the most of the observed ArBH bands is shown in Fig. 1. Higher-resolution scans of the observed ArBH bands were also taken. We have observed 12 Ar BH bands with resolved rotational structure [shown in low resolution in Fig. 1] and, in addition, 9 diffuse bands at higher excitation energy. We believe that the latter are predissociating since they lie above the lowest excited asymptote [BH( $A^1\Pi$ ,  $v'=0$ ,  $j'=1$ ) + Ar]. From the observed convergence limits of these bands and the shifts from the BH diatom transition, we estimate the ground and excited state binding energies as  $D_0'' \approx 92$   $\text{cm}^{-1}$  and  $D_0' \geq 176$   $\text{cm}^{-1}$ .

We have been able to derive satisfactory rotational analyses for most of the bands shown in Fig. 1. Both perpendicular [ $P' = 1 \leftarrow P'' = 0$ ] and parallel [ $P' = 0 \leftarrow P'' = 0$ ]

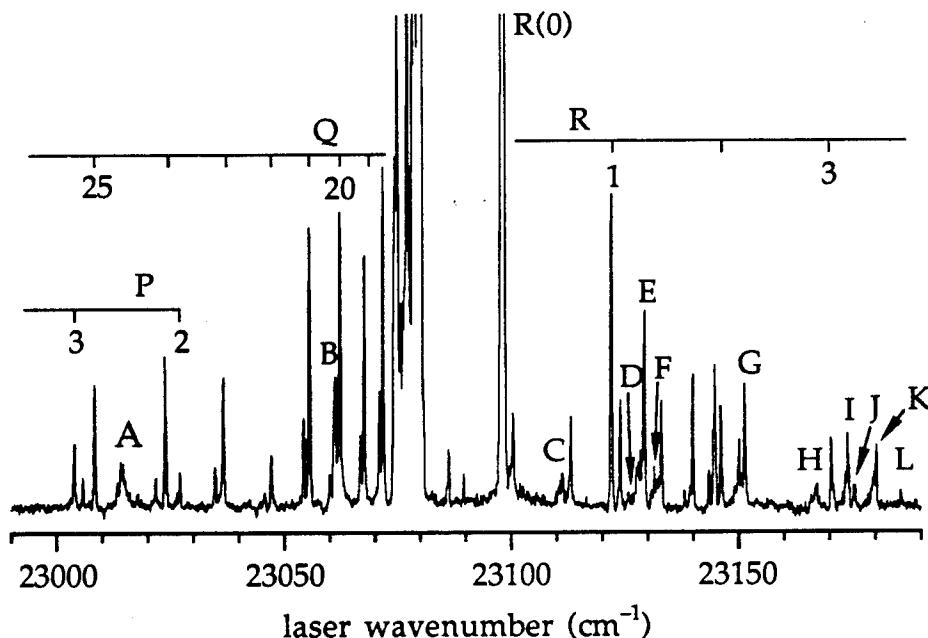


Figure 1. Survey laser fluorescence excitation spectrum of the ArBH complex around the region of the BH  $A^1\Pi - X^1\Sigma^+$  (0,0) band [individual lines of the diatomic  $P$ ,  $Q$ ,  $R$  branches marked]. Features marked A through L are rotationally resolved bands of ArBH.

parallel bands, where  $P$  is the projection of the rotational angular momentum onto the Ar–BH axis, are observed. The rotational constant of the ground vibrational level of  $\text{Ar}^1\text{BH}(X^1\Sigma^+)$  was found to equal  $0.1330(21) \text{ cm}^{-1}$ . This corresponds to an average Ar–BH separation  $R_0'' = [\langle R^{-2} \rangle_0]^{-1/2}$  of  $3.70 \text{ \AA}$ .

The vibrational structure in the excited  $\text{ArBH}(A^1\Pi)$  electronic state was found to be quite complicated. Since the diatom electronic state is orbitally degenerate, *two* potential energy surfaces (PES's), of  $A'$  and  $A''$  symmetry, arise from the interaction of  $\text{BH}(A^1\Pi)$  with Ar. In concurrent collaborative work, Millard Alexander's group has calculated *ab initio* PES's for the interaction of argon with  $\text{BH}(X^1\Sigma^+, A^1\Pi)$ .<sup>6</sup> Unlike the situation for the well studied  $\text{ArNO}(X^2\Pi)$  and  $\text{ArOH}(X^2\Pi)$  complexes, the differences between the  $A'$  and  $A''$  PES's are large. Because of the orbital degeneracy of  $\text{BH}(A^1\Pi)$ , there are in fact *two* bender curves of each projection quantum  $P'$  correlating with each  $\text{BH}(A^1\Pi) + \text{Ar}$  rotational asymptote. We find that there is a spectroscopic selection rule which forbids the observation of one type of  $P' = 0$  levels in transitions from the ground ( $P'' = 0$ )  $\text{ArBH}(X^1\Sigma^+)$  vibronic level.

These PES's have been used to compute  $\text{ArBH}$  vibronic energies.<sup>6</sup> Our observed complicated pattern of  $\text{ArBH}(A^1\Pi)$  vibrational energies has been found to be due to this large difference potential. For the understanding of the pattern of vibrational energies, we have found to very useful to employ an *adiabatic bender* model, in which one first diagonalizes the full Hamiltonian as a function of the atom–molecule distance and then subsequently obtains the vibrational eigenvalues of the resulting one dimensional adiabatic bender potentials.<sup>6</sup> We find that there are two kinds of bender curves, a strongly bound set with relatively short equilibrium Ar–BH separations and another more weakly bound set with larger distances. The more strongly bound set correspond to internal helicopter-like rotor motion of the more attractive ( $A''$ ) of the two  $\text{ArBH}(A^1\Pi)$  PES's.

With the help of these calculations, we have been able to assign van der Waals stretch and bend vibrational quantum numbers to most of the observed  $\text{ArBH}(A^1\Pi)$  levels. Table I presents the derived excitation energies, rotational constants, and assigned vibrational quantum numbers for the assigned bands. It can be seen that there is almost a factor of 3 variation in the rotational constant, due in part to the large differences in the equilibrium Ar–BH separation for the different bender curves.

### *Complexes Involving the AlH Radical*

We have also investigated the weak, nonbonding interactions of the homologous AlH molecule with rare gases with the help of laser fluorescence excitation spectra of van der Waals complexes involving this diatom. In these experiments, the AlH diatom is

TABLE I. Excitation energies and rotational constants (in  $\text{cm}^{-1}$ ) for assigned  $\text{ArBH}(A^1\Pi)$  levels.

band ID	$P'$	$j'$ <sup>a)</sup>	$v_S'$ <sup>a)</sup>	excitation energy <sup>b)</sup>	$B'$ <sup>c)</sup>
A	1	$1_l$	0	23 013.70	0.1669(21)
B	1	$1_l$	1	23 060.53	0.1530(18)
C	1	$1_u$	0	23 110.43	0.1149(15)
D	1	$1_l$	3	23 124.65	0.1166(23)
E	0	$1_+$	0	23 129.31	0.1032(23)
F	1	$1_u$	1	23 131.63	0.1138(11)
G1	1 <sup>d)</sup>	$1_u$	2	23 149.11	[0.115] <sup>e)</sup>
G2	0	$1_+$	1	23 150.89	0.0967(25)
H1	1 <sup>d)</sup>	$1_u$	3	23 166.05	[0.095] <sup>e)</sup>
H2	0	$1_+$	2	23 166.98	0.0643(15)

- a) The quantities  $j'$  and  $v_S'$  are the asymptotic  $\text{BH}(A^1\Pi)$  diatom rotational quantum number for the adiabatic bender curve and the van der Waals stretching quantum number, respectively, assigned by comparison with the calculations of Alexander *et al.* (Ref. 6). The subscripts + and - for  $P' = 0$  denote levels with the same symmetry as  $\Sigma^+$  and  $\Sigma^-$  levels, respectively; the subscripts  $l$  and  $u$  for  $P' = 1$  denote the upper and lower bender curves, respectively, of the same  $P'$  and  $j'$ .
- b) Estimated uncertainty  $\pm 0.1 \text{ cm}^{-1}$ .
- c) Quoted uncertainties are one standard deviation in units of the last significant digit.
- d) Assignment not definite from experimental spectrum and was made, in part, by comparison with the calculated vibrational energies of Alexander *et al.* (Ref. 6).
- e) On the basis of an observed complicated rotational structure and the calculated vibrational energies, this band is assigned as a strong transition to a  $P' = 0^+$  level overlapped by a weak transition to a weak  $P' = 1$  level. The approximate rotational constant for the latter was estimated by comparison with simulated spectra.

generated by 193 nm photolysis of trimethylaluminum. The laser fluorescence excitation spectrum of the  $\text{ArAlH}$  spectrum has been observed in the vicinity of the  $A^1\Pi - X^1\Sigma^+$  (0,0) band of diatomic  $\text{AlH}$ . A pattern of bands similar to those observed for  $\text{ArBH}$  has been found. Rotational analyses have been obtained for most of the resolved bands, and both perpendicular and parallel transitions have been found.

From the shift of the lowest-energy band from the lowest  $\text{AlH}$  diatomic line [ $R(0)$ ] and the onset of diffuse bands, the ground and excited state binding energies have been estimated as  $D_0'' \approx 126 \text{ cm}^{-1}$  and  $D_0' \geq 234 \text{ cm}^{-1}$ . These values are somewhat larger

larger the corresponding values for ArBH. The rotational constant of the ground vibrational level of ArAlH( $X^1\Sigma^+$ ) was found to equal  $0.069(9) \text{ cm}^{-1}$ . This corresponds to an average Ar–AlH separation  $R_0$  of  $3.85 \text{ \AA}$ , which is only slightly greater than for ArBH. Our analysis of the ArAlH spectrum is continuing. The principal remaining work to be done is the rotational analysis and vibrational assignment of a number of weakly resolved bands. The latter should be greatly facilitated by forthcoming calculations of ArAlH vibrational energies which will be obtained with newly computed *ab initio* PES's.<sup>7</sup>

Most recently, we have been recording the laser fluorescence excitation spectrum of KrAlH, in order to gain further insight into the differences in the structure and energetics of these atom-diatom complexes with the identity of the rare gas partner. Preliminary rotational analyses yield a rotational constant of the ground vibrational level of KrAlH( $X^1\Sigma^+$ ) of  $0.056(2) \text{ cm}^{-1}$ , which corresponds to an average Kr–AlH separation of  $3.83 \text{ \AA}$ , which is slightly *smaller* than the average Ar–AlH separation. This difference presumably reflects the increased interaction energy for Kr–AlH as compared to Ar–AlH. Thus far, all of the rotationally analyzed bands have involved perpendicular transitions.

- 
1. P. J. Dagdigian, E. Hwang, and M. H. Alexander, in *Proceedings of the High Energy Density Matter Contractor's Conference*, Wood's Hole, MA, 1993, p.180.
  2. E. Hwang, Y.-L. Huang, P. J. Dagdigian, and M. H. Alexander, *J. Chem. Phys.* **98**, 8484 (1993).
  3. E. Hwang, P. J. Dagdigian, and M. H. Alexander, *Can. J. Chem.* **72**, xxxx (1994).
  4. M. H. Alexander, unpublished work.
  5. E. Hwang and P. J. Dagdigian, *J. Chem. Phys.* **101**, xxxx (1994).
  6. M. H. Alexander, S. Gregurick, and P. J. Dagdigian, *J. Chem. Phys.* **101**, xxxx (1994).
  7. M. Yang and M. H. Alexander, work in progress.

# Weakly Bound Complexes involving Atomic B

*Millard Alexander*

*Department of Chemistry and Biochemistry*

*University of Maryland, College Park, MD 20742-2021*

During the past year, and with the collaboration of Anne McCoy and Benny Gerber, we completed our study<sup>1</sup> of the structure and energetics of clusters of B atoms with multiple  $p\text{-H}_2$  molecules. The underlying potential energy surfaces (PESs) were constructed from pairwise interactions, based on our earlier *ab initio* calculations,<sup>2</sup> with a simple geometrical treatment of the electronic aspect of the interaction. Due to the non-sphericity of the unpaired valence  $p$ -electron on the B atom, the interaction is far more attractive when the  $\text{H}_2$  approaches the B atom in a plane perpendicular to the orientation of the  $p$  orbital. This governs the features of the small  $\text{B}(p\text{-H}_2)_n$  clusters. We used classical molecular dynamics and quantum diffusion Monte-Carlo<sup>3, 4</sup> techniques to investigate the structure and stability of the clusters.

The energetics and structure of these highly quantum clusters was significantly different from what would be predicted by methods based on classical mechanics.<sup>5</sup> The distribution of the B- $\text{H}_2$  distances were considerably narrower than those of the  $\text{H}_2\text{-H}_2$  distances, and nearly indistinguishable for all clusters studied. The strong B- $\text{H}_2$  interaction governs the structure of these relatively small complexes. The hydrogens distribute themselves with a distribution of B- $\text{H}_2$  distances quite similar to that in the  $\text{B}(p\text{-H}_2)$  dimer.

In these calculations no provision was made for the deviation from sphericity of the  $\text{H}_2$  molecule in the clusters containing more than one hydrogen molecule. The assumption that  $p\text{-H}_2$  can be treated as spherical has been made consistently in prior simulations of both pure  $p\text{-H}_2$  clusters<sup>6, 7</sup> and of atomic Li solvated by  $p\text{-H}_2$ .<sup>8</sup> Due to the stronger anisotropy of the B- $\text{H}_2$  interaction, when

compared to the Li-H<sub>2</sub> or the H<sub>2</sub>-H<sub>2</sub> potentials, our calculations on the BH<sub>2</sub> dimer, show that the effects of the anisotropy of the interaction on the wavefunction and energy are virtually negligible.

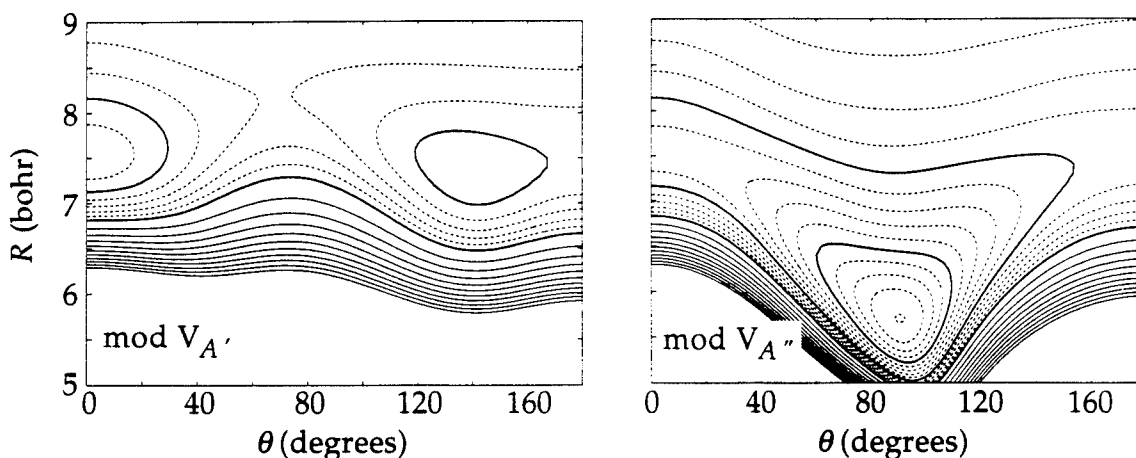
The heterogeneous B(*p*-H<sub>2</sub>)<sub>*n*</sub> clusters investigated here represent a bridge between highly quantum clusters, such as those of *p*-H<sub>2</sub> or He, in which the large zero-point energy and lack of structured minima result in broad, unstructured probability distributions of the geometrical parameters, and those of heavier atoms, with deeper minima, in which relatively few structures play an important role. In B(*p*-H<sub>2</sub>)<sub>*n*</sub> the probability distributions of the geometric parameters reflect an interplay between the light mass of the hydrogen ligands, which contributes to the spreading of the vibrational wavefunctions, and the relative strength of the B-H<sub>2</sub> interaction, which imposes significant energetic constraints on the structure of the cluster.

A second project involved the study of the Ar-BH cluster, stimulated by experimental work in Dagdigian's laboratory. There has been considerable recent interest, both experimental as well as theoretical, in complexes of argon with diatomic free-radical hydrides.<sup>9</sup> To provide a theoretical framework with which to interpret the ArBH spectrum, we carried out CASSCF-CI(D) calculations of the PESs for the interaction of Ar with the BH radical in its ground (*X*<sup>1</sup>Σ<sup>+</sup>) and first excited (*A*<sup>1</sup>Π) electronic states. In these calculations we used the augmented correlation-consistent valence quadruple zeta (*avqz-f*) basis of Dunning and co-workers<sup>10</sup> with the exclusion of *g* functions on B and Ar and the exclusion of *f* functions on H.

In contrast to the well-studied ArOH(*X*<sup>2</sup>Π) cluster,<sup>11</sup> for ArBH(*A*<sup>1</sup>Π) there is a large difference in the interaction energies when the unpaired π electron lies in or perpendicular to the triatomic plane. To compensate for our inability to include higher order excitations involving the Ar electrons, we introduce a slight transformation of the *ab initio* PES which deepens the van der Waals well depths and shifts the position of the minimum ~ 0.2 – 0.3 bohr closer in. For or the state

of  $A'$  symmetry, there are two minima of depth  $\sim 120 \text{ cm}^{-1}$ , at ArBH angles of  $0^\circ$  and  $140^\circ$ , at an Ar-BH distance of  $\sim 7.7$  bohr. For the state of  $A''$  symmetry, the minima lies at  $88.5^\circ$  at a Ar-BH distance of 6 bohr, with a depth of  $280 \text{ cm}^{-1}$ .

Contour plots of the two PESs are shown below.



Contour plots of the ArBH(A) PESs for the states of  $A'$  (left panel) and  $A''$  (right panel) reflection symmetry. The linear BHAr geometry corresponds to  $\theta = 0^\circ$ . The dashed contours indicate negative energies with the first contour at  $-10 \text{ cm}^{-1}$  and a spacing of  $10 \text{ cm}^{-1}$ . The solid contours designate positive energies; the contours are equally spaced with the first contour at  $50 \text{ cm}^{-1}$ , a spacing of  $50 \text{ cm}^{-1}$ , and the last (innermost) contour at  $500 \text{ cm}^{-1}$ . For clarity, the contours at  $0$ ,  $-100$ , and  $-200 \text{ cm}^{-1}$  are drawn with heavy solid curves.

With these PESs and using our earlier formulation of the interaction of a  ${}^1\Pi$  molecule with a structureless atom,<sup>12</sup> we can obtain the wavefunctions and energies of the bend-stretch levels of the cluster. Variational calculations were carried out, using both a full close-coupled expansion, and also within a centrifugal decoupling approximation where the projection of the BH rotational angular momentum along the Ar-BH separation vector is held constant. These agreed very closely, which indicates that Coriolis coupling is small at the low values of the total angular momentum which characterize ArBH molecules produced in supersonic nozzle expansions.<sup>13</sup> The calculated energies and rotational constants also compared extremely well with the predictions of our *adiabatic bender* model,<sup>14</sup> closely related to the pioneering work of Klemperer



and co-workers.<sup>15</sup> In this model the matrix of the two-dimensional ArBH interaction energy is prediagonalized in the bending degree of freedom. This provides a one-dimensional potential for the assignment and quantitative determination of the stretch-bend energies of the ArBH complex. The success of this model is indicative of the lack of significant bend-stretch coupling.

With only a slight modification of the *ab initio* PES's, which preserves the qualitative aspects of these PES's, we were able to predict accurately and, more importantly, *assign* the experimentally observed spectra of the ArBH van der Waals complex, as will be described by Dagdigian in a separate abstract.

1. A. Vegiri, M. H. Alexander, S. Gregurick, A. McCoy, and R. B. Gerber, *J. Chem. Phys.* 100, xxxx (1994), work in progress.
2. M. H. Alexander, *J. Chem. Phys.* 99, 6014 (1993).
3. J. B. Anderson, *J. Chem. Phys.* 63, 1499 (1975).
4. M. A. Suhm and R. O. Watts, *Phys. Repts.* 204, 293 (1991).
5. F. H. Stillinger and T. A. Weber, *Phys. Rev. A* 25, 978 (1982).
6. P. Sindzingre, D. M. Ceperly, and M. L. Klein, *Phys. Rev. Lett.* 67, 1871 (1991).
7. D. Scharf, M. L. Klein, and G. J. Martyna, *J. Chem. Phys.* 97, 3590 (1992).
8. D. Scharf, G. J. Martyna, D. Li, G. A. Voth, and M. L. Klein, *J. Chem. Phys.* 99, 9013 (1993).
9. For a good recent review, see M. C. Heaven, *J. Phys. Chem.* 97, 8567 (1993).
10. R. A. Kendall, T. H. Dunning Jr., and R. J. Harrison, *J. Chem. Phys.* 96, 6796 (1992).
11. M. I. Lester, W. H. Green Jr., C. Chakravarty, and D. C. Clary in *Molecular Dynamics and Spectroscopy by Stimulated Emission Pumping*, edited by H.-L. Dai and R. W. Field (World Scientific, New York, 1993).
12. M. H. Alexander, *Chem. Phys.* 92, 337 (1985).
13. E. Hwang and P. J. Dagdigian, *J. Chem. Phys.* (1994), (submitted).
14. M. H. Alexander, S. Gregurick, and P. J. Dagdigian, *J. Chem. Phys.* XXX, yyyy (1994), submitted.
15. S. L. Holmgren, M. Waldman, and W. Klemperer, *J. Chem. Phys.* 67, 4414 (1977).

## TIME RESOLVED DYNAMICS IN MOLECULAR CLUSTER IONS

W. Carl Lineberger, Stephen R. Leone, Robert P. Parson and Stephen V. O'Neil  
Department of Chemistry and Biochemistry  
Joint Institute for Laboratory Astrophysics  
University of Colorado  
Boulder, Colorado, 80309-0440

Our experiments involving studies of the structure and reactivity of dications have led in the past year to the conclusion that the demonstrated stabilities of doubly charged molecular species were insufficient to warrant further investigation as fuel additives. As a consequence, we have directed our recent efforts toward studies involving ultrafast lasers to probe clustered species, caging dynamics and wave packet dynamics in species such as  $\text{Li}_2$ . In the last 12 months, Leone has been setting up ultrafast laser experiments to study wave packet dynamics in  $\text{Li}_2$ , designed to address the fundamental question of the HEDM program, concerning the maximum achievable number densities of fuel-additive species. The ultimate goal is to understand the dissociation dynamics and interactions of  $\text{Li}_2$  species clustered with a solvent shell of  $\text{H}_2$  molecules, and to learn about the fundamental limits of additive densities by studying caging phenomena. The first experiments will investigate the wave packet dynamics in this extended-bond shelf state ( $E^1\Sigma_g^+$ ) of isolated  $\text{Li}_2$ . The  $E^1\Sigma_g^+$  state provides a unique opportunity to explore a wide range of internuclear separations in the  $\text{Li}_2$  molecule, from 2.4-6 Å. Since the outer turning point of this state corresponds to the  $\text{Li}^+-\text{Li}^-$  ionic configuration, while the inner turning point corresponds to neutral  $\text{Li}-\text{Li}$ , it will be possible to explore real time dynamics to elucidate the electronic character of the state with and without the solvent shell. The interaction with  $\text{H}_2$  is expected to be significantly stronger in the ionic configuration at the outer turning point. The interactions of this state as a function of internuclear separation with a surrounding solvent shell of  $\text{H}_2$  molecules and potential caging effects relating to dissociative dynamics are the ultimate goals. Since  $\text{H}_2$  molecules are not strongly bound to  $\text{Li}_2$ , it may be difficult to form these clusters in a jet expansion. Another possibility is to cluster  $\text{H}_2$  with the ionic  $\text{Li}_2^+$  species, which would increase the interaction strength and formation rates. If the desired cluster formation cannot be achieved, we perform experiments on odd hydrogen species, such as  $\text{Li}_2\text{H}$ , which will exhibit much stronger bonding interactions and provide some key new concepts for the HEDM program.

While it may well be difficult to produce neutral clusters with large numbers of  $\text{H}_2$  solvents, the complementary experiments of Lineberger employ ionic cores which can much more readily acquire a solvent shell. The initial experiments will focus on oxidizers and additives to such as O, Li and  $\text{Li}_2$ . In those cases where the additive has a small electron affinity, the excess charge will largely remain on the solvent and the ion may serve as a reasonable "mimic" for the neutral. Photoabsorption in the mass-selected cluster ions is detected via evaporation of solvent molecules from the cluster. The shape and size evolution of the absorption spectrum with cluster size provides a mechanism to identify the chromophore and to detect the extent of charge delocalization in the cluster ion. These changes will be interpreted in terms of structure using the solvent field models being advanced by Parson. Finally, ultrafast pump-probe techniques will be employed to follow reaction dynamics and the breakup of the solvent shell after photoexcitation. The goal will be to understand the limits on storing such species in  $\text{O}_2$  or  $\text{H}_2$  matrices.

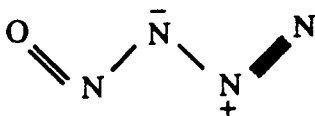
# HIGH ENERGY DENSITY MATTER CONTRACTORS CONFERENCE

## The Newly Synthesized Tetranitrogen Monoxide Molecule: Why is the Observed Form Higher in Energy than the Unobserved Cyclic Structure?

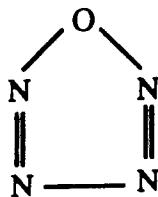
John Morrison Galbraith and Henry F. Schaefer III  
Center for Computational Quantum Chemistry  
University of Georgia  
Athens, Georgia 30602

### Abstract

In December of 1993 Thomas Klapötke and coworkers at the Technical University of Berlin reported (*Angew. Chem. Int. Ed. Engl.* **32**, 1610) the preparation of a new oxide of nitrogen, namely  $N_4O$ . The work has been described in popular terms in the November 29 issue of *Chemical and Engineering News*. The synthesized tetranitrogen monoxide appears to have the structure



even though there may be a cyclic (perhaps aromatic with six  $\pi$  electrons) structure



that is lower in energy. High level quantum mechanical methods are used to address some of the questions arising from the Klapötke synthesis.

# MCD Spectroscopy of Metal/Rare Gas and Metal/Hydrogen Systems

HEDM Contractors' Conference  
Lake Tahoe, Nevada  
June 1994

*John W. Kenney, III*  
*Chemical Physics Laboratory*  
*Eastern New Mexico University*  
*Portales, NM 88130*

## INTRODUCTION

In this report, we cover recent developments in the electronic absorption and magnetic circular dichroism (MCD) spectroscopy of cryogenic metal/rare gas matrices in which high kinetic energy metal atom vapors are generated by laser ablation of a metal target. The chief experimental challenge hinges around the geometrical constraints imposed by incorporating a magnet into or around a suitable cryostat for low temperature spectroscopy. The primary theoretical challenge is to develop rigorous models of metal/matrix systems that faithfully reproduce the experimental spectroscopic data based upon fundamental quantum mechanical principles.

## EXPERIMENTAL

**Preparation of Metal/Rare Gas Matrices.** Laser-ablated alkali metal atoms are trapped in cryogenic noble gas matrices according to the procedures developed by Fajardo et al.<sup>1</sup> The matrices are deposited onto a cooled 0° sapphire window in a cryostat that is positioned between the pole pieces of a large electromagnet capable of generating magnetic fields on the order of 0.7 T (7 000 Gauss).

**MCD/Absorption Spectrophotometer.** The design of the MCD spectrophotometer (Figure 1) is straightforward but carefully planned for precise control of light polarization both for the MCD and absorption spectroscopic measurements. Circularly Polarized light for MCD experiments is generated and analyzed in the following manner. Collimated monochromatic light emerging from a monochromator is passed through a computer-controlled light attenuator comprised of two quartz Glan-Taylor linear polarizers (see Figure 1f-g). The first polarizer is fitted in a stepper-motor-actuated rotator capable of 360° rotation; the second polarizer is fixed at 0°, which we define to be parallel to the vertical exit slit of the monochromator. The linear

---

<sup>1</sup>(a) Fajardo, M. E.; Carrick, P. G.; Kenney, J. W., III *J. Chem. Phys.* **1991**, *94*, 5812-5825.  
(b) Fajardo, M. E. *J. Chem. Phys.* **1993**, *98*, 110-118. (c) Tam, S.; Fajardo, M. E. *J. Chem. Phys.* **1993**, *99*, 854-860. (d) Corbin, R. A.; Fajardo, M. E. *J. Chem. Phys.* **1994**, *101*, 2678-2683.

polarizers provide a simple and elegant way to adjust light levels for constant photocurrent output from the photomultiplier tube (PMT) across the wavelength range of interest. *A constant, wavelength independent PMT output is crucial for the proper measurement of MCD spectra and preferable for the measurement of high quality UV-visible absorption spectra.*<sup>2</sup> Immediately after passing through the polarizers, the light is chopped by a two ring mechanical chopper. The inner chopper ring, set to chop at ~325 Hz, is aligned along the main optical axis. It chops the light that passes through the sample region of the MCD instrument. The outer chopper ring, which chops at ~390 Hz, is set slightly off of the main optical axis. It chops the reference beam, which is picked off immediately after passing through the outer ring of the chopper and directed around the sample region to the PMT via a series of right angle prisms (Figure 1k). The main on-axis light, vertically polarized by the second Glan-Taylor polarizer and chopped at ~325 Hz, is directed through a quartz PEM mounted at 45° with respect to the reference axis of the second linear polarizer. The PEM acts as a variable wavelength quarter wave ( $1/4\lambda$ ) plate. The linearly polarized monochromatic light that strikes the PEM at 45° is converted into pulses of LCP and RCP light, of equal amplitudes, at ~50 kHz. The PEM control unit automatically adjusts the piezoelectric control voltage on the quartz bar to preserve the quarter wave retardation condition as the wavelength changes across the scan. The sample beam, chopped at 325 Hz and modulated at 50 kHz, is directed through a small hole drilled in the pole pieces of the magnet and onto the sample, which in this case is a metal/rare gas matrix deposited onto a cryogenically cooled sapphire window housed in a low temperature cryogenic refrigerator or cryostat. The emergent light from the sample goes through the hole in the other magnet pole piece and impinges on the photocathode of a PMT set in a magnetically shielded, thermoelectrically cooled housing. The reference beam bypasses the sample and impinges directly on the PMT. This particular PMT is an end-on unit equipped with a flat quartz optical window and a flat photocathode. The PMT dynode chain is specifically chosen to be more than fast enough to handle the 50 kHz modulation of the PEM. The photocurrent emerging from the dynode chain of the PMT is a combined signal comprised of three distinct components

$$i_{\text{total}} = i_{\text{ref}} + i_{\text{UV-vis}} + i_{\text{MCD}} \quad (1)$$

with three distinct frequency modulation signatures, where as noted previously,  $\nu_{\text{ref}} = \sim 390$  Hz,  $\nu_{\text{UV-vis}} = \sim 325$  Hz, and  $\nu_{\text{MCD}} = \sim 50$  kHz. This photocurrent is fed into a fast current-to-voltage converter/amplifier to obtain the final amplified voltage signal (gain  $\sim 10^6$ )

---

<sup>2</sup> Drake, A. F. *J. Phys E: Sci. Instrum.* **1986**, *19*, 170-181. A superb and highly detailed review article covering every aspect of the measurement of CD and MCD spectra that includes a valuable reference list.

$$V_{\text{total}} = V_{\text{ref}} + V_{\text{UV-vis}} + V_{\text{MCD}} \quad (2)$$

whose components have the same frequency signatures and the same relative amplitudes as the photocurrent components. This triply-modulated voltage signal is fed into three lock-in amplifiers that are locked in, respectively, on  $v_{\text{ref}}$ ,  $v_{\text{UV-vis}}$ , and  $v_{\text{MCD}}$ . The outputs from the lock-in amplifiers (0 to 10 V range analog or direct digital) are read by computer as a function of wavelength and stored for subsequent reconstruction of the MCD and UV-visible absorption spectra. It is easier to use the analog signals when setting up and calibrating the instrument. The direct digital lock-in outputs are read over the IEEE-488 GPIB interfaces once instrument operating parameters have been established. The IEEE-488 lock in signal recovery option is illustrated in Figure 1. The center dots in the lock in amplifier block diagrams represents the analog output option, which are shown not connected in Figure 1.

**MCD Spectroscopy with Absorption Polarization Control.** Precise control of the polarization of the absorption beam can be achieved in several ways. *Method A:* The MCD signal is recovered in the usual manner by locking in on the  $v_{\text{MCD}} = 50$  kHz modulation. The absorption (or transmission) signal may be recovered by locking in at  $2v_{\text{MCD}}$ , which effectively allows addition of the  $V_{\text{LCP}}$  and the  $V_{\text{RCP}}$  signals. A mechanical chopper is not used unless a reference beam is required. *Method B:* The lock in frequency is left at 50 kHz and the PEM controller is commanded via the IEEE-488 computer interface to go to  $1/2\lambda$  retardation for an absorption measurement involving linearly polarized light. Recall that the combination of a fixed linear polarizer with a  $1/2\lambda$  retarder gives linearly polarized light polarized  $90^\circ$  to the pass direction of the linear polarizer. Once the appropriate constant absorption signal level is achieved by attenuating the light intensity or adjusting the PMT high voltage, the PEM control is switched by computer command back to  $1/4\lambda$  retardation for the MCD measurement. *The important point here is that precise absorption polarization control can be achieved while scanning the MCD and absorption spectra in a simultaneous, coordinated double scan.*

## EXPERIMENTAL RESULTS

**MCD Spectra of Metal/Rare Gas Systems.** It has been demonstrated that the laser ablation technique for generating alkali metal/rare gas (M/Rg) cryogenic matrices can be incorporated around the tight geometrical constraints imposed by the necessity of placing the matrix-isolated sample between the pole pieces of a large electromagnet. MCD spectra of M/Rg systems prepared by laser ablation method have been acquired. Of particular note is the successful acquisition of blue triplet MCD spectra for Li/Ar and mixed matrix MCD spectra of Li/Ar;Xe.

Through the use of MCD spectroscopy in conjunction with the laser ablation for generating metal atom vapors, distinct differences between the Knudsen oven produced "red triplet" trapping site and the laser ablation produced "blue triplet" trapping site in M/Rg systems have been demonstrated (see Figures 2-5).

The M/Rg cryogenic matrices exhibit a characteristic three peaked or "triplet" electronic absorption pattern (see Figures 2-5). For alkali metals such as Li or Ni, this triplet arises as a matrix perturbation of the  $[\text{core}]ns^1 \rightarrow [\text{core}]np^1$  or  $^2S \rightarrow ^2P$  atomic transition in the metal. Previous electronic absorption spectroscopy studies by Fajardo et al. have identified "red triplet", "blue triplet", and "violet triplet"  $^2S \rightarrow ^2P$  alkali metal spectra in cryogenic rare gas hosts.<sup>1</sup> The red triplet is centered on the atomic  $^2S \rightarrow ^2P$  transition energy. The blue and violet triplets appear at progressively higher energies with respect to the atomic transition energy. It is postulated that the red, blue, and violet triplets arise from  $^2S \rightarrow ^2P$  transitions in alkali metal atoms trapped in progressively tighter substitutional sites in the matrix: i.e., sites from which progressively fewer Rg atoms are removed to accommodate the metal atom dopant.

The MCD spectra of M/Rg systems, like the electronic absorption spectra, also exhibit characteristic red, blue, and violet triplet spectral patterns, with the MCD "peaks" essentially coinciding with the peaks of the corresponding triplet absorption spectrum. This research represents the first reported study of the MCD spectra of matrix-isolated alkali metal atoms in which laser ablation is employed as the metal atom vaporization technique. The Li/Xe MCD pattern exhibits one up peak and two down peaks ( $\uparrow\downarrow\downarrow$ ) with increasing wavelength (Figure 2) for a Li/Xe matrix prepared by trapping laser ablated Li atoms in a Xe cryogenic matrix. An up peak in MCD spectroscopy ( $\uparrow$ ) corresponds to the absorption of more left circularly polarized (LCP) light than right circularly polarized (RCP) light ( $\Delta A' = A'_{\text{LCP}} - A'_{\text{RCP}} > 0$ ); a down peak ( $\downarrow$ ) corresponds to the opposite situation in which RCP light is preferentially absorbed ( $\Delta A' = A'_{\text{LCP}} - A'_{\text{RCP}} < 0$ ). It should be noted that the ( $\uparrow\downarrow\downarrow$ ) MCD spectral pattern for laser ablation prepared Li/Xe is similar to the pattern reported by Schatz et al. in an earlier series of experiments using the Knudsen oven metal vapor deposition method.<sup>3</sup> Apparently, the same trapping site for the Li in the Xe matrix is accessed regardless of the deposition method: laser ablation vs. Knudsen oven. The MCD spectrum for the laser ablated blue triplet in Li/Ar is characterized by two up peaks and one down peak ( $\uparrow\uparrow\downarrow$ ) as wavelength increases (Figure 3). This MCD pattern is roughly similar to what was observed by Schatz et al. for Knudsen oven deposited Li/Ar matrices that almost certainly represented a mixture of red and blue metal trapping sites.<sup>3</sup> It is clear that that the

---

<sup>3</sup>(a) Lund, P. A.; Smith, D.; Jacobs, S. M.; Schatz, P. N. *J. Phys. Chem.* **1984**, *88*, 31. (b) Rose, J.; Smith, D.; Williamson, B. E.; Schatz, P. N. *J. Phys. Chem.* **1986**, *90*, 2608.

characteristic MCD spectral patterns exhibit a strong, obvious trapping site dependence; blue triplets give a different MCD pattern than red triplets.

**MCD Spectra of Mixed Li/Rg;Rg' Systems.** In the mixed rare gas matrices, those in which the host matrix is composed of a mixture of two rare gases in varying concentrations, a triplet pattern is still detectable in the absorption<sup>1d</sup> and MCD spectra. In this case, however, the overall MCD spectral pattern observed depends on the Ar/Xe mol ratios. When Ar is in excess, the MCD spectral pattern is ( $\uparrow\uparrow\downarrow$ ) as  $\lambda$  increases; when Xe is in excess the MCD pattern becomes ( $\uparrow\downarrow\downarrow$ ) with increasing  $\lambda$  (see Figures 4 and 5). In all cases, the MCD spectral pattern coincides peak-for-peak with the corresponding observed triplet electronic absorption spectrum.

## THEORY

**Origins of Triplet Patterns in  $2S \rightarrow 2P$  Electronic Spectra.** The characteristic triplet spectral pattern observed by us and others in the electronic spectra of alkali metal/rare gas systems appears to be a general feature of matrix-isolated P electronic states.<sup>1,3</sup> This triplet pattern is not confined to cryogenic metal/rare gas matrices. Triplets also are observed in the F center states of alkali halides<sup>4</sup> and other inorganic crystals<sup>5</sup> and in the P states of metals doped into solid silicon matrices.<sup>6</sup> The origin of the triplets has been ascribed variously to multiple metal trapping sites in the matrix host, spin-orbit coupling, static crystal field distortions of the P site by the surrounding lattice (static Jahn-Teller effect), and dynamic distortions of the P site by lattice vibrations (dynamic Jahn-Teller effect).<sup>1</sup> Recent work by Fajardo et al.<sup>1</sup> indicates that different trapping sites each give rise to their own characteristic triplet spectral patterns. Tighter sites with fewer rare gas vacancies give higher energy triplets; looser sites with larger rare gas vacancies produce lower energy triplets. For the lighter alkali metals (e.g., Li, Na) with small atomic spin-orbit coupling constants it seems reasonable to ascribe the triplet patterns (whether in a tight substitutional matrix site or a loose substitutional matrix site) to a combination of static and dynamic Jahn-Teller effects that effectively act to remove the threefold orbital degeneracy of the  $2P$  state.<sup>1</sup> The existence of similar  $2S \rightarrow 2P$  triplet spectral patterns in the alkali metal/rare gas series Li/Ar, Li/Kr, Li/Xe makes assigning the triplet features to spin-orbit coupling via a rare gas heavy atom effect somewhat problematical. However, spin-orbit coupling is indeed a viable splitting mechanism for the  $2P$  states of the heavier alkali metals (e.g., K, Rb, Cs) and the coinage metals (Cu, Ag, Au) when these metals are trapped in cryogenic rare gas matrix hosts. It is entirely

<sup>4</sup>(a) Moran, P. R. *Phys. Rev.* **1965**, *137*, A1016-1027. (b) Fulton, T. A.; Fitchen, D. B. *Phys. Rev.* **1969**, *179*, 846-859. (c) O'Brien, M.C.M. *J. Phys. C: Solid State Phys.* **1976**, *9*, 3153-3164.

<sup>5</sup>Rodriguez, S.; Schultz, T. D. *Phys. Rev.* **1968**, *178*, 1252-1263.

<sup>6</sup>Toyozawa, Y.; Inoue, M. *J. Phys. Soc. Japan* **1966**, *21*, 1663-1679.



reasonable to assume that in heavy metal/rare gas matrices *both* spin-orbit coupling and Jahn-Teller effects could contribute significantly to the observed triplet splitting patterns.

**Patterns in  $^2S \rightarrow ^2P$  MCD Spectra.** Earlier detailed MCD studies of alkali metal/rare gas systems were confined primarily to moment analysis interpretations. For example, the pioneering MCD studies of Schatz et al. on the Na/Xe and Li/Xe systems using Knudsen-oven-generated metal vapors assumed a single substitutional site model with spin orbit-coupling parameters extracted from moment analyses of the MCD and electronic absorption spectra.<sup>3</sup> Large negative  $^2P$  spin-orbit coupling constants were predicted for Li/Xe and Na/Xe even though the free metals have small positive spin-orbit coupling constants. Hormes and Schiller, however, predicted small positive spin-orbit coupling constants based upon their own independent experimental data and moment analysis scheme.<sup>7</sup> Recent MCD simulation studies by Boatz and Terrill-Stolper using a Monte Carlo treatment of alkali metal/rare gas lattice vibrations give rise to observed MCD patterns with modest atomic-like metal spin-orbit coupling constants.<sup>8</sup> This simulation approach has the advantage that multiple trapping site vacancies can be modeled--hence red, blue, or violet triplet sites can be incorporated into the model--and the light alkali metal spin-orbit coupling constants need not vary greatly from their atomic values. It is instructive to look at a simple group theoretical analysis of the MCD  $C/D$  ratio for a  $^2P$  metal state trapped in an octahedral rare gas substitutional site where, within the octahedral ( $O_h$ ) environment, the  $^2P$  state becomes a  $^2T_{1u}$  state. The prediction is that the  $^2T_{1u}$  manifold will contain both a positive MCD  $C/D$  component  $\uparrow$  and a negative MCD  $C/D$  component  $\downarrow$ . If one of these components is further split by a lattice interaction specific to the trapping site itself and not the overall geometry of the trapping site (keeping in mind that many octahedral substitutional sites representing a wide range of removed rare gas atoms are, in principle, possible), then the distinctive variations observed in the MCD spectra of Li/Ar ( $\uparrow\uparrow\downarrow$ ) and Li/Xe ( $\uparrow\downarrow\downarrow$ ) can be accounted for qualitatively. These ideas are fully consistent with a Jahn Teller model of  $^2P$  triplet structure in alkali metal/rare gas systems where the some of the spectral features are common to all sites but also where details of the Jahn-Teller interaction vary from trapping site to trapping site (e.g., red, blue, or violet). It appears that some key differences in trapping sites are indeed detectable via MCD spectroscopy!

### FURTHER WORK

Further studies will concentrate on the MCD spectra of alkali metal/hydrogen systems. Also planned for future studies are magnetic circularly polarized luminescence (MCPL) spectra of metal/rare gas systems, which are known to have luminescent  $^2S \leftarrow ^2P$  transitions. A number of

---

<sup>7</sup>Hormes, J.; Schiller, J. *Chem. Phys.*, **1983**, *74*, 433-439.

<sup>8</sup>Boatz, J.; Terrill-Stolper, H. A., private communication.

experiments involving careful control and/or measurement of the polarization properties of the exciting light and emitted light are possible, each of which has the potential to give unique insights about the nature of the trapping sites involved. Finally, feasibility studies are under way to determine how to load alkali metal/rare gas matrices into diamond anvil cells. This is a most challenging experimental problem. However, these high pressure experimental studies are of key importance in determining how the trapped metal atoms behave under lattice stress. This is of considerable practical interest in determining the practical utility of atom-doped cryogenic solids as storable, reasonably stable and shock-insensitive rocket propellants.

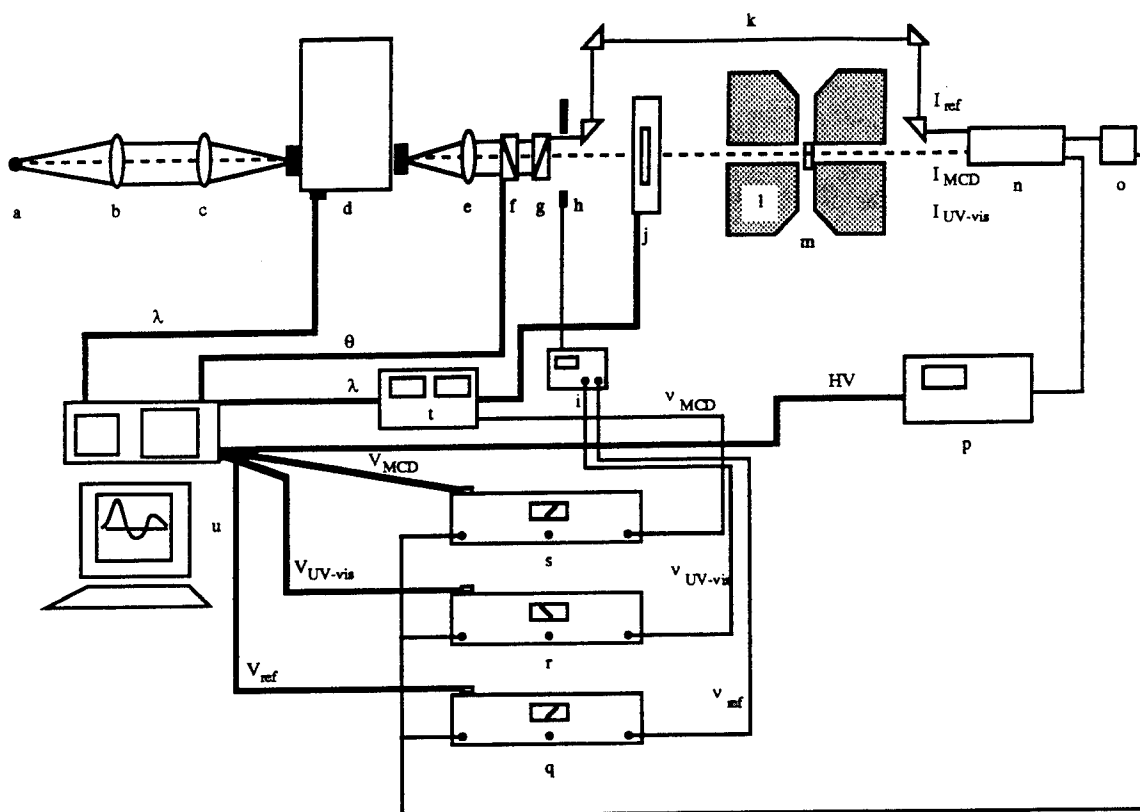


**Figure 1.** MCD/Absorption Spectrophotometer: (a) 100 W quartz halogen lamp; (b) and (c) quartz lenses; (d) monochromator, Acton SpectraPro 275; (e) quartz collimating lens; (f) Glan-Taylor polarizer, quartz, rotating; (g) Glan-Taylor polarizer, quartz, fixed; (h) 2-ring mechanical chopper, SRS; (i) chopper controller; (j) PEM, Hinds PEM 90, quartz; (k) reference beam; (l) electromagnet; (m) sample; (n) PMT, Hamamatsu R562, thermoelectrically cooled; (o) current-to-voltage converter/amplifier, Hamamatsu; (p) PMT high voltage controller, SRS; (q) reference lock in amplifier, SRS 510; (r) UV-visible lock in amplifier, SRS 510; (s) MCD lock in amplifier SRS 530; (t) PEM 90 controller; (u) computer and data acquisition/instrument controller, Hewlett Packard 3497A, 9816. Note: dark lines represent IEEE-488 computer cables; light lines represent standard BNC type cables.

Li/0%Ar;100%Xe

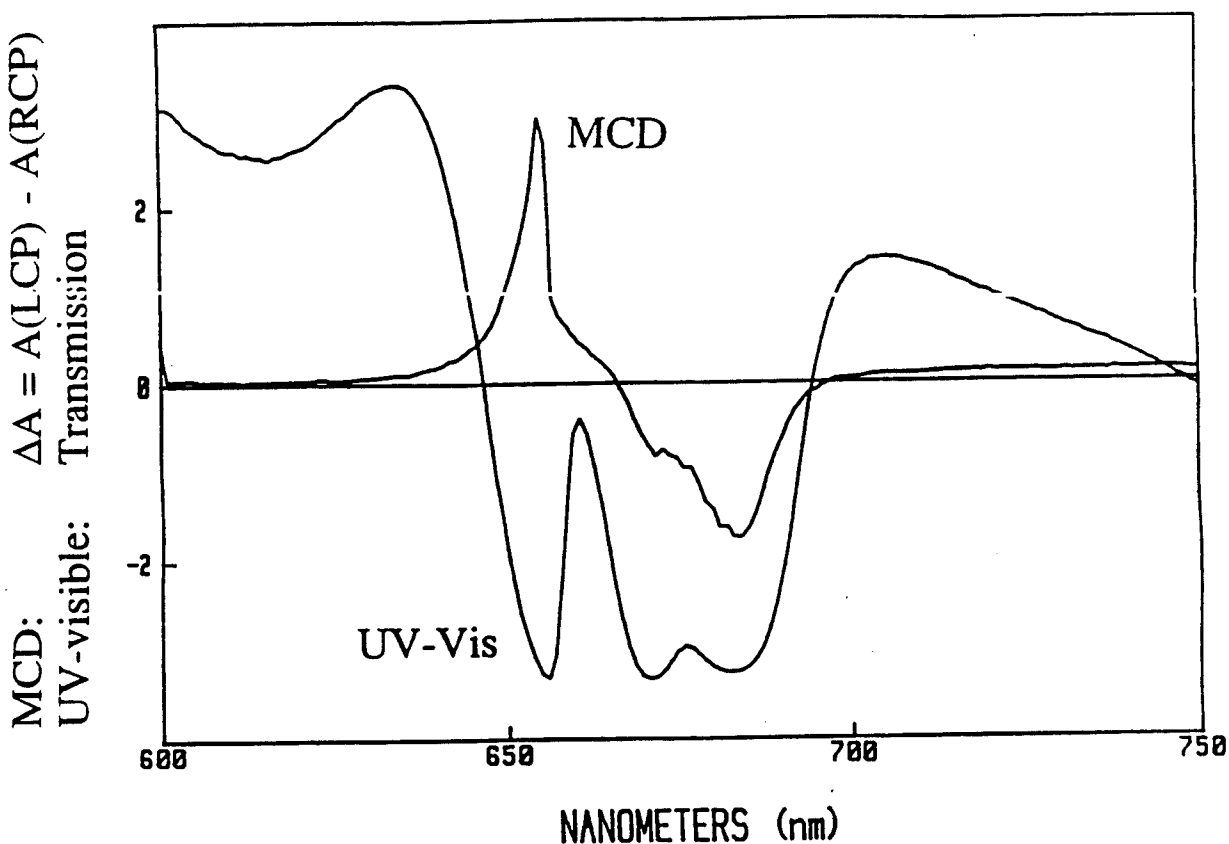


**Figure 2.** MCD/UV-visible spectra of Li/0%Ar;100%Xe.

The figure shows MCD and UV-visible transmission spectra of Li/0%Ar;100%Xe prepared by laser ablation of Li vapor from a rotating target by 308 nm excimer laser light (~5 mJ/pulse, 5 Hz, 10 min). The cryogenic sapphire sample window temperature is maintained at ~20 K during matrix deposition and during subsequent spectroscopic measurements. The MCD spectral pattern [(↑↓) with increasing  $\lambda$ ] is essentially identical to the pattern observed by Schatz et al. for Li/Xe matrices generated from Knudsen oven vaporized Li.

Li/100%Ar;0%Xe

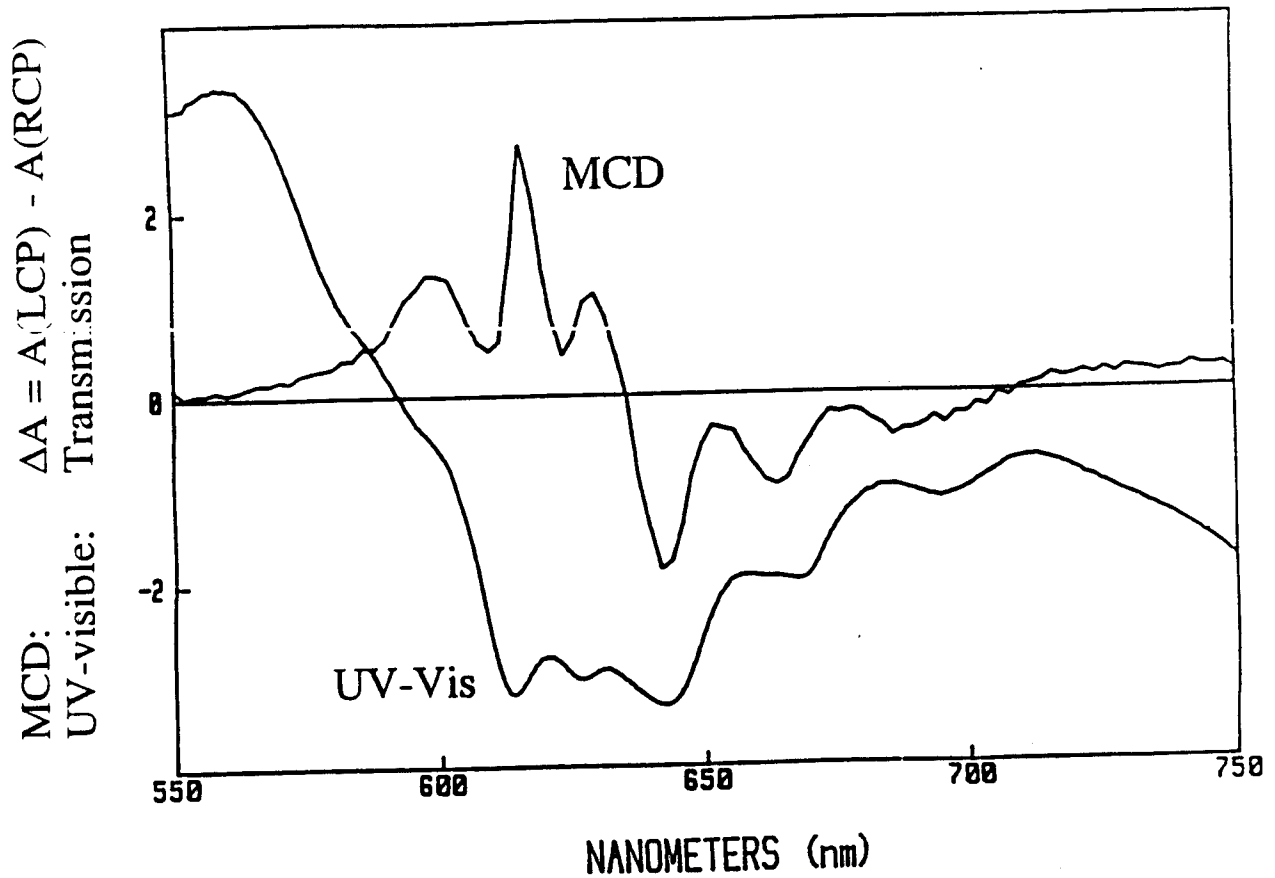


**Figure 3.** MCD/UV-visible spectra of Li/100%Ar;0%Xe. "Blue Triplet"

The figure shows MCD and UV-visible transmission spectra of Li/100%Ar;0%Xe prepared by laser ablation of Li from a rotating target by 308 nm excimer laser light (~5 mJ/pulse, 5 Hz, 10 min). This is the Li/Ar "blue triplet". The cryogenic sapphire sample window temperature is maintained at ~20 K during matrix deposition and during subsequent spectroscopic measurements. The MCD spectral pattern [(↑↑↓) with increasing  $\lambda$ ] is similar to the pattern observed by Schatz et al.<sup>3</sup> for Li/Ar matrices generated from Knudsen oven vaporized Li. The Schatz et al. spectra clearly contain both red and blue triplet spectral features.

Li/50%Ar;50%Xe

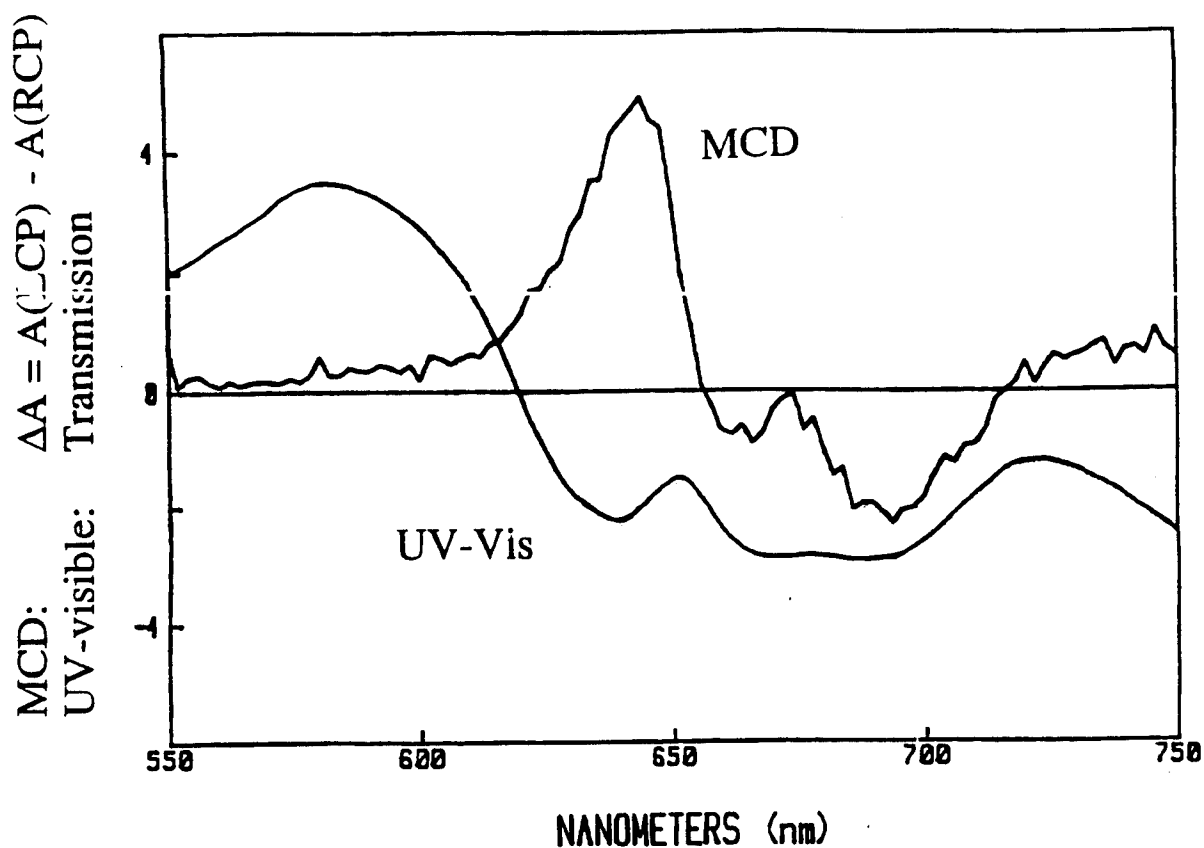


Figure 4. MCD/UV-visible spectra of Li/50%Ar;50%Xe.

The figure shows MCD and UV-visible transmission spectra of Li/50%Ar;50%Xe prepared by laser ablation of Li from a rotating target by 308 nm excimer laser light (~5 mJ/pulse, 5 Hz, 10 min) to give a mixed matrix triplet. The cryogenic sapphire sample window temperature is maintained at ~20 K during matrix deposition and during subsequent spectroscopic measurements. The MCD spectral pattern [(↑↓) with increasing  $\lambda$ ] is similar to the Li/Xe MCD pattern observed in Figure 2.

Li/90%Ar;10%Xe

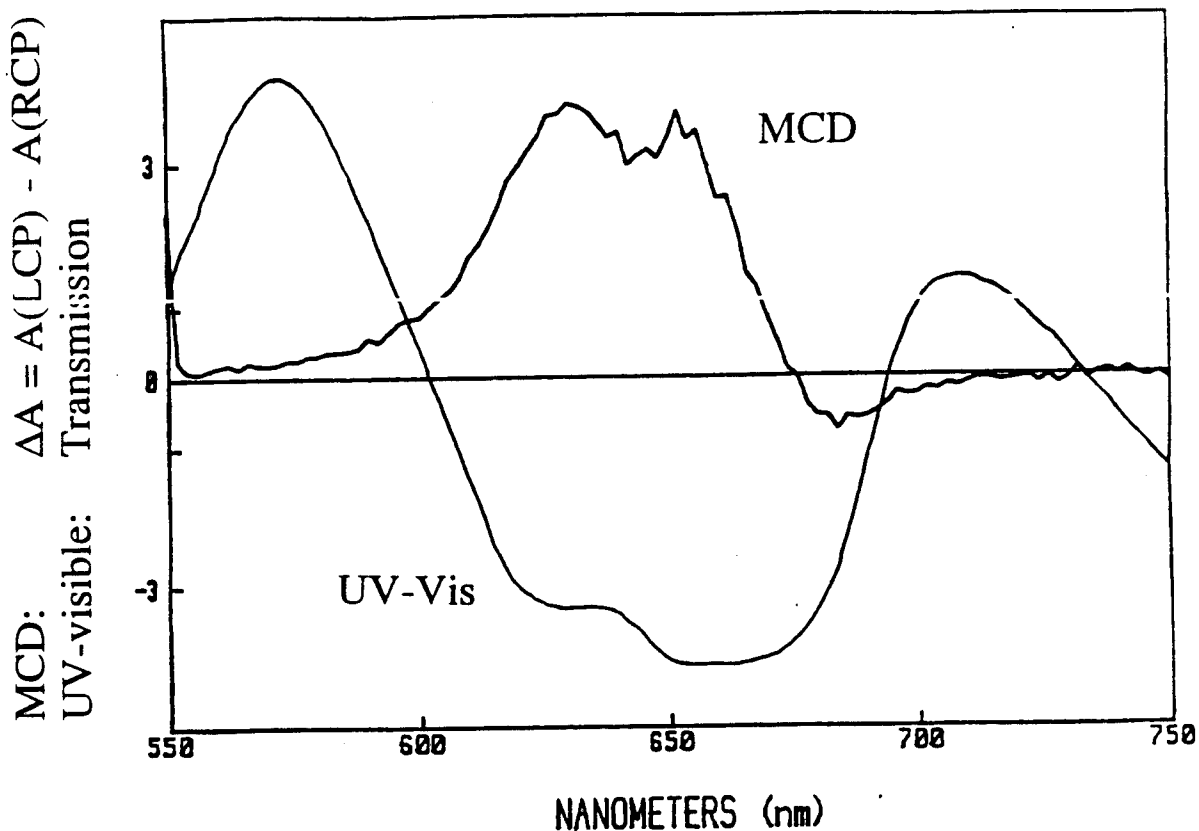


Figure 5. MCD/UV-visible spectra of Li/90%Ar;10%Xe.

The figure shows MCD and UV-visible transmission spectra of Li/90%Ar;10%Xe prepared by laser ablation of Li from a rotating target by 308 nm excimer laser light (~5 mJ/pulse, 5 Hz, 10 min) to give a mixed matrix triplet. The cryogenic sapphire sample window temperature is maintained at ~20 K during matrix deposition and during subsequent spectroscopic measurements. The MCD spectral pattern [(↑↑↓) with increasing  $\lambda$ ] is similar to the Li/Ar MCD pattern observed in Figure 3.

HEDM Contractors' Meeting  
Crystal Bay, NV  
June 1994

## **Demonstration of a High Gain Visible Wavelength Chemical Laser Based on Energy Transfer from Metastable $\text{NF}(a^1\Delta)$ to Boron Hydride**

D.J. Benard and E. Boehmer  
Rockwell International Science Center  
Thousand Oaks, CA 91358

### **EXTENDED ABSTRACT**

The development of visible wavelength chemical lasers is based upon the principles of spin-conservation which allows formation of metastable products in chemical reactions, energy transfer and pooling to excite a suitable emitting species, and stimulated emission as a means of relaxing an inverted distribution. Our work is centered on the 1.4 eV metastable species  $\text{NF}(a^1\Delta)$ , which is efficiently generated in large ( $\sim 3 \times 10^{16} / \text{cm}^3$ ) concentrations by rapid dissociation of fluorine azide ( $\text{FN}_3$ ). This unique molecule is highly energetic and easily split apart over a  $\sim 0.5$  eV barrier by either thermal or vibrational excitation. Since, the central bond in  $\text{FN}_3$  is the weak link, the most favored dissociation products are  $\text{NF}$  and  $\text{N}_2$ . Conservation of spin, however, blocks formation of the triplet  $\text{NF}(X)$  ground state and allows production of the excited singlet (metastable) state instead. Since the  $\text{N}_2$  byproduct is also a slow quencher of  $\text{NF}(a^1\Delta)$ , scaling of this generation scheme is limited only by the metastable self-annihilation reaction.

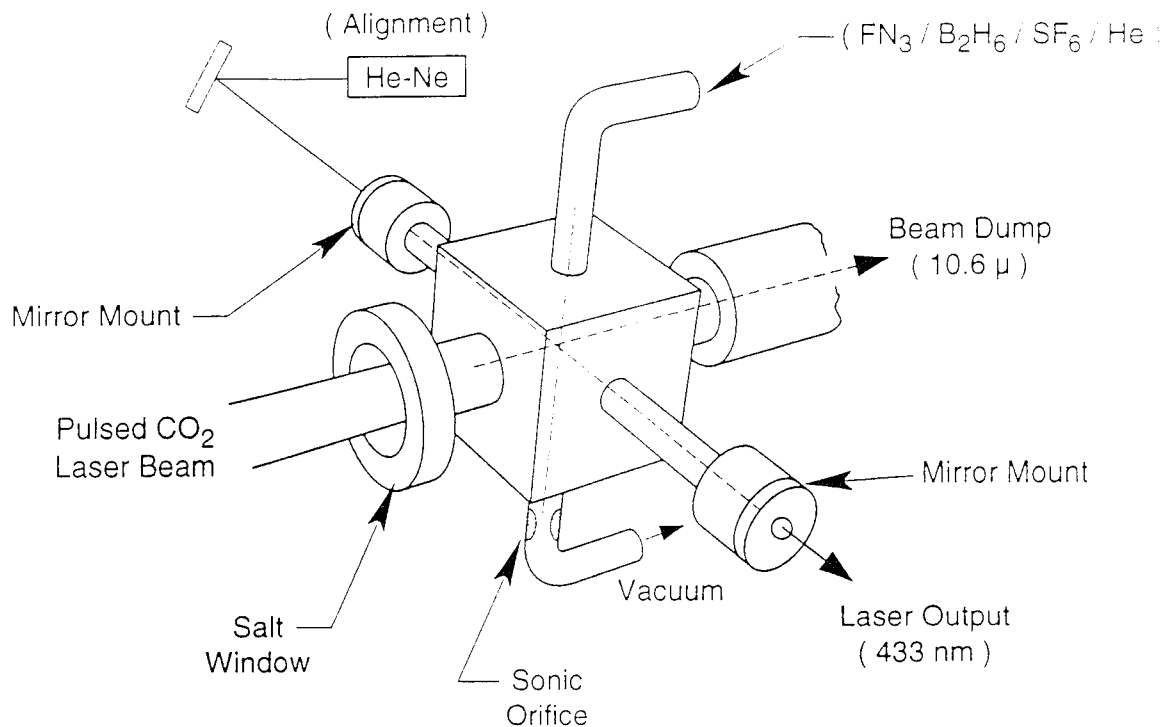
Resonances between the forbidden  $\text{NF}(a-X)$  transition and the forbidden  $\text{BH}(a-X, A-a)$  transitions allow efficient pumping of the allowed  $\text{BH}(A-X)$  transition at 433 nm by energy transfer and pooling reactions. The  $\text{BH}$  radicals are obtained in situ by decomposition of  $\text{B}_2\text{H}_6$  in parallel with the azide dissociation reaction. Once the active species are generated, the  $\text{BH}$  radicals act as cyclic catalysts for conversion of electronic energy stored as  $\text{NF}(a^1\Delta)$  into photons, and this process continues until the metastable population is depleted. Inversion occurs when the  $\text{NF}(a^1\Delta)$  concentration is large enough to drive the  $\text{BH}$  cycle faster than the rate of spontaneous  $A-X$  radiation. Since the rate coefficients for energy transfer in this system are extremely fast, inversion can be obtained at achievable metastable concentrations.

The magnitude of the gain coefficient depends on the density of  $\text{BH}$  radicals and the stimulated emission cross section. The radical concentration is determined by



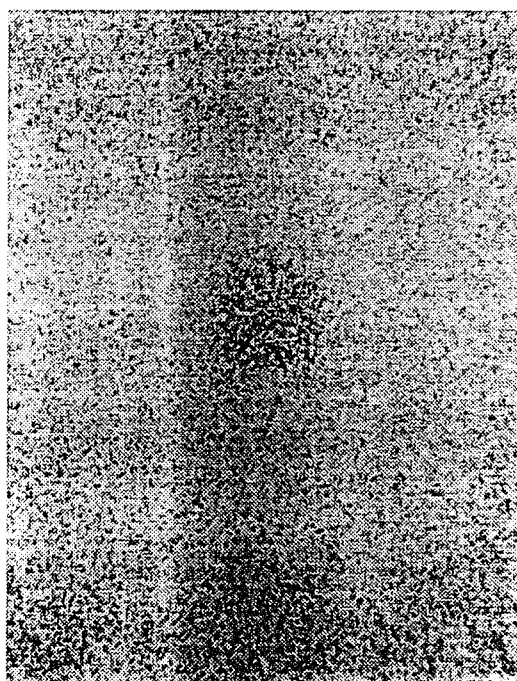
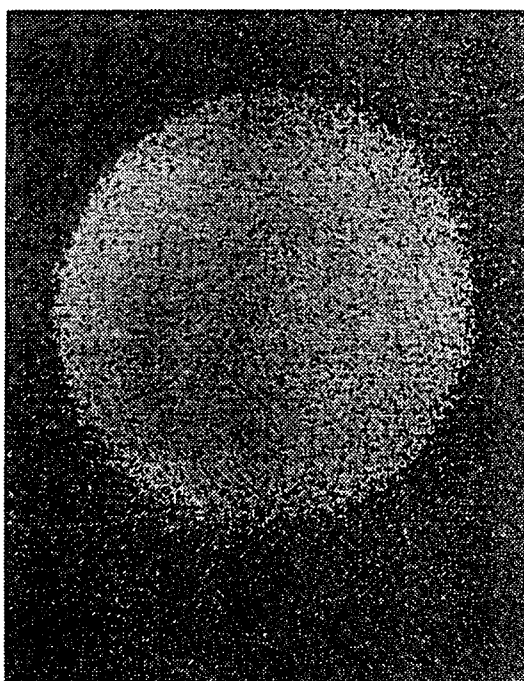
# NF/BH Visible Chemical Laser Demo

SCP0603E.C21534



## Aperture / Beam Photos

SCP0603E.C21534



the yield from dissociation of  $B_2H_6$  and the tolerance of  $NF(a^1\Delta)$  to addition of donor molecules. In this case, small yields are compensated by a large tolerance factor, since the BH donors do not quench metastables significantly. The cross section of the BH(A-X) transition, on the other hand, is favored by a relatively short radiative lifetime, highly vertical potential energy curves and minimal rotational-vibrational dilution of the inversion density compared to other diatomic emitters. Consequently, the NF/BH concept is capable of generating exceptionally high gain coefficients.

A demonstration experiment was performed in which  $FN_3$ ,  $B_2H_6$ ,  $SF_6$  and He were mixed on the fly and then excited by a pulsed  $CO_2$  laser. The infrared photons were resonantly absorbed by the  $SF_6$  molecules, which (on the  $\mu s$  time scale) dissociated the azide and donor molecules upon subsequent collisions. A population inversion was then obtained due to energy transfer and pooling between the metastable and emitting products. The reaction was carried out inside an optical resonator with a threshold gain of 2.5 %/cm and an active gain length (volume) of 1 cm (2  $\mu$ liter). Since the reaction volume was  $\sim 1 \text{ cm}^3$ , only a small fraction of the chemistry was allowed to contribute to laser output. Evidence of lasing at 433 nm was obtained by recording photographic images of the cavity output, which demonstrated an axial mode of  $\sim 1 \text{ mm}$  diameter that was much brighter than the surrounding chemiluminescence, which filled the  $\sim 6 \text{ mm}$  diameter cavity aperture.

The metastable electronic energy stored by  $NF(a^1\Delta)$  in this pulsed laser demonstration is  $\sim 5 \text{ J/liter}$ , which is sufficient to generate an approximately 10 watt (1  $\mu s$ ) output pulse from the active volume of the resonator. Much weaker outputs were obtained, however, as the concentration of BH radicals was too low to remove the  $NF(a^1\Delta)$  before it decayed by self-annihilation. This same concentration of  $NF(a^1\Delta)$  can, nonetheless, generate very high energy outputs, if the BH concentration is increased. In a supersonic laser, using a Mach 3 nozzle (1 x 100  $\text{cm}^2$  area), energy storage of 5 J/liter equates to a continuous output of 150 KW at 100% extraction efficiency. Scaling this laser for high energy applications therefore requires both chemistry improvements to increase the BH concentration and reactor/resonator engineering to efficiently process the gas stream at a high volumetric flow rate. Energetic molecules such as tetra-azido diborane are potential high yield donors that can improve power extraction efficiency.

This work was supported by the Innovative Science and Technology Office of the Ballistic Missile Defense Organization, which provided funding through the Air Force Office of Scientific Research.

**Irvine University Research Initiative  
on  
Advanced Cryogenic Propellants**

Presented at the 1994 HEDM conference (Lake Tahoe)

V. A. Apkarian	Chemistry
R. B. Gerber	Chemistry
K. C. Janda	Chemistry
J. E. Rutledge	Physics
P. Taborek	Physics

The University Research Initiative on Advanced Cryogenic Propellants was established at UCI a year ago, with a membership of two physicists and three chemists as co-principle investigators. The aim of this center is to provide a cross-disciplinary, multi-pronged yet focused approach to deliver the fundamental science and technology required to transfer vague concepts on potential cryogenic propellants to practicality. The main theme in these concepts involves the enrichment of quantum solids and fluids with atomic or radical dopants. These concepts and the approaches taken to address them define the master plan of the research activities of the group. The group is organized around a central laboratory, and four satellites. The effort involves both experiment and theory. In addition to research, the center is active in:

- a) preparation of future scientists with cross-disciplinary education, who are in position to advance and execute the science at issue,
- b) creating an active center at UCI for cryogenic physics and chemistry,
- c) maintaining contacts with other investigators in related disciplines,
- d) maintaining contacts with potential end-users of the emerging technologies, through visits and exchange of personnel.

An overview of the activities of the group and its mode of operation, were presented. The planned research, its rationale and the accomplishments to date were highlighted. This was followed by five technical reports.

**Photodynamics in cryogenic solids (V. A. Apkarian):**

A) Femtosecond time resolved studies can yield descriptions of many-body interactions and dynamics with unprecedented detail. This is illustrated through studies of the breaking and remaking of the I<sub>2</sub> bond for molecules isolated in solid Ar and Kr. The experiments consist of pump-probe studies, in which an initial pulse excites I<sub>2</sub>(A) on the repulsive part of its potential, at energies of 1000-3000 cm<sup>-1</sup> above dissociation. The probe pulse then interrogates the time evolution on the nested A/A' surfaces via laser induced fluorescence from the I<sub>2</sub> ion-pair states. The time resolution of the system, 150 fs, is sufficient to follow the reaction coordinate from reagent to product configurations for heavy atoms, hence the choice of I<sub>2</sub> for these experiments. An example of the observed signals

is shown in figure 1, in which the oscillations due to coherent evolution of dynamics that lasts for ~8 ps can be observed. Frequency analysis of the transients yields a description of not only the I<sub>2</sub> motion, but also the motions of the cage atoms immediately surrounding the molecule. Detailed analysis of this data is possible via molecular dynamics simulations, and nearly quantitative reproduction of the transients has been possible using classical dynamics and the classical Franck principle in synthesizing the data. Early reports of this work has already appeared in print.<sup>1</sup> The methodology can be used for lighter atoms, which are more appropriate in HEDM applications, by shortening the pulse width of the lasers. This extension is now in planning stages.

B) Solid hydrogen, doped with atomic oxygen, is one of the potential propellant concepts, which with proper optimization, can deliver the targeted advance in specific impulse. The initial experimental studies on this prototype are quite encouraging. It has been possible to isolate O<sub>2</sub> in D<sub>2</sub> at a concentration of 1:500. Excitation of the molecule at 193 nm, via the B←X transition, leads to predissociation of a sub-ensemble isolated at defect sites. A primitive molecular dynamics simulation shows that photodissociation in these quantum solids is qualitatively different from classical van der Waals solids, such as rare gases. The predissociation generates O atoms with 0.25 eV each, which upon collision with D<sub>2</sub> undergo three-body exchange refilling the O atom vacancy. This is dramatically different from I<sub>2</sub> dissociation-recombination in Ar, although the mass asymmetries involved, I/Ar versus O/D<sub>2</sub>, are quite similar. The photodynamics in this reactive quantum host is rather fascinating. Using laser induced fluorescence spectroscopy, it has been determined that at temperatures of ~4K, not only O(<sup>3</sup>P) but also O(<sup>1</sup>S) and O(<sup>1</sup>D) are stable with respect to reaction with D<sub>2</sub>. This can be discerned from the LIF spectrum shown in figure 2a, in which the stable emissions from O<sub>2</sub>(A'→X) and O(<sup>1</sup>S→<sup>1</sup>D) can be seen. The thermal histories of the atomic and molecular emissions are used to establish that the visible O atoms are mostly stored as O<sub>2</sub>(<sup>3</sup>Σ<sub>g</sub><sup>-</sup>).O(<sup>3</sup>P) complexes. These are stable up to 7.5 K. Upon warm-up above 7.5 K, the atoms recombine as evidenced by the thermoluminescence illustrated in figure 2b. The spectroscopic methods used only give indirect measures of the energy density of these solids. To quantify the energy content of such systems, absolute calorimetric and gravimetric measurements, using quartz microbalance technologies developed in the URI (see below) are now being implemented. Possible methods of optimization are considered. Scaling to bulk hydrogen is the next logical step in this work.

---

1 R. Zadoyan, P. Ashjian, Z. Li, C. C. Martens, and V. A. Apkarian, Chem. Phys. Lett. 218, 504 (1994).

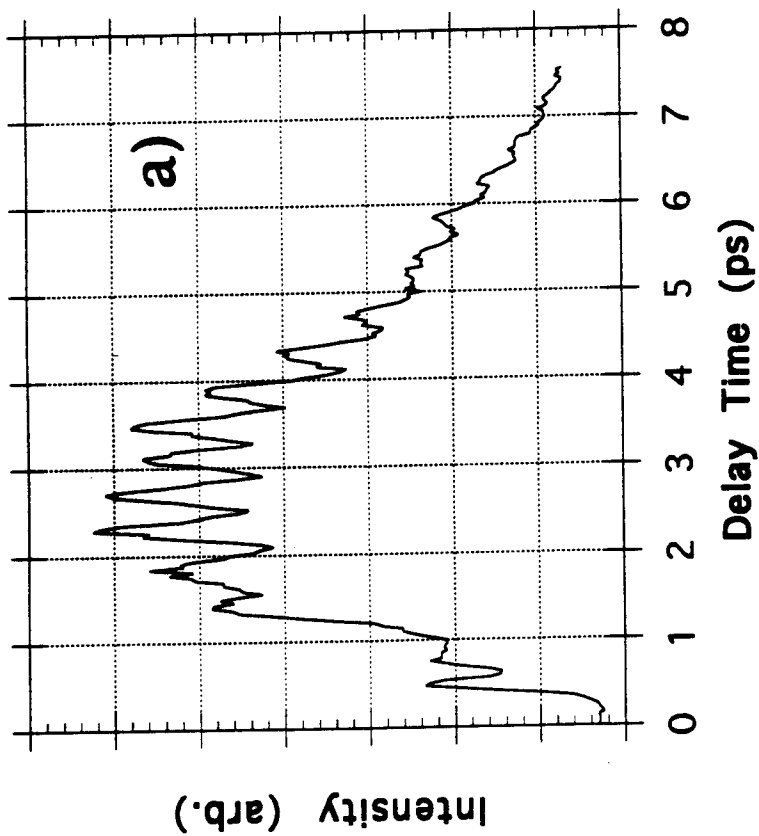
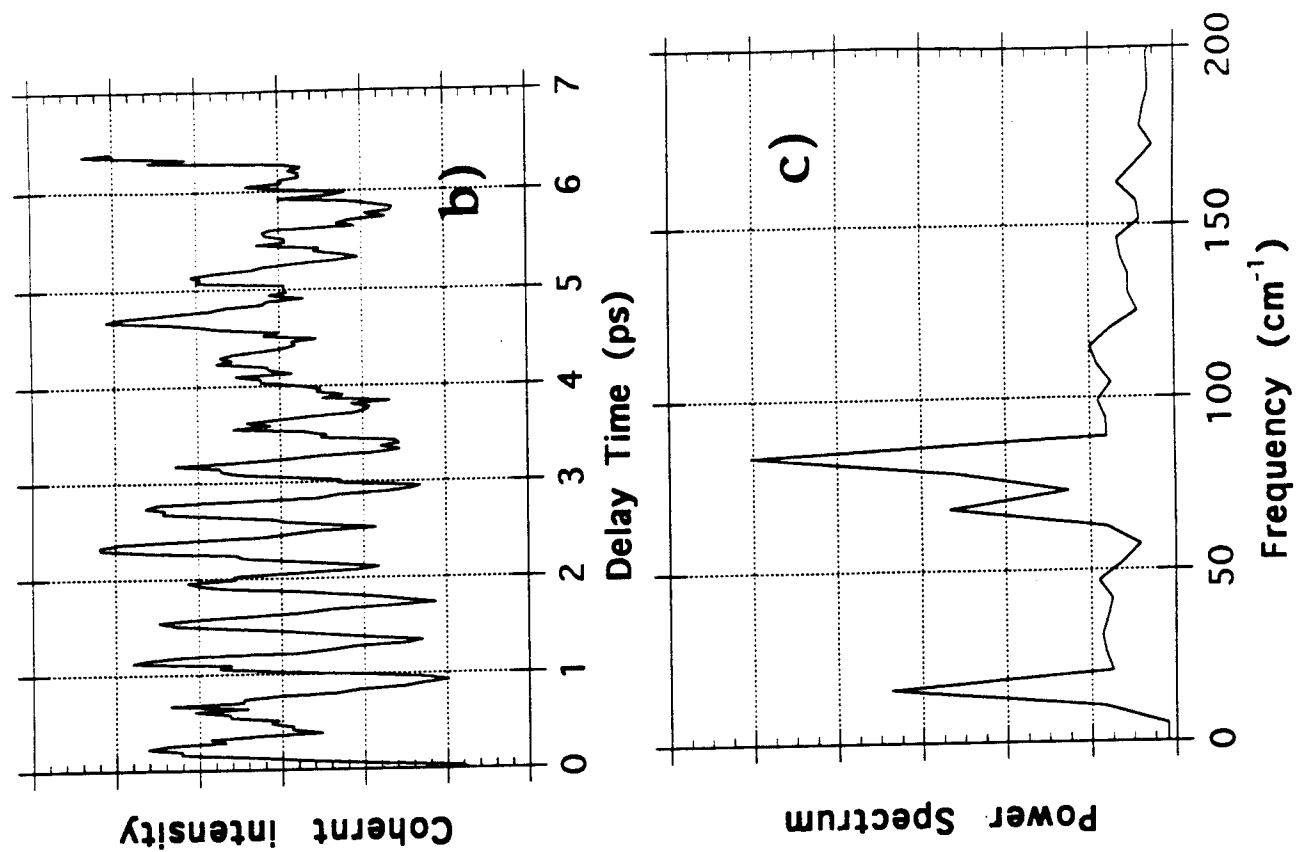


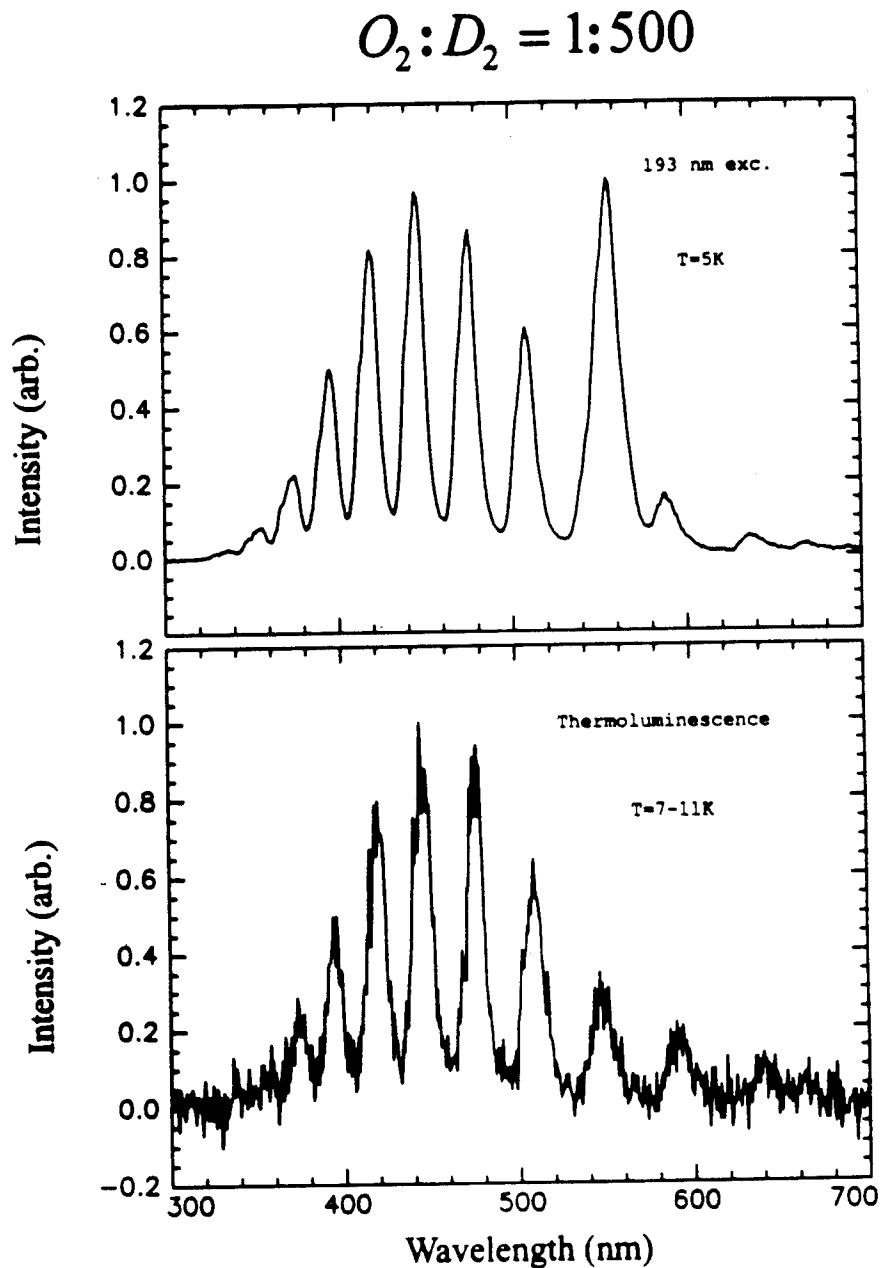
**Figure 1:**

- a) Time evolution of pump-probe signal.
- b) Coherent part of time evolution.
- c) Fourier transform of oscillatory part

**Figure 2:**

Top panel: Fluorescence of  $O_2(A' \rightarrow X)$  and O atom ( $^1S \rightarrow ^1D$ ) at 569 nm, from an  $O_2/D_2$  sample of 1:500, after irradiation at 193 nm.  
Lower panel: Thermoluminescence of  $O_2$  due to thermally induced O+O recombination at 7.5K.

## LIF and Thermoluminescence



### Growth kinetics of solid hydrogen (P. Taborek and J.E. Rutledge)

A special cryostat has been designed and built for hydrogen experiments over the temperature range from 1 to 30 K. As shown in Figure 3, it features a carefully heat sunk copper sample chamber to ensure the highly isothermal conditions these studies require and contains a port for the addition of an atom source. We have been investigating atom sources with particular attention to minimizing the power consumption to allow in situ low temperature growth. The potentially promising technique of forming solid hydrogen with high concentrations of atomic dopants by direct condensation will be conducted in this apparatus.

The first experiments have been studies of the growth of solid molecular hydrogen films under thermal equilibrium conditions using a quartz microbalance technique. A surprising wealth of phenomena are known to accompany the growth of surface films. Among these are surface phase transitions such as wetting and roughening transitions. The location of these transitions in the P-T plane are indicated schematically in Figure 4. The sub-monolayer mass sensitivity of quartz microbalances have made them an important means of exploring these phases. We have modified the microbalance to include thin film heaters and thermometers, as shown in the inset to Figure 3. These modifications will allow calorimetric studies to more thoroughly characterize the growth. The experimental challenges include adding the devices and the leads without sacrificing the mass sensitivity and developing thin film thermometers that can be applied to the quartz surface without substantially increasing the heat capacity of the device. We have developed a technique for sputtering niobium doped silicon films that are well suited for resistance thermometry in the temperature range of interest. A measurement of the resistance versus temperature for one of these thermometers is shown in Figure 5. We have also succeeded in bonding leads onto the films in a way which does not degrade the performance of the microbalance.

To study the growth of solid hydrogen films at temperatures not far below the bulk triple point, we have measured adsorption isotherms. In these experiments, the temperature of the can is held constant and the pressure increased from zero to the bulk sublimation pressure while the mass signal from the microbalance is recorded. The trajectory of such an experiment in the  $\mu$ -T plane and the resulting isotherm are shown in Figure 4 and 6. The result is typical of most solid films well below the triple point. As the film grows strains develop as the adsorbate accommodates its structure to that of the substrate. After a few layers, the thermodynamic costs of the strains overwhelms the thermodynamic advantage of being in the attractive potential well of the substrate and film growth stops.

At lower temperatures the drastically reduced sublimation pressure is too low to permit direct measurements of isotherms. To study the growth below 4 K we are pursuing thermal desorption experiments. A pulse of heat is applied to the heater sufficient to remove the film from the microbalance. The mass signal is then monitored as a function of time as gas phase molecules collide with and

stick to the surface. At 4 K the molecules hit the surface at the rate of one solid monolayer per second, while at 2.4 K the growth rate is a monolayer per year. The result of one such experiment is shown in Figure 7. After the topmost layers of the film are removed and readsorption begins, an instability that affects the resonant frequency of the microbalance develops. Onset time of the instability scales roughly with the monolayer time. Attempts to understand this signal and relate it to properties of the growing film are current under way.

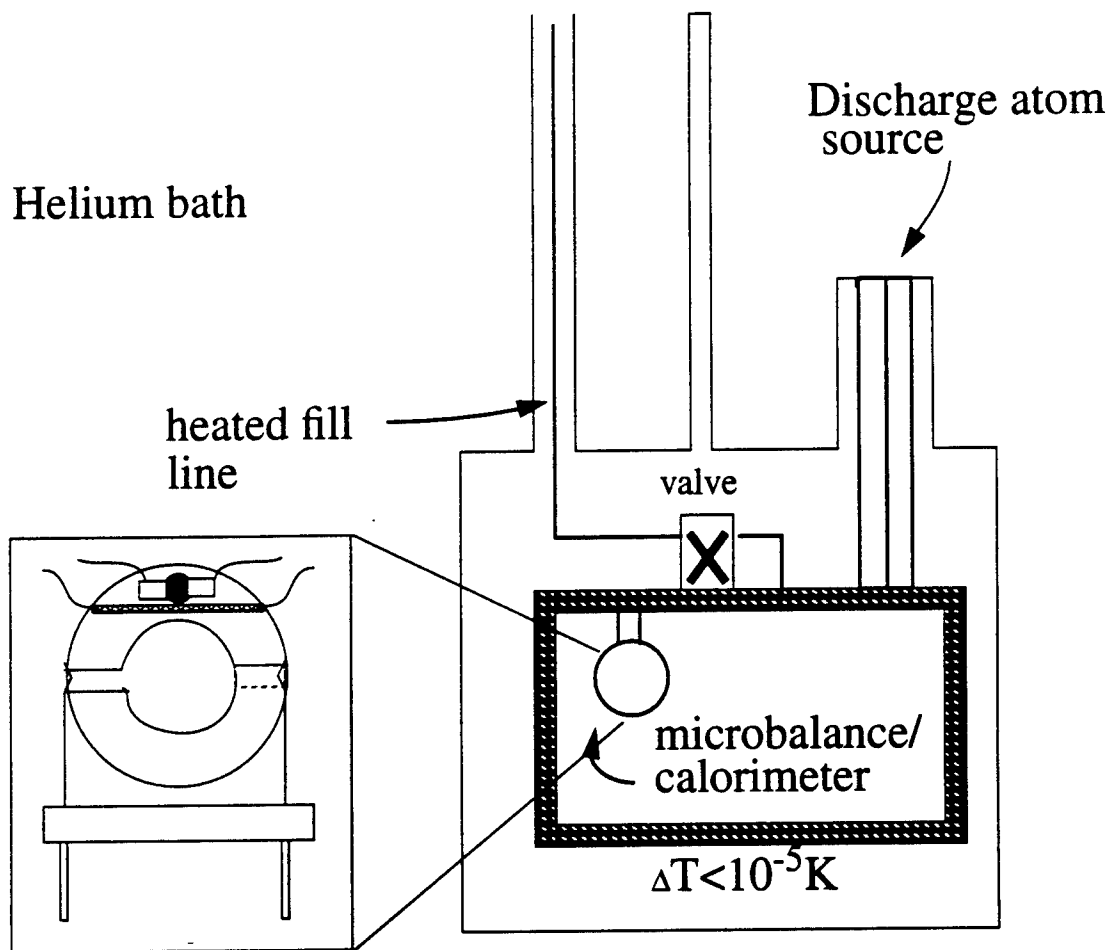


Figure 3. Apparatus for studying growth of hydrogen films. The inset shows details of the thin film heater and thermometer on the microbalance/calorimeter.



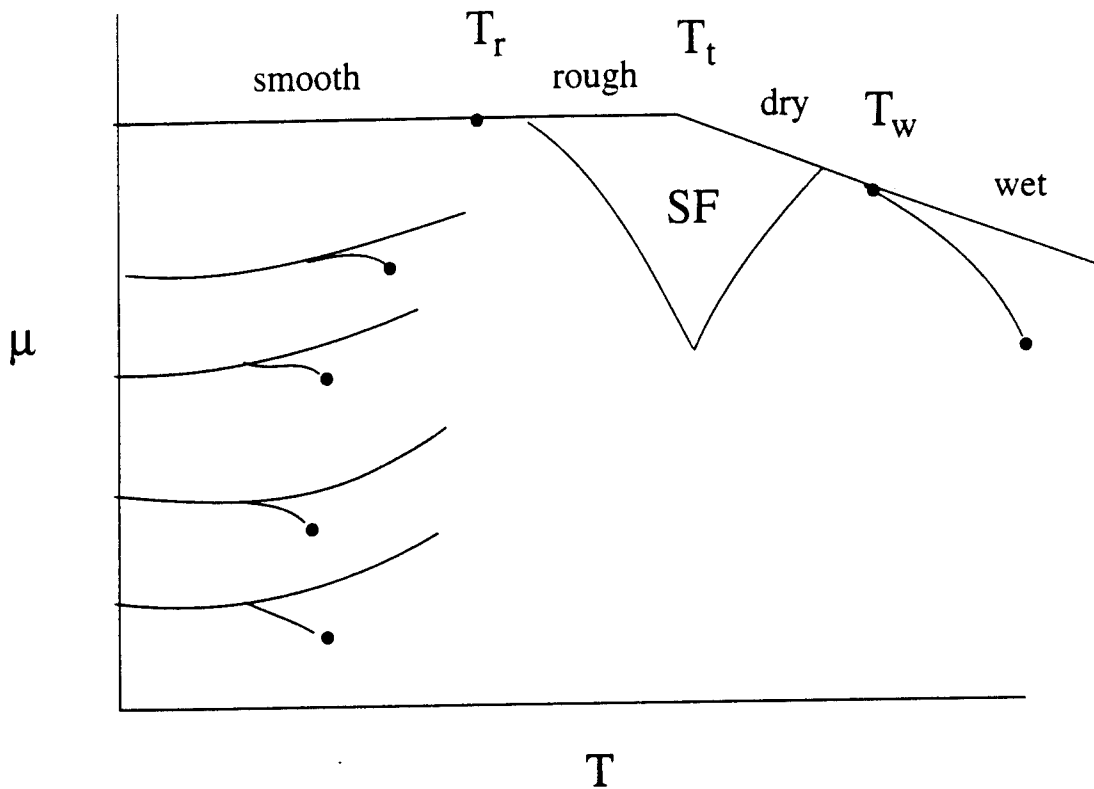


Figure 4. Schematic phase diagram in the  $\mu$ - $T$  plane of a material growing on a substrate, showing solid, liquid and vapor phases in the adlayers. The 2D liquid-vapor critical points converge to the roughening transition at  $T_r$  at bulk coexistence. Other possible phase transitions are wetting at  $T_w$  which separates wet and dry regions of the coexistence curve, and prewetting which separates thin and thick film phases. In the vicinity of the triple temperature  $T_t$ , it is possible to have stratified films (SF) which consist of layers of solid covered with a fluid layer.

# Resistance of Nb/Si vs. Temperature

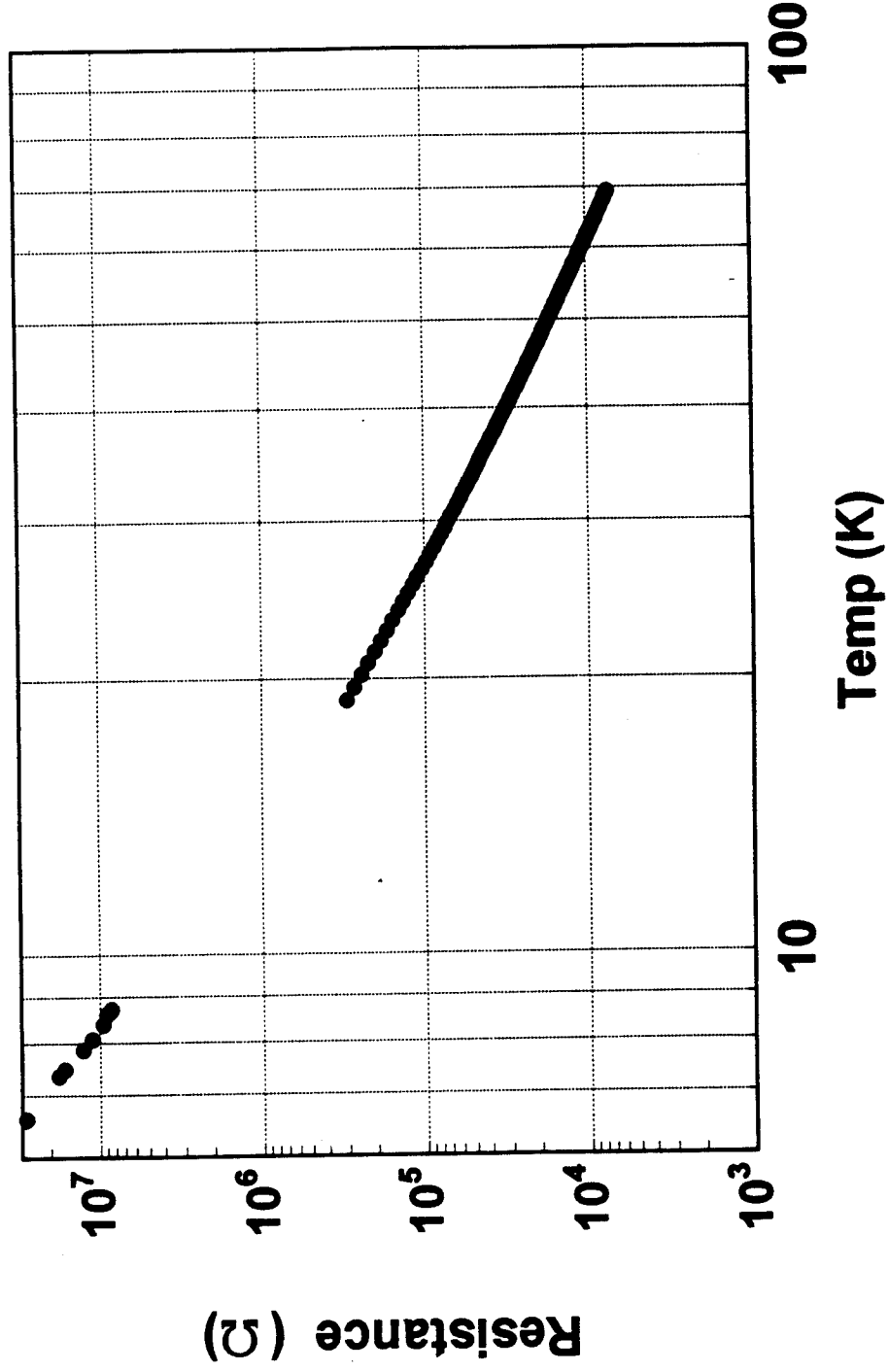


Figure 5.

147.

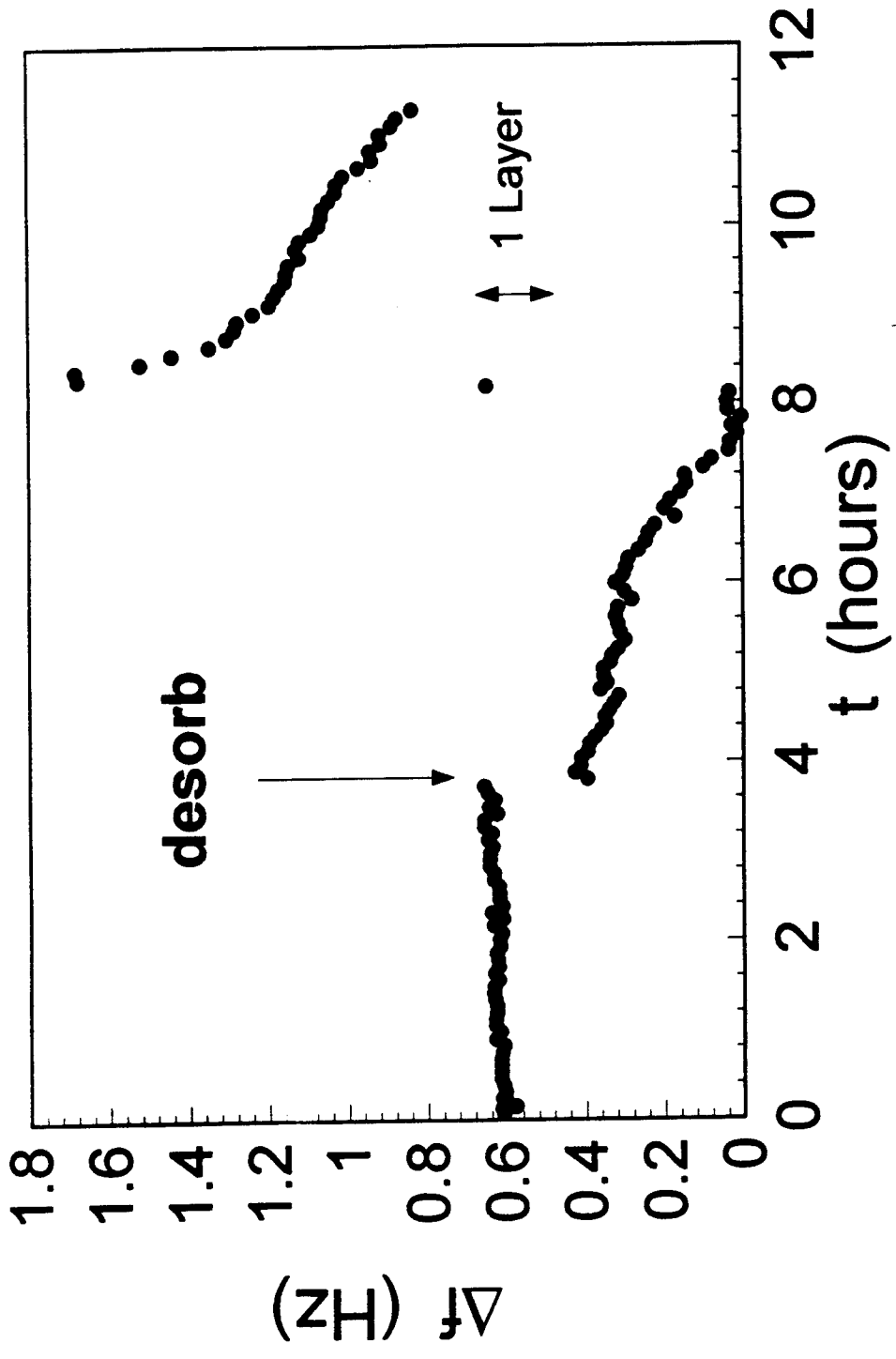


Figure 7. Response of microbalance to flash desorption at  $t=4$  hrs.

### Development of soft delivery techniques (K. C. Janda):

If we are to achieve 5% doping of solid H<sub>2</sub> with B, C, N or O atoms, then two things are clear. First, we can not depend on statistical deposition processes. Second, the resulting solid will not be well described as a slight perturbation of solid H<sub>2</sub>. Most of the H<sub>2</sub> molecules in the solid will be in contact with one of the reactive atoms. Since the potential between the reactive atom and H<sub>2</sub> will be stronger than the H<sub>2</sub>-H<sub>2</sub> interaction, the reactive atom properties will strongly influence the properties of the solid. In order to achieve high densities of reactive atoms in solid H<sub>2</sub>, we will try to pre-form stoichiometric clusters using the "pick-up" technique of Scoles, and then "soft land" the cluster on the surface of the solid H<sub>2</sub> matrix.

In what follows, we will use carbon atoms as our example for a reactive atom. Carbon provides the highest potential increase in  $I_{sp}$ . However, carbon is also the most reactive atom in the sense that its barrier to reaction with H<sub>2</sub> is very small. This means that if the carbon atom is to survive its encounter with a hydrogen molecule without reacting then the two species must encounter each other at close to zero kinetic energy. We are prepared to investigate several methods of imbedding C atoms in clusters, but only one will be outlined here. First, large He clusters will be generated using a cryogenic, super-sonic nozzle source similar to that of Scoles. Next, a pulsed beam of C atoms will be generated by a spark discharge of C<sub>3</sub>O<sub>2</sub>. The He atom beam and the C atom beam will be crossed at right angles. Since the He atom beam has much higher total mass ( $N_{He}=1000$ ), it will "pick up" some of the carbon without being deflected from its original trajectory. It is expected that the C atom will be imbedded deep into the He cluster since the He-C interaction is expected to be quite strong. The He/C cluster will then pass through a "pick-up" cell containing H<sub>2</sub> molecules. In early experiments, the pressure in the "pick-up" cell will be adjusted so that the cluster picks up one or two hydrogen molecules. This provides the gentlest possible introduction of H<sub>2</sub> to carbon. Since the incident H<sub>2</sub> molecule will first encounter the He portion of the cluster, the relative kinetic energy of H<sub>2</sub> and He will be thermalized at 1 K before they meet. The cluster will then be probed by multiphoton ionization to see if they form a van der Waals molecule or if they directly react.

If the carbon atoms and hydrogen molecules are found to form a cluster without reacting, then more hydrogen will be added to the pick up cell in an attempt to make a cluster with the stoichiometry C(H<sub>2</sub>)<sub>12</sub>HeN. This will provide a single solvation shell of H<sub>2</sub> for the carbon, and the "reactive core" would still be shielded by helium. If this can be achieved, the cluster will be deposited on a surface and MPI spectroscopy will be used to probe whether the reactive core survives the collision with the surface.

So far we have built and are testing the He cluster source, we have built a spark source for reactive atoms. We have used laser excited fluorescence spectroscopy to test the spark source for producing boron atoms from diborane precursor. We are currently completing the MPI detector system that will be

significant advantages over conventional beam source nozzles for cluster production. In a conical nozzle the beam expansion is constricted to occur over a longer distance and time. This keeps the beam density high as the temperature decreases, and allows for the formation of more clusters. We have investigated this technique for the production of HeBr<sub>2</sub>. As shown in Fig. 2, HeBr<sub>2</sub> can be produced with high enough number densities to record the pump-probe laser excited fluorescence spectrum out to high values of J. This, in turn, has allowed us to determine the structure and bond energy of the molecule with considerable precision. Finally, the conical supersonic nozzle expansion allowed us to resolve rotational structure in a transition to an excited bending mode of the He-Br<sub>2</sub> bond for the first time. This will allow the first direct test of the anisotropy of the HeBr<sub>2</sub> potential. This work is currently being prepared for publication.

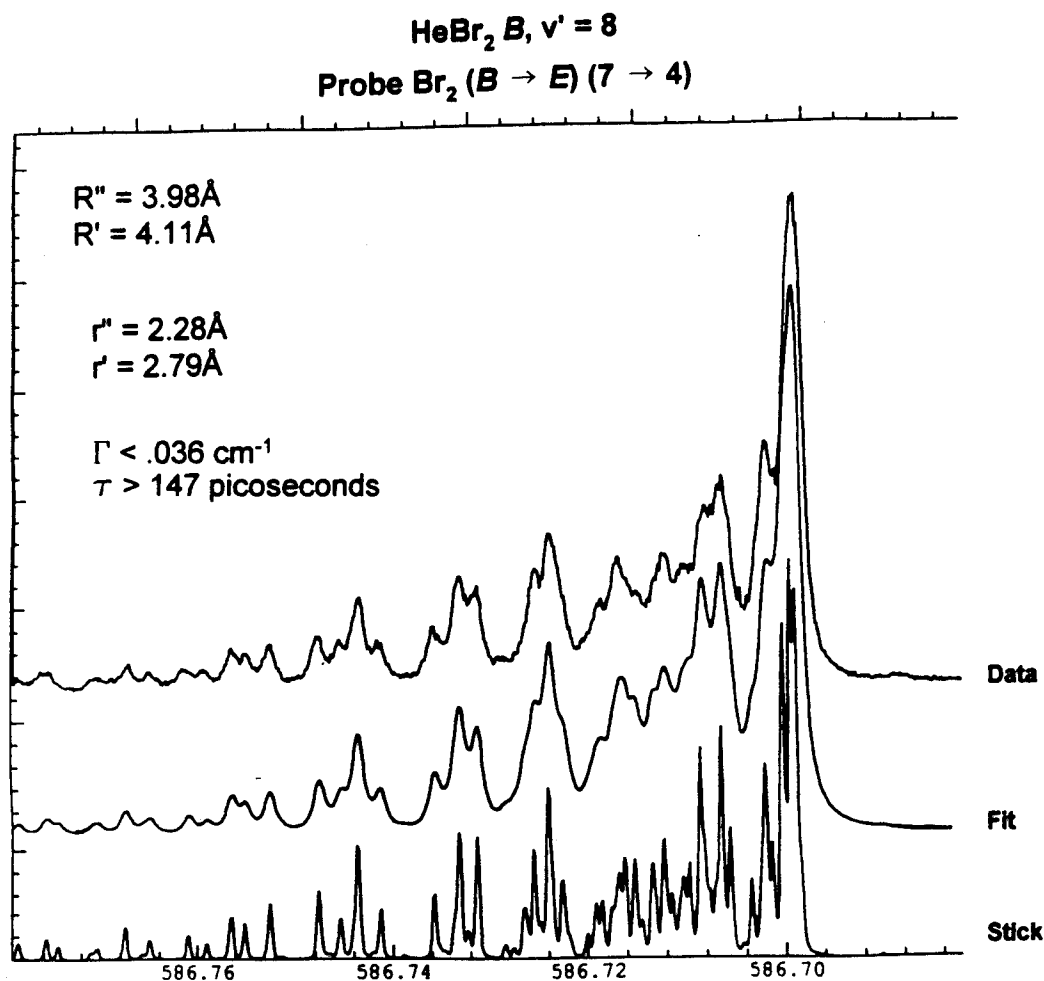


**Figure 8:** The pump-probe, laser induced fluorescence spectrum of HeBr<sub>2</sub>. The top trace is the spectrum as recorded using a conical super-sonic nozzle source. The signal to noise of this spectrum is much higher than previously obtained using conventional nozzles. The fit to the spectrum uses a rigid rotor Hamiltonian in which the molecules is assumed to have a "T" shaped structure.  $R''$  and  $R'$  are the He-Br<sub>2</sub> distances in the ground and electronic excited states, respectively.  $r''$  and  $r'$  are the Br<sub>2</sub> distances. The lifetime broadened line width is  $0.036\text{ cm}^{-1}$ .

### Theoretical developments (R. B. Gerber):

Theoretical calculations in support of the various experimental efforts, is being carried at different levels, using computational approaches appropriate for treating many quantum degrees of freedom. The energetics, and photo-induced and collision-induced dynamics of doped hydrogen clusters  $A(H_2)_n$ , where A is an atom, is the present focus. Among the results obtained to date are:

The ground state wavefunctions of  $A(H_2)_n$  are computed using diffusion Monte Carlo to assess the stability, and utility of various dopants in solid hydrogen as propellants. Among the systems that have already been completed are:  $(H_2)_n$  with  $n \leq 100$ ;  $Li(H_2)_n$  with  $n \leq 12$ ;  $B(H_2)_n$  with  $n \leq 8$ ;  $Hg(H_2)_n$  with  $n \leq 55$  ( $H_g$  being a model for Mg);  $O(^3P)H_2$  and  $FH_2$ . Insights on the vibrational dynamics and spectroscopic probes will be presented.

The survival probabilities of quantum clusters upon collision with  $H_2$  molecules was studied using time-dependent quantum mechanical methods. Despite the weak binding of these clusters, relatively high survival probabilities are observed. These insights are crucial to considerations of methods of preparation of the propellants.

Reactive photodynamics in  $Li(H_2)_2$  and  $Hg(H_2)_{12}$  has also been investigated. In the first case, the different channels for the break-up of the cluster is characterized. In the second case, abstraction of H and subsequent coherent chain reaction in the cluster is observed. This data is crucial in experiments involving optical probing of the clusters, or the extended solids.

# **Current Experiments on the Combustion of Cryogenic Solid Propellants**

**Patrick G. Carrick**

**Phillips Laboratory, Propulsion Directorate  
Edwards Air Force Base, CA 93524-7680**

**Several techniques for the use of cryogenic solid HEDM propellants are under consideration. One promising method is the direct combustion of the cryogenic solid in a hybrid configuration. Either the fuel or the oxidizer can be used as the solid in this configuration, with the complimentary component in the form of a conventional (usually cryogenic) liquid.**

**We are investigating the combustion of cryogenic solid ethylene (and other low melting point hydrocarbons) using liquid nitrogen as the coolant and gaseous oxygen as the oxidizer. This combination forms a relatively easy-to-study model system that can simulate the possible combustion of solid hydrogen.**

**The solid ethylene/additive system itself may also be of interest as a possible low cost, simple and relatively high performance rocket. This design would be less complicated and contain fewer "moving parts" that conventional LOX/RP-1 rocket engines.**

## ***Why are we interested in cryogenic solid propellants?***

### **Greater propellant density:**

- ◆ **Liquid Hydrogen = 0.070 g/cc, Solid = 0.087 g/cc**
- ◆ **Liquid Oxygen = 1.149 g/cc, Solid = 1.55 g/cc (20K)**

### **Can store energetic additives to improve performance:**

- ◆ **Atoms and small molecules in solid hydrogen**
- ◆ **Ozone, oxygen atoms, and others in solid oxygen**
- ◆ **Acetylene, energetic strained rings in “ethylene”**



## **Summary of $I_{sp}$ Research Results**

- 1. Boron and Carbon atoms in solid  $H_2$  give best  $I_{sp}$  increases. Carbon is potential monopropellant.**
- 2. Aluminum and Silicon in solid  $H_2$  give moderate  $I_{sp}$  increases.**
- 3. Ozone in solid Oxygen gives about 20 seconds increase in  $I_{sp}$  over LOX/ $LH_2$ .**
- 4. Oxygen atoms could give over 40 seconds increase.**
- 5. Small molecules may help improve  $I_{sp}$  increases.**

# Conclusions

1. Boron and carbon atoms in H<sub>2</sub> give the best I<sub>sp</sub> increases. Carbon is a potential monopropellant. However, carbon may not be stable in solid hydrogen.
2. The homonuclear diatomic molecules generally do not reduce the specific impulse. For low additive concentrations, higher *effective* atomic loading can be obtained with diatomic molecules, except for carbon.
3. At the 5% level, LiB gives the best I<sub>sp</sub> increase (other than Be compounds).
4. Formation of other small molecules during the deposition process may not significantly reduce the I<sub>sp</sub>.

POC: Dr. Patrick G. Carrick, (805)275-5883  
PL/RKFE, 10 E. Saturn Blvd., Edwards AFB, CA,  
93524-7680

## Structure, Thermochemistry and Performance of Advanced Propellants

H. H. Michels and J. A. Montgomery, Jr.  
United Technologies Research Center  
East Hartford, CT 06108

Donald D. Tzeng and Edmund Lee  
United Technologies Chemical Systems  
San Jose, CA 95150

### ABSTRACT

Environmental concerns and the requirements for increased payload delivery into earth orbit have brought about the need for new chlorine-free propellants with a high energy content. Nitramines, which exhibit one or more covalently bonded N-NO<sub>2</sub> groups, constitute one important class of compounds. Examples are RDX, HMX, and polycyclic caged structures such as wurtzitanes and [n]-prismanes.

Several new compounds have recently been synthesized based on the dinitramide anion [N(NO<sub>2</sub>)<sub>2</sub><sup>-</sup>]. Using *ab initio* calculations at the SCF and MP2 levels of theory, we have examined the stability and thermochemistry of several dinitramide compounds including: ammonium dinitramide (ADN), hydroxylammonium dinitramide (HADN), methyl dinitramide (MDN), lithium dinitramide (LDN) and the closely related oxidizers: tetranitrohydrazine [N<sub>2</sub>(NO<sub>2</sub>)<sub>4</sub>] and trinitramine [N(NO<sub>2</sub>)<sub>3</sub>]. A comparison of the performance of these new compounds, many of which have now been synthesized, indicates significant improvements over conventional oxidizers such as ammonium perchlorate (AP) or ammonium nitrate (AN).

A new family of energetic compounds are the polynitrogen azidamines. We have examined the stability and available energy content of several of these compounds, including diazidamine [HN(N<sub>3</sub>)<sub>2</sub>], triazidamine [N(N<sub>3</sub>)<sub>3</sub>] and salts of the diazidamide anion [N(N<sub>3</sub>)<sub>2</sub><sup>-</sup>]. All of these compounds are highly energetic materials with large positive heats of formation. Since azidamines do not require synthetically difficult ring closing methods, they may be more amenable to chemical synthesis than the corresponding cyclic compounds. Several nitrated forms of this class of compounds also show structural stability. Nitrosyl azide [NON<sub>3</sub>] and nitryl azide [NO<sub>2</sub>N<sub>3</sub>] represent the elementary structures in this category.

The development of explosives with lessened sensitivity to detonation by shock is another area of considerable current interest. The compound, 3-nitro-1,2,4-triazole-5-one (NTO), is an example of a high energy material with less shock sensitivity than TNT. Preliminary studies indicate several nitrated triazole and tetraazole structures with large positive heats of formation. The structures and decomposition routes of these compounds are currently being investigated.

---

Supported in part by AFPL under Contract F04611-90-C-0009.

## Discussion

There has been growing interest in the development of chlorine-free oxidizers and high energy compounds for use in advanced propellant formulations. Nitramines, which contain one or more covalently bonded N-NO<sub>2</sub> groups, constitute a promising class of chlorine-free energetic molecules. Examples of such compounds are the well-known explosives RDX and HMX<sup>1,2</sup>, and the recently synthesized hydrogen and ammonium dinitramide.<sup>3,4,5</sup> Other examples of energetic molecules are those containing the azide (N<sub>3</sub>) group such as FN<sub>3</sub><sup>6</sup> and ClN<sub>3</sub>.<sup>7</sup> Halogen azide compounds, which exhibit a 15-20 kcal/mol barrier to decomposition, have high positive heats of formation (~100 kcal/mol) owing to their conformational stability as a local minimum on a potential surface that lies significantly higher in energy than dissociation to NF(Cl) + N<sub>2</sub>.

Recently, Bottaro and Schmitt<sup>3</sup> have synthesized several new compounds that exhibit a dinitramide anion [N(NO<sub>2</sub>)<sup>-</sup>] structure. These compounds form as salts similar to ammonium nitrate or ammonium perchlorate, rather than as the less stable organic alkyldinitramines.<sup>8</sup> In our studies, we have examined the structure of this new inorganic anion and have reported estimates of its vibrational spectra and thermodynamic stability.<sup>5</sup>

*Ab initio* calculations on N(NO<sub>2</sub>)<sub>2</sub><sup>-</sup>, NH<sub>4</sub>N(NO<sub>2</sub>)<sub>2</sub>, LiN(NO<sub>2</sub>)<sub>2</sub>, HN(NO<sub>2</sub>)<sub>2</sub>, CH<sub>3</sub>N(NO<sub>2</sub>)<sub>2</sub>, and NH<sub>3</sub>OHN(NO<sub>2</sub>)<sub>2</sub> have been performed at both the HF and MP2 levels of theory using the standard 6-31G\*\*, 6-31+G\*\*, and 6-311+G\*\* basis sets. The inclusion of diffuse basis functions is necessary for reliable predictions of the thermochemistry of these species. Gradient optimizations were performed to locate the geometries of the stationary points. Harmonic vibrational frequencies were then computed to verify that the calculated structures are true minima. The results for the dinitramide ion and the lithium salt are shown in Fig. 1 and Tables 1-2. A detailed study of hydrogen dinitramides, which exists both as the simplest member of an alkyldinitramines series and as a very strong dinitramidic acid has been previously reported.<sup>5</sup>

The successful synthesis of halogen azides and dinitramide structures has led us to examine the possibility of stability in other unusual nitrogen structures. Previous theoretical studies have examined the stability of several energetic forms of N<sub>n</sub>.<sup>9-12</sup> Although nitrogen and the CH group are pseudoelements<sup>13</sup> and numerous stable (CH<sub>n</sub>) compounds, such as benzene, or polyacetylene are well known, the analogous polynitrogen compounds, N<sub>n</sub>, where n exceeds 3, have so far not been prepared. The main reasons for this difference are the relative energies of their triple, double, and single bonds. For nitrogen, the average thermochemical bond energy of the triple bond (946 kJ mol<sup>-1</sup>) is 368 kJ mol<sup>-1</sup> larger than the sum of a double (418 kJ mol<sup>-1</sup>) and a single (160 kJ mol<sup>-1</sup>) bond.<sup>14</sup> Thus, dinitrogen, N<sub>2</sub>, is by far the most stable polynitrogen compound. For carbon the situation is reversed. The bond energy of a triple bond (813 kJ mol<sup>-1</sup>) is 141 kJ mol<sup>-1</sup> smaller than the sum of a double (598 kJ mol<sup>-1</sup>) and a single (356 kJ mol<sup>-1</sup>) bond.<sup>14</sup> Thus, acetylene, (CH)<sub>2</sub>, is thermodynamically unstable with respect to its higher homologues.

In view of the above energetic considerations, it is not surprising that the polynitrogen compounds with  $n > 2$  are highly energetic and thus, are of interest for halogen-free high energy density materials (HEDM). The obvious challenge to their use is their thermodynamic instability which renders their syntheses and handling very difficult. Most publications dealing with polynitrogen compounds have been limited to theoretical predictions of their behavior and experimental studies, such as the one by Vogler,<sup>15</sup> are rare. Previously calculated, but presently still unknown polynitrogen ( $n > 3$ ) compounds include  $N_4$ <sup>16</sup>,  $N_4^+$ <sup>17-21</sup>,  $N_5^-$ <sup>22</sup>,  $N_6$ <sup>16, 22-24</sup>,  $N_8$ <sup>16, 23, 25</sup>,  $N_{12}$ <sup>26</sup> and  $N_{20}$ <sup>26, 27, 28</sup>. Most of these compounds are cyclic or polycyclic and, hence, would require synthetically very difficult ring closing methods. In order to avoid this difficulty, we are searching for stable polynitrogen structures which would be more amenable to an actual synthesis.

As an exploratory step, we have calculated energies, stabilities, and vibrational spectra of a set of polynitrogen compounds, the azidamines. *Ab initio* molecular orbital (MO) calculations were carried out using the Gaussian 92 programs.<sup>29</sup> RHF/6-31G\* and MP2/6-31G\* geometry optimizations were performed for all species; additional calculations with the 6-31G\* set augmented with diffuse functions (RHF/6-31+G\*) were performed for the anion. The density functional theory<sup>30</sup> calculations were done with the program DGauss<sup>31</sup>, which employs Gaussian basis sets. DGauss was implemented on a Cray YMP computer.

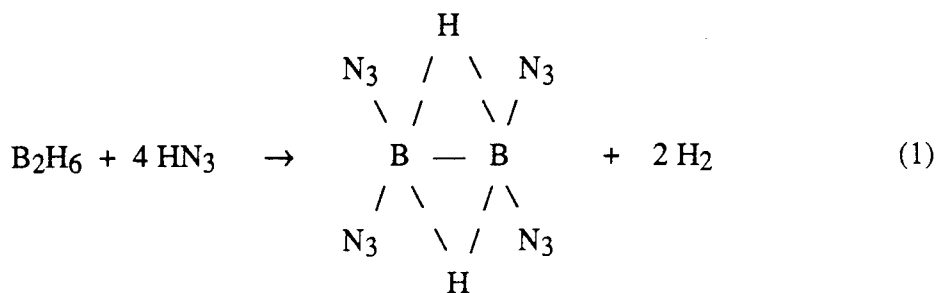
The basic azidamide anion is  $N(N_3)_2^-$  which was found to be stable as an open chain with  $C_2$  symmetry. This anion is shown in Fig. 2 where the central  $N_1-N_2$  bond distance of 1.44 Å is only slightly larger than the 1.38 Å value reported for the dinitramide anion,  $N(NO_2)_2^-$ .<sup>5</sup> Adding a proton to  $N(N_3)_2^-$  yields diazidamine,  $HN(N_3)_2$ , which is shown in Fig. 3. We find the lowest energy conformation to exhibit  $C_2$  symmetry but a stable  $C_1$  structure is also found to lie ~9 kJ/mol higher.

In analogy with trinitramine, we examined the structure of the triazidamine molecule,  $N(N_3)_3$ . A stable structure of  $C_3$  symmetry was found as shown in Fig. 4. This very energetic structure exhibits a central  $N_1-N_2$  bond distance of 1.46 Å, very close to the value found for the anion. This suggests that strong electrostatic interactions (crowding) are not observed in this system in contrast to the situation found for trinitramine.<sup>32</sup> Finally we examined the tetraazidammonium cation,  $N(N_3)_4^+$ . A stable  $D_{2d}$  structure was found at both the MP2/6-31G\* and DFT levels of theory as illustrated in Fig. 5. Again, we find only a small stretching (.02 Å) of the central  $N_1-N_2$  bond distance.

The gas phase heats of formation of these azidamines were calculated from the reactions listed in Table 1. The heats of reaction given in Table 1 are based on calculated MP2 and DFT energies. In Table 2, we list the derived heats of formation of this family of polynitrogen compounds. This is a very energetic class of compounds. Potential methods for their synthesis are being explored including the replacement of halogen ligands in nitrogen halides, such as  $NCl_3$ , by azido groups using reagents such as trimethylsilylazide,  $(CH_3)_3SiN_3$ .

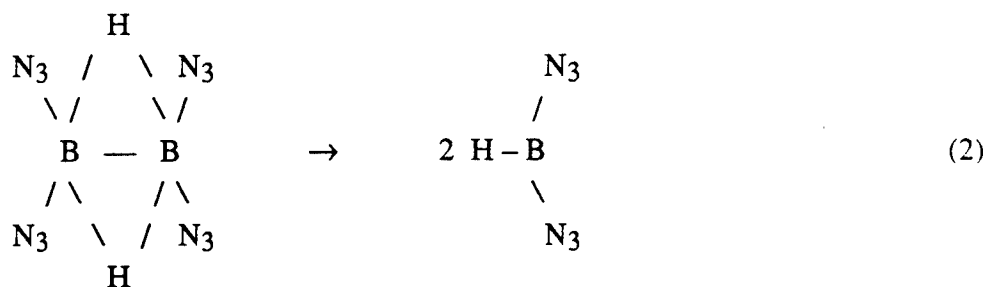
Another family of energetic compounds is the azidoboranes. Wiberg and Michaud<sup>33</sup> have shown that  $HN_3$  and  $B_2H_6$  react in ether by abstracting  $H_2$  to form azidoboranes. The gas phase

reaction could proceed as:



provided the reaction products are stable. *Ab initio* calculations were performed to explore the possible existence and stability of the tetraazidoborane (TADB) structure suggested in reaction (1). The calculations indicate the likely existence of a vibrationally stable  $D_2$  structure for TADB. Calculated heats of reaction and heats of formation are reported in Table 3. These results include vibrational zero-point corrections obtained from the calculated vibrational frequencies (scaled by 0.8929). The MP2/6-31G\*\*/RHF/6-31G\* heat of formation of TADB, given in Table 3, indicates that reaction (1) is exothermic by 73.2 kcal/mol.

In a fashion similar to  $\text{B}_2\text{H}_6$ , TADB can dissociate upon heating, yielding diazidoborane (DAB):

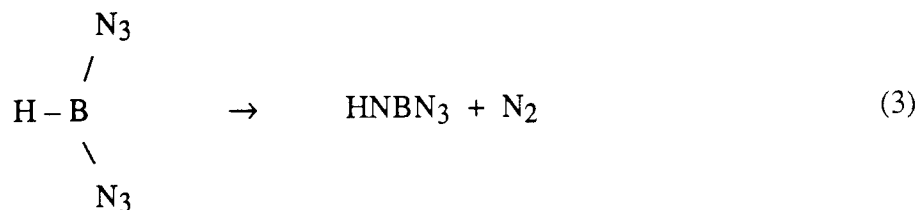


*Ab initio* calculations of diazidoborane indicate a vibrationally stable  $C_{2v}$  structure. The calculated energies in Table 3 indicate that reaction (2) is exothermic by about 9.8 kcal/mol.

DAB, like the halogen azides, can eliminate a terminal  $\text{N}_2$  group. Calculations at the RHF/6-31G\* level of theory indicate that the barrier for  $\text{N}_2$  elimination is 17.9 kcal/mol, a value slightly greater than that found for  $\text{FN}_3$  (10.8 kcal/mol calc., 13.6 kcal/mol exp.). The molecular

fragment  $\begin{array}{c} \text{N} \\ / \\ \text{H} - \text{B} \\ \backslash \\ \text{N}_3 \end{array}$  that results from  $\text{N}_2$  elimination from DAB undergoes a conformational

change by migration of the lone N atom away from the N<sub>3</sub> group and insertion into the H-B bond to form a planar HNBN<sub>3</sub> structure. Calculations at the RHF/6-31G\* level of theory indicate that this compound is vibrationally stable. The overall reaction:



is exothermic by 41.1 kcal/mol as calculated from the data in Table 3.

### Performance Characteristics

Although several of the compounds discussed above have not yet been synthesized, it is of interest to compare their relative value in improving the performance characteristics of solid propellant formulations. Heats of formation for all of these compounds have been calculated at the MP2/6-31G\* level of theory from isodesmic reactions. The use of isodesmic reactions permits cancellation of errors that can otherwise accumulate if heats of formation are based on atomization energies. Solid densities were estimated using Cady's method<sup>34</sup> for evaluating explosives. These calculated data are given in Table 4.

The new energetic materials are separated into three groups: oxidizers, monopropellants, and oxygen deficient energetic materials. These compounds are formulated in propellants and the I<sub>sp</sub>'s of these propellants are calculated through the AFAL theoretical I<sub>sp</sub> program. The oxidizers are calculated as ADN substitutes in an ADN/GAP smokeless propellant. The monopropellants replace HMX in a smokeless/PEG propellant. The oxygen-deficient materials are formulated in an aluminized/HTPB propellant as replacements of HMX.

#### Oxidizers

Tetranitrohydrazine, trinitramine, nitrosyl azide, and nityl azide are the oxidizers formulated in a GAP/smokeless propellants. The calculated I<sub>sp</sub> are shown in Table 5. An average of 30 to 40 sec improvement in the specific impulse over the formulation containing ADN as an oxidizer is achieved. Similar improvement is also seen in density I<sub>sp</sub>. The large improvement in performance also comes with much lower percentages of oxidizer contents. Lower solid contents make propellant processing easier. Lower solid contents also produce propellants with better physical properties.

## Monopropellants

Triazidamine (TAA), a monopropellant, is used in replacement of HMX, also a monopropellant, in a selected formulation. A generic energetic smokeless/PEG formulation is chosen for comparison. The base formula is not optimized. This base formulation contains HMX (60 %), PEG (13 %), NG (25 %), and N-3200 (2 %). As shown in Table 5 more than 50 sec. improvement is achieved.

## Oxygen Deficient Energetic materials

Diazidoborane, imidoazidoborane, 1-amino-3-nitro-1,2,4-triazol, and the two nitrotriprismanes are oxygen deficient energetic materials. We have not yet found a good way to incorporate these materials into existing propellant formulations for a quick performance comparison. For now, an aluminized/HTPB system is chosen as a base propellant. The propellant has the following formulation: HTPB (8.25 %), DDI (1.25 %), aluminum (20 %), AP (58 %), and HMX (12 %). Again, this generic formulation is used for comparison only and is not optimized. Diazidoborane and 1-amino-3-nitro-1,2,4-triazol are used to replace HMX in the base formula. The percentages of aluminum and AP are adjusted to maximize the calculated performance. Table 5 lists the calculated results. We believe that improvement in performance can be realized upon finding a suitable propellant.

## References

1. G. F. Adams, R. W. Shaw, Jr., *Annu. Rev. Phys. Chem.* **43**, 311 (1992).
2. *Chemistry and Physics of Energetic Materials*, Ed. S. N. Bulusu, Kluwer: London, (1990).
3. R. J. Schmitt, J. C. Bottero: Private Communication.
4. R. J. Schmitt, M. Krempp, V. M. Bierbaum, *Int. J., Mass Spectrom.* **117**, 621 (1992).
5. H. H. Michels and J. A. Montgomery, Jr., *J. Phys. Chem.*, **97**, 6602 (1993).
6. D. J. Benard, B. K. Winkler, T. A. Seder and R. H. Cohn, *J. Phys. Chem.* **93**, 4790 (1989).
7. D. J. Benard, M. A. Chowdhury, B. K. Winkler, T. A. Seder and H. H. Michels, *J. Phys. Chem.* **94**, 7507 (1990).
8. L. V. Cherednichenko, B. A. Ledebev and B. V. Gidasov, *Zh. Org. Khim.* **14**, 735 (1978).
9. P. Saxe and H. F. Schaefer III, *J. Am. Chem. Soc.* **105**, 1760 (1983).
10. R. Engelke, *J. Phys. Chem.* **93**, 5722 (1989).
11. M. T. Nguyen, *J. Phys. Chem.* **94**, 6923 (1990).



12. W. J. Lauderdale, J. F. Stanton and R. J. Bartlett, *J. Phys. Chem.* **96**, 1173 (1992).
13. a) A. Haas, *Chemiker Zeitung*, **106**, 239 (1982). b) A. Hass, *Adv. Inorg. Chem. Radiochem.*, **28**, 167 (1984).
14. F. A. Cotton and G. Wilkinson in "Advanced Inorganic Chemistry", Third Ed., Interscience Publishers, John Wiley & Sons, NY, 1972, pg. 113.
15. A. Vogler, R. E. Wright and H. Kunkley, *Angew. Chem. Int. Ed. Engl.* **19**, 717 (1980).
16. K. F. Ferris, R. J. Bartlett, *J. Am. Chem. Soc.* **114**, 8302 (1992), b) W. J. Lauderdale, J. F. Stanton and R. J. Bartlett, *J. Phys. Chem.* **96**, 1173 (1992).
17. K. Hiraoka, and G. J. Nakajima, *J. Chem. Phys.* **88**, 7709 (1989).
18. K. Norwood, G. Luo, C. Y. Ng, *J. Chem. Phys.* **91**, 849 (1989).
19. L. B. Knight, K. D. Johannessen, C. B. Cobranchi, E. A. Earl, D. Feller and E. R. Davidson, *J. Chem. Phys.* **87**, 885 (1987).
20. G. P. Smith and L. C. Lee, *J. Chem. Phys.* **69**, 5393 (1978).
21. W. E. Thompson and M. E. Jacox, *J. Chem. Phys.* **93**, 3856 (1990).
22. a) M. T. Nguyen, M. T., *J. Phys. Chem.* **94**, 6923 (1990), b) M. T. Nguyen, M. Sana, G. Leroy, J. Elguero, *Can. J. Chem.* **61**, 1435 (1983), c) M. T. Nguyen, M. A. McGinn, A. F. Hegarty, J. Elguero, *Polyhedron, Part A*, 1721 (1985).
23. a) R. Engelke, *J. Phys. Chem.* **96**, 10789 (1992), b) R. Engelke, *J. Phys. Chem.* **93**, 5722 (1989), c) R. Engelke, J. R. Stine, *J. Phys. Chem.* **94**, 5689 (1990), d) R. Engelke, *J. Org. Chem.* **57**, 4841, 1992.
24. M. N. Glukhovtsev, P. von Rague Schleyer, *Chem. Phys. Lett.* **198**, 547 (1992).
25. Cano, J. A. Gorini, J. Farras, M. Feliz, S. Olivella, A. Sole and J. Villarasa, *J. Chem. Soc., Chem. Commun.* 959 (1986).
26. a) I. Alkorta, J. Elguero, I. Rozas and A. T. Balaban, *J. Mol. Struct.* **228**, 47 (1991).
27. A. A. Bliznyuk, M. Shen and H. F. Schaefer III, *Chem. Phys. Lett.* **198**, 249 (1992).
28. C. Chen, L.-H Lu and Y.-W. Yang, *J. Mol. Struct.* **253**, 1 (1992).
29. Gaussian 92. M. J. Frisch, G. W. Trucks, M. Head-Gordon, P. M. W. Gill, M. W. Wong, J. B. Foresman, B. G. Johnson, H. B. Schlegel, M. A. Robb, E. S. Replogle, R. Gomperts, J. L. Andrews, K. Raghavachari, J. S. Binkley, C. Gonzales, R. L. Martin, J. Fox, D. J. DeFress, J. Baker, J.J. P. Stewart and J. A. Pople, Gaussian Inc., Pittsburg, PA (1992).
30. a) R. G. Parr and W. Yang, "Density Functional Theory of Atoms and Molecules", Oxford University Press, New York, 1989; b) D. R. Salahub in "Ab Initio Methods in Quantum Chemistry-II, ed. Lawley, K. P., J. Wiley & Sons, New York, 1987, p. 447, c) E. Wimmer, A. J. Freeman, C.-L. Fu, P.-L. Cao, S.-H. Chou, and B. Delley in "Supercomputer Research in Chemistry and Chemical Engineering" K. F. Jensen, D. G. Truhlar, Eds: ACS Symposium Series, American Chemical Society, Washington, D. C. p.49, 1987, d) R. O. Jones and O. Gunnarsson, *Rev. Mod. Phys.* **61**, 689 (1989), e) T. Zeigler, *Chem. Rev.* **91**, 651 (1991).

31. a) J. Andzelm, E. Wimmer, D. R. Salahub in "The Challenge of d and f Electrons: Theory and Computation", Eds. D.R. Salahub and M. C. Zerner in ACS Symposium Series, No. 394, American Chemical Society, Washington, D. C., 1989, b) J. Andzelm in "Density Functional Methods in Chemistry", Ed. J. Labanowski and J. Andzelm, Springer-Verlag: New York, 1991, p. 101, c) J. W. Andzelm and E. Wimmer, J. Chem. Phys. **96**, 1280 (1992). DGauss is a local density functional program available via the Cray Unichem Project.
32. J. A. Montgomery, Jr. and H. H. Michels, J. Phys Chem. **97**, 6774 (1993).
33. E. Wiber and H. Michaud, Z. Naturf. **9B**, 497 (1954).
34. H. H. Cady, "Estimation of the Density of Organic Explosives from their Structural Formulas", LA-7760-MS, University of California, Los Alamos Scientific Lab., Los Alamos, New Mexico (1979).

HEDM8revpaper.5/94

Table 1. Reactions Used to Calculate Heats of Formation of Azidamines.

Reaction	$\Delta H_f$ , kJ/mol
2 $\text{NH}_3 + 2\text{HN}_3 \rightarrow \text{HN}(\text{N}_3)_2 + 2\text{H}_2$	296.2
3 $\text{NH}_3 + 3\text{HN}_3 \rightarrow \text{N}(\text{N}_3)_3 + 3\text{H}_2$	443.5
4 $[\text{NH}_2]^- + 2\text{HN}_3 \rightarrow [\text{N}(\text{N}_3)_2]^- + 2\text{H}_2$	- 4.5
5 $[\text{NH}_4]^+ + 4\text{HN}_3 \rightarrow [\text{N}(\text{N}_3)_4]^+ + 4\text{H}_2$	746.0
6 $\text{HN}_3 + \text{NH}_3 \rightarrow \text{H}_2 + \text{H}_2\text{N}(\text{N}_3)$	158.5
7 $\text{H}_2\text{NN}_3 + \text{HN}_3 \rightarrow \text{H}_2 + \text{HN}(\text{N}_3)_2$	137.6
8 $\text{HN}(\text{N}_3)_2 + \text{HN}_3 \rightarrow \text{H}_2 + \text{N}(\text{N}_3)_3$	147.3
9 $\text{NH}_3 + \text{H}^+ \rightarrow [\text{NH}_4]^+$	- 856.2
10 $[\text{N}(\text{N}_3)_2]^- + \text{H}^+ \rightarrow \text{HN}(\text{N}_3)_2$	- 1425.9
11 $\text{HN}(\text{N}_3)_2 + \text{H}^+ \rightarrow [\text{N}(\text{N}_3)\text{H}_2]^+$	- 771.7
12 $2 [\text{N}(\text{N}_3)_2\text{H}_2]^+ \rightarrow [\text{NH}_4]^+ + [\text{N}(\text{N}_3)_4]^+$	- 60.2
13 $[\text{NH}_2]^- + \text{H}^+ \rightarrow \text{NH}_3$	- 1726.5
14 $\text{NH}_3 + 2\text{HN}_3 \rightarrow [\text{N}(\text{N}_3)_2]^- + \text{H}^+ + 2\text{H}_2$	1721.7

Table 2. Experimental and Calculated Heats of Formation (298 K) in kJ/mol

<u>Molecule</u>	<u><math>\Delta H_f^\circ</math></u>	
H <sub>2</sub>	0.0 (expt)	
NH <sub>3</sub>	-45.9 (expt)	
[NH <sub>2</sub> ] <sup>-</sup>	113±4 (expt)	
[NH <sub>4</sub> ] <sup>+</sup>	630 (expt)	
[H] <sup>+</sup>	1530.0 (expt)	
HN <sub>3</sub>	294.1 (expt)	
HN(N <sub>3</sub> ) <sub>2</sub>	825.4(MO/R2)	838.4(DFT/R2)
N(N <sub>3</sub> ) <sub>3</sub>	1247.8(MO/R3)	1279.9(DFT/R3)
[N(N <sub>3</sub> ) <sub>2</sub> ] <sup>-</sup>	660.6(MO/R4)	751.5(MO+/R4)
	791.6(MO/R14)	744.3(MO+/R14)
[N(N <sub>3</sub> ) <sub>4</sub> ] <sup>+</sup>	2453.8(MO/R5)	2552.4(DFT/R5)
H <sub>2</sub> NN <sub>3</sub>	406.7(DFT/R6)	
[H <sub>2</sub> N(N <sub>3</sub> ) <sub>2</sub> ] <sup>+</sup>	1596.8(DFT/R11)	
		734.3(DFT/R10)
		734.0(DFT/R14)
		2503.4(DFT/R12)
		696.7(DFT/R4)

( /Rn) = reaction number from Table 1.

Table 3. Calculated Energies (hartrees) and Thermochemistry (kcal/mol).

DAB

Level of Theory	E	$\Delta H_f$
RHF/6-31G*	-351.86757	117.6
MP2/6-31G**/RHF/6-31G*	-352.92725	106.2
MP2/6-31+G**/RHF/6-31G*	-352.94539	108.3

HNBN<sub>3</sub>

Level of Theory	E	$\Delta H_f$
RHF/6-31G*	-243.01229	40.4
MP2/6-31G**/RHF/6-31G*	-243.73651	60.0
MP2/6-31+G**/RHF/6-31G*	-243.75290	56.9

Table 4. Thermochemistry of Advanced Propellants

<u>Compound</u>	<u>Formula</u>	<u>Mol. Wt.</u>	<u>Density gm/cm<sup>3</sup></u>	<u><math>\Delta H_f(25^\circ\text{C})</math> kcal/mol</u>
Triprismane	$\text{C}_6\text{H}_6$	78.12	1.29	+134.7
Nitrotriprismane	$\text{C}_6\text{H}_5\text{NO}_2$	123.11	1.55	+125.3
Dinitrotriprismane	$\text{C}_6\text{H}_4(\text{NO}_2)_2$	168.11	1.71	+121.5
Tetranitrohydrazine	$\text{N}_2(\text{NO}_2)_4$	212.04	2.17	+140.0
Trinitramine	$\text{N}(\text{NO}_2)_3$	152.02	2.15	+90.0
Diazidamine	$\text{HN}(\text{N}_3)_2$	99.06	1.56	+199.0
Triazidamine	$\text{N}(\text{N}_3)_3$	140.07	1.58	+302.0
Diazidoborane	$\text{HB}(\text{N}_3)_2$	95.86	1.52	+108.0
Imidoazidoborane	$\text{HNBN}_3$	67.85	1.34	+56.0
Nitrosylazide	$\text{NON}_3$	72.03	1.54	+105.0
Nitrylazide	$\text{NO}_2\text{N}_3$	88.03	1.76	+90.0
3-nitro-1,2,4-triazol-5-one (NTO)	$\text{C}_2\text{H}_2\text{N}_4\text{O}_3$	130.06	1.75	-3.2
1-amino-3-nitro-1,2,4-triazol	$\text{C}_2\text{H}_3\text{N}_5\text{O}_2$	129.08	1.61	+55.6

Density is calculated by the method of Cady.<sup>34</sup>

Table 5. Theoretical Performance Characteristics ( $I_{sp}$ ) of Advanced Propellants

Oxidizers

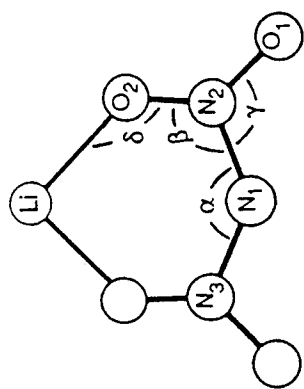
Oxidizer	$I_{sp}$ , sec	$I_{sp}$ (vac)	$I_{sp}$ *density	$I_{sp}$ (vac)*density	Density	% Oxidizer
AP	255	277	16.2	17.5	1.75	78
-----						
ADN	265	287	16.2	17.6	1.69	83
$N_2(NO_2)_4$	293	320	18.6	20.3	1.75	62
$N(NO_2)_3$	293	319	18.2	19.9	1.71	64
$NON_3$	305	331	16.4	17.8	1.48	81
$NO_2N_3$	294	319	17.1	18.6	1.61	74

Monopropellants

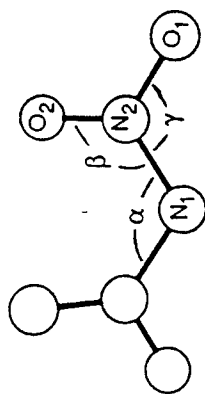
Ingredient	$I_{sp}$ , sec	$I_{sp}$ (vac)	$I_{sp}$ *Density	$I_{sp}$ (vac)*density	Density
HMX	243	261	14.7	15.8	1.67
TAA	296	318	16.2	17.4	1.51

Oxygen Deficient Energetic Materials

Ingredient	$I_{sp}$ , sec	$I_{sp}$ (vac)	$I_{sp}$ *Density	$I_{sp}$ (vac)*density	Density
HMX	266	291	17.7	19.3	1.84
ANT	265	291	17.2	18.9	1.79
DAB	266	291	17.0	18.7	1.76



(b)  $1A - C_2$  structure  
(lithium salt)



(a)  $1A - C_2$  structure  
(anion)

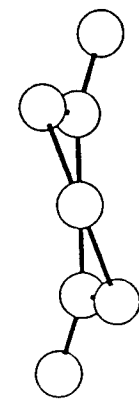


Fig. 1  $N(NO_2)^-$  and  $LiN(NO_2)_2$  are shown in (a) and (b), respectively.



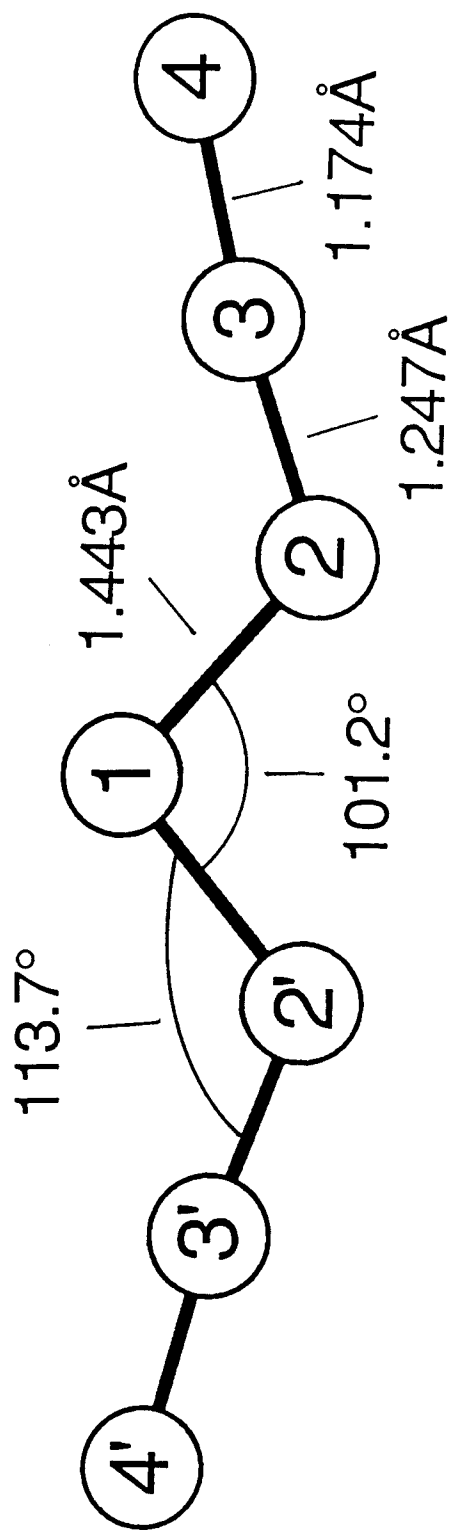


Fig. 2 Geometry of  $\text{N}(\text{N}_3)_2^-$  at the MP2/6-31G\* Level of Theory

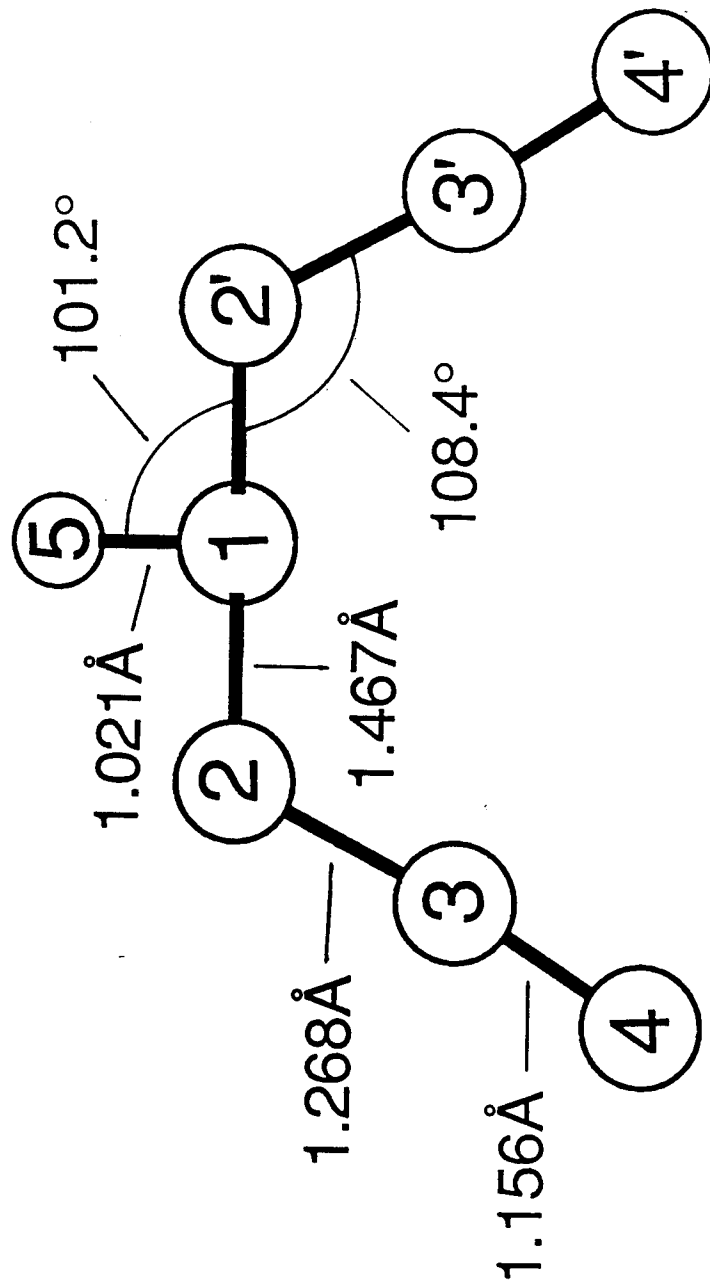


Fig. 3 Geometry of HN(N<sub>3</sub>)<sub>2</sub> (C<sub>2</sub> symmetry) at the MP2/6-31G\* Level of Theory

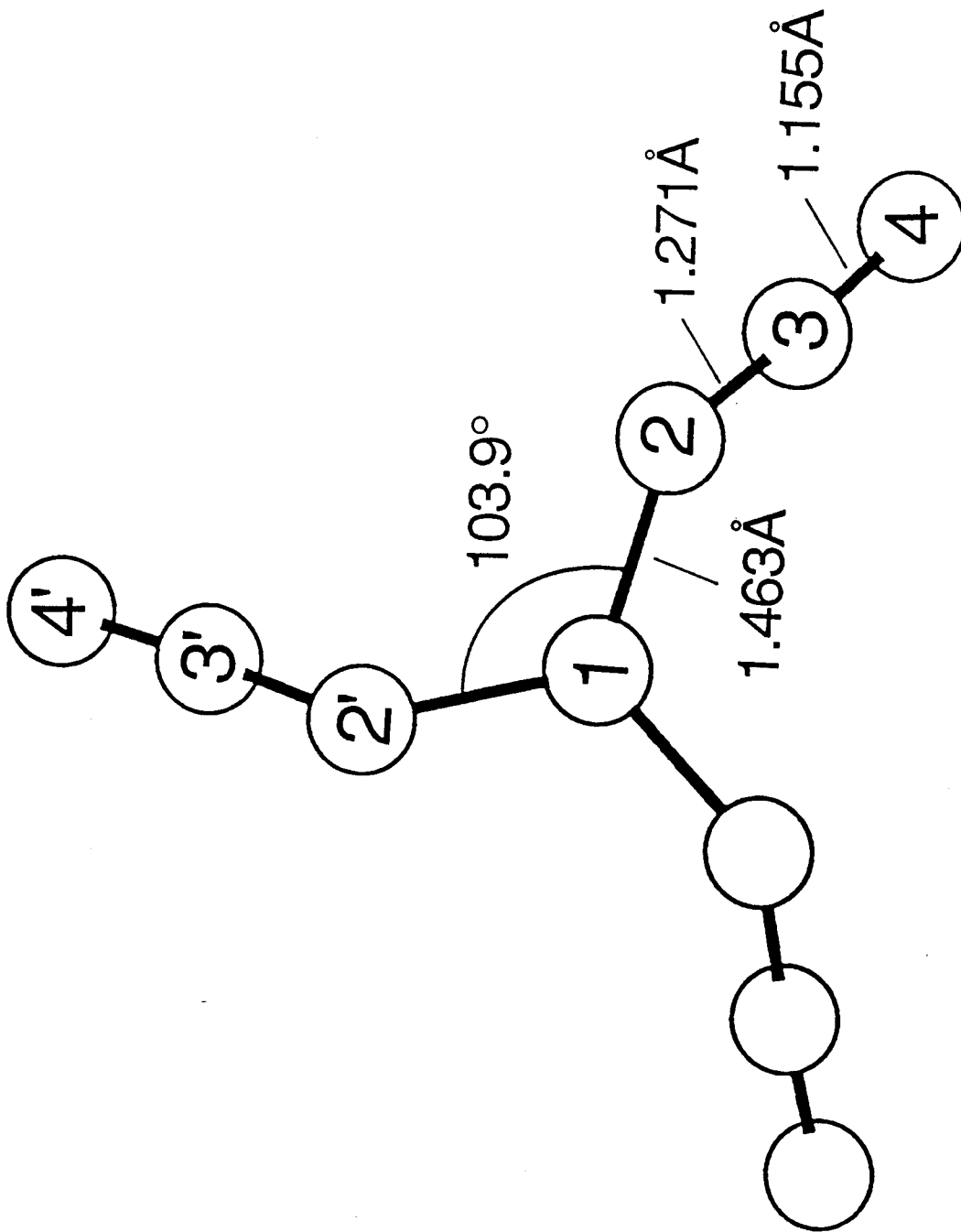


Fig. 4 Geometry of  $N(N_3)_3$  at the MP2/6-31G\* Level of Theory

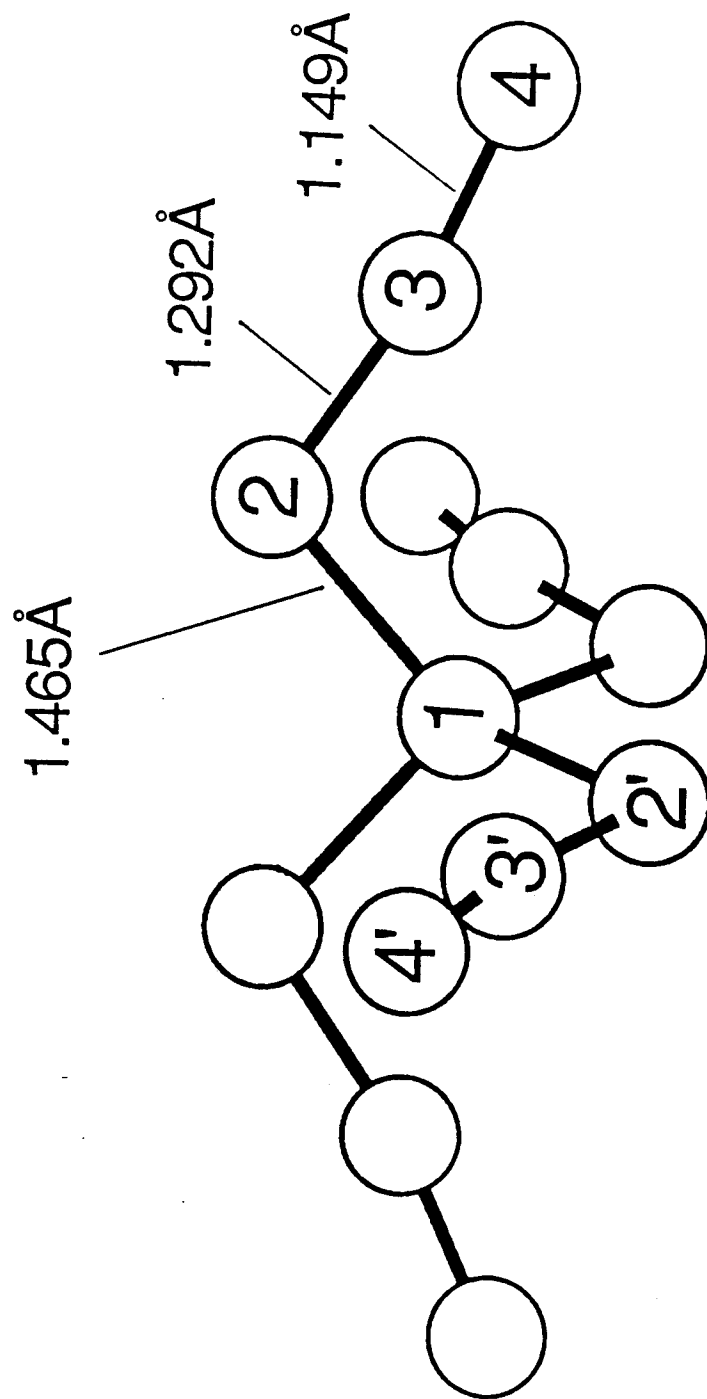


Fig. 5 Geometry of  $N(N_3)_4^+$  at the MP2/6-31G\* Level of Theory

# A Survey of Rocket Propulsion Systems

E. J. Wucherer, Hughes STX  
OLAC PL/RKF  
Edwards AFB, CA 93524-7680

This presentation briefly discusses some aspects of current rocket propulsion technology. It is intended as an overview to help chemists, chemical physicists and physicists understand current technology and see where their research, experience and expertise may find application in rocket propulsion.

Conceptually there are five topics to consider: Liquid Bipropellant Systems, Solid Propellant Systems, Hybrid Propulsion Systems, Monopropellant and Electric Propulsion Systems, and the Relevant Physics and Thermodynamics. The latter topic is the basic science which is common to the previous four, we will begin the discussion here.

Thrust (F) is the force exerted by a rockets liquid engines or solid motors. Specific Impulse (Isp) is the thrust divided by the propellant weight flow rate. Conceptually, thrust is like the horse power rating of an automobile - higher thrust gets you out of the gate and moving more quickly. Isp is a measure of efficiency, more like the mpg rating of your auto - for the long haul to a far away place you need efficiency. Often the product (propellant density)\*(Isp) is considered as a measure of the thrust produced per volume of propellant. Denser propellant results in smaller propellant tanks and hence a less inert mass for the vehicle.

Thrust or force is the time rate of change of momentum. In the case of rocket propulsion this is best written as the rate of change of mass (propellant flow) times the propellant velocity. Practically, the propellant gas exit velocity is limited by the combustion temperatures that can be contained so high thrust is often obtained by having high mass flow. High thrust is crucial for a launch vehicle, since insufficient thrust will result in a negative vehicle acceleration.

## Momentum Thrust

$$F = \frac{dP}{dt} = m \frac{dv}{dt} + v \frac{dm}{dt} = \dot{m}v_n$$

where

$\dot{m}$  = propellant mass flow rate (kg / s)

$v_n$  = propellant gas velocity (m / s)

## Launch

$$a = (F_o / w_o)g_o - g_o$$

$F_o / w_o$  = Initial Thrust to Weight Ratio

Specific Impulse can be related to the enthalpy change which occurs as propellants are burned in the combustion chamber, and using the ideal gas approximations, further related to a complex function of several variables. The strongest influence on this equation are the root dependence on combustion temperature and the

inverse root dependence on mean molar mass of exhaust gas. Chamber pressure and gas heat capacities play a less direct role in Isp. The highest Isp is obtained at the highest combustion temperature with the lowest mean exhaust gas mass.

$$I_{sp} = v_n / g_o = \frac{1}{g_o} \sqrt{2(h_c - h_n) + v_c^2}$$

$$I_{sp} = \frac{1}{g_o} \sqrt{\frac{2\gamma(1 - (p_n / p_c)^{\gamma-1/\gamma})R T_c}{(\gamma - 1) M}}$$

$$\gamma = \frac{C_p}{C_v} \text{ of the exhaust gases}$$

R = gas constant, Tc = chamber temperature

M = mean molar mass of exhaust gas

p<sub>n</sub>, p<sub>c</sub> = pressure in nozzle and chamber

h<sub>n</sub>, h<sub>c</sub> = enthalpy in nozzle and chamber

Chemical rocket motors function by burning propellants in a high pressure combustion chamber and allowing the hot exhaust gases to pass through a constricting throat with supersonic expansion out a nozzle cone. Thermodynamic equilibrium is usually reached in the high temperature, high pressure combustion chamber during the ca. 100ms residence time. Expansion through the throat and nozzle usually results in a non-equilibrium situation as the temperature, pressure and residence time all drop rapidly. The high temperature coupled with chemical and mechanical erosion provide a real challenge to the construction of combustion chambers and throat assemblies.

Liquid bipropellant rocket engines generally have the highest performance and versatility. LOX/Ethanol (V2) had Isp=279s under standard conditions while LOX/LH2 has Isp=390s. Liquid engines are versatile and very complex. Engine systems consist of propellant tanks, pressurizing gases, turbo-pumps, pre-burners to drive the pumps, piping and ducting to circulate propellant around hot engine parts (regenerative cooling of combustion chamber, throat and nozzle), injector, ignitor, combustion chamber, throat and nozzle. These components are subject to high dynamic loads as the vehicle accelerates upwards, thermal shocks as cryogenic propellants are vaporized or combusted, and stresses as pump blades spin at 50k rmp and propellants burn at 2500K. Liquid engines often can be throttled and restarted. A variety of cryogenic (non-storable) and ambient liquid (storable) propellants have been used. The Space Shuttle Main Engine (SSME) uses LOX/LH2 at nearly 3000psi to produce 470Klb of thrust, Isp=455s.

Solid propellant motors are mechanically much simpler than liquid engines and are correspondingly less versatile. Solid propellant is contained in a combination propellant tank/combustion chamber - no pumps, tubes or cooling lines. Solid motors cannot be restarted, throttling is limited and they cannot be tested before use. Materials of construction are designed to function without cooling. Solid propellant performance is generally lower than liquid engines. The strap on boosters for the Space Shuttle operate at 918 psi with Isp=267s. Each of the two boosters produce 2.65Mlb of thrust however, more than twice as much as the three SSME's combined.

While mechanically much simpler than liquid engines, the solid propellant grain is chemically very complex. Often ten ingredients must be mixed in precise quantities

then cured under controlled conditions to produce the rubbery, tough uniform grain of a solid propellant. Typically, a solid oxidizer such as ammonium perchlorate (60%) is mixed with a solid fuel such as aluminum (20%) in a binder such as hydroxy terminated polybutadiene (HTPB, 15%). Curing agents, cure catalyst, burn rate catalyst, plasticizer, and stabilizers account for the last 5% of ingredients.

Hybrid engine systems represent a blend of liquid and solid technologies. Solid rubbery fuel grain is burned when a liquid oxidizer is pumped into the combustion chamber/fuel tank. Hybrid systems can be throttled and restarted. They have less pump and pipe hardware than a liquid system. One major drawback is efficient combustion as the liquid or gaseous oxidizer must mix with the solid fuel grain. Microscopically this is a complex series of steps as heat is transferred to the fuel grain which partially decomposes to vaporize and mix with oxidant, combust, and produce heat to vaporize more fuel and produce propellant gases. Hybrid systems have a hard time producing the thrust levels and burn rates of solids.

Other chemical propulsion systems can be gathered into a family of liquid monopropellant and electric propulsion systems. These small systems are typically used for orbital transfer, station keeping, and maneuvering. Hydrazine and hydrogen peroxide are common monopropellants which have Isp's around 230s. A high pressure He gas bottle is used to drive the monopropellant over a catalyst bed which causes the propellant to decompose. Satellite systems often perform thousands of restarts to nudge the vehicle gently back to the correct orbit. Monopropellant engines have been augmented with ohmic or electric arc heating to form resisto-jets and arc-jets with Isp's of up to 300s and 1500s resp. While these latter systems have very good Isp's, they also have very complex and heavy electric power generation, storage and delivery systems, so the Isp comparison is not a good overall barometer of system desirability.

A satellite launch mission illustrates the use of some of these propulsion systems. Delta II rockets are used to launch satellites from Vandenberg AFB. At ignition the first stage LOX/RP1 (kerosene) liquid main engine and six solid boosters fire to push the vehicle up and away from the earth. After about 60s the first six solid motors burn out and three more are ignited, these also burn out about 60s later. The main liquid engine continues to burn for a further two minutes. During these first sequences the vehicle trajectory is basically straight up, away from the earth and away from all the atmospheric drag. Four minutes into the flight the first stage engine and solid boosters are spent and jettisoned. The Delta II second stage liquid engine (hydrazine/nitrogen tetroxide) kicks in to provide the payload with the velocity needed for orbit. The hydrazine/NTO engine is hypergolic - the propellants ignite upon mixing. Often the second stage firing will be interrupted to allow the vehicle to coast to adjust the orbit. After an appropriate coast the 2nd stage engine is readily restarted to continue to gain the necessary vehicle velocity. When the second stage is expended and jettisoned, the remaining vehicle may make several coasting orbits until the correct positioning is acquired for the final satellite injection. The third stage - for Delta often a solid motor - then fires to place the payload into the correct orbit. Once on station, a satellite will use small hydrazine monopropellant thrusters to maintain position or adjust orientation for transmitting data.

I hope that this report provides you with some sense of the present state of rocket propulsion to assist you in pushing new concepts in propulsion toward application. The material presented here is largely abstracted from two sources: "Rocket Propulsion Elements" Sixth Edition, G. P. Sutton, John Wiley & Sons Inc, New York, 1992, ISBN 0-471-52938-9; and "The Performance of Chemical Propellants", Glassman and Sawyer. Technivision Services, Slough England, 1970, ISBN 85102-018-6.

*Poster Presentations*



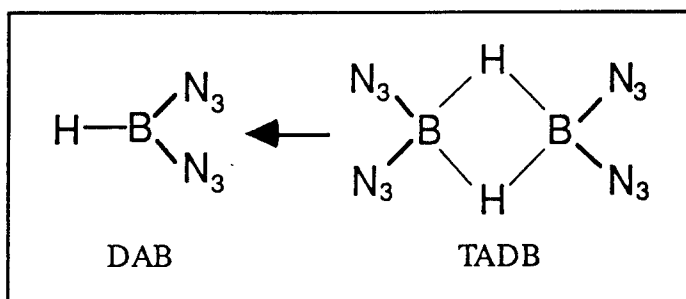
# Production and Decay of Diazidoborane (DAB) and Tetra-Azidodiborane (TADB)

E. Boehmer  
Rockwell International Science Center  
P.O. Box 1085 - Mail Stop: A9  
Thousand Oaks, CA 91358  
805/373-4139

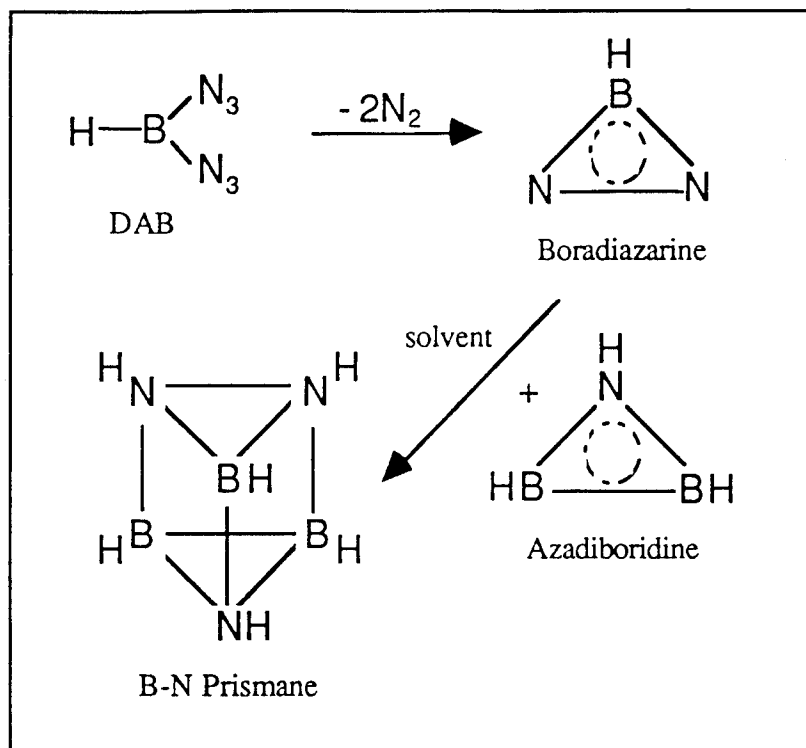
## Extended Abstract

New synthetic pathways to strained ring and cage structures are a main target in the search for new rocket fuels and rocket fuel additives. Ideal HEDM's of this type are characterized by a compact structure, large positive heat of formation, amenability to large scale synthesis, compatibility with existing fuels and a large specific impulse boost. In this context, ring and cage structures containing boron and nitrogen such as B-N prismane and three membered BBN and BNN rings, which function as its precursors, are especially promising.

B-N prismane has been investigated theoretically and is predicted to be stable, however, its synthesis remains an experimental challenge. As precursors for B-N prismane, the BBN ring and BNN ring derivatives have been identified, but only the BBN structure can be routinely and easily obtained. In addition, state-of-the-art synthetic routes to hetero rings generally involve the use of ring precursors, which are protected by large organic groups. Unfortunately these groups add unwanted bulk and weight and can hinder cage closures needed, for example, in the formation of B-N prismane. At Rockwell Science Center, a unique new synthetic concept was recently discovered based on the compounds diazidoborane (DAB) and tetra-azidodiborane (TADB). These compounds are potential precursors for a



BNN ring structure, boradiazirine, without the involvement of large organic protection groups. Boradiazirine is a potential precursor in the synthesis of B-N prismane.



Two macroscopic approaches exist for the preparation of DAB and TADB. The first method is the fluid phase synthesis performed by Wiberg and Michaud (1954), who codeposited  $B_2H_6$  and  $HN_3$  in form of an etheric slush at  $-60\text{ }^\circ\text{C}$ . When slowly defrosting the slush these authors observed a lively hydrogen production starting between  $-20\text{ }^\circ\text{C}$  and  $-10\text{ }^\circ\text{C}$ . They were able to link the total amount of hydrogen released by the reaction with the production of azides such as  $B(N_3)_3$ ,  $HB(N_3)_2$  and  $H_2BN_3$ . The isolation of the products was difficult due to strong solvent-azide interactions, and only successful for  $B(N_3)_3$ . Based on the observations made by Wiberg and Michaud, the gas phase reaction between  $HN_3$  and  $B_2H_6$  was investigated at Science Center as a possible way to generate suitable azide precursors of the BH radical. For these studies  $HN_3$  and  $B_2H_6$  were diluted in noble gas and reacted in a capillary metal oven at temperatures of  $\sim 400\text{ }^\circ\text{C}$  and pressures of  $\sim 500\text{ Torr}$ . Depending on the reaction time (0.01 - 0.1 s) DAB, TADB, polymers and other products were obtained. Characterization of the products (DAB and TADB) was

achieved by comparing experimental FT-IR spectra to calculated IR frequencies obtained from Dr. Michels at United Technologies Research Center.

To optimize the existing synthetic procedures for production of DAB and TADB, and especially to tailor synthetic pathways to boradiazirine and B-N prismane, it is desirable to selectively study the influence of experimental parameters, such as interactions with the solvent, reactant activation by heat or radiation, and catalysis by metal walls. These goals can be achieved by working in an organic glass environment, where the diluent may consist of differing Lewis bases to evaluate the effect of solvent base strength on reaction initiation and product stabilization. Radiation and heat effects can be studied independently of solvent effects by use of a noble gas matrix. In these experiments, changes in the products are investigated as a function of annealing the matrix and optical pumping by selected IR lasers that are tuned to specific reactant vibrational transitions. The goal of these future investigations is to identify reaction conditions which lead selectively to DAB, TADB, boradiazirine and finally to energetic cage structures such as B-N prismane.

This work was supported by the Innovative Science and Technology Office of the Ballistic Missile Defense Organization, which provided funding through the Air Force Office of Scientific Research, Contract No. F49620-90-C-0025, and by the High Energy Density Materials Office of the Air Force Phillips Laboratory, Contract No. F04611-90-C-0009.

# CHARACTERIZATION OF QUADRICYCLANE

Dr. E.J. Wucherer and Angelica C. Wilson -Hughes STX; Phillips Laboratory, Edwards  
AFB, CA

The composition of commercially available quadricyclane was determined using a standard gas chromatograph analysis. A Hewlett Packard 5890 G.C. with a flame ionization detector was used to analyze quadricyclane samples versus prepared impurity standards. Quadricyclane samples were found to be at least 99% pure with major impurities of 0.6% Norbornadiene and 0.2% Toluene. Test methods and equipment have been identified to fully characterize the quadricyclane compound.

**INTRODUCTION:** Theoretical predictions have identified the hydrocarbon quadricyclane as a possible replacement for, or additive to, current rocket propellants. Quadricyclane offers the advantages of increased performance and environmentally friendly characteristics compared to current rocket fuels. Under the High Energy Density Matter (HEDM) program at Phillips Laboratory, experimental research is being conducted to fully characterize the quadricyclane compound. Initial work has focused on determining the composition, including impurities, of commercially available samples. Test methods and necessary equipment have been identified for the full characterization of quadricyclane. Phillips Laboratory will perform small-scale research testing to determine key physical parameters such as thermal conductivity, density, specific heat, and vapor pressure. NASA White Sands will conduct hazards tests and Armstrong Laboratory will carry out toxicity tests on quadricyclane. After characterization, the program will transition to testing of quadricyclane in the Atlas Vernier rocket engine. Potential applications for quadricyclane may then be determined based on the characterization effort and subsequent testing.

**OBJECTIVE:** Conduct experimental research to fully characterize Quadricyclane propellant compound for possible replacement of and/or mixture with current propellant combinations.

**APPROACH:**

- Small scale Research Testing at Phillips Laboratory to determine key physical properties.
- Hazards Testing at NASA White Sands
- Toxicity Testing at Armstrong Laboratory
- Transition to testing on Atlas Vernier Rocket
- Look for potential applications

## PHYSICAL PROPERTIES

**DENSITY:** High density is desirable to accommodate a smaller vehicle tank size in a given required weight of propellants. Also used in propellant loading and mixture ratio calculations.

**FREEZING POINT:** Low freezing point permits operation of rockets in cold weather.

**BOILING POINT:** High boiling point desirable for propellants that are used for thrust chamber cooling, also able to operate in vehicles where propellant temperature rises due to aerodynamic heating during flight.

**VAPOR PRESSURE:** Low vapor pressure permits easier handling of propellants, lighter tank weights for storable propellants, and a more effective pump design (reduced cavitation).

**VISCOSITY:** Used in propellant flow and pump calculation. If viscosity is too high, pumping and flow through the injection system may become difficult.

**THERMAL CONDUCTIVITY:** High values are desired for propellants that are used for thrust chamber cooling. Enables heat of combustion products to be carried away from the thrust chamber walls.

**SPECIFIC HEAT:** Used in engine power balance calculations .

**FLASHPOINT:** High flashpoint desirable for safety and handling considerations.

**HEAT OF FORMATION:** Want a high energy release in the combustion process of the propellant combinations.

**HEAT OF VAPORIZATION:** Needed for injector design and engine power balance calculations.

**REFRACTIVE INDEX:** Used for quality and purity checks of samples.

**MOLECULAR WEIGHT AND FORMULA:** A low molecular mass of the product gases of the propellant combination is desired. This can be accomplished by using fuels rich in hydrogen.

## **HAZARDS TESTS- NASA WHITE SANDS**

**IMPACT:** 2.5 Kg mass dropped onto sample from various heights to determine if this mechanical impact will cause the propellant to react.

**ADIABATIC COMPRESSION:** Propellant in tube is rapidly pressurized to stimulate "slamming" against a closed valve to determine if this will cause the propellant to react.

**CRITICAL DIAMETER:** Determine the critical diameter of material that will propagate detonation.

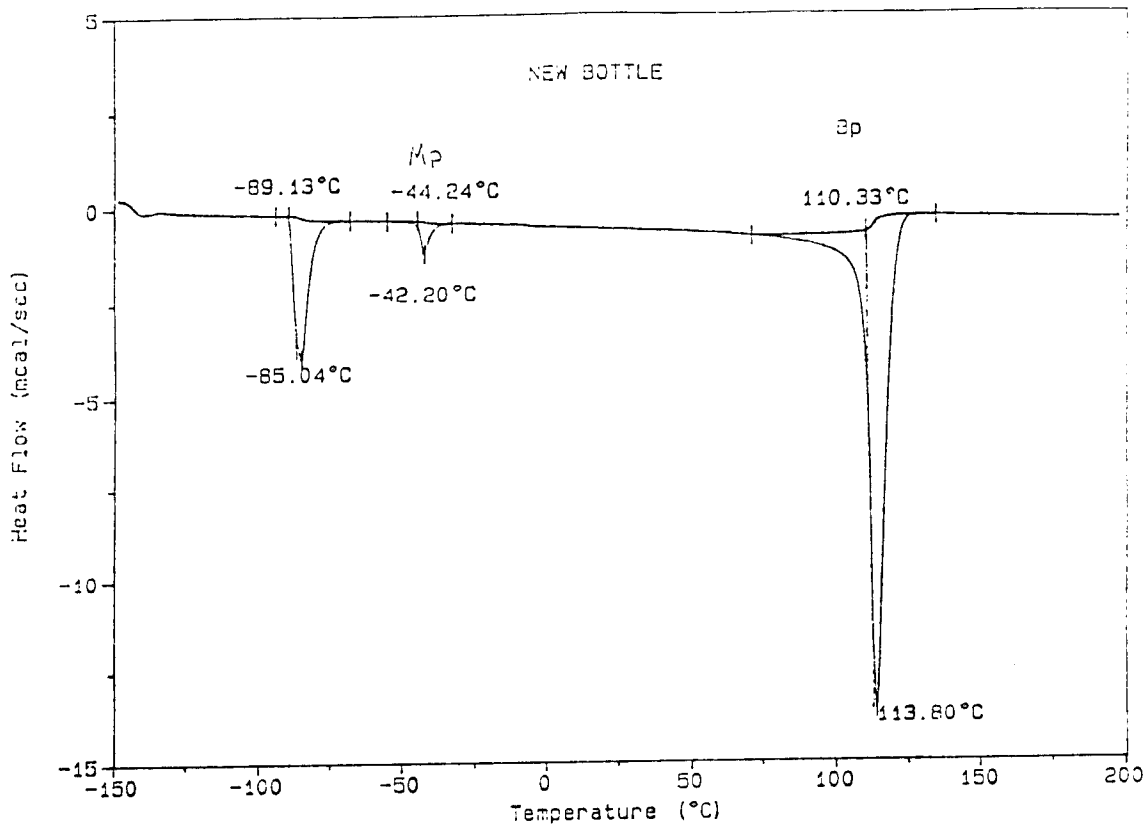
## KNOWN PHYSICAL CHARACTERISTICS OF QUADRICYCLANE

Formula weight:	92.14 g
Density:	0.9937 g/ml at 10°C <sup>3</sup> 0.9887 g/ml at 15°C <sup>3</sup> 0.9835 g/ml at 20°C <sup>3</sup> 0.9787 g/ml at 25°C <sup>3</sup>
Viscosity:	10°C 1.2212 centistokes <sup>3</sup> 20°C 1.0614 centistokes <sup>3</sup> 30°C 0.9372 centistokes <sup>3</sup> 50°C 0.7465 centistokes <sup>3</sup> 60°C 0.6745 centistokes <sup>3</sup> 70°C 0.6177 centistokes <sup>3</sup> 80°C 0.5715 centistokes <sup>3</sup>
Boiling point:	108 C/740 mmhg <sup>1,3,4</sup>
Flashpoint:	52 °F, 11 °C <sup>1</sup>
Heat capacity:	1.664 J/g °C <sup>3</sup>
Melting point:	-44.38 °C <sup>3</sup>
Index of refraction:	1.4850 <sup>1</sup>
Heat of formation:	302.1 kJ/mol <sup>5</sup>
Heat of vaporization:	37.0 kJ/mol <sup>5</sup>
Major Impurities:	Norbornadiene 0.6 % <sup>3</sup> Toluene 0.2 % <sup>3</sup>
Thermal Conductivity:	-40°C 0.0003969 cal/(sec <sup>2</sup> ) (cm) (°C/cm) <sup>2</sup> -10°C 0.0003787 cal/(sec <sup>2</sup> ) (cm) (°C/cm) <sup>2</sup> 20°C 0.0003515 cal/(sec <sup>2</sup> ) (cm) (°C/cm) <sup>2</sup> 50°C 0.0003250 cal/(sec <sup>2</sup> ) (cm) (°C/cm) <sup>2</sup> 80°C 0.0003121 cal/(sec <sup>2</sup> ) (cm) (°C/cm) <sup>2</sup> 100°C 0.0002844 cal/(sec <sup>2</sup> ) (cm) (°C/cm) <sup>2</sup>

1. Aldrich Chemical Company, Inc., (1990) 1125
2. Institute for Research, Inc. 1994
3. Phillips Laboratory, Chemistry Research Lab, 1994
4. Smith, C. D., *Organic Synthesis*, **51**, 133-136
5. Steele, V. W., *J. Chem. Thermodynamics*, (1978) **10**, 919-927

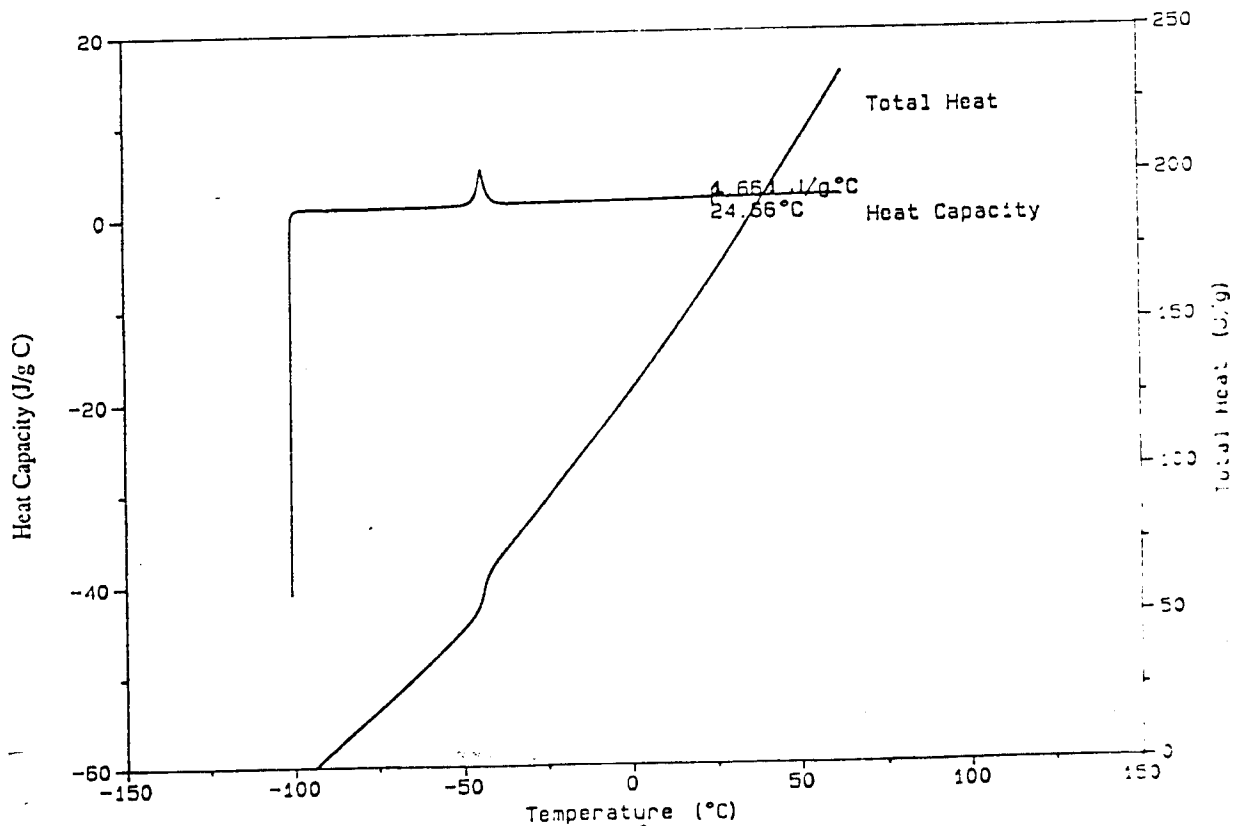
# DIFFERENTIAL SCANNING CALORIMETER

Boiling and melting point-rate 10°C/min, GN2 50 ml/min, ind. Al pans, sample size 7.12 mg



# DIFFERENTIAL SCANNING CALORIMETER

Heat Capacity-rate 10°C/min, GN2 atm, hermetic Al pans, ref pan wt. 57.20 mg, sample size 3.44 mg



## Thermoluminescence Studies of Atomic Nitrogen in Cryogenic Solid Deuterium

T.L. Thompson, M.E. Cordonnier, M.E. Fajardo  
Propulsion Directorate, OL-AC PL/RKFE, Edwards AFB, California

The objective of the US Air Force High Energy Density Matter (HEDM) program is to improve chemical rocket performance. One proposed HEDM concept is the trapping of atomic species in cryogenic solid hydrogen. We have had preliminary successes trapping Li, Al, and B atoms in solid hydrogen matrices.<sup>1</sup> We are examining issues arising from the storage and handling of such HEDM materials. We propose to use luminescence from atomic recombination to measure the decay of the trapped atoms with storage time, and during temperature excursions encountered during handling.

In this experiment model HEDM samples, consisting of nitrogen atoms isolated in solid deuterium, are prepared from a microwave discharged precursor gas co-deposited with a separate flow of deuterium gas onto a liquid helium cooled, 4K sapphire substrate. We present data from thermoluminescence experiments on these samples, and compare our results with previous studies of condensed "activated nitrogen" samples prepared by similar techniques and by in-situ radiolysis.<sup>2</sup>

Figure 1 shows total luminescence from the Vegard-Kaplan bands of nitrogen versus temperature for both nitrogen atoms in solid nitrogen and nitrogen atoms in solid deuterium. As can be seen, the thermoluminescence from the nitrogen atom/solid deuterium matrix is concentrated between 4 - 8K while the thermoluminescence from the nitrogen atom/solid nitrogen matrix is spread across a 25K temperature range.

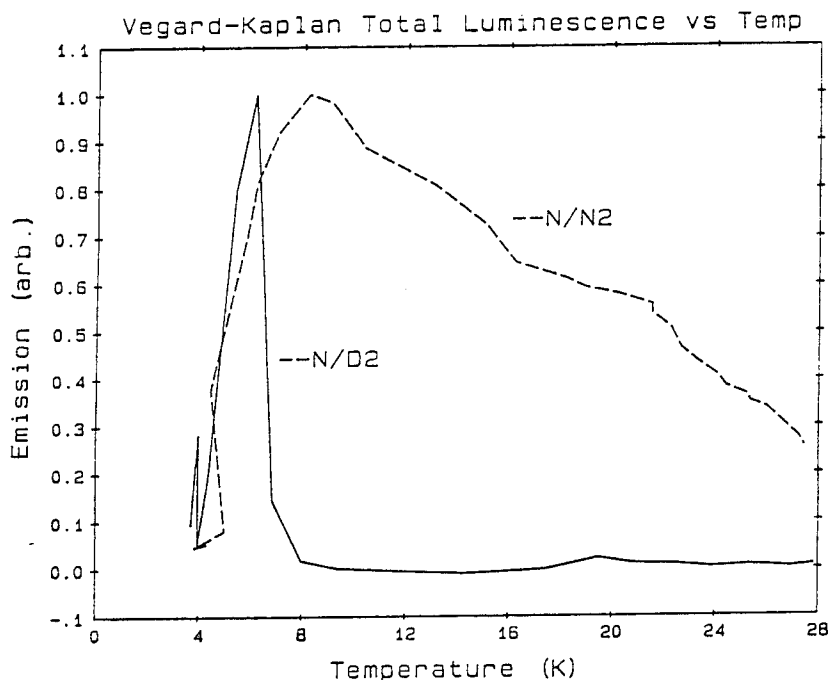
We have shown that ground state nitrogen atoms,  $N(^4S)$ , can be trapped in solid deuterium below temperatures of 5K. Above this temperature, recombination occurs rapidly and is accompanied by atomic and molecular emission. Further, nitrogen atoms in solid deuterium is a valuable analog of a cryogenic high energy material. The nitrogen atoms recombine over a short temperature range (4 - 8K) and their emission can be used as a valid temperature probe. Future work will involve using this tool to scale up and learn to handle cryogenic solids with these high energy additives.

Plans are to use the thermoluminescence from this model HEDM sample as a probe to measure temperature excursions during storage and



transport of a solid hydrogen sample. A gaseous mixture of deuterium and microwave discharged nitrogen will be sprayed onto the surface of a superfluid liquid helium bath. During the transport of the resulting solid from the liquid helium cryostat into a room temperature chamber, we will observe the thermoluminescence to determine when the sample has lost its HEDM additives to recombination. It is planned that results from this effort will be presented at the next HEDM Contractor's Conference.

1. M.E. Fajardo, S. Tam, T.L. Thompson, and M.E. Cordonnier, Chem. Phys., to be published.
2. D.S. Tinti and G.W. Robinson, J. Chem. Phys., **49**, 3229 (1968).



# Collision Dynamics of Small Molecular Hydrogen and Deuterium Clusters with Light Atoms

Zhiming Li<sup>(a)</sup> and R. Benny Gerber<sup>(a)(b)</sup>

(a) Department of Chemistry, University of California, Irvine, CA 92717

(b) Department of Physical Chemistry and the Fritz Haber Center for Molecular Dynamics, the Hebrew University of Jerusalem, Jerusalem 91904, Israel

## Abstract

The dynamics of highly anharmonic, weakly bound quantum clusters of molecular hydrogen and deuterium colliding with light atoms (Li, B) and diatomic molecules ( $H_2$ ,  $D_2$ ) are investigated by an exact time-dependent quantum scattering method. As a simplification, molecular hydrogen and deuterium are constrained to the lowest ( $J=0$ ) rotational level of  $p$ - $H_2$ . The calculations are performed for a collinear model system on the ground electronic state, which reveal an unusually high survival probability of such weakly bound quantum clusters, even at relatively high collision energy (room temperature). Such a high survival probability can be understood by an argument based on the large spread of the ground electronic state vibrational wave function of the quantum molecular clusters. The results of the collinear hydrogen and deuterium trimers colliding with other particles as calculated by a classical path method are also reported.

## 1. Introduction

The recent molecular beam scattering experiments show that  $(H_2)_2$  dimer has a substantially large survival probability when scattered from a crystalline LiF surface, even at collision energy close to the room temperature[1]. The result is somewhat surprising because the binding energy of  $(H_2)_2$  dimer is only a few wave numbers. The present work is thus directed toward understanding the collision dynamics of such weakly bound cluster of hydrogen by studying a model system of  $(H_2)_2$  dimer colliding collinearly with other light particles, such as Lithium and Boron atoms. It has been suggested that light atoms, such as Lithium and Boron atoms could be potential propellant additives in solid hydrogen. A recent experiment shows Lithium atoms have been trapped and stored in cryogenic  $H_2$  for hours [2]. This work also attempt to address the issues of the stability of such atoms in solid hydrogen by studying the survival probability of B-- $H_2$  van der Waals cluster following collision with other light particles. Because of the light masses and weakly bound nature of such species, quantum dynamics approaches are necessary in order to understand the collision process. We organize the paper as follows. In Section 2 we describe the methodology of the exact quantum wave packet approach to study the dimer survival probability after colliding with another particle. In Section 3 the classical path formalism for studying the collision dynamics of a particle with larger cluster, such as  $(H_2)_3$  and  $(D_2)_3$  trimer, is discussed. Section 4 describes the interaction potential functions used in our calculations. The simulation results are given in Section 5 followed by the conclusion in Section 6.

## 2. Methodology of Exact Quantum Dynamics

The exact quantum dynamics study starts from solving the following time-dependent Schrodinger equation:

$$i\hbar \frac{\partial \Psi(q_1, \dots, q_n; t)}{\partial t} = \hat{H} \Psi(q_1, \dots, q_n; t), \quad (1)$$

where

$$\hat{H} = -\sum_{i=1}^n \frac{\hbar^2}{2m_i} \frac{\partial^2}{\partial q_i^2} + V(q_1, \dots, q_n), \quad (2)$$

where  $q_1, \dots, q_n$  are the coordinates of the system and  $m_1, \dots, m_n$  are the masses of each particle in the system.

We formulate the approach by considering a collinear model system of a particle A colliding with a weakly bound anharmonic oscillator BC. Let's denote three particles A, B and C with masses  $m_i$  ( $i=1,2,3$ ), using Jacobi coordinates  $(R,r)$ , where  $R$  is the distance from the atom A to the center of mass of BC,  $r$  is the BC inter-particle distance, the quantum Hamiltonian operator of the model system can be written as:

$$\hat{H} = -\frac{1}{2\mu_R} \frac{\partial^2}{\partial R^2} - \frac{1}{2\mu_r} \frac{\partial^2}{\partial r^2} + V(R,r), \quad (3)$$

where

$$\mu_R = \frac{m_1(m_2 + m_3)}{m_1 + m_2 + m_3}, \quad \mu_r = \frac{m_2 m_3}{m_2 + m_3} \quad (4)$$

are the corresponding reduced masses. The potential  $V(R,r)$  used is from *ab initio* calculations and will be discussed in Section 4.

The wave packet propagation procedure used is adapted from several existing grid method [3-6], i.e., the 2-D wave function is discretized: they are represented by their values at a set of 2-D grid points. The grid used here is a two dimensional lattice in the coordinates  $(R,r)$  and chosen to encompass the coordinates space of interest. To calculate the time evolution of the wave function, it is necessary to evaluate the Hamiltonian operation  $\hat{H}\psi$ . The operation of potential operator  $V$  on  $\psi$  is evaluated simply by multiplication at each of the discrete grid points. The kinetic operation  $\hat{T}\psi$  is evaluated by the Fourier transform method [9]: first  $\psi(R,r)$  is Fourier transformed to  $\bar{\psi}(p_R, p_r)$  in momentum space, then multiplied by  $-\hbar^2 p_R^2 / 2\mu_R$  and  $-\hbar^2 p_r^2 / 2\mu_r$  to each dimension, and the products are inverse Fourier transformed back to the coordinate space.

In our simulations, the initial wave packet is chosen as a product of a ground state vibrational wave function of the dimer and a plane wave describing the incoming collision particle, i.e.,

$$\psi(t=0) = G_{k_0}(R)\Phi(r) \quad (5)$$

where  $\Phi(r)$  is the ground state vibrational eigenfunction of the oscillator and  $G_{k_0}(R)$  is a Gaussian wave packet of width  $\sigma$ , centered at  $R_0$  away from the center of mass of the oscillator, with an average wave vector  $k_0$ :

$$G_{k_0}(R) = \left( \frac{1}{\sigma\sqrt{\pi}} \right)^{1/2} e^{-(R-R_0)/2\sigma^2} e^{ik_0 R} \quad (6)$$

In all the calculations the value of  $\sigma$  has been chosen to be 1.0 Å, which corresponds to approximately 15% spread in the momentum of the colliding particles. The grid size and the numerical parameters used in the wave packet propagation are listed in Table I. Such an initial

wave function is propagated in time by Chebychev method [3-6]. The final wave packet is projected to the eigenstate of the dimer to yield the survival probability of the collision process.

**Table I.** The grid boundaries and numerical parameters used in the wave packet propagation.

$R_{\min}$	$R_{\max}$	$r_{\min}$	$r_{\max}$	$N_x, N_y$	$t$
2.0 Å	40.0 Å	2.0 Å	40.0 Å	128,64	2.5 fsec

### 3. Formulation of Classical Path Approach

To study the survival probability of a collision process of an atom with large clusters, such as  $(H_2)_3$  and  $(D_2)_3$  trimers, the classical path approach is employed. The method involves two steps; first a classical trajectory is calculated for the system of interest by solving the corresponding Hamilton's equations of motion, then the system is treated quantum mechanically in a reduced dimension by substituting certain dynamical variables with their classical trajectories obtained from the classical simulations. The method has been used for studying molecular roto-vibrational energy transfer [7], and it is related to the reduced dimensionality theories of quantum reactive scattering developed by Bowman [8].

Consider a model system which consists of four particles with  $m_i$  ( $i=1, \dots, 4$ ). Let's denote particle 1 the colliding particle and the particles 2 to 4 forming a collinear triatomic cluster. The particle positions are represented by the Cartesian coordinates  $\{q_i, i=1, \dots, 4\}$ , based on which, the three new coordinates  $\{r, r_1, r_2\}$  can be defined as:

$$r = q_2 - q_1, r_1 = q_3 - q_2, r_2 = q_4 - q_3. \quad (7)$$

In these coordinates, the classical Hamiltonian of the model system can be written as follows:

$$H = \frac{1}{2\mu} p^2 + \frac{1}{2\mu_1} p_1^2 + \frac{1}{2\mu_2} p_2^2 - \frac{pp_1}{m_2} - \frac{p_1 p_2}{m_3} + V(r) + V(r_1) + V(r_2) \quad (8)$$

where

$$\mu = \frac{m_1 m_2}{m_1 + m_2}, \mu_1 = \frac{m_2 m_3}{m_2 + m_3}, \mu_2 = \frac{m_3 m_4}{m_3 + m_4}. \quad (9)$$

Using atomic units and by substitute the  $p_j \rightarrow -i\hbar \frac{\partial}{\partial r_j}$  ( $j=1,2$ ), the classical path Hamiltonian is obtained as:

$$\hat{H}(t) = \frac{p(t)^2}{2\mu} - \frac{1}{2\mu_1} \frac{\partial^2}{\partial r_1^2} - \frac{1}{2\mu_2} \frac{\partial^2}{\partial r_2^2} + \frac{ip(t)}{m_2} \frac{\partial}{\partial r_1} + \frac{1}{m_3} \frac{\partial^2}{\partial r_1 \partial r_2} + V(r_1, r_2; r(t)). \quad (10)$$

Here we have used classical trajectories for  $p(t)$  and  $r(t)$  in deriving the quantum Hamiltonian. Such an obtained Hamiltonian is explicitly time-dependent. For a system with time-dependent Hamiltonian, instead of using Chebychev propagation method, we use a second order differencing (SOD) scheme[9] for the wave packet propagation because the Chebychev scheme only valid for systems with time-independent Hamiltonian[9]. The SOD scheme can be expressed as:

$$\psi(t + \Delta t) = \psi(t - \Delta t) - 2i\hat{H}\psi(t), \quad (11)$$

where the operation of the Hamiltonian on a wave packet is evaluated by the FFT method as discussed above.

#### 4. Interaction Potentials

The intermolecular interaction potential of  $(\text{H}_2)_2$  has been investigated both experimentally [10] and theoretically [11-12]. In the simulation describe in this work, we always represent the  $\text{H}_2$  molecules as spherical particles interacting via a semi-empirical pair potential. Thus we are simulating the para-hydrogen species, i.e.,  $\text{H}_2$  is in the rotational ground state ( $J=0$ ). The ratio of the minor to the major axis of the ellipsoidal electronic charge distribution of the  $\text{H}_2$  molecule is very close to unity [13].

Silvera and Goldman [11] have used solid hydrogen pressure-volume data to determine the isotropic part of the intermolecular potential. Such an obtained semi-empirical potential has been used in the path-integral Monte-Carlo (PIMC) simulation of  $\text{H}_2$  cluster [15-17] and  $\text{H}_2$  surface [18]. Recently, high level *ab initio* calculations for the potential energy surface of  $(\text{H}_2)_2$  dimer have been performed by Wind and Roggen [12], which we believe is most accurate potential for the dimer existed in the literature. The isotropic part of the *ab initio* data and the fit of a Morse function to the data, which is used in our simulation, are shown in Figure 1(A). The comparison of Wind et al's potential data with Silvera-Goldman's potential and others are given by Ref. [12].

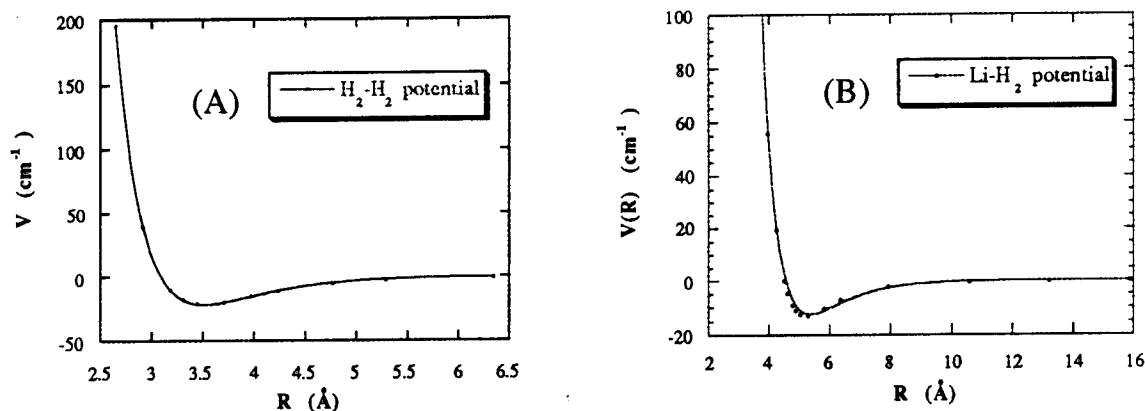


**Figure 1.** (A) The best fitted Morse potential function of Wind et al's [12] *ab initio* data for  $\text{H}_2$ - $\text{H}_2$  interaction. (B) Fitting of the *ab initio* data [19] for the  $\text{Li-H}_2$  interaction potential by a Morse function.

**Table II.** The Morse potential parameters used in the calculations.

	$D$ ( $\text{cm}^{-1}$ )	$\beta$ ( $\text{\AA}^{-1}$ )	$r_0$ ( $\text{\AA}$ )
$\text{pH}_2$ -- $\text{pH}_2$	24.26	1.571	3.418
$\text{Li}$ -- $\text{pH}_2$	12.39	0.865	5.360
$\text{B}$ -- $\text{pH}_2$ ( $\Sigma$ )	18.26	1.341	4.412
$\text{B}$ -- $\text{pH}_2$ ( $\Pi$ )	60.62	1.315	3.482

Until recently, the accurate data on the  $\text{Li-H}_2$  interaction is rather limited [18]. Recently, state-of-art quantum (ISCF-CI) calculation have been performed on this system [19]. The detailed

interaction potential surface data is now available to us. In the present study, the isotropic part of the potential is fitted to a Morse function and is shown in Figure 1(B). The numerical parameters from a least-squared fit by a Morse function for both H<sub>2</sub>-H<sub>2</sub> and Li-H<sub>2</sub> interaction potentials are listed in Table II. The B-H<sub>2</sub> potential is obtained from the multi-reference configuration-interaction calculation results by Alexander [20]. The system consists of the interaction of H<sub>2</sub> with Boron atom in its ground ( $2s^2 2p^2 P$ ) electronic state. The Morse potential parameters for the two diabatic interaction potential curves,  $\Sigma$  and  $\Pi$  states, are listed in Table II.

## 5. Simulation Results

To understand the interesting dynamical properties of such highly anharmonic, weakly bound quantum systems, Figure 2 shows the H<sub>2</sub>-H<sub>2</sub> potential surface and the J=0 vibrational ground state wave functions of (H<sub>2</sub>)<sub>2</sub> and (D<sub>2</sub>)<sub>2</sub> dimers. For the J=0 vibrational state, (H<sub>2</sub>)<sub>2</sub> and (D<sub>2</sub>)<sub>2</sub> dimers are bounded only by 1.68 and 5.79 cm<sup>-1</sup> respectively. Thus the interaction is extremely weak. It is also important to note that the large zero-point motion indicated by the broad distribution in the coordinate space. The half widths of the inter-particle distance distribution are 3.88 Å and 2.22 Å for (H<sub>2</sub>)<sub>2</sub> and (D<sub>2</sub>)<sub>2</sub> dimers respectively. These special properties of the dimers are important in the later discussion of the high survival probability of the dimers colliding with other particles.

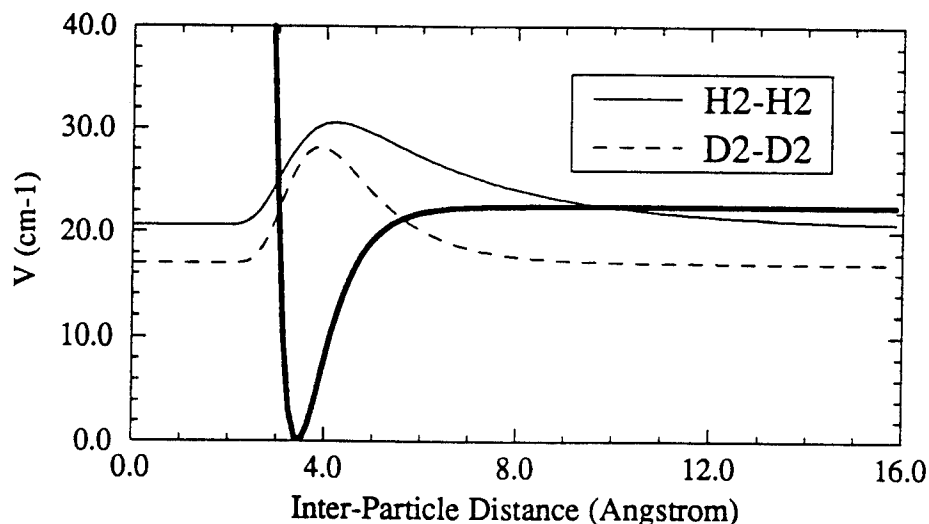


**Figure 2.** The interaction potential surface and the J=0 vibrational wave functions for the (H<sub>2</sub>)<sub>2</sub> and (D<sub>2</sub>)<sub>2</sub> dimers.

### A. (H<sub>2</sub>)<sub>2</sub> and (D<sub>2</sub>)<sub>2</sub> Dimers Survival Probability

Figure 3 shows the exact quantum wave packet calculation results of a Lithium atom colliding with (H<sub>2</sub>)<sub>2</sub> and (D<sub>2</sub>)<sub>2</sub> dimers. The survival probabilities of the dimers are plotted versus the relative collision energy. At low collision energy, <20 cm<sup>-1</sup>, the survival probabilities for the (D<sub>2</sub>)<sub>2</sub> dimer are less than that for the (H<sub>2</sub>)<sub>2</sub> dimer. This is because the binding energy for the (D<sub>2</sub>)<sub>2</sub> dimer is slightly higher than that for the (H<sub>2</sub>)<sub>2</sub> dimer as shown in Figure 2. Nevertheless, at collision energy about 20 cm<sup>-1</sup>, which is much large than the binding energy of the dimers, the survival probability of ~38% is surprisingly high. More interestingly is the cross over of the survival probability curves when the collision energy is increased to higher than 20 cm<sup>-1</sup>. Now the survival probabilities for the (H<sub>2</sub>)<sub>2</sub> dimer are large than for the (D<sub>2</sub>)<sub>2</sub> dimer, which is contrary to the energetic consideration as discussed previously.

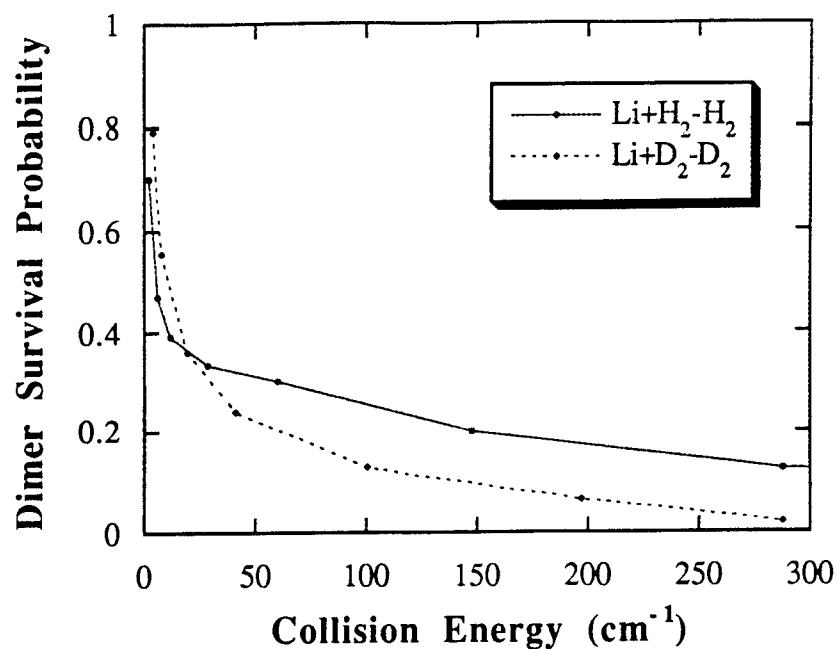


**Figure 3.** The survival probability for a collinear collision of Li atoms with (H<sub>2</sub>)<sub>2</sub> and (D<sub>2</sub>)<sub>2</sub> dimers.

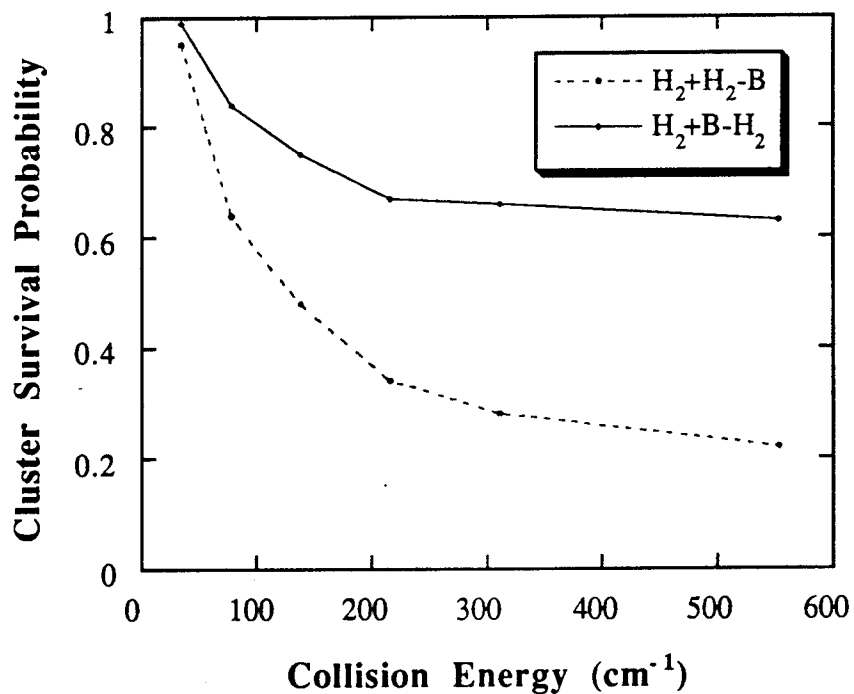


**Figure 4.** The survival probability of the collinear collision of the H<sub>2</sub> atom with H<sub>2</sub>-B clusters.

For the (H<sub>2</sub>)<sub>2</sub> dimer, because of the broad distribution of the vibrational wave function (see Figure 2), the energy transfer process from the colliding particle to the dimer could be inefficient. I

the case, the dimer acts like a very soft object which makes the hard-sphere like, energy transfer-efficient collision process a very rare event. Based on this argument, because the vibrational wave function for the  $(\text{H}_2)_2$  dimer is broader than for the  $(\text{D}_2)_2$  dimers, we can expect that the  $(\text{H}_2)_2$  dimer's survival probability will be large than that of  $(\text{D}_2)_2$  dimers. The recent preliminary experimental results [2] of  $(\text{H}_2)_2$  and  $(\text{D}_2)_2$  dimer scattering from a LiF surface seem to also suggest that deuterium dimer fragmentation is substantially greater than in the case of hydrogen dimer, at the collision energy approximately  $75 \text{ cm}^{-1}$  experimental beam conditions.

### B. $\text{H}_2$ -B Cluster Survival Probability

The survival probability of a heterogeneous cluster of  $\text{H}_2$ -B colliding with another  $\text{H}_2$  is also calculated. In the present collinear collision model, there are two collision arrangements for a  $\text{H}_2$  molecule colliding collinearly with a  $\text{H}_2$ -B cluster, arrangement (a)  $\text{H}_2 + \text{H}_2$ -B and (b)  $\text{H}_2 + \text{B}$ - $\text{H}_2$ . The survival probability of such two processes is quite different due to the difference in the strength of the kinetic coupling, which is inversely proportional to the square root of the mass of the center particle.

In Figure 4, the survival probabilities of the  $\text{H}_2$ -B cluster are plotted versus the collision energy of the  $\text{H}_2$  molecule. The survival probability of the process (b) is always greater than that of the process (a), which is due to the light atom ( $\text{H}_2$ ) as a center particle between the two bond of the collision complex  $\text{H}_2$ - $\text{H}_2$ -B. The ratio of survival probability between process (a) and (b) is asymptotically approaching to  $\sqrt{m_B/m_{\text{H}_2}} = 2.23$  at high collision energy ( $>200 \text{ cm}^{-1}$ ), which indicated that this energy range the collision process is dominated by kinetics.

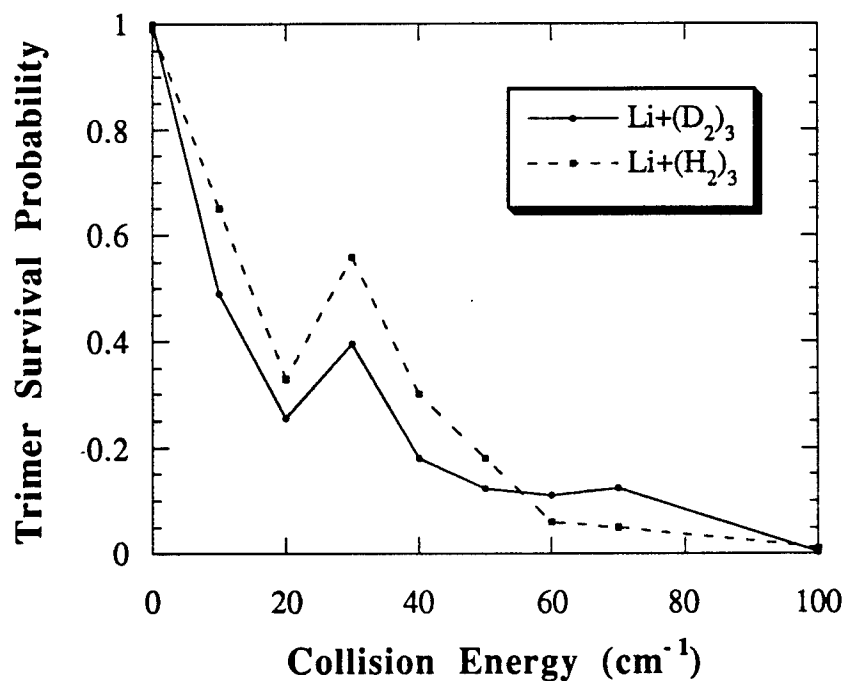


Figure 5. The survival probability of the collinear collision of a Li atom with the  $(\text{H}_2)_3$  and  $(\text{D}_2)_3$  trimers.

### C. $(\text{H}_2)_3$ and $(\text{D}_2)_2$ Trimers Survival Probability

Within the classical path approximation, the survival probabilities of  $(\text{H}_2)_3$  and  $(\text{D}_2)_3$



timers when collide with Li atom are calculated as shown in Figure 5. The general trend of the survival probability for the  $(\text{H}_2)_3$  and  $(\text{D}_2)_3$  trimers is similar. The important point of this result is that at collision energy of  $100 \text{ cm}^{-1}$ , the trimer, both  $(\text{H}_2)_3$  and  $(\text{D}_2)_3$  are complete fragmented. While at this collision energy, the  $(\text{H}_2)_2$  and  $(\text{D}_2)_2$  dimers still have more than 10% survival probabilities as shown in Figure 4.

## 6. Conclusion

Using an exact quantum wave packet propagation technique and a classical path approach, the collision dynamics and the survival probability of highly anharmonic, weakly bound quantum cluster such as  $(\text{H}_2)_2$  and  $(\text{D}_2)_2$  dimers and trimers colliding with other light particles including  $\text{H}_2$ , Li and B atoms are investigated. An unusual large survival probability of the  $(\text{H}_2)_2$  dimer, even at room temperature collision energy, is obtained which is in consistent with the recent molecular beam experiment results [1,2] of scattering  $(\text{H}_2)_n$  clusters from crystalline LiF surface. We also found that the survival probabilities for the trimers are much smaller than that for the dimers. For the B- $\text{H}_2$  cluster colliding with another hydrogen molecule, we found that the survival probabilities of more than 10% at room temperature. This indicate that Boron atoms could be potentially stabilized in the molecular hydrogen solid environment.

## 7. Acknowledgments

We thank Professor V.A. Apkarian for helpful discussions. This research was supported by the US Air Force Philips Laboratory (AFMC) under the contract F29601-92K-0016. We also thank the Office for Academic Computing, University of California, Irvine for partial support through the allocation of computer time on the CONVEX C240 computer.

## References

- [1] G. Tepper and D. R. Miller, Phys. Rev. Lett. **69** (1992) 2977. G. Tepper and D. R. Miller, J. Chem. Phys. **98** (1993) 9585.
- [2] M. E. Fajardo, J. Chem. Phys. **98** (1993) 110.
- [3] H. Tal-Ezer and R. Kosloff, J. Chem. Phys. **81**(1984) 3967.
- [4] D. Kosloff and R. Kosloff, J. Comput. Phys. **52** (1983) 35.
- [5] R. Kosloff and D. Kosloff, J. Chem. Phys. **79** (1983) 1823.
- [6] R. Bisseling and R. Kosloff, J. Comput. Phys. **59**(1985) 136.
- [7] G. D. Billing, Chem. Phys. **9** (1975) 359. G. D. Billing, Comput. Phys. Rep. **1**(1984) 237.
- [8] J. M. Bowman, Adv. Chem. Phys. **65** (1985) 115.
- [9] R. B. Gerber, R. Kosloff and M. Berman, Comp. Phys. Rep. **5** (1986) 59.
- [10] U. Buck, F. Huisken, A. Kohlhase and D. Otten, J.Chem. Phys. **78** (1983) 4439.
- [11] I. F. Silvera nad V.V. Goldman, J.Chem.Phys. **69** (1978) 4209.
- [12] P. Wind and I. Roeggen, Chem. Phys. **167**(1992) 247, *ibid* **167**(1992) 263; *ibid* **174** (1992) 345.
- [13] I. F. Silvera, Rev. Mod. Phys. **52** (1980) 393.
- [14] P. Sindzingre, D. M. Ceperley, and M. L. Klein, Phys. Rev. Lett. **67** (1991) 1871.
- [15] D. Scharf, G. J. Martyna, and M. L. Klein, J. Chem. Phys. **97** (1992) 3590.
- [16] D. Scharf, G. J. Martyna, and M. L. Klein, *ibid.* **99** (1993) 8997.
- [17] M. Walgner and D. M. Ceperley, J. Low. Temp. Phys. **94** (1994) 161.
- [18] J. C. Tully, J. Chem. Phys. **59** (1973) 5122; A. F. Wagner, A. C. Wahl, A. M. Karo, and R. Krejci, J. Chem. Phys. **69** (1978) 3746.
- [19] D. D. Konowalow, (private communication).
- [20] M. L. Alexander, J. Chem. Phys. **99** (1993) 6014.

## Molecular Impurities in Quantum Clusters: Cl<sub>2</sub>He<sub>N</sub>

Michele A. McMahon and K. Birgitta Whaley  
Department of Chemistry  
University of California, Berkeley  
CA 94720

The study of atomic and molecular additives to quantum condensed systems is a key component in the development of high energy density propellants based on solid hydrogen. In order to understand how to maximize the concentration of such additives it is necessary to first understand both how they are affected by the cryogenic quantum environment, and also how they modify the local structure of their environment. We are investigating this general issue for quantum clusters of He and of H<sub>2</sub>, using quantum Monte Carlo techniques. Using variational (VMC) and diffusion Monte Carlo (DMC) we have analyzed the energetic, structural and dynamical consequences of embedding/attaching single molecules. Ground state results for Cl<sub>2</sub> in He<sub>N</sub> are presented here and compared with the previously analyzed SF<sub>6</sub>He<sub>N</sub>.<sup>1</sup> Both of these result in strong perturbation and localization of the helium density about the impurity. The effects of cluster rotation are then studied for both pure and impurity-containing He clusters and for pure H<sub>2</sub> clusters, and are seen to result in marked centrifugal distortion. We also present a novel scheme for the Monte Carlo evaluation of energy transfer rates from impurity to cluster, and show how this may be used to determine the effective rotation/vibration energy levels of the solvated species. Both rotational excitation and energy transfer calculations are made for Cl<sub>2</sub>He<sub>N</sub>.

### Theory

Monte Carlo methods have proven extremely powerful in addressing the energetic and structural analysis of quantum clusters of helium and molecular hydrogen.<sup>2</sup> Both ground and low-lying excited states can be studied by variational and diffusion Monte Carlo methods. We have extended theoretical studies of these quantum clusters to include the analysis of clusters containing molecular impurities. The variational functions contain exponentially correlated two-particle impurity-helium factors, in addition to the usual two- and three-particle helium-helium correlation factors contained in  $\Psi_0(\mathbf{R})$ :

$$\Psi(\mathbf{R}, \mathbf{R}_I) = \Psi_0(\mathbf{R}) \exp \left[ \sum_{i=1}^N t_i(\mathbf{r}_{iI}) \right] \quad (1)$$

The correlation factor  $t_i(\mathbf{r}_{iI})$  is designed to make  $\Psi(\mathbf{R}, \mathbf{R}_I)$  small whenever the potential becomes large. When the impurity-helium potential is anisotropic,  $t_i(\mathbf{r}_{iI})$  is correspondingly anisotropic. Full details of the wavefunctions and of the VMC and DMC algorithms employed are given in refs. 1 and 3. For a cluster with non-zero angular momentum deriving from overall rotation, the variational cluster wave function is given by

$$\Psi_{LM} = \chi_{LM} \Psi_0 \quad (2)$$

Here  $\Psi_0$  is of the ground state form and is variationally determined while  $\chi_{LM}$  is of a fixed form and gives the correct angular symmetry as well as the rotational character. In the absence of magnetic fields we restrict ourselves to  $M=L$ . The form used in these studies is

$$\chi_{LL} = \sum_{i=1}^N \left[ \sum_{j=1}^N (\mathbf{x}_{ij} + i\mathbf{y}_{ij}) \right]^L \quad (3)$$

For pure  $\text{He}_N$  the sums extend over all  $N$  helium atoms, while for clusters with an impurity,  $\text{XHe}_{N-1}$ , the sum extends over  $N-1$  helium atoms and the impurity which constitutes particle  $N$ . Details of the wavefunctions for rotating clusters are given in ref. 4.

These quantum Monte Carlo methods may be used to obtain energetics and structural quantities, expressed as averages over the lowest state of a given symmetry. VMC gives variational estimates of the energy and structural information which may depend on the form of the wave function. We employ DMC with importance sampling, using the optimized variational wave function as the trial function. Importance sampling improves the efficiency and yields exact results for operators commuting with the Hamiltonian. Mixed expectation values are obtained for operators which do not commute with the Hamiltonian and in these cases second order estimators are reported,

$\langle A \rangle_{2\text{nd. order}} = 2\langle A \rangle_{\text{DMC}} - \langle A \rangle_{\text{VMC}}$ . For operators commuting with the Hamiltonian, DMC gives exact results, provided convergence is achieved. When using these methods for the study of isolated impurities in large clusters ( $N > 20$ ) one should bear in mind that the energy may be somewhat insensitive to the position of the impurity, and hence to the trial form used for  $t_1(\mathbf{r}_{i1})$ . Therefore, structural results for the impurity may depend to some extent on the particular form used. This problem is less severe for the solvating species, which for larger clusters provides the greater contribution to the energy.

We have recently also developed a mixed VMC/DMC algorithm which enables one to calculate energy transfer rates between an embedded molecule and the solvating cluster, and hence to analyze spectral line widths and line shifts for embedded chromophores. The method takes the Golden Rule expression for the energy transfer rate out of state  $\Psi_I$ :

$$T_I(\omega) = \frac{2\pi}{\hbar} \sum_F \left| \langle \Psi_I | V | \Psi_F \rangle \right|^2 \delta(E_I - E_F + \hbar\omega) \quad (4)$$

and Laplace transforms this to yield a pseudo-correlation function in imaginary time:

$$\tilde{T}_I(t) = \frac{2\pi}{\hbar} \int d\omega \langle \Psi_I | V e^{-(H_0 - E_I)t} V | \Psi_I \rangle \quad (5)$$

This quantity is then evaluated by a VMC sampling of  $\Psi_I$  in which a DMC sidewalk is made at each step in order to develop the propagator.<sup>5</sup> Similar sidewalk methods have been used to calculate exact dipole moment matrix elements<sup>6</sup> and to evaluate Euclidean response functions for nuclei.<sup>7</sup> For a given variational function  $\Psi_I$ , taking the inverse Laplace transform of the pseudo-correlation function yields both the prefactor of the rate and the energy differences  $E_F - E_I$ . The former gives the line width and hence the lifetime of the molecular excited state, while comparison of the latter with the bare molecule energies gives the energy shifts due to the solvating environment. In principle, this scheme could also be implemented with the ground state wave function obtained from an outer DMC walk, but this would be computationally far more intensive. Using the VMC form for  $\Psi_I$ , the primary computational problem is time step error accumulating in the propagator at long times which in practice allows only a bound on  $E_F - E_I$  to be obtained. Computational details on this method will be supplied elsewhere.<sup>5</sup> We have applied this approach to

rotational energy transfer from Cl<sub>2</sub> in He<sub>N</sub>; preliminary results for this system are summarized below.

## Cl<sub>2</sub>He<sub>N</sub>

### 1. Energetics

We employ the anisotropic He-Cl<sub>2</sub> potential of Cline et al.,<sup>8</sup> separating this into isotropic and anisotropic components by expanding in spherical harmonics of the Cl<sub>2</sub> orientation at the center of mass in a lab-fixed frame.<sup>5</sup> (Ref. 8 contains two important typographical errors: i) the term  $V_{vdw}$  is missing from eq.(3b), ii) the parameters  $C_{60}$  and  $C_{62}$  in Table IV are one order of magnitude too small, i.e., they should be  $13.3 \times 10^4 \text{ cm}^{-1}$  and  $1.88 \times 10^4 \text{ cm}^{-1}$  respectively.<sup>9</sup>) Use of a lab-fixed reference is convenient when the summation over  $N$  He-Cl<sub>2</sub> interactions is made in the cluster. The potential curves for the two extreme orientations are shown together with our isotropic approximation in Figure 1. The well depth for the isotropic potential is 30.2 K. The energetics of Cl<sub>2</sub>He<sub>N</sub>,  $N=1, 6$  and  $20$  obtained with the isotropic potential are summarized in Table 1. For  $N=6$  we have determined the minimum of the multi-dimensional potential and used this with the ground state energy to determine the zero point energy,  $E_{ZPE}=157.88 \text{ K}$ . For this size,  $E_{ZPE}$  is given to 99% by the analytic pair-wise model of Bacic et al.<sup>10</sup> as would be expected for less than one solvation shell of helium atoms. The binding of Cl<sub>2</sub>He<sub>20</sub> is about one third that of SF<sub>6</sub>He<sub>N</sub> ( $626.2(3) \text{ K}$  DMC result<sup>3</sup>), reflecting the greater strength of the isotropic He-SF<sub>6</sub> potential (well depth  $62.2 \text{ K}$ ). The rotationally excited Cl<sub>2</sub>He<sub>6</sub> cluster has a higher energy than that for the non-rotating ground state. The energy difference,  $\Delta E_{20} = 2.3 \text{ K}$ , is larger than the corresponding difference for He<sub>7</sub>,  $\Delta E_{20} = 1.3 \text{ K}$  (VMC result<sup>4</sup>), suggesting a greater degree of rigidity in the substituted cluster. This is consistent with the general phenomena of impurity induced localization of helium which we have seen previously for SF<sub>6</sub>He<sub>N</sub>.<sup>1</sup>

### 2. Structure

The radial structure of the  $N=6$  and  $N=20$  clusters is summarized in Figures 2 and 3 respectively, for the isotropic He-Cl<sub>2</sub> potential. Figures 2a and 3 plot the radial number profile  $P(r) = 4\pi r^2 \rho(r)$ , rather than the density profile in order to be able to display both impurity and helium structures on the same scale. The radial profiles are all plotted as a function of the distance from the geometric center of the cluster,  $r_g = \frac{1}{N+1} \sum_{i=1}^{N+1} r_i$ . For these systems  $r_g$  is approximately equal to the center of mass of the He<sub>N</sub> constituents, and differs by a small amount from the cluster center of mass. For these relatively small clusters the He distribution is located in one or two shells about the impurity. For  $N=6$  a single shell is seen.

These radial profiles clearly show the effect of the difference in both impurity size and binding strength to He. Thus for Cl<sub>2</sub>He<sub>20</sub> we see a longer tail in the helium density, which may be the start of a second solvation shell. In contrast, for SF<sub>6</sub>, there is clearly still only one solvation shell at  $N=20$ . Integration of helium density in Cl<sub>2</sub>He<sub>20</sub> for  $r > 6.5 \text{ \AA}$  yields one particle, suggesting that the first shell closes at  $N \sim 19-20$ . For SF<sub>6</sub> the first shell is completed at  $N=22-23$ .<sup>1</sup> In addition, the greater binding of SF<sub>6</sub> to He is reflected in the greater localization of SF<sub>6</sub> near the center of the cluster. This is consistent with the general trend we have observed previously, namely that light, more weakly bound impurities are more delocalized throughout the cluster.<sup>11</sup> The extreme case of this is H<sub>2</sub>.

which shows a maximum in the surface region and is delocalized over the entire cluster for  $N \sim 20$ .<sup>3</sup> For larger clusters the precise location of the impurity is still a major concern, since the cluster energy becomes relatively less sensitive to this feature and then the structural bias imposed by the trial wave function becomes important.<sup>12</sup> We are currently investigating this for  $\text{SF}_6$  with both VMC/DMC methods and with finite temperature path integral methods which are free from wave function bias.<sup>13</sup>

The density profiles of  $\text{Cl}_2$  in Figures 2a and 2b clearly show that the  $\text{Cl}_2$  is displaced away from the center of the cluster in a rotationally excited state. This centrifugal distortion, which is more apparent when density contours are plotted in a cylindrical coordinate system about the axis of quantization and which corresponds to the  $\text{Cl}_2$  moving away from the axis of quantization, is entirely consistent with the oblate distortions we have previously seen for pure  $\text{He}_7$  and  $(\text{H}_2)_7$  clusters.<sup>4</sup> Of interest however is the fact that a noticeable centrifugal distortion occurs for the impurity already at  $L=2$ , whereas the He density is virtually unchanged. Again, the He atoms appear to be more rigid than in a pure  $\text{He}_N$  system where at  $L=2$  there is more distortion. Most importantly, this differential centrifugal displacement raises the possibility that for larger  $L$  states even a strongly bound impurity may be preferentially pushed from the center to a surface region of the cluster. This kind of effect has possible implications for the impurity spectral shifts.<sup>14</sup>

### 3. Lifetimes

For rotational energy transfer from initially excited  $\text{Cl}_2$  we factorize the total wave function according to

$$\Psi_1 = \psi_1 \chi_{\text{Cl}_2}(j) \quad (6)$$

where  $\chi_{\text{Cl}_2}(j)$  is the  $\text{Cl}_2$  rigid rotor function for state  $j$  and  $\psi_1$  is the ground state  $\text{Cl}_2\text{He}_N$  function. This amounts to making a sudden, or 'vertical' excitation, and implies that we neglect the possibility of adiabatic relaxation of the He about the  $\text{Cl}_2$  in its excited state in the zeroth order wave function. These zeroth order states are solved for with the isotropic He- $\text{Cl}_2$  interaction potential, i.e., they are precisely the states we have been analyzing above. The potential coupling in eqs. (4) and (5) then becomes

$$\sum_f |\chi_i\rangle \langle \chi_i | V_{\text{anis}} | \chi_f\rangle \langle \chi_f | \quad (7)$$

and these matrix elements are now readily evaluated since we have expanded  $V_{\text{anis}}$ , the anisotropic component of the interaction potential, in spherical harmonics of the  $\text{Cl}_2$  orientation. Eq. (7) together with eq. (5) then allow state-to-state energy transfer rates to be calculated. Note that if just the energy transfer rates are required, these are given by the pre-factor in eq. (4), and so correspond to the zero time integral in eq. (5). Therefore these may be evaluated directly by VMC sampling alone. The rates for  $j = 2 \rightarrow 0$ ,  $j = 4 \rightarrow 2$  and  $j = 4 \rightarrow 0$  are summarized for  $\text{Cl}_2\text{He}_6$  in Table 2. We quote rates summed over all contributing  $m \rightarrow m'$  values,  $T_{j \rightarrow j'}$ , from which an averaged rate can be obtained by dividing by the number of  $m \rightarrow m'$  transitions,  $N_{mm'}$ . Given these state-to-state rates, the line widths  $\Gamma_j$  and lifetimes  $\tau_j$  are calculated from

$$\Gamma_j = \frac{\hbar}{2} \sum_j T_{j \rightarrow j}, \quad \tau_j = \left( \sum_j T_{j \rightarrow j} \right)^{-1} \quad (8)$$

The line widths correspond to the full width at half maximum of a Lorentzian absorption to the  $j$  state. These fall within the range of current experimentally achievable line widths for direct absorption of chromophores in  $\text{He}_N$ ,<sup>14,15</sup> although  $\text{Cl}_2$  itself does not have an infra-red spectrum. The rates in Table 2 may be compared to the classical rotational periods of the  $j=2$  and 4 rotational states, defined by  $E_j = I(\tau_j^{\text{cl}})^{-2} / 2$ . This yields  $\tau_2^{\text{cl}} = 4.47$  psec and  $\tau_4^{\text{cl}} = 2.45$  psec. Thus the rotational lifetimes of these states are about 58 and 10 rotational periods for  $j=2$  and 4 respectively, where the rates summed over all  $m$  transitions have been employed. This implies that the rotational excitations are quite stable with respect to rotational energy transfer to the cluster as a whole, and also suggests that the anisotropic coupling is small enough that the first order perturbation treatment employed here is valid. Future work will concentrate on the estimation of the perturbed energy levels from the time decay of eq. (5), and also on application of this approach to vibrational energy transfer from embedded molecules such as HF.

## References

1. R. N. Barnett and K. B. Whaley, *J. Chem. Phys.* **99**, 9730 (1993).
2. K. B. Whaley, *Int. Rev. Phys. Chem.* **13**, 41 (1994).
3. R. N. Barnett and K. B. Whaley, *J. Chem. Phys.* **96**, 2953 (1992).
4. M. A. McMahon, R. N. Barnett and K. B. Whaley, *J. Chem. Phys.* **99**, 8816 (1993).
5. M. A. McMahon and K. B. Whaley, to be published.
6. R. N. Barnett, Ph. D. Thesis, Univ. Calif. Berkeley, 1989.
7. J. Carlson and R. Schiavilla, *Phys. Rev. Lett.* **68**, 3682 (1992).
8. J. I. Cline, B. P. Reid, D. D. Evard, N. Sivakumar, N. Halberstadt and K. C. Janda, *J. Chem. Phys.* **89**, 3535 (1988). Note the typographical errors in the potential, eq. (3b) and Table IV, corrected above.
9. K. C. Janda, private communication.
10. Z. Bacic, M. Kennedy-Manziuk, J. W. Moskowitz and K. E. Schmidt, *J. Chem. Phys.* **98**, 7165 (1993).
11. M. A. McMahon, R. N. Barnett and K. B. Whaley, *Z. Phys. B* in press.
12. For example, a recent DMC calculation for  $\text{SF}_6\text{He}_N$  by S. A. Chin using different trial function from ours gives a quite different  $\text{SF}_6$  distribution for  $N > 20$  (S. A. Chin and E. Krotscheck, preprint 1994).
13. Y. K. Kwon, D. M. Ceperley and K. B. Whaley, work in progress.
14. S. Goyal, D. L. Schutt and G. Scoles, *Phys. Rev. Lett.* **69**, 933 (1992).
15. R. Froechtenicht, J. P. Toennies and A. Vilesov, *Chem. Phys. Lett.* **229**, 1, (1994).

Table 1. Energetics of  $\text{Cl}_2\text{He}_N$  calculated with the isotropic He- $\text{Cl}_2$  potential.<sup>5,8,9</sup> Energies are in Kelvin, distances in Å. For the dimer  $\langle r_{\text{He-Cl}_2} \rangle = 4.5281$ .

\* Energy obtained by diagonalization (exact).

N	$\langle E \rangle_{\text{DMC}}$	$\langle E \rangle_{\text{VMC}}$	$\frac{\langle E \rangle_{\text{VMC}}}{\langle E \rangle_{\text{DMC}}}$	$\sqrt{\langle r_{\text{He}}^2 \rangle}$	$\sqrt{\langle r_{\text{Cl}}^2 \rangle}$
1	-13.0798*	-13.0796(3)	99.99%		
6 (L=0)	-82.5(1)	-81.50(1)	98.8%	4.32(2)	1.21(5)
6 (L=2)	-80.2(1)	-78.87(2)	98.3%	4.33(2)	1.34(6)
20 (L=0)	-249.2(15)	-218.12(7)	87.5%	4.94(3)	0.55(2)

Table 2. Energy transfer rates, line widths and lifetimes of  $\text{Cl}_2$  in  $\text{He}_6$ , calculated by the mixed VMC/DMC method, eqs. (4) and (5). Numbers in parentheses indicate the statistical error in the last digit(s).

Transition	$T_{j \rightarrow j} (10^9 \text{ s}^{-1})$	$N_{\text{mm}}$
$2 \rightarrow 0$	3.87(2)	5
$4 \rightarrow 2$	0.1587(5)	9
$4 \rightarrow 0$	42.4(2)	64
State j	$\Gamma_j (\text{cm}^{-1})$	$\tau_j (\text{psec})$
j=2	0.01027(9)	258.4(11)
j=4	0.1130(5)	23.48(11)

### Figure Captions

1. He- $\text{Cl}_2$  pair potential from ref. 8 (corrected for typographical errors, see above), plotted at perpendicular approach of He to  $\text{Cl}_2$  ( $\gamma = 90^\circ$ ) and at parallel approach ( $\gamma = 0^\circ$ ). The isotropic component after expansion in spherical harmonics<sup>5</sup> is shown for comparison.
2. a) Radial number profile  $P(r) = 4\pi r^2 \rho(r)$  for  $\text{Cl}_2$  and He in  $\text{Cl}_2\text{He}_6$  with L=0 and L=2. The  $\text{Cl}_2$  is in its ground rotational state, j=0, in both cases and the cluster wavefunction is given by eqs. (2) and (5). The number profile for pure  $\text{He}_7$  is shown for comparison. All results are second order estimates.  
b) Radial density profile  $\rho(r)$  for  $\text{Cl}_2$  in  $\text{Cl}_2\text{He}_6$  with L=0 and L=2.
3. Radial number profiles  $P(r) = 4\pi r^2 \rho(r)$  for  $\text{Cl}_2\text{He}_{20}$  and  $\text{SF}_6\text{He}_{20}$ .<sup>1</sup> All results are second order estimates.

Figure 1

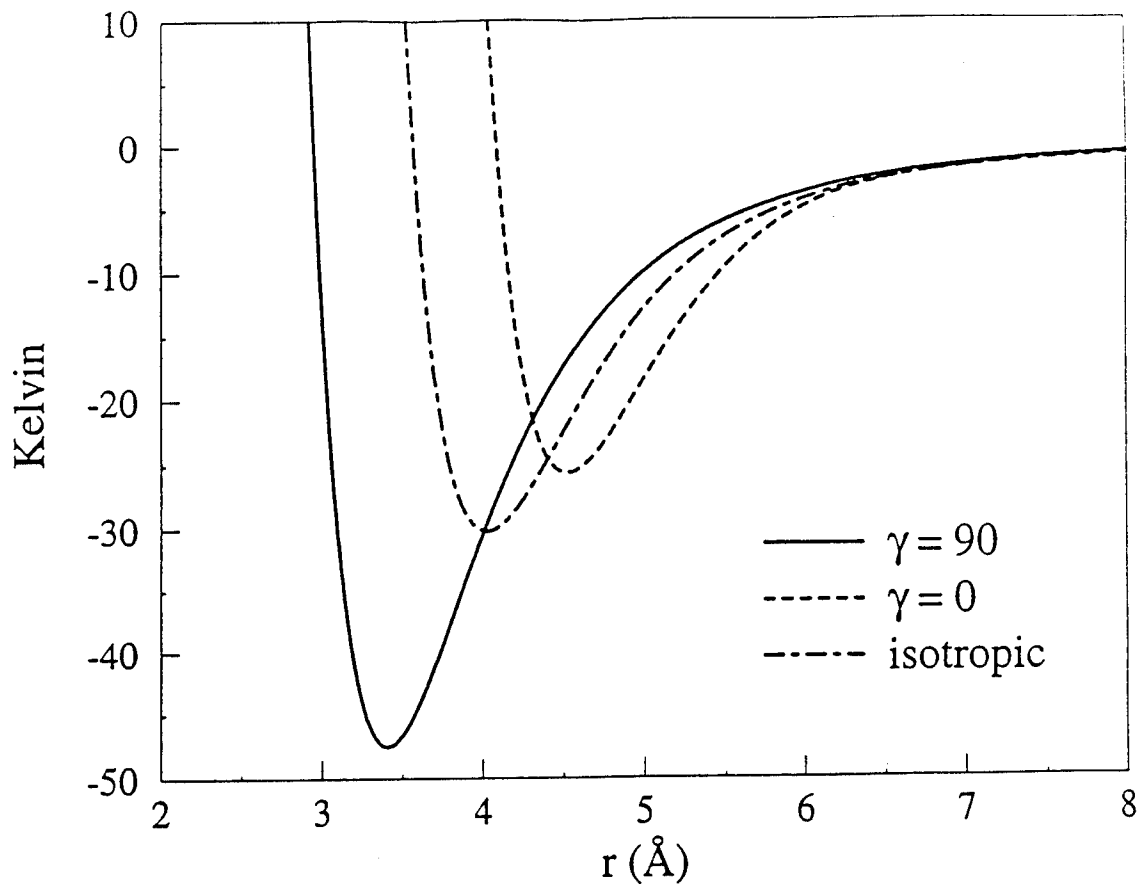


Figure 2a

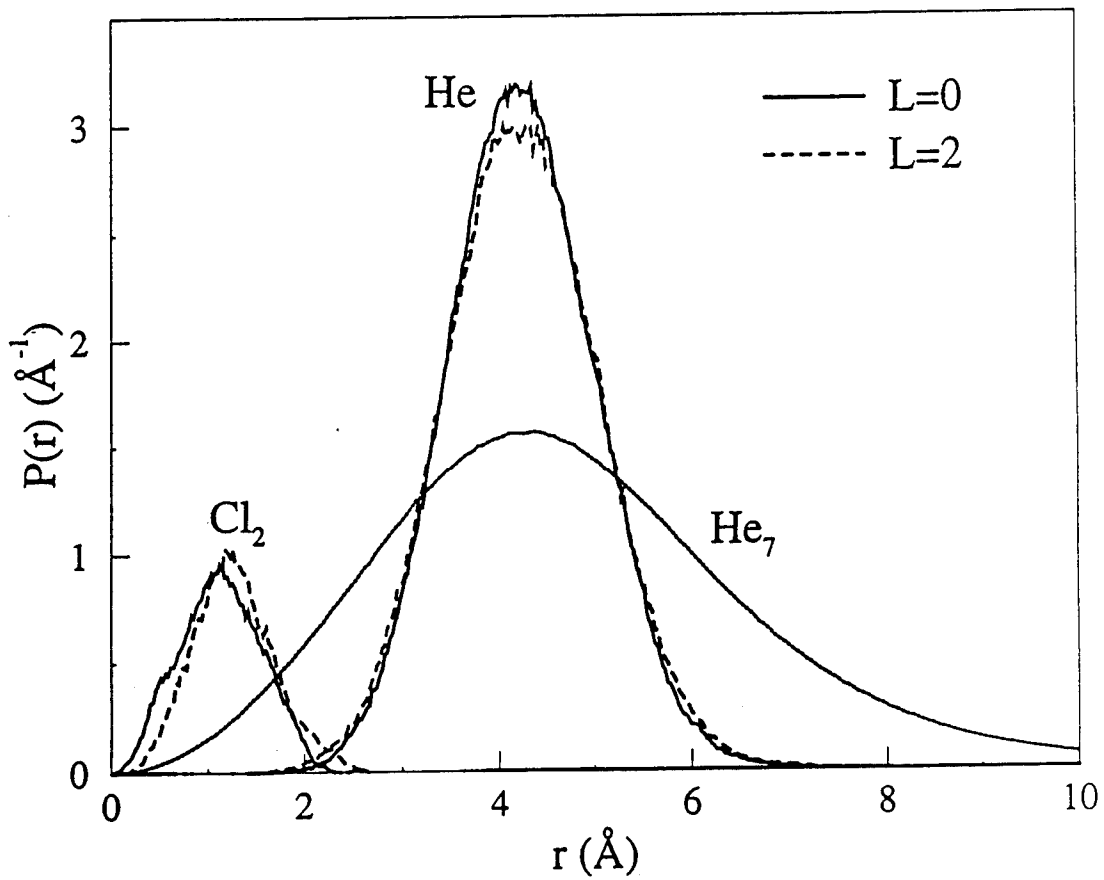




Figure 2b

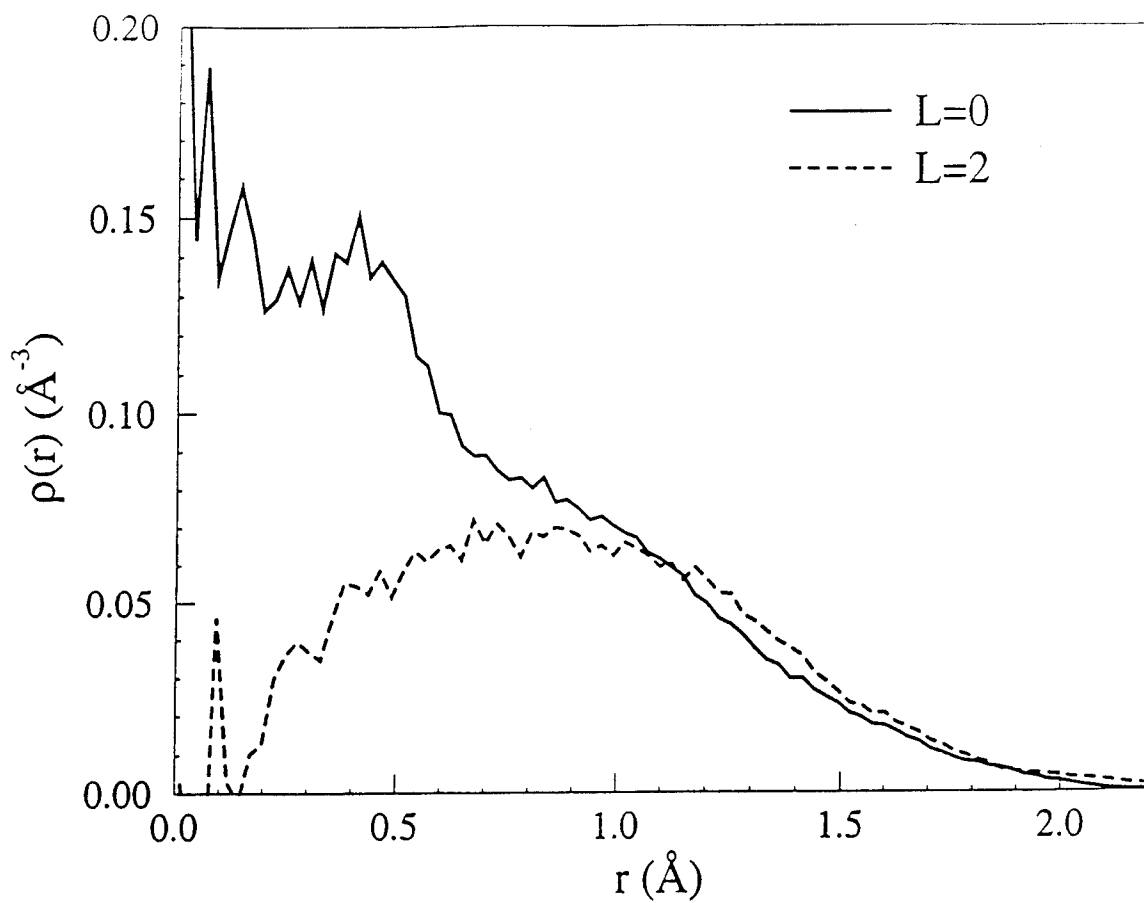
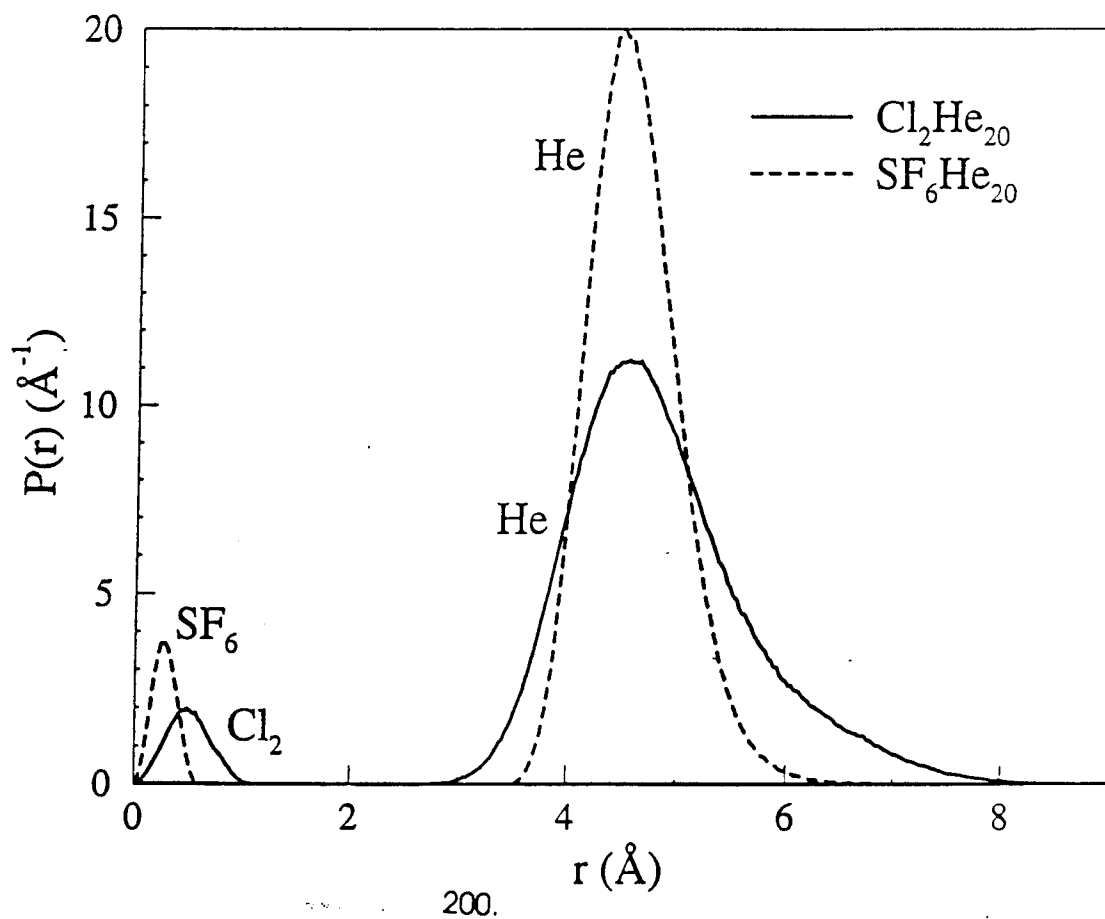


Figure 3



## Dynamics of Processes in Doped Hydrogen Clusters

R.B. Gerber, Z. Li, S. Broude and A.B. McCoy  
Department of Chemistry  
University of California  
Irvine, CA 92717

### Abstract

Theoretical calculations are presented for photoinduced and collision-induced processes in doped molecular hydrogen clusters of the type  $A(H_2)_n$ , where A is an atom. The data obtained provide indications for the potential usefulness of several HEDM propellants based on doped solid hydrogen systems. Some of the main results are:

(1) Using the Diffusion Quantum Monte Carlo Method, implemented on massively parallelized computers, the vibrational ground state wavefunctions of several hydrogen and doped hydrogen clusters were computed. Systems for which calculations were carried out include include  $(H_2)_n$ , with  $n \leq 100$ ;  $Li(H_2)_n$  with  $n \leq 12$ ;  $B(H_2)_n$  with  $n \leq 8$ ;  $Hg(H_2)_n$  with  $n \leq 100$  (the latter being a model for  $Mg(H_2)_n$  which is of HEDM interest);  $O(^3P)H_2$  and  $FH_2$ . The results have implications for the the stability of the corresponding atomic impurities in solid hydrogen.

(2) Approximate model wavefunctions were developed for these clusters, by fitting the numerical wavefunctions. For small clusters, e.g.  $Li(H_2)_2, (H_2)_3$ , the wavefunction is found to be separable to an excellent approximation in hyperspherical oscillators. For large clusters, e.g.  $Hg(H_2)_{12}$ , a relatively "spherical" wavefunction model was found to provide a good description. The results have useful applications for spectroscopy, and provide insights to the vibrational dynamics of these systems.

(3) Using a time-dependent quantum mechanical method, we carried out calculations for collisions of  $H_2$  molecules with quantum clusters such as  $LiH_2$  and  $BH_2$ . The survival probability of the cluster in such collisions is useful data for a method proposed for the preparation of HEDM systems. Despite the extremely weak binding of the clusters, relatively high survival probabilities were found even at high collision energies. This surprising behavior was shown to be due to a quantum effect.

(4) The dynamics following photoexcitation of the Li atom in  $Li(H_2)_2$  was calculated using a time dependent quantum-mechanical algorithm. The time-dependent

spectroscopy of the system was computed, and the decay rates for the channels  $\text{Li}(\text{H}_2)_2 \rightarrow \text{LiH}_2 + \text{H}_2$ ,  $\text{Li} + (\text{H}_2)_2$  were obtained. The results should be useful for the spectroscopic characterization of the quantum clusters.

(5) The dynamics following photoexcitation of Hg in  $\text{Hg}(\text{H}_2)_{12}$  was studied. The excitation gives rise to a reaction  $\text{Hg}^* + \text{H}_2 \rightarrow \text{HgH} + \text{H}$  within the cluster, and to a subsequent chain reaction  $\text{H}' + \text{H}_2 \rightarrow \text{H}'\text{H} + \text{H}$  that can propagate for several steps in the cluster. This chain propagation is found to be coherent at least over 2-3 steps. This coherent chain reaction is a new and interesting dynamical phenomenon in clusters.

With regard to assessing the HEDM promise of various doped hydrogen systems, some of the above calculations point to B in solid  $\text{H}_2$  as a potential HEDM propellant of major advantages. Also Mg in  $\text{H}_2$  and  $\text{O}(^3P)$  in  $\text{H}_2$  appear to be among the more advantageous potential HEDM materials.

## I. Introduction

This paper presents results on properties of hydrogen clusters doped by a single foreign atom. These systems, which we denote by  $\text{A}(\text{H}_2)_n$  where A is an atom, belong in the category of quantum clusters and exhibit exotic behavior, associated with the highly delocalized state of the hydrogen molecules within the system. The systems are obviously linked to a class of High Energy Density Materials (HEDM), based on doped solid hydrogen.<sup>(1)</sup> The topic is thus of interest both for basic scientific reasons, and for the potential applications. Several questions are explored here. First, we study the vibrational ground state wavefunctions of these systems, by "numerically exact" simulations and by physically-based models fitted to the computational data. Our aim is to characterize the vibrational behavior and to throw light on the nature of the "good vibrational modes" for these systems. These issues are essential for understanding the vibrational and the electronic spectroscopy of the quantum clusters. Very little is known in these issues, especially for large clusters. A second topic pursued here deals with the collision dynamics of quantum clusters, namely what are the survival probabilities of clusters of the type of  $\text{A}(\text{H}_2)_n$  in collisions with molecules or atoms. The question is pertinent to proposed methods for preparing doped solid hydrogen HEDM systems. While quantum clusters have been extensively pursued recently, little is still known on the dynamics of processes where such clusters are involved. The third topic is in a similar spirit: We present results on the

dynamics of clusters such as  $\text{Li}(\text{H}_2)_2$ , following photoexcitation of the metal atom. The results described deal with the fragmentation dynamics of the quantum cluster, and with the description of the process in terms of the time evolution of the wavepacket of the system. Finally, a fourth topic is touched upon as we present preliminary findings on the photoexcitation of Hg atoms in  $\text{Hg}(\text{H}_2)_n$  clusters. In this case, the  $\text{Hg}^*$  reacts with an  $\text{H}_2$  molecule within the cluster, giving rise to chemical processes in a highly quantum medium.

The material is organized as follows: Sect. II deals with the vibrational ground state calculations of large clusters. Sec. III presents results on collisions of quantum clusters with  $\text{H}_2$  molecules. Sec. IV describes results on dynamics following photoexcitation of  $\text{Li}(\text{H}_2)_2$ . Sec. V is a brief report on a preliminary finding on reaction dynamics in  $\text{Hg}(\text{H}_2)_{12}$ , induced by photoexcitation of Hg.

## II. Vibrational Properties of $\text{A}(\text{H}_2)_n$ Clusters

(a) *Simulation Method*: The method used to obtain the "numerically exact" ground-state vibrational wavefunction was the Diffusion Quantum Monte-Carlo (DMC), pioneered by Anderson.<sup>(2)</sup> Both this method, and several related methods such as Green's function Monte-Carlo and Variational Monte-Carlo were applied extensively, among other systems, to the vibrational ground state of clusters, including quantum clusters.<sup>(3)-(7)</sup> The method is well-g geared to producing a nodeless ground state wavefunction of a highly anharmonic system having many coupled modes. We will not discuss here the computational details and the algorithm used.<sup>(8)</sup> An important point was, however, the implementation of the method on massively parallelized SIMD computers. Overcoming issues of load balancing was a major aspect of the implementation. MasPar computers with 4000 and with 16,000 processes were used. The largest systems treated in our calculations so far were  $\text{Hg}(\text{H}_2)_{100}$  and  $(\text{H}_2)_{100}$ .

(b) *Spherical Cluster Model*: To gain insight into the physical properties described by the numerical wavefunctions, we introduced a simple wavefunction model, and fitted the latter to the numerical data. The main form used for  $\text{Hg}(\text{H}_2)_n$  was

$$\psi(\mathbf{r}_1, \dots, \mathbf{r}_n) = \prod_{i>j} J(r_{ij}) \prod_{k=1}^n f(|\mathbf{r}_k|) \quad (1)$$

where  $\mathbf{r}_i$  is the distance vector between the  $i$ -th hydrogen and the Hg.  $r_{ij}$  denotes the

distance between the  $i$  and the  $j$  hydrogen molecule. The  $H_2$  is treated in the spherical approximation. Eq. (1) is clearly a Jastrow-type approximation.<sup>(9)</sup> However, in this study the functions  $f(r)$  and  $J(r)$  were determined by fitting the "numerically exact" results. The  $J(r)$  so obtained may differ from Jastrow functions postulated, or employed in variational calculations.<sup>(9)</sup>

(c) *Vibrational Properties of  $Hg(H_2)_n$* : The spherical wavefunction model, Eq. (1), was found of accuracy in reproducing the numerical Quantum Monte Carlo results. Comparisons between the model and the numerical results for  $Hg(H_2)_{12}$  are shown in Figs. 1, 2. Fig. 1 shows the  $H_2 - H_2$  distance distribution in this cluster as obtained from the DQMC numerical results and from the fitted model wavefunction. Fig. 2 shows the corresponding comparison for the  $Hg - H_2$  distance distribution. In both cases the agreement is very good. The model wavefunction offers simple interpretations of the  $Hg(H_2)_{12}$  vibrational dynamics. Each of the  $H_2$  molecules carries out essentially independent radial oscillations against the heavy Hg. Looking at the wavefunctions at any distance  $r$  from the Hg, the  $H_2$  molecules can be described by the wavefunction as moving freely on the hypersphere of this radius, except for mutual  $H_2 - H_2$  avoidance at short distances. There are thus localized, radial vibrations, and in additions motions on a hypersphere that are collective only for configurations where short-range repulsions occur, and otherwise these motions are decoupled. The validity of the model has been demonstrated only for the ground state, but it obviously suggests possible simple models for "radial" and "angular" (on the hypersphere) excitations. It is interesting to inquire to what extent does the spherical nature of the model apply also to the numerical wavefunction for  $Hg(H_2)_{12}$ . *Classical* clusters of this type are known to be icosahedral. We used several criteria to examine the extent to which  $Hg(H_2)_{12}$  has a remaining icosahedral behavior. In a geometric icosaheron, there are 30 bonds of equal length on the surface. Any count of the number of equal bonds in the present system must allow for large tolerances, since the  $H_2$  molecules are extremely delocalized, and the probability of exact symmetry configurations is negligible. Fig. 3 shows the percent of Monte Carlo configurations that can be considered icosahedral but the number of equal bonds, as a function of the tolerance (with respect to deviation from equality). The spherical model for  $Hg(H_2)_{12}$  is compared with the Monte Carlo results for this system and with Quantum Monte Carlo simulations for  $Ar_{13}$ , that is a typical icosahedral cluster. As noted,  $Hg(H_2)_{12}$  is only slightly icosahedral, much closer to the spherical model than to a true icosahedron such as  $Ar_{13}$ . While Fig. 3 is for qualitative purposes,

# $n_2-n_2$ Distance Distribution

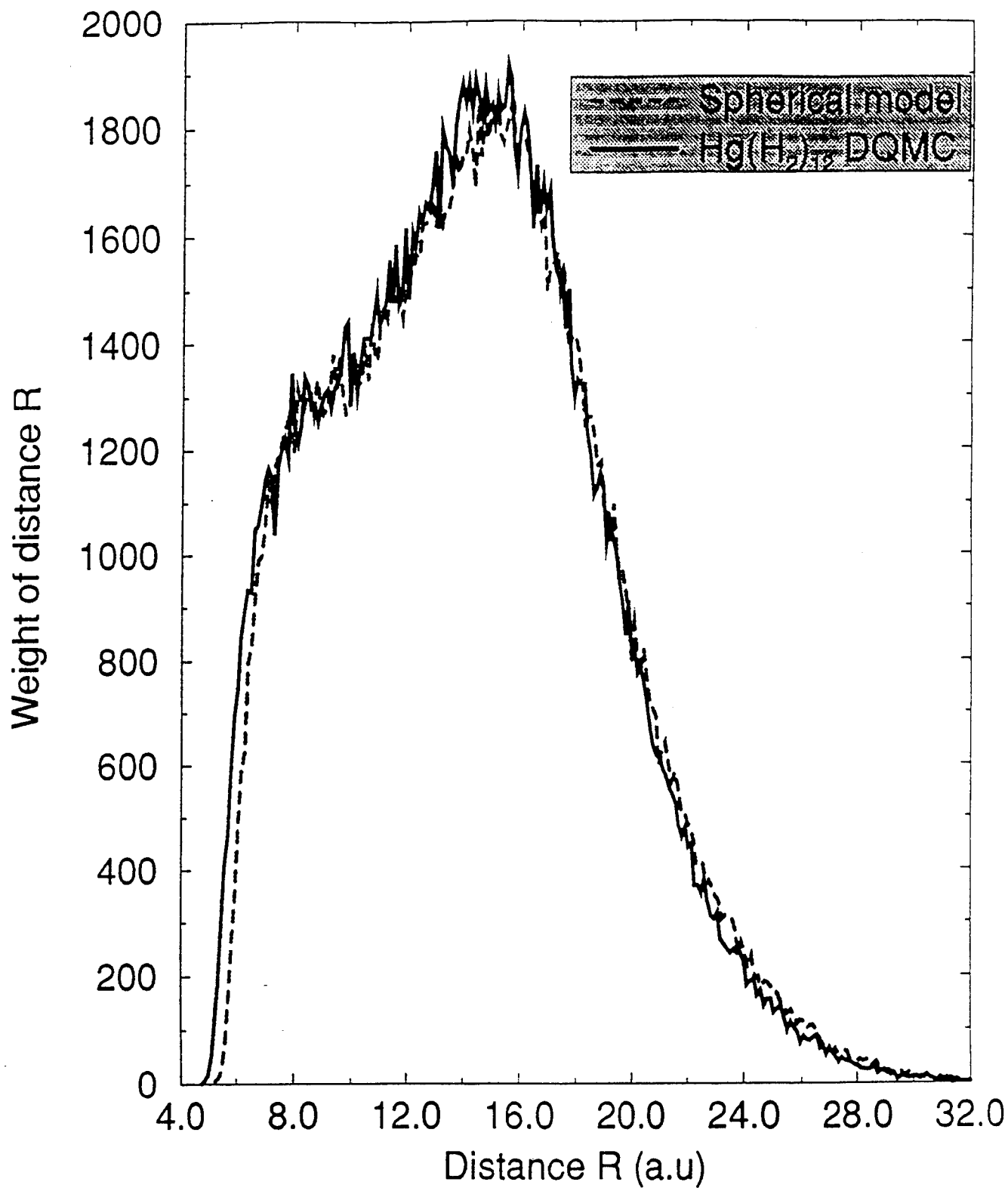


Fig. 1: H<sub>2</sub> - H<sub>2</sub> Distance Distribution in Hg(H<sub>2</sub>)<sub>12</sub>.

DQMC and Spherical Model Wavefunction results are compared.

# Hg-H<sub>2</sub> Distance Distribution

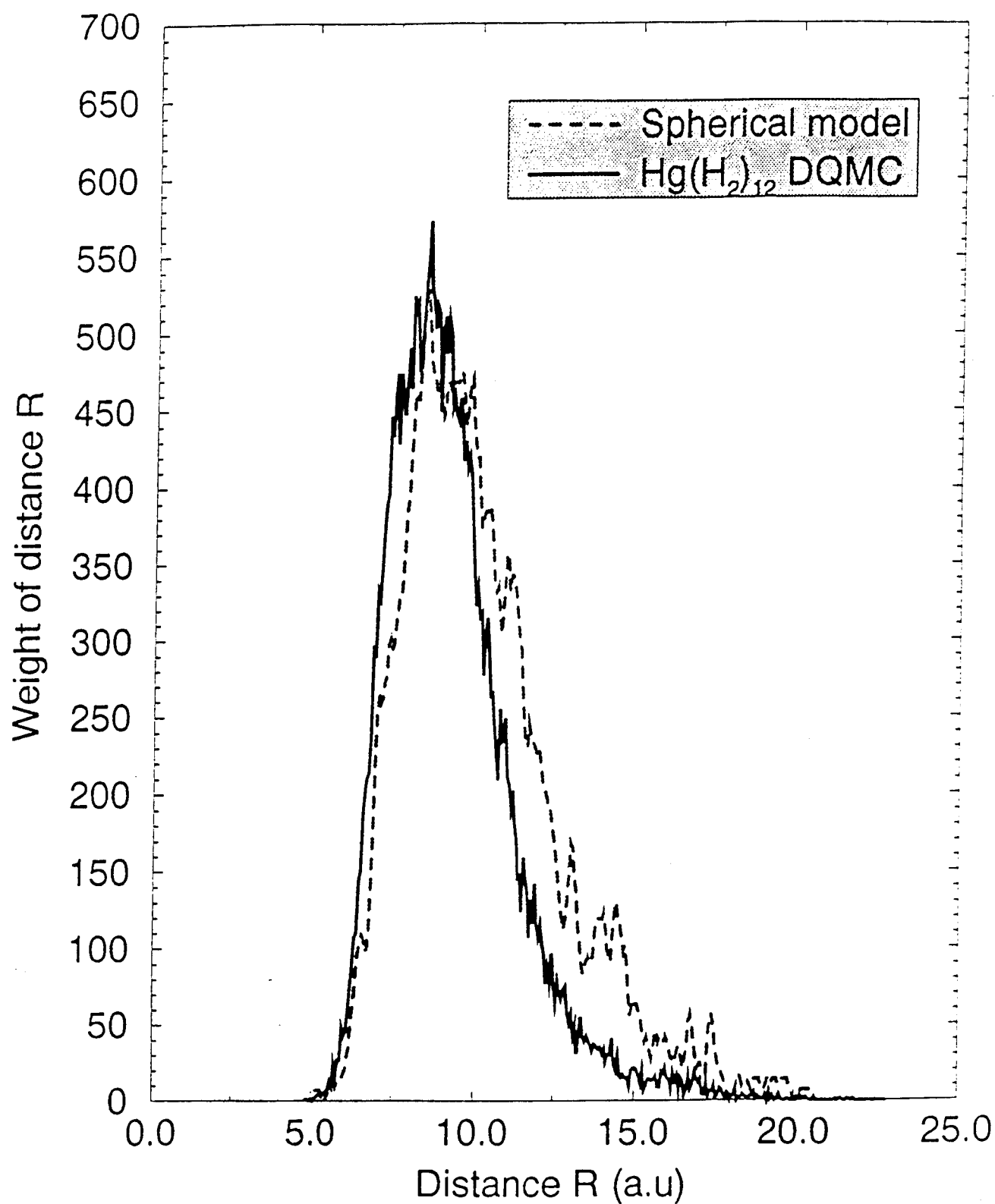


Fig. 2: Mg – H<sub>2</sub> Distance Distribution in Hg(H<sub>2</sub>)<sub>12</sub>.

DQMC and Spherical Model Wavefunction results are compared.

# Proximity to Icosahedral Behaviour

Criterion: 30 equal bond lengths

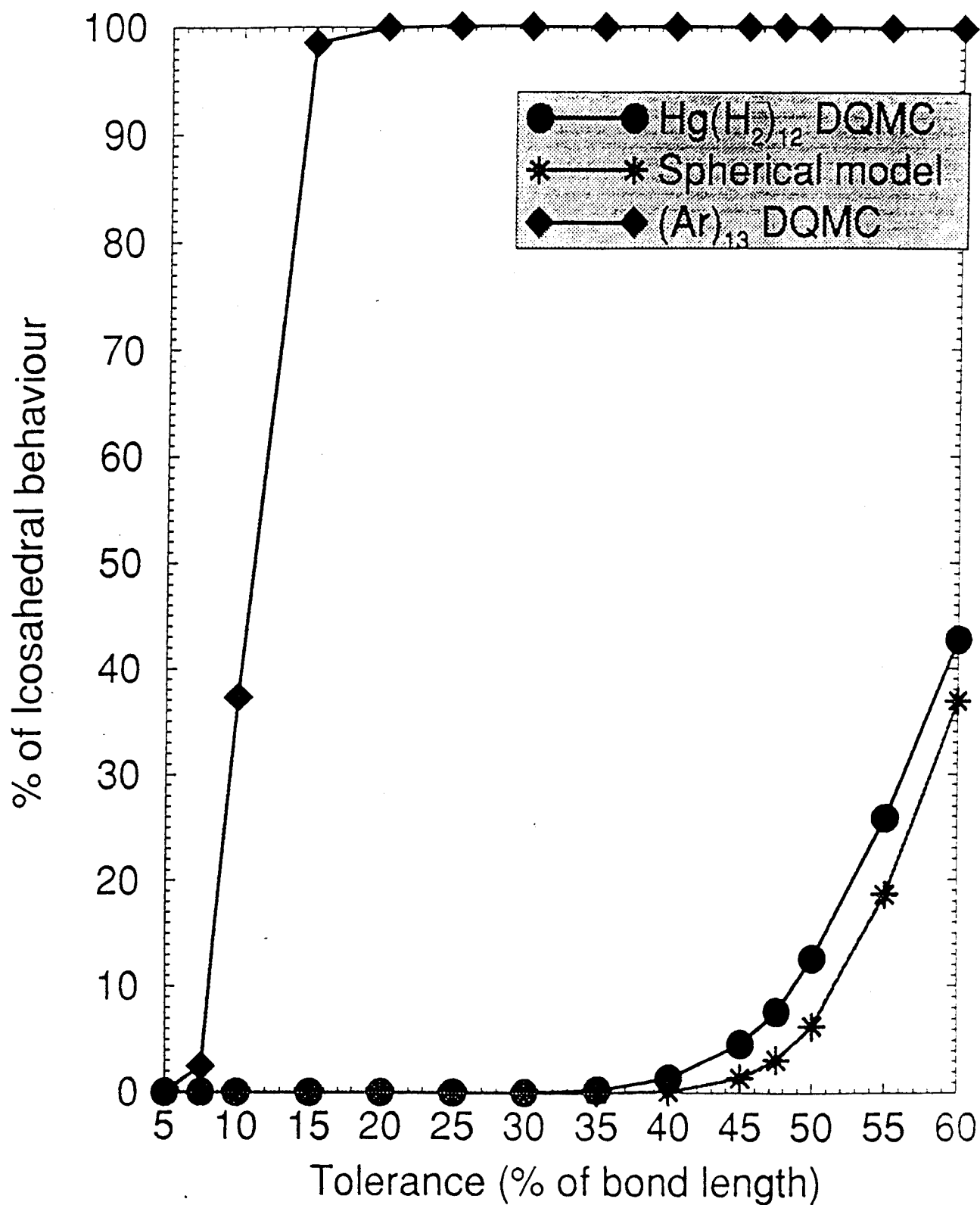


Fig. 3: Percent of Icosahedral Configurations in Clusters versus Tolerance.

The criterion used is the existence of 30 equal bond lengths at surface, within the tolerance.  $\text{Ar}_{13}$ , Spherical Model, and Monte-Carlo<sup>(13)</sup>  $\text{Hg}(\text{H}_2)_{12}$  are compared.



the comparison with  $Ar_{13}$  suggests that  $Hg(H_2)_{12}$  is in the order of a few percent of icosahedral character.

(d) *Small Quantum Clusters as Hyperspherical Oscillators*: Numerical tests we carried out suggest that *three particle quantum clusters are separable to excellent extent in hyperspherical coordinates*. Consider three atoms having position vectors  $r_1, r_2, r_3$ . The set of hyperspherical coordinates is defined by

$$\chi = \cos^{-1} \left\{ \frac{R \cdot r}{|r||R|} \right\} \quad (2.a)$$

$$\rho = [C^2|r|^2 + C^{-2}|R|^2]^{-1/2} \quad (2.b)$$

$$k = 2 \arctan(C^2|r|/|R|) \quad (2.c)$$

where, in terms of the position vectors  $r_1, r_2, r_3$ :

$$r = r_2 - r_1 \quad (3.a)$$

$$R = r_3 - [(m_1 r_1 + m_2 r_2) \frac{1}{m_1 + m_2}] \quad (3.b)$$

and  $C$  is given by:

$$C^4 = \frac{(m_1 + m_2 + m_3)m_1 m_2}{m_3(m_1 + m_2)^2} \quad (4)$$

where  $m_i$  denotes the mass of particle  $i$  in the cluster. The factorization property mentioned above means that to excellent approximation

$$\Psi(\chi, \rho, k) = \psi_1(\chi)\psi_2(\rho)\psi_3(k) \quad (5)$$

The validity of this factorization for the ground state, as well as for the excited vibrational states of the quantum cluster  $XeHe_2$  was established in Ref. 10. It was later shown by Horn *et al.*<sup>(11)</sup> that even for the much more harmonic and classical cluster  $Ar_3$  this factorization is somewhat better than the factorization of the wavefunction in conventional normal modes. Our recent studies suggest that the approximation (5) seems to hold very well for any weakly-bound quantum cluster of three particles, including  $A(H_2)_2$  clusters. This suggests that such clusters should be viewed as "hyperspherical oscillators", in analogy to nearly harmonic molecules that are normal-mode oscillators. The result has obvious applications to vibrational and electronic spectroscopy of such systems. We are currently

studying whether the same conclusion can be extended to larger clusters.

### III. Survival of Quantum Clusters in Collisions

This Section examines the dynamical stability of quantum clusters in a particular class of processes. Specifically, we study the probabilities for such clusters to survive in collisions with atoms or molecules. This data is relevant to certain methods proposed for the preparation of doped hydrogen systems. We present here results of calculations using time-dependent quantum wavepacket algorithms on collinear collisions of particles with quantum clusters. The collision in the collinear configurations are expected to be especially effective in dissociating the clusters. One would expect very high yields for the breaking of the cluster, since the calculations are for energies much greater than the dissociation threshold for the cluster.

Below we give the results of the calculations. The method and the potentials used will be discussed elsewhere.<sup>(12)</sup> Fig. 4 shows the survival probability of the dimer in collisions of Li atoms with  $(\text{H}_2)_2$  and with  $(\text{D}_2)_2$ , as a function of the collision energy. Two interesting effects are seen: First, the survival probabilities are substantial, even at relatively high collision energies. Second, at higher energies the survival probability of  $(\text{H}_2)_2$  is greater than that of  $(\text{D}_2)_2$ , although the latter has a higher binding energy (due to its lower Zero Point Energy). The explanation for both effects lies in the structure of the wavefunction of the dimer. The configurations most effective for dissociation upon impact are those where the relative distance in the dimer is at one of the turning points. While classically these configurations are very probable, the opposite is true for the wavefunctions of these highly quantum mechanical systems. In  $(\text{D}_2)_2$ , which is somewhat more classical than  $(\text{H}_2)_2$ , these configurations are more probable, hence it has a greater yield for dissociation. Fig. 5 shows the probability of survival of the  $\text{B} \cdots \text{H}_2$  cluster in collisions with  $\text{H}_2$ . Since this is a collinear calculation, it is useful to examine the process for the two configurations  $\text{H}_2 + \text{B} \cdots \text{H}_2$  and  $\text{H}_2 + \text{H}_2 \cdots \text{B}$ . In both cases very high survival probabilities are found despite the high energies. Collisions in which the  $\text{H}_2$  strikes the  $\text{H}_2$ -end of the cluster are more conducive to dissociation, since in the latter case energy transfer upon impact is more effective due to the 1:1 mass ratio. We conclude that quantum clusters have relatively large survival probabilities in collisions, also at energy orders of magnitude greater than the binding energy.

# Collinear Collisional Study

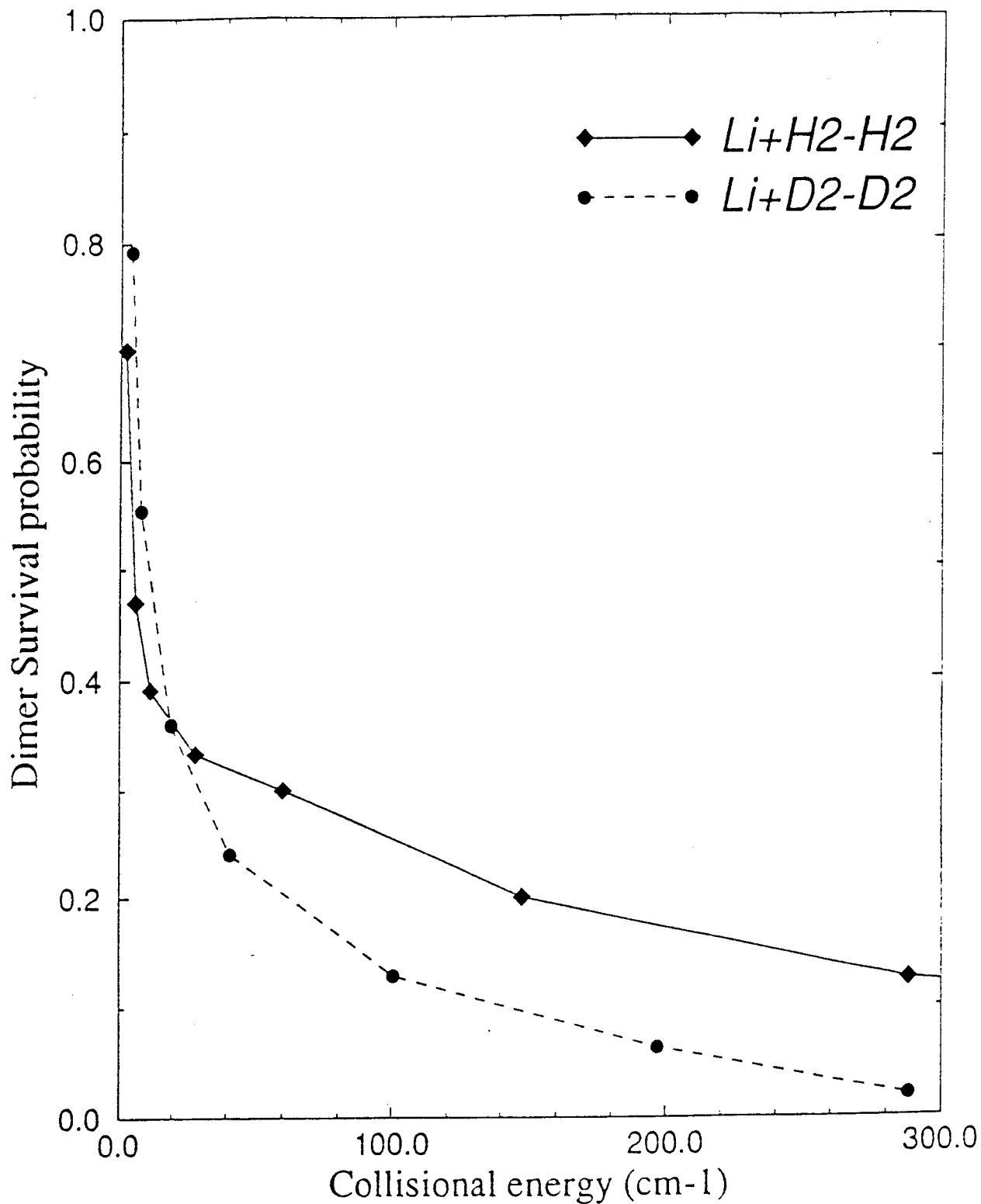


Fig. 4: Survival Probability of (H<sub>2</sub>)<sub>2</sub> and of (D<sub>2</sub>)<sub>2</sub> in Collisions with Li, as a Function of Collision Energy.

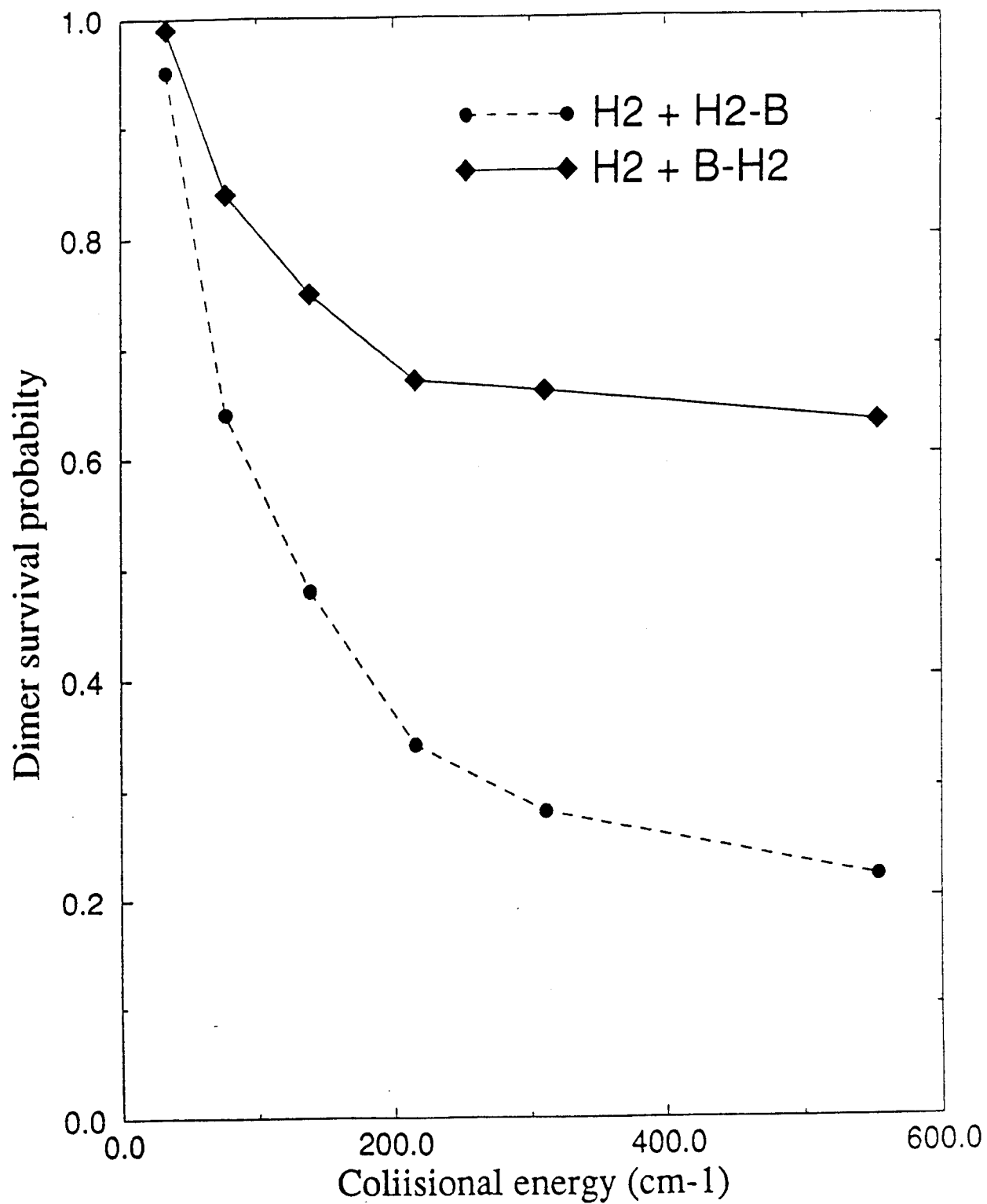
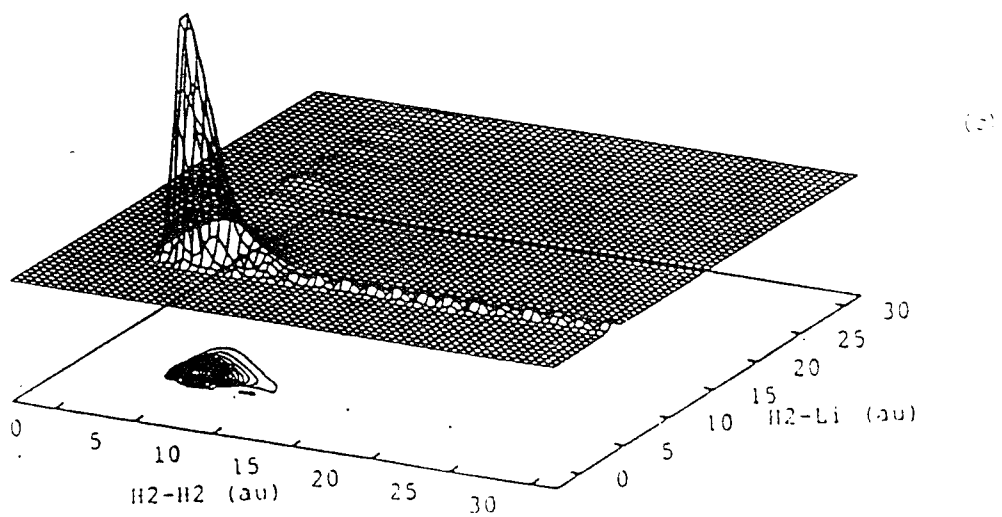
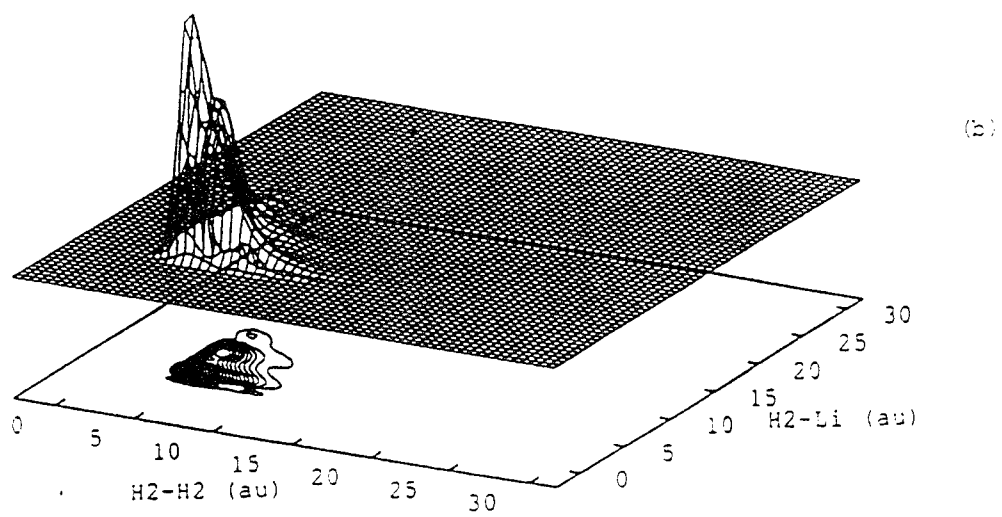
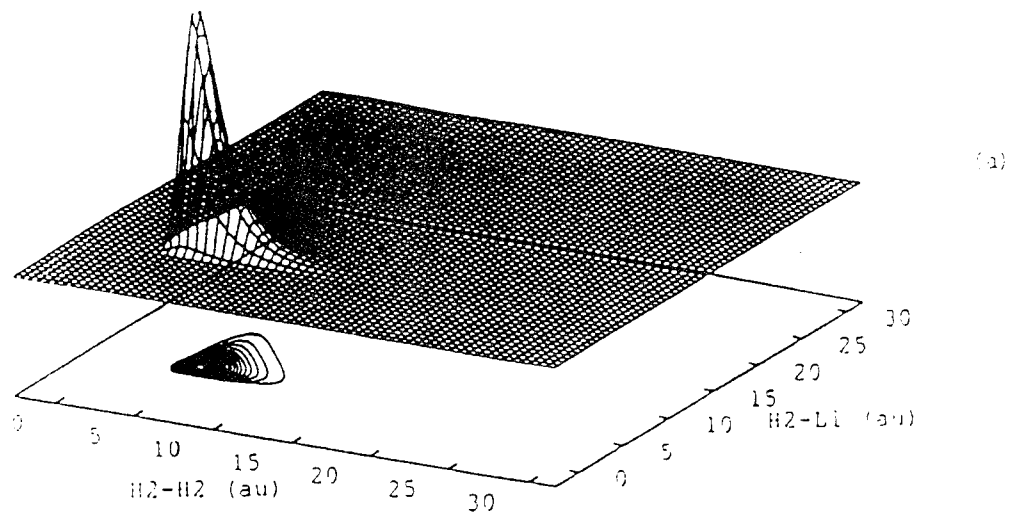


Fig. 5: Survival Probability of B - H<sub>2</sub> in Collisions with H<sub>2</sub> versus Collision Energy.

#### IV. Dynamics Following Electronic Excitation of Li in $\text{Li}(\text{H}_2)_2$

To take full advantage of the data provided by electronic excitation experiments, in quantum clusters, it is useful to study also the dynamics following the initial excitation. We note that photoabsorption lineshape experiments are generally sensitive to the very short time domain only. We studied the excitation dynamics for a collinear  $\text{H}_2 \cdots \text{H}_2 \cdots \text{Li}$  cluster. Three potential surfaces contribute in principle to the process, but estimates indicate that non-adiabatic coupling after the initial excitation is rather weak. Only the dynamics on a single potential surface, corresponding to the  ${}^2B_1$  state of the system was calculated. The calculations used a time-dependent quantum wavepacket algorithm. An infinitely fast excitation pulse was assumed, and the subsequent dynamics in time was computed over a timescale of  $> 100$  ps. The potential surface of the  ${}^2B_1$  state is a strongly attractive one. In fact, the excited state species does not have the properties of a (weakly bound) quantum cluster, but is a fairly strongly interacting complex, with a well-depth of the order of 0.4 eV. As a result, a long predissociation takes place. Several time-snapshots are shown in Fig. 6. The upper curve is the initial wavepacket which, in this case, given the fast excitation pulse, corresponds to the vibrational ground-state wavefunction of the weakly bound quantum cluster  $\text{Li}(\text{H}_2)_2$ . The potential is steeply attractive along the  $\text{Li} \cdots \text{H}_2$  coordinate, thus the initial dynamics develops along this mode. The second figure in (6) shows the situation after 0.72 ps, and a nodal pattern along the  $\text{Li} - \text{H}_2$  mode is beginning to emerge. The bottom picture is for  $t = 7.20$  ps. The picture shows that at this stage the decay channels  $\text{Li}^* - \text{H}_2 - \text{H}_2 \rightarrow \text{Li} - \text{H}_2 + \text{H}_2$ ;  $\text{Li} + (\text{H}_2)_2$  are already significant. The most important decay is into  $\text{Li} - \text{H}_2$ , which is formed in a highly excited state, and an  $\text{H}_2$  molecule. Direct decay into  $\text{Li} + \text{H}_2 + \text{H}_2$  seems to be negligible on this timescale. The process has a timescale of over 100 ps (not shown in Fig. 6). The conclusion that emerges is that electronic excitation of Li in  $\text{Li}(\text{H}_2)_2$  gives rise, in the  $B_1$  state, to a slow predissociation process - in fact the excited state is a resonance which decays into two channels, the main one results in formation of vibrationally excited  $\text{Li}^* - \text{H}_2$  (in addition to an  $\text{H}_2$  molecule). The process should be very suitable for time-resolved experiments on the picosecond timescale.



**Fig. 6:** Wavepackets for Dissociation of Electronically Excited Collinear  $\text{Li} - \text{H}_2 - \text{H}_2$ .

(a) Initial State; (b) Wavepacket at  $t = 0.72$  ps; (c) Wavepacket at  $t = 7.2$  ps.

## V. Photoinduced Chemical Reactions in $\text{Hg}(\text{H}_2)_n$ Clusters

The results of the above Section show that dynamics in the excited electronic state of clusters such as  $\text{A}(\text{H}_2)_n$  may be not far from the classical one, since the interactions are much steeper and the energies involved far higher than in the ground state. A very attractive approach to such systems is to sample the initial conditions based on the ground state wavefunction, and to pursue the excited state dynamics *classically*.<sup>(13)</sup> We have pursued this approach for  $\text{Hg}(\text{H}_2)_{12}$ , using the excited state  $\text{Hg}^* - \text{H}_2$  interaction of Bernier and Millie. Only very preliminary results are at hand. The results show a fast initial reaction:  $\text{Hg}^* + \text{H}_2 \rightarrow \text{HgH} + \text{H}$ , between the Hg and one of the hydrogens within the cluster. A substantial probability is found for the  $\text{H} + \text{H}_2$  process in the cluster to occur as a subsequent step. Trajectories corresponding to several *coherent* steps of the chain reaction  $\text{H} + \text{H}_2 \rightarrow \text{H}_2 + \text{H}$  were found. The existence of *coherent* chain reactions in doped solid hydrogen appears to be of great interest, and is being pursued by us. An important aspect is that these reactions are impulsive, rather than thermal.

**Acknowledgement:** This work was supported by Contract F2601-92K-0016 from the Air Force Phillips Laboratory (AFMC), and by the AFOSR in the framework of the University of California, Irvine, Research Initiative on Advanced Cryogenic Propellants.

## References

- (1) P. Carrick in "Proceedings of the HEM Conference" (Woods Hole, MA, June 1993). Edited by T.L. Thompson. Special Report published by the Phillips Laboratory, Air Force Material Command, 1993. p. 412.
- (2) J.B. Anderson, J. Chem. Phys. **63**, 1499 (1975).
- (3) R.N. Barnett and K.B. Whaley, J. Chem. Phys. **99**, 9730 (1993).
- (4) H. Sun and R.O. Watts, J. Chem. Phys. **92**, 603 (1990).
- (5) M. Quack and M.A. Sirhan, J. Chem. Phys. **95**, 28 (1991).
- (6) V. Buch, J. Chem. Phys. **97**, 726 (1992).
- (7) A. Vegiri, M.H. Alexander, S. Gregurick, A.B. McCoy and R.B. Gerber, J. Chem. Phys. (in press).
- (8) S. Broude and R.B. Gerber (to be published).

- (9) R.N Barnett and K.B. Whaley, Phys. Rev. A**47**, 4082 (1993).
- (10) T.R. Horn, R.B. Gerber and M.A. Ratner, J. Chem. Phys. **91**, 1813 (1989).
- (11) T.R. Horn, R.B. Gerber, J.J. Valentini and M.A. Ratner, J. Chem. Phys. **94**, 6728 (1991).
- (12) Z. Li and R.B. Gerber (to be published).
- (13) A.B. McCoy, Y. Hurwitz and R.B. Gerber, J. Phys. Chem. **97**, 12516 (1993).
- (14) A. Bernier and P. Millie, J. Chem. Phys. **88**, 4843 (1988).



**Fourier transform vibrational spectroscopy of novel  $\text{Li}_x\text{B}_y$  propellant additive clusters in solid Ar**

**J. D. Presilla-Márquez and P. G. Carrick  
Phillips Laboratory/Propulsion Directorate  
OLAC PL/RKFE  
10 East Saturn Blvd  
Edwards AFB CA 93524-7680**

$\text{Li}_x\text{B}_y$  molecular additives stored in solid hydrogen at cryogenic temperatures (4K) have the potential of improving the specific energy density (energy to mass ratio) and impulse (thrust per weight flow rate of propellant) compared to conventional  $\text{LH}_2/\text{LO}_2$  propellants. While small clusters are expected to result in improvements in propulsion, the role of larger clusters is still not clear.

We present preliminary results of the FTIR spectroscopy of some of these  $\text{Li}_x\text{B}_y$  clusters and their reaction products with  $\text{H}_2$ ,  $\text{O}_2$ ,  $\text{N}_2$ , and  $\text{H}_2\text{O}$ . These clusters were produced by pulsed laser ablation of Li/B targets, co-depositing the products with Ar, or Ar seeded with the gases mentioned above, onto CsI windows maintained at  $\sim 10$  K.

Jerry A. Boatz

Phillips Laboratory  
OLAC PL/RKFE  
10 East Saturn Blvd  
Edwards AFB, CA 93524-7680

**ABSTRACT**

The geometries, electronic structures, and harmonic vibrational frequencies and intensities of the lowest singlet and triplet states of  $\text{Li}_2\text{B}_2$  have been predicted using *ab initio* electronic structure theory. The geometries and harmonic frequencies were calculated using multiconfigurational self-consistent field (MCSCF) wavefunctions of the complete active space (CAS) variety, with the 6-31G(d) basis set (denoted as MCSCF/6-31G(d)). The MCSCF active space consists of all configurations generated by distributing the eight valence electrons in all possible ways among the eight active orbitals which correlate with the boron atom 2s and 2p atomic orbitals. Relative energies were refined using first-order and second-order configuration interaction (FOCI and SOCI, respectively) single-point energy calculations.

At the MCSCF/6-31G(d) level, the bent  $C_{2v}$  geometry is a local minimum on the lowest singlet potential energy surface ( $^1A_1$  electronic state.) The planar  $D_{2h}$  structure ( $^1A_g$ ) is the inversion transition state (imaginary frequency =  $57i \text{ cm}^{-1}$ ) and lies 0.4 kcal/mol above the  $^1A_1$  minimum. On the lowest triplet potential energy surface, the planar  $D_{2h}$  structure ( $^3B_{1u}$ ) is a local minimum and lies 13.2 kcal/mol above the  $^1A_1$  state. At the SOCI/6-31G(d)//MCSCF/6-31G(d) level, the  $^1A_g$  and  $^3B_{1u}$  states lie 0.9 and 6.5 kcal/mol, respectively, above the  $^1A_1$  state.

Analysis of the electrostatic potential, total electron density, and the natural orbitals of  $\text{Li}_2\text{B}_2$  reveals that the Li-B bonding takes place via  $\pi$ -complex formation rather than  $\sigma$  bonding. Indeed, the bonding in  $\text{Li}_2\text{B}_2$  can perhaps best be described as a charge transfer interaction with each lithium atom formally donating its single valence electron into the half-filled  $1\pi_u$  orbitals of  $\text{B}_2$ .

The MCSCF/6-31G(d) predicted harmonic frequencies of  $^1A_1$   $\text{Li}_2\text{B}_2$  are 78, 306, 458, 520, 606, and  $1109 \text{ cm}^{-1}$ . The most intense vibration is the  $606 \text{ cm}^{-1}$  asymmetric Li-B stretch.

**I. Introduction**

A currently proposed method of improving the performance of rocket propellants is to dope (or possibly replace) the fuel/working fluid with one or more types of high energy density material (HEDM). These dopants can range in size and complexity from simple metal atoms and clusters to highly strained organic compounds, such as derivatives of cubane and

quadricyclane, and inorganic species, such as tetrasilabicyclo[1.1.0]butane ( $\text{Si}_4\text{H}_8$ ) and the prismane isomer of borazine ( $\text{B}_3\text{N}_3\text{H}_6$ ).

The current study focuses on the characterization of the potential HEDM cluster  $\text{Li}_2\text{B}_2$ . Previous theoretical calculations<sup>1,2</sup> on  $\text{Li}_2\text{B}_2$  have examined a variety of singlet and triplet structures at the RHF/6-31G(d) level of theory. In these studies, the planar and bent singlets were found to be the preferred structures. At the MP4/6-31G(d)//RHF/6-31G(d) level,  $^1\text{A}_g$   $\text{Li}_2\text{B}_2$  was preferred by 9 kcal/mol over the  $^1\text{A}_1$  structure. Although efforts are underway in this laboratory<sup>3</sup> to synthesize and characterize  $\text{Li}_2\text{B}_2$ , as yet it has not been detected experimentally. The purpose of this work is to predict vibrational frequencies and infrared intensities of the ground state of  $\text{Li}_2\text{B}_2$  to aid in the experimental identification of this molecule.

## II. Theoretical Methods

The geometries and harmonic vibrational frequencies and intensities of  $\text{Li}_2\text{B}_2$  were calculated using MCSCF/6-31G(d) wavefunctions of the complete active space (CAS) variety. The active space consisted of all eight valence electrons distributed in the eight active orbitals arising from the 2s, 2p boron atomic orbitals. The predicted relative energies were refined using both first-order and second-order configuration interaction (FOCI and SOCI, respectively) single-point energy calculations.

The molecular geometries were fully optimized within the constraints of the point group symmetry. Stationary points were verified as local minima or transition states by diagonalization of the energy second derivative matrices; i.e., hessian matrices. All calculations were performed using the *ab initio* electronic structure programs GAMESS<sup>4</sup> and MESSKIT.<sup>5</sup>

## III. Results and Discussion

Geometries: Since previous theoretical studies<sup>1,2</sup> of  $\text{Li}_2\text{B}_2$  have indicated that the planar  $D_{2h}$  and/or bent  $C_{2v}$  structures are likely to be the preferred geometries, the present effort is confined to characterization of only those structures. Table I shows the MCSCF/6-31G(d) optimized structures of the  $^1\text{A}_1$ ,  $^1\text{A}_g$ , and  $^3\text{B}_{1u}$  electronic states of  $\text{Li}_2\text{B}_2$ .<sup>6</sup> All three states adopt a geometry in which there is a bond between the boron atoms and each lithium atom is attached to both boron atoms, presumably via a bridging two-electron, three-center bond (which, as will be shown below, is not an accurate description of the Li-B interaction.) The B-B bond lengths in the  $^1\text{A}_1$  and  $^1\text{A}_g$  states are virtually identical (1.567 Å vs. 1.566 Å, resp.), while the  $^1\text{A}_1$  Li-B bond length (2.186 Å) is slightly longer than its  $^1\text{A}_g$  counterpart (2.171 Å.) In the  $^3\text{B}_{1u}$  state, the B-B (Li-B) bond length is approximately 0.06 Å (0.04 - 0.05 Å) longer than in the singlet states.

Energies: Table II summarizes the relative energies, both with and without zero-point energy corrections, of the three electronic states of  $\text{Li}_2\text{B}_2$  as determined at the MCSCF, FOCI, and SOCI levels. At all three levels of theory, the  $^1\text{A}_1$  state is energetically favored; however, the  $^1\text{A}_g$  state is consistently less than one kcal/mol above the  $^1\text{A}_1$  state. (This is in

contrast to an earlier study by Lammertsma<sup>1</sup> in which  ${}^1A_g$   $Li_2B_2$  was found to be lower in energy than the  ${}^1A_1$  state by 9 kcal/mol at the MP4/6-31G(d)//RHF/6-31G(d) level.) Therefore, given the similarity in energies of the  ${}^1A_1$  and  ${}^1A_g$  states as determined in the present study, it is not possible to definitively identify the ground state of  $Li_2B_2$  as the  ${}^1A_1$  state. Furthermore, while the present study predicts the  ${}^3B_{1u}$  state to lie several kcal/mol above the  ${}^1A_1$  state, more accurate calculations (e.g., using a more extensive basis set and/or a larger active space) may reduce the relative energy of the  ${}^3B_{1u}$  state or perhaps even reverse the order of relative stability.<sup>7</sup>

Harmonic frequencies and infrared intensities: Table III summarizes the six computed harmonic frequencies for each of the  ${}^1A_1$ ,  ${}^1A_g$ , and  ${}^3B_{1u}$  states of  $Li_2B_2$ , at the MCSCF/6-31G(d) level. For all three electronic states, the lowest frequency mode is a torsional motion. Note that for the  ${}^1A_g$  state, this mode has an imaginary frequency. Therefore, this state is not a local minimum but rather is an inversion transition state. However, since this transition state is less than 1 kcal/mol above the  ${}^1A_1$  state (see Table I), and the corresponding frequency of the  ${}^1A_1$  state is quite small ( $78\text{ cm}^{-1}$ ),  ${}^1A_1$   $Li_2B_2$  is likely to exhibit fluxional behavior and may be "quasi-planar" at sufficiently high temperatures. For all three electronic states, the four intermediate frequencies correspond to Li-B stretching modes, while the highest frequency mode is a B-B stretch.

Five of the six vibrational modes of  ${}^1A_1$   $Li_2B_2$  are infrared-active. The computed frequencies combined with the computed relative intensities are summarized in the IR "stick spectrum" shown in Figure 1. The asymmetric  $b_2$  Li-B stretch occurring at  $606\text{ cm}^{-1}$  is the most intense vibration (and therefore experimentally should be the most easily detectable of the 5 IR active modes) while the  $a_1$  Li-B stretch at  $520\text{ cm}^{-1}$  has the weakest infrared intensity.

Electronic structure: A cursory examination of the MCSCF/6-31G(d) natural orbitals (not shown) arising from the 8 CAS orbitals of the  ${}^1A_1$  state of  $Li_2B_2$  reveals that there are essentially no contributions from the lithium atomic orbitals. Indeed, the  $Li_2B_2$  natural orbitals qualitatively resemble those of the  $B_2$  diatom, in spite of the presence of the lithium atoms. Therefore, in the following discussion, the natural orbitals will be described in terms of  $B_2$  " $\sigma_{g,u}$ " and " $\pi_{g,u}$ " orbitals, even though for instance the  $\pi_x$  and  $\pi_y$  components of the  $\pi_{g,u}$  orbitals will not have identical occupation numbers, as would be required for orbitals which are truly degenerate.

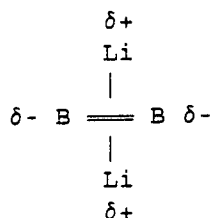
Table IV summarizes the MCSCF/6-31G(d) natural orbital occupation numbers for the  ${}^1A_1$  state of  $Li_2B_2$ . The occupation numbers for the formally occupied orbitals ( $2\sigma_g$ ,  $2\sigma_u$ ,  $1\pi_{ux}$ , and  $1\pi_{uy}$ ) range from 1.98 for the  $2\sigma_g$  orbital to 1.74 for the  $2\sigma_u$  orbital. Note that for a single-configuration wavefunction such as RHF, each of these orbitals would be constrained to contain exactly two electrons. The marked decrease in occupation numbers from the RHF-imposed value of 2 (most notably for the  $2\sigma_u$  orbital) and the concomitant non-trivial occupations of the formally empty orbitals (in the RHF sense) is an indication of the multiconfigurational character of  $Li_2B_2$  and the inability of a single-configuration wavefunction to accurately describe the electronic structure of this molecule.

Table IV also contains the MCSCF/6-31G(d) natural orbital occupation numbers for the ground state ( $^3\Sigma_g^-$ ) of  $B_2$ . With the exception of the  $1\pi_u$  orbitals, the corresponding occupation numbers for  $B_2$  and  $Li_2B_2$  differ by less than 0.07 electrons. In  $Li_2B_2$ , each component of the  $1\pi_u$  orbital is occupied by nearly a full electron more than the  $1\pi_u$  orbital in  $B_2$ . This suggests that in  $Li_2B_2$ , each lithium atom donates its single valence electron to complete the half-filled  $1\pi_u$  orbital in  $B_2$ , thereby increasing the B-B bond order by approximately one. The decrease in predicted B-B bond length in  $Li_2B_2$  (1.567 Å) relative to that in  $B_2$  (1.618 Å) as well as the increase in the calculated B-B vibrational stretching frequency (1109  $cm^{-1}$  in  $Li_2B_2$  versus 1034  $cm^{-1}$  in  $B_2$ ) are consistent with a strengthening of the B-B bond in  $Li_2B_2$ .

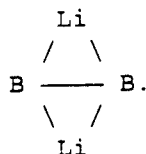
Figure 2 is a contour plot of the electrostatic potential of  $^1A_1 Li_2B_2$ , in a plane parallel to the plane containing both boron atoms and one of the lithium atoms. The solid contours, which denote regions of positive electrostatic potential, are centered on the lithium atom. Conversely, the regions of negative electrostatic potential (dashed contours) are localized primarily on the boron atoms. This is consistent with a transfer of electron density from the lithium atoms to the  $B_2$  moiety (*vide supra*.)

A contour plot of the total electron density of  $^1A_1 Li_2B_2$  in a plane containing both boron atoms and one of the lithium atoms is shown in Figure 3. This plot shows the existence of a single bond critical point<sup>8</sup> linking the lithium atom to the  $B_2$  moiety. Within the setting of a "Bader" analysis of molecular total electron densities,<sup>8</sup> this implies that the lithium atoms are **not** sigma-bonded directly to each boron atom. Rather, the plot in Figure 3 suggests that each lithium atom is bonded to the  $B_2$  fragment via a " $\pi$ -complex" interaction between the lithium 2s orbital and the partially filled  $B_2 \pi_u$  HOMO.

The above analysis of the bonding in  $Li_2B_2$  suggests a  $\pi$ -complex, charge transfer interaction between each lithium atom and the  $B_2$  moiety. Thus, the Li-B bonding is best described pictorially as



rather than as 2 electron, 3 center bonding such as



#### IV. Conclusions

The present study predicts a bent  $C_{2v}$  geometry as a local minimum on the lowest singlet potential energy surface of  $Li_2B_2$ . The planar  $D_{2h}$  structure is the inversion transition state and is less than one kcal/mol above the  $C_{2v}$  minimum. Since the energy difference between the  $C_{2v}$  and  $D_{2h}$  stationary points is so small, it cannot be stated with certainty that the  $C_{2v}$  structure is energetically preferred over the  $D_{2h}$  form. The closeness in energy of these two geometries suggests that the structure of  $Li_2B_2$  will be highly fluxional. The lowest triplet structure of  $Li_2B_2$  is planar ( $D_{2h}$ ) and is predicted to lie about 7 kcal/mol above the  $^1A_1$  minimum, at the SOCI/6-31G(d)//MCSCF/6-31G(d) level.

The bonding in  $^1A_1$   $Li_2B_2$  is best described as a  $\pi$  complex, charge-transfer interaction between the lithium atoms and the  $B_2$  moiety, in which each Li atom donates its single valence electron to the half-filled  $1\pi_u$  bonding orbital of  $B_2$ . Of the five IR-active vibrational modes in  $^1A_1$   $Li_2B_2$ , the  $b_2$  Li-B stretch with a predicted harmonic frequency of  $606\text{ cm}^{-1}$  has the largest intensity.

#### Acknowledgements

The author gratefully acknowledges several insightful discussions with Txomin Presilla, Patrick Carrick, and Michael W. Schmidt.

### Figure Captions

1. MCSCF/6-31G(d) infrared vibrational spectrum for  ${}^1A_1$   $Li_2B_2$ .
2. MCSCF/6-31G(d) electrostatic potential plot for  ${}^1A_1$   $Li_2B_2$ . Solid (dashed) contours denote regions of positive (negative) electrostatic potential. The increment between contours is 2.5 kcal/(mol\*e), where "e" represents the unit of electron charge. The plotting plane is parallel to one of the two planes containing both boron atoms and one of the lithium atoms, at a perpendicular distance of approximately 1.5 angstroms from the molecular plane. All four atoms lie behind the plotting plane.
3. MCSCF/6-31G(d) total electron density plot for  ${}^1A_1$   $Li_2B_2$ . The increment between contours is 0.005 electrons/bohr<sup>3</sup> (contours greater than 0.20 electrons/bohr<sup>3</sup> are not shown.) The plotting plane contains both boron atoms and one lithium atom. "X" denotes the bond critical point (see text.)

### References

1. K. Lammertsma and O.F. Güner, "Proceedings of the Air Force High Energy Density Materials Contractors Conference", L.P. Davis and F.J. Wodarczyk, eds., 1988.
2. G.F. Adams, "Proceedings of the High Energy Density Matter (HEDM) Conference, T.G. Wiley and R.A. van Opijnen, eds., 1989.
3. T. Presilla and P. Carrick, private communication.
4. a) M. Dupuis, D. Spangler, and J.J. Wendoloski, NRCC Software Catalog, 1980, 1, Program QG01.; M.W. Schmidt, J.A. Boatz, K.K. Baldridge, S. Koseki, M.S. Gordon, S.T. Elbert, and B. Lam, *Quantum Chemistry Program Exchange Bulletin* 7, 115(1987).  
b) M.W. Schmidt, K.K. Baldridge, J.A. Boatz, J.H. Jensen, S. Koseki, M.S. Gordon, K.A. Nguyen, T.L. Windus, S.T. Elbert, *Quantum Chemistry Exchange Bulletin*, 10, 52(1990).  
c) M.W. Schmidt, K.K. Baldridge, J.A. Boatz, S.T. Elbert, M.S. Gordon, J.H. Jensen, S. Koseki, N. Matsunaga, K.A. Nguyen, S. Su, and T.L. Windus, *J. Comp. Chem.* 14, 1347(1993).
5. R.A. Kendall, E. Earl, R. Hernandez, H.L. Taylor, D. O'Neal, J. Nichols, M. Hoffmann, M. Gutowski, X.-C. Wang, J.A. Boatz, J. Anchell, K. Bak, and M. Feyereisen, University of Utah, 1990.
6. The bent triplet structure ( ${}^3A_1$ ) optimizes to the planar ( ${}^3B_{1u}$ ) geometry.
7. More extensive calculations of this kind are currently in progress.
8. See, for example, R.F.W. Bader, *Chem. Rev.* 91, 893-928(1991).

Table I. Geometries of  $\text{Li}_2\text{B}_2$ .<sup>a</sup>

Electronic State	$^1A_1$	$^1A_g$	$^3B_{1u}$
Parameter			
$R_e$ (B-B)	1.567	1.566	1.630
$R_e$ (Li-B)	2.186	2.171	2.222
$R_e$ (Li-Li)	3.722	4.050	4.133
$\omega_e$ <sup>b</sup>	131.5	180.0	180.0

<sup>a</sup> Bond lengths in angstroms, dihedral angles in degrees.

<sup>b</sup> " $\omega_e$ " denotes the Li-B-B-Li torsional angle.

Table II. Relative Energies of  $\text{Li}_2\text{B}_2$ .<sup>a</sup>

Electronic State	$^1A_1$	$^1A_g$	$^3B_{1u}$
Level of Theory			
MCSCF	0.0	0.4	13.2
MCSCF + ZPE <sup>b</sup>	0.0	0.3	13.7
Number of CSFs	(480)	(264)	(296)
FOCI	0.0	0.3	4.8
FOCI + ZPE <sup>b</sup>	0.0	0.2	5.3
Number of CSFs	(28,816)	(14,572)	(22,436)
SOCI	0.0	0.9	6.5
SOCI + ZPE <sup>b</sup>	0.0	0.8	7.0
Number of CSFs	(802,256)	(402,764)	(683,124)

<sup>a</sup> Energies given in kcal/mol. All geometries fully optimized at the MCSCF/6-31G(d) level. The number of configuration state functions (CSFs) are given in parentheses.

<sup>b</sup> "ZPE" denotes inclusion of MCSCF/6-31G(d) zero-point energy corrections.



Table III. Predicted Harmonic Vibrational Frequencies of  $\text{Li}_2\text{B}_2$ .<sup>a</sup>

Electronic State	${}^1\text{A}_1$	${}^1\text{A}_g$	${}^3\text{B}_{1u}$
	78 $a_1$	571 $b_{1u}$	102 $b_{1u}$
	306 $b_1$	259 $b_{3u}$	172 $b_{3u}$
	458 $a_2$	503 $b_{1g}$	340 $b_{1g}$
	520 $a_1$	524 $a_g$	493 $a_g$
	606 $b_2$	623 $b_{2u}$	582 $b_{2u}$
	1109 $a_1$	1106 $a_g$	985 $a_g$

<sup>a</sup> In  $\text{cm}^{-1}$ . The symmetry of the vibrational mode is given after the computed frequency.

Table IV. Natural Orbital Occupation Numbers for  $\text{Li}_2\text{B}_2$  and  $\text{B}_2$ .<sup>a</sup>

	$\text{B}_2$ ( ${}^3\Sigma_g^-$ )	$\text{Li}_2\text{B}_2$ ( ${}^1\text{A}_1$ )
Orbital		
$3\sigma_u$	0.0184	0.0140
$1\pi_{gy}$	0.0605	0.0898
$1\pi_{gx}$	0.0605	0.1100
$3\sigma_g$	0.3000	0.2456
$1\pi_{uy}$	0.9658	1.9010
$1\pi_{ux}$	0.9658	1.9162
$2\sigma_u$	1.6672	1.7412
$2\sigma_g$	1.9620	1.9822

<sup>a</sup> Units are number of electrons.

Li<sub>2</sub>B<sub>2</sub> 1A<sub>1</sub> IR Spectrum  
Li<sup>7</sup>B<sub>11</sub>

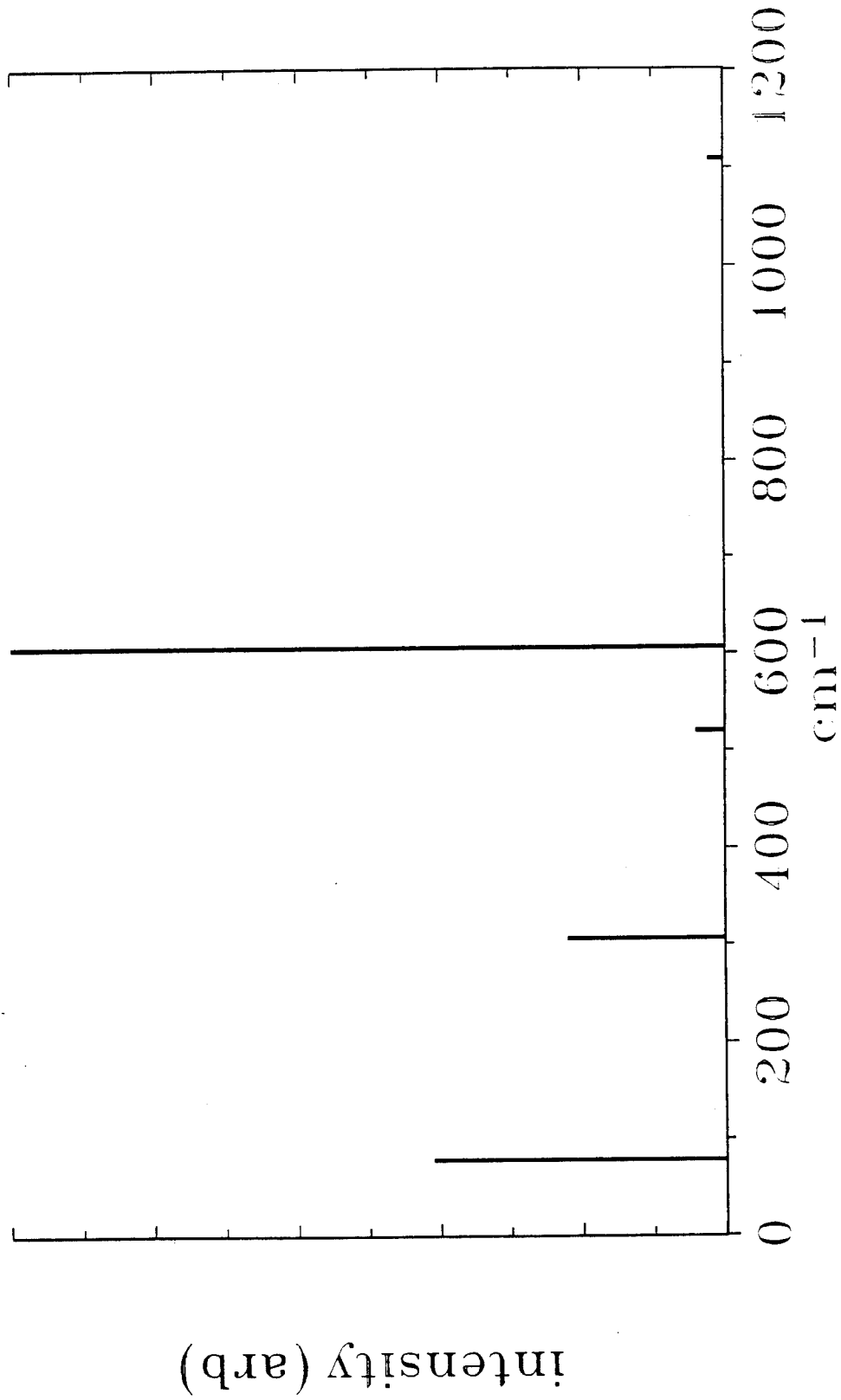


Figure 1  
225

MEPMAP

ONE BOHR IS

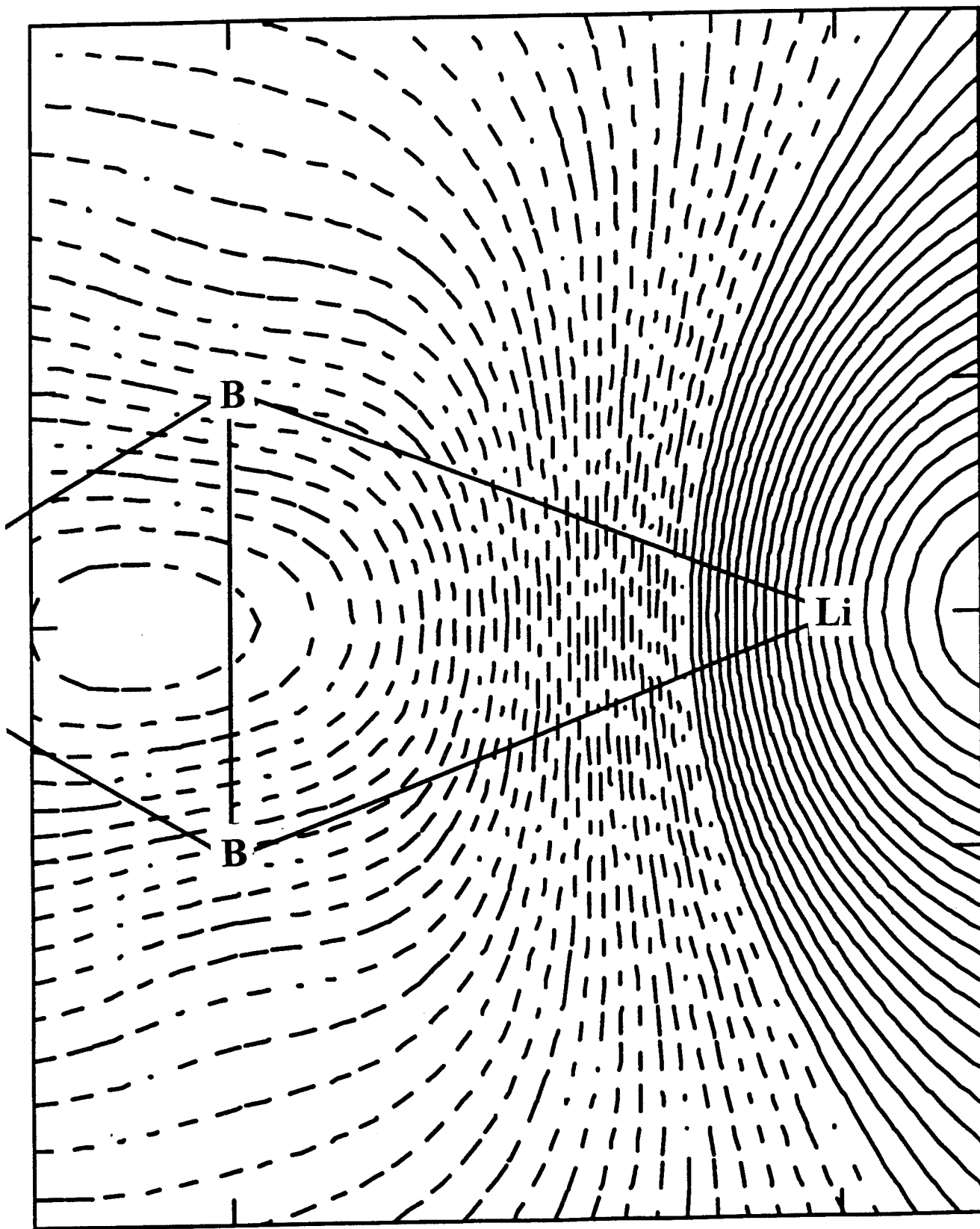
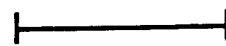


Figure 2

MCSCF(8e,8o)/6-31G(d) Li2B2

1A1 total density

DENDIF

ONE BOHR IS

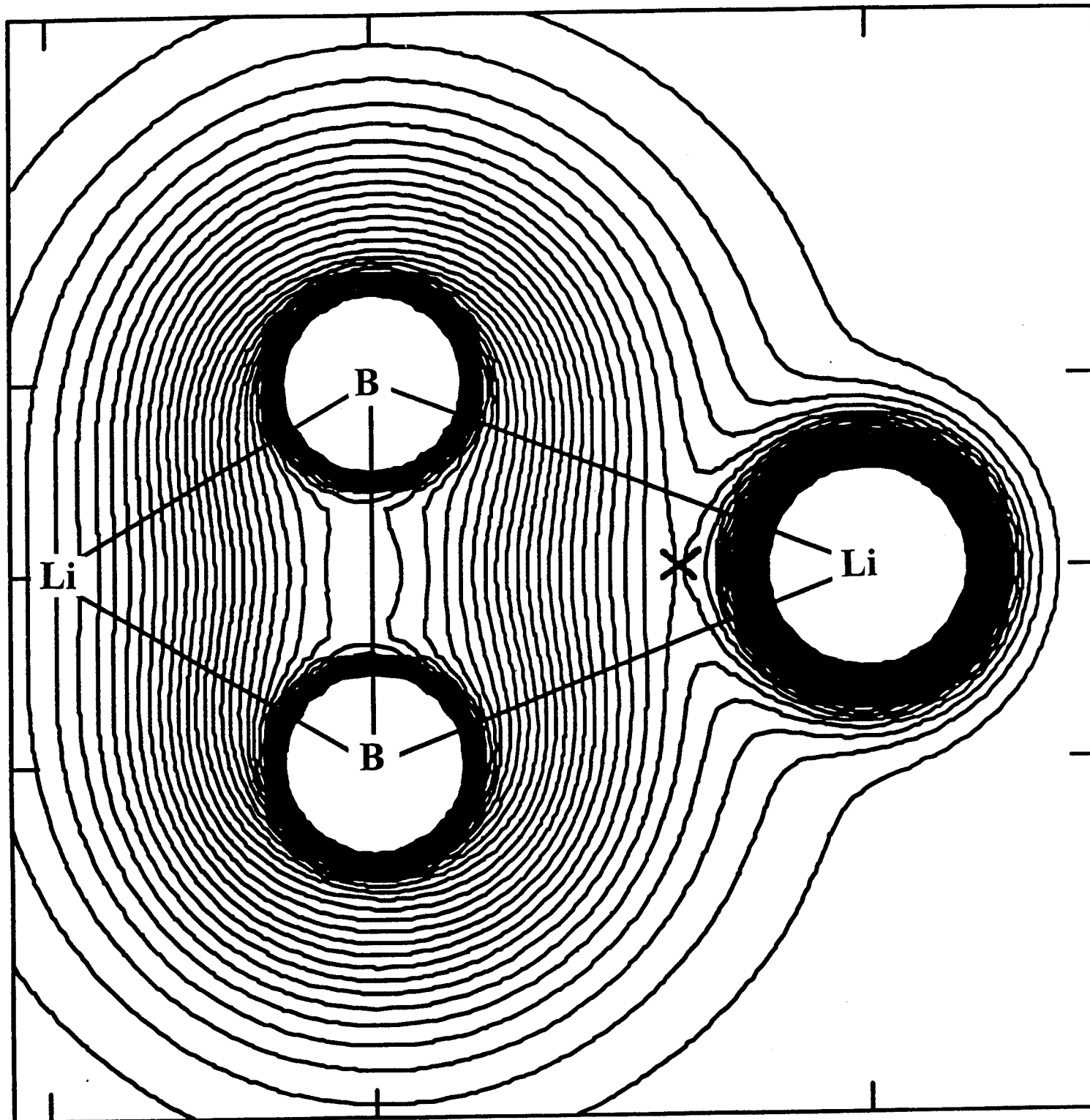


Figure 3

227

HIGH ENERGY DENSITY MATTER CONTRACTORS CONFERENCE  
North Lake Tahoe, NV 5 to 7 June, 1994

**Prediction of "Triplet" Absorption Lineshape for Na Atoms in Liquid Ar**

Mario E. Fajardo and Jerry Boatz

Emerging Technologies Branch, Propulsion Directorate, Phillips Laboratory  
(OLAC PL/RKFE Bldg. 8451, Edwards AFB, CA 93524-7680)

**ABSTRACT**

We are in the process of performing Monte Carlo based simulations of the absorption spectra of alkali atoms in disordered condensed phase systems. Preliminary results from simulations of Na atoms in liquid Ar have yielded a "triplet" (i.e. three peaks) absorption lineshape, however with much broader and more widely split peaks than those observed in matrix isolation studies. We discuss our results in the context provided by recent experimental work on Li atoms trapped in mixed Ar/Xe matrices<sup>1</sup>, and on metal atoms in superfluid liquid helium<sup>2-5</sup>.

1. R.A. Corbin and M.E. Fajardo, J. Chem. Phys. 101, 2678 (1994).
2. H. Bauer, M. Beau, A. Bernhardt, B. Friedl, and H.J. Reyher, Phys. Lett. A 137, 217 (1989).
3. G. zu Putlitz and M.R. Beau, in Topics in Applied Physics, Vol. 70, ed. M. Stuke (Springer-Verlag, Berlin, 1992).
4. Y. Takahashi, K. Sano, T. Kinoshita, and T. Yabuzaki, Phys. Rev. Lett. 71, 1035 (1993).
5. Y. Takahashi, K. Sano, T. Kinoshita, and T. Yabuzaki, Phys. Rev. Lett. 71, 1039 (1993).

**NO SEPARATE ABSTRACT WAS SUBMITTED FOR THIS PRESENTATION.  
PLEASE SEE SHORT DISCUSSION IN THE PAPER ENTITLED:**

**"Progress on Atom Doped Cryogenic Solid Propellants"**

Mario E. Fajardo, Simon Tam, Jerry Boatz, Michelle Cordonnier, Tim Thompson, and  
Michel Macler (NRC Research Associate)

**ELSEWHERE IN THESE PROCEEDINGS.**

# THEORETICAL METHODS FOR CRYOGENICALLY TRAPPED METAL RADICAL SPECTRA<sup>†</sup>

P. W. Langhoff

Department of Chemistry  
Indiana University  
Bloomington, IN 47405-4001

and

J. Boatz & M. E. Fajardo

Emerging Technology Branch  
Phillips Laboratory - OLAC PL/RKFE  
Edwards AFB, CA 93524-7680

## ABSTRACT

A formally complete solution is provided to the problem of constructing adiabatic electronic potential energy surfaces for a single metal radical perturbed by  $N$  rare gas atoms employing individual metal-rare gas pair information and the pair-wise-additive nature of the full Hamiltonian operator. The potential surfaces are obtained from diagonalization of a sum of matrices of the form

$$\mathbf{V}^{(A)}(R, \phi, \theta) = \mathbf{R}(\phi, \theta)^\dagger \cdot \mathbf{U}(R)^\dagger \cdot \mathbf{V}^{(D)}(R) \cdot \mathbf{U}(R) \cdot \mathbf{R}(\phi, \theta),$$

where  $(R, \phi, \theta)$  gives the position of any individual rare-gas atom perturber,  $\mathbf{V}^{(D)}(R)$  is the diagonal matrix of pair potentials,  $\mathbf{R}(\phi, \theta)$  is comprised of rotation matrices, and  $\mathbf{U}(R)$  is the unitary transform from atomic to molecular eigenstates. Applications are described for dilute Na radicals trapped in Ar cryogenic matrices, in which case appropriate pair-potential and related theoretical and experimental information is available. The development is seen to incorporate metal-radical charge distortions corresponding to mixing of spectroscopically active states, providing realistic potential surfaces in the angles and radial distances of rare-gas perturbers from the metal radical. In this way significant angle-dependent blue shifts of absorption lines and band centroids are obtained from the present development, in contrast to the predictions of perturbation methods. The latter results are obtained from the present development in the limit of negligible mixing between spectroscopically active radical states.

## 1. Introduction

Adiabatic electronic potential energy surfaces are required in predictions of the optical spectra and other attributes of metal radicals trapped in rare-gas cryogenic matrices [1-3]. Perturbation approximations [4-6] to  $N$ -body metal-rare gas potential surfaces based on individual pair potentials and related information [7,8] can provide useful first approximations in computational simulations of such optical absorption spectra [9]. These studies are of largely qualitative value in the absence of incorporation of the spatial distortions of the spectroscopically active radical states due to the perturbing  $N$ -body rare-gas matrix in which they are trapped [10]. It would be useful to devise non-perturbative methods for construction of  $N$ -body potential surfaces which incorporate the correct spectroscopic state mixings employing only individual metal-rare gas pair potentials and related theoretical or experimental pair information. A parameter-free method of this nature is reported here which employs only pair-wise atomic interactions in Hamiltonian matrix form. Since the full Hamiltonian operator is exactly pair-wise in the atomic interactions, the method is in principle exact [11], although it is implemented in an approximate form in the present application. The development is shown to reduce to familiar perturbation approximations in the appropriate limit [4-6].

<sup>†</sup> Work supported in part by AFOSR through Research and Development Laboratories, Inc.

Let the column vector  $\Phi$  represent the molecular electronic eigenstates ordered in accordance with increasing asymptotic ( $R \rightarrow \infty$ ) energy and conventional spectroscopic notation;  $\Phi = (X^2\Sigma, A^2\Pi_{+1}, B^2\Sigma, A^2\Pi_{-1}, \dots)$ , and let  $V^D(R)$  be the (diagonal) adiabatic electronic potential energy curve matrix in this basis [see Eq. (1)]. Let the column vector  $\Psi$  represent the corresponding atomic-product electronic eigenstates ordered in accordance with increasing energy and conventional spectroscopic notation;  $\Psi = (3^1S, 4^1S, 4^1P, \dots) \otimes (3^2S, 3^2P_{+1}, 3^2P_0, 3^2P_{-1}, 4^2S, 4^2P_{+1}, 4^2P_0, 4^2P_{-1}, 3^2D_{+2}, \dots)$ . The atomic and molecular eigenstates are related by the transformation

$$\Phi = U(R) \cdot \Psi, \quad (2)$$

where, as indicated,  $[U(R)]_{i,j} = \langle \Psi_i | \Phi_j \rangle$  depends only upon the distance of the rare-gas perturber from the metal radical (see left side of Figure 1). The adiabatic electronic potential energy curve matrix in the atomic-product eigenbasis is given by the expression

$$V^{(A)}(R) = U(R)^\dagger \cdot V^{(D)}(R) \cdot U(R), \quad (3)$$

where  $V^{(D)}(R)$  is the diagonal potential energy curve matrix in the molecular eigenbasis,  $V^{(A)}(R)$  is the corresponding non-diagonal matrix in the atomic-product eigenbasis, and  $U(R)^\dagger$  is the adjoint of  $U(R)$ . The specific form and construction of the matrix  $U(R)$  is described in the implementation section below.

The adiabatic electronic potential energy curve matrix for the M-Rg configuration shown on the right in Figure 1 is obtained from Eq. (3) by applying a rotation matrix  $R(\phi, \theta)$  in the form

$$\begin{aligned} V^{(A)}(R, \phi, \theta) &= R(\phi, \theta)^\dagger \cdot V^{(A)}(R) \cdot R(\phi, \theta), \\ &= R(\phi, \theta)^\dagger \cdot U(R)^\dagger \cdot V^{(D)}(R) \cdot U(R) \cdot R(\phi, \theta). \end{aligned} \quad (4)$$

Here, the matrix  $R(\phi, \theta)$  is a direct product of rotation matrices for the metal and rare gas spectroscopic eigenstates

$$R(\phi, \theta) = D^{(M)}(\phi, \theta, 0) \otimes D^{(Rg)}(\phi, \theta, 0), \quad (5)$$

where the individual matrices  $D^{(M)}$  and  $D^{(Rg)}$  are block diagonal, having rotation matrices [12] of appropriate angular momentum values along the diagonal, arranged in accordance with the ordering of the atomic product eigenbasis indicated above.

Finally, the  $(N+1)$ -body adiabatic electronic potential surface matrix for a single metal radical interacting with  $N$  rare-gas perturbers is given by

$$H^{(A)}(\mathbf{R}) = E^{(D)} + \sum_{k=1}^N \{V^{(A)}(R_k, \phi_k, \theta_k) - E_k^{(D)}\}, \quad (6)$$

where  $E^{(D)} [= H^{(A)}(\mathbf{R} \rightarrow \infty)]$  is a diagonal matrix of atomic energies and  $E_k^{(D)} [= V^{(A)}(R_k \rightarrow \infty, \phi_k, \theta_k)]$  is a corresponding diagonal matrix of atomic energies for the M-Rg<sub>k</sub> pair interaction.

#### 4. Perturbation Theory Limit

Although the forgoing results are formally exact and the development can be implemented computationally as given, it is convenient to describe its application in terms of information currently available in the literature [7,8]. Accordingly, the approach is illustrated in the case of Na-Ar interactions depicted in Figure 2, considering first the perturbation theory limit [4-6].

The perturbation theory limit in the case of Na-Ar interactions is obtained by (i) restricting the rare-gas atomic states contributing to the development to the  $^1S$  ground state, since the first excited Ar state is

$\approx 93,140 \text{ cm}^{-1}$  above the ground state [15], and (ii) setting the metal-radical spectroscopic state mixing inherent in the  $U(R)$  matrix to zero [ $U(R) \rightarrow I$ ]. In this case, Eq. (4) takes the form

$$V^{(A)}(R, \phi, \theta) = \mathbf{R}(\phi, \theta)^\dagger \cdot \mathbf{V}^{(D)}(R) \cdot \mathbf{R}(\phi, \theta). \quad (7)$$

where

$$\mathbf{R}(\phi, \theta) = \mathbf{D}^{(M)}(\phi, \theta, 0), \quad (8)$$

with Eq. (6) giving the full interaction matrix.

Since the rotation matrix of Eq. (8) is block diagonal, it is instructive to write out Eq. (7) for specific states to clarify its equivalence with perturbation theory developments [4-6].

For the ground-state ( $3^2S - X^2\Sigma$ ) Na-Ar interaction (Figure 2.), Eqs. (7) and (8) give

$$V_{3^2S}^{(A)}(R, \phi, \theta) = \mathbf{D}^{(0)}(\phi, \theta, 0)^\dagger \cdot \mathbf{V}_X^{(D)}(R) \cdot \mathbf{D}^{(0)}(\phi, \theta, 0), \quad (9)$$

or, simply,

$$V_{3^2S}^{(A)}(R) = V_X^{(D)}(R). \quad (10)$$

The ground-state potential surface in this case is obtained from Eq. (6) in the form

$$E_{3^2S}^{(A)}(\mathbf{R}) = E_{3^2S}^{(Na)} + N E_g^{(Ar)} + \sum_{k=1}^N \{V_X^{(D)}(R_k) - (E_{3^2S}^{(Na)} + E_g^{(Ar)})\}, \quad (11)$$

where, as indicated above, the Ar-Ar interaction energies are not included [11]. Evidently, there is no angular ( $\phi_k, \theta_k$ ) dependence in this case, corresponding to the neglect of atomic metal-radical state mixing inherent in the perturbation theory approximation.

In the case of the  $3^2P - A^2\Pi, B^2\Sigma$  Na-Ar interaction manifold (Figure 2.), Eqs. (7) and (8) give

$$V_{3^2P}^{(A)}(R, \phi, \theta) = \mathbf{D}^{(1)}(\phi, \theta, 0)^\dagger \cdot \mathbf{V}_{A,B}^{(D)}(R) \cdot \mathbf{D}^{(1)}(\phi, \theta, 0), \quad (12)$$

where  $\mathbf{D}^{(1)}(\phi, \theta, 0)$  is the familiar  $L=1$  rotation matrix [12]

$$[\mathbf{D}^{(1)}(\phi, \theta, 0)]_{M',M} = D_{M',M}^{(1)}(\phi, \theta, 0), \quad (13)$$

and  $\mathbf{V}_{A,B}^{(D)}(R)$  is the diagonal  $3 \times 3$   $A^2\Pi, B^2\Sigma$  M-Rg electronic energy matrix (Figure 2.). The  $3 \times 3$  adiabatic electronic energy surface matrix in this case is obtained from Eq. (6) in the form

$$E_{3^2P}(\mathbf{R}) = (E_{3^2P}^{(Na)} + N E_g^{(Ar)})\mathbf{I} + \sum_{k=1}^N \{V_{3^2P}^{(A)}(\mathbf{R}_k) - (E_{3^2P}^{(Na)} + E_g^{(Ar)})\mathbf{I}\}. \quad (14)$$

The equivalence of Eq. (14) with previously described perturbation theory results [4-6] is established by direct matrix multiplication or use of the D-matrix addition theorem [12].

Evidently, the eigenvalue surfaces in the case of Eq. (14) will depend upon the angular arrangement of rare-gas perturbers about the metal radical. However, since the ground-state surface [Eq. (11)] is independent of these angles, and the diagonal sum [ $V_\Sigma(R) + 2V_\Pi(R)$ ] of the matrix of Eq. (12) is also independent of angles, the centroid of the perturbed  $3^2S \rightarrow 3^2P$  absorption band predicted by the perturbation theory development will also be independent of the angular arrangement of rare-gas perturbers [9].



## 5. Non-Perturbative Illustration

As an illustration of the general development, the effects of configuration mixing between the ground  $3^2S$  and excited  $3^2P_0$  states of atomic Na perturbed by Ar atoms on the four lowest-lying adiabatic electronic potential energy surfaces is described here. These results are obtained by (i) restricting the rare-gas atomic states contributing to the development to the ground  $1S$  state, (ii) setting  $U(R) \rightarrow I$  everywhere except for the  $2 \times 2$  unitary matrix describing the atomic eigenstate mixing, and (iii) estimating the  $3^2S - 3^2P_0$  mixing coefficients in the ground  $X^2\Sigma$  and excited  $B^2\Sigma$  states from the calculated ground-state dipole moment function and the  $X \rightarrow B$  dipole transition moment function [7,8], as described below.

Of course, the foregoing approximations neglect a number of important effects in the interaction between metal radical and rare-gas perturbers, but nevertheless help to clarify the additional features of the new development not incorporated in the perturbation theory limit. A more complete description of the development is reported separately elsewhere [11].

With the above assumptions, Eq. (4) takes the form of a  $4 \times 4$  matrix

$$V^{(A)}(R, \phi, \theta) = \begin{pmatrix} V_{aa} & V_{ab} \\ V_{ba} & V_{bb} \end{pmatrix} \quad (15)$$

where the indicated  $1 \times 1$ ,  $1 \times 3$ ,  $3 \times 1$ , and  $3 \times 3$  matrices are

$$V_{aa} = D^{(0)}(\phi, \theta, 0)^\dagger \cdot V_{11}(R) \cdot D^{(0)}(\phi, \theta, 0) \quad (16a)$$

$$V_{ab} = D^{(0)}(\phi, \theta, 0)^\dagger \cdot V_{12}(R) \cdot D^{(1)}(\phi, \theta, 0) \quad (16b)$$

$$V_{ba} = D^{(1)}(\phi, \theta, 0)^\dagger \cdot V_{21}(R) \cdot D^{(0)}(\phi, \theta, 0) \quad (16c)$$

$$V_{bb} = D^{(1)}(\phi, \theta, 0)^\dagger \cdot V_{22}(R) \cdot D^{(1)}(\phi, \theta, 0), \quad (16d)$$

respectively, and where

$$V_{11}(R) = a(R)^2 V_X(R) + b(R)^2 V_B(R) \quad (17a)$$

$$V_{12}(R) = (0, \quad a(R)b(R)\{V_X(R) - V_B(R)\}, \quad 0) \quad (17b)$$

$$V_{21}(R) = V_{12}(R)^\dagger \quad (17c)$$

$$V_{22}(R) = \begin{pmatrix} V_{\Pi}(R) & 0 & 0 \\ 0 & a(R)^2 V_B(R) + b(R)^2 V_X(R) & 0 \\ 0 & 0 & V_{\Pi}(R) \end{pmatrix}. \quad (17d)$$

Here, the mixing coefficients  $a(R)$  and  $b(R)$  are given by

$$a(R) = [1 - b(R)^2]^{1/2}, \quad (18a)$$

$$a(R)b(R) = \mu_X(R)/2\mu_{X \rightarrow B}(R \rightarrow \infty), \quad (18b)$$

where  $\mu_X(R)$  is the calculated molecular ground-state dipole moment function, and  $\mu_{X \rightarrow B}(R \rightarrow \infty)$  is the  $X \rightarrow B$  transition dipole moment evaluated in the indicated asymptotic limit [7,8]. Note that  $b(R)$  varies from  $\approx 0.15$  to zero in the interval  $R \approx 5 a_0$  to  $\infty$  [7,8]. Accordingly, the effect of the configuration mixing in this case is small but not negligible.

It is convenient to represent the eigenvalue surfaces obtained from Eqs. (6) and (15) to (18) in terms of optical potentials using matrix partitionings [16]. For the ground-state surface Eqs. (6) and (15) to (18) give

$$E_g(\mathbf{R}) = E_{3^2S}^{(Na)} + NE_g^{(Ar)} + \sum_{k=1}^N \{a(R_k)^2 V_X(R_k) + b(R_k)^2 V_B(R_k) - (E_{3^2S}^{(Na)} + E_g^{(Ar)})\} +$$

$$\left\{ \sum_{k=1}^N V_{ab}(\mathbf{R}_k) \right\} \cdot \left\{ (E_g(\mathbf{R}) - E_{3^2P}^{(Na)} - NE_g^{(Ar)}) \mathbf{I}_{bb} - \sum_{m=1}^N \{V_{bb}(\mathbf{R}_m) - (E_{3^2P}^{(Na)} + E_g^{(Ar)}) \mathbf{I}_{bb}\} \right\}^{-1} \cdot \left\{ \sum_{k'=1}^N V_{ba}(\mathbf{R}_{k'}) \right\}. \quad (19a)$$

It is seen the ground-state potential surface is given by the perturbation theory term [Eq. (11), using  $a(R) > b(R)$ ] and a correction term involving the strength of the atomic state mixing [Eqs. (16b) and (17b)], which can be as large as  $\approx 150 \text{ cm}^{-1}$  per rare-gas perturber in the R interval of interest [9]. The angular dependence of the correction term, which predicts a caging-like effect missing in the perturbation theory limit [4-6], is displayed explicitly by an approximation to Eq. (19b) of the form

$$E_g(\mathbf{R}) \approx E_{3^2S}^{(Na)} + NE_g^{(Ar)} + \sum_{k=1}^N \{a(R_k)^2 V_X(R_k) + b(R_k)^2 V_B(R_k) - (E_{3^2S}^{(Na)} + E_g^{(Ar)})\}$$

$$+ \frac{1}{\{E_{3^2S}^{(Na)} - E_{3^2P}^{(Na)}\}} \sum_{k=1}^N \sum_{k'=1}^N (k > k') V_{12}(R_k) V_{12}(R_{k'}) \cos(\hat{\mathbf{R}}_k \cdot \hat{\mathbf{R}}_{k'}), \quad (19b)$$

where  $V_{12}(R_k)$  is the non-zero element of the matrix  $\mathbf{V}_{12}(R_k)$  [Eq. (17b)], and  $\hat{\mathbf{R}}_k$  and  $\hat{\mathbf{R}}_{k'}$  are unit vectors in the direction of  $\mathbf{R}_k$  and  $\mathbf{R}_{k'}$ , respectively.

The  $3^2P$  manifold adiabatic electronic energy surfaces [ $E_I(\mathbf{R})$ ,  $I=1,2,3$ ] are the eigenvalues of the 3x3 matrix

$$\mathbf{H}_{3^2P}^{(A)}(\mathbf{R}) = (E_{3^2P}^{(Na)} + NE_g^{(Ar)}) \mathbf{I}_{bb} + \sum_{k=1}^N \{V_{bb}(\mathbf{R}) - (E_{3^2P}^{(Na)} + E_g^{(Ar)}) \mathbf{I}_{bb}\} +$$

$$\left\{ \sum_{k=1}^N V_{ba}(\mathbf{R}_k) \right\} \cdot \left\{ (E_I(\mathbf{R}) - E_{3^2S}^{(Na)} - NE_g^{(Ar)} - \sum_{m=1}^N \{V_{aa}(\mathbf{R}_m) - E_{3^2S}^{(Na)} - E_g^{(Ar)}\}) \right\}^{-1} \cdot \left\{ \sum_{k'=1}^N V_{ab}(\mathbf{R}_{k'}) \right\}. \quad (20a)$$

The three roots of Eq. (20a) are evidently given by the perturbation theory matrix of Eq. (14) and the indicated angular-dependent correction terms. Note that even though there is no explicit configuration mixing of the  $3^2P_{+1}$  and  $3^2P_{-1}$  atomic eigenstates with other levels, the rotation matrices bring the  $3^2S - 3^2P_0$  mixing into the  $3^2P_{+1,-1}$  manifold. Accordingly, there are additional angular dependences not present in the perturbation theory limit. Since the magnitude of the additional terms is  $\approx 150 \text{ cm}^{-1}$  per rare-gas perturber in the R interval of interest [7,8], and the ground and excited surfaces repel one another, angular-dependent band-centroid blue shifts of the order of  $\approx 300 \text{ cm}^{-1}$  per rare-gas perturber are possible in the R interval of interest on basis of the present development.

Computationally useful approximations to the three excited-state potential surfaces [ $E_I(\mathbf{R})$ ] are obtained from Eq. (20a) in the form

$$\mathbf{H}_{3^2P}^{(A)}(\mathbf{R}) \approx (E_{3^2P}^{(Na)} + NE_g^{(Ar)}) \mathbf{I}_{bb} + \sum_{k=1}^N \{V_{bb}(\mathbf{R}) - (E_{3^2P}^{(Na)} + E_g^{(Ar)}) \mathbf{I}_{bb}\}$$

$$+ \frac{1}{\{E_{3^2P}^{(Na)} - E_{3^2S}^{(Na)}\}} \left\{ \sum_{k=1}^N V_{ba}(\mathbf{R}_k) \right\} \cdot \left\{ \sum_{k'=1}^N V_{ab}(\mathbf{R}_{k'}) \right\}. \quad (20b)$$

## 6. Concluding Remarks

A formally exact generalization of perturbation theory methods [4-6] is described for calculations of the optical spectra of metal radicals trapped in low-temperature rare gas matrices [1-3]. The development uses only metal-rare gas pair information, which can be obtained from quantum mechanical calculations supplemented by available experimental data. Accordingly, there are points of similarity between the present results and early semi-empirical procedures that introduce experimental atomic or pair energies into potential energy surface determinations [13,14]. In contrast to these semi-empirical procedures, which appear to be based formally on use of an over-complete atomic basis [14], the present development is rigorous, unambiguous, and free of arbitrary parameters when sufficient pair information is available.

Preliminary implementation of the method in the case of Na-Ar pairs indicates more realistic many-body adiabatic electronic potential energy surfaces are obtained than in the perturbation theory limit. Specifically, the optically active potential energy surfaces obtained are seen to include additional terms and dependences involving the angular arrangement of rare-gas perturbers around the metal radical which are not present in the perturbation theory limit. Accordingly, larger blue shifts are obtained from the present development for individual  $3^2S \rightarrow 3^2P$  transitions, and band centroid shifts are seen to depend upon the angular arrangement of perturbers, in contrast to the perturbation limit results [9]. Computational simulations of trapped radical spectra employing the new approach for constructing adiabatic electronic potential energy surfaces are reported separately.

## Acknowledgments

We thank AFOSR for support of PWL provided under the auspices of the Research Associates Program, Phillips Laboratory, Edwards AFB, administered by Research and Development Laboratories, Inc.

## References

- [1] M.E. Fajardo, P.G. Carrick, and J.W. Kenney, *J. Chem. Phys.* **94**, 5812 (1991).
- [2] M.E. Fajardo, *J. Chem. Phys.* **98**, 110 (1993).
- [3] S. Tam and M.E. Fajardo, *J. Chem. Phys.* **99**, 854 (1993).
- [4] W.E. Baylis, *J. Phys. B* **10**, L477 (1977).
- [5] K.M. Sando, G.J. Erickson, and R.C. Binning, *J. Phys. B* **12**, 2697 (1979).
- [6] L.C. Balling and J.J. Wright, *J. Chem. Phys.* **79**, 2941 (1983).
- [7] R.P. Saxon, R.E. Olson, and B. Liu, *J. Chem. Phys.* **67**, 2692 (1977).
- [8] B.C. Laskowski, S.R. Langhoff, and J.R. Stallcop, *J. Chem. Phys.* **75**, (1981).
- [9] J.A. Boatz and M.E. Fajardo, *J. Chem. Phys.* (to be published).
- [10] C. Tsou, D.A. Estrin, and S.J. Singer, *J. Chem. Phys.* **93**, 7187 (1990).
- [11] P.W. Langhoff, *Chem. Phys. Letters* (to be published).
- [12] A.R. Edmonds, *Angular Momentum in Quantum Mechanics* (Princeton, NJ, 1957).
- [13] W. Moffit, *Proc. Roy. Soc. (Lond.)* **A210**, 245 (1951).
- [14] J.C. Tully in, *Modern Theoretical Chemistry*, Edited by G.A. Segal, (Plenum, NY, 1977), Vol. 7. pp 173-200.
- [15] C.E. Moore, *Atomic Energy Levels, I*, Circular 467 (NBS, US Government Printing Office Washington, DC, 1949).
- [16] M.R. Hermann and P.W. Langhoff, *Int. J. Quantum Chem.* **23**, 135 (1983).

## 2. Statement of Problem

Given the adiabatic electronic potential energy curves for metal-rare gas pair interactions

$$V_i(R) = \langle \Phi_i | H | \Phi_i \rangle, i = 1, 2, \dots, \quad (1)$$

where the  $\Phi_i$  are corresponding molecular eigenfunctions in cylindrical ( $C_{\infty v}$ ) symmetry and  $H$  is the total molecular Hamiltonian in adiabatic approximation, determine the  $(N+1)$ -body adiabatic electronic potential energy surfaces  $E_I(\mathbf{R})$ , ( $I=1,2,\dots$ ), where  $\mathbf{R} = (R_1, R_2, \dots, R_N)$  specifies the positions of  $N$  rare-gas (Rg) perturber atoms relative to a single metal radical  $M$  (Figure 1). Additional information from the eigenstates  $\Phi_i$ , such as molecular dipole or transition moments, may also be available and should be incorporated in the development in so far as is possible.

## 3. Formal Solution

It is useful as a specific example to refer to the calculated adiabatic electronic potential curves for Na-Ar pairs depicted in Figure 2 [7,8], although the development given here applies generally to optically active radicals weakly perturbed by non-bonding host-lattice rare-gas atoms. In the following, the molecular electronic eigenstates  $\Phi_i$  quantized in the coordinate frame on the left of Figure 1 will be represented in terms of the spectroscopic atomic eigenstates  $\Psi_j$  of the metal radical and rare-gas atom comprising the diatomic pair, the two sets of orthonormal complete states ( $\Phi$ ,  $\Psi$ ) being connected by a unitary transformation matrix  $U(R)$ . The atomic eigenstates can be related to a corresponding atomic set quantized along a  $z$ -axis having angles  $\theta$ ,  $\phi$  as indicated on the right in Figure 1, employing a rotation matrix  $R(\phi, \theta)$  [12]. Application of the two transformation matrices  $U(R)$  and  $R(\phi, \theta)$  to the initially diagonal adiabatic electronic potential energy curve matrix provides the corresponding matrix for the interaction of a single rare-gas atom with a metal radical as on the right in Figure 1. Summation over all such atoms at positions  $R_k$ ,  $\phi_k$ ,  $\theta_k$  gives the  $(N+1)$ -body adiabatic electronic potential energy surface matrix, which must be diagonalized to obtain the appropriate eigenvalues. The Rg-Rg interaction terms are not included here, although they can be incorporated into the formalism, in which event the present development becomes formally exact [11,13,14].

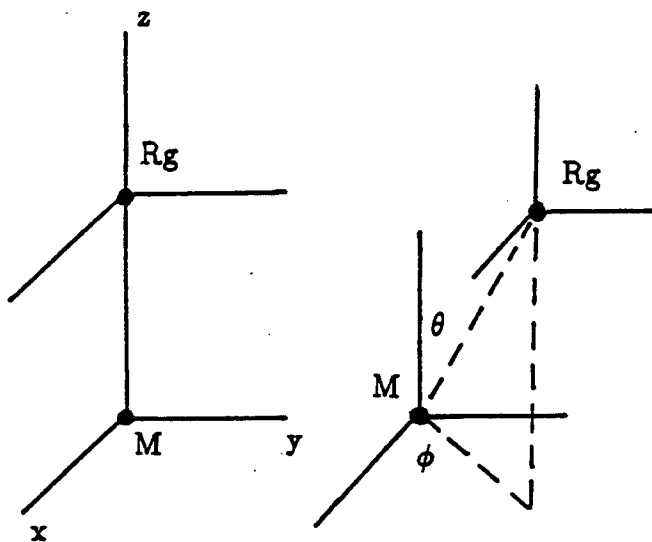


Figure 1. Metal-radical (M) rare-gas perturber (Rg) pairs arranged (left) along the  $z$ -axis and (right) along an axis at the indicated angles ( $\phi, \theta$ ).

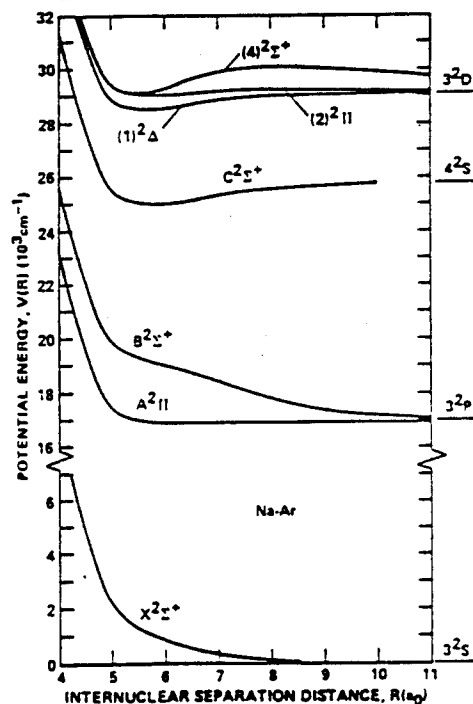


Figure 2. Calculated adiabatic electronic potential energy curves for Na-Ar pairs having asymptotic ( $R \rightarrow \infty$ ) limits as indicated [7,8].

## Optical Spectroscopy and Photochemistry of Atoms in Solid Molecular Hydrogen

William C. Stwalley and John T. Bahns, Department of Physics and Institute of Materials Science, University of Connecticut, Storrs, CT 06269-3046

We hope in the near future to begin studies of the two-photon ultraviolet absorption spectroscopy of solid molecular hydrogen. Tunable ultraviolet (~180-210 nm) light will be generated to two-photon excite  $H_2(s)$  to the E,F  $1\Sigma_g^+$  state (which in the gas phase occurs at ~202 nm). Infrared fluorescence E,F  $1\Sigma_g^+ \rightarrow B^1\Sigma_u^+$  will be detected near 1.1  $\mu m$ . Unlike the single photon VUV  $H_2(s)$  absorption, where vibrational but not rotational structure can be observed because of dipole broadening, the two-photon excitation spectrum is expected to be sufficiently narrow that individual vibrational-rotational levels can be detected. Thus ortho/para concentration ratios and temperatures can then be estimated. The linewidths and shifts may also indicate crystal structure and quality. If such studies are successful with pure  $H_2(s)$ , impurity (e.g. Li, B) doped  $H_2(s)$  will subsequently be studied. Of particular interest are photochemical cycles for preparation of doped  $H_2(s)$  samples with high energy content.

# OPTICAL ABSORPTION, EMISSION, AND RADIATION TRAPPING IN HIGH-TEMPERATURE METAL VAPORS†

J. D. Mills, C. W. Larson  
Emerging Technology Branch  
Phillips Laboratory - OLAC PL/RKFE  
Edwards AFB, CA 93524-7680

and

P. S. Erdman, W. C. Stwalley  
Department of Physics  
University of Connecticut  
Storrs, CT 06269-3046

and

P.W. Langhoff  
Department of Chemistry  
Indiana University  
Bloomington, IN 47405-4001

## ABSTRACT

Theoretical and computational studies are reported in support of optical absorption and emission measurements performed on buffered lithium, sodium, and aluminum vapors in a high-temperature ( $\approx 2,000\text{K}$ ) spectroscopic cell designed for this purpose. Emphasis is placed on production of metal seedants for high-energy-density cryogenic propellants and on precise determinations of the radiative properties of metal vapors for applications in high-temperature solar-power-conversion devices. A comprehensive state-to-state quantum and statistical mechanical treatment of atoms (Li, Al) and diatoms ( $\text{Li}_2$ ,  $\text{Al}_2$ , ...) which incorporates available spectroscopic and quantum-chemical data is used to calculate the vibrationally and rotationally rich one-photon absorption cross sections at high resolution in the visible spectrum. Absorption and emission profiles are derived appropriate to both uniform and nonuniform gaseous samples under a variety of thermodynamic and associated spectral lineshape conditions, ranging from optically thin to thick circumstances. Detailed comparisons with measured values emphasize the critical importance of lineshapes and radiative trapping effects in accounting for the emission spectra from optically thick gases. Diagnostic uses of the calculated optical profiles in characterizing completely the temperature conditions and the coupled mass and energy flow in the spectroscopy cell employed are also reported.

## 1. Introduction

Production of doped, cryogenic solid fuels might proceed via the corresponding high-temperature vapors. A means of predicting the optical characteristics of equilibrium mixtures of buffered metals is briefly outlined. Not only does this assist in characterizing the conditions within a current prototype apparatus, but it allows insight into the relative importance of the various transport and radiative processes determinative of the performance of these entrained high-energy species as absorbing seedants in solar-power-conversion devices.

## 2. Experimental

The Plasma Spectroscopy Cell, described extensively elsewhere,<sup>1</sup> allows spectroscopic interrogation of slowly flowing, laminar jets of equilibrated rare-gas- or hydrogen-buffered metal vapors at high temperatures (up to 2000K) and elevated pressures (up to 100 atm). Coupled with a detector array, this instrument has been used to obtain spatially resolved absorption and emission spectra, examples of which will be displayed subsequently (e.g. Figures 3 and 9).

† Work supported by AFOSR through RDL, Inc. and the Air Force Palace Knight Program.

### 3. Theoretical Modeling of Absorption in the Li/Li<sub>2</sub> System

The absolute optical transmission of a spatially uniform sample can be expressed in terms of the energy-dependent absorption coefficient,  $k(E)$ , the per atom or molecule absorption cross section,  $\sigma_q(E)$ , and the number density of each specie,  $(\frac{N}{V})_q$ , by:

$$\frac{I(E)}{I_0(E)} \equiv T(E) = e^{-k(E)\Delta x}$$

$$k(E) = \sum_{\text{species } q} \sigma_q(E) \left(\frac{N}{V}\right)_q.$$

#### a. Absorption by Atoms

The atomic absorption cross section is given in an explicit sum over transitions between initial, I, and final, F, levels by the oscillator strengths, temperature-dependent fractional state populations, and line shape functions,  $\phi_{IF}(E)$ , centered at the transition energies, according to:

$$\sigma_q(E) = \frac{2\pi^2 e^2 \hbar}{mc} \sum_{I,F} f_{IF} \frac{(\frac{N}{V})_I}{(\frac{N}{V})_q} \phi_{IF}(E).$$

Published values of transition energies<sup>2</sup> and strengths<sup>3</sup> allow modeling of the main atomic feature of the experimental spectra, that due to the  $2s \rightarrow 2p$  resonance transition, in addition to the other transitions apparent in the higher temperature atomic transmission displayed in Figure 1.

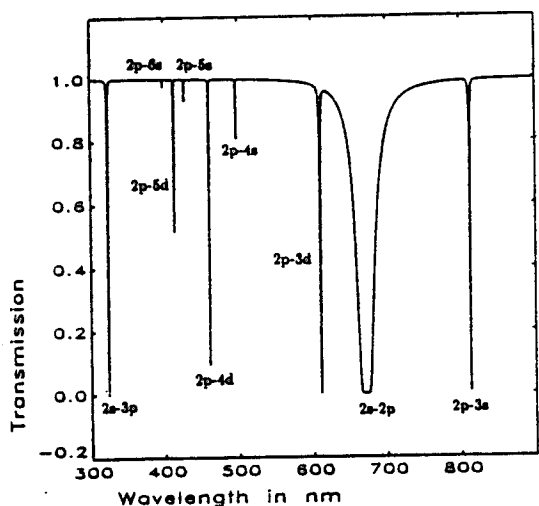


Figure 1—Model absorption by lithium atoms at a temperature of 3000K with number density,  $7.9 \times 10^{17} / \text{cm}^3$ , and pathlength,  $\Delta x = 3.5$  mm.

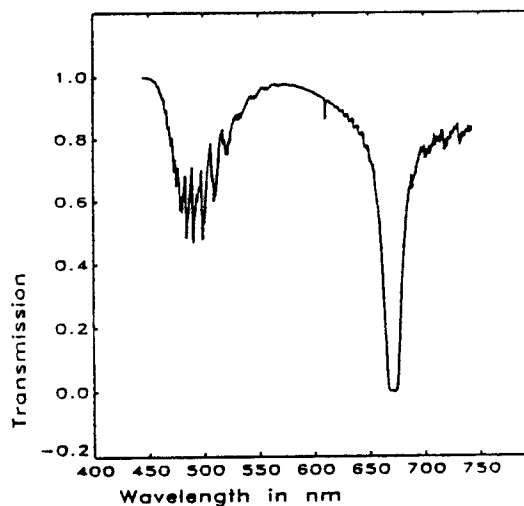


Figure 2—Rovibronic model spectrum of an equilibrated mixture of lithium atoms (at the same number density as in Figure 1) and diatoms at a temperature of 1703 K.

#### b. Absorption by Diatomic Molecules

A similar summation over the rovibronic levels of a diatomic absorber yields the per molecule absorption cross section:

$$\sigma_q(E) = \frac{2\pi^2 e^2 \hbar}{mc} \sum_{\epsilon_i, \epsilon_f} \bar{f}_{\epsilon_i \epsilon_f}^{\text{abs}} \sum_{v_i, v_f} \sum_{J_i, J_f} \chi_{v_i, J_i, v_f, J_f} \frac{E_{IF}}{\bar{E}_{\epsilon_i \epsilon_f}^{\text{abs}}} \xi_{J_i, J_f}^{\text{rot}} \frac{(\frac{N}{V})_I}{(\frac{N}{V})_q} \phi_{IF}(E)$$

in terms of effective electronic-band transition energies and strengths,  $\bar{E}_{\epsilon_i \epsilon_f}^{\text{abs}}$  and  $\bar{f}_{\epsilon_i \epsilon_f}^{\text{abs}}$ , relative rovibrational strengths (Franck-Condon factors or normalized, squared transition-dipole

matrix elements),  $\chi_{v,J_i,v_f,J_f}$ , normalized London-Hönl-type factors,  $\xi_{J_i J_f}^{\text{rot}}$ , fractional state populations, and lineshape functions. Calculated using the results of previous experimental and theoretical studies,<sup>4,5</sup> the spectroscopically rich diatomic contributions to a model spectrum for typical experimental conditions can be seen in Figure 2.

### c. Determination of Species Particle Densities

The partition functions which determine the equilibrium constant:

$$K_{\text{eq}} = \frac{\left(\frac{N}{V}\right)_{\text{Li}_2}}{\left[\left(\frac{N}{V}\right)_{\text{Li}}\right]^2} = \frac{\left(\frac{Q_{\text{Li}_2}}{V}\right)}{\left(\frac{Q_{\text{Li}}}{V}\right)^2}$$

are provided by a direct summation over atomic and molecular levels with the correct electronic, rotational, and nuclear spin degeneracy factors,  $g$ , as:

$$Q_{\text{Li}} = V \left( \frac{2\pi m_{\text{Li}} k_B T}{h^2} \right)^{\frac{3}{2}} \sum_{\mathbf{K}} g_{\mathbf{K}} e^{-E_{\mathbf{K}}/k_B T}$$

$$Q_{\text{Li}_2} = V \left( \frac{2\pi 2m_{\text{Li}} k_B T}{h^2} \right)^{\frac{3}{2}} \sum_{\epsilon_{\mathbf{K}} v_{\mathbf{K}} J_{\mathbf{K}}} g_{\epsilon_{\mathbf{K}}} g_{\mathbf{K}}^{\text{rot}} g_{\mathbf{K}}^{\text{ns}} e^{-E_{\mathbf{K}}/k_B T}$$

Mass conservation along the flow path of the apparatus from an evaporator containing equilibrated vapor and condensed phases then unambiguously fixes the particle densities of both atoms and diatoms in the observation region.

### d. Lineshapes and Widths

In this study atomic and diatomic transition profiles are represented by a simple phenomenological Voigt function:

$$\phi_{\text{IF}}(E) = \int_{-\infty}^{+\infty} \left[ \frac{1}{2\pi} \frac{\delta}{(E' - E_{\text{IF}})^2 + (\delta/2)^2} \right] \left[ \frac{2\sqrt{\ln 2}}{\gamma\sqrt{\pi}} e^{-(4\ln 2)(E - E')^2/\gamma^2} \right] dE'$$

in which the principal convolved Gaussian component represents the effects of instrumental resolution ( $\gamma = 0.5 \text{ nm}$  or  $8 - 30 \text{ cm}^{-1}$  depending on the transition energy) and the predominant Lorentzian contribution is due to pressure broadening. For lithium atoms under the present experimental conditions, both self-broadening and foreign-gas-broadening by the buffer contribute to the total width according to:

$$\delta_{\text{Li}} = C_{\text{Li-Li}} \left(\frac{N}{V}\right)_{\text{Li}} + C_{\text{Li-B}} \left(\frac{N}{V}\right)_{\text{B}}$$

where the well known rare-gas broadening coefficients<sup>6</sup> yield total width contributions of approximately  $0.1 \text{ cm}^{-1}$ . Coefficients for self broadening are less well established with extrapolations from theory<sup>7,8</sup> giving  $C_{\text{Li-Li}} = 1.6 \times 10^{-17} \text{ cm}^{-1}/\text{cm}^{-3}$  and somewhat indirect measurement<sup>9</sup> yielding  $C_{\text{Li-Li}} = 1.1 \times 10^{-18} \text{ cm}^{-1}/\text{cm}^{-3}$ . By comparing measured and model spectra in the current investigation, the range of possible values of this parameter so clearly critical to the bulk optical absorption of these samples has been narrowed to  $3 - 6 \times 10^{-18} \text{ cm}^{-1}/\text{cm}^{-3}$  with total width components in the interval,  $\delta_{\text{Li-Li}} = 0.1 - 2.5 \text{ cm}^{-1}$ .

### e. Overall Comparison of Model and Experiment

In Figures 3 and 4 measured transmission spectra of lithium vapors obtained under a variety of conditions can be compared to those calculated using thermodynamic parameters within the experimental uncertainties. It is to be understood that the rather favorable



agreement between experiment and theory comes without any arbitrary adjustable scale factors.

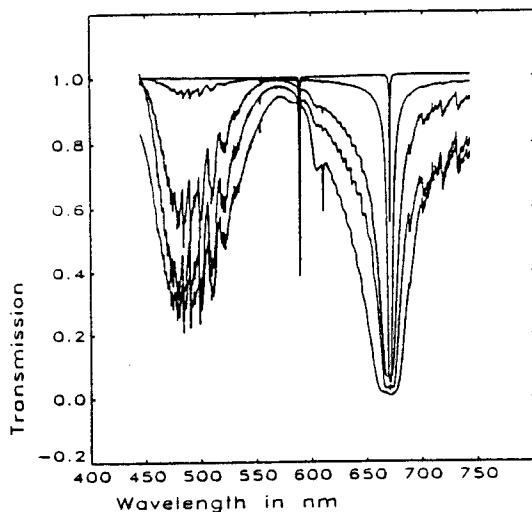


**Figure 3**—Experimental transmission spectra (with baseline adjustment).  $T_{obs} = 1580 - 2030\text{K}$ ,  $T_{evap} = 970 - 1390\text{K}$ , and  $P_{tot} = 1\text{ atm}$ .

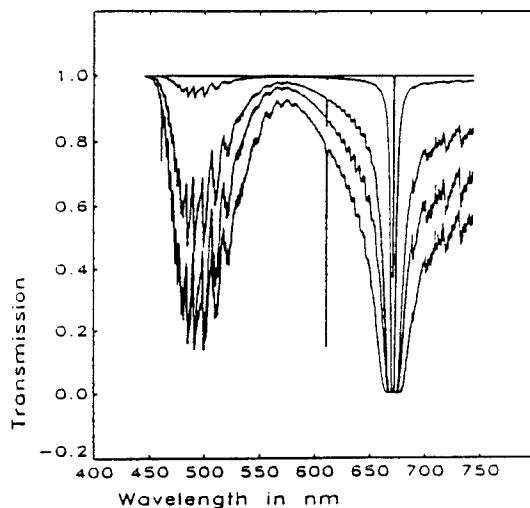


**Figure 4**—The corresponding model absorption spectra.  $(N/V)_{Li} = 5 \times 10^{13} - 2 \times 10^{18} / \text{cm}^3$ ,  $(N/V)_{Li_2} = 6 \times 10^7 - 2 \times 10^{16} / \text{cm}^3$ , and  $\Delta x = 3.5\text{ mm}$ .

#### 4. The Effects of Instrument Resolution

In order to guide the course and predict the results of further experimental endeavors, it is possible to calculate model spectra for various instrumental widths. Both the detailed state-specific nature of the present calculations and the gross broadening effects of the present experimental resolution can be seen in Figure 5 where on an arbitrary scale a model of the intrinsic physical structure of a single dilithium vibronic band obtained using a reasonable estimate of the unknown molecular pressure width is displayed with the spectrum obtained upon broadening with the indicated experimental width. Figure 6 provides a comparison of the actual measured profile in this narrow wavelength region with a corresponding intrinsic model spectrum in which all transitions have been included.

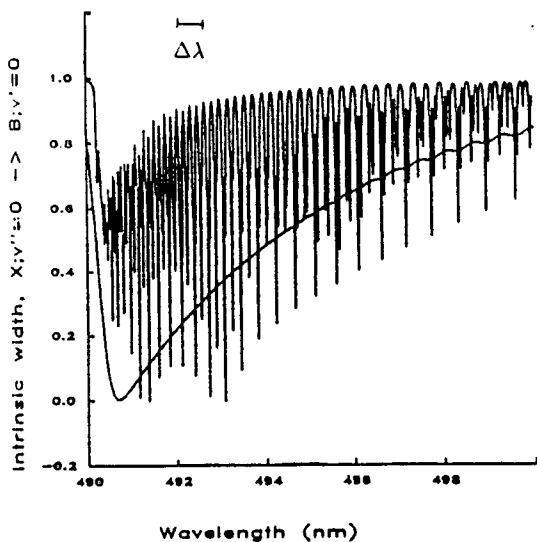


**Figure 5**—Model of the Intrinsic Physical Structure of the  $X: v'' = 0 \rightarrow B: v' = 0$  Band of  $\text{Li}_2$  and the Convolution with the Instrument Resolution Function ( $\Delta\lambda = 0.5\text{ nm}$ ).  $T_{obs} = 1600\text{K}$ .

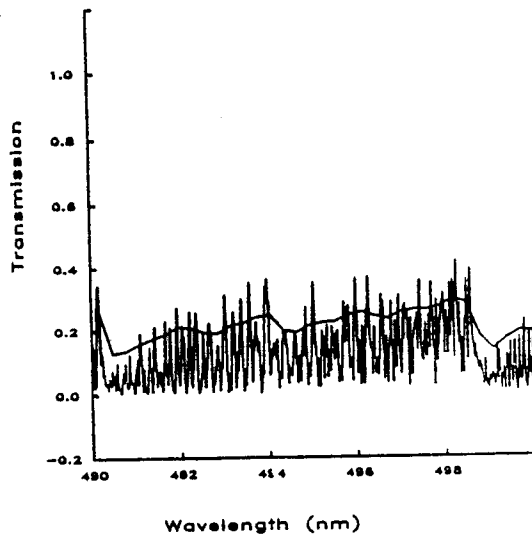


**Figure 6**—Experiment ( $T_{obs} = 1600\text{K}$ ,  $T_{evap} = 1305\text{K}$ , and  $P = 1\text{ atm}$ ) and High-resolution Model ( $(N/V)_{Li-Li} = 2 \times 10^{16}$ ,  $\Delta x = 3.5\text{ mm}$ , and  $\delta_{Li-Li} = 1.0\text{ cm}^{-1}$ ) for the Same Narrow Spectral Region.

Careful comparison of model and high-resolution experimental spectra would thus seem to provide a simple means of determining or at least delimiting the insufficiently characterized molecular linewidths which would be critical, for example, to the radiation exchange between samples with such highly structured absorption profiles.

## 5. Al<sub>2</sub> Spectroscopy and the Search for AlLi

Modeling of prospective experiments can even be extended to unknown or heretofore unobserved species. In support of an attempt to produce the aluminum-lithium diatomic, the spectral characteristics of all atomic and homonuclear diatomic species in an equilibrium mixture of lithium and aluminum vapors can be accumulated to predict the condition-dependent transmission background upon which any AlLi signal would need to be observed (Figure 7). The extremely weak bound-bound and bound-free absorption due to diatomic aluminum is constructed principally from molecular structure calculations<sup>10</sup> and is displayed separately in Figure 8. Theoretical information concerning the potential energy curves of the AlLi molecule<sup>11</sup> also allows prediction of the thermodynamic conditions most appropriate to maximization of the desired specie and minimization of interfering signals.

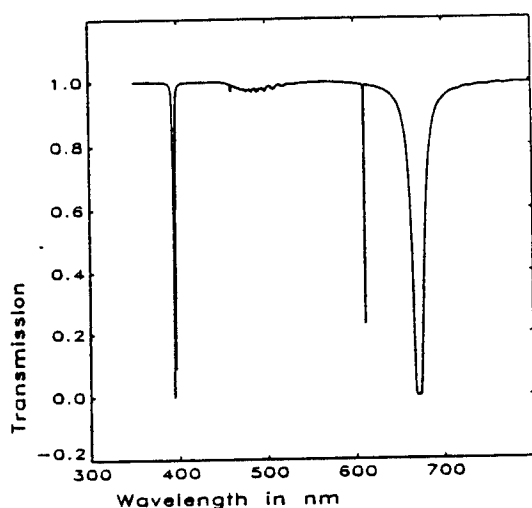


**Figure 7**—Anticipated Spectral Background of an Al/Li Mixture Including only Al, Li, Al<sub>2</sub>, and Li<sub>2</sub> Components ( $T_{\text{evap}}^{\text{Li}} = 1350\text{K}$ ,  $T_{\text{evap}}^{\text{Al}} = T_{\text{obs}} = 2100\text{K}$ ).

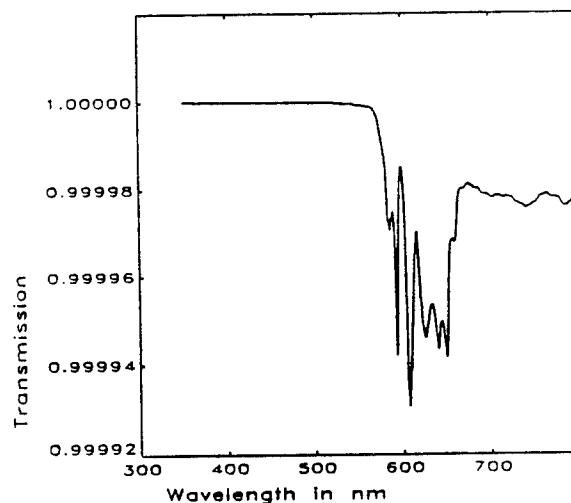
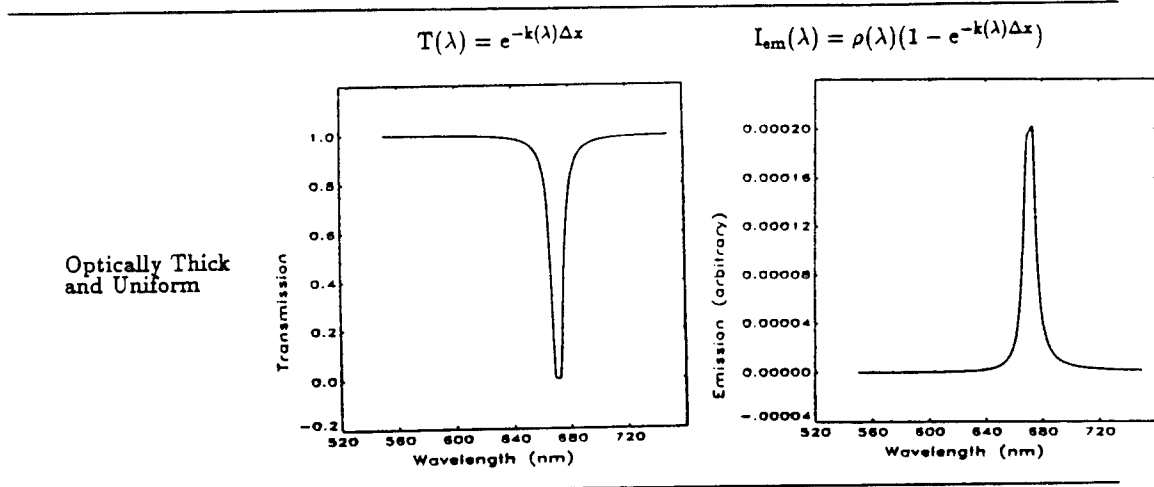
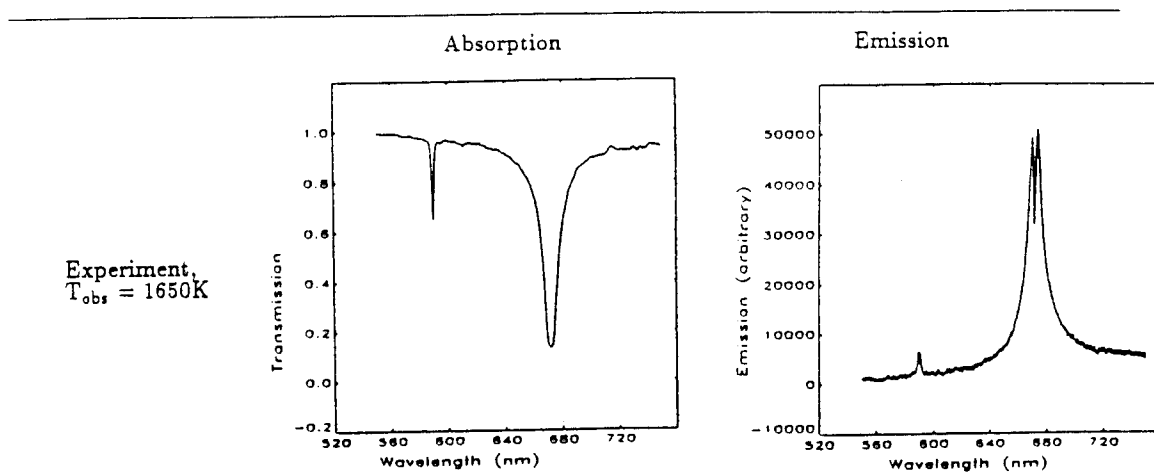


**Figure 8**—Bound-bound and Bound-Free Spectrum of Al<sub>2</sub> ( $T_{\text{obs}} = T_{\text{evap}} = 2100\text{K}$ ).

With model backgrounds of this type, novel absorption features in a congested experimental spectrum might be obtained by simple subtraction.

## 6. Emission Spectra and the Effects of Sample Nonuniformity on Atomic Lineshape

Figure 9 begins with the absorption and emission spectra measured under the same conditions for a mixture of alkali metals in which lithium predominates over sodium (manifested by the small resonance feature around 590 nm). As the next pair of spectra illustrate, unlike the general features of the transmission, a theoretical treatment which assumes a uniform distribution of absorbing species is not able to account for the line reversal apparent in emission. The final set of figures demonstrate that this characteristic can however be produced with one simple concentration profile in which diffuse outer regions subject to a relatively narrow pressure broadening re-absorb some of the light emitted by a more concentrated inner region. (In each case the Planck distribution function,  $\rho(\lambda)$ , associated with a constant observation-zone temperature provides the indicated relationship between the emitted power and the absorption coefficient.)



By Explicit Integration along the Optical Path from Back to Front:

$$I(\lambda, \Delta x) = \int_0^{\Delta x} k(\lambda, x) [I(\lambda, x) + \rho(\lambda)] dx$$

$$T(\lambda) = \frac{I(\lambda, \Delta x)}{I_0(\lambda)}$$

for  $I(\lambda, 0) = I_0(\lambda)$

$$I_{em}(\lambda) = I(\lambda, \Delta x)$$

for  $I(\lambda, 0) = 0$

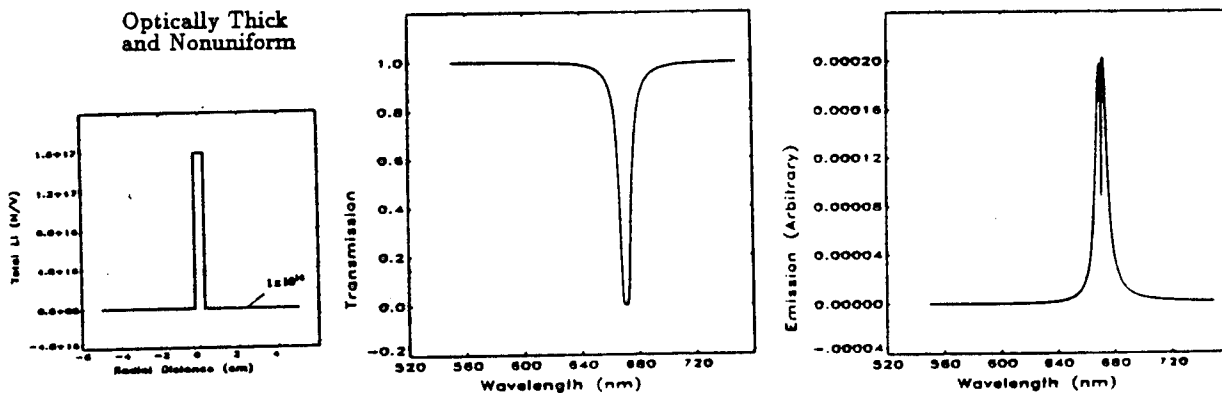


Figure 9

As linewidths and specie distributions become better characterized and comparison with experiment is improved, not only will insight be gained into the specific flow properties of the experimental apparatus, but foundations will have been laid for a more accurate accounting of the radiative and thermal properties of such anisotropic samples, particularly their critical

dependence upon secondary emission and absorption. Thus, conditions responsible for radiation trapping and novel spatial temperature variations might be determined.

## 7. Conclusions

A quantum- and statistical-mechanical, state-to-state theoretical approach in a tractable computational framework has been shown to be applicable to optical absorption and emission by the atoms and diatoms of several buffered metal vapors. The existent conditions and important processes in a prototype metal-seedant production device can be thereby diagnosed and elucidated, the results of prospective spectroscopic experiments can be predicted, and the energy-exchange characteristics of high-temperature flowing metal vapors can be quantitatively investigated.

## 8. Acknowledgments

This work was supported by AFOSR through RDL, Inc., Research Associates Program (JDM, PSE, PWL), the Air Force Palace Knight Program (JDM), and the Indiana University Chemistry Department (JDM and PWL). M.E. Fajardo, P.G. Carrick, and M.E. Cordonnier of the Emerging Technology Branch of Phillips Laboratory were instrumental in collecting much of the experimental data.

## 9. References

1. C.W. Larson, "The Spectroscopy of Hydrogen/Metal Mixtures at High Temperatures and Pressures," *AL-TR-88-080*, Edwards AFB, CA, August 1990.
2. C.E. Moore, *Atomic Energy Levels*, Nat. Bur. Stand. Circ. 467, (U.S. G.P.O, Washington, D.C., 1949), Vol. I.
3. W.L. Wiese, M.W. Smith, and B.M. Glennon, *Atomic Transition Probabilities*, Nat. Stand. Ref. Data Ser., Nat. Bur. Stand. Circ. 4, (U.S. G.P.O, Washington, D.C., 1966), Vol I.
4. See references cited in: Jeff Mills, "Theoretical Absorption Spectroscopy of High-Temperature Metal Vapors: Model and Experiment Compared," Air Force Technical Report, submitted May 1994.
5. See also: C.W. Larson, M.E. Fajardo, P.G. Carrick, P.S. Erdman, W.C. Stwalley, J.D. Mills, and P.W. Langhoff, "Absorption and Emission Spectroscopy of High-Temperature Metal Vapors for Solar Thermal Propulsion," *JANNAF Propulsion Meeting*, Monterey, CA, Nov. 1993, Vol. V, pp. 281-296.
6. N. Allard and J. Kielkopf, *Rev. Mod. Phys.*, **54**, 1103 (1982).
7. K. Niemax and G. Pichler, *J. Phys. B*, **8**, 179 (1975).
8. B. Bussery and M. Aubert-Frècon, *J. Chem. Phys.*, **82**, 3224 (1985).
9. B. Ya'akobi, *J. Quant. Spectrosc. Radiat. Transfer*, **9**, 309 (1969).
10. S.R. Langhoff and C.W. Bauschlicher, Jr., *J. Chem. Phys.*, **92**, 1879 (1990).
11. M.E. Rosenkrantz, *unpublished results*.

# Emission Spectroscopy of BH and B<sub>2</sub>

C.R. Brazier

Hughes STX

Phillips Lab. /RKFE

Edwards AFB, CA 93524-7680

## Introduction

The long term aim of this research is to develop new rocket propellants by isolating small atoms and molecules in solid hydrogen. The atomization energy of these species is trapped in the cryogenic matrix and is recovered on combustion. This results in a significant increase in the  $I_{sp}$  of the rocket which in turn should lead to a large increase in the payload. The best non-toxic diatomic species for such a system is B<sub>2</sub> [1]. The BH radical which is likely to be present in any B<sub>2</sub> or B atom source is also a fairly good HEDM species. Although the optimum  $I_{sp}$  of 563 sec [1] may be impossible to achieve as it requires 28% loading.

The BH molecule is also being considered as a candidate for a chemical laser [2]. The BH molecule can be chemically excited from the ground  $X^1\Sigma^+$  state to the  $A^1\Pi$  state in two steps by NF\* via the  $a^3\Pi$  state. Very little is known about the  $a^3\Pi$  state of BH or the  $b^3\Sigma^- - a^3\Pi$  transition which is used for monitoring the intermediate triplet population. The spectroscopic results discussed here will provide an important guide to the characterization of the BH chemical laser system.

The work reported here on B<sub>2</sub> is part of an ongoing study of the spectroscopy of this important HEDM species [3,4]. The  $(1)^3\Pi_g$  and  $(2)^3\Pi_g$  states of B<sub>2</sub> undergo an avoided crossing and interact strongly with each other over most of the lower part of the potentials of both species. Results have previously been reported on the  $(2)^3\Pi_g - A^3\Pi_u$  system of B<sub>2</sub> [4] and recent improvements in the sensitivity of the experimental apparatus has now allowed the extension of this investigation to the  $(1)^3\Pi_g - A^3\Pi_u$  system which is much weaker, as it only gains intensity by mixing with the  $(2)^3\Pi_g - A^3\Pi_u$  transition.

The BH and B<sub>2</sub> molecules were produced in a corona excited supersonic expansion of diborane seeded in helium (typically between 200 and 500 ppm). The spectra were recorded using either a 1.3m monochromator and OMA or the 1m Fourier transform spectrometer at Kitt Peak National Observatory.

## The $b^3\Sigma^- - a^3\Pi$ System of the BH Molecule

The singlet systems of the BH molecule have been extensively studied. The triplet system (only one is known) was first observed in 1937 by Almy and Horsfall [5] and has not been studied again until the present investigation. They observed the 0-0 band of the main  $^{11}\text{B}$ H isotopomer and performed a graphical analysis of the line positions to determine the rotational constants for a band that they identified as  $^3\Sigma^- - ^3\Pi$ . There was no further work on this system until the recent interest prompted by the possibility of making a BH chemical laser [2]. Besides this work there have also been two recent theoretical investigations of triplet BH by Pederson et al. [6,7].

The current spectroscopic data was originally recorded as a supplement to the extensive investigation of new bands of  $\text{B}_2$  observed throughout the visible and near UV

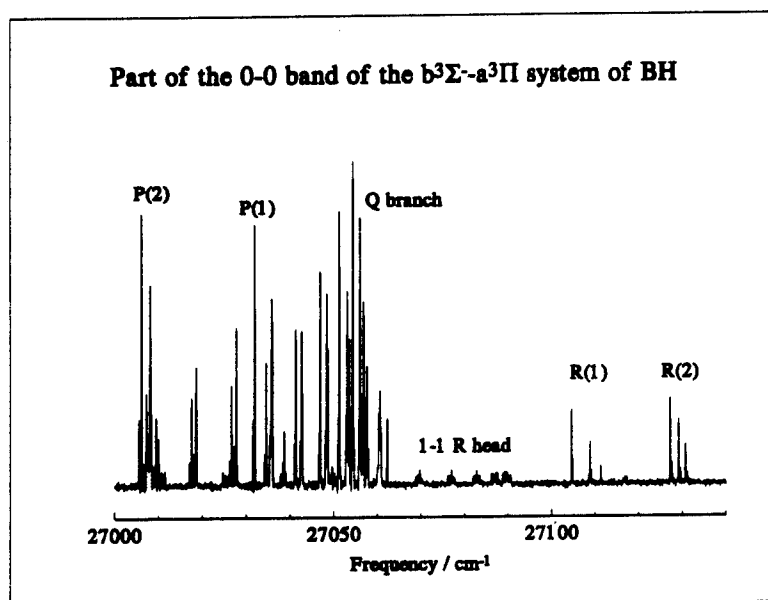


Figure 1

parts of the spectrum [3,4]. The BH singlet and triplet bands were extremely strong, and as very little was known about the triplet system a series of spectra of the  $\Delta v=0$  sequence around  $27000 \text{ cm}^{-1}$  were recorded using the Fourier transform spectrometer at Kitt Peak National Observatory. This provides essentially Doppler limited resolution, resulting in an observed linewidth of  $0.12 \text{ cm}^{-1}$ . The spectrum is dominated by the strong 0-0 band, the origin region of which is shown in Fig. 1. The spectrum is clearly  $^3\Sigma^- - ^3\Pi$  with one line missing at the start of the R branch and each rotational transition split into three components. This can be seen most clearly in the R branch. Each line also has an isotopic satellite on the side away from the origin. The minor  $^{10}\text{B}$  isotope is present naturally at about 20% of the main  $^{11}\text{B}$  isotope. The bandhead for the R branch of the 1-1 band can be seen weakly in the origin gap. The BH molecules are produced in a Corona Excited Supersonic Expansion but they are clearly not rotationally cold. The lines near the origin are best described by a rotational temperature of  $\sim 200\text{K}$ , while the high J lines indicate an

effective temperature in excess of 3000K. While it is possible that part of the temperature range is due to simultaneously viewing different parts of the jet, the primary effect is most likely a lack of rotational cooling due to the short radiative lifetime of this transition (~200 nsec) [6,7]. The observed rotational distribution then represents the nascent rotational population when the BH molecules are formed.

Constant	v=0	v=1
B	12.681974(52)	12.24399(16)
D	0.00124142(29)	0.00124208(97)
$10^7 H$	1.0202(51)	1.006(19)
$10^{11} L$	-1.322(25)	-1.91(11)
A	4.4034(11)	4.4352(38)
$A_D$	0.00217(40)	
$\lambda$	-0.0145(12)	-0.0252(51)
$o$	0.39679(75)	0.3870(20)
$10^5 o_D$	-1.01(56)	-1.01
$p$	0.00549(14)	0.00500(23)
$10^6 p_D$	-3.09(90)	-3.09
$10^9 p_H$	2.1(11)	
$q$	0.019748(16)	0.018869(39)
$10^6 q_D$	-7.78(11)	-7.99(19)
$10^9 q_H$	1.54(20)	1.47(20)
$10^{13} q_L$	-3.4(11)	

Constant	v=0	v=1
Transition Energy	27059.2443(4)	26872.8708(12)
B	12.122905(52)	11.66805(17)
D	0.00126338(29)	0.0012584(10)
$10^7 H$	1.0204(51)	1.036(21)
$10^{11} L$	-1.355(37)	-1.91(11)
$10^{16} M$	3.4(14)	
$\lambda$	0.2407(11)	0.2329(45)
$\gamma$	-0.00612(34)	-0.00724(20)
$10^6 \gamma_D$	3.33(47)	3.83(68)
$10^9 \gamma_H$	-1.30(52)	

and peaking at 4-3. All of the bands in this sequence from 1-0 through 8-7 were observed. A few weak  $\Delta v=-1$  and  $\Delta v=+2$  bands were also observed. A section of the 5-4 band showing the origin of the Q branch and the R branch is shown in Fig. 2. The weak R branch

The line positions for the 0-0 band were extracted from the spectrum and fitted using standard  $^3\Sigma$  and  $^3\Pi$  Hamiltonians. The results of this fit are shown in Tables I and II. Due to the high rotational levels observed a large number of molecular constants were required to reproduce the data. The 1-1, 2-2, 3-3, 4-4 and 5-5 bands were also observed in the Fourier transform spectrum. The lines for all of these bands were also identified and fitted. Due to the bandpass filters used to enhance the signal to noise ratio of the Fourier transform spectrum, no off-diagonal bands were observed. To complete the analysis and obtain information on the vibrational frequencies in both electronic states a search for off-diagonal bands was carried out using a 1.3m monochromator and OMA. This system has higher sensitivity than the FTS but the resolution is only of the order of  $0.8 \text{ cm}^{-1}$  in the region of interest. The  $\Delta v=+1$  bands were found to be quite strong, with the intensity increasing for higher vibrational levels

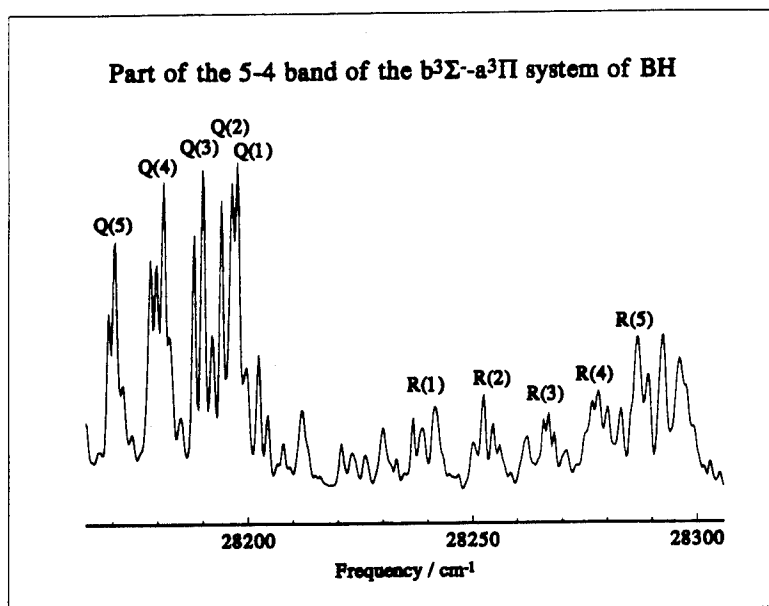


Figure 2

lines are somewhat overlapped by lines from other bands. It was also possible to extend the  $\Delta v=0$  sequence using the monochromator/OMA data. High J rotational lines were observed in the 0-0 through 5-5 bands, in addition the weak 6-6 and 7-7 bands were found.

The analysis of the  $b^3\Sigma^- - a^3\Pi$  system of

BH is still in progress and a simultaneous fit of all of the observed data has not yet been performed. The band origins and rotational constants have been fitted to power series to obtain equilibrium constants. These are shown in Table III. The rotational and vibrational data were inverted using an RKR procedure. The potential curves that were obtained are shown in Fig. 3. The levels observed for the ground state extend more than 80% of the way to the dissociation limit, which is estimated to be about  $18900 \text{ cm}^{-1}$ . The molecular

<p style="text-align: center;">Equilibrium Constants for the <math>a^3\Pi</math> State of BH (in <math>\text{cm}^{-1}</math>)</p> <p style="text-align: center;"><math>\omega_e = 2632.83</math>   <math>\omega_e x_e = 62.00</math>  <math>\omega_e y_e = 1.443</math>   <math>\omega_e z_e = -0.2735</math>  <math>B_e = 12.8667</math>   <math>\alpha_e = 0.3786</math>   <math>\gamma_e = -0.0182</math></p> <p style="text-align: center;">Equilibrium Constants for the <math>b^3\Sigma^-</math> State of BH (in <math>\text{cm}^{-1}</math>)</p> <p style="text-align: center;"><math>T_e = 27154.13</math>  <math>\omega_e = 2441.43</math>   <math>\omega_e x_e = 58.24</math>  <math>\omega_e y_e = 0.377</math>   <math>\omega_e z_e = -0.0761</math>  <math>B_e = 12.3416</math>   <math>\alpha_e = 0.4358</math>   <math>\gamma_e = -0.0059</math></p>
---

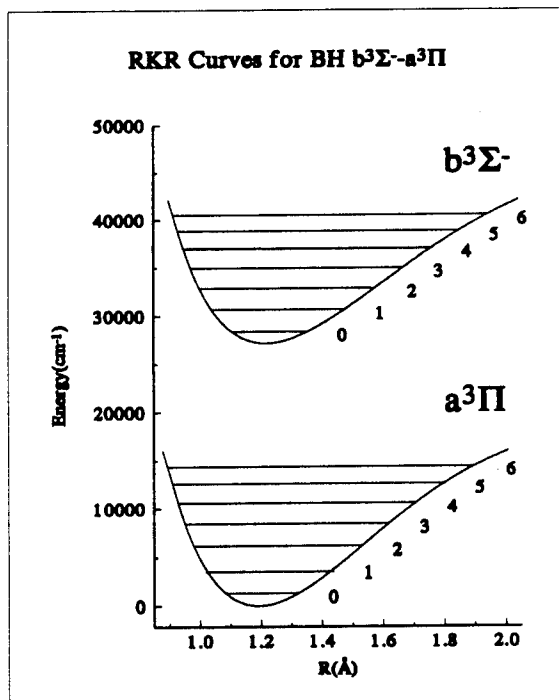


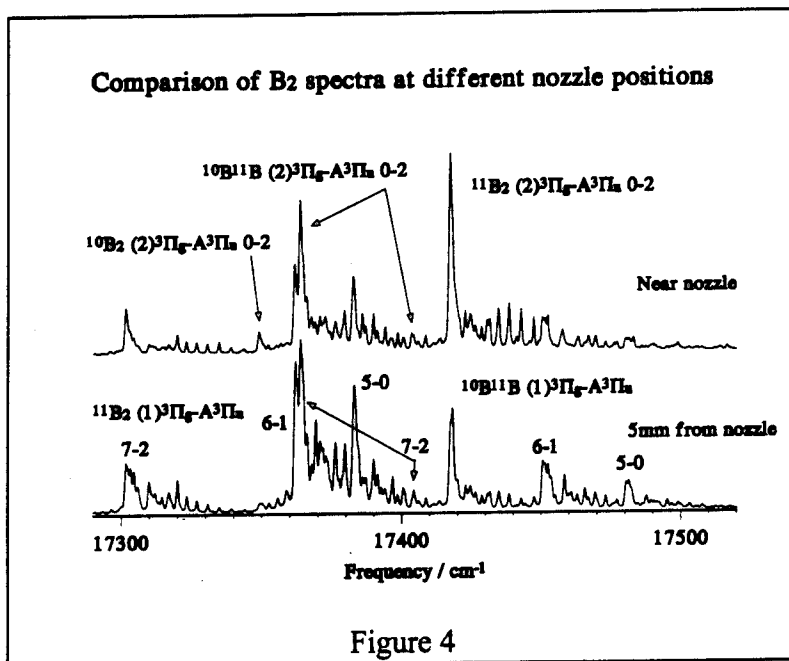
Figure 3



constants determined for the  $b^3\Sigma^- - a^3\Pi$  system are in very close agreement with the most recent theoretical calculations [6].

### The $(1)^3\Pi_g - A^3\Pi_u$ System of the $B_2$ Molecule

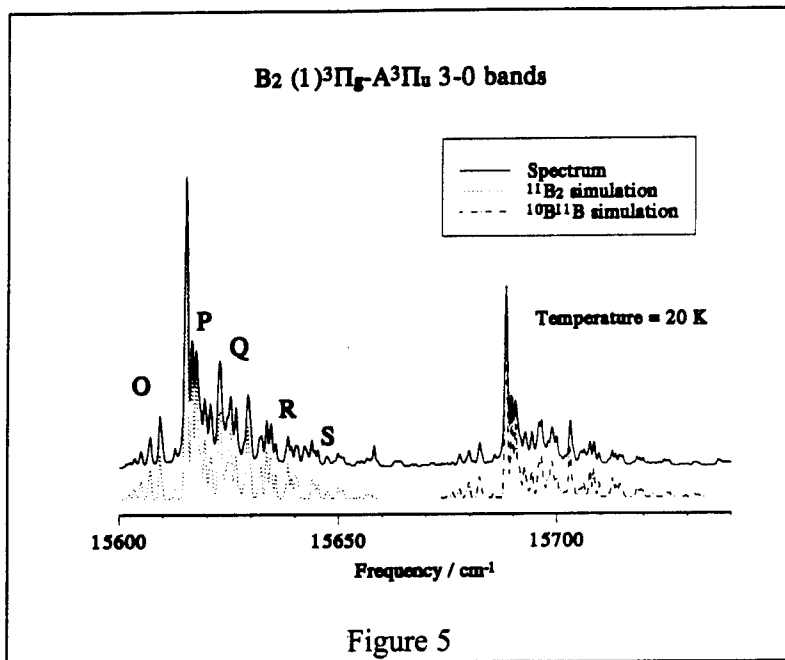
In the course of analyzing the  $(2)^3\Pi_g - A^3\Pi_u$  system of  $B_2$  a series of weaker bands of somewhat similar appearance was observed on the red side of the main 0-0 and 0-1 bands. These bands overlapped the weaker 0-2 and 0-3 transitions and became stronger than the  $(2)^3\Pi_g - A^3\Pi_u$  system far out in the expansion. The new bands were part of the  $(1)^3\Pi_g - A^3\Pi_u$  system. The  $(1)^3\Pi_g$  and  $(2)^3\Pi_g$  states are formed from an avoided crossing and hence interact strongly. The 1-0, 2-0, 3-0, 4-0, 5-0, 6-1, 7-2 and 8-3 bands of the  $(1)^3\Pi_g - A^3\Pi_u$  system have been analyzed for both  $^{11}B_2$  and  $^{10}B^{11}B$ . In addition the 1-1, 2-1, 2-2, 3-1, 3-2, 3-3, 4-1, 4-2, 4-3, 5-1, 5-2, 5-3, 5-4, 6-0, 6-2, 6-3, 6-4, 6-5, 7-1, 7-4, and 8-2 bands have been identified.



The transfer of population from the  $(2)^3\Pi_g$  state to the  $(1)^3\Pi_g$  state is illustrated in Fig. 4 which shows emission spectra from two different regions of the expansion. The spectrum near the nozzle is dominated by the 0-2 band of the  $(2)^3\Pi_g - A^3\Pi_u$  system. Further out in the expansion the  $(1)^3\Pi_g - A^3\Pi_u$  bands become more prominent. For the 0-0

and 0-1 transitions the  $^{10}B^{11}B$  band was found to be split into two components of equal intensity due to perturbation of  $v=0$  of  $(2)^3\Pi_g$  by  $v=7$  of  $(1)^3\Pi_g$ . For the 0-2 transition the perturbed  $^{10}B^{11}B$  band has much higher intensity in the lower component. The normal and perturbing transitions now have almost equal intensity and when they interact the two bands have intensities corresponding to the sum and difference of the original intensities.

As the system is followed down to lower vibrational levels in the  $(1)^3\Pi_g$  state the structure of the bands changes. This is due to the spin-orbit constant becoming increasingly negative. As a result the low rotational levels of the  $(1)^3\Pi_g$ - $A^3\Pi_u$  transition have significant case a inverted to case a regular character. This is illustrated in Fig. 5 which



shows the 3-0 bands for both isotopomers. The O and S form branches have significant intensity and there is also significant spin-structure apparent. The match between the simulated spectra, using a rotational temperature of 20K, and the experimental observations is extremely good.

The data for the strongest band from each excited state level between  $v=1$  and  $v=8$  was analyzed, with the constants for the  $A^3\Pi_u$  state held fixed to the values determined from the high resolution spectra of the  $(2)^3\Pi_g$ - $A^3\Pi_u$  transition [4]. The most important results of this analysis are shown in Table IV. The  $v=0$  level was not observed but its rotational constants are known from the  $(2)^3\Pi_u$ - $(1)^3\Pi_g$  system. The rotational and vibrational constants were fitted to power series ex-

The data for the strongest band from each

v	Energy <sup>a</sup>	A	B
0	~12650	-4.43	1.371
1	13887.8	-4.27	1.353
2	15001.4	-3.66	1.320
3	16027.9	-2.72	1.280
4	16952.5	-1.69	1.231
5	17796.0	-0.83	1.185
6	18578.7	-0.29	1.147
7	19307.7	+0.19	1.110
8	19985.5	+0.72	1.064

<sup>a</sup>Energies are relative to  $A^3\Pi_u$  at equilibrium

$T_e = 11989.43$	$\omega_e = 1358.34$
$\omega_e x_e = 65.496$	$\omega_e y_e = 1.9217$
$B_e = 1.3661$	$\alpha_e = -0.01681$
$\delta_e = 0.00261$	$\epsilon_e = -0.000120$
$r_e = 1.4971 \text{ \AA}$	

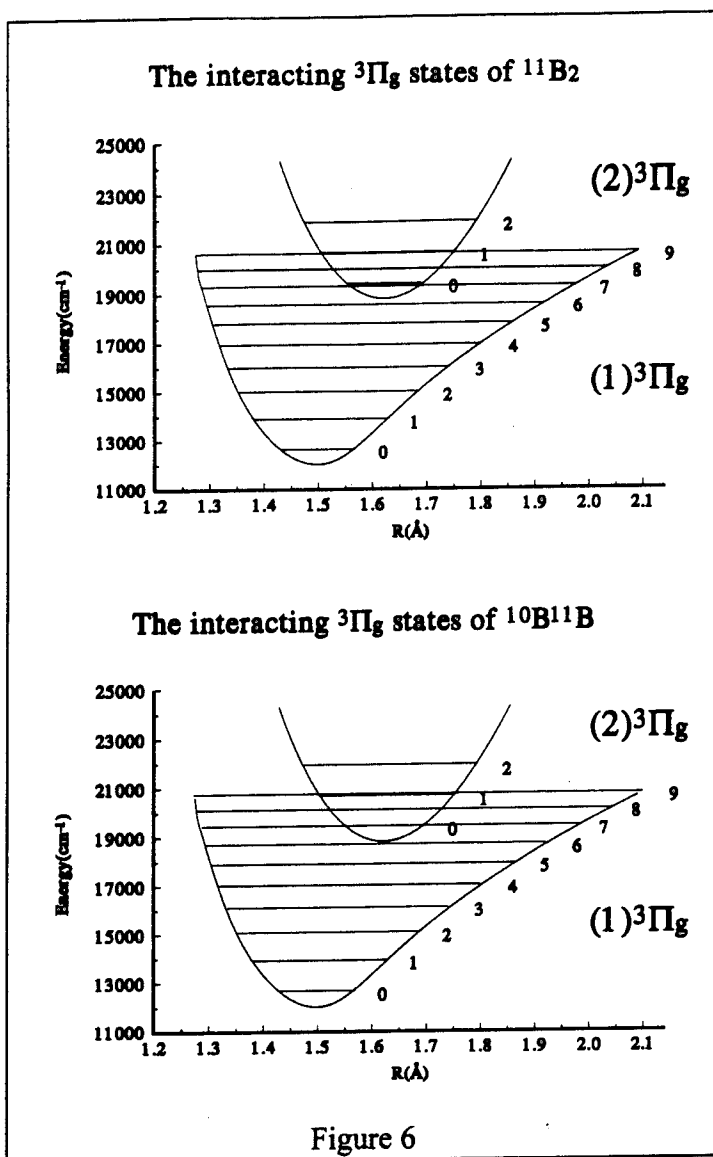


Figure 6

predissociated.

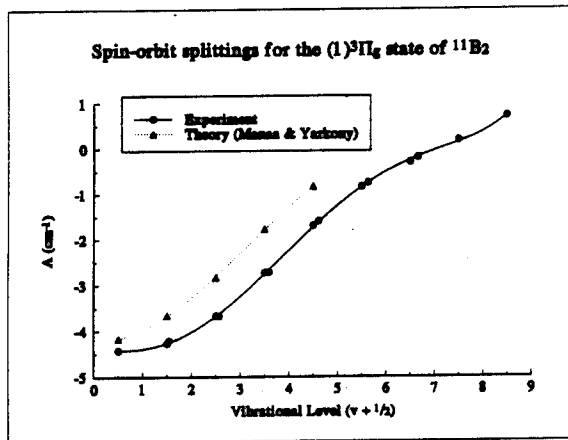


Figure 7

pansions. The resulting equilibrium constants are shown in Table V. These constants were then used to generate an RKR potential curve. This is shown in Fig. 6 together with the interacting  $(2)^3\Pi_g$  state. The energy scale is relative to the  $A^3\Pi_u$  state. Only  $v=0$  and  $v=1$  have been observed for  $(2)^3\Pi_g$ . The  $v=0$  level shows a strong perturbation for the  $^{10}\text{B}^{11}\text{B}$  isotopomer as the  $v=7$  level of  $(1)^3\Pi_g$  is almost coincident. Weaker interactions occur for the other isotopomers for  $v=0$ . For  $v=1$  both the  $^{11}\text{B}_2$  and  $^{10}\text{B}^{11}\text{B}$  isotopomers are significantly affected by the interaction with  $v=9$  of  $(1)^3\Pi_g$ . No emission was observed from  $v=2$  of  $(2)^3\Pi_g$  indicating that it lies above the barrier to dissociation for  $(1)^3\Pi_g$  and hence is

The spin-orbit constant for the  $(1)^3\Pi_g$  state shows a substantial variation with vibrational level. This is indicated graphically in Fig. 7. The  $^{10}\text{B}^{11}\text{B}$  data have been included by scaling the vibrational levels to  $^{11}\text{B}_2$ . The recent theoretical calculations of Manaa and Yarkony [8] have been included for comparison. The dominant configuration of the  $(1)^3\Pi_g$  state at equilibrium is  $\sigma_g^2\sigma_u\pi_u^3$ , this leads to a first order approximation for the spin-orbit splitting of  $A=-5\text{ cm}^{-1}$ . The dominant configu-

ration for  $(2)^3\Pi_g$  is  $\sigma_g^2\sigma_u\pi_u\sigma_g^2$  which implies  $A=+5\text{ cm}^{-1}$ . The observed value for  $v=0$  of  $(2)^3\Pi_g$  is  $A=1.5\text{ cm}^{-1}$ . This suggests considerable mixing of  $\pi^3$  character into the  $(2)^3\Pi_g$  wavefunction near equilibrium. The  $(1)^3\Pi_g$  state shows a rapid change in spin-orbit splitting from  $v=0$  through  $v=8$  as the configuration changes from primarily  $\pi^3$  to a mix of  $\pi$  and  $\pi^3$ . At energies near the bottom of the  $(2)^3\Pi_g$  potential both spin-orbit constants are small and positive due to the admixture of a small amount of the  $\sigma_g^2\sigma_u^2\pi_u\sigma_u$  configuration. This configuration is repulsive and is the dominant configuration for the  $(1)^3\Pi_g$  state from the potential barrier to dissociation.

## Conclusion

Spectroscopic studies of two important HEDM species, BH and  $B_2$ , have been performed. This information is important to the understanding of the energetics of these species as well as a possible diagnostic when producing doped HEDM solids. The triplet system of BH is also important for characterizing the BH chemical laser as the chemical excitation proceeds via the  $a^3\Pi$  state.

## References

1. P.G. Carrick, USAF Technical Report No. PL-TR-93-3014 (1993) and in *Proceedings of the HEDM Contractors Conference* (1993), T.L. Thompson ed. PL-TR-93-3041, p412-418.
2. D.J. Benard, E. Boehmer, H.H. Michels and J.A. Montgomery, *J. Phys. Chem.* **98**, 8952-8958 (1994).
3. C.R. Brazier and P.G. Carrick, *J. Chem. Phys.* **96**, 8684-8690 (1992).
4. C.R. Brazier and P.G. Carrick, *J. Chem. Phys.* **100**, 7928-7937 (1994).
5. G.M. Almy and R.B. Horsfall, Jr., *Phys. Rev.* **51**, 491-500 (1937).
6. L.A. Pederson, H. Hetta and D.R. Yarkony, *J. Phys. Chem.*, *in press*.
7. L.A. Pederson and D.R. Yarkony, *Mol. Phys.*, *submitted*.
8. M.R. Manaa and D.R. Yarkony, *J. Chem. Phys.* **100**, 8204-8211 (1994).

# Emission Spectra of the $(1)^1\Sigma_u^+ - (1)^1\Sigma_g^+$ Transition of $B_2$

Michelle E. Cordonnier, Patrick G. Carrick, and Christopher R. Brazier<sup>a</sup>

Phillips Laboratory/Propulsion Directorate

OL-AC PL/RKFE

10 East Saturn Blvd

Edwards AFB CA 93524-7680

Presented at the eighth annual High Energy Density Matter Contractor's Conference  
5-7 June 1994  
Crystal Bay NV

## Abstract

Emission spectra of the  $(1)^1\Sigma_u^+ - (1)^1\Sigma_g^+$  electronic transition of  $B_2$  produced by discharging dilute mixtures of diborane followed by expansion through a Corona Excited Supersonic Expansion source have been recorded and analyzed for the first time. The spectrum and rotational analysis of the 0-0 and 1-1 vibrational bands of this transition will be presented along with the rotational analyses of the 2-2, 3-3, and 4-4 bands. The molecular parameters that resulted from fitting the data to a Dunham type expansion will be reported and compared with recent theoretical calculations.

## Introduction

Calculations show that atomic and diatomic boron additives could provide significant increases in specific impulse for cryogenic propellant systems<sup>1</sup>. The low atomic weight, high heat of combustion, and increased specific impulse of boron make atomic boron and small boron and boron-containing molecules attractive propellant additive candidates. The  $B_2$  molecule has

<sup>a</sup>Hughes STX Corporation

been the focus of much of this research in the past and continues to be of interest.

Past work in this laboratory reported the observation of the emission spectrum and rotational analyses of the  $(2)^3\Pi_u - (1)^3\Pi_g$  and  $(1)^1\Delta_u - b^1\Delta_g$  transitions of  $B_2$  produced with a Corona Excited Supersonic Expansion (CESE) source<sup>2</sup> and the high resolution spectrum and rotational analysis of the  $(2)^3\Pi_g - A^3\Pi_u$  transition<sup>3</sup>. The current investigation of  $B_2$  resulted from the previous observation in a series of uncalibrated survey scans of a band system around  $33960\text{ cm}^{-1}$ . The calculations of Hachey et al.<sup>4</sup> predicted a transition energy of 4.41 eV ( $35568\text{ cm}^{-1}$ ) for the  $(1)^1\Sigma_u^+ - (1)^1\Sigma_g^+$  transition and inspired us to further investigate this band system. We present here our observations and the results of our assignments and analysis of the 0-0, 1-1, 2-2, 3-3, and 4-4 vibrational bands of the  $(1)^1\Sigma_u^+ - (1)^1\Sigma_g^+$  transition.

## Observations

The experimental procedure used in this work has been described previously<sup>2</sup>.

We began by taking data of the strong 0-0 and 1-1 overlapped band system at  $33960\text{ cm}^{-1}$  and then took a series of uncalibrated survey scans by stepping the monochromator and taking data in all spectral regions that looked interesting. After studying the survey scans and determining which bands potentially belonged to the system of interest, we went back and took calibrated data in these areas. The upper spectrum in Fig. 1 shows the data for the overlapped 0-0 and 1-1 bands and the lower spectrum is a computer generated simulation. After numerous attempts, no acceptable data for the 0-1, 1-0, or higher off-diagonal bands was obtained due to low signal and obstruction of these bands by other species.

## Analysis

The basic analysis process has been discussed previously<sup>2,3</sup> and will be discussed in an upcoming paper<sup>6</sup> so will not be discussed here.

It should be noted that isotope bands were omitted in the analysis of all five bands presented here. Boron occurs naturally in the form of two isotopes,  $^{11}\text{B}$  (approximately 80%) and  $^{10}\text{B}$  (approximately 20%), resulting in three isotopic forms for the dimer:  $^{11}\text{B}_2$ ,  $^{10}\text{B}^{11}\text{B}$ , and  $^{10}\text{B}_2$  in the ratio of about 16:8:1. Since the amount of  $^{10}\text{B}_2$  is relatively small compared to the other two isotopes, it is unobservable and its omission has a minimal effect on the results of the analysis. This leaves a ratio of 2:1 for the remaining combinations, meaning the intensity of the

$^{10}\text{B}^{11}\text{B}$  bands should be about half that of the  $^{11}\text{B}_2$  bands. Because of the difficulty in resolving the spectra and assigning lines to the isotope bands, the  $^{10}\text{B}^{11}\text{B}$  isotope bands, which become more apparent at high rotational quantum number ( $J$ ) and in the hot spectra and are especially split out in the 3-3 and 4-4 bands, were not rotationally analyzed. Calculated isotope bands were used only for the purpose of confirming that our predictions and assignments were correct.

The analysis of the 0-0 and 1-1 bands were fairly straightforward and only became slightly troublesome for some peaks in the region where the two bands overlap (approximately  $33896\text{ cm}^{-1}$  to  $33918\text{ cm}^{-1}$ ). The data file shown in Fig. 1 was used in the analysis because of its high signal-to-noise ratio and low rotational temperature of approximately 30 K (referred to as "cold" data). A file containing data of approximately 165 K (referred to as "hot" data) was used only when necessary to assign peaks that could not be definitely assigned with the cold data (due to low signal intensity or the peaks being poorly resolved) and to assign high  $J$  lines that become more intense at higher temperatures. The lower spectrum is the 0-0 and 1-1 simulations added together. The simulation matches rather well except for in the region where the two bands overlap and at high  $J$ .

The analysis of the 2-2 band proved to be more difficult due to another band, tentatively assigned as a  $\Pi$ - $\Sigma$  band, that overlaps the P branch of the 2-2 band. The overlapping band is more prominent in the cold data than in the hot data possibly because it has a longer fluorescence lifetime than the  $\text{B}_2$   $\Sigma$ - $\Sigma$  band and therefore survives farther out into the jet than the  $\Sigma$ - $\Sigma$  band. Taking data from close to the tip of the nozzle where the jet is hotter thus resulted in data with a higher ratio of molecules in the  $\Sigma$ - $\Sigma$  transition to molecules in the supposed  $\Pi$ - $\Sigma$  transition.

The 3-3 and 4-4 bands were initially difficult to analyze but once it was determined where the isotope bands were located, the analysis became fairly straightforward. The 3-3 and 4-4 isotopes are shifted farther out from their corresponding main bands than the 0-0, 1-1, and 2-2 isotopes, thus making them quite apparent. To calculate the simulated spectra of these isotopes, the constants from the 3-3 and 4-4 main bands were multiplied by the appropriate isotopic ratios and the simulated spectra for the isotopes were generated from the resulting constants. The line positions for all 5 bands for the  $^{11}\text{B}_2$  isotopomer are shown in Table I.

At this point, the lines of all five analyzed bands were fit to a Dunham type expansion of the molecular parameters. The results of this fit are given in Table II. As we did not observe any off-diagonal vibrational bands, the lower state  $\omega_e$  and  $\omega_e x_e$  were held fixed to the values calculated by Hachey, Karna, and Grein<sup>4</sup>. The  $D_e$  for both states was held fixed to that estimated

from the Kratzer relation ( $D_e = 4B_e^3/\omega_e^2$ ). The comparison of our experimental  $r_e$  and  $T_e$  for both states, and  $\omega_e$  for the upper state, with theory is shown in Table III. The rapid increase in the separation of the observed bands from 0-0 through 4-4 arises from the large difference in the anharmonicity constants,  $\omega_e x_e (= -Y_{20})$ , for the two states. The vibrational constants ( $Y_{10}$  through  $Y_{40}$ ) determined for the  $(1)^1\Sigma_u^+$  state are only phenomenological fitting constants that represent the observed irregularly spaced band origins. Comparison with the calculated potential curves for both  $(1)^1\Sigma_u^+$  and  $(1)^1\Sigma_g^+$  states shows that such irregular spacings should be expected as both states have strong interaction with other states of the same symmetry leading to highly anharmonic potential curves.

## Conclusion

Diatomic boron molecules have been produced with a Corona Excited Expansion Source. The emission spectra of the 0-0, 1-1, 2-2, 3-3, and 4-4 vibrational bands of the  $(1)^1\Sigma_u^+ - (1)^1\Sigma_g^+$  transition of  $B_2$  have been recorded with an optical multichannel analyzer and analyzed. Bond lengths were calculated for both states, and as shown in Table III, agree well with theoretical calculations, with the largest difference being less than 0.02 Å. In addition, the experimental  $\omega_e$  for the upper state and the  $T_e$  for the transition agree well with the theoretical predictions of Langhoff and Bauschlicher<sup>5</sup> and Hachey, Karna, and Grein, as also shown in Table III. Since the lower state  $\omega_e$  was held fixed and the upper state  $\omega_e$  is relative to the fixed lower state value, the upper state value should not be considered absolute.

## References

1. P.G. Carrick, Proceedings of the High Energy Density Matter (HEDM) Contractors Conference, report number PL-TR-93-3041, T.L. Thompson, p. 412-418, USAF Phillips Laboratory, Edwards AFB, CA, 1993.
2. C.R. Brazier and P.G. Carrick, *J. Chem. Phys.*, **96**, 8684-8690 (1992).
3. C.R. Brazier and P.G. Carrick, *J. Chem. Phys.*, **100**, 7928-7937 (1994).
4. M. Hachey, S.P. Karna, and F. Grein, *J. Phys. B: At. Mol. Opt. Phys.*, **25**, 1119-1136 (1992).
5. S.R. Langhoff and C.W. Bauschlicher, Jr., *J. Chem. Phys.*, **95**, 5882-5888 (1991).
6. M.E. DeRose, P.C. Carrick, and C.R. Brazier, submitted.



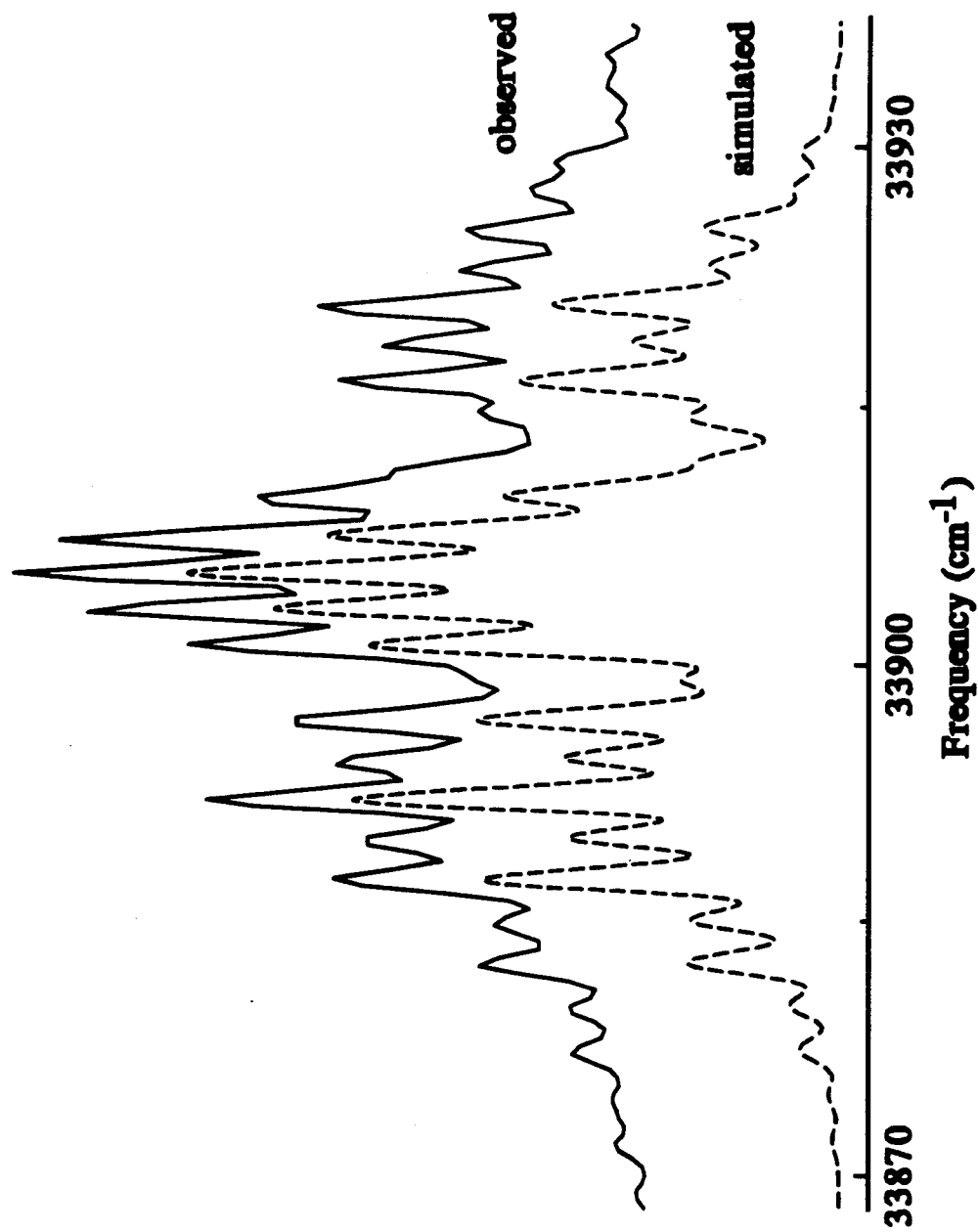


Figure 1. Comparison of experimental and simulated emission spectra of the overlapped 0-0 and 1-1 bands of the  $(1)^1\Sigma_u^+ - (1)^1\Sigma_g^+$  transition of B<sub>2</sub> produced by discharging and expanding diborane in a CESE source. The simulated spectra was produced by adding the 0-0 and 1-1 simulations. The rotational temperature of the data is approximately 30 K.

Table I. Line Positions for the  $(1) \Sigma_u^+ - (1) \Sigma_g^+$  System of  ${}^1\text{B}_2$  (in  $\text{cm}^{-1}$ ).

J	0-0		1-1		2-2		3-3		4-4	
	v	$\Delta v$	v	$\Delta v$	v	$\Delta v$	v	$\Delta v$	v	$\Delta v$
P(1)	33 897.135	-0.066	33 910.356	0.159			34 193.340	-0.224	34 373.400	-0.027
P(2)	33 894.780	-0.104	33 908.001	0.005						
P(3)	33 892.471	-0.047	33 905.952	0.153			34 189.830	-0.142	34 370.000	0.081
P(4)	33 889.952	-0.151	33 903.706	0.099						
P(5)	33 887.620	-0.019	33 901.527	0.106						
P(6)	33 885.036	-0.089	33 899.190	-0.050						
P(7)	33 882.587	0.024	33 897.135	0.070						
P(8)	33 879.894	-0.058	33 894.780	-0.114			34 184.084	-0.068		
P(9)	33 877.328	0.036	33 892.471	-0.259						
P(10)	33 874.924	0.341								
P(11)	33 871.942	0.116								
P(12)	33 869.219	0.200								
P(13)	33 866.238	0.074								
P(14)	33 863.173	-0.087								
P(15)	33 860.283	-0.024								
P(16)	33 857.451	0.147								
P(17)	33 854.013	-0.240								
R(0)	33 901.527	-0.158	33 914.566	-0.048			34 197.662	0.051	34 379.793	0.189
R(1)	33 903.706	-0.146	33 916.866	0.037	34 025.187	0.133	34 200.009	0.206	34 381.929	0.023
R(2)	33 905.952	-0.017	33 919.106	0.058	34 027.539	0.205	34 202.221	0.112	34 384.237	-0.092
R(3)	33 908.001	-0.034	33 921.308	0.037	34 029.814	0.134	34 204.559	0.032	34 386.758	-0.114
R(4)	33 910.356	0.306	33 923.511	0.013	34 032.022	-0.069	34 207.037	-0.020	34 389.509	-0.027
R(5)	33 912.119	0.104	33 925.701	-0.027	34 034.594	0.027	34 209.631	-0.068	34 392.249	-0.071
R(6)			33 928.069	0.109	34 037.024	-0.085	34 212.492	0.039	34 395.286	0.062
R(7)			33 930.018	-0.178	34 039.585	-0.130	34 215.407	0.090	34 398.048	-0.199
R(8)			33 932.398	-0.035	34 042.167	-0.218	34 218.400	0.107	34 401.737	0.349
R(9)			33 934.538	-0.134	34 044.866	-0.252			34 404.728	0.079
R(10)					34 050.612	-0.163	34 227.900	0.019		
R(11)					34 053.522	-0.175	34 231.211	-0.084		
R(12)					34 056.736	0.055	34 234.588	-0.230		
R(13)					34 059.774	0.047	34 238.463	0.013		
R(14)					34 062.869	0.036				
R(15)					34 066.257	0.257				
R(16)					34 069.422	0.196				
R(17)										

Table II. Dunham parameters for  $1^1B_2$

	(in $\text{cm}^{-1}$ )	
	$(1)^1\Sigma_g^+$	$(1)^1\Sigma_u^+$
Y <sub>00</sub>	33 928.80(21)	
Y <sub>10</sub>	859 <sup>a</sup>	779.00(59)
Y <sub>20</sub>	-47.4 <sup>a</sup>	-7.46(49)
Y <sub>30</sub>		6.12(15)
Y <sub>40</sub>		-1.365(15)
Y <sub>01</sub>	1.1249(88) <sup>b</sup>	1.0914(93)
Y <sub>11</sub>	0.038(16)	0.050(15)
Y <sub>21</sub>	-0.0442(81)	-0.0337(72)
Y <sub>31</sub>	0.0062(12)	0.0043(10)
Y <sub>02</sub>	-8.2661x10 <sup>-6c</sup>	-9.2073x10 <sup>-6c</sup>

<sup>a</sup>Held fixed to theoretical values from ref. 4.

<sup>b</sup>Values in parentheses represent one standard deviation error from the least squares fit.

<sup>c</sup>Held fixed at calculated values from Kratzer relation.

Table III. Comparison of experimental and theoretical constants for the  $(1)^1\Sigma_u^+ - (1)^1\Sigma_g^+$  system of  $B_2$

	Experiment	L and B <sup>a</sup>	H, K, and G <sup>b</sup>
$(1)^1\Sigma_g^+ r_e$ (Å)	1.650	1.664	1.631
$(1)^1\Sigma_g^+ \omega_e$ ( $\text{cm}^{-1}$ )	859 <sup>c</sup>	859	859
$(1)^1\Sigma_u^+ - (1)^1\Sigma_g^+ T_e$ ( $\text{cm}^{-1}$ )	33 929		35 568
$(1)^1\Sigma_u^+ r_e$ (Å)	1.675		1.660
$(1)^1\Sigma_u^+ \omega_e$ ( $\text{cm}^{-1}$ )	779		773

<sup>a</sup>Ref. 5

<sup>b</sup>Ref. 4

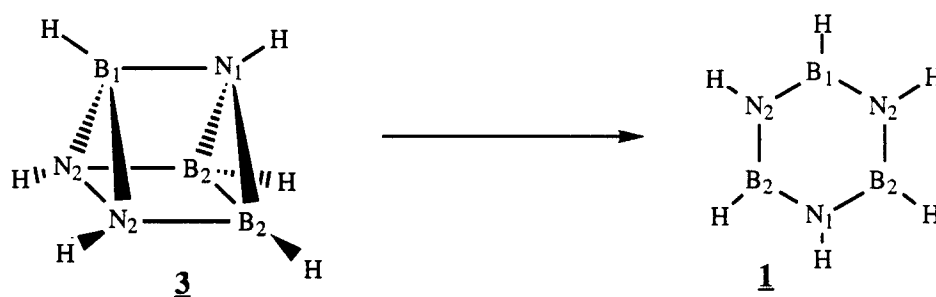
<sup>c</sup>Held fixed to theoretical value.

## A Theoretical Study of High Energy B-N Prismane

Nikita Matsunaga and Mark S. Gordon  
Department of Chemistry  
Iowa State University  
Ames, IA 50011

### Introduction

Our preliminary calculations[1] have shown that the B-N analog of prismane is a high energy minimum on its potential energy surfaces (PES). The relative energy of the B-N prismane with respect to borazine, including zero-point energy correction, is 185.0 kcal/mol at the restricted Hartree-Fock (RHF) level of theory using effective core potential and basis sets of Stevens *et. al* (SBK(d))[2]. The relationship between the B-N prismane and borazine can be thought of as an intramolecular isomerization reaction, such that the bond between B<sub>1</sub> and N<sub>1</sub> breaks and followed by breaking two other bonds, *i.e.* B<sub>2</sub>-B<sub>2</sub> and N<sub>2</sub>-N<sub>2</sub> (**Scheme 1**) to obtain borazine.



**Scheme 1**

The synthesis of B-N analog of prismane could be conceived by reacting two ring systems, diiminoborane and iminodiborane[3]. Part of our effort goes into cooperation between our synthetic colleagues and our group to facilitate the synthesis of B-N prismane. At the first stage of our effort includes the mapping of the PES of B-N

prismane in order to understand the thermodynamic and kinetic stabilities, and also to learn about the nature of diiminoborane.

In this abstract, a part of the PES of the B-N prismane and related molecules are explored in an attempt to achieve the isomerization reaction above. Also, the total electron density analysis was performed in order to shed light into the stabilities and the nature of bonding in the B-N primane.

### **Computational Approach**

The geometries were optimized with the restricted Hartree-Fock (RHF) using GAMESS[4] quantum chemistry programs. The basis sets used here include the Steven-Basch-Krauss-Jasien (SBK) effective core potentials (ECP) and basis sets[2] for all heavy atoms and the -31G basis[5] for hydrogen, also using 6-31G(d,p) basis[5]. All heavy atoms are augmented with d-polarization functions[6].

Reaction path was followed for each transition state located by using Gonzalez-Schlegel method[7] in order to connect a transition state to the associated two minima.

Due to the fact that the RHF level of theory fails to find a transition state connecting B-N prismane and borazine directly, MCSCF wave function was utilized. For the preliminary results presented here STO-3G[8] basis set was used. Active space of the prismane consists of the three bonding and anti-bonding orbitals (orbitals that lie on  $N_1-B_1$ ,  $N_2-N_2$  and  $B_2-B_2$ ). This 6 electron-6 orbital active space generates 175 configuration state functions(CSF).

Bonding was analyzed by using localized molecular orbitals (LMO), constructed with the method of Mezey and Pipek[9]. The AIM-PAC system of programs[10] was also used to elucidate the nature of bonding. A bond critical point exists between two atoms if there is a saddle point in the electron density between two atoms. At such a point the Hessian of the electron density has one positive eigenvalue along the axis orthogonal to the bond axis. The existence of a bond critical point implies the existence of a bond path

(path of maximum electron density passing through the bond critical point), and the two atoms are said to be bonded.

## **Results**

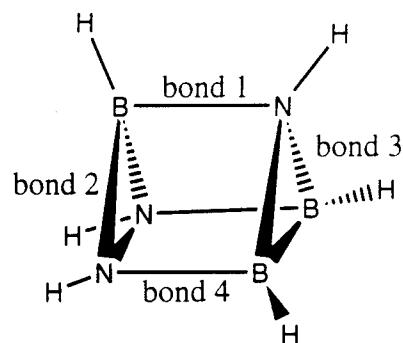
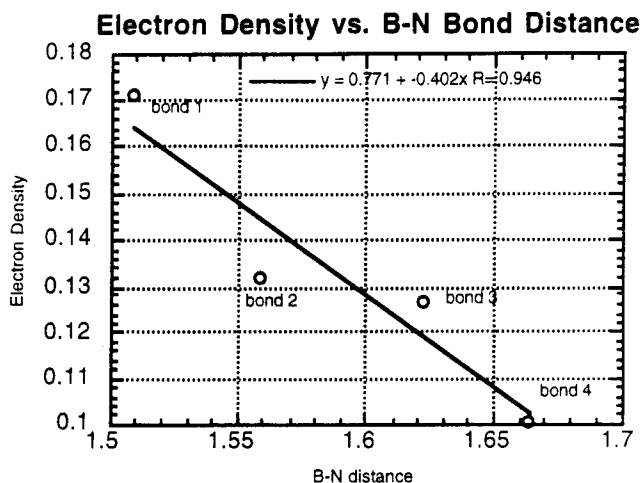
Geometries of the B-N prismane and the related molecules along with the relative energies of each molecule with respect to the B-N prismane are shown in Figure 1. The normal modes corresponding to the negative eigenvalue of the energy hessian for the transition state found are also shown in Figure 1. The bond lengths of B-N bonds in prismane form is substantially larger than that of the borazine. All the rectangular faces of the B-N prismane possess up to about 5° deviations from the ideal angle of 90°. The two triangular faces deviates less than 4° from the ideal angle, 60°, found in a prismane.

Dewar-benzene analog of borazine was found (**4**) at the MCSCF/STO-3G level of theory, even though the RHF/SBK(d) failed to do so. The transition state (**14**) connecting the Dewar-benzene analog and the prismane can be found in Figure 1. At the transition state the reference configuration function consists 75% of the total contribution, and the occupation number of one of the anti-bonding orbitals is 0.565 (Figure 2).

The bond critical points found for the bonds B<sub>1</sub>-N<sub>2</sub> and N<sub>1</sub>-B<sub>2</sub> (of **Scheme 1**) are located inside the ring. Especially, the bond critical points of the N<sub>1</sub>-B<sub>2</sub> bond can be found close to the ring critical point associated with the ring N<sub>1</sub>-B<sub>2</sub>-B<sub>2</sub>. It means that the ring has small ring strain. One could think of it as a "T-shaped" bond, though the total electron density contour map shows two distinct bond paths. The localized orbitals do not show such characteristics, either. On the other hand, prismane (carbon only) possesses the bond critical points associated with the triangular face are located outside the ring.

There seems to be some correlation between the bond strength of a given bond type and the value of electron density at the bond critical point. The graph below shows

the values of electron density at the bond critical points plotted against the B-N bond distances.



The bond between the  $N_1-B_1$  (bond 1) possesses the highest electron density among B-N bonds, and the smallest value is assigned to the bond  $N_2-B_2$  (bond 4). Then the reaction is likely to occur (or to initiate) by breaking the bond  $N_2-B_2$  first.

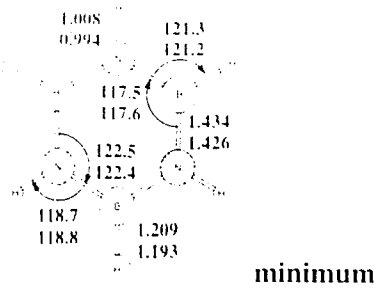
### Al-N and Ga-N analogs of prismane

There are other possible HEDM candidates. We have found that prismane structures of  $(AlH-NH)_3$  and  $(GaH-NH)_3$  to be high energy species, 90.7 and 96.4 kcal/mol with respect to the corresponding benzene structures. They are both minima on the PES and the corresponding benzene structures are also minima.

### References

- [1] N. Matsunaga and M. S. Gordon *J. Ame. Chem. Soc.*, submitted for publication
- [2] W. J. Stevens, H. Basch and M. Krauss *J. Chem. Phys.* **81** (1984) 6026
- [3] personal communication with Ellen Boehmer
- [4] M. W. Schmidt, K. K. Baldridge, J. A. Boatz, S. T. Elbert, M. S. Gordon, J. H. Jensen, S. Koseki, N. Matsunaga, K. A. Nguyen, S. Su, T. L. Windus, M. Dupuis, and J. A. Montgomery *J. Comput. Chem.* **14** (1993) 1347
- [5] R. Ditchfield, W. J. Hehre and J. A. Pople *J. Chem. Phys.* **54** (1971) 724
- [6] We have used  $B=0.6$  and  $N=0.8$
- [7] C. Gonzales and H. B. Schlegel *J. Phys. Chem.* **94** (1990) 5523
- [8] W. J. Hehre, R. F. Stewart and J. A. Pople *J. Chem. Phys.* **51** (1969) 2657
- [9] J. Pipek and P. G. Mezey *J. Chem. Phys.* **90** (1989) 4916
- [10] R. F. W. Bader *Atoms in Molecules--A Quantum Theory* (University of Oxford, Oxford, 1990)

1



Relative Energies wrt Prismane:

RHF/SBK(d)//RHF/SBK(d)	-185.0 kcal/mol
MP2/SBK(d)//RHF/SBK(d)	-161.2
RHF/6-31G(d,p)//RHF/6-31G(d,p)	-186.0
MP2/6-31G(d,p)//MP2/6-31G(d,p)	-

Vibrational Frequencies:

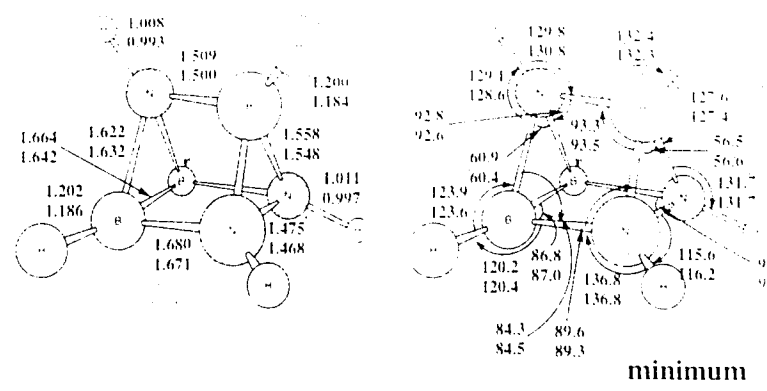
RHF/6-31G(d,p) vibrational frequencies (in cm<sup>-1</sup>)

295.8	295.8	407.3	555.1	555.1
737.0	737.0	761.8	912.1	991.9
991.9	1003.3	1004.9	1004.9	1022.7
1125.1	1142.8	1142.8	1300.3	1424.8
1495.5	1495.5	1590.6	1590.6	2708.5
2708.5	2722.0	3881.6	3883.1	3883.1

RHF/SBK(d) vibrational frequencies (in cm<sup>-1</sup>) and intensities (in km/mol)

293.9(0.0)	293.9(0.0)	395.2(55.1)	543.0(0.1)	543.0(0.1)
714.5(0.0)	714.5(0.0)	752.8(98.9)	900.2(0.0)	975.3(0.3)
975.3(0.3)	986.2(0.0)	994.9(0.0)	994.9(0.0)	998.7(296.8)
1095.8(0.0)	1118.5(1.5)	1118.5(1.5)	1288.9(0.0)	1381.6(0.0)
1461.0(58.9)	1461.0(58.9)	1564.8(760.8)	1564.8(760.8)	2716.7(499.2)
2716.7(499.2)	2738.3(0.0)	3792.8(0.0)	3794.7(54.5)	3794.7(54.4)

2



Relative Energies:

RHF/SBK(d)//RHF/SBK(d)	0.0 kcal/mol
MP2/SBK(d)//RHF/SBK(d)	0.0
RHF/6-31G(d)//RHF/6-31G(d,p)	0.0
MP2/6-31G(d)//RHF/6-31G(d,p)	0.0

Vibrational Frequencies:

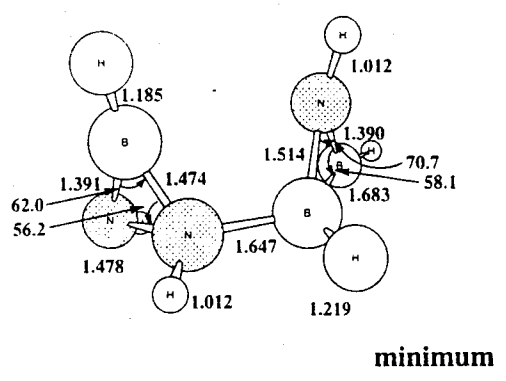
RHF/6-31G(d,p) vibrational frequencies (in cm<sup>-1</sup>)

383.4	478.6	522.8	560.6	628.2
665.5	678.1	690.1	796.9	834.4
892.9	907.3	936.9	950.7	981.2
1024.1	1029.1	1040.1	1125.9	1169.6
1237.7	1250.2	1306.8	1451.8	2736.3
2758.0	2774.9	3858.6	3869.9	3888.3

RHF/SBK(d) vibrational frequencies (in cm<sup>-1</sup>) and intensities (in km/mol)

370.8(1.6)	462.7(13.4)	483.4(1.9)	546.9(63.4)	623.1(21.5)
655.3(36.4)	664.8(25.4)	665.5(6.4)	767.0(0.1)	814.9(31.5)
879.0(50.6)	894.6(41.8)	916.2(9.2)	935.2(27.4)	960.6(57.9)
1007.2(30.5)	1017.5(132.0)	1020.7(39.7)	1099.2(15.9)	1157.5(96.5)
1205.7(50.2)	1227.1(220.3)	1277.5(114.3)	1425.3(25.3)	2721.1(321.9)
2745.1(186.2)	2763.8(169.7)	3789.3(19.6)	3799.4(19.9)	3805.1(64.8)

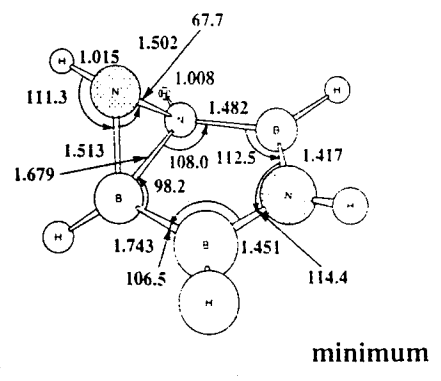
5



Relative Energies:

RHF/SBK(d,p)//RHF/SBK(d,p)	15.8 kcal/mol
MP2/SBK(d,p)//RHF/SBK(d,p)	22.5

8



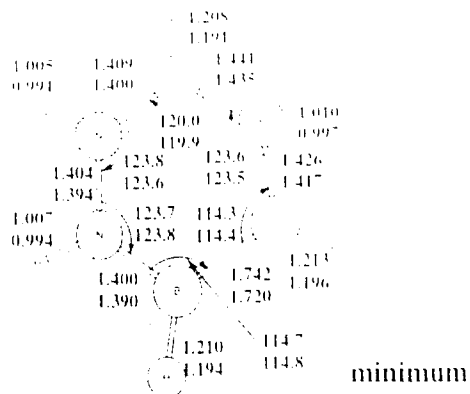
Relative Energies:

RHF/SBK(d)//RHF/SBK(d)	-53.7 kcal/mol
MP2/SBK(d)//RHF/SBK(d)	-36.0

Figure 1. Structures and Energetics of B-N Prismane and its Isomers



3



## Relative Energies:

RHF/SBK(d)//RHF/SBK(d)	-86.3 kcal/mol
MP2/SBK(d)//RHF/SBK(d)	-66.4
RHF/6-31G(d,p)//RHF/6-31G(d,p)	-86.8
MP2/6-31G(d,p)//RHF/6-31G(d,p)	

## Vibrational Frequencies:

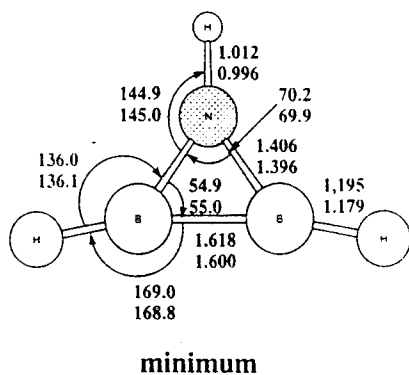
RHF/6-31G(d,p) vibrational frequencies (in  $\text{cm}^{-1}$ )

152.9	265.7	346.2	482.8	491.6
568.5	592.5	753.1	801.5	913.5
928.2	931.7	987.6	999.0	1005.4
1105.7	1129.9	1277.1	1335.4	1449.1
1512.2	1527.3	1613.3	1718.3	2671.4
2700.9	2730.5	3843.6	3879.7	3922.5

RHF/SBK(d) vibrational frequencies (in  $\text{cm}^{-1}$ ) and intensities (in  $\text{kmol}^{-1}$ )

103.0(15.6)	245.3(9.8)	331.5(0.0)	475.3(28.7)	476.6(9.9)
556.3(0.8)	579.3(117.6)	739.5(2.1)	798.8(5.2)	895.5(4.0)
911.3(127.3)	919.6(5.0)	974.8(81.7)	982.6(5.4)	988.2(46.1)
1081.6(22.2)	1106.6(1.2)	1251.6(55.4)	1311.7(50.0)	1428.5(61.6)
1474.4(41.6)	1508.6(342.7)	1590.4(40.2)	1679.4(80.3)	2651.4(279.5)
2700.3(560.1)	2710.0(3.6)	3766.6(20.3)	3844.1(15.9)	3880.4(64.6)

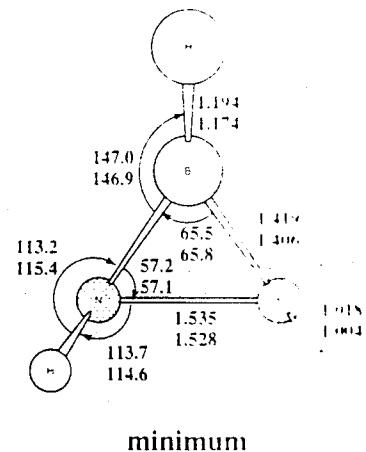
6a



## Relative Energies of 6a + 6b with respect to Prismane:

RHF/SBK(d)//RHF/SBK(d)	20.7 kcal/mol
MP2/SBK(d)//RHF/SBK(d)	30.0
RHF/6-31G(d,p)//RHF/6-31G(d,p)	21.5
MP2/6-31G(d,p)//RHF/6-31G(d,p)	

6b



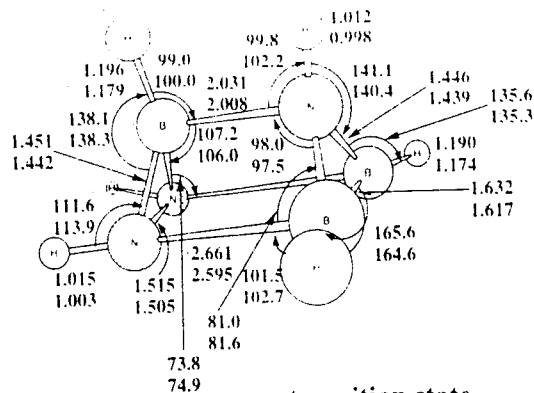
## Vibrational Frequencies:

RHF/6-31G(d,p) vibrational frequencies (in  $\text{cm}^{-1}$ )

597.7	712.8	819.8	883.3
1121.2	1134.1	1443.4	1453.3
3729.5	3746.0		

RHF/SBK(d) vibrational frequencies (in  $\text{cm}^{-1}$ ) and intensities (in  $\text{kmol}^{-1}$ )

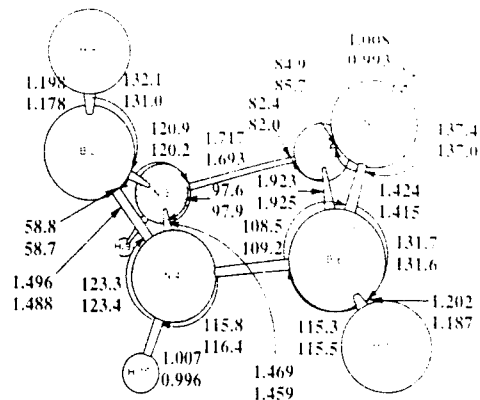
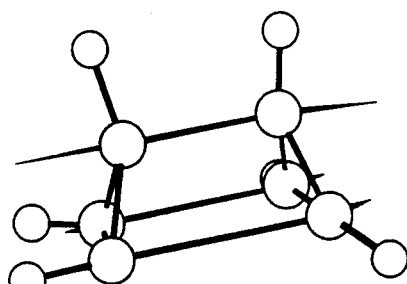
604.5(101.5)	687.8(80.8)	816.4(13.7)	883.3(115.7)
1081.6(70.6)	1134.8(8.3)	1427.5(102.4)	1453.3(126.8)
3686.8(0.6)	3703.6(11.3)		



transition state  
*i* 260.7 cm<sup>-1</sup> RHF/SBK(d)  
 2*i* 288.7 cm<sup>-1</sup> RHF/6-31G(d,p)

Relative Energies:

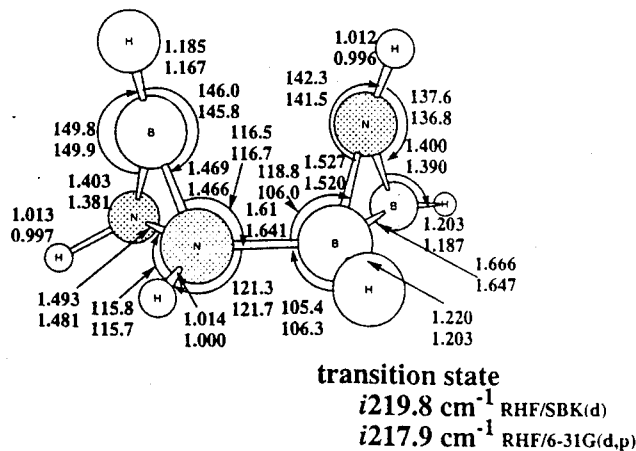
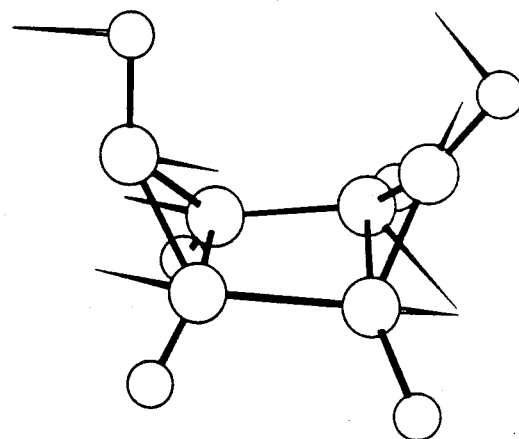
RHF/SBK(d)//RHF/SBK(d)	32.1 kcal/mol
MP2/SBK(d)//RHF/SBK(d)	45.1
RHF/6-31G(d,p)//RHF/6-31G(d,p)	30.9



transition state:  
*i* 788.6 cm<sup>-1</sup> RHF/SBK(d)  
*i* 790.3 cm<sup>-1</sup> RHF/6-31G(d,p)

Relative Energies:

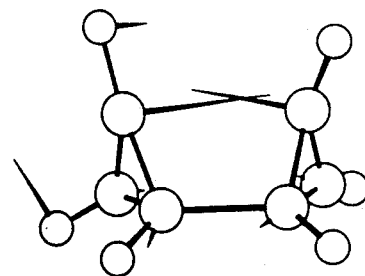
RHF/SBK(d)//RHF/SBK(d)	72.1 kcal/mol
MP2/SBK(d)//RHF/SBK(d)	43.2
RHF/6-31G(d,p)//RHF/6-31G(d,p)	74.0



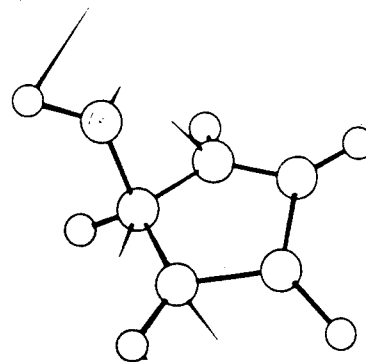
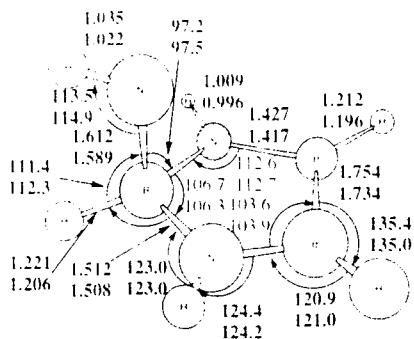
transition state  
*i* 219.8 cm<sup>-1</sup> RHF/SBK(d)  
*i* 217.9 cm<sup>-1</sup> RHF/6-31G(d,p)

Relative Energies:

RHF/SBK(d)//RHF/SBK(d)	26.4 kcal/mol
MP2/SBK(d)//RHF/SBK(d)	35.3
RHF/6-31G(d,p)//RHF/6-31G(d,p)	23.6



11



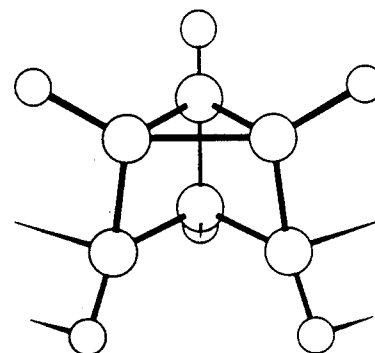
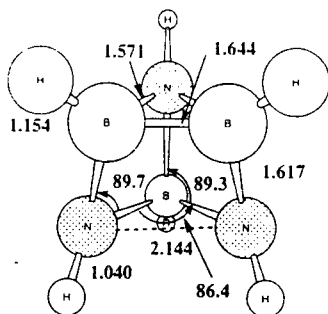
transition state  
*i* 644.1  $\text{cm}^{-1}$  RHF/SBK(d)  
*i* 685.2  $\text{cm}^{-1}$  RHF/6-31G(d,p)

Relative Energies:

RHF/SBK(d)//RHF/SBK(d)	8.4 kcal/mol
MP2/SBK(d)//RHF/SBK(d)	32.1
RHF/6-31G(d,p)//RHF/6-31G(d,p)	9.1

14

Geometries optimized at (6,6)MCSCF/STO-3G



transition state:  
*i* 246.1  $\text{cm}^{-1}$

Relative Energies:

(6,6)MCSCF/STO-3G	11.2 kcal/mol
-------------------	---------------

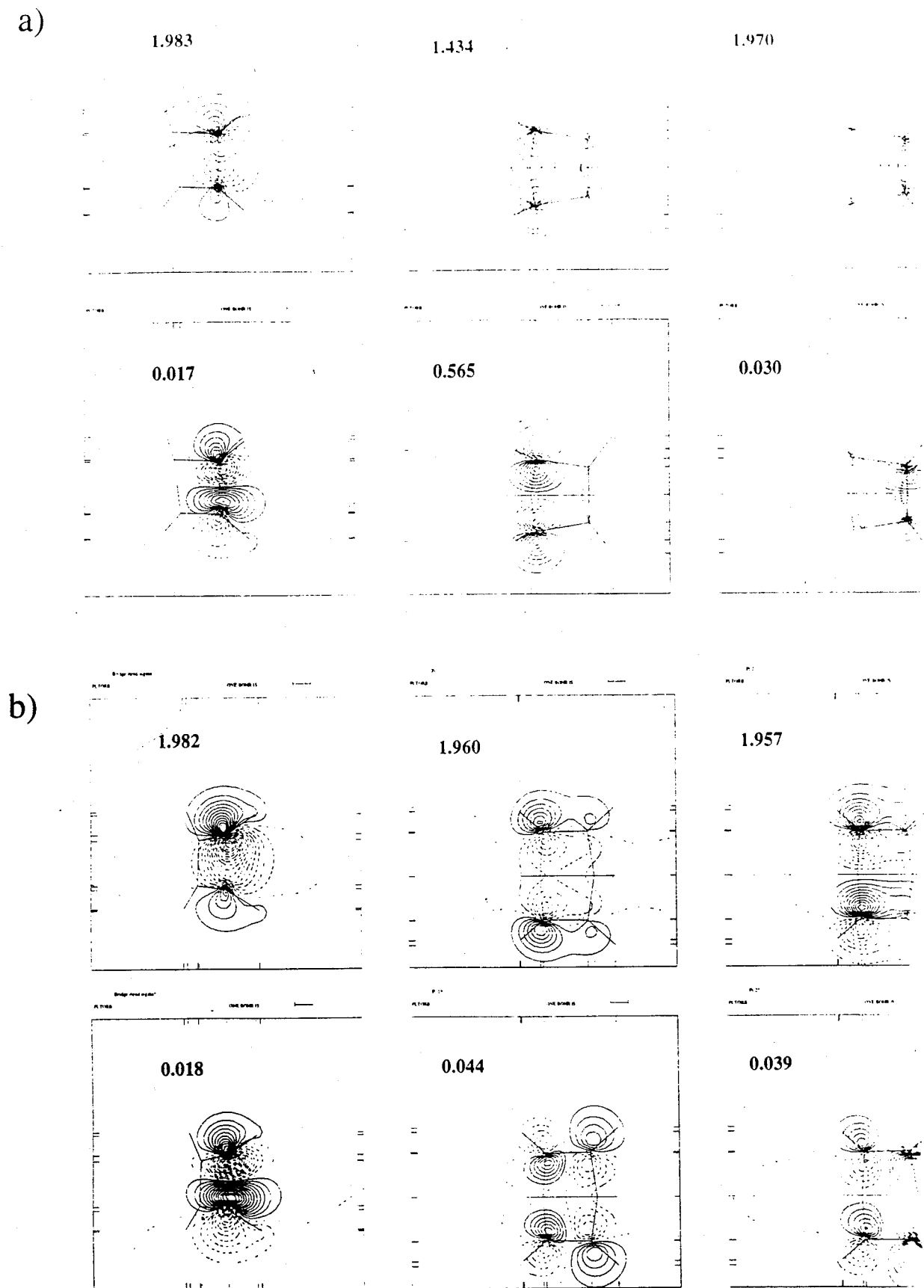


**Figure 2. MCSCF Optimized Orbitals and their Occupation Numbers.**  
 a) Transition state (14) and b) Dewar-benzene (4)

## Potential Energy Surfaces for High Energy Compounds Containing Nitrogen

Galina Chaban, Kiet A. Nguyen and Mark S. Gordon

Department of Chemistry

Iowa State University

Ames, Iowa 50011

Potential energy surfaces (PES) have been studied for isoelectronic compounds containing nitrogen ( $N_3F$ ,  $N_2O_2$ , and  $N_4H_2$ ) which might be possible candidates for high energy materials. The purpose of our study is to identify high lying isomers and to determine pathways connecting them to lower energy products. The next step will be to study possible surface crossings of states with different multiplicity.

Several computational methods were used in our study. Single-configurational perturbation theory (MP2-MP4) and configuration interaction (QCISD) calculations were performed in the regions of PES's corresponding to minima, and the multi-configurational MCSCF, CASPT2, and MRCI wavefunctions were used for study of dissociation processes where the configurational mixing is significant.

### 1. $N_3F$

The ground state open isomer of the  $N_3F$  molecule (fluorine azide) and the process of its decomposition to  $N_2+NF$  ( $^1\Delta$ ) has been studied in a number of experimental and theoretical works<sup>1-6</sup>. It was found that the barrier height of the dissociation is about 15 kcal/mol and that the triplet state crosses the singlet PES on the side of dissociation products.

In this work we report two new, previously unknown metastable isomers found on both the singlet and triplet  $N_3F$  potential energy surfaces. The local minimum on the singlet PES corresponds to the cyclic isomer with  $C_s$  symmetry (see Fig.1), which is less stable energetically than the open fluorine azide by 15-16 kcal/mol (at the QCISD(T)//MP2/6-31G(d) and CASPT2//MCSCF(10,10)/6-31G(d) levels of theory). The process of decomposition of the singlet cyclic isomer to  $N_2+NF$  ( $^1\Delta$ ) was studied using multiconfigurational MCSCF(6,6) wavefunction. The corresponding reaction path is shown in Fig.1. The height of the dissociation barrier is estimated to be about 14 kcal/mol at the CASPT2(10,10)/6-311G(2d)//MCSCF(10,10)/6-31G(d) level of theory, which is close to the barrier height for dissociation of the open isomer.

Two structures (open and cyclic) were found to be minima on the triplet PES of  $N_3F$  at the

ROHF and UHF levels. However, the open isomer is very weakly bound and dissociates at the MP2 level of theory. The cyclic triplet is more stable kinetically. It is separated from the dissociation products  $N_2 + NF(3\Sigma)$  by a barrier of about 15-16 kcal/mol (see Fig.2). The triplet cyclic isomer is very high in energy: 70 kcal higher than the open singlet isomer and about 106 kcal/mol above the dissociation products  $N_2 + NF(3\Sigma)$ .

Since the triplet dissociation products are much lower in energy than the singlet products (about 40 kcal/mol), the singlet and triplet surfaces must cross. The single point CASPT2/MCSCF(10,10) energy for the triplet state at the geometry of the singlet transition state is very close (1 kcal/mol lower) to the corresponding singlet energy. Unlike the case of the open isomer dissociation, in our case the triplet surface crosses the singlet one in the region of the singlet transition state. If the spin-orbit coupling is significant, the singlet cyclic isomer may dissociate to the ground state (triplet) dissociation products.

According to our calculations, the intramolecular rearrangement between singlet cyclic and open isomers is impossible since the isomerization barrier is higher than the barrier of dissociation to  $N_2 + NF$ . The transition state for isomerization was found only at the GVB(1P) level. At all other levels of theory, including MCSCF, the cyclic isomer dissociates before it reaches the isomerization transition state.

Four other transition states were found on the singlet potential energy surface at the RHF and GVB levels of theory, which correspond to rearrangements between two open or two cyclic isomers, but all they are much higher in energy than the transition states for dissociation of both the open and cyclic isomers.

## 2.N<sub>2</sub>O<sub>2</sub>

A number of metastable high energy species has been found on the singlet and triplet surfaces of  $N_2O_2$  molecule.<sup>7</sup> Four of them are shown in Fig.3. They all correspond to minima on the singlet PES and are very high in energy compared with 2 NO and  $N_2 + O_2$  products.

The spin-forbidden decomposition of isomer 4 (a- $N_2O_2$ ) to  $N_2O(X^1\Sigma^+) + O(3P)$  has been studied and the minimum energy crossing point was found to lie only 2 kcal/mol above the a- $N_2O_2$  isomer.<sup>8</sup>

The part of the potential energy surface connecting the bicyclic isomer 2 with the planar isomer 1 was studied previously.<sup>9</sup> The two isomers were found to be separated by a barrier of 40 kcal/mol.

The next step in our study is to consider different dissociation channels for isomers 1-3. Work on the dissociation of these isomers to 2 NO molecules is in progress now. Here we report

preliminary results on the dissociation process of the planar  $D_{2h}$  isomer to 2 NO molecules. Using the MCSCF(10,10)/6-31G(d) wavefunction we found the transition state with the geometry shown in Fig.4. The initial MCSCF active space included four  $\sigma$ (N-O) bonding orbitals, four corresponding antibonding orbitals,  $\pi$  (N-N), and  $\pi^*$ (N-N) orbitals. In the region of the transition state where one N-O bond is broken, the wavefunction has essentially diradical character (the  $\sigma$  and  $\sigma^*$  orbitals corresponding to the broken bond are almost singly occupied). Single point calculations were performed using multi-configurational perturbation theory (CASPT2) based on the MCSCF(10,10) and MCSCF(14,12) reference wavefunctions. The height of the barrier is estimated to be about 50 kcal/mol (see Fig.4). The triplet state is found to intersect the singlet curve on the side of the  $D_{2h}$  isomer in the region about 40 kcal/mol above the isomer.

These results show that the  $D_{2h}$  isomer is kinetically stable with respect to dissociation to two NO molecules. The next step will be to study other possible channels of dissociation (to  $N_2 + O_2$ ,  $NO_2 + O$ ,  $N_2O + N$  products) and barriers for isomerization to the lower energy isomers.

### 3. $N_4H_2$

The MP2/6-31G(d) geometrical parameters and QCISD(T)/6-311G(2df,2pd) relative energies are shown for a number of structural isomers found on the singlet PES of  $N_4H_2$  (Fig.5). All structures shown were verified to be minima at the MP2/6-31G(d) level of theory.

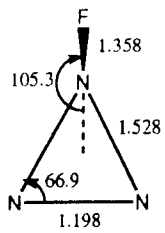
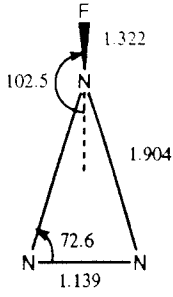
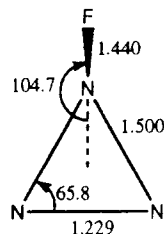
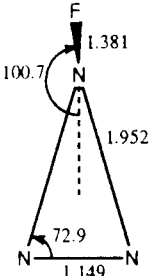
Structures (3)-(6) have been considered previously in theoretical studies<sup>10,11</sup>. Geometrical parameters of the tetrazadiene isomers (4)-(6) have been calculated at the RHF/STO-3G level of theory<sup>10</sup>. A four-membered cyclic isomer (3) has been studied along with other compounds containing 4-membered rings<sup>11</sup> and found to be a minimum at the RHF/6-31G\*\* level of theory. No experimental data is available for geometrical parameters of any of the  $N_4H_2$  compounds.

In addition to these species we found several new isomers: aminoazide (1), which is the ground state isomer, 3-membered cyclic isomer (2), about 28 kcal/mol higher in energy, and three bicyclic isomers (7)-(9), very high in energy (60-65 kcal/mol above the isomer (1)). All  $N_4H_2$  species are much higher in energy than their dissociation products ( $N_2 + N_2H_2$  and  $2N_2 + H_2$ ) and may be considered as possible candidates for high energy material. As a future work we plan to study the kinetic stability of these isomers, considering reaction paths connecting these isomers to each other and to different dissociation products.

## References

1. Peters, N.J.S.; Allen, L.C.; Firestone, R.A. *Inorg. Chem.* **1988**, 27, 755.
2. Christen, D.; Mack, H.G.; Schatte, G.; Willner, H. *J. Am. Chem. Soc.* **1988**, 110, 707.
3. Benard, D. J.; Winker, B. K.; Seder, T. A.; Cohn, R.H. *J. Phys. Chem.* **1989**, 93, 4790.
4. Michels, H. H.; Montgomery, J. A. Proceedings of the High Energy Density Materials Contractors Conference.; AFOSR, Washington, DC, 1989.
5. Kestner, N.R.; Brener, N.E.; Callaway, J. Proceedings of the High Energy Density Materials Contractors Conference.; AFOSR, Washington, DC, 1990.
6. Otto, M.; Lotz, S.D.; Frenking, G. *Inorg. Chem.* **1992**, 31, 3647.
7. Nguyen, K. A.; Gordon, M. S.; Montgomery, Jr. J. A.; Michels, H. H. *J. Phys. Chem.* Submitted.
8. Nguyen, K. A.; Gordon, M. S.; Montgomery, Jr. J. A.; Michels, H. H.; Yarkony, D. R. *J. Chem. Phys.* **1993**, 98, 3845.
9. Nguyen, K. A.; Gordon, M. S. Boatz, J. A. *J. Am. Chem. Soc.* Submitted.
10. Inagaki, S.; Goto, N. *J. Am. Chem. Soc.* **1987**, 109, 3234.
11. Geert van Zandwijk; Janssen, R. A. J.; Buck, H. M. *J. Am. Chem. Soc.* **1990**, 112, 4155.



	<u>singlet cyclic isomer</u>	<u>transition state</u>	<u>N<sub>2</sub> + NF (<sup>1</sup>Δ)</u>
MCSCHF(6,6)/6-31G* geometry			
MCSCHF(6,6)/6-31G*	<b>0.0</b>	<b>10.6</b>	<b>-24.5</b>
SOCI/6-31G*//MC(6,6)	<b>0.0</b>	<b>11.2</b>	<b>-14.5</b>
MRCI/6-31G*//MC(6,6)	<b>0.0</b>	<b>12.2</b>	<b>-12.0</b>
CASPT2/6-31G*//MC(6,6)	<b>0.0</b>	<b>13.2</b>	<b>-12.4</b>
MCSCHF(10,10)/6-31G* geometry			
MCSCHF(10,10)/6-31G*	<b>0.0</b>	<b>18.0</b>	<b>-11.9</b>
SOCI/6-31G*//MC(10,10)	<b>0.0</b>	<b>20.1</b>	<b>0.1</b>
CASPT2/6-31G*//MC(10,10)	<b>0.0</b>	<b>16.9</b>	<b>-8.4</b>
CASPT2/6-311G*//MC(10,10)	<b>0.0</b>	<b>17.6</b>	<b>-11.0</b>
CASPT2/6-311G(2d)//MC(10,10)	<b>0.0</b>	<b>13.7</b>	<b>-13.7</b>

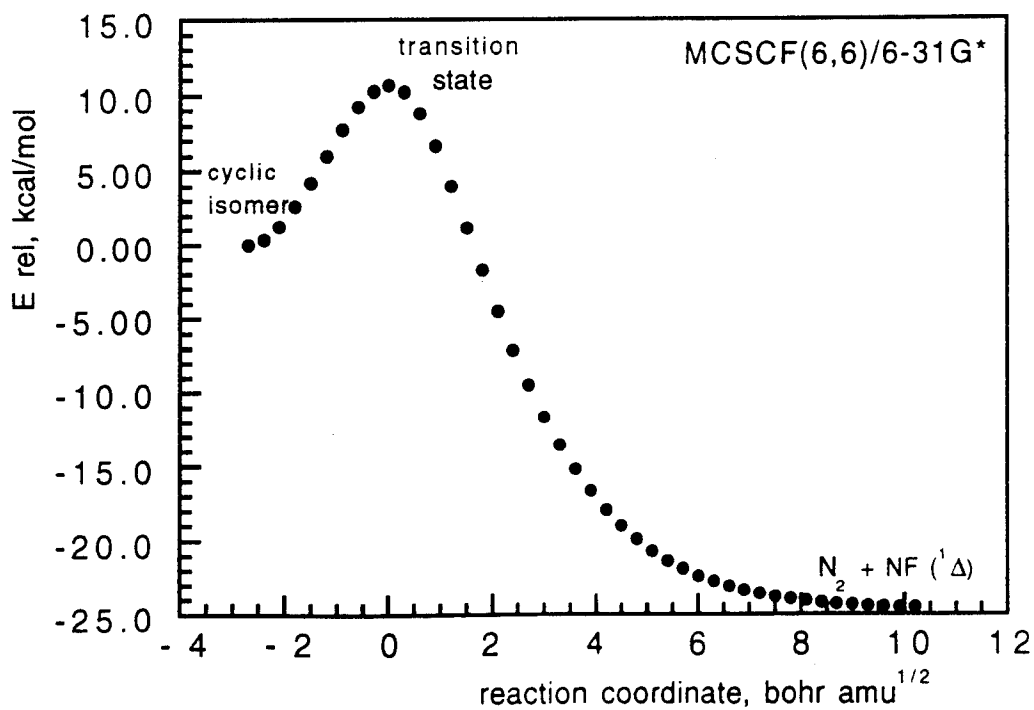
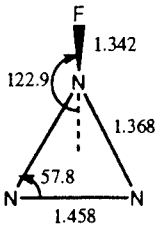
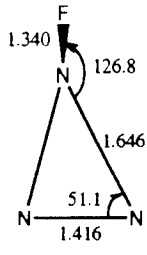


Figure 1. Reaction path for decomposition of singlet cyclic N<sub>3</sub>F

	<u>triplet cyclic isomer</u>	<u>transition state</u>	<u>N<sub>2</sub> + NF (<sup>3</sup>Σ)</u>
MCSCF(6,6)/6-31G* geometry			
MCSCF(6,6)/6-31G*	0.0	9.6	-152.3
CASPT2/MCSCF(6,6)	0.0	15.1	-107.2
MCSCF(10,10)/MCSCF(6,6)	0.0	13.0	-137.6
CASPT2(10,10)/MCSCF(10,10)	0.0	16.3	-106.2

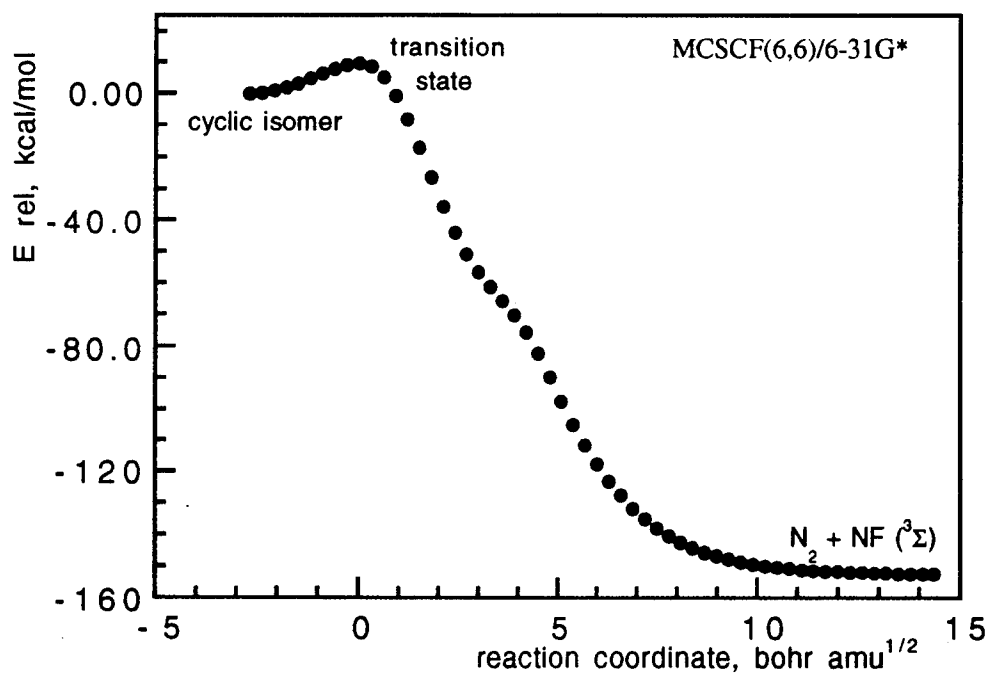


Figure 2. Reaction path for decomposition of triplet cyclic N<sub>3</sub>F

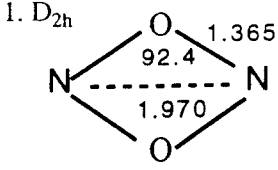
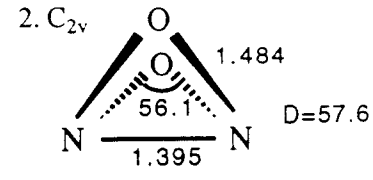
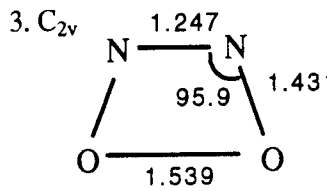
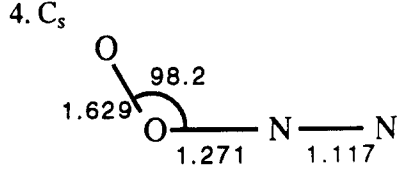
MCSCF(10,10)/6-31G(d) geometries (A,deg.)	1. $D_{2h}$ 	2. $C_{2v}$ 
<u>E rel., kcal/mol</u>		
MCSCF/6-31G(d)	<b>71.0</b>	<b>71.2</b>
CASPT2/6-31G(d)	<b>49.0</b>	<b>77.3</b>
MCSCF/6-311+G(2d)	<b>71.7</b>	<b>73.2</b>
CASPT2/6-311+G(2d)	<b>48.7</b>	<b>81.9</b>
	3. $C_{2v}$ 	4. $C_s$ 
MCSCF/6-31G(d)	<b>43.4</b>	<b>60.3</b>
CASPT2/6-31G(d)	<b>49.4</b>	<b>79.3</b>
MCSCF/6-311+G(2d)	<b>44.4</b>	<b>57.1</b>
CASPT2/6-311+G(2d)	<b>52.9</b>	<b>75.5</b>

Figure 3. Relative energies of high energy  $N_2O_2$  isomers with reference to 2 NO

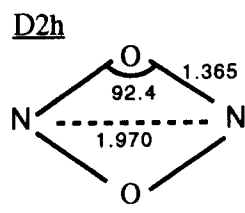
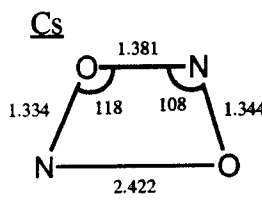
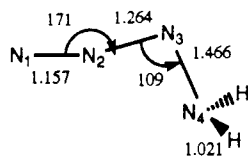
	<u>minimum</u>	<u>transition state</u>	<u>dissociation products</u>
	$D_{2h}$ 	$C_s$ 	2 NO
MCSCF(10,10)/6-31G(d) geometries			
<u>E rel. kcal/mol</u>			
MCSCF(10,10)/6-31G(d)	<b>0.0</b>	<b>50.9</b>	<b>-71.0</b>
CASPT2/MCSCF(10,10)	<b>0.0</b>	<b>54.3</b>	<b>-49.0</b>
MCSCF(14,12)/6-31G(d)	<b>0.0</b>	<b>52.1</b>	<b>-71.2</b>
CASPT2/MCSCF(14,12)	<b>0.0</b>	<b>50.1</b>	<b>-48.9</b>
CASPT2(10,10)/6-311+G(2d)	<b>0.0</b>	<b>52.2</b>	<b>-48.7</b>

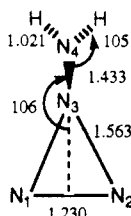
Figure 4. Dissociation of  $D_{2h}$  cyclic isomer of  $N_2O_2$

MP2/6-31G(d)  
geometry

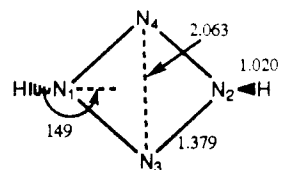
(1)  $C_s$



(2)  $C_s$



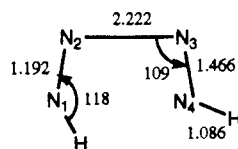
(3)  $C_{2h}$



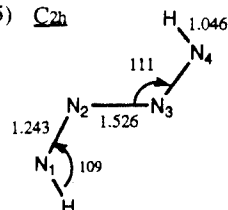
$\Delta E$ , kcal/mol

1. MP2/6-31G(d)	<b>0.0</b>	<b>28.9</b>	<b>26.5</b>
2. MP4SDQ/6-311G(2df,2pd)	<b>0.0</b>	<b>28.8</b>	<b>35.6</b>
3. QCISD(T)/6-311G(2df,2pd)	<b>0.0</b>	<b>27.5</b>	<b>34.0</b>

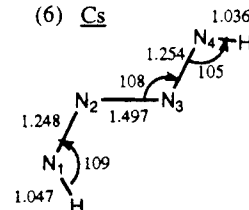
(4)  $C_s$



(5)  $C_{2h}$

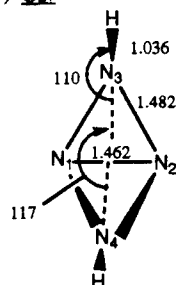


(6)  $C_s$

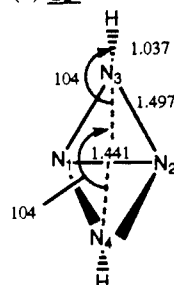


1. MP2/6-31G(d)	<b>8.6</b>	<b>14.7</b>	<b>16.0</b>
2. MP4SDQ/6-311G(2df,2pd)	<b>14.1</b>	<b>8.1</b>	<b>9.3</b>
3. QCISD(T)/6-311G(2df,2pd)	<b>9.2</b>	<b>7.9</b>	<b>9.5</b>

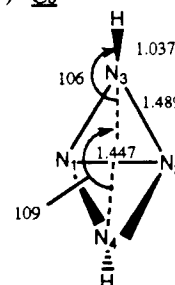
(7)  $C_{2v}$



(8)  $C_{2v}$



(9)  $C_s$



$\Delta E$ , kcal/mol

1. MP2/6-31G(d)	<b>71.5</b>	<b>66.3</b>	<b>63.7</b>
2. MP4SDQ/6-311G(2df,2pd)	<b>68.8</b>	<b>64.8</b>	<b>62.4</b>
3. QCISD(T)/6-311G(2df,2pd)	<b>66.2</b>	<b>62.3</b>	<b>60.0</b>

#### DISSOCIATION PRODUCTS OF $N_4H_2$

	$N_2 + N_2H_2$	$2 N_2 + H_2$
1. MP2/6-31G(d)	<b>-50.7</b>	<b>-103.6</b>
2. MP4SDQ/6-311G(2df,2pd)	<b>-54.0</b>	<b>-96.4</b>
3. QCISD(T)/6-311G(2df,2pd)	<b>-50.2</b>	<b>-92.1</b>

Figure 5. Geometrical parameters and relative energies for  $N_4H_2$  structural isomers

METAL CLUSTERS AND METAL COMPLEXES: MODELS FOR METAL-SEEDED  
ENERGETIC MATERIALS

Michael A. Duncan

Department of Chemistry, University of Georgia, Athens, GA 30602

We are studying a variety of clusters and weakly bound complexes containing the metals lithium, aluminum and magnesium. These complexes are produced in supersonic molecular beams using a laser vaporization cluster source. Metal dimers and neutral complexes are studied with photoionization spectroscopy and "mass analyzed threshold ionization spectroscopy" (MATI), while ion systems are studied with mass selected photodissociation spectroscopy. We will describe our latest results in this area, including photoionization spectroscopy of the new metal dimer, LiAl,<sup>1</sup> and ongoing MATI experiments on lithium and aluminum complexes.

The metal dimer LiAl is produced by laser vaporization using a XeCl excimer laser (Lumonics) at 308 nm on an alloy sample containing 5% lithium and 95% aluminum (Goodfellow). Photoionization is accomplished with a Nd:YAG pumped dye laser system (Spectra-Physics PDL-2 or Lambda Physik "Scanmate" system). The ionization scheme is two-color two-photon, with a tunable ultraviolet laser generated by frequency doubling in a KDP crystal as the first photon and a second dye laser with fixed red wavelengths used to complete the ionization. The isotopic species of the parent ion (<sup>6</sup>Li<sup>27</sup>Al and <sup>7</sup>Li<sup>27</sup>Al) are detected in a homemade time-of-flight mass spectrometer.

Two excited electronic states have been studied for LiAl with electronic origins at

29,391 and 29,888  $\text{cm}^{-1}$ . A portion of the R2PI excitation spectrum is shown in Figure 1. As indicated, both ground and excited state progressions and sequence bands are observed. The vibrational constants determined for the ground and excited states are shown in Table 1. The ground state is of particular interest for comparison to previous theoretical studies. The ground state vibrational frequency is  $\omega_e=317 \text{ cm}^{-1}$ , and the ground state dissociation energy is  $D_e=0.867 \text{ eV}$  (determined from a Morse potential fit to the  $v=0$  to  $v=5$  ground state vibrational levels observed). As indicated in the table, these data are in good agreement with theory.<sup>1,2</sup>

## References

- 1) L.R. Brock, J.S. Pilgrim and M.A. Duncan, to be published.
- 2) A.I. Boldyrev, J. Simons and P.v.R. Schleyer, *J. Chem. Phys.* **99**, 8793 (1993).
- 3) M.E. Rosenkrantz, Air Force Systems Command Interim Report No. PL-TR-91-3088 (1992).

Table 1. Spectroscopic constants ( $\text{cm}^{-1}$ ) for the  ${}^7\text{Li-Al}$  (A),  $\langle\text{B}\rangle$  and ground states, and the comparison to the theory.

	Observed	Theory	
ground state		${}^1\Sigma^+$	
$\omega_e$ "	318	322 <sup>1</sup>	
		331.47 <sup>2,a</sup>	304.78 <sup>2,b</sup>
$\omega_e x_e$ "	4.05	4.19 <sup>2,a</sup>	3.29 <sup>2,b</sup>
$D_e$	6242	6557.7 <sup>2,a</sup>	7098.1 <sup>2,b</sup>
(A) state			
$v_{00}$	29383.9		
$\omega_e$	233		
$\omega_e x_e$	2.55		
$\langle\text{B}\rangle$ state			
$v_{00}$	29882.3		
$\omega_e$	261		
$\omega_e x_e$	0.802		

(a)MCSCF, (b)MRCI

1. A.I. Boldyrev, J. Simons and Paul von R. Schleyer, *J. Chem. Phys.*, **99**, 8793 (1993)
2. Marcy E. Rosenkrantz, Air Force Systems Command Interim Report No. PL-TR-91-3088 (1992)

# The Photoionization Spectrum of LiAl

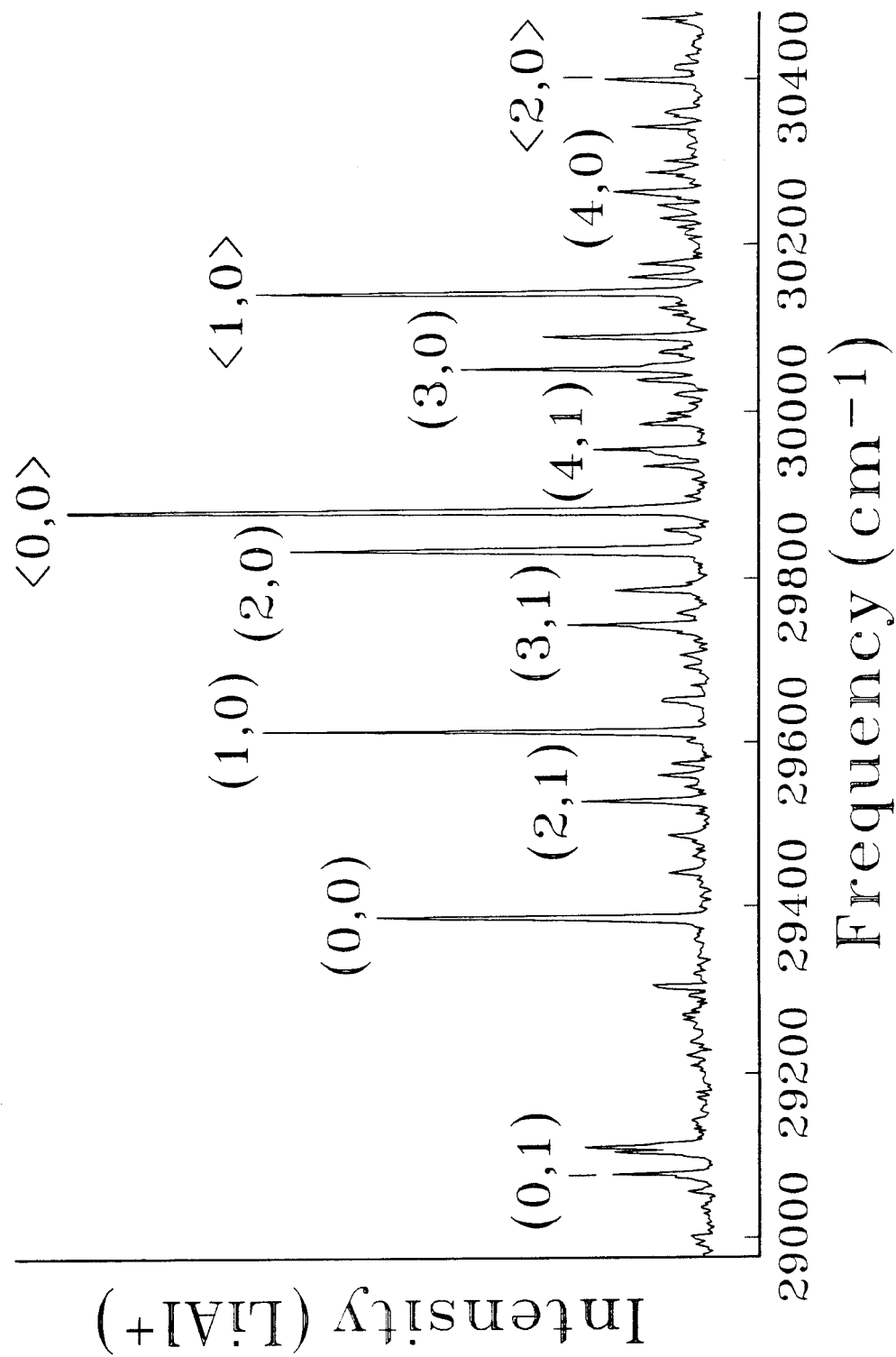


Figure 1.



## VELOCITY SELECTED LASER ABLATION METAL ATOM SOURCE

MICHEL MACLER\* AND MARIO E. FAJARDO

Emerging Technologies Branch, Propulsion Directorate, Phillips Laboratory,  
OLAC PL/RKFE, 10 East Saturn Boulevard, Edwards Air Force Base, CA 93524-7680.

\*AFMC PL/NRC Post-doctoral Research Associate.

### ABSTRACT

We report the successful demonstration of velocity selection of fast aluminum atoms by a novel, non-mechanical, technique. Pulses of atoms with broad velocity distributions are produced by laser ablation of aluminum metal. A second pulsed laser, delayed by  $\sim 1 \mu\text{s}$  and crossed at a right angle to the atomic beam, is used to photoionize only those atoms with unwanted velocities, i.e.: atoms moving too fast or too slow to be hidden behind an opaque mask placed  $\sim 1 \text{ cm}$  from the ablated surface. The photoions are subsequently deflected from the beam by a static magnetic field. We have demonstrated velocity selected Al atom fluxes equivalent to  $\Phi \sim 10^{11} \text{ atoms}/(\text{cm}^2\text{-eV-pulse})$  at a working distance of 10 cm.

### INTRODUCTION

Our research has recently focused on the mechanisms of vapor deposition of impurity atom doped cryogenic van der Waals solids<sup>1,2</sup>. We have conjectured that the incident kinetic energies (KEs) of the codeposited impurity metal atoms is a key factor influencing the reactive and nonreactive microscopic dynamics of these processes. Resolution of these issues would be facilitated by the availability of a compact source for producing an intense, directed beam of nearly monoenergetic metal atoms with KEs tunable throughout the chemically important 1 to 20 eV range. Unfortunately, existing sources<sup>3</sup> based on neutralized ion beams are of limited utility due to low space charge limited fluxes at the lower KEs<sup>4,5</sup>. An alternative compact ion acceleration/neutralization scheme<sup>6</sup> cannot be used in corrosive environments (e.g.: B or Al vapor) due to materials incompatibilities. Also, for the lightest atoms of interest (e.g.: Li, B), KEs  $> 10 \text{ eV}$  require atomic velocities well over  $10^6 \text{ cm/s}$  -- above the capabilities of compact mechanical velocity selectors<sup>7-9</sup> with working distances of order 10 cm. (see Fig. 1.)

However, laser ablation of metals provides a copious source of neutral and ionic, atomic and molecular, metallic species with broad kinetic energy distributions (KEDs) overlapping the desired range<sup>10,11</sup>. We recently reported on measurements of KEDs of laser ablated Al atoms made close to ( $x = 0.5 \text{ cm}$ ) and far from ( $x = 22.5 \text{ cm}$ ) the ablated metal surfaces<sup>12</sup>. The good agreement between these measurements demonstrates the existence of a strong one-to-one correlation between atomic velocity and distance traveled from the surface on the  $\sim 1 \mu\text{s}$  timescale of the short range measurement. In this manuscript, we describe experiments which take advantage of this spatial separation of the various velocity components within the ablated plume to provide the proof-of-concept demonstration of a novel, velocity selected, laser ablation based metal atom source.

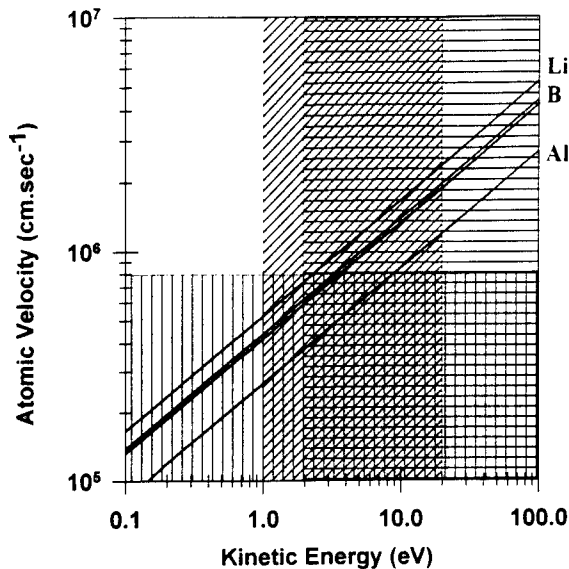


FIG. 1. The vertical line zone depicts the compact mechanical velocity selector region, the horizontal line zone displays the ion charge neutralization regime, whereas the diagonal line zone shows the velocity selected laser ablation atom source regime. Data for Li, B, and Al illustrate zone crossing in the 1-20 eV range.

## EXPERIMENTAL

Figure 2 shows a schematic diagram of the experiment. The ablation source region configuration is described in greater detail in ref. 12. Briefly: the ablated plumes are generated by a focused ablation laser ( $\lambda = 308$  nm, incident intensities,  $I_{abl}$ , of  $5 \times 10^7$  to  $7 \times 10^7$  W/cm<sup>2</sup>); the plume products pass through a magnetic field region ( $|B| = 2.8$  kG) which deflects and rejects Al<sup>+</sup> ions with KE  $\leq 30$  eV; the undeflected products pass through a 0.2 cm diameter aperture located at  $x = 6.0$  cm from the ablated surface. Restricting the source operation to the mild ablation conditions described above yields a beam composed primarily of fast Al atoms (we will report elsewhere<sup>13</sup> on the photofragmentation and photoionization of aluminum clusters and particles produced in quantity at higher ablation intensities).

We characterize the resulting "atomic" beam with a commercially available electrostatic energy analyzer / time of flight mass spectrometer (EEA/TOFMS) system<sup>14</sup> employing pulsed laser photoionization (PI) of neutrals. We use an ArF excimer laser for the PI step, since the output at  $\lambda = 193$  nm is coincident with an extremely strong ( $\sigma = 2 \times 10^{-16}$  cm<sup>2</sup>) Al atom autoionization resonance<sup>15</sup>. Easily attainable PI laser fluences of  $F_{PI} = 15$  mJ/cm<sup>2</sup> result in calculated and observed PI efficiencies of over 95 %. The ions of the proper KE that transit the EEA are accelerated to 2.0 keV, pass through the 1 m TOF tube, and are detected by a low gain ( $\times 10^3$ ) microchannel plate (MCP) detector. By scanning the delay between the ablation and PI lasers and integrating the MCP signals over the range of arrival times corresponding to Al<sup>+</sup> ions, we obtain the TOF distributions of the Al atoms arriving at the PI region with a given KE. These TOF distributions for each KE are in turn integrated to yield directly the contributions to the KEDs. Further details, characteristics, and potential pitfalls of this detection scheme are discussed in ref. 12.

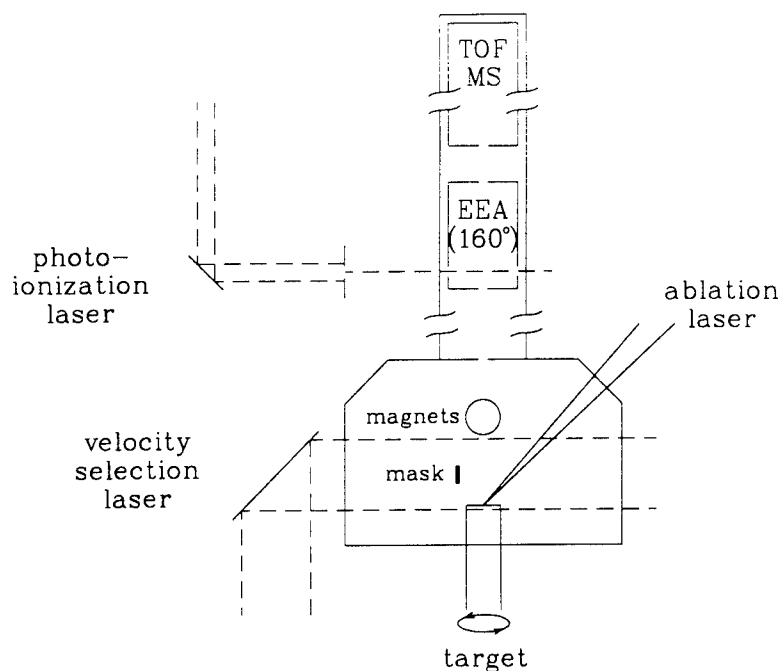


FIG. 2. Experimental diagram.

We also performed a series of Al film deposition rate measurements using a quartz crystal microbalance (QCM) in an attempt to estimate the order of magnitude of the absolute fluxes of the velocity selected Al atoms.

## RESULTS AND DISCUSSION

### (i) KEDs Measurements

We accomplish velocity selection (VS) of the Al atoms by Temporally And Spatially Specific Photolization (TASSPI) of the unwanted velocity components using a third excimer laser (ArF), labeled "velocity selection laser" in Fig. 2, and rejection of the resulting  $\text{Al}^+$  ions by the magnetic deflection field. We use a simple opaque mask consisting of a metal wire of thickness,  $\Delta x$ , centered at a distance,  $x$ , from the ablation target surface, and offset about 1 cm from the atomic beam axis. The mask serves to protect the Al atoms hidden behind it at the arrival time of the VS laser pulse,  $t_{\text{VS}}$ , following the ablation pulse. The surviving Al atoms have a spread of velocities,  $\Delta v$  (full width at half maximum, FWHM), centered around a mean velocity,  $v$ , and a corresponding spread of kinetic energies,  $\Delta \text{KE}$ , all related by:

$$\frac{\Delta \text{KE}}{\text{KE}} \approx 2 \frac{\Delta v}{v} \approx 2 \left[ \left( \frac{\Delta x}{x} \right)^2 + \left( \frac{\Delta t_{\text{VS}}}{t_{\text{VS}}} \right)^2 \right]^{\frac{1}{2}} \quad (1)$$

in which  $\Delta t_{\text{VS}}$  is taken as the sum of the duration of the VS laser pulse and the jitter between the ablation and VS pulses ( $\Delta t_{\text{VS}} \approx 50 \text{ ns}$ ).

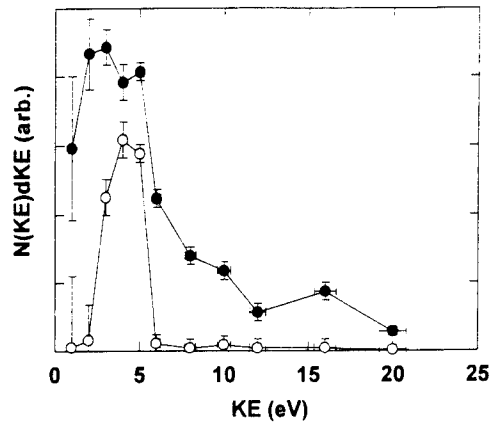


FIG. 3. Velocity selection using a coarse wire mask placed close to the ablation target surface. The closed circles show the nascent Al atom KED, the open circles show the result of the VS laser. The experimental conditions were:  $I_{abl} = 7 \times 10^7 \text{ W/cm}^2$ ,  $F_{VS} = 15 \text{ mJ/cm}^2$ ,  $\Delta x = 0.16 \text{ cm}$ ,  $x = 0.45 \text{ cm}$ ,  $t_{VS} = 0.94 \mu\text{s}$ . The error bars represent the estimated  $\pm 1 \sigma$  limits.

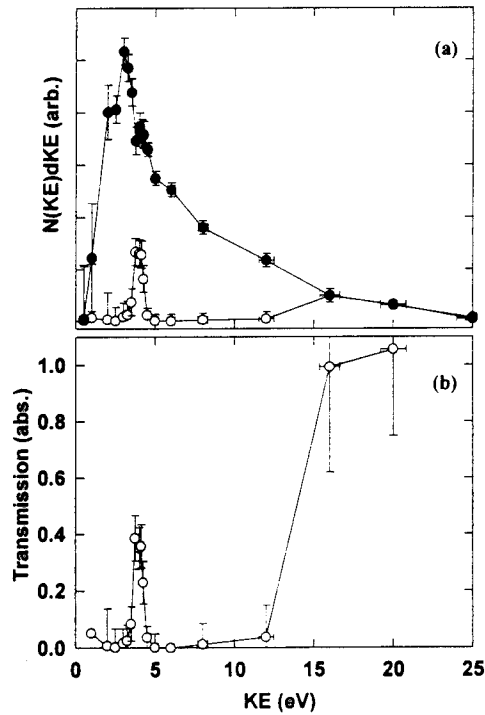


FIG. 4. Velocity selection using a thinner wire mask placed near the middle of the velocity selection port window. In panel (a) the closed circles show the nascent Al atom KED, the open circles show the result of the VS laser. The experimental conditions were:  $I_{abl} = 7 \times 10^7 \text{ W/cm}^2$ ,  $F_{VS} = 15 \text{ mJ/cm}^2$ ,  $\Delta x = 0.064 \text{ cm}$ ,  $x = 0.90 \text{ cm}$ ,  $t_{VS} = 1.70 \mu\text{s}$ . Panel (b) shows the transmission function of the velocity selection process for these conditions. The error bars represent the estimated  $\pm 1 \sigma$  limits.

Figure 3 shows the results of our first attempt at VS by TASSPI in which we used a rather thick wire mask placed close to the ablation target surface. The KED of the transmitted Al atoms has a peak near 4 eV, and a width of  $\Delta KE \approx 3$  eV. This data also demonstrates good peak transmission,  $T_{Al}(KE)$ , of the selected Al atoms ( $T_{Al}(4 \text{ eV}) \approx 80\%$ ) as well as strong rejection of the unwanted velocity components throughout the rest of the 1 to 20 eV range.

Figure 4 shows a subsequent attempt to produce a beam with a narrower KED by placing a thinner wire mask farther away from the ablated target surface. Indeed, the KED of the transmitted Al atoms, again peaked at 4 eV, has sharpened to  $\Delta KE = 0.65$  eV. The data also show one of the limitations of our experimental setup: attempts to produce narrow KEDs by placing the mask too far from the target surface can be accompanied by an increase in the transmission of the fastest Al atoms. This is due to the relatively short overall length of our VS region, only 2 cm, so that metal atoms with velocities in excess of  $v \approx (2 \text{ cm})/t_{VS}$  escape the effects of the VS laser and continue through the magnetic field and beam defining aperture. This puts an upper limit on the range of useful delays between ablation and VS laser pulses; *i.e.*: ensuring that Al atoms with KEs up to  $\approx 30$  eV are rejected in our apparatus requires maintaining  $t_{VS} \leq 1.4 \mu\text{s}$ . Thus, tuning of the desired KE of the transmission peak can be accomplished either by scanning  $t_{VS}$ , within the allowable limits, or by mechanically moving the opaque mask to change  $x$ .

We have observed VS of Al atoms to produce KEDs peaked at 2 and 8 eV. We have produced Al atom KEDs peaked at 2 eV with widths as narrow as  $\Delta KE \approx 0.2$  eV (with:  $x = 1.1$  cm,  $\Delta x = 0.06$  cm,  $t_{VS} = 2.9 \mu\text{s}$ ,  $T(KE = 2 \text{ eV}) = 50\%$ ,  $T(KE > 6 \text{ eV}) = 100\%$ ). These results are not pictured here.

The FWHM of the experimental and calculated KEDs have been compared for various VS conditions (Fig. 5). The agreement between measured and calculated reduced FWHM is good. Eqn. 2 illustrates the quantitative relationship between calculated and experimental reduced FWHM.

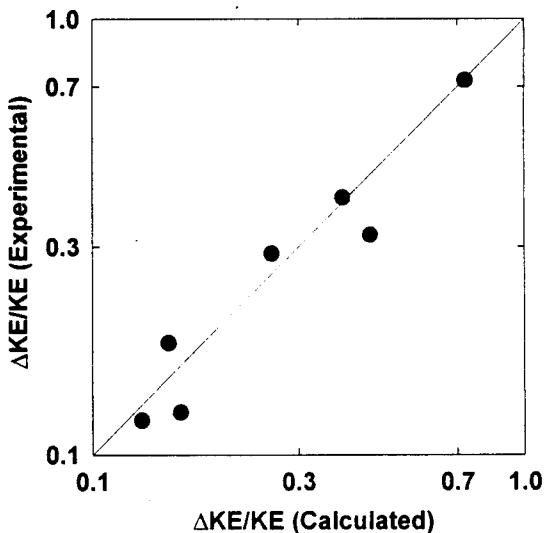


Fig. 5. The solid line corresponds to a 1 to 1 correlation between calculated and experimental reduced FWHM. The solid circles are the actual points.

$$\frac{\Delta KE}{KE}(\text{exp.}) \approx (0.96 \pm 0.045) \frac{\Delta KE}{KE}(\text{calc.}) \quad (2)$$

Within uncertainty, experimental and calculated reduced FWHM are equal. Thus, eqn. 1 describes accurately the behavior of the VS source.

The magnitude of the transmission function maximum decreases as we use progressively thinner wire masks, indicating that diffraction of the VS laser beam by the mask is significant in our current setup.

## (ii) Atomic Fluxes Measurements

Atomic fluxes were derived from deposition rates measurements. The QCM outputs were thickness vs. time. These curves were essentially straight lines, the slope of which was proportional to a mass of Al/time. Knowing the actual diameter of the quartz microcrystal, assuming a film density of  $2.7 \text{ g.cm}^{-3}$ , and a KE independent Al sticking coefficient of unity, these thicknesses can be converted into number of Al atoms. As the lasers' repetition rates were known, we could derive the flux of atoms per pulse per crystal area, at the distance  $x$  from the target surface at which the microcrystal was located.

First, we removed the deflection magnets and beam defining aperture, and placed the QCM at a working distance of  $x = 8.0 \text{ cm}$  from the ablation target. We estimated a total incident Al flux of  $\Phi(I_{\text{abl}} = 7 \times 10^7 \text{ W/cm}^2, x = 8 \text{ cm}) \approx 1.2 \times 10^{12} \text{ atoms/cm}^2$ . The ratio of the Al deposition rates obtained with this geometry at  $I_{\text{abl}} = 7 \times 10^7 \text{ W/cm}^2$  to  $I_{\text{abl}} = 5 \times 10^7 \text{ W/cm}^2$  was  $R \approx 1.8$ , in fair agreement with the corresponding ratio of total Al atom fluxes previously measured using the EEATOFMS system (*i.e.*:  $R \approx 1.6$ , see ref. 12, fig. 3). Second, we replaced the deflection magnets and beam defining aperture, moved the QCM back to a working distance of  $x' = 18.0 \text{ cm}$ , and confirmed that the Al deposition rates scaled roughly as  $(x/x')^2$ , *e.g.*:  $\Phi(I_{\text{abl}} = 7 \times 10^7 \text{ W/cm}^2, x = 18 \text{ cm, no VS}) \approx 2.1 \times 10^{11} \text{ atoms/cm}^2$ . Finally, we measured the Al deposition rates at  $x = 18 \text{ cm}$ , while employing VS by TASSPI under conditions similar to those used in the original experiment depicted in fig. 2, and obtained  $\Phi(I_{\text{abl}} = 7 \times 10^7 \text{ W/cm}^2, x = 18 \text{ cm, } \Delta KE \approx 3 \text{ eV}) \approx 1.2 \times 10^{11} \text{ atoms/cm}^2$ . The ratio of selected to unselected deposition rates at  $x = 18 \text{ cm}$  is  $R \approx 0.5$ , about twice the ratio of selected to unselected total Al atom fluxes in the KEDs shown in fig. 2, an appropriate reminder of the rough nature of these comparisons. From these measurements, we estimate that this source delivers velocity selected Al atom fluxes of  $\Phi \sim 10^{11} \text{ atoms/(cm}^2\text{-eV-pulse)}$  at a working distance of  $10 \text{ cm}$ .

## CONCLUSION

We have demonstrated a novel method for producing velocity selected beams of neutral Al with tunable kinetic energies throughout the 2-8 eV range with a flux  $\Phi \sim 10^{11} \text{ atoms/(cm}^2\text{-eV-pulse)}$ . The kinetic energy range can be extended to 1-20 eV without any apparatus modification. The widths of the KED resulting from VS are quantitatively predicted by eqn. 1. The velocity distribution of the velocity selected metal atoms decreases as the mask is made narrower, down to a fundamental limit imposed by:

- The finite duration of the ablation laser pulses and the initial plume formation.
- The finite duration of the ionization laser pulses.

- Diffraction limitations on imaging the masked ionization laser onto the plume. The durations mentioned in the first two items will not be altered in our laboratory, as 20-30 ns laser pulses are the only pulses that will permit reasonable velocity selected atomic fluxes. However, we hope to reduce the effect of laser beam diffraction by adopting laser lithographic techniques and imaging the mask onto the atomic beam.

In principle, TASSPI is almost universal, as: any material which can be formed into a solid target can be ablated and any neutral species which can be photoionized intact can be velocity selected. It is compact (10 cm working distance from the ablation target to the reaction zone or deposition substrate) and does not involve high velocity moving mechanical parts.

TASSPI has some potential commercial applications, as the KE of incident atoms in device growth is a crucial parameter with respect to layer/film quality. The growth of semiconductor, superconductors, and nonlinear optical thin films and microstructures are all potential applications for VS by TASSPI. In particular, velocity selected Al atoms are of interest for:

- AlAs/AlGaAs microstructures.
- Al based Josephson Junctions and Field Effect Transistors.

TASSPI is a true example of DUAL USE TECHNOLOGY.

Our plans for the immediate future include:

- Investigation of the velocity selected Al beam purity (evidence of clusters and particulates.)
- Attempt VS of laser ablated B and Li atoms.

We hope that by using resonance enhanced multiphoton photoionization (REMPI) schemes, we will be able to apply our velocity selection method to other atomic or molecular species.

## REFERENCES

1. M.E. Fajardo, J. Chem. Phys. **98**, 110 (1993).
2. S. Tam and M.E. Fajardo, J. Chem. Phys. **99**, 854 (1993).
3. Atomic and Molecular Beam Methods, Volume 1, edited by G. Scoles, D. Bassi, U. Buck, and D. Laine (Oxford, New York, 1988).
4. M. Hollstein and H. Pauly, Z. Phys. **196**, 353 (1966).
5. S. Kita, H. Hubner, W. Kracht, and R. Duren, Rev. Sci. Instrum. **52**, 684 (1981).
6. R.K.B. Helbing and E.W. Rothe, Rev. Sci. Instrum. **39**, 1948 (1968).
7. H.U. Hostettler and R.B. Bernstein, Rev. Sci. Instrum. **31**, 872 (1960).
8. L.T. Crowley, M.A.D. Fluendy, and K.P. Lawley, Rev. Sci. Instrum. **41**, 666 (1970).
9. G.O. Este, B. Hilko, D. Sawyer, and G. Scoles, Rev. Sci. Instrum. **46**, 223 (1975).
10. J.F. Friichtenicht, Rev. Sci. Instrum. **45**, 51 (1974).
11. H. Kang and J.L. Beauchamp, J. Phys. Chem. **89**, 3364 (1985).
12. M. Macler and M.E. Fajardo, Appl. Phys. Lett. **62**, xxxx (1994).
13. M. Macler and M.E. Fajardo, submitted to Appl. Phys. Lett.
14. M.J. Shea, R.N. Compton, and R.L. Hettich, Phys. Rev. A **42**, 3579 (1990).
15. R.D. Hudson and L.J. Kieffer, Atomic Data **2**, 205 (1971).

## Laser Pyrolysis of Explosives

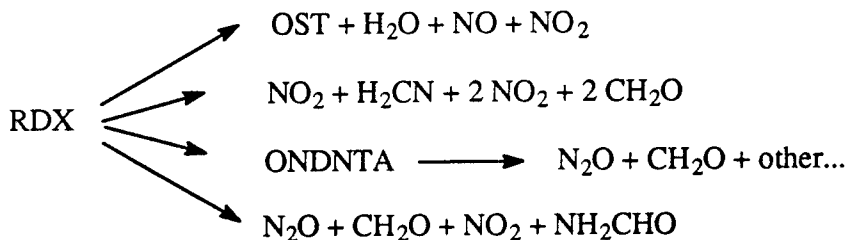
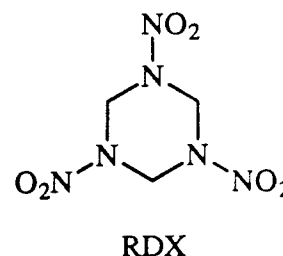
Charles A. Wight

Department of Chemistry  
 University of Utah  
 Salt Lake City, UT 84112

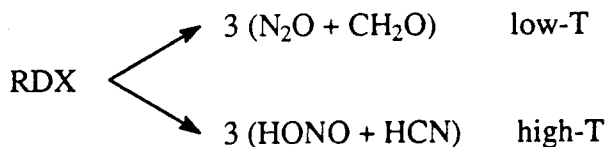
### Introduction

The design of new explosives and propellants that are both powerful and insensitive to accidental ignition is a formidable challenge. This is because the details of what causes some explosives to be more sensitive than others are poorly understood. It is widely believed that the keys to this issue are to be found in the combustion mechanisms of explosives. However, the combination of many parallel and sequential reaction steps and the large amounts of heat released make it difficult to unravel the mechanisms by conventional kinetic techniques.

An good example can be found in the work of Behrens and Bulusu<sup>1,2,3,4</sup> on the thermal decomposition mechanism of hexahydro-1,3,5-trinitro-1,3,5-triazine, better known as RDX. These workers found that there are at least four independent decomposition pathways that are significant when RDX is heated at rates of about 2 K/min. Although the initial step in the decomposition has been widely assumed to be N-N bond scission (release of an NO<sub>2</sub> radical), Behrens and Bulusu found that only 10% of the products could be directly associated with this mechanism.



It is well known that the distribution of gaseous products undergoes a distinct shift as the heating rate is increased (i.e., the decomposition occurs at higher temperature). Brill and co-

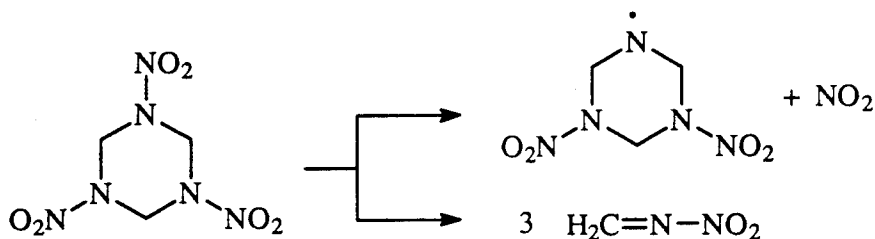


workers have developed a technique<sup>5</sup> whereby gaseous products are detected by FTIR following



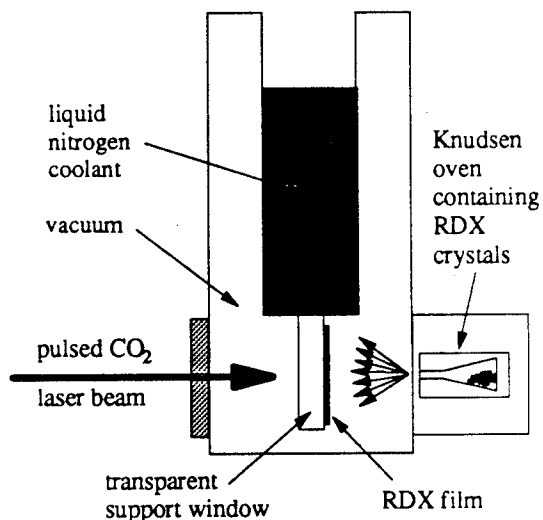
rapid heating of RDX at up to 2000 K/s. They noted that the low-temperature channel is exothermic, whereas the high-temperature channel is substantially endothermic. This switch in the kinetic pathway provides a built-in regulatory mechanism that controls the burning rate of the RDX propellant.

In the late 1980's, Y.T. Lee and co-workers<sup>6</sup> carried out a molecular beam thermal decomposition experiment on RDX, in which the gaseous molecules were heated with a CO<sub>2</sub> laser at about 10<sup>9</sup> K/s. The time-of-flight distributions of the products strongly suggested that the major decomposition pathway under these conditions is concerted depolymerization to three identical molecules of methylene nitramine. Only about a third of the product yield was consistent with the



more conventional N-N bond scission pathway. Lee's experiment suggested that the concerted depolymerization pathway could be an important mechanism in the combustion of RDX under explosive conditions, where heating rates of the propellant can be extremely high. However, in order to prove it, a comparable experiment has to be done in the condensed phase under conditions that simulate a thermal explosion.

This consideration prompted us to develop a thin film laser pyrolysis technique to study thermal decomposition of RDX and other energetic materials under conditions that simulate a thermal explosion. Details of the experimental methodology have been described elsewhere.<sup>7</sup> Briefly, a thin film (~10 μm) of propellant is formed by vapor deposition onto the surface of a transparent support window (CaF<sub>2</sub> or CsI) which is maintained at 77 K (see the schematic diagram). Following deposition, the film is irradiated with the output of a line-tunable CO<sub>2</sub> laser at 944 cm<sup>-1</sup>. The laser energy is absorbed directly by the RDX film, and is heated to a peak temperature of approximately 1000 K in 35 μs (the nominal pulse duration of the laser). The peak temperature can be controlled simply by adjusting the fluence of the laser. Because the film is thin, the excess heat is conducted into the substrate window on a time scale of about 1 ms. The return of the film temperature to 77 K traps the initial thermal decomposition products for subsequent detection by Fourier-transform infrared spectroscopy.



#### Results for RDX

The figure below shows FTIR spectra of an RDX film before and after laser pyrolysis at relatively high fluence. Several small molecule products are observed, including N<sub>2</sub>O<sub>4</sub> (the dimer

of  $\text{NO}_2$ ), HCN,  $\text{N}_2\text{O}$ , and NO. Experiments carried out just above the threshold fluence for product formation show that the initial product is  $\text{N}_2\text{O}_4$ . There is no evidence for formation of  $\text{CH}_2\text{NNO}_2$  in any of the FTIR spectra, so we conclude that *condensed phase* thermal decomposition of RDX is initiated by N-N bond scission.

Several different types of experiments were performed to elucidate further details of the decomposition process. Firstly, the pyrolysis was performed on films that were sandwiched between two cryogenic support windows in order to prevent loss of RDX or reaction products by vaporization. Measurements of the  $\text{N}_2\text{O}_4$  product yields were made by comparing the integrated band intensities to calibration experiments in which thin films of authentic  $\text{N}_2\text{O}_4$  were prepared. These measurements suggested that one  $\text{N}_2\text{O}_4$  product molecule is formed for every two RDX molecules destroyed (i.e., *one  $\text{NO}_2$  molecule per RDX*, on average).

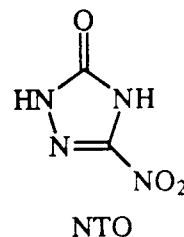
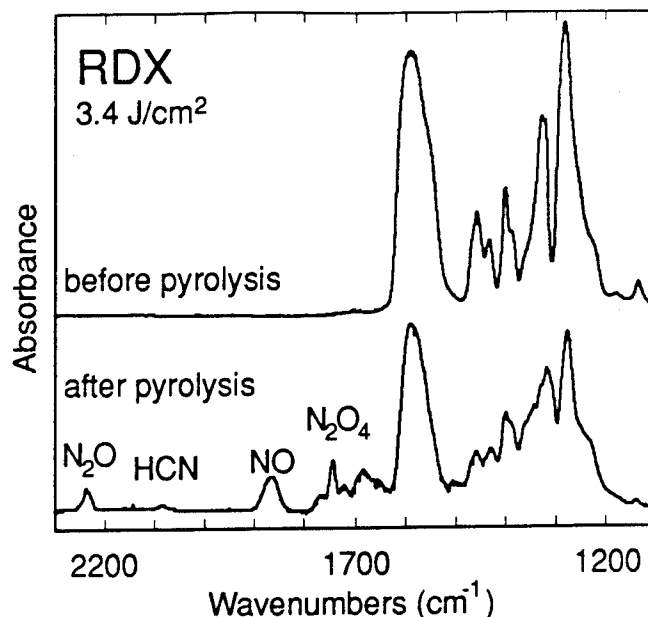
Secondly, RDX films were pyrolyzed at various laser fluences without a cover window. In this way, products formed in the gas phase could escape the sample window and not be detected by the FTIR analysis. Comparison of these results with the double-window experiments showed that  $\text{N}_2\text{O}_4$  is definitely a *condensed phase reaction product*. All of the other products are formed only under conditions where a substantial fraction of the RDX film is vaporized.

The vapor deposition process at 77 K forms RDX films that are amorphous (non-crystalline) as evidenced by substantial inhomogeneous broadening of the bands in the FTIR spectra. However, it was also possible to produce crystalline films by annealing to 35°C followed by recooling to 77 K. Pyrolysis experiments carried out on amorphous and crystalline films under otherwise similar conditions afforded essentially identical yields of  $\text{N}_2\text{O}_4$ . This observation provides strong evidence that the N-N bond scission mechanism is unimolecular rather than bimolecular, because the latter would be expected to be sensitive to variations in the relative orientations of neighboring molecules in the film.

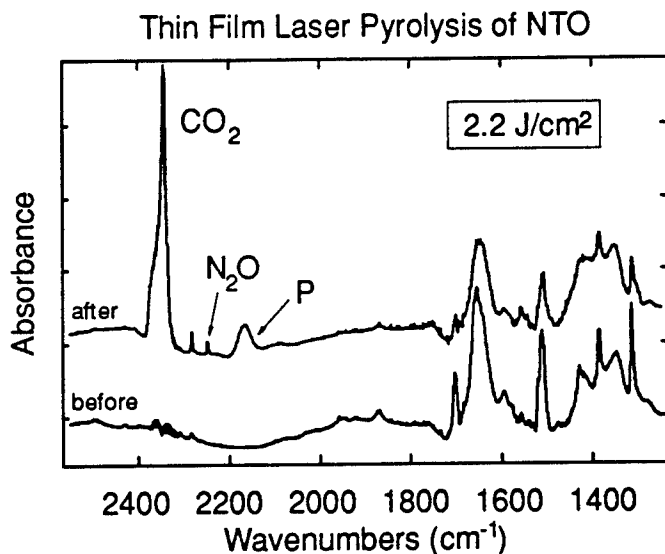
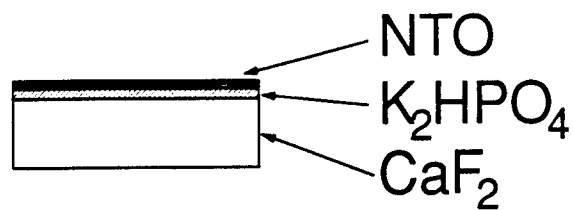
Finally, we were able to show that the  $\text{N}_2\text{O}_4$  product is formed by recombination of  $\text{NO}_2$  product molecules from separate RDX parent molecules. This was accomplished in an isotopic crossover experiment in which RDX and RDX- $^{15}\text{N}_8$  were randomly mixed in a film and subjected to laser pyrolysis.<sup>8</sup> The  $\text{N}_2\text{O}_4$  product consisted of a statistical mixture of  $^{15}\text{N}$  and  $^{14}\text{N}$  isotopomers, showing that each RDX molecule affords only a single  $\text{NO}_2$  product. The other nitrogen atoms are evidently converted to  $\text{N}_2\text{O}$ , HCN, NO and  $\text{N}_2$ .

#### Extension of the Method to Other Explosives

The thin film laser pyrolysis of RDX works well because this molecule has a strong absorption bands within the tuning range of the  $\text{CO}_2$  laser. Unfortunately, other explosives such as 3-nitro-1,2,4-triazol-5-one (NTO) do not. However, it is nevertheless possible to heat materials of this type indirectly. This is done by preparing a three-layer sample as depicted below. A  $\text{CaF}_2$  window is first covered with a thin layer of  $\text{K}_2\text{HPO}_4$ , which has an absorption band in the range of the  $\text{CO}_2$  laser. This is followed by a layer of



NTO. Laser pyrolysis of such a sample at high fluence results in formation of a large  $\text{CO}_2$  product band in the FTIR spectrum. A small amount of  $\text{N}_2\text{O}$  is also formed, along with an unidentified product having an absorption feature at  $2166\text{ cm}^{-1}$ . This feature persists even after the film is warmed to room temperature, so the corresponding product is relatively non-volatile. Experiments are in progress to clarify the decomposition mechanism, including identification of the initial products in the first step of the process.



#### Acknowledgments

Virtually all of the thin film laser pyrolysis experiments described in this paper were performed by Tod Botcher, who recently defended his Ph.D. thesis in Chemistry. The work on RDX was supported by the Army Research Office. The project on NTO is currently supported by the Air Force Office of Scientific Research.

#### References

1. Behrens, Jr., R. *J. Phys. Chem.* **1990**, *94*, 6706.
2. Behrens, Jr., R.; Bulusu, S. *J. Phys. Chem.* **1991**, *95*, 5838.
3. Behrens, Jr., R.; Bulusu, S. *J. Phys. Chem.* **1992**, *96*, 8877.
4. Behrens, Jr., R.; Bulusu, S. *J. Phys. Chem.* **1992**, *96*, 8891.
5. Brill, T.B.; Brush, P.J. *Phil. Trans. R. Soc. Lond. A* **1992**, *339*, 377.
6. Zhao, X.; Hintsä, E. J.; Lee, Y. T. *J. Chem. Phys.* **1988**, *88*, 801.
7. Botcher, T.R.; Wight, C.A. *J. Phys. Chem.* **1993**, *97*, 9149.
8. Botcher, T. R.; Wight, C. A. *J. Phys. Chem.* **1994**, in press.

## Strained Ring Hydrocarbon Pyrolysis

Angelo J. Alfano  
Hughes STX  
Air Force Phillips Laboratory  
Edwards Air Force Base, CA

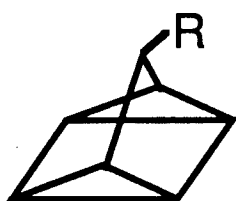
HEDM (high energy density) fuel molecules encompass a wide range of varieties. This includes the potential use of strained ring hydrocarbons as additives to conventional fuels (RP1). The specific impulse increases expected from these additives would result in larger deliverable payloads with significant economic benefits. However, to successfully recover the stored energy from a thermodynamically attractive HEDM system, an understanding of the available decomposition pathways is needed. We have begun a mechanistic and kinetic study of the bridgehead substituted quadricyclane/norbornadienes (Figure 1) to provide some general strained ring structure-combustion properties guidelines.

A well-stirred reactor (Figure 2) in conjunction with gas chromatography is being used to study pyrolysis/combustion mechanisms in the 298-1000 K range. To clarify the role of surface effects on the mechanisms and to reach higher temperatures and heating rates, an infrared laser sensitized pyrolysis apparatus has also been constructed. A baseline study on unsubstituted quadricyclane (Figure 3) agrees with the accepted pyrolysis mechanism and the published rate constants. Our gas phase results for the 7-t-butoxy substituted norbornadiene (Figure 4) indicate a pyrolysis mechanism with one dominant unimolecular reaction which yields a substituted cycloheptatriene. The rate for cycloheptatriene production is 5 orders of magnitude greater in 7-t-butoxynorbornadiene as compared to norbornadiene at 523 K.

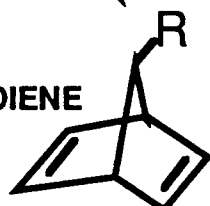
# SUBSTITUTED QUADRICYCLANE PYROLYSIS

R = H, Cl, t-butoxy, phenyl

QUADRICYCLANE



NORBORNADIENE



ADDITIONAL  
PRODUCTS

CYCLOHEPTATRIENE

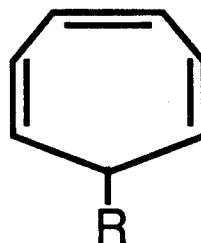


FIGURE 1

# WELL-STIRRED REACTOR AND ANALYTICAL INSTRUMENTATION FOR PYROLYSIS STUDIES

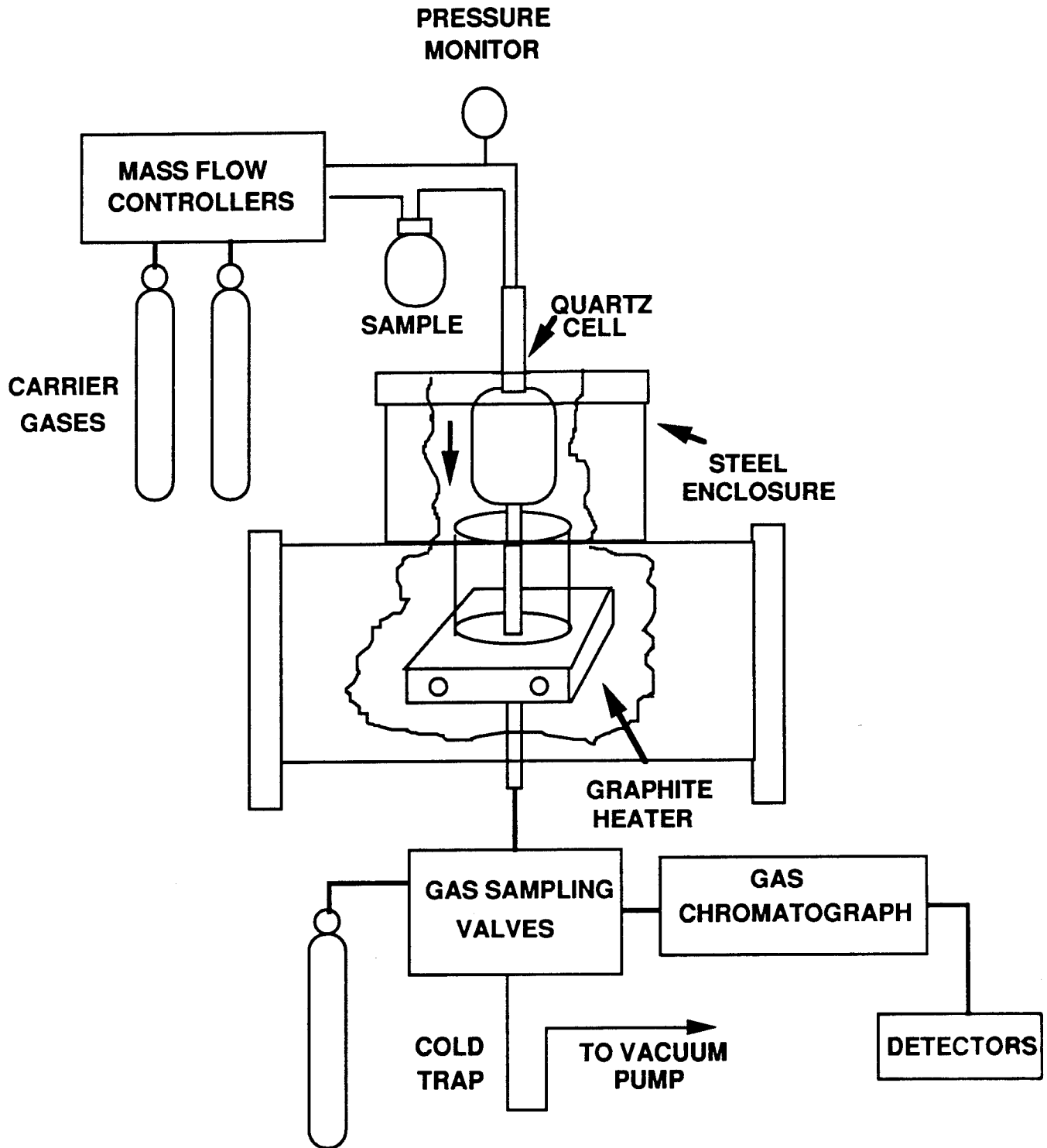
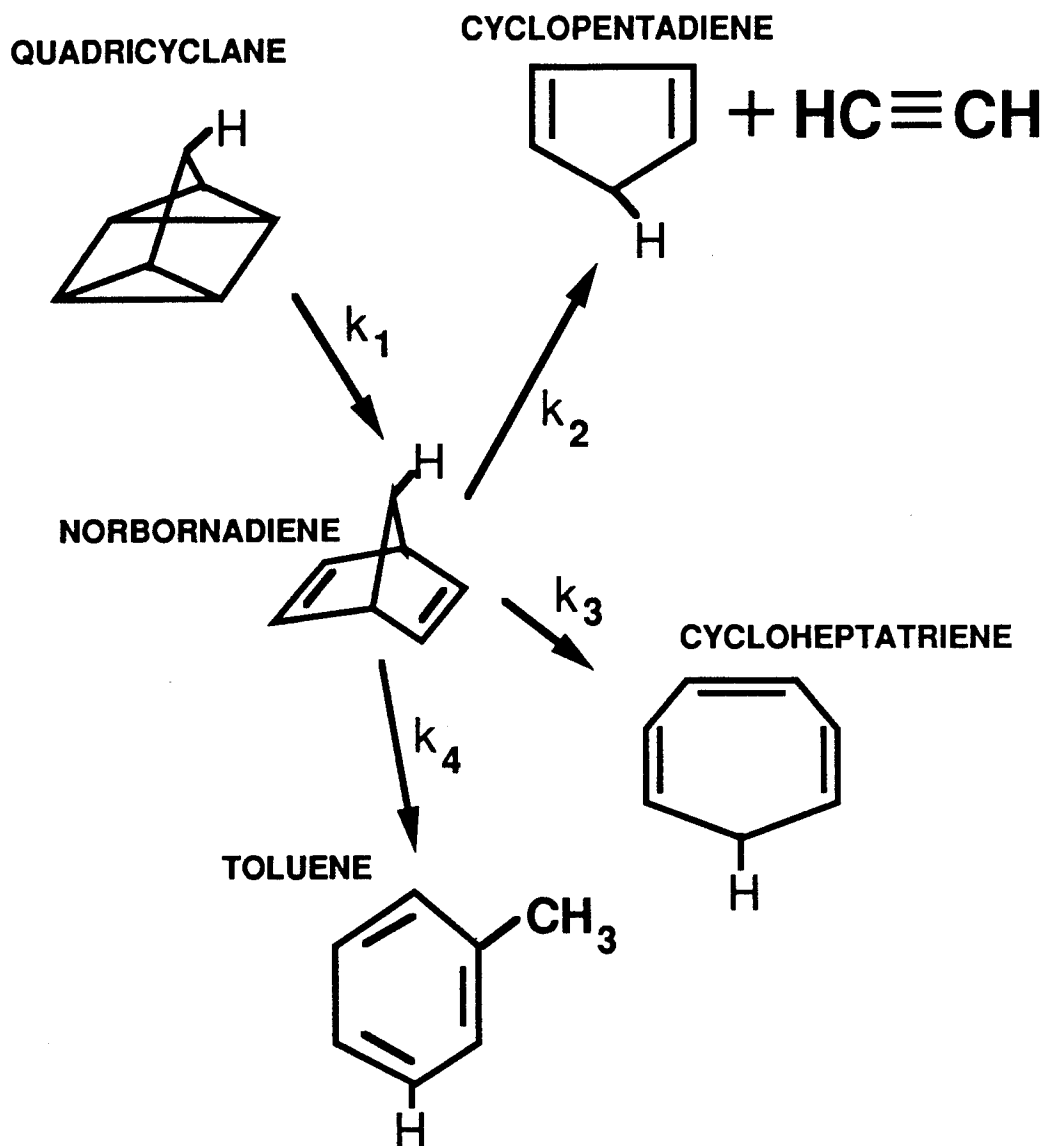


FIGURE 2

# QUADRICYCLANE DECOMPOSITION MECHANISM



$$k_1 = 7.4 \times 10^{14} e^{-\frac{37.8}{RT}} \quad T=484-544K$$

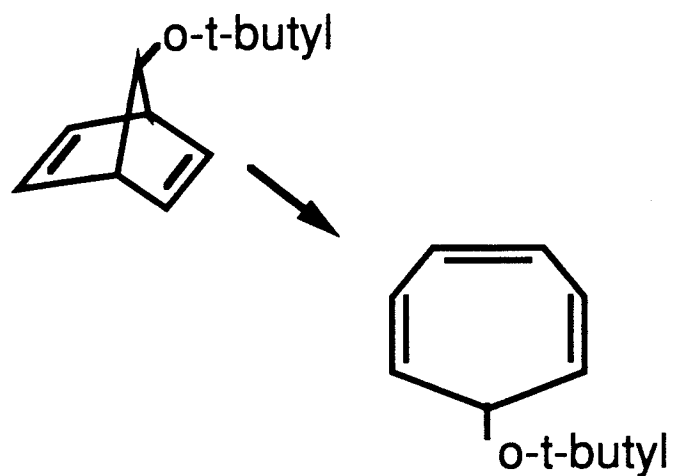
$$k_2 = 9.3 \times 10^{14} e^{-\frac{51.2}{RT}} \quad T=641-715K$$

$$k_3 = 9.6 \times 10^{13} e^{-\frac{47.9}{RT}} \quad T=641-715K$$

$$k_4 = 2.3 \times 10^{13} e^{-\frac{49.6}{RT}} \quad T=641-715K$$

FIGURE 3

# THERMAL DECOMPOSITION MECHANISM FOR 7-t-BUTOXYNORBORNADIENE



T=513-543K

FIGURE 4



## Spectroscopy of Atom-Dihydrogen van der Waals Complexes

James M. Spotts, Matthew S. Johnson, Gary T. Olsen, and Mitchio Okumura

*Arthur Amos Noyes Laboratory of Chemical Physics  
California Institute of Technology  
Pasadena, CA 91125*

The introduction of light atoms such as boron and lithium into a solid hydrogen matrix can in principle lead to a significant improvement in the  $I_{sp}$  of hydrogen as a propellant.<sup>1</sup> Li atoms have already been observed in matrix isolation studies in Ne,<sup>2</sup> and progress has been reported on trapping B and Al in H<sub>2</sub>.<sup>1</sup> In order to model the behavior of these atoms within the matrix, the intermolecular forces between the atoms and molecular hydrogen must be accurately determined. Because these are van der Waals interactions, pair potentials can reasonably be used to model condensed phase behavior. The small number of electrons within these systems has permitted *ab initio* CI calculations of the potential energy surfaces to be performed for both the Li·H<sub>2</sub> and B·H<sub>2</sub> complexes.<sup>3,4</sup> The calculated spherical part of the Li·H<sub>2</sub> potential has been used in recent simulations to investigate the behavior of lithium atom in clusters and bulk hydrogen, as well as trapping sites in *para*-hydrogen and *ortho*-deuterium.<sup>5,6</sup> Spectroscopic studies of the Li·H<sub>2</sub> and B·H<sub>2</sub> complexes as well as their higher cluster analogues will provide critical experimental tests of these calculated potentials.

We have completed an apparatus and are presently perfecting an atom source to investigate these weakly bound van der Waals complexes using a number of spectroscopic techniques, including laser-induced fluorescence, dispersed emission, multiphoton ionization, and infrared spectroscopy. The Li·H<sub>2</sub> and B·H<sub>2</sub> clusters present a number of experimental challenges, both in their formation and in their spectroscopic detection.

**Li·H<sub>2</sub> Complexes.** The dimer of atomic lithium and dihydrogen has been calculated to have a shallow, fairly isotropic well with a depth of 10-20 cm<sup>-1</sup> that varies with Jacobi angle and H<sub>2</sub> bond length.<sup>3</sup> The ground state potential is in many ways analogous to the previous experimental<sup>7</sup> and theoretical<sup>8</sup> studies of rare gas-dihydrogen complexes in which the H<sub>2</sub> behaves as a near free rotor. The spherical component of the potential calculated

by Konowalow<sup>3</sup> supports only one bound vibrational state which we estimate has a dissociation energy of energy  $D_0 \approx 4 \text{ cm}^{-1}$ . This energy is comparable to the binding energy of the hydrogen dimer  $(\text{H}_2)_2$  of  $2.3 \text{ cm}^{-1}$ . In contrast, the B-Ar system, which has been observed by Hwang *et al.*<sup>9</sup>, has been calculated to have a dissociation energy of  $D_0 = 75 \text{ cm}^{-1}$ .

We are nearing completion of a cryogenically cooled laser vaporization source for  $\text{Li} \cdot \text{H}_2$ . Our experience has shown that hydrogen dimers and larger clusters are readily formed when the stagnation temperature is below 100 K. The piezo-actuated pulsed gas valve and laser vaporization assembly is shown in Figure 1. Since the piezo element must operate at  $T > 273 \text{ K}$ , the poppet is extended over 3 in. to thermally isolate the liquid nitrogen cooled seal from the actuating element, a design based on that of Continetti and Lee.<sup>10</sup> This allows the gas behind the seal to equilibrate to a temperature near 80 K. This design also ensures that no impurities, especially water, expand with the gas and react with vaporized metal. The cooling serves a second purpose of enhancing the

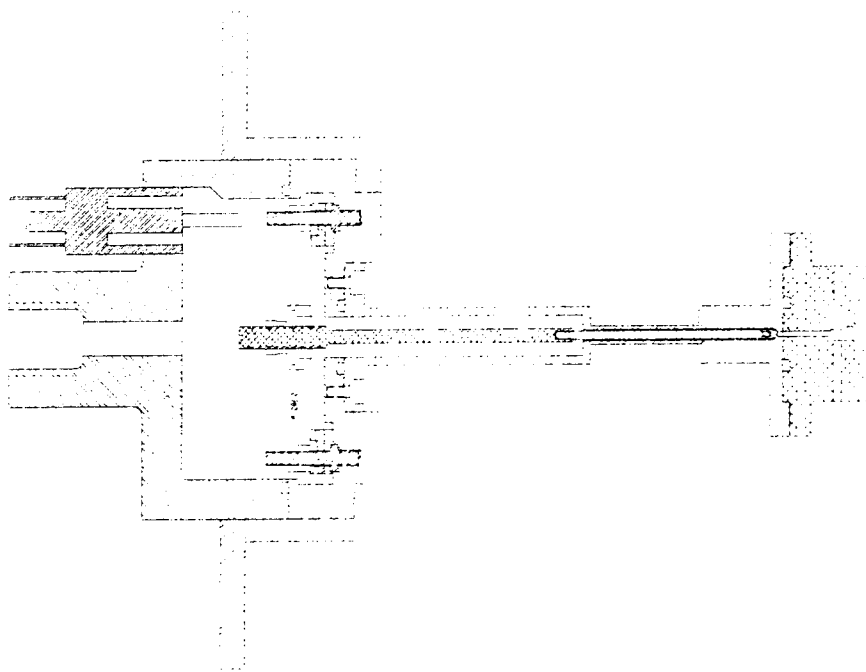


Figure 1. Assembly drawing of piezo-driven, cryogenically cooled pulsed valve and laser vaporization source.

mechanical stiffness of soft metals such as lithium when used as a rotatable laser vaporization target rod.

Excitation of the Li  $2s \rightarrow 2p$  transition leads to three states, one of which is weakly bound and essentially repulsive, and two that possess minima with  $C_{2v}$  symmetry. Konowalow's potentials indicate that, due to the large change in the intermolecular bond distance  $R$ , the transitions with the largest Franck-Condon factors will be to the highest  $v$  levels near the top of the potential. These transitions will occur at 671 to 687 nm. In this region, we expect transitions to both of the more strongly bound levels, with their vibronic bands interleaved. Although the potentials are strongly anisotropic, at the large intermolecular distances at the outer turning points of the excited state wells, the anisotropy should be quite weak. This suggests that in the Franck-Condon region, the molecule may behave similarly to a rare gas-dihydrogen complex.

**B-H<sub>2</sub> Complexes.** Alexander<sup>4</sup> has calculated that the adiabatic potential for parahydrogen bound to ground state atomic boron, when averaged over the  $j=0$  rotational wavefunction, has a zero-point corrected dissociation energy of  $D_0 = 25 \text{ cm}^{-1}$ . While this system should be formed more readily than Li-H<sub>2</sub>, the first excited state of boron, the  $3s^2S$  state, lies at 249.8 nm, well above the limit to form BH + H. Yang and Dagdigian<sup>11</sup> have already observed BH chemiluminescence upon excitation of B atoms to the  $4p^2P$  state in the presence of H<sub>2</sub>. In order to explore alternate methods for observing the spectra of B-H<sub>2</sub> complexes, we have considered the possibility of detecting vibrational transitions of the H<sub>2</sub> moiety.

The vibrational transition moment arises from the dipole moment induced by intermolecular interactions. As Dunker and Gordon have shown for rare gas atom-dihydrogen clusters, there are three terms responsible: one quadrupole induction term, and two overlap induction terms. Unlike rare gases (or lithium), the B atom should possess a quadrupole moment. Thus, there will be two quadrupole induction contributions, one from the quadrupole on the boron atom interacting with the H<sub>2</sub> polarizability, and one from the H<sub>2</sub> interacting with the B atom polarizability. Both will contribute to a vibrational transition moment. Since the B atom is open shell, it is somewhat more polarizable than a rare gas atom, and we estimate the two contributions

to be

$$\frac{Q_B \langle 1|\alpha_{H_2}|0\rangle}{R^4} \approx 15ea_0^2 \cdot 1a_0^3 \cdot \frac{1}{(6.4a_0)^4} = 0.011ea_0 = 0.022D$$

$$\frac{\langle 1|Q_{H_2}|0\rangle \alpha_B}{R^4} \approx 1ea_0^2 \cdot 6.9a_0^3 \cdot \frac{1}{(6.4a_0)^4} = 0.004ea_0 = 0.01D$$

These dipole moments, while considerably larger than the rare gas-dihydrogen moments, are still quite small. Such transitions, however, can be pumped with the pulsed optical parametric oscillator available in our laboratory ( $\approx 5$  mJ/pulse). *If the  $BH_2$  state does not predissociate during the pulse width of the laser (6 ns)*, then an IR-UV photoionization experiment would yield detectable signals, with the added advantage of mass selection. In any event, the magnitude of these transition moments also suggest that nearest neighbor  $H_2$  molecules adjacent to an impurity B atom should be readily detectable in infrared experiments on B atoms doped in solid hydrogen.

### References

1. Proceedings of the HEDM Contractor's Meeting, T.L. Thompson Ed., Woods Hole, MA, 1993; P. G. Carrick, Specific Impulse Calculations of High Energy Density Solid Crogenic Rocket Propellants in Solid  $H_2$ , Phillips Laboratory, Edwards AFB, Report PL-TR-93-3014.
2. M. Fajardo, J. Chem. Phys. **98**, 110 (1993); *ibid.* 119.
3. D. Konowalow, unpublished.
4. M. Alexander, J. Chem. Phys. **99**, 6014 (1993).
5. D. Scharf, G. J. Martyna, and M. L. Klein, J. Chem. Phys. **99**, 8997 (1993).
6. D. Scharf, G. J. Martyna, D. Li, G. A. Voth, and M. L. Klein, J. Chem. Phys. **99**, 9013 (1993).
7. A. R. W. McKellar, Faraday Disc. Chem. Soc., **73**, 89 (1982), and references therein.
8. R. J. LeRoy and J. M. Hutson, J. Chem. Phys. **86**, 837 (1987).
9. E. Hwang, Y. L. Huang, P. Dagdigan, and M. H. Alexander, J. Chem. Phys. **98**, 1 (1993).
10. R. E. Continetti, Ph.D. thesis, University of California, Berkeley, CA, 1990.
11. X. Yang and P. J. Dagdigan, Chem. Phys. Lett. **200**, 217 (1992).